

Theoretical Biology

Naoki Masuda
Petter Holme *Editors*

Temporal Network Epidemiology

 Springer

Theoretical Biology

Series editor

Yoh Iwasa, Faculty of Science, Kyushu University, Fukuoka, Japan

The “Theoretical Biology” series publishes volumes on all aspects of life sciences research for which a mathematical or computational approach can offer the appropriate methods to deepen our knowledge and insight.

Topics covered include: cell and molecular biology, genetics, developmental biology, evolutionary biology, behavior sciences, species diversity, population ecology, chronobiology, bioinformatics, immunology, neuroscience, agricultural science, and medicine.

The main focus of the series is on the biological phenomena whereas mathematics or informatics contribute the adequate tools. Target audience is researchers and graduate students in biology and other related areas who are interested in using mathematical techniques or computer simulations to understand biological processes and mathematicians who want to learn what are the questions biologists like to know using diverse mathematical tools.

More information about this series at <http://www.springer.com/series/15703>

Naoki Masuda • Petter Holme
Editors

Temporal Network Epidemiology

 Springer

Editors

Naoki Masuda
Department of Engineering Mathematics
University of Bristol
Bristol, UK

Petter Holme
Institute of Innovative Research
Tokyo Institute of Technology
Yokohama, Japan

ISSN 2522-0438

Theoretical Biology

ISBN 978-981-10-5286-6

DOI 10.1007/978-981-10-5287-3

ISSN 2522-0446 (electronic)

ISBN 978-981-10-5287-3 (eBook)

Library of Congress Control Number: 2017952199

© Springer Nature Singapore Pte Ltd. 2017

This work is subject to copyright. All rights are reserved by the Publisher, whether the whole or part of the material is concerned, specifically the rights of translation, reprinting, reuse of illustrations, recitation, broadcasting, reproduction on microfilms or in any other physical way, and transmission or information storage and retrieval, electronic adaptation, computer software, or by similar or dissimilar methodology now known or hereafter developed.

The use of general descriptive names, registered names, trademarks, service marks, etc. in this publication does not imply, even in the absence of a specific statement, that such names are exempt from the relevant protective laws and regulations and therefore free for general use.

The publisher, the authors and the editors are safe to assume that the advice and information in this book are believed to be true and accurate at the date of publication. Neither the publisher nor the authors or the editors give a warranty, express or implied, with respect to the material contained herein or for any errors or omissions that may have been made. The publisher remains neutral with regard to jurisdictional claims in published maps and institutional affiliations.

Printed on acid-free paper

This Springer imprint is published by Springer Nature

The registered company is Springer Nature Singapore Pte Ltd.

The registered company address is: 152 Beach Road, #21-01/04 Gateway East, Singapore 189721, Singapore

Contents

1	Introduction to Temporal Network Epidemiology	1
	Naoki Masuda and Petter Holme	
2	How Behaviour and the Environment Influence Transmission in Mobile Groups	17
	Thomas E. Gorochowski and Thomas O. Richardson	
3	Sensitivity to Temporal and Topological Misinformation in Predictions of Epidemic Outbreaks	43
	Petter Holme and Luis E.C. Rocha	
4	Measuring Propagation with Temporal Webs	57
	Aaron Bramson, Kevin Hoefman, Milan van den Heuvel, Benjamin Vandermarliere, and Koen Schoors	
5	Mean Field at Distance One	105
	Ka Yin Leung, Mirjam Kretzschmar, and Odo Diekmann	
6	Towards Identifying and Predicting Spatial Epidemics on Complex Meta-population Networks	129
	Xiang Li, Jian-Bo Wang, and Cong Li	
7	Epidemic Threshold in Temporally-Switching Networks	161
	Leo Speidel, Konstantin Klemm, Víctor M. Eguíluz, and Naoki Masuda	
8	Control Strategies of Contagion Processes in Time-Varying Networks	179
	Márton Karsai and Nicola Perra	
9	Leveraging Topological and Temporal Structure of Hospital Referral Networks for Epidemic Control	199
	Vitaly Belik, André Karch, Philipp Hövel, and Rafael Mikolajczyk	

10	Surveillance for Outbreak Detection in Livestock-Trade Networks ..	215
	Frederik Schirdewahn, Vittoria Colizza, Hartmut H. K. Lentz, Andreas Koher, Vitaly Belik, and Philipp Hövel	
11	Optimal Containment of Epidemics in Temporal and Adaptive Networks	241
	Masaki Ogura and Victor M. Preciado	
12	Mapping Out Emerging Network Structures in Dynamic Network Models Coupled with Epidemics	267
	István Z. Kiss, Luc Berthouze, Joel C. Miller, and Péter L. Simon	
13	Disease Spreading in Time-Evolving Networked Communities	291
	Jorge M. Pacheco, Sven Van Segbroeck, and Francisco C. Santos	
14	Toward a Realistic Modeling of Epidemic Spreading with Activity Driven Networks	317
	Alessandro Rizzo and Maurizio Porfiri	

Chapter 1

Introduction to Temporal Network Epidemiology

Naoki Masuda and Petter Holme

Abstract In this introductory chapter, we start by briefly summarising temporal and adaptive networks, and epidemic process models frequently used in this volume. Then, we introduce a couple of what we think are key studies in the field, which are fundamental for various chapters in this volume. Finally, we give an overview of each chapter and discuss future work.

1.1 Introduction

Epidemic processes are one of the most studied type of dynamics on networks for at least two reasons. First, pandemic occurs on both global and local scales in every part of the world and very frequently. Some infectious diseases are fatal. Even if not, infectious diseases are health burdens to infected individuals, and societal economic burdens to their families and the whole society. Therefore, understanding them and devising efficient intervention methods are of a paramount importance to the whole society. Furthermore, computer viruses and viral information spread in a similar fashion (but with some notable differences) to biological contagions. Networks of individuals that specify who is connected to whom are a significant determinant of how epidemic processes behave. Second, relatively simple dynamics models of epidemic processes tell us how infection spreads in a population, often at a realistic level, in terms of quantities such as the epidemic threshold, the fraction of infected individuals in the equilibrium or at the final stage of spreading, and speed of spreading. The development of network epidemiology and perhaps the whole of mathematical epidemiology may have been very different if basic epidemic process models were already too complicated to accommodate mathematical analysis or they were analytically tractable but too far away from the reality.

N. Masuda (✉)

Department of Engineering Mathematics, University of Bristol, Merchant Venturers Building,
Woodland Road, BS8 1UB, Clifton, Bristol, UK
e-mail: naoki.masuda@bristol.ac.uk

P. Holme

Institute of Innovative Research, Tokyo Institute of Technology, Yokohama, Japan
e-mail: holme@cns.pi.titech.ac.jp

The present volume is a collection of recent developments on network epidemiology when networks are themselves dynamic in nature. Such temporal or adaptive networks (distinctions between them are given in Sect. 1.2.2) are not just for theoretical curiosity. Most empirical networks to which epidemic processes are relevant *are* dynamic, and dynamics of networks probably make epidemic dynamics different from the same epidemic dynamics occurring on static networks. Seminal work on epidemic dynamics in temporally varying populations already appeared in 1980s and early 1990s [5, 35], which can be regarded as precursors of the field of research presented in this volume. One can also argue that the concept of *concurrency*—that was developed in the 1990s in the context of HIV epidemiology—has a temporal component [19]. It emphasizes the number of other persons that, at a given point in time, a person had sex with before and will have sex with again. More research on temporal and adaptive networks is ongoing, supported by an increasing amount of temporally varying network data and developments of new theory, algorithms, measurements and concepts.

In the present introductory chapter, we start by explaining basics of temporal and adaptive networks and epidemic process models. Then, we discuss some key studies in the field, briefly summarise what each chapter is about, and conclude by discussing some future directions.

1.2 Preliminaries

1.2.1 Temporal Networks

Contact networks between individual humans and animals as well as many other networks are dynamic in nature. Static networks, which are studied in a majority of empirical and theoretical/computational work, including work on epidemics, neglect temporal variations of the contacts (links or edges in network terminology). Temporal networks or time-varying networks are a modelling and data analysis framework where we explicitly take into account the time of contacts. There are comprehensive reviews [12, 14], a volume collecting recent advancements [15], a monograph on mathematical and computational tools [22], and reviews focussing on epidemics [1, 21] on temporal networks.

There are different representations of temporal network data [12]. A major one of which is a list of events, where each event is specified by the two nodes that form an event, an event time, and additionally the duration of the event if the information is available. It should be noted that events and edges are now distinguished, because an edge formed between a given pair of nodes generally has multiple events at different times. In a static network representation, we simply count the number of events and use it as the weight of the edge. In a temporal network representation, we are usually interested in specific time of the events so we do not aggregate the events on an edge into the edge weight.

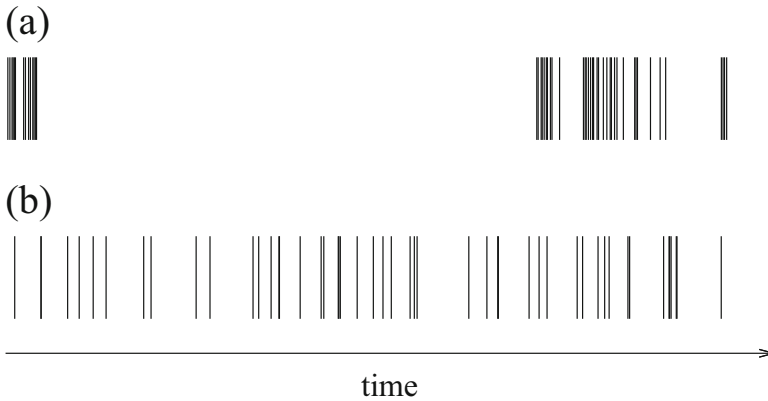


Fig. 1.1 (a) Bursty and (b) non-bursty event sequences with the same number of events, $n = 30$

Temporal information contained in network data may change dynamics of epidemic processes and designs of efficient intervention methods that have predominantly been based on models and data of static networks. Although there are plenty of factors of temporal networks that would affect epidemic dynamics on networks, here we explain a few of them. See [12, 14, 22] for more.

First, inter-event times (i.e., interval between consecutive contacts between a given pair of nodes, i.e., individuals, or that between consecutive contact events for a given node) are quite often heterogeneously distributed. Empirical distributions of inter-event times are typically long-tailed (Fig. 1.1a). Then, there are some bursts of events with short inter-event times, and some inter-event times are very large. In contrast, epidemic process models on static networks (Sect. 1.2.3) implicitly assume that events on each edge occur as a Poisson process. This assumption is equivalent to inter-event times obeying an exponential distribution, lacking bursts and very long inter-event times (Fig. 1.1b). In addition, if data are recorded across different days, events tends to be more frequent during the daytime than the night. Similarly, the frequency of events is typically different between weekdays and weekends. Second, the duration of contacts can also be long-tailed, even between the same pair of nodes. Third, events on different edges are often correlated. For example, suppose that nodes v_1 and v_2 meet at a certain point of time. Then, it may be more likely that v_2 contacts a specific node v_3 rather than v_4 within a short time, as compared to the expectation from the static network ignoring temporal information. Fourth, nodes and edges may enter or leave the network during the observation period. For example, an individual may register to an online networking service that we are monitoring, in the middle of the recording period. As another example, an edge between two workmates may be lost permanently in the middle of recording because one of the two individuals has changed the job.

1.2.2 Adaptive Networks

Adaptive networks are also a family of networks where edges or their weights vary over time. A common classification is that, in contrast to temporal networks, dynamics of edges in adaptive networks are assumed to be influenced by dynamics occurring on networks such as epidemic processes [7, 9, 28]. For example, if an infected person has noticed that he/she is unwell and has decided to stay home, then edges connected to this infected individual are temporarily deactivated, changing the structure of the network. In temporal network frameworks, we usually assume that network dynamics are given exogenously, by a time series of events given by a data set or produced by a generative model.

Considering adaptive networks is important for better understanding epidemics for at least two reasons. First, people may proactively adapt their edges according to their status (e.g., upon contracting an infection) and other input (e.g., news). Such proactive behavioural changes may considerably change the extent of epidemic spreading. Second, intervention strategies, which can depend on the history of epidemic dynamics and network dynamics up to the current time point, may induce changes in the network structure thereafter (e.g., specific individuals quarantined by an authority for a certain period of time). These adaptive changes in social networks caused by intentional or unintentional behaviour of individuals, or by interventions implemented at an institution level, are collectively called social distancing [6, 18, 25].

1.2.3 Basic Epidemic Process Models

In contemporary temporal and adaptive network epidemiology (as well as static network cases), we have been primarily studying stochastic variants of the following three so-called compartmental models of epidemic processes [10], e.g., the susceptible-infected-susceptible (SIS) model, the susceptible-infected-recovered (SIR) model and the susceptible-infected (SI) model. The rules of the three models are schematically summarised in Fig. 1.2. Most of the chapters in this volume also use some of the three models.

The SIS model assumes two states: susceptible (i.e., healthy) and infected, for each node. When a susceptible node interacts with an infected node, the susceptible node changes its state from susceptible to infected at rate β . In a discrete-time representation, the probability that a susceptible node gets infected in time $\Delta t (\ll 1)$ is equal to $\beta \Delta t$. If a susceptible node is adjacent to k infected neighbours, the transition rate is equal to $k\beta$ (Fig. 1.2b). An infected node recovers at rate μ irrespectively of the neighbours' states, and then enters the susceptible state. Therefore, a node may be reinfected in the SIS model.

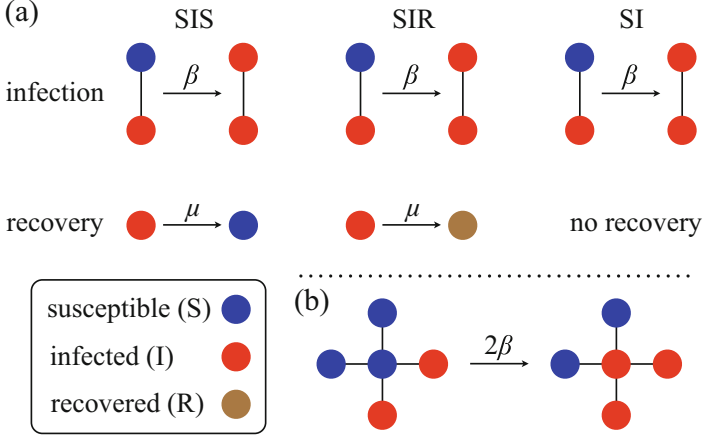


Fig. 1.2 (a) Infection and recovery rates in three epidemic process models. (b) Infection rate when a susceptible node is surrounded by two susceptible nodes and two infected nodes

In a sufficiently large well-mixed population (i.e., no network structure), where each node is adjacent to each other with a normalised weight $1/N$, the deterministic SIS dynamics are given by

$$\frac{dI(t)}{dt} = \beta S(t)I(t) - \mu I(t), \quad (1.1)$$

where $I(t)$ is the fraction of infected individuals at time t , and $S(t) = 1 - I(t)$ is the fraction of susceptible individuals at time t . By setting $dI(t)/dt = 0$, we obtain the fraction of infected individuals in the equilibrium, I^* , as follows:

$$I^*(\beta S^* - \mu) = 0, \quad (1.2)$$

where $S^* = 1 - I^*$, which leads to

$$I^* = 1 - \frac{\mu}{\beta} \quad (1.3)$$

or $I^* = 0$. We obtain $I^* > 0$ if and only if

$$\frac{\beta}{\mu} > 1. \quad (1.4)$$

Therefore, the epidemic threshold in terms of β/μ is equal to unity in the well-mixed population. If the infection rate β is larger than the recovery rate μ , the infection can stay in the population. Otherwise, it will die out after a transient.

The epidemic threshold depends on the network structure. A central result for static networks is that in uncorrelated random networks with a general degree distribution, the epidemic threshold is equal to $\langle k \rangle / \langle k^2 \rangle$, where $\langle \cdot \rangle$ denotes the mean and k is the degree [23, 24]. For scale-free networks (i.e., with a power-law degree distribution), the epidemic threshold can be very small (theoretically can be zero) because $\langle k^2 \rangle$ can be much larger than $\langle k \rangle$. Therefore, infection is likely to persist in scale-free networks as compared to well-mixed populations.

The SIR model assumes three states, i.e., susceptible, infected and recovered. The only difference to the SIS model is that when an infected node recovers at rate μ , it enters the recovered state, not going back to the susceptible state. A recovered node will not infect others or will not be reinfected. The recovered state can also be interpreted as the dead state because a dead node would not infect others or be infected. Different from the SIS model, the infected state gets extinct in the end in the SIR dynamics. The final population always consists of susceptible and recovered nodes, but not infected nodes. We typically start the SIR model from a single infected node or a small fraction of infected nodes, and all the other nodes are initially in the susceptible state. Main interests for the SIR model are the final size, i.e., the number of recovered individuals (who have undergone infection) when the dynamics have terminated, and the speed at which infection spreads in the network.

A primary concern of the SIS model is the equilibrium. In contrast, SIR model is suitable for describing transient contagion dynamics of a population triggered by an initial set of infected individuals. Because such one-shot epidemic dynamics are relevant to many real phenomena, including outbreaks of various emerging infectious diseases and viral spreading in online media, the SIR model and its variants are probably more frequently used than the SIS model unless births and deaths of individuals are relevant on the simulated time scale.

The deterministic SIR dynamics for an infinitely large well-mixed population are described by

$$\frac{dI(t)}{dt} = \lambda I(t)S(t) - \mu I(t), \quad (1.5)$$

$$\frac{dR(t)}{dt} = \mu I(t), \quad (1.6)$$

where $R(t)$ is the fraction of recovered individuals and $S(t) = 1 - I(t) - R(t)$. If and only if $dI(t)/dt > 0$ at $t = 0$, the number of infectious individuals increases to a macroscopic (i.e., $O(N)$) number before they recover. Therefore, the epidemic threshold is given by $dI(t)/dt|_{t=0} = 0$, resulting in the same epidemic threshold as that for the SIS model (Eq. (1.4)). For uncorrelated random heterogeneous networks, the epidemic threshold in terms of β/μ is equal to $\langle k \rangle / (\langle k^2 \rangle - \langle k \rangle)$ [23, 24], which is similar to the case of the SIS model if the degree is sufficiently heterogeneous (i.e., $\langle k^2 \rangle \gg \langle k \rangle$).

The SI model is a simplified version of the SIR model and assumes two states, i.e., susceptible and infected states, for each node. Infection occurs in the same manner as in the SIS and SIR models. Different from the SIS and SIR models, an

infected node never recovers in the SI model. Therefore, if dynamics start from a single infected node in a connected static network, all nodes will be infected in the end. Therefore, the final size is not a relevant question for the SI model unless the time horizon is relatively short (as determined by the length of a temporal network data set) or a network is composed of multiple connected components. It should be noted that a finite observation period is typical in temporal network data, such that the final size is often a relevant question to the SI model on temporal networks. Likewise, the epidemic threshold is also an irrelevant issue for the SI model. Instead, we are interested in the speed at which infection propagates. The dynamics in the well-mixed population are described by

$$\frac{dI(t)}{dt} = \lambda S(t)I(t). \quad (1.7)$$

The SI model is unrealistic in many scenarios. However, we often employ it in studies of epidemic processes in temporal networks. This is probably because temporal network data are already complicated objects so we want to simplify the epidemic process model to gain better insight into epidemic dynamics on temporal networks. If we start the SIR dynamics from a small number of infected individuals, we obtain $S(t) \approx 1$ and $I(t), R(t) \approx 0$ in an early stage of dynamics. Then, Eq. (1.5) coincides with Eq. (1.7). Therefore, the dynamics of the SI model approximates that of the SIR model in an early stage. This feature of the SI model was exploited to derive the speed of spreading of infection in an early stage of dynamics in the SIR as well as SI model on static scale-free networks [3].

As already touched upon, these and other epidemic processes have been studied on various networks. A majority of books and reviews on network science devote much text to epidemic processes because they are one of the most studied type of dynamics for networks. Influential books and reviews extensively discussing (static) network epidemiology include [2, 17, 24].

1.3 Computational Considerations

In addition to solving compartmental models analytically one can simulate them. It is fairly straightforward, but there are some technicalities worth mentioning. First, as an alternative to the constant recovery rate introduced above, many computational studies use a fixed period of infection, mostly because it allows some program simplifications and speed-up [11]. From an epidemiological point of view, these are both rather large simplifications. A constant recovery rate assumes an exponential distribution of disease durations, which is not much closer to reality than a constant duration [20]. On the other hand, one can expect other aspects of epidemic simulations to have a larger impact.

Another technicality worth pointing out is that the seed of the outbreak should be only one node at one time. There are two reasons for this. First, real epidemic outbreaks are thought to start from only one person. For example, the handful known

strains of HIV are thought to have originated from each occasion the simian immunodeficiency virus infected a human and started spreading in the population [29]. Since the compartmental models above assume a closed population, it follows that it would be misleading to have more than one seed (except some special scenarios e.g. bioterrorism). The early period can also provide great insights. Essentially any early outbreak has two possible fates—either it dies out immediately, or it spreads to a substantial part of the population. In the real world, we cannot study the first case directly—so that is one motivation for not leaving the initial phase out. Furthermore, the early phase is heavily dependent on the number of infection seeds.

For temporal networks, one also needs to choose a time of the first infection. The most principled way would be to pick a time at random between the beginning and the end of the sampling time. This would lead to many outbreaks not spreading beyond the seed—if the seed infection time is late, then it might not be involved in many more contacts. This also means that the possible duration of the infections will vary much. One can argue that this would be the case if one studies a limited time of a real system. However, for some types of epidemiological questions this could be a problem, leading to biased statistics. Then, some authors have studied infection seeds in the beginning of the sampling time of the temporal networks (e.g. Ref. [26]) or at the moment the seed node enters the data (e.g. Ref. [13]). Qualitative results, like the existence of an epidemic phase, should be independent of such choices, but quantitative results are not, which is important to keep in mind.

Finally, we note that there are many ways of speeding up epidemiological simulations. For temporal networks the disease can spread over a contact only once. This means that one can prune the temporal network—delete a random fraction $1 - \lambda$ contacts that would not spread the disease—and then simulate the SIR or SI dynamics with infection probability one on these pruned data sets. The simulated outbreaks of one pruned network is then exceptionally fast, meaning that one can allow averages over many simulations per pruned network, and the averages over prunings will be the computational bottleneck. For temporal network models one can perform very fast exact simulations by the temporal Gillespie algorithm of Vestergaard and Génois [32]. If one allows some approximations, another approach is the individual-based approximation [27, 31]. When we consider the SIS dynamics on a temporal network data set, we have to assume periodic boundary conditions in time or random sampling of events. This is because the endemicity is the concern of the SIS model and therefore we have to generate infinitely long temporal networks to use the SIS model.

1.4 A Few Key Papers in Temporal and Adaptive Network Epidemiology

This book introduces recent key advances in temporal and adaptive network epidemiology, from theoretical, computational and data-analysis perspectives. In this section, we briefly explain just a few papers that we think are key theoretical

and computational papers in the field, which underlie many of the chapters in this volume directly and indirectly. Our choice is necessarily biased (but not in favour of our own work), and we are aware that there are many more important and interesting papers than can be presented here.

Karsai et al. numerically investigated how temporal nature of empirical contact data affects the speed of epidemic spreading using the SI model [16]. They shuffled time stamps of contact events on edges according to various rules to create artificial temporal networks and compared the speed at which infection spreads on an original temporal network and on synthesised temporal networks created by the shuffling. For example, if one randomly shuffles inter-event times on each edge, temporal correlation on each edge and across different edges is lost, whereas the distribution of inter-event times is preserved. If one redraws the event times on each edge from a Poisson process such that the (mean) number of events agrees between the original and synthesised temporal networks, the distribution of inter-event times in addition to temporal correlation is destroyed, whereas the structure of the network as static network is still conserved. A main finding in the article is that bursty activity patterns of humans present in empirical temporal network data slow down epidemic spreading. Now, various types of randomisation (shuffling and other ways of randomisation) of events and edges (and other quantities) are a popularly used tool for examining factors of temporal networks that contribute to epidemic and other dynamics [12, 14].

Volz and Meyers proposed a so-called neighbour exchange model of network dynamics combined with epidemic spreading [33]. Network dynamics are modelled by edge swapping involving two pairs of connected dyads (hence four nodes in total). In other words, an arbitrary pair of edges (v_1, v_2) and (v_3, v_4) is replaced by two new edges (v_1, v_3) and (v_2, v_4) at a fixed rate. The network is assumed to be undirected and unweighted. Link swapping does not alter the degree of any node. Therefore, this model allows us to examine the effect of network dynamics (i.e., temporal network, because edge swapping occurs independently of epidemic dynamics), here modelled as edge swapping, on the final size and other quantities, with the aggregate network (i.e., time average of the network) fixed. Using generation function formalisms, the authors semi-analytically examined the dynamics of the SIR model on the neighbour exchange model. They developed an accurate approximation to the epidemic dynamics by a set of ODEs with a small number of variables, which were solved numerically. Their approximation is a type of pair approximation, which has been widely used for analysing epidemic processes on networks [24] and beyond. They showed that edge swapping, i.e., temporality of networks, suppresses epidemic spreading. For further theoretical approaches to the model, see [34]. For an analysis of a simplified case, see [22].

Gross et al. studied SIS epidemic dynamics on a model of adaptive networks, where susceptible nodes actively avoid to be adjacent to infected nodes, a type of social distancing [8]. On top of the behavioural rules defining the SIS model, they assumed that each edge having a susceptible node on one end and an infected node on the other end is severed by the susceptible node at a constant rate (or probability). Then, the susceptible node reconnects to another susceptible node

selected uniformly at random, dynamically changing the network structure. They found that the epidemic threshold increases as the rewiring rate increases. In other words, rewiring behaviour of susceptible individuals suppresses epidemics, which is intuitive. Susceptible nodes tend to be connected to susceptible nodes and infected nodes to other infected nodes as time goes by. The mean degree is larger for susceptible than for infected nodes. They also developed a pair approximation to analytically determine the bifurcation diagram, revealing oscillations, hysteresis (implying bistability), and first-order phase transitions among other things.

1.5 What This Book Is About

The present book is a collection of recent advancements in temporal and adaptive network epidemiology, focussing on theoretical, computational, modelling, and data-analytic approaches. The organisation of the volume is as follows.

The following seven chapters discuss theoretical and computational aspects of epidemic processes on temporal networks.

In Chap. 2, Gorochowski and Richardson proposed an agent-based simulation model on a two-dimensional arena to investigate effects of indirect pathways of disease spreading. The indirect pathway means that an infected individual leaves a trail that acts like a “pheromone”, such as a pathogen whose infectiousness decays exponentially in time once it is placed. Then, if a susceptible individual visits the same site within a relatively short time, the individual may contract infection owing to the remaining pathogen. Because a trail is disposed randomly according to the assumed random movement of each agent and the infectiousness of a deposited pathogen decays over time, agents are effectively connected as a temporal network. Even if such indirect pathways are absent, a system of randomly walking agents creates a temporal network, where infection is transmitted from agent to agent when the two agents are physically close to each other (direct pathway). The authors found that the effects of indirect pathways in addition to direct ones were massive.

In Chap. 3, Holme and Rocha analysed effects of imperfect information about temporal networks on the behaviour of the SIR model. This is a practical concern because it is probably a norm rather than exception that one cannot collect some information about social networks that underly epidemic processes. In temporal networks, the information that one can gain may be imperfect in terms of temporal properties of the network as well as static properties of the network. If results of running epidemic processes, either numerically or theoretically, are highly sensitive to such perturbation, we have to be cautious in interpreting the obtained results because the results may drastically change if we gain a little bit more information about temporal networks. The authors explored the effects of lacking some temporal and structural information about networks on SIR dynamics by numerical means.

In Chap. 4, Bramson et al. proposed a framework to analyse temporal network data, called temporal webs. The idea is to consider a network in which a directed edge is placed from node v_1 at time t to node v_2 at time $t + 1$ to represent a causal

relationship. A node in this representation does not necessarily correspond to a node in the original network data, such as an individual human/animal. In this way, a temporal network data is transformed to a directed acyclic graph, or frankly a feed-forward network, where the direction of the entire network is shaped by the arrow of time. This framework is useful in representing chains of causal events including spread of infectious diseases (as in the SI and SIR models). For example, the out-component of node v at time t in the temporal web tells us how many nodes can be infected by v and when. They applied the methods to alliance networks in an online game, interbank loan network data, and Twitter social networks, in each of which propagation of “infection”, such as frustration, bankruptcy, and mood is a salient question.

In Chap. 5, Leung et al. analytically studied continuous-time dynamics of temporal networks in which nodes form and dissolve pairs at given rates. Each node is assumed to have binding sites, or stubs, which the node can use to connect to other nodes, as in the configuration model of static networks. In particular, they assessed when their mean field assumption exactly holds. When demographic turnover of nodes (i.e., death and birth) is added on top of dynamics of networks, the mean field assumption is only approximate. In this situation, positive degree correlation between adjacent nodes emerges through positive age (i.e., time since the birth of the node) correlation between them, although the amount of positive correlation is admittedly small in realistic situations. As they discuss in a dedicated section, analytical knowledge of such network dynamics derived in this chapter (though not combined with disease dynamics) brings useful insights into epidemic dynamics on top of the network dynamics.

In Chap. 6, Li et al. analysed the SI model dynamics on metapopulation models. In metapopulation models, a node is container of individual agents, i.e., a subpopulation or location, not an individual agent. Individuals diffuse from subpopulation (i.e., node) to another randomly or according to a mobility rule. Although the relationship between metapopulation models and temporal networks have not actively been explored, metapopulation models can be regarded as temporal networks for individual agents, because individuals are assumed to interact only when they are visiting the same subpopulation. The authors took analytical approaches to provide algorithms to infer transmission pathways on networks of subpopulations and parameter values of the model such as the infection rate.

In Chap. 7, Speidel et al. analysed the SIS model on temporal network models, in which static networks switch from one to another at constant time intervals. By modulating the switching interval, they tuned the timescale of the network dynamics relative to that of epidemic dynamics. They took analytical and numerical approaches to suggest that the epidemic threshold is small when the switching interval is long, corresponding to the temporal network because infinitesimally fast switching corresponds to the aggregate network. This result is contrary to some known results in previous literature on SIR and SI Models on temporal networks. They also suggested that whether different adjacency matrices commute or not (and deviation from the perfect commutation) was a key indicator to predict the epidemic threshold in the temporal networks.

In Chap. 8, Karsai and Perra reviewed immunisation strategies on temporal networks. An immunisation strategy is commonly defined as a rank order of nodes according to which one immunises nodes, i.e., one removes the selected nodes from the network before an epidemic spreading possibly happens. They distinguished global and local immunisation strategies depending on the amount of information that one can use. They started with discussing the case of static networks, then the activity-driven model of temporal networks, and then several heuristic immunisation strategies assessed on empirical temporal networks. As the authors also discuss in the concluding section, we still do not have a solid understanding of immunisation strategies on temporal networks and also on adaptive networks, which contrasts to the situation of static networks.

The following two chapters discuss analysis of unique data sets to which epidemic spreading and temporal networks are both relevant.

In Chap. 9, Belik et al. analysed a data set of hospital referral networks, which were generated by a record of time-stamped relocation events of patients from a hospital to another. The data were provided by a major insurance provider of a federal state in Germany and mainly covered that region, involving approximately one million patients and three years. Such a hospital network provides information complementary to that provided by within-hospital contact networks of individuals. They investigated the heterogeneity in activity in days of the week, the network structure and then the SIS, SIR and SI dynamics on the networks of hospitals. They particularly examined the following practical scenario: Patients dismissed from a hospital may be readmitted to a hospital after some time. Because that individual spent some time in community, he/she may have acquired infection, which is introduced to the hospital upon the readmission of this individual.

In Chap. 10, Schirdewahn et al. analysed an empirical temporal network of pig trades in Germany. They regarded each premise (e.g., farm, slaughterhouse) rather than a single pig as a node. Time-stamped edges are defined by trades of animals between two premises. They investigated epidemic spreading using a deterministic SIR model, where a time-stamped edge was assumed to always transmit infection. They provided methods to identify sentinels, i.e., nodes to be monitored for early detection of epidemic outbreaks. Understanding of infectious diseases in livestock and their early detection, as studied in this chapter, has huge economic as well as health implications.

The following four chapters discuss adaptive networks, at least partly in the chapter.

In Chap. 11, Ogura and Preciado analytically bounded the epidemic threshold for the SIS model on temporal and adaptive networks, which occur as continuous-time Markovian dynamics of networks. Then, they formulated the problem of optimal allocation of containment resources as modelled by a decrease in the infection rate, an increase in the recovery rate, and rate to cut undesired edges (in the case of adaptive networks), each of which came at a cost. They connected their optimisation problems to geometric programmes, which can be converted to a convex optimisation problem and hence solved with realistic computational resources. They demonstrated that different optimisation problems yielded considerably different

optimal allocations of resources at nodes. The proposed formulation is expected to inform various other intervention methods, many of which so far rely on agent-based numerical simulations, in particular for networks changing over time.

In Chap. 12, Kiss et al. presented analytical approaches to the SIS epidemic model on adaptive networks. To analyse such dynamics with an improved accuracy, one has to track the fraction of pairs of connected nodes that have certain states (e.g., susceptible or infected) and certain connectivity (e.g., degree) as well as the fraction of nodes in certain states as used in the mean field theory. The authors used an approximation scheme to close the set of differential equations composed of the variables coding the state of nodes and pairs. This is generally called a pair approximation. Using the resulting closed system, the authors mapped out oscillatory and bistability regimes in the epidemic dynamics and revealed bifurcations in network structure. Crucially, such rich dynamics are caused by the interplay between epidemic dynamics on the network and the dynamics of the network. They also make a case for more emphasis on extending the bifurcation analysis of the epidemic dynamics to mapping out changes in the dynamic network, either in the transient regime or at the steady state.

In Chap. 13, Pacheco et al. developed analytical approaches to investigate the SIS, SIR and SI models on adaptive networks. They assumed that an individual has information to be able to cut an edge to an infected neighbour at a higher rate than an edge to a non-infected neighbour. Link creation occurred randomly for simplicity. They found that the disease was less likely to progress as compared to the case of the non-adaptive network. Hinted from the theory of evolutionary dynamics in finite populations, the authors particularly focussed on stochastic disease dynamics in finite populations, which were boiled down to one or two dimensional biased random walks. For example, the state of the chain was specified by the number of the infected individuals in the case of the SIS or SI model. This analytical framework makes it possible to understand the effect of population size on epidemic dynamics on adaptive networks, as well as the effect of other main parameters such as the rate to sever edges.

In Chap. 14, Rizzo and Porfiri extended and applied the SIS model on activity-driven network models of temporal networks in three strands. First, they extended the model by considering individual agent's behaviour. For example, infected individuals were assumed to reduce connectivity because of quarantine or their compromised health condition. In a different scenario, susceptible individuals were assumed to reduce connectivity when the prevalence in the population increased. By exploiting the analytical tractability of the activity-driven model, the authors derived the epidemic threshold in these and other adaptive network scenarios. Second, they further extended the epidemic dynamics to a seven-state compartmental model, taking into account the reality of the Ebola, and fitted the model to the 2014–2015 Ebola outbreak in Liberia. The model offered a reasonable fit to the field data and a one-year prediction of the number of infected individuals. Third, going back to the basic activity-driven model, the authors provided a continuous-time variant of the model that enabled analytical estimation of the dynamics of the SIS model.

1.6 Future Work

We conclude this chapter by discussing some challenges in this research field.

Strong intervention methods exploiting temporal and/or adaptive nature of networks should be developed. For example, what is an efficient vaccination strategy (to prioritise nodes to be vaccinated before an epidemic dynamic occurs) given statistics of temporal network data? Or, can we design a vaccination strategy that allocates resources in a manner responsive to ongoing epidemic dynamics to achieve an efficient containment (using adaptive networks)? How about quarantine strategies? Designing of transportation systems and traffic flows of passengers and cattles? Can we do better by using temporal/adaptive networks as compared to static networks? There questions have already been addressed by many articles including Chap. 8 of this volume, and we expect more in coming years.

A large part of temporality of network structure is contributed by mobility of individuals. They simply move on various time scales to which epidemic dynamics is relevant, changing partners to interact with. Metapopulation models are a powerful framework to model mobility coupled with epidemic dynamics [4], as discussed in Chap. 6 of this volume. How can temporal/adaptive network epidemiology approaches marry with those and other mobility models? When should we take temporal/adaptive network approaches (without metapopulation components) rather than metapopulation approaches? Interacting random walks on the Euclidean space (e.g., two-dimensional arena) are also a promising tool to connect mobility of individuals and temporal networks [30].

Working together with real epidemiologists and practitioners would benefit both fields. The data analyses presented in Chaps. 9 and 10 are towards this direction. Admittedly, this research field has been mostly contributed by theoreticians in a broad sense, having backgrounds in, e.g., mathematics, statistical physics, computer science and engineering, and affiliations with such departments. For instance, we tend to publish relevant papers in physics journals (e.g., *Physical Review E* or *Physical Review Letters*), mathematical or computational, biology or epidemiology journals (e.g., *PLOS Computational Biology*, *Journal of Theoretical Biology*, or *Mathematical Biosciences*), or general audience journals (e.g., *Proc. Natl. Acad. Sci. USA*, *Nature Communications*, *Scientific Reports*, *PLOS ONE*). Medical epidemiologists may prefer different sorts of journal including specialist journals in epidemiology. Some people including authors of the present volume are now collaborating with epidemiologists and publishing in epidemiology and medicine journals. Hopefully more and more temporal/adaptive network epidemiology ideas and analysis tools will be exploited in field and clinical epidemiology contexts in a near future.

Acknowledgements NM acknowledges the support provided through JST, ERATO, Kawarabayashi Large Graph Project and JST, CREST.

References

1. Bansal, S., Read, J., Pourbohloul, B., Meyers, L.A.: The dynamic nature of contact networks in infectious disease epidemiology. *J. Biol. Dyn.* **4**, 478–489 (2010)
2. Barrat, A., Barthélemy, M., Vespignani, A.: *Dynamical Processes on Complex Networks*. Cambridge University Press, Cambridge, UK (2008)
3. Barthélemy, M., Barrat, A., Pastor-Satorras, R., Vespignani, A.: Velocity and hierarchical spread of epidemic outbreaks in scale-free networks. *Phys. Rev. Lett.* **92**, 178701 (2004)
4. Colizza, V., Pastor-Satorras, R., Vespignani, A.: Reaction-diffusion processes and metapopulation models in heterogeneous networks. *Nat. Phys.* **3**, 276–282 (2007)
5. Dietz, K.: On the transmission dynamics of HIV. *Math. Biosci.* **90**, 397–414 (1988)
6. Glass, R.J., Glass, L.M., Beyeler, W.E., Min, H.J.: Targeted social distancing designs for pandemic influenza. *Emerg. Infect. Dis.* **12**, 1671–1681 (2006)
7. Gross, T., Blasius, B.: Adaptive coevolutionary networks: a review. *J. R. Soc. Interface* **5**, 259–271 (2008)
8. Gross, T., D’Lima, C.J.D., Blasius, B.: Epidemic dynamics on an adaptive network. *Phys. Rev. Lett.* **96**, 208701 (2006)
9. Gross, T., Sayama, H. (eds.): *Adaptive Networks*. Springer, Berlin (2009)
10. Hethcote, H.W.: The mathematics of infectious diseases. *SIAM Rev.* **42**, 599–653 (2000)
11. Holme, P.: Model versions and fast algorithms for network epidemiology. *J. Logist. Eng. Univ.* **30**, 1–7 (2014)
12. Holme, P.: Modern temporal network theory: a colloquium. *Eur. Phys. J. B* **88**, 234 (2015)
13. Holme, P., Liljeros, F.: Birth and death of links control disease spreading in empirical contact networks. *Sci. Rep.* **4**, 4999 (2014)
14. Holme, P., Saramäki, J.: Temporal networks. *Phys. Rep.* **519**, 97–125 (2012)
15. Holme, P., Saramäki, J.: *Temporal Networks*. Springer, Berlin (2013)
16. Karsai, M., Kivela, M., Pan, R.K., Kaski, K., Kertész, J., Barabási, A.L., Saramäki, J.: Small but slow world: how network topology and burstiness slow down spreading. *Phys. Rev. E* **83**, 025102(R) (2011)
17. Keeling, M.J., Eames, K.T.D.: Networks and epidemic models. *J. R. Soc. Interface* **2**, 295–307 (2005)
18. Kelso, J.K., Milne, G.J., Kelly, H.: Simulation suggests that rapid activation of social distancing can arrest epidemic development due to a novel strain of influenza. *BMC Public Health* **9**, 117 (2009)
19. Kretzschmar, M., Morris, M.: Measures of concurrency in networks and the spread of infectious disease. *Math. Biosci.* **133**, 165–195 (1996)
20. Lloyd, A.L.: Realistic distributions of infectious periods in epidemic models: changing patterns of persistence and dynamics. *Theor. Pop. Biol.* **60**, 59–71 (2001)
21. Masuda, N., Holme, P.: Predicting and controlling infectious disease epidemics using temporal networks. *FI000Prime Rep.* **5**, 6 (2013)
22. Masuda, N., Lambiotte, R.: *A Guide to Temporal Networks*. World Scientific, Singapore (2016)
23. Newman, M.E.J.: *Networks—An Introduction*. Oxford University Press, Oxford (2010)
24. Pastor-Satorras, R., Castellano, C., Van Mieghem, P., Vespignani, A.: Epidemic processes in complex networks. *Rev. Mod. Phys.* **87**, 925–979 (2015)
25. Reluga, T.C.: Game theory of social distancing in response to an epidemic. *PLoS Comput. Biol.* **6**, e1000793 (2010)
26. Rocha, L.E.C., Liljeros, F., Holme, P.: Simulated epidemics in an empirical spatiotemporal network of 50,185 sexual contacts. *PLoS Comput. Biol.* **7**, e1001109 (2011)
27. Rocha, L.E.C., Masuda, N.: Individual-based approach to epidemic processes on arbitrary dynamic contact networks. *Sci. Rep.* **6**, 31456 (2016)
28. Sayama, H., Pestov, I., Schmidt, J., Bush, B.J., Wong, C., Yamanoi, J., Gross, T.: Modeling complex systems with adaptive networks. *Comput. Math. Appl.* **65**, 1645–1664 (2013)

29. Sharp, P.M., Hahn, B.H.: Origins of HIV and the AIDS pandemic. *Cold Spring Harb. Perspect. Med.* **1**, a006841 (2011)
30. Starnini, M., Baronchelli, A., Pastor-Satorras, R.: Modeling human dynamics of face-to-face interaction networks. *Phys. Rev. Lett.* **110**, 168701 (2013)
31. Valdano, E., Ferreri, L., Poletto, C., Colizza, V.: Analytical computation of the epidemic threshold on temporal networks. *Phys. Rev. X* **5**, 021005 (2015)
32. Vestergaard, C.L., Génois, M.: Temporal Gillespie algorithm: fast simulation of contagion processes on time-varying networks. *PLoS Comput. Biol.* **11**, e1004579 (2015)
33. Volz, E., Meyers, L.A.: Susceptible-infected-recovered epidemics in dynamic contact networks. *Proc. R. Soc. B* **274**, 2925–2933 (2007)
34. Volz, E., Meyers, L.A.: Epidemic thresholds in dynamic contact networks. *J. R. Soc. Interface* **6**, 233–241 (2009)
35. Watts, C.H., May, R.M.: The influence of concurrent partnerships on the dynamics of HIV/AIDS. *Math. Biosci.* **108**, 89–104 (1992)

Chapter 2

How Behaviour and the Environment Influence Transmission in Mobile Groups

Thomas E. Gorochoowski and Thomas O. Richardson

Abstract The movement of individuals living in groups leads to the formation of physical interaction networks over which signals such as information or disease can be transmitted. Direct contacts represent the most obvious opportunities for a signal to be transmitted. However, because signals that persist after being deposited into the environment may later be acquired by other group members, indirect environmentally-mediated transmission is also possible. To date, studies of signal transmission within groups have focused on direct physical interactions and ignored the role of indirect pathways. Here, we use an agent-based model to study how the movement of individuals and characteristics of the signal being transmitted modulate transmission. By analysing the dynamic interaction networks generated from these simulations, we show that the addition of indirect pathways speeds up signal transmission, while the addition of physically-realistic collisions between individuals in densely packed environments hampers it. Furthermore, the inclusion of spatial biases that induce the formation of individual territories, reveals the existence of a trade-off such that optimal signal transmission at the group level is only achieved when territories are of intermediate sizes. Our findings provide insight into the selective pressures guiding the evolution of behavioural traits in natural groups, and offer a means by which multi-agent systems can be engineered to achieve desired transmission capabilities.

T.E. Gorochoowski (✉)

BrisSynBio, University of Bristol, Life Sciences Building, Tyndall Avenue, BS8 1TQ, Bristol, UK

School of Biological Sciences, University of Bristol, Life Sciences Building, Tyndall Avenue, BS8 1TQ, Bristol, UK

e-mail: thomas.gorochoowski@bristol.ac.uk

T.O. Richardson (✉)

Department of Ecology and Evolution, University of Lausanne, 1015, Lausanne, Switzerland

e-mail: thomas.richardson@unil.ch; tom.richardson30@gmail.com

2.1 Introduction

Animal societies consist of many individuals that must interact to coordinate their actions. The cohesion of such groups is typically achieved through a distributed network of short-range ‘direct’ interactions between neighbouring individuals. These serve to rapidly transmit information throughout the group [61, 92]. Short-range contacts also represent a channel for the transmission of harmful pathogens, with the potential for large-scale epidemics being closely linked to the structure of the group interaction network [72, 77, 80, 81, 89]. Whilst information often spreads via dedicated interactions that have evolved for the purpose of communication, diseases often ‘piggyback’ over a diverse range of different interaction types that have evolved for other purposes, such as sexual contacts [67, 86] or face-to-face conversations [96, 107]. Furthermore, while information and disease play different roles, they may both be viewed as ‘signals’ that can be transmitted across a group. Although direct interactions based on physical contact are the most obvious means by which such signals can spread, other forms of transmission are possible. For example, some signals remain viable after being deposited into the environment. If such a signal is still viable when that location is later visited by another individual, then the second individual could acquire the signal. As this pathway does not require the sender and receiver to be present at the same time, this is termed ‘indirect’ transmission [23, 38, 84].

Indirect communication is ubiquitous. It is found in species where individuals are generally solitary (Fig. 2.1a), as well as in highly cooperative species where individuals live together in tightly-knit societies (Fig. 2.1b–e). A commonly used example is that of pheromone trails in ant colonies where individual workers deposit chemical markers that recruit nestmates to rewarding food sources [30] (Fig. 2.1c). Disease can also exploit indirect pathways for transmission. Pathogens such as smallpox and influenza are able to remain intact outside a host for extended periods of time in ‘environmental reservoirs’ (Fig. 2.1f). These increase the number of opportunities for transmission and can lead to multiple waves of infection. Whilst researchers of animal behaviour have long appreciated that the shared environment can act as a substrate for indirect communication [29, 32, 46, 73, 98, 115], epidemiologists are only starting to quantify the important role that indirect transmission has during disease spread [2, 19, 28, 58, 87, 88, 103, 114, 116].

Over the last decade there has been an increasing number of studies focusing on the transmission properties of contact networks in humans [31, 56, 69, 95, 105–108] and other social animals [1, 14, 17, 17, 21, 75, 77, 94, 101]. Similarly, there has been a rapid growth in the effort devoted to understanding how adaptive collective behaviours such as swarming, flocking and shoaling [6, 22, 74, 92] emerge from the underlying peer-to-peer interactions. To date, these studies have exclusively focused on the role of direct interactions, without considering the potential for indirect transmission of materials or information. Although there are many species in which environmentally-mediated transmission is not viable because

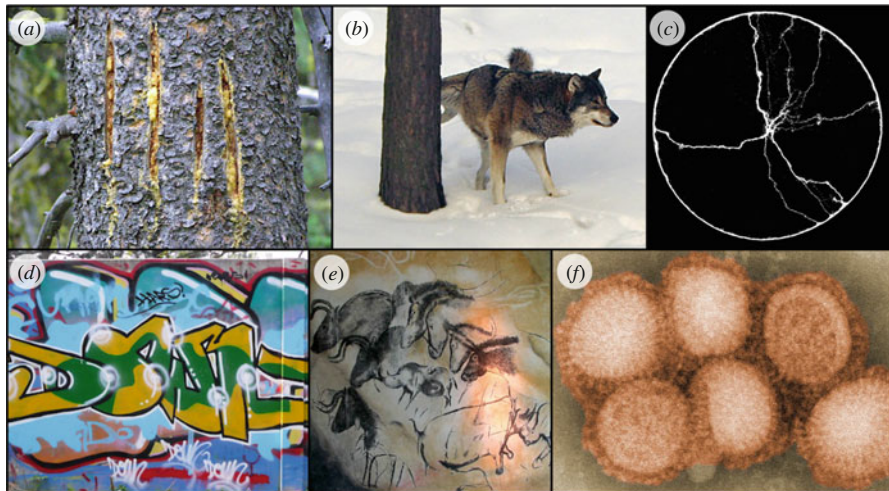


Fig. 2.1 Indirect transmission of information and disease. (a) Territorial bear markings on a tree in Paradise Valley, Montana, USA (Image attribution: Suzanna Soileau, USGS). (b) Eurasian Wolf (*Canis lupus*) marking its territory. (c) Pheromone trails of Argentine ants (*Linepithema humile*) used to coordinate colony behaviours such as foraging [82]. (d) Modern graffiti. (e) Ancient human murals from the Chauvet cave. (f) Influenza A (H1N1) virus more commonly known as swine flu that can be transmitted indirectly through the air and infected surfaces (Image attribution: Cybercobra at English Wikipedia)

the environment cannot physically support such transmission (e.g. flocking birds), there are many species for which the potential is clear (e.g. those living within or upon the ground).

To address this shortcoming, we previously developed an analytical framework that combines both direct and indirect interactions within a single dynamic network representation [84]. Individuals are represented by nodes and weighted edges represent direct and indirect interactions (Fig. 2.2a). When a direct physical interaction occurs between two individuals, an edge with a weight of 1 is drawn between them. As both individuals are at the same place at the same time, they may both play the role of either sender or receiver, hence the edge is bidirectional. In contrast, indirect interactions occur when an individual j visits a location previously visited by another individual i . Assuming that i carries some signal (information or disease) that it deposits into the environment, that the signal decays at a rate α , and that j visits the location at time t , this indirect interaction is represented by a directed edge from i to j with weight,

$$\omega_{i \rightarrow j}(t) = e^{-\alpha \tau_{i \rightarrow j}(t)}. \quad (2.1)$$

Here, $\tau_{i \rightarrow j}(t)$ is the time delay between the visits of i and j , which is used to calculate the proportion of the signal that would remain viable given its environmental decay (Fig. 2.2b). This formalism allows any given time point to be represented as a static network ‘slice’ consisting of both strongly weighted direct interactions and more weakly weighted indirect interactions. Over time edges are created and

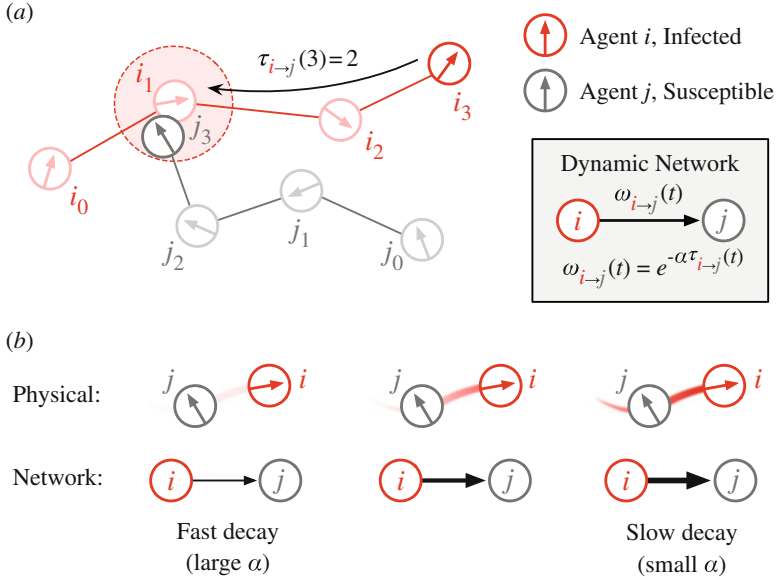


Fig. 2.2 Extracting a dynamic network containing direct and indirect interactions from the paths of mobile agents. Example shows an indirect interaction between an infected (*red*) and susceptible (*grey*) agent. (a) Methodology for calculating edge weights for the dynamic interaction network. A susceptible agent j intersects a previously visited location of an infected agent i at $t = 3$. This gives an intersection delay of $\tau_{i \rightarrow j}(3) = 2$ time steps. The *shaded circle* represents the maximum distance over which the signal can be transmitted. The edge weight is calculated using both the intersection delay $\tau_{i \rightarrow j}$ and decay rate α of the signal. Positions at time points 1 to 4 are denoted i_0, i_1, i_2 and i_3 for agent i and j_0, j_1 and j_2, j_3 for agent j , respectively. (b) The weight of an indirect interaction is modulated by the decay rate α of the transmitted signal. Fast decay of a signal in the environment leads to weak trails and weakly weighted edges. Conversely, slow decay of a signal produces strong trails and highly weighted edges (Figure adapted from Ref. [84])

destroyed. Direct edges appear and disappear whenever two agents make and break contact. An indirect edge appears when one agent (the receiver) visits a location that was previously visited by another agent (the sender), and disappears when the receiving agent leaves that location. As such events are intermittent, the instantaneous static network slices are typically sparse. The overall network structure consists of a sequence of static slices, with direct interactions linking nodes within each slice, and with indirect edges linking nodes between slices. In the literature, such networks have been referred to as multi-slice, multiplex, dynamic, time-ordered, and temporal.

In our previous work [84], we used this approach to study the transmission properties of interactions within a colony of ants. Trajectories of individual worker ants were collected and used to create temporal networks where edges represented the direct and indirect interactions between the workers (referred to as ‘combined’ networks). To investigate the transmission properties of these temporal networks, we ran simulations inspired by susceptible-infected (SI) models of epidemiological

processes [52, 54]. In addition to simulating disease spread, SI models and their variants have been used to simulate transmission processes over a wide range of social and technological networks, including infrastructure networks [4], email and mobile phone call records [59, 62], and face-to-face conversation logs [56, 107]. In an SI model each individual may take one of two states; infected (I) or susceptible (S). Once an individual is infected it carries the signal of interest. The model is initiated with one node infected, and all others susceptible. To represent transmission between individuals, an infected individual i that interacts (either directly or indirectly) with a susceptible individual j , may result in j changing its state to infected. The probability that this state-change occurs is given by,

$$\Pr(j \rightarrow I \mid i \in I \wedge j \in S) = p_s \omega_{i \rightarrow j}(t), \quad (2.2)$$

where p_s is the transmission probability for direct interactions, and $\omega_{i \rightarrow j}(t)$ is the edge weight defined above. Because the edge weight $\omega_{i \rightarrow j}(t)$ decreases as a negative exponential function of the time delay $\tau_{i \rightarrow j}(t)$, direct interactions (which all have $\tau_{i \rightarrow j}(t) = 0$) are much more likely to result in transmission than indirect interactions (which have $\tau_{i \rightarrow j}(t) > 0$).

This SI model was applied to the ant colony interaction networks using the NetEvo software library [41, 42]. By systematically varying the transmission probability p_s and signal decay rate α , we were able to analyse how the transmission properties of the ant interaction networks changed depending upon the characteristics of the signal being transmitted. We showed that both signal characteristics—the decay rate and transmission probability—significantly influenced the speed of signal transmission over the ant interaction networks. But do real-world signals exhibit such characteristics?

Signals that have evolved for the purpose of delimiting the borders of an animal territory or home-range, are expected to have a low environmental decay rate, particularly if the population is small or widely-spaced. In such cases, a small decay rate is essential, otherwise the territory-holder would need to allocate all of their time to re-marking. Whilst data concerning the environmental persistence of such signals is scarce, the prions that cause Chronic Wasting Disease (CWD) in deer can persist in the environment for several years [2], and the visual scratch marks used by some vertebrates to indicate territory borders (Fig. 2.1a) are essentially permanent (i.e. $\alpha \approx 0$). Similarly, the scent- and scat-marks made by other vertebrates [25, 79] to indicate territory (Fig. 2.1b) and the pheromone marks used by invertebrates [57, 64] for communication (Fig. 2.1c), typically dissipate after a few days or weeks, and therefore correspond to signals with intermediate values of α . At the other end of the scale, there are many examples of pathogens that decay so quickly that they cannot readily persist within the environment at all, and are therefore constrained to spreading by direct interactions (i.e. $\alpha = \infty$). Most sexually-transmitted diseases fall into this category.

The second key characteristic of a signal is the transmission probability, which reflects the ability of a given signal to spread from one host to another when given the chance to do so. Diseases such as SARS which have evolved to have

a high virulence also have a very high probability of spreading during close-proximity interactions [76]. In terms of information transmission, unambiguous or high intensity signals such as elaborate courtship displays or eye-catching billboards (Fig. 2.1d, e) are unlikely to be missed or misinterpreted by the targeted recipient, and should therefore also have a high transmission probability. Interestingly, examples of signals with low transmission probabilities are scarce, probably because both information-bearing signals and pathogens have evolved to efficiently utilize any and all available transmission opportunities.

Whilst our previous study provided a mechanistic understanding of how the mixture of direct and indirect interactions produced by a real animal society determines how different types of signal may spread through it [84], we could not directly control the motion of the ants. Therefore, we were not able to provide a causal understanding of how individual-level behaviours determine the transmission properties of the overall interaction network. In this chapter, we overcome this limitation by defining an agent-based model in which the movement of virtual individuals (referred to as ‘agents’) is systematically varied. The motion of each agent takes the form of a parameterisable two-dimensional random walk. The environment within which these move also contains a spatially-explicit ‘signal field’ representing signals deposited by infected agents. This field is dynamically updated to reflect signal decay. By feeding the interaction data produced by this more physically realistic agent-based model into our previous network abstraction [84], we are able to establish a causal link between the behaviours of the individuals and the emergent group-level transmission properties.

2.2 Modelling Approaches

Numerous modelling approaches and formalisms have been developed to identify the key factors influencing the transmission of information and disease within populations of interacting individuals. In this section, we provide a brief overview of some of the most commonly used and discuss the benefits and limitations of each approach.

2.2.1 *Compartment Models*

Many of the earliest attempts to provide a quantitative description of spreading processes involve the use of compartment models. These employ deterministic or stochastic mathematical equations to describe contagious transmission of a signal (typically disease) through a population that is divided into compartments. In epidemiology, these compartments typically reflect an individual’s clinical status, for example, susceptible, exposed, infected or recovered [60, 102].

Compartment models remain popular today because their precise mathematical formulation can allow for the derivation of exact analytical solutions [55]. However, many simplifying assumptions are often made to ensure a tractable solution. For this reason, these models generally use deterministic differential equations to represent the flux of individuals between different states and assume that the population is infinite and well-mixed [66]. These simplifications are often not a good approximation for real-world systems where a finite number of individuals are non-uniformly distributed across space and behave stochastically rather than deterministically [7]. Furthermore, the physical laws governing real-world environments impose severe limits on how individuals can move and interact, yet compartment models assume no such constraints. Some attempts have been made to extend this approach to incorporate network structures that capture the heterogeneous mixing of populations, but generally such changes come at the cost of reduced analytical tractability.

2.2.2 *Network Models*

More recently, it has become popular to treat the spread of information or disease through spatially structured populations, as a contagious process propagating over a network. Nodes represent individuals and edges capture the interactions or contacts between them [15]. Although space is not explicitly modelled, the ability to constrain the interactions present between individuals allows for the effective description of the heterogeneous connectivity observed in many real-world systems (e.g. long-tailed degree distributions [9–11]). This has led to network-based approaches becoming common not only in epidemiology, but in a huge variety of different fields where contagious processes are observed, from the spread of rumours and gossip over social networks [68, 93], to cascading failures in power distribution networks [4, 20]. Attempts have also been made to combine the benefits of network models with other modelling approaches. For example, the GLocal Epidemic and Mobility (GLEaM) model makes use of structured metapopulation simulations that are linked to realistic networks capturing known mobility links (e.g. train and airline routes). Simulations using this combined model are able to accurately simulate the spatial propagation of disease pandemics at both regional and global scales [4, 5, 112].

The vast majority of network-based epidemic models investigate transmission using static networks where the structure is fixed over time. Doing so ignores the fact that in almost every real-world system the connectivity between individuals varies with time. For example, studies of the contact networks of both humans and other animals, have shown that interactions can be 'bursty' [9] or even cyclical [85], with large numbers of interactions concentrated in a short period of time. In cases where the dynamics of the epidemic process is much slower than the evolution of the network, this is not a problem as time-scale separation makes it possible to consider an 'annealed' network describing the averaged structure the process will encounter

[113]. However, if the process has a similar time-scale to the network dynamics, it is essential that both these aspects are modelled concurrently. Temporal networks are well suited to describing such intermittent fluctuations, as they represent the dynamics as a sequence of static network slices [15, 43, 53, 54]. Other approaches have also been developed to describe networks with dynamic topologies. Adaptive networks [49] and evolving dynamic networks [27, 43] make use of dynamical equations and stochastic rules to describe how the strength of each edge varies with time, whilst also allowing for changes in the size of the network through the birth and death of nodes. Although these more complex approaches can capture an even richer range of behaviours, they are a challenge to apply to real-world systems because a unified and accepted theory of time-varying networks is still emerging and new forms of analysis are often required [44].

2.2.3 *Agent-Based Models*

Agent-based models attempt to simplify the description of real-world systems by modelling the behaviours of large numbers of autonomous ‘agents’ that move and interact within a virtual environment [40, 51] (Fig. 2.3). Unlike compartmental and network models, they provide a spatially- and physically-explicit representation of a population of mobile interacting individuals. As an agent-based model is essentially a physical representation of a given system, it is considerably more detailed than the compartmental and network abstractions described above. Agents can be used to represent any autonomous entity, from cells [45] to animals [110]. Each agent typically follows a prescribed set of rules controlling their behaviour and interactions with their peers. In a cellular context, these rules might represent the genetic circuits that control the expression of key genes in response to particular stimuli [71, 109], whereas in the context of shoals of fish or swarms of insects they would embody the behavioural responses each member makes in response to neighbouring individuals [22].

A major benefit of using an agent-based approach, as opposed to considering averaged group behaviours, is that the system is modelled as a set of discrete elements. This makes it possible to directly include heterogeneity and stochasticity into the behaviour of agents. Moreover, agent-based models allow for environmental processes (e.g. diffusion of a chemical) to be more easily described and incorporated using known physical laws [43, 51]. Including such processes in other more abstract methodologies, such as network models, is difficult due to the simplifications that are made.

Agent-based models are also ideally suited to the study of how complex group-level features emerge from the behaviour of the individuals and their use of a shared environment. By varying the rules that agents follow and observing the changes in the group-level behaviours, it is possible to understand how these organisational levels are linked and the causal factors controlling them. It is important to note that by representing the discrete individuals in a system, we are able to capture features

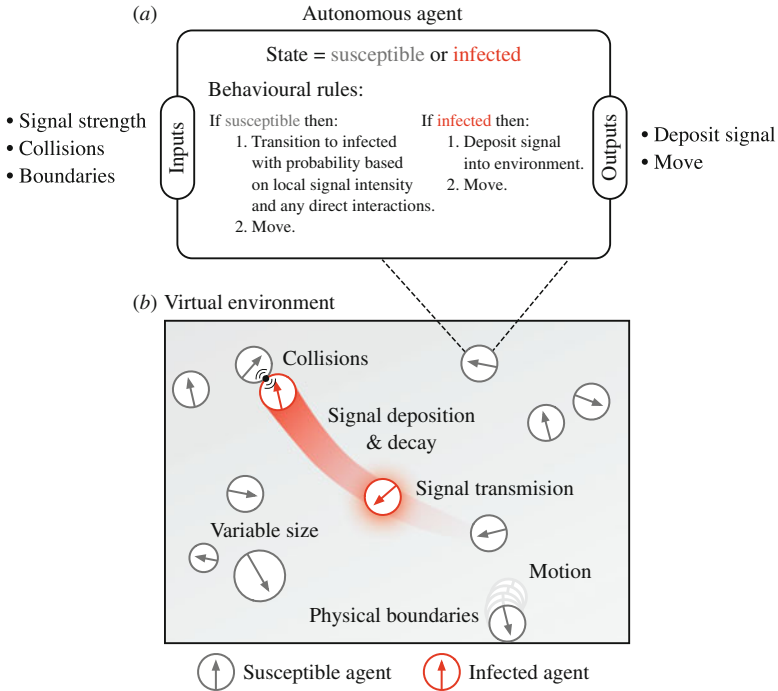


Fig. 2.3 Overview of an agent-based model. (a) Agent-based models contain a number of autonomous individuals that follow their own individual set of rules defining how they respond to different external stimuli. (b) The agents are placed in an environment in which they can interact with each other and other processes within the environment (e.g. deposit a signal at a specific location)

that averaging across the population would miss. For example, cells often exploit noise and stochastic effects to differentiate their behaviours. A famous example of this is the *lac* operon that encodes genes required for the transport and metabolism of lactose [78]. In this system, cells that are genetically homogeneous use stochastic noise to differentiate themselves into two separate populations: those that are active and strongly expressing the *lac* operon, and those that are not. The fraction of cells in an active state varies depending on the concentration of lactose. However, two separate populations are always maintained. If an average of *lac* operon expression was taken across the entire population, it would look as if each cell was tuning its expression to match the concentration. Only when the individual cells are modelled, as is done when using agent-based modelling, is an accurate understanding of the bistable structure of the system gained.

The need to capture the dynamics of each component of a system results in agent-based models being computationally expensive to run. While this limited their use initially, recent advances in high-performance computing have opened up the possibility to efficiently simulate large complex systems consisting of millions

of interacting components [40, 51]. In many cases this is sufficient to provide an accurate representation of real-world systems, and as a result, agent-based models are now commonplace in many different fields including social behaviour [3], ecology [48], microbiology [51] and economics [111]. The major difficulty that remains is the requirement for a detailed understanding of the individual-level rules, as such information is often unavailable.

2.3 Studying Signal Transmission Using an Agent-Based Model

In this section we describe the agent-based model we use to assess how high-level properties of the group, such as the transmission properties of the interaction network, emerge from the underlying behaviours of the individual agents. This model enables us to parameterise the random walk performed by each agent as well as environmental properties such as physical collisions and the decay rate of any signals deposited into the environment. We apply this model to a number of different scenarios to explore the role of these factors and link the observed changes in transmission to characteristics of the underlying interaction networks that are generated.

2.3.1 Agent-Based Model Definition

The agent-based model consists of a population of N agents, each performing a random walk in a two-dimensional environment with periodic boundary conditions. Each agent is defined by a set of four variables describing its current infection state s (either susceptible ‘S’ or infected ‘I’), its position within the environment \mathbf{x} stored as a two-dimensional vector, its two-dimensional heading vector $\hat{\theta}$ (of unit length, arbitrary length units), and the time remaining t_r before a new heading is randomly selected. Each agent is represented as a circle of unit radius $r = 1$, unit mass (arbitrary mass units), and can propel itself with a constant force of 0.3 force units per time unit in the direction it is heading. Furthermore, agents display no inertia (i.e. the velocity of an agent will be zero when no force is applied) and no friction is present in the environment. Parameter values and variables for the model are shown in Table 2.1.

In order to allow indirect signal transmission via the shared environment, the model includes a ‘signal field’ that records the signal strength at every location within the environment. As an infected agent moves through the environment, it leaves a ‘trail’ of the signal behind it, which is modelled as a local increase in the signal field strength (Fig. 2.3b). At each time step $t_s = 0.02$ time units, we begin by updating the field to simulate signal decay. Assuming the signal has decay rate α

Table 2.1 Model features and parameters

Aspect	Parameter	Description	Value(s)	Units
Simulation	t_s	Simulation time step	0.02	Time unit
Environment	N	Number of agents	2–1500	–
	–	Environment dimensions	$100 \times 100, 25 \times 25$	Length unit ²
	–	Boundary conditions	Periodic, Solid	–
	–	Physical collisions between agents	On, Off	–
Agent	r	Radius of agent	1	Length unit
	κ	Turn-angle distribution bias	–	–
	s	Infection state	S, I	–
	γ	Strength of attraction	0.001–0.2	–
Signal	p_s	Transmission probability	0.01–1.0	–
	α	Decay rate	0.001–1.0	Time unit ⁻¹

per time unit, then the value of the field at each position has $\alpha t_s F$ subtracted, where F is the current value of the field. Next, we cycle through each agent and if $t_r > 0$ then their position is updated according to $\mathbf{x} + 0.3\hat{\theta}t_s$ and t_s is subtracted from t_r . Otherwise, if t_r has reached zero, a new heading $\hat{\theta}$ is chosen by generating a unit length vector in the direction of a randomly selected angle over the interval $[-\pi, \pi]$. In addition, t_r is set to a constant agent movement time (default is 1 time unit) and the agent is then moved as described above. Finally, if the agent is infected, we update the signal field to have a value of 1 for the entire space covered by the agent. Conversely, if the agent is susceptible, then a transition to an infected state occurs with probability $p_s F$, where p_s is the signals' probability of transmission through a direct contact, and F is the maximum value of the signal field for the space occupied by the agent. Because the path of each agent is determined by random sampling of the heading vectors, agents move independently of one another.

In addition to agents following simple random walks, we also extended the model to allow each agent to have its own point of attraction, which enabled the formation of territories in space. When an agent is close to its point of attraction it moves randomly, but as the distance from the point of attraction increases, the heading distribution (which in the basic model is uniformly distributed around the circle), becomes increasingly biased towards the point of attraction. This allowed us to constrain the motion of each individual to a limited region of space. To implement this behaviour we adapted the basic model such that new headings for agents were sampled using a circular normal (von Mises) distribution over the range $[-\pi, \pi]$. The probability density function was given by,

$$f(x | \mu, \kappa) = \frac{e^{\kappa \cos(x-\mu)}}{2\pi I_0(\kappa)}, \quad (2.3)$$

where μ is the mean, κ is the bias (analogous to the variance of a normal distribution), and $I_0(\kappa)$ is the modified Bessel function of order zero [70]. This

distribution was orientated such that its mean value μ pointed from the agent towards its' point of attraction. The bias of the distribution around the mean was then given by $\kappa = d_a\gamma$, where d_a is the distance between the agent and the point of attraction, and γ is a parameter governing the strength of attraction (Table 2.1). Hence, the further away the agent is from its point of attraction, the more strongly its heading will be biased towards it.

Although in the model described above, each agent occupies a non-zero area in space, agents do not physically interact with one another. Hence, two agents are allowed to occupy the same position at the same time. Clearly this is not realistic, as packing constraints impose an upper limit on real world animal population densities. Therefore, we optionally allow for the inclusion of physical collisions between agents. To implement this feature a reaction force was applied whenever two agents' boundaries touched one another. For a distance d between the boundaries of two agents, a reaction force of $R_f = 25d \times \log(d/2r)$ was applied to both agents in opposing directions. For the chosen parameters of our simulations (Table 2.1) this enabled some limited overlap of agents, but prevented agents passing through one another.

We initiated each simulation by randomly-selecting a single 'seed' individual whose state was set to infected. We then followed the propagation of the infection across the rest of the population. As transmission was stochastic, 1000 simulations were run for each parameter combination and the average of these runs was used to calculate the proportion of the population infected over time.

2.3.2 *Role of Indirect Transmission Pathways*

Interaction networks composed of both direct and indirect interactions (referred to as 'combined' networks) have been shown to have fundamentally different transmission characteristics from those composed solely of direct interactions (referred to as 'direct-only' networks) [84]. To confirm that the addition of indirect interactions affects the transmission properties of the group, we measured the progression of signals spreading across the combined interaction networks generated by the agent based model. This was then compared to signals spreading across groups where the agents could only interact by direct physical contacts. Signal progression over both network types was quantified by simulating SI transmission of a wide range of signals that varied in both their transmission probability p_s , and their decay rate α .

For both network types and for all combinations of transmission probability p_s , and decay rate α of a signal, the SI model produced sigmoid shaped infection curves (Fig. 2.4a). Sigmoidal curves are a hallmark of density-dependent processes, such as the spread of information or disease through a finite population. The early explosive growth is due to the exponential nature of the SI dynamics where contact between one infected and one susceptible agent can result in two infected agents. The later slowing of spread arises from the gradual depletion of the pool of uninfected agents. To compare the transmission among different types of signals, it is necessary to

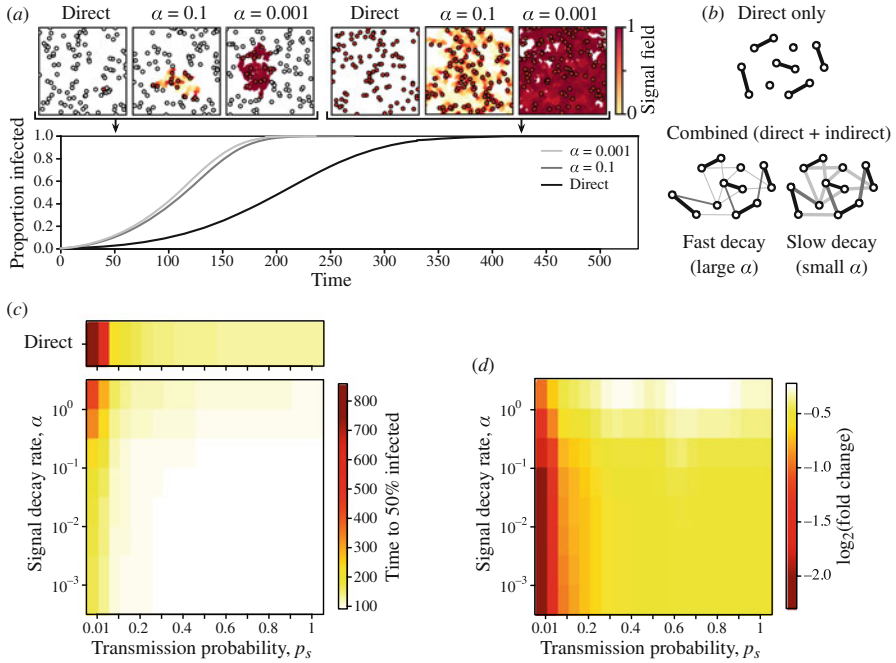


Fig. 2.4 Influence of indirect pathways on transmission rate. **(a)** The spread of three different signals are shown. In one, the signal decays immediately (i.e. $\alpha = \infty$) and so infections can only spread via direct interactions. In the other two, the signals have decay rates of $\alpha = 0.1$ and 0.001 , respectively, making indirect transmission possible. All three signals have a transmission probability $p_s = 0.1$. *Small panels above* show a time point from the agent-based model for a representative simulation. Agents are shown by *circles*, which are *grey* if susceptible and *red* if infected. The *background colour* denotes the strength of the environmental signal field; *dark red* = 1 to *white* = 0. **(b)** Illustration of the static network ‘slice’ for a single point in time. *Circles* denote agents, *thick black edges* denote direct interactions and *thinner grey edges* denote indirect interactions. *Line thickness* corresponds to edge strength. **(c)** Average time to reach 50% of the population infected t_c for a range of signal decay rates α and transmission probabilities p_s . **(d)** Comparison of the \log_2 fold change difference in t_c between simulations using only direct interactions and those incorporating both direct and indirect interactions. Simulations for all panels contained 250 agents and are the average of 1000 simulations

define a feature of each growth curve that reflects the overall transmission speed. We chose to use the time taken for 50% of the population to become infected to define the characteristic time of infection t_c . Larger t_c values correspond to slower transmission through a population. In order to more easily assess the size of changes in transmission, we normalized (divided) the t_c for the combined networks by the respective t_c times for the direct-only networks. This provided a fold change in the t_c value that could then be compared for all signal decay rates α and transmission probabilities p_s (Fig. 2.4d). Positive log fold changes would indicate that collisions lead to a slower transmission, whereas negative values correspond to an accelerated transmission rate.

A comparison of the t_c times between the direct-only and combined networks revealed that transmission was considerably slower in the direct-only networks for signals with identical transmission probabilities (Fig. 2.4c). The addition of indirect interactions reduced the t_c time by up to 80% for signals with a low transmission probability and small decay rate (Fig. 2.4d; $p_s = 0.01$, $\alpha = 0.001$). In contrast, for signals with high transmission probability and rapid decay rate, the addition of indirect interactions had a much weaker effect, reducing the t_c times by only 15% (Fig. 2.4d; $p_s = 1$, $\alpha = 1$). Therefore, the addition of indirect transmission opportunities greatly increases the speed of transmission between group members.

This accelerated transmission derives from the impact of indirect interactions upon the connectivity (i.e. the degree) of the agents. When direct interactions are possible, the transmission rate is fully dependent on the rate of physical contacts generated by the random walks performed by each member of the population to transmit the signal. Moreover, this rate scales linearly as the number of infected individuals grows. In contrast, when indirect transmission becomes possible because an infected agent deposits a signal into the environment, the effective area for indirect transmission grows. It is as though the size of the agent grows over time, and has the effect of increasing the number of interactions, and therefore the connectivity, of infected agents. For fast decaying signals, this effect will be constrained as the signal trail will be of a limited length (see Fig. 2.4a, $\alpha = 0.1$ top panels). However, if the decay rate of a signal is sufficiently small, the trail will continue to grow enabling the entire environment to quickly become a potential transmission pathway, even though the infected agents only take up a small fraction of the total area (see Fig. 2.4a, $\alpha = 0.001$ top panels). In all cases, the increased connectivity that is gained by the indirect pathways will lower the overall diameter of the interaction network and help accelerate transmission [84].

Another major factor influencing the interaction rate between individuals in a group is their density. To assess how the density of individuals affects the rate of transmission, we produced combined networks from the agent based simulations as before, but with 10, 50 and 250 agents. As the size of the environment was fixed, the agent density varied over an order of magnitude (0.3–8% of the total area). For all agent densities, we again found that the transmission speed over combined networks was increased relative to networks composed of direct edges; signals with a low transmission probability and small decay rate saw the greatest enhancement in transmission for the combined networks (Fig. 2.5). Furthermore, the agent density also modulated the magnitude of the transmission enhancement brought about by the addition of indirect edges; at low agent densities, the strength of the enhancement was maximal (Fig. 2.5, $N = 10$), whereas at high agent densities the enhancement was weaker (Fig. 2.5, $N = 250$). In the case of a slow decaying signal with high transmission probability ($\alpha = 0.001$, $p_s = 1.0$), the difference in t_c between direct and combined networks rose from 1.4-fold to 2.3-fold for 250 to 10 agents, respectively. This suggests that the beneficial role of indirect pathways has a greater impact when agents are sparse, raising the interesting possibility that natural populations broadly distributed in space will more heavily rely on indirect transmission pathways [25].

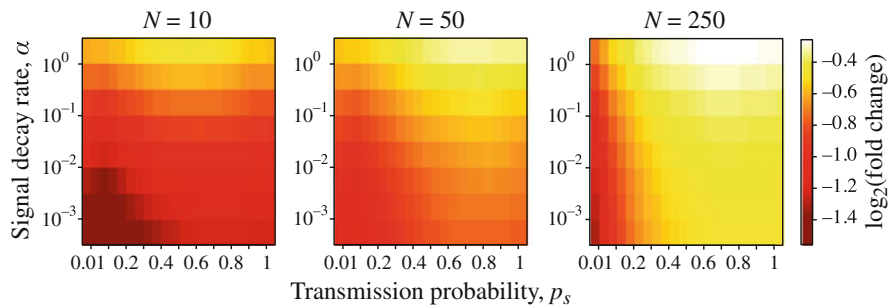


Fig. 2.5 Influence of agent density on transmission rate. Comparison of the \log_2 fold change difference in t_c between simulations using only direct interactions and those incorporating both direct and indirect interactions, when 10, 50, and 250 agents are present (densities of 0.3%, 1.6% and 8% of the total area, respectively). All values are the average of 1000 simulations

The reason for this density dependence derives from the presence of indirect edges. At low agent densities infected agents will have a low rate of physical contacts, whereas they may frequently visit locations that were previously visited by other agents. Hence, at low agent densities indirect interactions are the primary channel for transmission. As the density of the agents increases, so does the contact rate. Therefore, transmission at high agent densities will occur primarily via the strongly-weighted direct interactions.

2.3.3 Role of Territories in Space

Studies of the mobility patterns of humans and other animals have shown that individuals often revisit specific locations over time [18] and maintain specific areas as territories. In humans, examples include homes, workplaces, restaurants, and the transit routes that connect them [108]. In other animals these locations take the form of watering holes, foraging patches, leks, valuable resources that must be defended, or nesting areas where there are brood that must be regularly provisioned. Depending upon the system and context, biases towards particular locations have been given many different names, including recurrence [18, 39, 104], recursion [8, 12, 13, 33], site tenacity [50], site allegiance [26], site recognition [97], site fidelity [36, 37, 65, 83, 99], spatial fidelity [100], ortstreue [91] and route fidelity [90].

The pervasive nature of this phenomenon across so many different animal species was the motivation for the first extension of the basic random walk model, to allow for the formation of territories. The aim was to investigate how individual-level spatial preferences influence transmission of a signal across the population. We hypothesized that compared to a population in which all agents perform random walks, a population of agents that exhibit spatial fidelity should display

slower transmission over the group-level interaction network. This is because a system composed of spatially constrained agents should intuitively be dominated by short-range local interactions. Put another way, when each agent interacts with only a small set of nearest neighbours, transmission should be slower than when agents move freely as then all agents can potentially interact with all other agents.

We used a simple model of territory formation where each agent performs a random walk biased towards a single point of attraction (method described above). A unique point of attraction was used for each of the 100 agents, and the points of attraction were arranged as a uniformly spaced grid within an environment with periodic boundary conditions. Simulations were then run for various territory sizes by varying the strength of attraction γ . This resulted in a range of agent movement, from distinct territories formed by agents that remained very close to their point of attraction ($\gamma = 0.2$), to nearly non-existent territories formed by agents that were only slightly attracted to their point of attraction, and which therefore moved much like a random walker ($\gamma = 0.001$). Examples of a representative simulation output and the paths taken by each agent are shown in Fig. 2.6a.

To measure the effect of territories upon signal transmission, we compared the t_c time of the combined networks with territories to those of the original agent-based model in which agents performed an unbiased random walk. For high strengths of attraction ($\gamma = 0.2$), we observed a more than 2-fold increase in t_c for all signal decay rates and transmission probabilities (Fig. 2.6c). This confirmed our hypothesis that spatially structured populations (i.e. those where an agent's movement is spatially restricted) also experience reduced transmission speeds. We also found that this increase was greater for signals with lower transmission probabilities and larger decay rates. Under these conditions, agents were so highly constrained to the vicinity of their point of attraction that they only had very limited connectivity to their nearest neighbours (Fig. 2.6a). This led to interaction networks that were highly compartmentalised with multiple sparsely connected components (Fig. 2.6b). These features reduce mixing of the agents and hamper the ability for a signal to propagate throughout the entire population [95] (Fig. 2.6c).

For low strengths of attraction ($\gamma = 0.001$), the t_c times were very similar to the original agent-based model in which agents performed unbiased random walks (Fig. 2.6c). This is to be expected given that as the strength of attraction decreases, a movement similar to an unbiased random walk is produced. Interestingly, for intermediate strengths of attraction ($\gamma = 0.05$), both decreases and increases in transmission speed were observed, depending on the signal transmission and decay characteristics (Fig. 2.6c). Slower transmission was found when signals had large decay rates ($\alpha = 1$) and low transmission probabilities ($p_s = 0.01$). Such signals will find it difficult to exploit indirect pathways. Faster transmission occurred for signals with low decay rates, as such signals are better able to use indirect pathways. Furthermore, the speed of transmission also increased for higher transmission probabilities, even when the signal decay rate was high.

The presence of both enhancement and inhibition of transmission at intermediate attraction strengths can be explained by considering the relation between the average

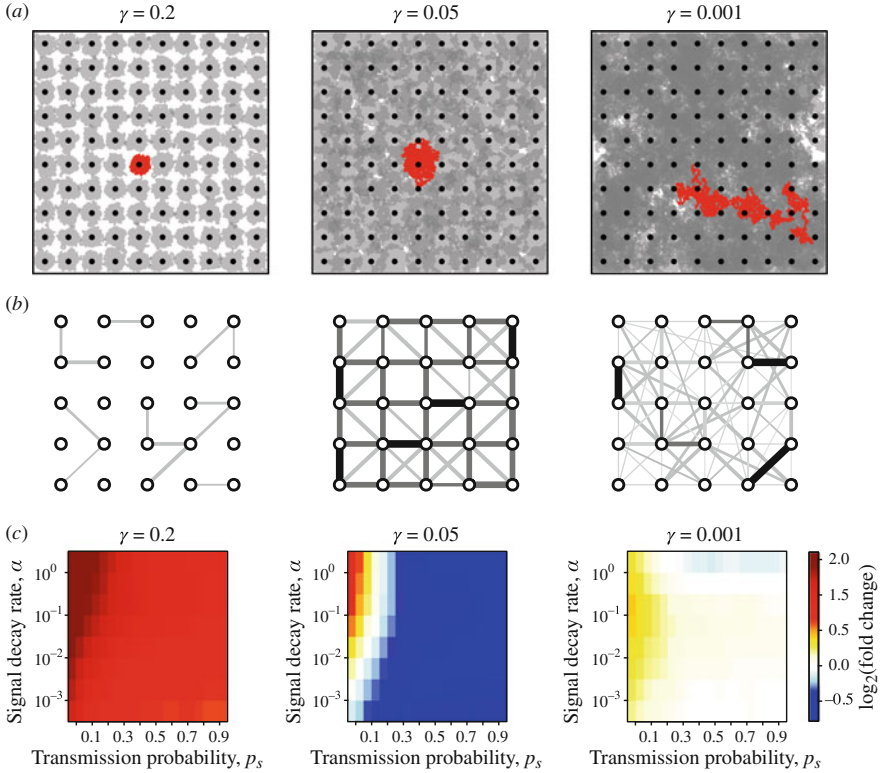


Fig. 2.6 Influence of agent territories on transmission rate. **(a)** Agent-based simulations shown at $t = 500$ time units for 100 agents with uniformly spaced points of attraction and attraction strengths $\gamma = 0.2, 0.05$ and 0.001 . *Black circles* denote the starting point of the agent, which also acts as the point of attraction. *Gray lines* show the path of each agent with *darker gray regions* denoting an overlap between multiple agents. *Red line* in each simulation shows the path of a single agent. **(b)** Illustrative time averaged interaction networks generated by the agent-based simulations. *Circles* denote agents, *thick black edges* denote direct interactions and *gray edges* denote indirect interactions. *Line darkness and thickness* corresponds to edge strength, with *darker and thicker* edges corresponding to stronger edges. **(c)** Comparison of the \log_2 fold change difference in t_c between simulations where the territory is present and those where agents perform random walks

number of interaction partners of each agent (their degree), and the average strength of their interactions (edge weights). At low attraction strengths ($\gamma = 0.001$), agents can move freely throughout the entire environment (Fig. 2.6a, right panel). This allows them to interact with potentially all other agents, but on average it results in weak interactions between any given pair of agents. This produces interaction networks in which agents have a high degree with many long-range links (i.e. links between agents with points of attraction very far from each other), but where the majority of these links are weak (Fig. 2.6c, right panel). In contrast, intermediate attraction strengths ($\gamma = 0.05$) lead to the formation of territories that significantly

overlap with all nearest neighbours, and potentially more distant agents (Fig. 2.6a, middle panel). In this scenario, an agent's movement is restricted to a much smaller area, resulting in a greater number of repeated interactions with neighbours over shorter periods of time. This generates an interaction network where each agent is connected by strongly weighted edges to its neighbours (Fig. 2.6c, middle panel). Varying the attraction strength alters the size of the territory and so also the number of neighbours it includes. However, as the attraction strength is reduced the potential area for movement also increases. This reduces the interaction rate between the agents and thus leads to an interaction network containing weaker edge strengths. Optimal transmission rates are achieved by trading-off these factors to generate a network in which the weighted diameter is minimised, which occurs when the shortest paths between agent pairs typically consist of a small number of strongly weighted edges.

2.3.4 *Role of Physical Collisions Between Agents*

Across the natural world, there are numerous examples of populations in which the individuals are so crowded that movement becomes difficult. For example, in bacterial colonies, nests of social insects [47], penguin huddles [117], and human crowds [16], the individuals may be so densely-packed together that the group itself becomes 'jammed' with some individuals unable to move. Most models of transmission over animal contact networks have ignored such physical considerations [63].

To assess how physical collisions between agents might influence signal transmission in mobile groups, we considered a simulated environment of 25×25 length units² with solid boundary conditions to allow for higher agent densities than in previous simulations. We ran three sets of simulations containing 10, 25 and 50 agents (densities of 5%, 12.5% and 25% of the total area, respectively) and measured t_c for each set. We hypothesized that the introduction of collisions would reduce transmission speeds via the constraint it places on an agent's movement, and that this slowing-down would be exaggerated at high agent densities.

As expected, we found that collisions slowed transmission for all types of signal (Fig. 2.7a). The magnitude of this effect was greater at high agent densities (Fig. 2.7b), and showed a non-linear dependence upon the signal characteristics (Fig. 2.7a). Specifically, for signals with a low transmission probability and high decay rate ($p_s = 0.01$, $\alpha = 1$), a more than 2-fold increase in the t_c time was observed.

An obvious explanation for the slower transmission when agents can collide is that the dense packing severely reduces individual movement, and constrains both direct and indirect interactions towards the immediate neighbours (Fig. 2.7c). This is in stark contrast to when collisions are absent, where infected agents can move

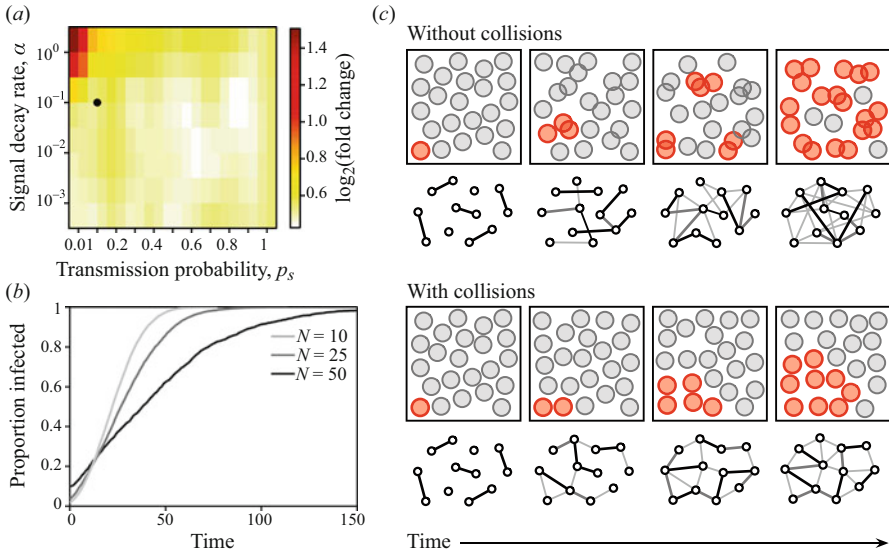


Fig. 2.7 Role of physical collisions between agents on transmission rate. (a) Comparison of the \log_2 fold change difference in t_c between simulations where collisions between agents are present and those where collisions are absent. (b) Infection time course for a signal with decay rate $\alpha = 0.1$ and transmission probability $p_s = 0.1$ (highlighted as *black point* in *panel above*) where simulations contained 10, 25 and 50 agents. (c) Illustration of simulations with physical collisions between agents absent and present. Hypothetical simulations are shown over time with *circles* representing agents that are susceptible if *grey* or infected if *red*. When collisions are absent, agents can overlap with one another. Networks below each simulation illustrate the general structural features over time. *Circles* denote agents, *thick black edges* denote direct interactions and *grey edges* denote indirect interactions. *Line darkness and thickness* corresponds to edge strength, with *darker and thicker edges* corresponding to stronger edges

throughout the environment to generate direct and indirect interactions with all other members of the population. As described previously, such increased mixing greatly reduces the overall diameter of the network and increases transmission speeds [84]. Long-range interactions also allow for a signal to be seeded at many different locations within the environment, leading to a rapid transmission across the entire population (Fig. 2.7c). Conversely, when collisions are present individuals become confined to a local area due to physical exclusion by nearby agents, hence an infected individual can only infect its nearest neighbours (Fig. 2.7c). At the highest densities, the interaction network is essentially a direct reflection of the agents' spatial locations, with the all edges reflecting short-range interactions between immediate neighbours. Such networks only allow transmission in the form of a moving infection 'front' passing through the densely-packed population. This limits the role of indirect transmission in 'seeding' infections in new areas and results in a slowing-down of transmission.

2.4 Conclusions and Future Directions

To understand how the behaviour of an individual within a group can affect the transmission of a signal, it is essential to establish causal relationships between these two organizational levels. In previous work, we applied a dynamic network methodology to an empirical dataset describing the movement and interactions of individual ants living within a communal nest [84]. However, because the behaviour of individuals could only be observed and not controlled, it was impossible to establish a direct link between individual-level behaviours and group-level transmission properties. Here, we used an agent-based model to simulate populations of individuals whose behaviour can be precisely controlled. This allowed for direct links to be made between an individual's behaviour (e.g. movement), environmental factors (e.g. signal decay rate, agent density and physical collisions), and transmission properties of the system.

Our simulations have revealed that indirect transmission pathways can play a significant role in shaping the spread of infections with differing environmental decay rates; even signals with a very low probability of transmission can when deposited into the environment propagate quickly throughout an entire group, if they are able to remain viable for some period of time. Both individual behaviour and group density also play an important role in the transmission capabilities of the group. Higher agent densities led to the faster spread of an infection. However, at very high densities, if physical collisions are considered then the movement of each individual becomes sufficiently impaired to reduce the ability for long-range interactions to form and slows transmission. More complex behaviours such as territory formation also modulated transmission rate, with a trade-off observed between maintaining stronger but shorter range interactions for smaller territories, or weaker but longer range interactions when an individual is free to diffuse throughout the entire environment. Optimal transmission was found when individuals maintained territories of intermediate size.

The focus of this work has been to simulate the transmission of a contagious signal across a group of mobile agents whose behavioural rule remains fixed over time. This idealised 'toy' model is deliberately simple to allow for an easier interpretation of the results and to provide clearer links between the behaviours of individuals and high-level collective transmission properties. Nevertheless, it is important to recognise that these simplifications ignore the fact that individuals in many real-world animal populations do exhibit strong behavioural responses to the presence of disease [35] and that these changes can significantly alter the transmission properties of the group [34]. Indeed, many animal species exhibit strong aversive behaviour to others that appear to be disease-carriers [24], and in highly social species, responses to the presence of disease may also be implemented by coordinated group-level responses. For examples, in human societies quarantines and curfews are used to reduce the potential for interactions between susceptible and infected individuals. Incorporating some form of adaptive behaviour would offer an interesting future direction for this work that the methodology is ideally suited to tackle.

This work was made possible by the availability of high-performance computing resources that enable large-scale simulations to be performed. A challenge often faced when using this type of approach is that the complexity of the underlying model makes interpretation of the results difficult. Here, we have exploited the wealth of knowledge in network theory to better understand how the structural features of the dynamic interaction networks generated by simulations influence the general transmission properties of the system. Such a combined approach offers a powerful means to bring together both numerical methods and proven mathematical theories to understand the role of direct and indirect pathways in natural systems, and provides a means to engineer new distributed systems with desired transmission capabilities.

Acknowledgements T.E.G. was supported by an EPSRC Institutional Sponsorship award from the University of Bristol (EP/P511298/1), and BrisSynBio, a BBSRC/EPSRC Synthetic Biology Research Centre (BB/L01386X/1). T.O.R is supported by an EU Marie Curie Actions Intra-European Fellowship, 'Mapping spatial interaction networks in honeybee colonies' (project number 30114). Simulations and analyses were carried out using the computational facilities of the Advanced Computing Research Centre, University of Bristol, UK.

References

1. Aiello, C., Nussear, K., Walde, A., Esque, T., Emblidge, P., Sah, P., Bansal, S., Hudson, P.: Disease dynamics during wildlife translocations: disruptions to the host population and potential consequences for transmission in desert tortoise contact networks. *Anim. Conserv.* **17**(S1), 27–39 (2014)
2. Almberg, E., Cross, P., Johnson, C., Heisey, D., Richards, B.: Modeling routes of chronic wasting disease transmission: environmental prion persistence promotes deer population decline and extinction. *PLoS One* **6**(5), e19896 (2011)
3. Axelrod, R.M.: *The Complexity of Cooperation: Agent-Based Models of Competition and Collaboration*. Princeton University Press, Harvard (1997)
4. Balcan, D., Gonçalves, B., Hu, H., Ramasco, J.J., Colizza, V., Vespignani, A.: Modeling the spatial spread of infectious diseases: the global epidemic and mobility computational model. *J. Comput. Sci.* **1**(3), 132–145 (2010)
5. Balcan, D., Hu, H., Gonçalves, B., Bajardi, P., Poletto, C., Ramasco, J.J., Paolotti, D., Perra, N., Tizzoni, M., Van den Broeck, W., Colizza, V., Vespignani, A.: Seasonal transmission potential and activity peaks of the new influenza a(h1n1): a monte carlo likelihood analysis based on human mobility. *BMC Med.* **7**(1), 45 (2009)
6. Ballerini, M., Cabibbo, N., Candelier, R., Cavagna, A., Cisbani, E., Giardina, I., Orlandi, A., Parisi, G., Procaccini, A., Viale, M., Zdravkovic, V.: Empirical investigation of starling flocks: a benchmark study in collective animal behaviour. *Anim. Behav.* **76**, 201–215 (2008)
7. Bansal, S., Grenfell, B.T., Meyers, L.A.: When individual behaviour matters: homogeneous and network models in epidemiology. *J. R. Soc. Interface* **4**(16), 879–891 (2007)
8. Bar-David, S., Bar-David, I., Cross, P.C., Ryan, S.J., Knechtel, C.U., Getz, W.M.: Methods for assessing movement path recursion with application to African buffalo in South Africa. *Ecology* **90**(9), 2467–2479 (2009)
9. Barabási, A.L.: The origin of bursts and heavy tails in human dynamics. *Nature* **435**, 207–211 (2005)

10. Barabási, A.L., Albert, R.: Emergence of scaling in random networks. *Science* **286**(5439), 509–512 (1999)
11. Barabási, A.L., Oltvai, Z.N.: Network biology: understanding the cell's functional organization. *Nat. Rev. Genet.* **5**, 101–113 (2004)
12. Benhamou, S., Riotte-Lambert, L.: Beyond the utilization distribution: identifying home range areas that are intensively exploited or repeatedly visited. *Ecol. Model.* **227**, 112–116 (2012)
13. Berger-Tal, O., Bar-David, S.: Recursive movement patterns: review and synthesis across species. *Ecol. Soc. Am.* **6**(9), 1–12 (2015)
14. Blonder, B., Dornhaus, A.: Time-ordered networks reveal limitations to information flow in ant colonies. *PLoS One* **6**(5), e20298 (2011)
15. Boccaletti, S., Latora, V., Moreno, Y., Chavez, M., Hwang, D.U.: Complex networks: structure and dynamics. *Phys. Rep.* **424**, 175–308 (2006)
16. Bode, N.W., Codling, E.A.: Human exit route choice in virtual crowd evacuations. *Anim. Behav.* **86**(2), 347–358 (2013)
17. Bohm, M., Hutchings, M., Whiteplains, P.: Contact networks in a wildlife-livestock host community: identifying high-risk individuals in the transmission of bovine TB among badgers and cattle. *PLoS One* **4**(4), e5016 (2009)
18. Boyer, D., Crofoot, M.C., Walsh, P.D.: Non-random walks in monkeys and humans. *J. R. Soc. Interface* **9**(70), 842–847 (2012)
19. Breban, R., Drake, J.M., Stallknecht, D.E., Rohani, P.: The role of environmental transmission in recurrent avian influenza epidemics. *PLoS Comput. Biol.* **5**(4), e1000346 (2009)
20. Brummitt, C.D., D'Souza, R.M., Leicht, E.: Suppressing cascades of load in interdependent networks. *Proc. Natl. Acad. Sci.* **109**(12), E680–E689 (2012)
21. Chen, S., White, B.J., Sanderson, M.W., Amrine, D.E., Ilany, A., Lanzas, C.: Highly dynamic animal contact network and implications on disease transmission. *Sci. Rep.* **4**, 4472 (2014)
22. Couzin, I.D., Krause, J., Franks, N.R., Levin, S.A.: Effective leadership and decision-making in animal groups on the move. *Nature* **433**, 513–516 (2005)
23. Crandall, D., Backstrom, L., Cosley, D., Surib, S., Huttenlocher, D., Kleinberg, J.: Inferring social ties from geographic coincidences. *Proc. Natl. Acad. Sci.* **107**(52), 22436–22441 (2010)
24. Croft, D.P., Edenbrow, M., Darden, S.K., Ramnarine, I.W., van Oosterhout, C., Cable, J.: Effect of gyrodactylid ectoparasites on host behaviour and social network structure in guppies *Poecilia reticulata*. *Behav. Ecol. Sociobiol.* **65**, 2219–2227 (2011)
25. Darden, S.K., Steffensen, L.K., Dabelsteen, T.: Information transfer among widely spaced individuals: latrines as a basis for communication networks in the swift fox? *Anim. Behav.* **75**(2), 425–432 (2008)
26. Dejean, A., Turillazzi, S.: Territoriality during trophobiosis between wasps and homopterans. *Trop. Zool.* **5**(2), 647–656 (1992)
27. DeLellis, P., di Bernardo, M., Gorochofski, T., Russo, G.: Synchronization and control of complex networks via contraction, adaptation and evolution. *IEEE Circuits Syst. Mag.* **10**, 64–82 (2010)
28. Devane, M.L., Nicol, C., Ball, A., Klena, J.D., Scholes, P., Hudson, J.A., Baker, M.G., Gilpin, B.J., Garrett, N., Savill, M.G.: The occurrence of campylobacter subtypes in environmental reservoirs and potential transmission routes. *J. Appl. Microbiol.* **98**, 980–990 (2005)
29. Dornhaus, A., Chittka, L.: Bumble bees (*bombus terrestris*) store both food and information in honeypots. *Behav. Ecol.* **16**(3), 661–666 (2005)
30. Dussutour, A., Nicolis, S.C., Shephard, G., Beekman, M., Sumpter, D.J.T.: The role of multiple pheromones in food recruitment by ants. *J. Exp. Biol.* **212**, 2337–2348 (2009)
31. Eagle, N., Pentland, A.S., Lazer, D.: Inferring friendship network structure by using mobile phone data. *Proc. Natl. Acad. Sci.* **106**(36), 15,274–15,278 (2009)
32. Edelman-Keshet, L., Watmough, J., Ermentrout, G.B.: Trail following in ants: individual properties determine population behaviour. *Behav. Ecol. Sociobiol.* **36**(2), 119–133 (1995)

33. Fagan, W.F., Lewis, M.A., Auger-Méthé, M., Avgar, T., Benhamou, S., Breed, G., LaDage, L., Schlügel, U.E., Tang, W.W., Papastamatiou, Y.P., Forester, J., Mueller, T.: Spatial memory and animal movement. *Ecol. Lett.* **16**(10), 1316–1329 (2013)
34. Fenichel, E.P., Castillo-Chavez, C., Ceddia, M.G., Chowell, G., Parra, P.A.G., Hickling, G.J., Holloway, G., Horan, R., Morin, B., Perrings, C., Springborn, M., Velazquez, L., Villalobos, C.: Adaptive human behavior in epidemiological models. *Proc. Natl. Acad. Sci.* **108**, 6306–6311 (2011)
35. Funk, S., Salathé, M., Jansen, V.A.: Modelling the influence of human behaviour on the spread of infectious diseases: a review. *J. R. Soc. Interface* **7**, 1247–1256 (2010)
36. Giuggioli, L., Bartumeus, F.: Linking site fidelity to animal movement. *J. Math. Biol.* **64**(4), 647–656 (2012)
37. Giuggioli, L., Potts, J.R., Harris, S.: Animal interactions and the emergence of territoriality. *PLoS Comput. Biol.* **7**(3), e1002008 (2011)
38. Godfrey, S.S., Bull, C.M., James, R., Murray, K.: Network structure and parasite transmission in a group living lizard, the gidgee skink, *Egernia stokesii*. *Behav. Ecol. Sociobiol.* **63**(7), 1045–1056 (2009)
39. Gonzalez, M.C., Hidalgo, C.A., Barabasi, A.L.: Understanding individual human mobility patterns. *Nature* **453**(7196), 779–782 (2008)
40. Gorochoowski, T.E.: Agent-based modelling in synthetic biology. *Essays Biochem.* **60**, 325–336 (2016)
41. Gorochoowski, T.E., di Bernardo, M., Grierson, C.: A dynamical approach to the evolution of complex networks. In: *Proceedings of the 19th International Symposium on Mathematical Theory of Networks and Systems*, pp. 1083–1087 (2010)
42. Gorochoowski, T.E., di Bernardo, M., Grierson, C.: Evolving enhanced topologies for the synchronization of dynamical complex networks. *Phys. Rev. E* **81**, 23,690 (2010)
43. Gorochoowski, T.E., di Bernardo, M., Grierson, C.S.: Evolving dynamical networks: a formalism for describing complex systems. *Complexity* **17**, 18–25 (2012)
44. Gorochoowski, T.E., di Bernardo, M., Grierson, C.S.: Using aging to visually uncover evolutionary processes on networks. *IEEE Trans. Vis. Comput. Graph.* **18**(8), 1343–1352 (2012)
45. Gorochoowski, T.E., Matyjaszkiwicz, A., Todd, T., Oak, N., Kowalska, K., Reid, S., Tsaneva-Atanasova, K.T., Savery, N.J., Grierson, C.S., di Bernardo, M.: BSIm: an agent-based tool for modeling bacterial populations in systems and synthetic biology. *PLoS One* **7**(8), e42790 (2012)
46. Grassé, P.P.: La reconstruction du nid et les coordinations interindividuelles chez *bellicositermes natalensis* et *cubitermes* sp. la théorie de la stigmergie: Essai d'interprétation du comportement des termites constructeurs. *Insect. Soc.* **6**(1), 41–80 (1959)
47. Gravish, N., Gold, G., Zangwill, A., Goodisman, M.A., Goldman, D.I.: Glass-like dynamics in confined and congested ant traffic. *Soft Matter* **11**(33), 6552–6561 (2015)
48. Grimm, V., Berger, U., Jeltsch, F., Mooij, W.M., Railsback, S.F., Thulke, H.H., Weiner, J., Wiegand, T., DeAngelis, D.L.: Pattern-oriented modeling of agent-based complex systems: lessons from ecology. *Science* **310**, 987–991 (2005)
49. Gross, T., Blasius, B.: Adaptive coevolutionary networks: a review. *J. R. Soc. Interface* **5**, 259–271 (2008)
50. Hahn, M., Maschwitz, U.: Foraging strategies and recruitment behaviour in the European harvester ant *Messor rufitarsis* (f.). *Oecologia* **68**(1), 45–51 (1985)
51. Hellweger, F.L., Clegg, R.J., Clark, J.R., Plugge, C.M., Kreft, J.U.: Advancing microbial sciences by individual-based modelling. *Nat. Rev. Microbiol.* **14**, 461–471 (2016)
52. Hethcote, H.: The mathematics of infectious diseases. *SIAM Rev.* **42**(4), 599–653 (2000)
53. Holme, P.: Modern temporal network theory: a colloquium. *Eur. Phys. J. B* **88**(9), 1–30 (2015)
54. Holme, P., Saramäki, J.: Temporal networks. *Phys. Rep.* **519**(3), 97–125 (2012)
55. Hoppensteadt, F., Waltman, P.: A problem in the theory of epidemics. *Math. Biosci.* **9**, 71–91 (1970)

56. Isella, L., Stehlé, J., Barrat, A., Cattuto, C., Pinton, J., Van den Broeck, W.: What's in a crowd? Analysis of face-to-face behavioral networks. *J. Theor. Biol.* **271**(1), 166–180 (2011)
57. Jackson, D., Martin, S., Holcombe, M., Ratnieks, F.: Longevity and detection of persistent foraging trails in pharaoh's ants, *Monomorium pharaonis* (L.). *Anim. Behav.* **71**(2), 351–359 (2006)
58. Joh, R.I., Wang, H., Weiss, H., Weitz, J.S.: Dynamics of indirectly transmitted infectious diseases with immunological threshold. *Bull. Math. Biol.* **71**(4), 845–862 (2009)
59. Karsai, M., Kivela, M., Pan, R.K., Kaski, K., Kertész, J., Barabási, A.L., Saramaki, J.: Small but slow world: How network topology and burstiness slow down spreading. *Phys. Rev. E* **83**, 025102 (2011)
60. Kermack, W.O., McKendrick, A.G.: Contributions to the mathematical theory of epidemics. III. Further studies of the problem of endemicity. *Proc. R. Soc. Lond. A Math. Phys. Eng. Sci.* **141**, 94–122 (1933)
61. King, A.J., Sueur, C., Huchard, E., Cowlshaw, G.: A rule-of-thumb based on social affiliation explains collective movements in desert baboons. *Anim. Behav.* **82**, 1337–1345 (2011)
62. Kivela, M., Pan, R.K., Kaski, K., Kertész, J., Saramäki, J., Saramaki, M.: Multiscale analysis of spreading in a large communication network. *J. Stat. Mech. Theory Exp.* **2012**(03), P03005 (2012)
63. Kramar, M., Goulet, A., Kondic, L., Mischaikow, K.: Persistence of force networks in compressed granular media. *Phys. Rev. E* **87**, 042207 (2013)
64. à l'Allemand, S., Witte, V.: A sophisticated, modular communication contributes to ecological dominance in the invasive ant *Anoplolepis gracilipes*. *Biol. Invasions* **12**(10), 3551–3561 (2010)
65. Lamb, A., Ollason, J.: Site fidelity in foraging wood-ants *Formica aquilonia* yarrow and its influence on the distribution of foragers in a regenerating environment. *Behav. Process.* **31**(2), 309–321 (1994)
66. Landau, H., Rapoport, A.: Contribution to the mathematical theory of contagion and spread of information: I. Spread through a thoroughly mixed population. *Bull. Math. Biophys.* **15**, 173 (1953)
67. Liljeros, F., Edling, C.R., Amaral, L.A.N., Stanley, H.E., Åberg, Y.: The web of human sexual contacts. *Nature* **411**(6840), 907–908 (2001)
68. Lind, P.G., da Silva, L.R., Andrade Jr, J.S., Herrmann, H.J.: Spreading gossip in social networks. *Phys. Rev. E* **76**(3), 036117 (2007)
69. Lloyd-Smith, J.O., Schreiber, S.J., Kopp, P.E., Getz, W.M.: Superspreading and the effect of individual variation on disease emergence. *Nature* **438**, 355–359 (2005)
70. Mardia, K., Jupp, P.: *Directional statistics*. John Wiley & Sons, New York (1999)
71. Mimee, M., Tucker, A., Voigt, C., Lu, T.: Programming a human commensal bacterium, *Bacteroides thetaiotaomicron*, to sense and respond to stimuli in the murine gut microbiota. *Cell Syst.* **1**, 62–71 (2015)
72. Moore, C., Newman, M.E.J.: Epidemics and percolation in small-world networks. *Phys. Rev. E* **61**, 5678–5682 (2000)
73. Moser, J.C., Blum, M.S.: Trail marking substance of the texas leaf-cutting ant: source and potency. *Science* **140**(3572), 1228–1228 (1963)
74. Nagy, M., Akos, Z., Biro, D., Vicsek, T.: Hierarchical group dynamics in pigeon flocks. *Nature* **464**, 890–893 (2010)
75. Naug, D.: Structure of the social network and its influence on transmission dynamics in a honeybee colony. *Behav. Ecol. Sociobiol.* **62**, 1719–1725 (2008)
76. Olsen, S.J., Chang, H.L., Cheung, T.Y.Y., Tang, A.F.Y., Fisk, T.L., Ooi, S.P.L., Kuo, H.W., Jiang, D.D.S., Chen, K.T., Lando, J., et al.: Transmission of the severe acute respiratory syndrome on aircraft. *N. Engl. J. Med.* **349**(25), 2416–2422 (2003)
77. Otterstatter, M., Thomson, J.: Contact networks and transmission of an intestinal pathogen in bumble bee (*bombus impatiens*) colonies. *Oecologia* **154**(2), 411–421 (2007)
78. Ozbudak, E.M., Thattai, M., Lim, H.N., Shraiman, B.I., van Oudenaarden, A.: Multistability in the lactose utilization network of *Escherichia coli*. *Nature* **427**, 737–740 (2004)

79. Paquet, P.C.: Scent-marking behavior of sympatric wolves (*Canis lupus*) and coyotes (*C. latrans*) in riding mountain national park. *Can. J. Zool.* **69**(7), 1721–1727 (1991)
80. Pastor-Satorras, R., Castellano, C., Van Mieghem, P., Vespignani, A.: Epidemic processes in complex networks. *Rev. Mod. Phys.* **87**, 925–979 (2015)
81. Pastor-Satorras, R., Vespignani, A.: Epidemic spreading in scale-free networks. *Phys. Rev. Lett.* **86**, 3200–3203 (2001)
82. Perna, A., Granovskiy, B., Garnier, S., Garnier, S.C., Labédan, M., Theraulaz, G., Fourcassié, V., Sumpter, D.J.T.: Individual rules for trail pattern formation in argentine ants (*Linepithema humile*). *PLoS Comput. Biol.* **8**, e1002592 (2012)
83. Richardson, T.O., Giuggioli, L., Franks, N.R., Sendova-Franks, A.B.: Measuring site fidelity and spatial segregation within animal societies. *Methods Ecol. Evol.* (2017). doi:10.1111/2041-210X.12751
84. Richardson, T.O., Gorochowski, T.E.: Beyond close-proximity interactions: the role of spatial coincidence in transmission networks. *J. R. Soc. Interface* **12**, 111 (2015)
85. Richardson, T.O., Liechti, J.I., Stroeymeyt, N., Bonhoeffer, S., Keller, L.: Short-term activity cycles impede information transmission in ant colonies. *PLoS Comput. Biol.* **13**(5), e1005527 (2017)
86. Rocha, L.E., Liljeros, F., Holme, P.: Simulated epidemics in an empirical spatiotemporal network of 50,185 sexual contacts. *PLoS Comput. Biol.* **7**(3), e1001109 (2011)
87. Roche, B., Drake, J.M., Rohani, P.: The curse of the pharaoh revisited: evolutionary bi-stability in environmentally transmitted pathogens. *Ecol. Lett.* **14**(6), 569–575 (2011)
88. Rohani, P., Breban, R., Stallknecht, D., Drake, J.: Environmental transmission of low pathogenicity avian influenza viruses and its implications for pathogen invasion. *Proc. Natl. Acad. Sci.* **106**(25), 10365–10369 (2009)
89. Rohani, P., Zhong, X., King, A.A.: Contact network structure explains the changing epidemiology of pertussis. *Science* **330**, 982–985 (2010)
90. Rosengren, R.: Route fidelity, visual memory and recruitment behaviour in foraging wood ants of the genus *Formica* (Hymenoptera, Formicidae), vol. 133. *Societas pro Fauna et Flora Fennica* (1971)
91. Rosengren, R., Fortelius, W.: Ortstreue in foraging ants of the *Formica rufa* group – hierarchy of orienting cues and long-term memory. *Insect. Soc.* **33**(3), 306–337 (1986)
92. Rosenthal, S.B., Twomey, C.R., Hartnett, A.T., Wu, H.S., Couzin, I.D.: Revealing the hidden networks of interaction in mobile animal groups allows prediction of complex behavioral contagion. *Proc. Natl. Acad. Sci.* **112**, 4690–4695 (2015)
93. Roshani, F., Naimi, Y.: Effects of degree-biased transmission rate and nonlinear infectivity on rumor spreading in complex social networks. *Phys. Rev. E* **85**(3), 036109 (2012)
94. Rushmore, J., Caillaud, D., Matamba, L., Stumpf, R.M., Borgatti, S.P., Altizer, S.: Social network analysis of wild chimpanzees provides insights for predicting infectious disease risk. *J. Anim. Ecol.* **82**(5), 976–986 (2013)
95. Salathé, M., Jones, J.H.: Dynamics and control of diseases in networks with community structure. *PLoS Comput. Biol.* **6**, e1000736 (2010)
96. Salathé, M., Kazandjieva, M., Lee, J., Levis, P., Feldman, M., Jones, J.: A high-resolution human contact network for infectious disease transmission. *Proc. Natl. Acad. Sci.* **107**(51), 22020–22025 (2010)
97. Salo, O., Rosengren, R.: Memory of location and site recognition in the ant *Formica uralensis* (hymenoptera: Formicidae). *Ethology* **107**(8), 737–752 (2001)
98. Schneirla, T.: Raiding and other outstanding phenomena in the behavior of army ants. *Proc. Natl. Acad. Sci.* **20**(5), 316 (1934)
99. Schwarzkopf, L., Alford, R.A.: Nomadic movement in tropical toads. *Oikos* **96**(3), 492–506 (2002)
100. Sendova-Franks, A., Franks, N.: Spatial relationships within nests of the ant *Leptothorax unifasciatus* (Latr.) and their implications for the division of labour. *Anim. Behav.* **50**(1), 121–136 (1995)

101. Sendova-Franks, A., Hayward, R., Wulf, B., Klimek, T., James, R., Planqué, R., Britton, N., Franks, N.: Emergency networking: famine relief in ant colonies. *Anim. Behav.* **79**(2), 473–485 (2010)
102. Serfling, R.: Historical review of epidemic theory. *Hum. Biol.* **24**, 145–166 (1952)
103. Smieszek, T., Salathé, M.: A low-cost method to assess the epidemiological importance of individuals in controlling infectious disease outbreaks. *BMC Med.* **11**(1), 1 (2013)
104. Song, C., Koren, T., Wang, P., Barabási, A.L.: Modelling the scaling properties of human mobility. *Nat. Phys.* **6**(10), 818–823 (2010)
105. Starnini, M., Baronchelli, A., Pastor-Satorras, R.: Modeling human dynamics of face-to-face interaction networks. *Phys. Rev. Lett.* **110**(16), 16871 (2013)
106. Starnini, M., Baronchelli, A., Pastor-Satorras, R.: Model reproduces individual, group and collective dynamics of human contact networks. *Soc. Networks* **47**, 130–137 (2016)
107. Stehlé, J., Voirin, N., Barrat, A., Cattuto, C., Isella, L., Pinton, J., Quaggiotto, M., Van den Broeck, W., Regis, C., Lina, B., Vanhems, P.: High-resolution measurements of face-to-face contact patterns in a primary school. *PLoS One* **6**(8), e23176 (2011)
108. Sun, L., Axhausen, K.W., Lee, D.H., Huang, X.: Understanding metropolitan patterns of daily encounters. *Proc. Natl. Acad. Sci.* **110**(34), 13774–13779 (2013)
109. Tabor, J., Levskaya, A., Voigt, C.: Multichromatic control of gene expression in *Escherichia coli*. *J. Mol. Biol.* **405**, 315–324 (2011)
110. Tang, W., D.A., B.: Agent-based modeling of animal movement: a review. *Geogr. Compass* **4**(7), 682–700 (2010)
111. Tesfatsion, L., Judd, K.L. (eds.): *Handbook of Computational Economics: Agent-Based Computational Economics*, vol. 2. Elsevier, Harvard (2006)
112. Tizzoni, M., Bajardi, P., Poletto, C., Ramasco, J.J., Balcan, D., Gonçalves, B., Perra, N., Colizza, V., Vespignani, A.: Real-time numerical forecast of global epidemic spreading: case study of 2009 a/h1n1pdm. *BMC Med.* **10**(1), 165 (2012)
113. Vespignani, A.: Modelling dynamical processes in complex socio-technical systems. *Nat. Phys.* **8**(1), 32–39 (2012)
114. Weber, D.J., Rutala, W.A., Miller, M.B., Huslage, K., Sickbert-Bennett, E.: Role of hospital surfaces in the transmission of emerging health care-associated pathogens: norovirus, *Clostridium difficile*, and *Acinetobacter* species. *Am. J. Infect. Control* **38**, S25–S33 (2010)
115. Wilson, E.O.: Chemical communication among workers of the fire ant *Solenopsis saevissima* (fr. smith) I. the organization of mass-foraging. *Anim. Behav.* **10**(1), 134–147 (1962)
116. Xiao, Y., French, N., Bowers, R., Clancy, D.: Pair approximations and the inclusion of indirect transmission: Theory and application to between farm transmission of *Salmonella*. *J. Theor. Biol.* **244**(3), 532–540 (2007)
117. Zitterbart, D.P., Wienecke, B., Butler, J.P., Fabry, B.: Coordinated movements prevent jamming in an emperor penguin huddle. *PLoS One* **6**(6), e20260 (2011)

Chapter 3

Sensitivity to Temporal and Topological Misinformation in Predictions of Epidemic Outbreaks

Petter Holme and Luis E.C. Rocha

Abstract Structures both in the network of who interact with whom, and the timing of these contacts, affect epidemic outbreaks. In practical applications, such information would frequently be inaccurate. In this work, we explore how the accuracy in the prediction of the final outbreak size and the time to extinction of the outbreak depend on the quality of the contact information. We find a fairly general stretched exponential dependence of the deviation from the true outbreak sizes and extinction times on the frequency of errors in both temporal and topological information.

3.1 Introduction

The propagation of infectious diseases in populations is an emergent property of the interaction between people and pathogens [1, 2]. Temporal networks is a stylized framework for describing the interaction within a population [3, 4]. It records who is in contact with whom, at what time, but omits information about the details of the encounters. In principle such details could also be important since individual, social and environmental variations affect contagion [5–7], but since our interest is to investigate the importance of temporal network structure, rather than accurate prediction, we leave them out by assuming identical individuals.

The theme of this book is to understand the role of structures in time and network topology on disease spreading. At the time of writing there are several different data sets recording the temporal contact networks of human proximity in which for example airborne diseases spread. Empirical data however is typically noisy

P. Holme (✉)

Institute of Innovative Research, Tokyo Institute of Technology, Tokyo, Japan
e-mail: holme@cns.pi.titech.ac.jp

L.E.C. Rocha

Department of Public Health Sciences, Karolinska Institutet, Stockholm, Sweden

Department of Mathematics, Université de Namur, Namur, Belgium

e-mail: luis.rocha@ki.se

either due to reporting or recording errors. This random information added to data affects the correlations in contact patterns and can potentially result in errors when analysing the data. In this chapter, we look at the sensitivity of epidemic variables with respect to simulated temporal and topological noise. Our work connects to the general questions about predictability of disease spreading [8, 9]. In this area, researchers have studied how different limitations to the models of disease spreading or incompleteness of the data affect the prediction results [10, 11]. Furthermore, researchers have investigated the internal fluctuations in the timings of contacts on the prediction of epidemic outbreaks [12–14]. The novel angle in our approach is to contrast two different types of misinformation—temporal and topological—and two different characteristics of an outbreak—the outbreak size and the time to extinction.

We use empirical, temporal proximity networks as the underlying contact structures for the disease spreading. Then we study the effects of inaccurate labeling of the nodes or time stamps on the predicted outbreak size and extinction time of susceptible-infectious-recovered (SIR) simulations on these modified data sets. The SIR model is the canonical compartmental model for diseases that gives immunity upon recovery [1]. It could be used to model e.g. HIV infection in case of treatment, that is, where the infectious individual becomes recovered after starting anti-retroviral treatment, Ebola in case of high death rate, measles and chickenpox. Simulations start with the entire population being susceptible. Then, at some point, one of the individuals becomes infectious. During this state, the infectious can spread the infection to other susceptible individuals that he or she is in contact with. As in other compartmental models, one assumes such a contagion to happen with a fixed probability per contact. After being infected for some fixed time, the infected individuals recover. When there are no infectious individuals, the outbreak is extinct. The severity of an outbreak can be quantified by various parameters. We use the outbreak size Ω (the fraction of recovered individual after the outbreak is extinct) and the extinction time τ (the duration of the outbreak in the population) as measures of the outbreak severity. In the remainder of this chapter, we will go over the background theory and technical details before we present our simulation results.

3.2 Preliminaries

3.2.1 Definitions

We represent the temporal network G as a sequence of *contacts* (i, j, t) —to be interpreted as individual i being in contact with individual j at time t [3, 4]. The number of individuals N (or *nodes*) is called the *size* of the temporal network. We use C to represent the number of contacts and M the number of pairs of individuals that are in contact at least one time. Furthermore, we let T represent the duration of the data (the time between the first and last contacts).

Table 3.1 Basic statistics of the network data sets. N is the number of individuals; C is the number of contacts; T is the total sampling time; Δt is the time resolution of the data set and M is the number of links in the projected static networks. We also list the original reference to the data

Data set	N	C	T	Δt	M	Ref.
<i>Prostitution</i>	16,730	50,632	6.00 y	1 d	39,044	[15]
<i>Conference</i>	113	20,818	2.50 d	20 s	2,196	[16]
<i>Hospital</i>	75	32,424	96.5 h	20 s	1,139	[17]
<i>School</i>	236	60,623	8.64 h	20 s	5,901	[18]
<i>Gallery</i>	200	5,943	7.80 h	20 s	714	[19]
<i>Office</i>	92	9,827	11.4 d	20 s	755	[20]

3.2.2 Contact Networks

We base our study on empirical data sets of human proximity. In other words, they capture when two persons are in close proximity, and who they are. Such data sets represent the structure over which infectious diseases spread. We list the basic statistics—sizes, sampling durations, etc.—of the data sets in Table 3.1.

Several of our data sets come from the Sociopatterns project (sociopatterns.org). These data sets are recorded by radio-frequency identification sensors that detect contacts between people within 1–1.5 m. One of these datasets comes from a conference [16] (*Conference*), another from a school (*School*) [18], a third from a hospital (*Hospital*) [17], a fourth from an art gallery (*Gallery*) [19] and a fifth from office (*Office*) [20]. The *Gallery* and *School* data sets comprise several days. We use the first day in both cases. Finally, the *Prostitution* data comes from self-reported sexual contacts between female sex-workers and their clients [15]. Since the contacts represent more than just proximity (i.e. sexual activity), this is a special form of proximity network.

3.2.3 Epidemic Simulation

The SIR simulations proceed as follows. First, all individuals are initialized to S (susceptible). Then, one node i_0 is selected randomly to become the seed of the infection. i_0 is made infectious at a random time t_0 between 0 and T . Then we go through the contacts of the data from the first to last. If the contact happens to be between a susceptible and an infectious individual, then, with a probability λ the susceptible becomes infectious. An infectious individual stays infectious δT time steps (in units of Δt) before turning recovered. In other words, δ is the fraction of the duration of the data set that a node is infectious. When there are no more infectious individuals the outbreak is considered extinct. This definition is slightly different from the most common [1], where an infectious individual has the same chance of getting recovered every time step. Our model is justified since the distribution of infectious times is narrow in real life [21] and this approach is also algorithmically simpler [22].

3.2.4 Controlling Misinformation

To model temporal misinformation, we replace a (randomly selected) fraction ϵ of the time stamps of the contacts of G by random times in the interval $[1, T]$. Similarly, for investigating the sensitivity with respect to the graph information, we randomly replace a fraction f of the node id-numbers by random numbers in the interval $[1, N]$. The only two constraints we impose in this randomization is that the resulting contacts should not be between a node and itself, and not already be present in the data. If a drawn node-id number does not satisfy the constraint, we redraw the node-id.

Technically, this approach is similar to randomization techniques [23, 24] where the temporal network structure is investigated by systematically replacing some aspect—like the timing of events—by random values and studying the response to quantities characterizing the functionality of the network (like average spreading speed, etc.). The difference is that we tune up the randomization, starting from zero (i.e. the original network).

3.2.5 Measuring Sensitivity to Misinformation

The two epidemiological variables we use to characterize an outbreak are the average final outbreak size Ω —the fraction of the population that are in state R after the outbreak is over—and the extinction time τ —the time between the first and last presence of an infected individual in the population. Let

$$\Delta_{\Omega t}(\epsilon, \delta, \lambda) = \langle \Omega(G_{\epsilon t}, \delta, \lambda) \rangle - \Omega(G, \delta, \lambda), \quad (3.1)$$

where $\langle \cdot \rangle$ denotes the average over an ensemble of networks $G_{\epsilon t}$ in which a fraction ϵ of misinformation has been imposed to the time stamps of the contacts (according to the preceding section) and G is the original network. Analogously, we define $\Delta_{\Omega n}$ for the deviation of outbreak sizes with respect to topological misinformation (i.e. rewiring of contacts generating network $G_{\epsilon n}$), and $\Delta_{\tau t}$ and $\Delta_{\tau n}$, for the deviations in the prediction of extinction times in the presence of temporal and topological noise respectively.

In principle, Δ (in any version) could be negative, but for our data sets that rarely happens—the practical minimum is $\Delta = 0$ for $\lambda = 0$. To study the ϵ dependence of Δ , we need to look at a summary statistic over the SIR parameter space. In this work, we will focus on the worst case scenario. We will use the summary statistic

$$\omega(\epsilon) = \max_{\delta, \lambda} \Delta(\epsilon, \delta, \lambda) - \min_{\delta, \lambda} \Delta(\epsilon, \delta, \lambda). \quad (3.2)$$

I.e. the difference in the range of Δ values. This quantity will be dominated by $\max_{\delta, \lambda} \Delta$, but also give a slight extra weight to networks with a negative $\min_{\delta, \lambda} \Delta$.

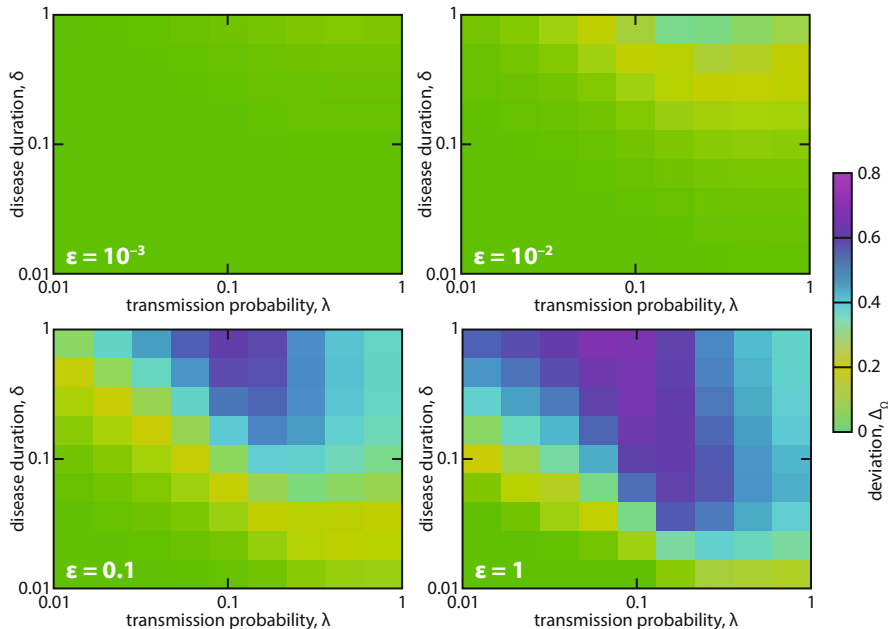


Fig. 3.1 Heatmap of the difference $\Delta\Omega$ between the average outbreak size Ω for the *Hospital* manipulated data set, where we vary a fraction ϵ of misinformation in the node identities, and the original data set. The different panels represent different values of the error rate ϵ

3.3 Results

3.3.1 Impact of Misinformation Throughout the SIR Parameter Space

As a first numerical study, we investigate $\Delta_{\Omega_n}(\epsilon, \delta, \lambda)$ (Fig. 3.1) and $\Delta_{\tau_n}(\epsilon, \delta, \lambda)$ (Fig. 3.2) for the *Hospital* data set. We chose this data set as a case study because it is of intermediate size and heterogeneity both in the temporal and topological structure. It is also highly relevant for the spread of healthcare associated infections [25]. We study an exponential sequence of ϵ -values— $\epsilon = 10^{-3}, 10^{-2}, 10^{-1}, 1$ —and, in the first place, only misinformation concerning the node identities. As seen in Fig. 3.1, the response to the noise is a non-linear function of both ϵ , δ and λ . For $\epsilon = 10^{-4}$, the impact is less than $\Delta_{\Omega_n} < 0.1$ throughout the SIR parameter space. For $\epsilon = 10^{-3}$, it reaches values around 0.2, while for larger ϵ -values, $\Delta_{\Omega_n} > 0.5$ for a large part of the parameter space. The shape of the region of high deviation also changes with ϵ . It seems, rather universally, the case that Δ reaches its maximum for large δ -values, but for large ϵ , also relatively small δ -values can show large deviations.

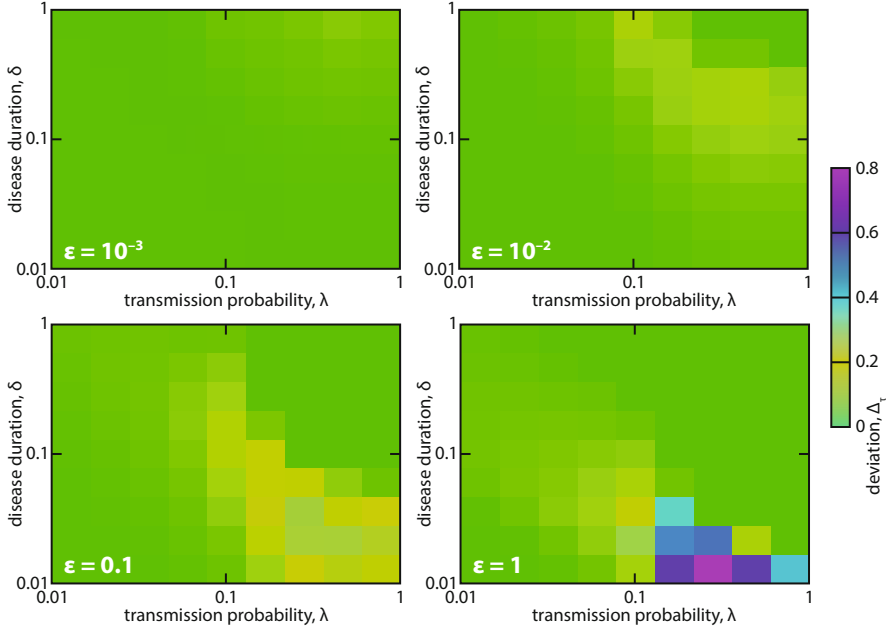


Fig. 3.2 Heat map of the difference $\Delta\tau$ between the average time to extinction τ for the *Hospital* manipulated data set, where we vary a fraction ϵ of misinformation in the node identities, and the original data set. The different panels represent different values of the error rate ϵ

For prediction of the extinction times, the absolute values of Δ are smaller for temporal misinformation in comparison to topological misinformation (Fig. 3.2). In other words, in the worst case, the prediction is somewhat better for τ than Ω . Furthermore, the parameter dependence is quite different. The maximal deviations happen for small δ -values. This is not so surprising—for relatively high values of δ and λ , the outbreak will last as long as the length T of the data set, thus making Δ small. If δ is small enough, the disease will die out without spreading much and thus Δ will also be rather small for small δ -values—the largest Δ_τ thus happens for intermediate δ .

The impact of temporal misinformation follows a similar picture to the impact of topological misinformation. The average outbreak sizes Ω differs most from the unperturbed network when the disease duration is as long as possible (Fig. 3.3). The impact changes non-linearly with both δ and λ . For the extinction time (Fig. 3.4), the situation is a bit different however. Now the largest impact does not necessarily happen for the largest δ -values. Whereas for $\epsilon \leq 10^{-2}$ it does happen at the largest δ , when $\epsilon > 10^{-2}$ the maximum is located at lower δ -values.

Several of the observations for the *Hospital* network holds for other data sets as well. However, the *Prostitution* network has a fairly different pattern (with negative $\Delta_{\Omega t}$ values for a large part of the parameter space). The origin of this anomalous behavior comes from the growth of the data (the number of contacts per time unit and the number of individuals present) was first pointed out in Ref. [14] and discussed further in Ref. [26].

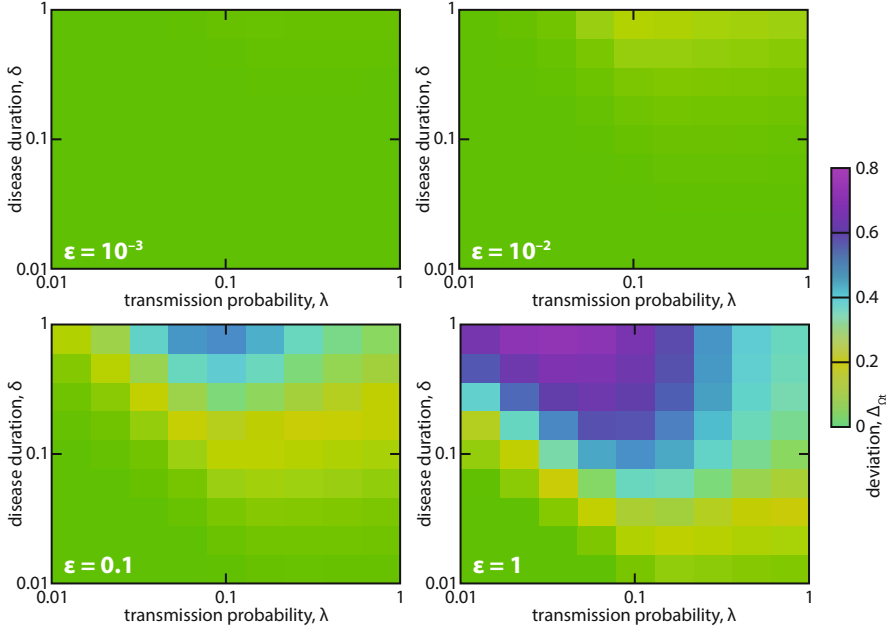


Fig. 3.3 Heat map corresponding to Fig. 3.1, but for misinformation about the timing of contacts

3.3.2 Impact of Error Rate on Prediction

To better understand the response of the level of misinformation on the prediction accuracy, we study $\omega(\epsilon)$ —the difference between the largest and smallest Δ -values (Eq. 3.2). The results for this quantity are displayed in Figs. 3.5 (for Ω) and 3.6 (for τ). The lower limit of ω is trivially $\omega(\epsilon = 0) = 0$. The shape of the $\omega(\epsilon)$ is concave (meaning the effect of increasing ϵ is largest for small ϵ). In fact, we find the functional form fitting well to a stretched exponential convergence

$$\tilde{\omega}(\epsilon) = \omega_{\max} [1 - \exp(-a\epsilon^b)], \quad (3.3)$$

where a and b are fitting parameters. The parameter b (typically in the interval $0 < b < 1$) is called the *stretching exponent* and its deviation from one indicates how much the tail is stretched compared to an exponential decay [27]. As far as we can see, there is no simple explanation for this functional form. Rather, we believe that in general the $\omega(\epsilon)$ -curves can have other shapes than stretched exponentials. Indeed, the points that are off the fitting curves (e.g. the second point in the *Gallery* graph of Fig. 3.6) are probably not a result of bad convergence, but structures in the data sets. The three fitting parameters of Eq. 3.3 are nevertheless concise ways of summarizing the shapes of the $\omega(\epsilon)$ -curves and revealing how the temporal network structure influences the impact of misinformation.

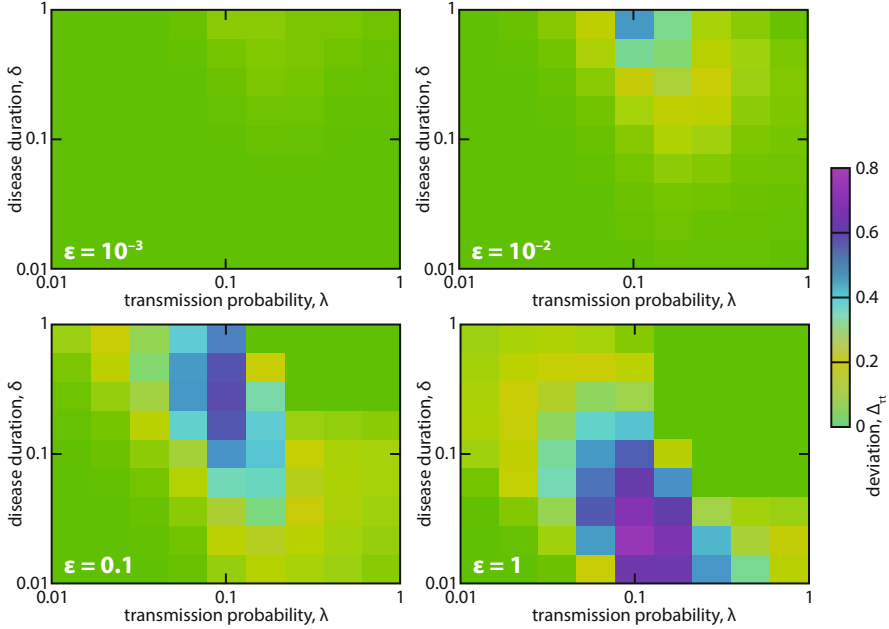


Fig. 3.4 Heat map corresponding to Fig. 3.2, but for misinformation about the timing of contacts

As alluded to, the perhaps most interesting parameter of the stretched exponential fits is the stretching exponent b . If $b = 1$, the decay is exponential. If $b < 1$ the decay is stretched (or slower than exponential). For a given error rate ϵ , the difference Δ is larger for small b . As seen in Fig. 3.7, it is indeed the case for all scenarios and data sets that $0 < b < 1$. The sparsest data set (in terms of number of contacts per individual), *Prostitution*, has a stretching exponent close to one. For the other data sets there is at least one exponent that is far off from one. There is, however, no straightforward explanation for the values of the stretching exponents in terms of the basic parameters of the temporal network data sets (as listed in Table 3.1). In future work, we will seek explanations in terms of quantities describing the temporal network structure [26, 28]. The smaller values of b for the *Conference* and *Hospital* data sets in case of τ_t happen because if we redistribute the time stamps, there will be less chance for the epidemics to die in comparison to the original data in which contacts are more concentrated at certain intervals of time. Note that in both cases, we consider night periods that correspond to absence of activity in the original data set. For the *School* data set, where individuals are clustered into network communities (i.e. the classes) the outbreak in the manipulated network is much larger since a weak randomization of id-numbers is sufficient to better distribute the links, making the network more random and thus facilitating the disease spread to the entire network. Note that in this case, there are many links at a given time step and thus the distribution of time stamps will not be much affected.

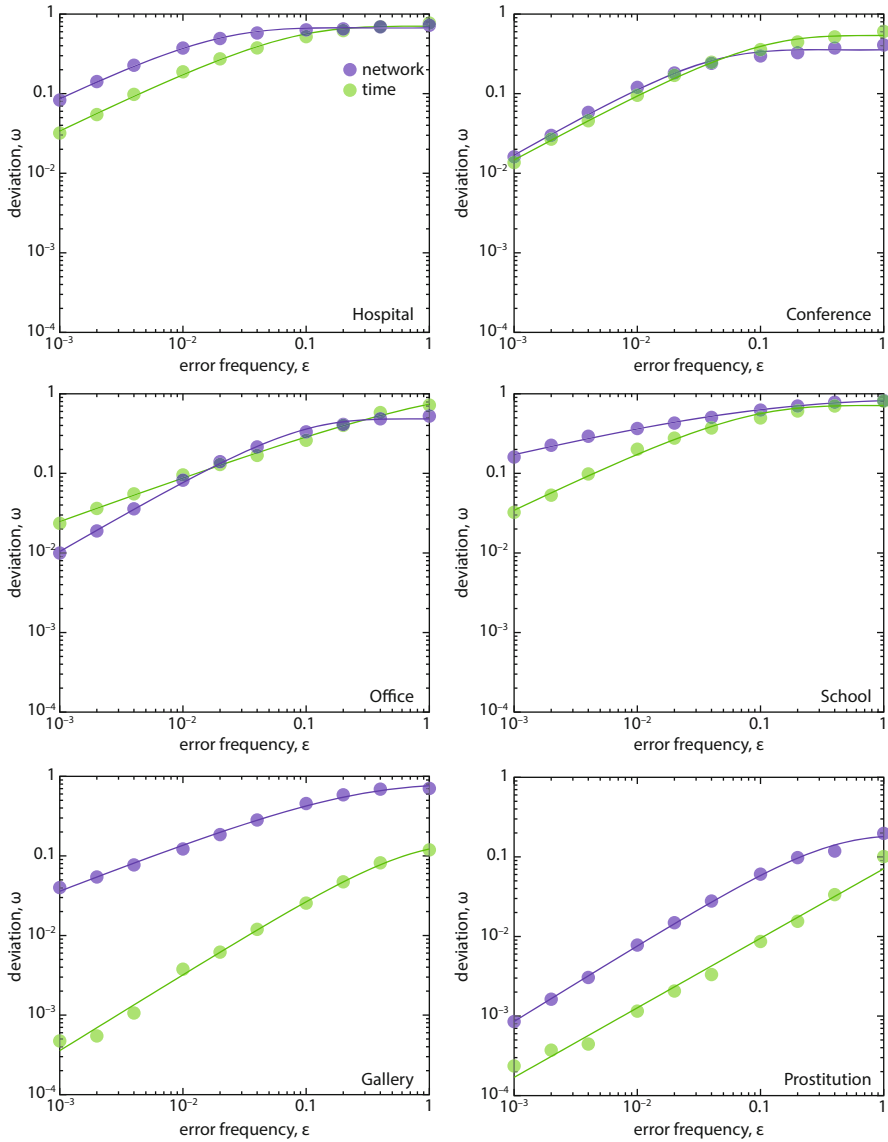


Fig. 3.5 ω_{Ω} , the difference between the largest and smallest Δ values over the SIR parameter space as a function of the node-identity misinformation frequency ϵ . The curves are Levenberg–Marquardt fits to a stretched exponential form, $\omega_{\max}(1 - e^{-a\epsilon^b})$

Gallery is a special case because groups of individuals visit the museum at fixed time slots. Possibly in this case, the disease spreads for longer times after redistributing the nodes because new links are now made between early and late museum visitors. This effect may sustain the disease for longer times and also affect the outbreak size.

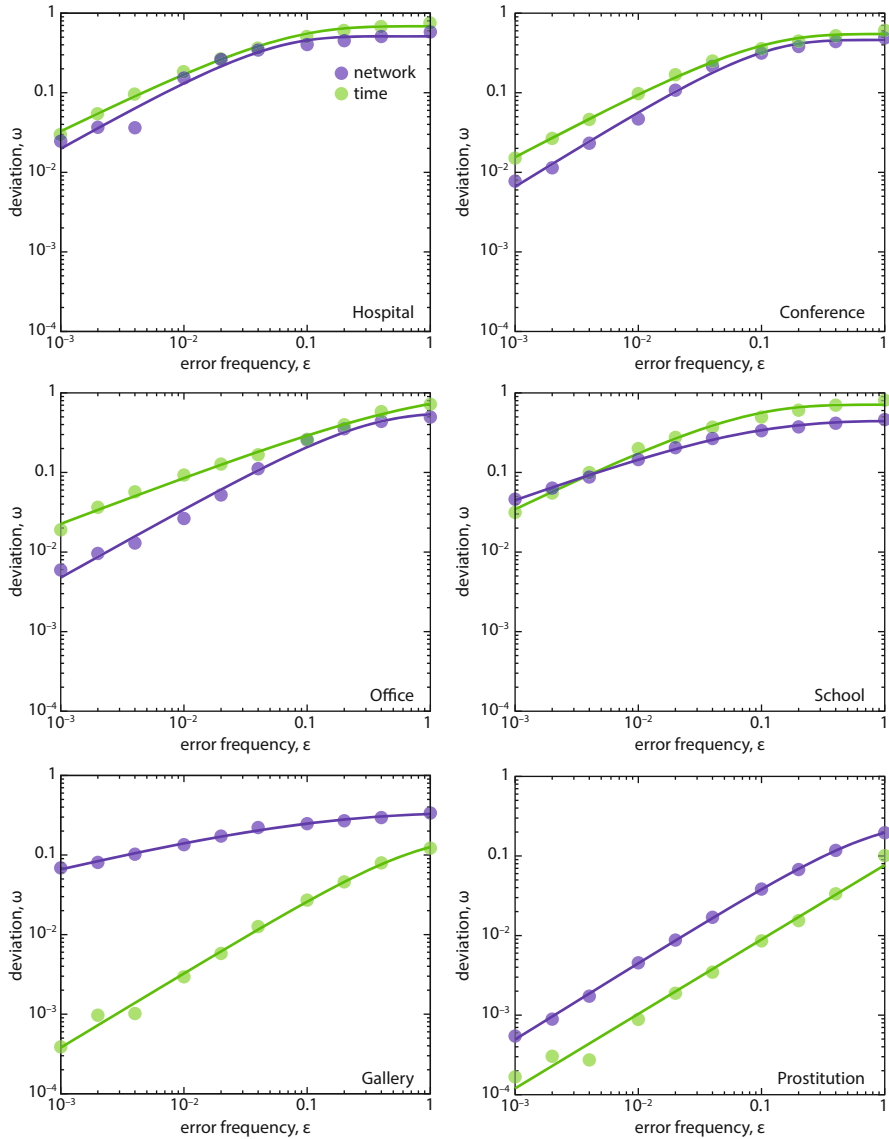
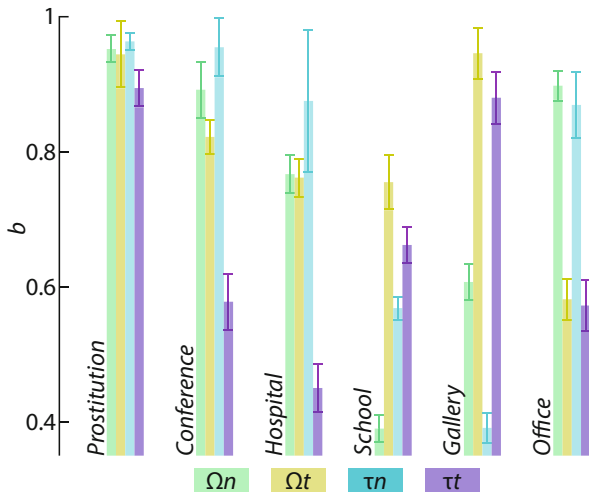


Fig. 3.6 The figure corresponding to Fig. 3.5 but for extinction times τ rather than outbreak sizes Ω

However, redistributing the time stamps will have little impact since individuals were not uniformly active during the day, for example, a new time stamp may occur at time $t = 10$ for an originally late visitor, i.e. all other connections are made at later times, therefore this new link does not contribute much to the disease spread.

Fig. 3.7 The the exponent b of the stretched exponential fits in Figs. 3.5 and 3.6. As elsewhere, Ωn relates to the response to the prediction of the average outbreak size Ω in the case of misinformation in the node identity information. Error bars represent standard errors



3.4 Discussion

In this work, we have investigated the ability to predict outbreaks of disease given imperfect data on the temporal contacts of a population. We contrast misinformation in the identities of the individuals and the time stamps of the contacts. For both misinformation scenarios, the deviation from the accurate prediction can reach 80% for 100% error frequency ϵ . Even for small errors, the deviation may differ 10 to 20% for some epidemiological parameters. However, the area in the parameter space of such a bad prediction is rather small. Furthermore, the functional dependency of the degree of mis-prediction on ϵ is similar for the two scenarios—a stretched exponential decay. At this point, we do not have any explanation for this behavior. It would be interesting to know the conditions on the temporal network structure for such a stretched exponential decay to occur.

In a wider context, this work further illustrates the importance of temporal structure for predicting disease spreading—it seems as important as the topological information. This is along the lines of observations in e.g. Refs. [26, 29–31], and a further reason for theoretical epidemiologists to investigate the role of the temporal structure in human contact patterns for disease spreading.

It would be interesting to explore this problem with alternative models for the misinformation. In real contact patterns, there would probably be more missing contacts [11] than false contacts—i.e. the assumption that the number of contacts is preserved as ϵ increases could probably be relaxed. Another step towards increased realism would be to assume the time stamps deviate from their true value by some random variable. This is expected in data collection surveys where participants have to remember the dates of events, for example, of sexual contacts [32], or when the date of the event is recorded at random times after the actual date of the event [15]. There are many other directions to proceed towards an understanding of the relation of incomplete information and the prediction of epidemics.

References

1. Hethcote, H.W.: Infectious diseases in humans. *SIAM Rev.* **32**(4), 599 (2000)
2. Keeling, M.J., Eames, K.T.: Social factors in epidemiology. *J. R. Soc. Interface* **2**(4), 295 (2005)
3. Holme, P., Saramäki, J.: Nosocomial infections. *Phys. Rep.* **519**(3), 97 (2012)
4. Holme, P.: The making of sixty nine days of close encounters at the science gallery. *Eur. Phys. J. B* **88**, 234 (2015)
5. Giesecke, J.: *Modern Infectious Disease Epidemiology*, 2nd edn. Arnold, London (2002)
6. Anderson, R.M., May, R.M.: *Infectious Diseases in Humans*. Oxford University Press, Oxford (1992)
7. Bauch, C.T., Galvani, A.P.: Compensating for population sampling in simulations of epidemic spread on temporal contact networks. *Science* **32**, 47 (2013)
8. Colizza, V., Barrat, A., Barthélemy, M., Vespignani, A.: Modern infectious disease epidemiology. *BMC Med.* **5**(1), 34 (2007)
9. Holme, P.: Data on face-to-face contacts in an office building suggest a low-cost vaccination strategy based on community linkers. *Sci. Rep.* **5**, 14462 (2015)
10. Dawson, P.M., Werkman, M., Brooks-Pollock, E., Tildesley, M.J.: The mathematics of infectious diseases. *Proc. R. Soc. Lond. B Biol. Sci.* **282**(1808), 20150205 (2015)
11. Génois, M., Vestergaard, C.L., Cattuto, C., Barrat, A.: Social organization patterns can lower disease risk without associated disease avoidance or immunity. *Nat. Commun.* **6**, 8860 EP (2015)
12. Meyers, L.A., Pourbohloul, B., Newman, M., Skowronski, D.M., Brunham, R.C.: Network reachability of real-world contact sequences. *J. Theor. Biol.* **232**, 7181 (2005)
13. Rocha, L.E.C., Blondel, V.D.: Model versions and fast algorithms for network epidemiology. *PLoS Comput. Biol.* **9**(3), e1002974 (2013)
14. Rocha, L.E.C., Liljeros, F., Holme, P.: Information content of contact-pattern representations and predictability of epidemic outbreaks. *PLoS Comput. Biol.* **7**(3), e1001109 (2011)
15. Rocha, L.E.C., Liljeros, F., Holme, P.: Modern temporal network theory: a colloquium. *Proc. Natl. Acad. Sci. USA* **107**, 5706 (2010)
16. Isella, L., Stehlé, J., Barrat, A., Cattuto, C., Pinton, J.F., van den Broeck, W.: Temporal network structures controlling disease spreading. *J. Theor. Biol.* **271**, 166 (2011)
17. Vanhems, P., Barrat, A., Cattuto, C., Pinton, J.F., Khanafer, N., Régis, C., Kim, B.A., Comte, B., Voirin, N.: Birth and death of links control disease spreading in empirical contact networks. *PLoS One* **8**, e73970 (2013)
18. Stehlé, J., Voirin, N., Barrat, A., Cattuto, C., Isella, L., Pinton, J.F., Quaggiotto, M., van den Broeck, W., Régis, C., Lina, B., Vanhems, P.: The basic reproduction number as a predictor for epidemic outbreaks in temporal networks. *PLoS One* **6**, e23176 (2011)
19. Van den Broeck, W., Quaggiotto, M., Isella, L., Barrat, A., Cattuto, C.: Temporal networks. *Leonardo* **45**(3), 285 (2012)
20. Génois, M., Vestergaard, C.L., Fournet, J., Panisson, A., Bonmarin, I., Barrat, A.: What's in a crowd? Analysis of face-to-face behavioral networks. *Netw. Sci.* **3**, 326 (2015)
21. Lloyd, A.L.: Small but slow world: how network topology and burstiness slow down spreading. *Theor. Popul. Biol.* **60**, 59 (2001)
22. Holme, P.: J. Networks and epidemic models. *Logist. Eng. Univ.* **5**, 51 (2014)
23. Holme, P.: Stretched exponential distributions in nature and economy: “fat tails” with characteristic scales. *Phys. Rev. E* **71**(4), 046119 (2005)
24. Karsai, M., Kivela, M., Pan, R.K., Kaski, K., Kertész, J., Barabási, A.L., Saramäki, J.: Realistic distributions of infectious periods in epidemic models: changing patterns of persistence and dynamics. *Phys. Rev. E* **83**(2), 025102R (2011)
25. Breathnach, A.S.: Network theory and SARS: predicting outbreak diversity. *Medicine* **33**(3), 22 (2005)

26. Holme, P.: Bursts of vertex activation and epidemics in evolving networks. *Phys. Rev. E* **64**, 022305 (2016)
27. Laherrère, J., Information dynamics shape the sexual networks of internet-mediated prostitution. Sornette, D.: *Eur. Phys. J. B* **2**(4), 525 (1998)
28. Holme, P., Masuda, N.: Simulated epidemics in an empirical spatiotemporal network of 50,185 sexual contacts. *PLoS One* **10**(3), e0120567 (2015)
29. Hock, K., Fefferman, N.H.: High-resolution measurements of face-to-face contact patterns in a primary school. *Ecol. Complex.* **12**, 34 (2012)
30. Holme, P., Liljeros, F.: Implementation of web-based respondent driven sampling among men who have sex with men in Sweden. *Sci. Rep.* **4**, 4999 (2014)
31. Valdano, E., Poletto, C., Giovannini, A., Palma, D., Savini, L., Colizza, V.: Predicting epidemic risk from past temporal contact data. *PLoS Comput. Biol.* **11**(3), e1004152 (2015)
32. Strömdahl, S., Lu, X., Bengtsson, L., Liljeros, F., Thorson, A.: Estimating potential infection transmission routes in hospital wards using wearable proximity sensors. *PLoS One* **10**(10), e0138599 (2015)

Chapter 4

Measuring Propagation with Temporal Webs

Aaron Bramson, Kevin Hoefman, Milan van den Heuvel,
Benjamin Vandermarliere, and Koen Schoors

Abstract We present a form of temporal network called a “temporal web” that connects nodes across time into a single temporally extended acyclic directed graph as a way to capture contingent behaviors. This representation is especially useful for uncovering and measuring social influence. We first present the general temporal web technique and then use it to analyze three empirical datasets: political relationships in the game EVE Online, interbank loans of the Russian banking system, and Twitter posts regarding the H1N1 vaccine. For each dataset we provide a detailed breakdown of the contingent behaviors using an approach we call temporal influence abduction. We then construct a temporal web for each one and describe the patterns of propagation found. Based on these patterns of propagation we infer more general properties of influence and the impact of certain types of behaviors in each system.

4.1 Introduction

Tracking and measuring the propagation of diseases, ideas, etc. across a population is an academic problem of great interest as well as a practical problem with important implications. There are many approaches using system dynamics and/or network contagion – and the use of various kinds of temporal networks is the latest advancement in this effort. Even within temporal networks there is significant

A. Bramson (✉)

Laboratory for Symbolic Cognitive Development, Riken Brain Science Institute, Wako, Japan

Department of General Economics, Ghent University, Ghent, Belgium

Department of Software and Information Systems, UNC Charlotte, Charlotte, NC, USA

e-mail: bramson@brain.riken.jp

B. Vandermarliere • M. van den Heuvel

Departments of General Economics and Physics, Ghent University, Ghent, Belgium

K. Schoors • K. Hoefman

Department of General Economics, Ghent University, Ghent, Belgium

© Springer Nature Singapore Pte Ltd. 2017

N. Masuda, P. Holme (eds.), *Temporal Network Epidemiology*,
Theoretical Biology, DOI 10.1007/978-981-10-5287-3_4

variation among approaches, as exemplified by the papers in this volume. Multiple demands of analysis have lead researchers towards temporal networks [31, 32]; two major pulls are preserving the time ordering of interactions [24, 39, 48, 58, 60] and constructing centrality measures for dynamic networks [8, 53, 55, 72].

Contributors to the field of temporal networks are still sorting out best practices and identifying which construction is most appropriate for which questions, and towards that end we demonstrate the use of a version of temporal networks and related measures called “temporal webs” to capture and analyze a variety of problems. Temporal webs are distinguished by their use of cross-temporal interaction and/or inheritance links. So, rather than being a sequence of network time slices connected by node membership, they are always monolithic graphs of the interaction structures across time. Similar, or perhaps even identical, structures have presumably gone by other names; we are not trying to make a serious nomenclature stake, just to identify the set of constructs we are addressing here. A pure temporal web has only cross-temporal edges to create a single acyclic directed graph. This construction has certain advantages in communication networks for which transmission and reception may take several time steps. It also embodies some specific advantages for analysis through the availability of approaches that work on large, sparse directed adjacency matrices.

In what follows we first describe the specifics in building one of the temporal web-style networks and some analysis approaches for them. The focus here is on how to approach problems, and especially the question of influence, by thinking about dynamic interactions as a temporal web. We then go on to demonstrate this approach by applying it to a variety of propagation problems on empirical networks. In this paper we use temporal webs to describe cascades of animosity on political alliance networks in the game EVE Online, understand risk propagation on the Russian interbank loan network, and the diffusion of emotional affect in the Twitter social network. Although we interpret the results in light of each subject matter, our focus here is on the methodology rather than the substantive issues, so no domain knowledge into these subjects is expected or required.

Temporal web thinking is particularly useful for identifying the most influential nodes in a network – one of the key pursuits in network epidemiology and network theory more generally [9, 12, 14, 19, 38, 40, 41, 47, 51, 52, 57, 66, 72, 73]. One can think of influence in two ways, one is to identify the role that an individual plays in a particular chain of events, and the other is to identify its potential role in all possible chains of events. In the first case it is specific to a sequence of observations and in the second it is a dispositional property (like being fragile or brave) that can only be assessed hypothetically (e.g., how much propagation would it cause under thus and such a scenario). In this paper we address the former concept of influence by examining the propagation of node characteristics in empirical temporal networks to assess the influence in that particular chain of events.

4.2 What Are Temporal Webs?

The general description of a temporal network is a mathematical structure that captures interactions across time. In the case of *dynamic networks* the key feature is that the conduits of interactions (i.e., the network edges) change across time so that the graph structure itself must be time-indexed. One can simulate dynamics across these networks, but the network properties of the nodes (e.g., how many friends one has) change over time and complicate the analysis. In contrast, a *time-layered network* typically has a static potential interaction structure and each layer reveals the interactions which occurred during that time step (e.g., how many friends one actually talked to). The difference between the two is fuzzy: if one captures a corporation's email sent each day as a temporal network it can be considered as either (1) a changing collection of interaction patterns or (2) a base set of cooperating colleagues and their de facto communications. This ambiguity is due largely to the primary strength of networks: the edges can represent any relationship among any objects, loosely defined. One is free to interpret the time-varying connections as changes in the link structure or activity across a link structure.

Here we describe a version of temporal networks that emphasizes the activity aspect, and especially transmission activity across time. Instead of capturing the interactions occurring within a time slice for each slice of time, a *temporal web* traces a link across time from the cause to effect. Although this may represent several different scenarios, it is most natural to think of it in terms of simulations with simultaneous updating in which an agent at time t has an effect on other agents at time $t + 1$. Each agent (whatever a node represents) has certain information (its state) at time t and that dictates its behavior, including its interaction behavior, at that time. Then each agent may change its state based on its behavior and input from other agents to reach a new state at $t + 1$. Thought of in this way it is obvious that for this situation the best representation is to have nodes at t interacting with (affecting) nodes at $t + 1$ instead of nodes at t . As mentioned earlier, one distinguishing feature of this approach is that the result is always a single acyclic digraph rather than connected layers of time-slice networks.

Naturally there is no limitation to discrete, integer, or uniform time increments; although that case is the simplest to represent.¹ It is possible, for example, that a message sent on Monday is read on Tuesday by some people, but on Wednesday or Friday by others. It is simple to incorporate links that connect a node at t to other nodes at $t + s$ ($s > 0$) for possibly heterogeneous s as long as the s times are discrete time steps. This is so because these connections would fit naturally into a temporal web adjacency matrix filling in spots outside the superdiagonal blocks of the t to

¹There is also no strict limitation that the interactions be instantaneous – they may be spans of time in which the agents are related – but that is a further extension beyond what we cover here. See [70, 71] for more information on link-stream graphs.

$t + 1$ connections. Allowing for continuous time dynamics is also possible, but it requires a switch in representation and an accompanying change in algorithms to analyze propagation dynamics, so we leave that out of the current work.

Pure temporal webs are a representation choice that is only appropriate for some purposes and datasets. Temporal webs can obviously be generated from temporally layered symmetric graphs by changing a link between nodes A and B at time t to a pair of directed links from $A(t)$ to $B(t + 1)$ and from $B(t)$ to $A(t + 1)$. But such a conversion naturally carries with it the assumptions and interpretation of temporal webs, which may or may not be appropriate for a particular temporally layered graph. Specifically, temporal webs (as interpreted here) are best used for actions such as the spread of a disease or communication of an idea and less appropriate for other relationships if those are not connections that happen across time (like co-location, club membership, or being connected by a road). In many cases actions are instantaneous in their effects, and a chosen time resolution (e.g., daily updates) masks the true behavioral pattern by obscuring the temporal ordering of events. Some of our methods presented below are designed to address exactly these issues by creating temporal webs from data so that they make the best of the actual influence relationships across time, even if that isn't a pure temporal network, and performing analyses using the general temporal web thinking as appropriate.

4.3 Analyzing Temporal Webs

Because pure temporal webs generate a single acyclic digraph from the entire system behavior over time, there are many off-the-shelf directed network measures that can be immediately applied. However, although these measures will return a value, the interpretation of that number is often twisted or impossible. They fail to actually inform our understanding of the system's dynamics. By analogy, I can find the average value of a list of phone numbers, but that doesn't mean the result is a viable phone number or meaningful in any other way.

As a specific example, the diameter of a temporal web is always equal to the time duration T (or infinity when some node at $t = 0$ has no time-order preserving path to some node at $t = T$). This is so because for any propagation there must be at least T steps along any path when the duration of the run is T to reach the final step. At each step all links connect from t to $t + 1$, meaning that along any path from $A(0)$ to $B(T)$ it can only make one network step per time step. So, even though diameter is a generally useful measure for assessing connectivity (even in acyclic directed social networks), it is not useful for temporal webs due to their specific construction.

Other measures, such as betweenness centrality and clustering coefficients are similarly uninformative for temporal webs for reasons discussed in [8]. There has been considerable attention paid to centrality measures on temporally layered networks [7, 32, 39, 61] as well as temporal clustering [16, 55]. The merits of these measures for those structures are still being evaluated, but their value after

adapting them for temporal webs is much more suspect. Certainly there is a desire for measures of centrality, clustering, communities and other network features on temporal webs, but they mean something slightly different than on other temporal networks and must be differently formulated. We do not put forward or test such temporal network measures in this work, but rather propose a way of thinking about transtemporal interaction data to ground the development of such measures.

4.3.1 *Temporal Knockout*

In order to benchmark the success of network measures in capturing all-things-considered influence, a measure called *temporal knockout score* (TKO) was presented in [8] and refined in [9]. At the limit of an infinite number of possible disease scenarios, this measure considers every possible disease transmission trajectory among a population, and then for each of those trajectories it tests how much the disease morbidity changes when each agent at each time is removed from the population. Because each agent at each time is represented as a node in a temporal web, these “agent-time” nodes constitute the unit of measure for infections. The agent-times (temporal nodes) that consistently have the greatest effect on the disease magnitude have the largest TKO score. Because this measure exhaustively covers all possible disease trajectories, it fully captures potential influence. By narrowing the set of test scenarios it can provide a more focused contingency analysis, such as to particular initial agents or particular interaction structures, and measure context-dependent influence.

Temporal knockout does not strictly depend on the temporal web structure, but the temporal magnitude measure of disease morbidity that it uses does depend on transtemporal records of the agent states. For example, in a hybrid temporal web in which the effects of interactions within a time-step are represented as a change in state during that period, then the interaction edges are not transtemporal; however, as long as there is inheritance of states across time it is possible to calculate the magnitude of the spread and therefore TKO. TKO does have its drawbacks however. Because it analyzes the removal of every agent at every time and reruns the dynamics in that counterfactual scenario it is extremely computationally intensive. Furthermore, the approach is intrinsically mechanistic. After the removal of an agent-time one must rerun the dynamics from that point forward, and doing so requires using some mechanism to change the agents’ states. The mechanism can be as simple as a probability of infection, but the resulting measure of influence is dependent on the mechanism used. In the case of the empirical temporal webs used in this analysis, we do not know the mechanism that produced the observed propagation, so we must either infer a mechanism and use that to determine TKO, or we can apply an alternative technique that still captures the essence of contingent marginal change in propagation magnitude.

4.3.2 Temporal Out Component Paths and Refinements

As a way to partially ameliorate the prohibitively long computational times of TKO analyses, [8] explored the use of various proxy measures on temporal webs of simulated disease spread. One class of such measures utilizes variations on the temporal out component of a node; i.e., all the nodes reachable from a given agent at a given time. One branch of variations included different ways of weighting the future: the number of reachable temporal nodes, the total length of all paths to those nodes, or the out component paths divided by the number of infections at that time step. Another branch of variations looked at ways to adjust the out component measures based on the history up to that point: weighing the contribution of each node in the out component by its in-degree, its in-component size, or the number of redundant paths leading to it. That paper also introduced a measure called *nexus centrality* as the sum of the lengths of all the paths running through that node as a way to capture bottlenecks.

Previously these measures were applied to simulated disease dynamics on a variety of network topologies to determine how well they matched TKO identifications. The results presented in [8] indicate that the temporal out component paths (TOCP) measures was highly correlated with TKO over 1000 simulations in both SEIR and SEIS dynamics. Although TOCP techniques consistently and drastically outperformed other network measures calculated on the base interaction network on average, the TKO values for temporal nodes is highly variable from run to run – sometimes even having negative values. Negative values occur when removing an agent at a certain time results in more overall infection. Though perhaps unintuitive, this results from the time varying network connections: the neighbors infected early on spread to only a few of their neighbors, but when infected later through another pathway they infect many more.

In addition to being much faster to calculate than TKO, the use of out component paths does not require a mechanism to evaluate influence. These measures can be calculated on the kinds of empirical networks examined below to provide an indication of influence. Although we won't have the TKO measure to benchmark against, it is still possible to assign a score to each temporal node for its potential impact (the full network) or actual impact (just through nodes that are “infected”) based on the temporal out components. In this chapter we analyze behavior by types of nodes rather than particular nodes and thus use aggregated measures of out component paths to assess patterns in propagation potential.

Another advantage of these out component based proxy measures for TKO is the ease of converting them into measures for quantitative (rather than categorical) propagation and to continuous time flows (rather than discrete time steps). Instead of counting the number of infected agent-time nodes in a temporal out component one can calculate the product of the time and quantity for each reachable agent-stream. This is essentially the area under the curve for the property across time starting after their interaction with the focal agent-time. The details depend on the nature of that property; for example, the calculation could use the value of the property at the time

of interaction as a baseline value and thus determine whether the interaction has had a net positive or negative effect on the property. These considerations are taken up in other work that explores continuous time temporal webs, but here we continue using temporally coarse-grained data.

4.3.3 *Temporal Influence Abduction*

When analyzing influence on empirical temporal webs, i.e., ones for which there is a particular thing that already happened, we need to rework the idea of temporal knockout to fit the application. We still would like to know how much of the propagation each agent at each time is uniquely responsible for, but the data provides what is essentially the result of one run of a simulation. In order to assess influence (rather than just the luck of how things turned out), we need to compare the observed system behavior to counterfactual behavior. As already mentioned, one way to do this is to model a generative mechanism that recreates the observed behavior and use it to populate hypothetical system behavior for comparison. Many machine learning techniques (such as Bayesian networks and Markov models) use this approach, and something like this could be developed that is specifically adapted to temporal webs. Although here we take a more direct statistical approach to describe consistent patterns in the dynamics, the behavioral patterns we uncover could very well be used for such a generative model in the future.

The general approach described here, called *temporal influence abduction* (TIA), uncovers the particular impact each agent has on the others conditional on its state (or its changing state). This is abductive because it infers the likely influence pattern as the best supported explanation for the available evidence, without proposing a mechanism by which the influence occurs. Take disease spreading as a familiar example. We can examine several relationships among nodes and their disease states to uncover whether they are playing a key role in spreading the disease: How many of one's neighbors become infected after interacting with an infected focal agent? How different is this proportion from the proportion when the focal agent is uninfected? How consistently do the each of disease states have this difference in effect across time? How similar are all the agents in these effects? Given these ideas about how influence would effect the actual spread, we can generate hypotheses about who is the most influential agent and quantitatively test them for being the best explanation.

A more concrete example makes this clearer. For categorical data, conditional infection rate can be assessed by collecting for each agent the number of (or proportion of infectable) neighbors that become infected each time step that the focal agent is infected. That is one distribution of values for each agent and across agents. Then do the same for when the agent is not infected. Those distributions can be compared using a Kolmogorov-Smirnov two-sample test to determine whether they are significantly different; the z-score acts as a measure of their being different

patterns. Of course one must also confirm that the distribution mean is higher when agents are infected than when uninfected because we are generating hypotheses about disease propagation. To check the consistency of the effect we can look at the dispersion of the two distributions; if the distribution is tight then it is more likely to be a systematic feature of propagation rather than a spurious connection. Finally, for a particular agent to be a key player in the spread of disease, an agent would also need to have consistently higher scores on all these measures than other agents.

Temporal influence abduction can also be performed on quantitative (rather than categorical) agent properties. Rather than a disease state of susceptible or infectious, one might be interested in how much confidence each person has in some idea and how that level of confidence spreads. In this case we can measure how much the confidence level of neighbors changes towards the confidence of a focal agent (total delta absolute distance) multiplied by the confidence of that focal agent (because a lack of confidence does not spread). With these values calculated at each time step we can also derive a distribution of values, but without categories we must discern patterns in the distribution endogenously. The details of such an analysis will vary from dataset to dataset depending on what the property is; for example, a lack of confidence should be down-weighted because a lack of something cannot propagate, but other properties (even other epistemic properties) may be just as contagious at every level. In what follows we provide hybrid TIA analyses of three datasets via a coarse-graining of the value ranges with the plan to follow up each one with a more in-depth continuous quantitative analysis in future work.

4.3.4 Measuring Empirical Propagation of Observed Properties

Measuring the influence of agents and times on the spread of hypothetical diseases on an abstracted social network is useful for many theoretical reasons. But capturing and understanding the observed spread of a property across an empirical network requires a distinct set of measures and methods. For one, rather than being in one or another disease state, the nodes in these systems may have multiple relevant properties that each take a range of values. Additionally, rather than probabilities of transmission, what we have is particular actual transmissions. Although we know which transmissions/interactions actually take place, we often don't have the potential interaction structure nor its implicit properties such as edge density or degree distribution. Furthermore, although we can trace the temporal node properties across the temporal web and provide measures of influence in terms of increased and decreased marginal spread, we cannot (as is usual in empirical science) bridge the correlation-causation divide nor eliminate exogenous influences.

Despite these limitations, the temporal web techniques described above can shed some new light on observed propagation dynamics. Below we examine three temporal network datasets with propagation, demonstrate the kind of conditional

effect analysis required for temporal influence abduction, examine the temporal out components of types of actors in each system, and tie these results back into substantive insights into each system.

4.4 Propagation of Frustration on Political Relation Networks

Our first dataset is a temporal web extension of Structural Balance Theory (SBT) [11, 28, 29] that makes the propagation dynamics of frustration explicit. SBT utilizes networks of positive and negative relationships among some sets of agents (typically people or countries) and provides a characterization of when such a signed social network is balanced or how frustrated it is. The implication is that frustrated relationships are more likely to change than balanced ones, and so the theory is implicitly one about the driver of signed social network dynamics. There exist analyses of how much the aggregate frustration changes over time according to generated dynamics [2, 33] or empirical networks [21, 49, 67], but no approaches that directly track the spread of frustration from triad to triad.

According to strict SBT a triad of nodes is frustrated whenever there is an odd number of negative links among them.² Thus if a triad of agents A , B , and C is frustrated then exactly one or exactly all three of its edges are negative. When any single edge (say $A \bullet \rightarrow B$) changes valence, the triad becomes balanced – regardless of whether that edge was originally positive or negative. Now consider that agents A and B were also in a triad with agent D , and that the Δ_{ABD} triad was balanced. When the edge $A \bullet \rightarrow B$ changes valence to balance the triad Δ_{ABC} , this *necessarily* causes the neighboring triad Δ_{ABD} to become unbalanced (that is, frustrated³). In fact, all triads using the $A \bullet \rightarrow B$ edge will flip between balanced and frustrated. In some cases these local changes can balance a large number of frustrated triads, increasing overall stability. This change can also create a large number of newly frustrated triads. These newly frustrated triads will likely then change other edge valences to become balanced, which serves to push the frustration starting with Δ_{ABC} through the social network. The methods presented in this section aim to track this frustration propagation using a temporal web of the network of triads.

²Originally it was formulated as an odd number of links across all paths, but the triad version has become dominant [1], cf. [22].

³For our analysis below we distinguish among strongly and weakly balanced and frustrated. Thus for us being unbalanced implies being one of the two kinds of frustrated, but that is not the only terminology. ‘Balanced’ can also refer to what we call ‘strongly balanced’, and hence our ‘weakly balanced’ would be ‘unbalanced’ but not frustrated.

4.4.1 Constructing a Network of Triads

In our general temporal web approach, the nodes carry the properties that are propagated, so to apply this technique to structural balance theory we first convert the social network with signed edges to one in which the nodes are frustrated or balanced. Our way of doing this is to construct a *triadic node* for each connected triplet of agents in the network that holds a property for the state of the triad (e.g., how many positive and negative edges or whether it is frustrated). Triadic nodes are connected by an edge whenever the triads they represent have an edge in common, but the triadic graph edge representing $A \bullet B$ in the original graph will occur as many times in the triadic graph as that edge is shared by triads.⁴ Although the number of triadic nodes depends on the structure of the network, and especially the edge density and clustering coefficient, because edges can be reused in many different triads, there are typically many times as many triadic nodes as there are agents in the social network. An example of converting a signed social network into such a triadic network appears in Fig. 4.1

In nearly all SBT analyses the network structure is static and only the sign of the links changes. For applications to empirical data, however, the approach must also accommodate dynamic networks to reflect both new or lost edges among existing

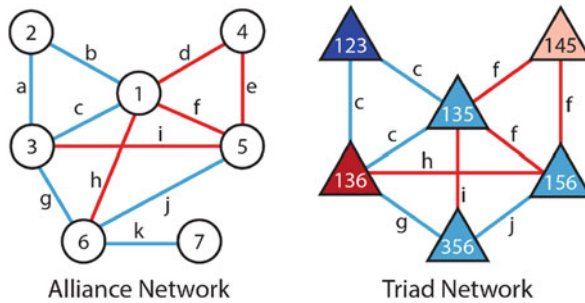


Fig. 4.1 An example of converting a signed social network into a triadic network with node properties corresponding to the frustration property of each triad in the alliance network. *Dark blue* is strongly balanced, *light blue* is weakly balanced; likewise *dark red* and *pink* are strongly and weakly frustrated, respectively. The frustrated triad Δ_{136} can become balanced by changing any one of the edges c , g , or h . Note that although changing c will balance Δ_{136} , that edge is also used by the triads Δ_{123} and Δ_{135} and so such a change will force both them to become frustrated. If Δ_{135} then rebalances itself by changing edge f this will propagate by balancing Δ_{145} and making Δ_{156} unbalanced. The triad network makes clear the level of frustration and the consequences of particular edge flips

⁴Triads can only share one or zero edges. If two triads share two edges, then they both also include the nodes that are the source and target of those edges. The minimum number of source and target nodes for two edges (in a non-reflexive and non-multigraph network) is three. If two triads share three nodes, then they are identical triads.

agents as well as agents entering and leaving the system. Just as a single edge sign flip can alter the frustration of a large number of triads that include that edge, the addition/deletion of a single new edge may sharply increase/decrease the number of triads; however, these changes cannot change the frustration of existing triads. In addition to frustration propagation we must therefore also consider exogenous events in both the changing of edge valences as well as edge creation and deletion. An aggregate approach to measuring system-wide frustration is inadequate for that task, so we focus on marginal changes in frustration in the temporal out component of state-changing triadic nodes conditional on each type of state change.

If the network is balanced, any cascade must be initiated by an exogenous change. Even in an unbalanced network, exogenous events can flip edge valences. However, as we will soon see, empirical political relationships are more tolerant to long-term frustration than SBT implies they should. Regardless of the spark, a single edge sign change will reveal itself as a change in state for all triadic nodes that use that edge. Then when any triadic node switches state – whether from frustrated to balanced or vice versa – all the neighboring triads must also flip their state unless: (1) an even number of changes occurs via multiple changing neighbors, or (2) a link is removed thus dissipating the triad.

4.4.2 Description of the Dataset

Here we apply our social frustration tracking technique to data of political standings from Eve Online (EVE), a massively multiplayer online game. Players in the game can create and run corporations, which have between zero and more than 10,000 player members. The leader (or an elected group of directors) of a corporation has complete power to determine corporate policies and represent the corporation. Corporations can (and usually do) form official collectives known as alliances. The number and sizes of alliances change over time, but most alliances have a few thousand character members (some are empty and the largest alliances include more than 17,000 members spread out over hundreds of corporations). The leadership of one of the member corporations will control the alliance and has the sole authority to set the lists of enemies, competitors, non-aggressors, and allies. These standings are set on a scale from -10 (enemy) to 10 (friend); setting it to zero means actively neutral (which is in effect like being an enemy), but they can also be removed completely. These alliance standings need not be reciprocal, though they almost always are. In the game, the icons for ships of an enemy alliance will show up as red on the screen, alerting players that they are both potential predators and potential prey. Friendly alliance ships appear green, while the icons for ships in alliances with unset standings appear white (as do asteroids, space bases, and other unaligned game objects). Attacking members of friendly alliances is possible, but such players are typically punished by their own alliance by paying a fine or being kicked out (potentially losing access to their personal assets).

The game environment is broken into 7930 solar systems of which 3524 are conquerable by the players. These conquerable systems are where the alliances can hold sovereignty over a system and ownership of its stations. Ownership allows them to decide who is allowed to place and retrieve resources from its stations, collect taxes on transactions occurring in that system, and have access to the natural resources in that system. There are many alliances that do not hold sovereignty over any systems, and therefore the political standings of these alliances only serve to establish conflict permissions. Here we perform an analysis of all alliances with more than 200 player members (which includes all sovereign alliances and many large alliances holding no territory).⁵

As already mentioned, the size and number of alliances change over time depending on player actions. We analyze the alliance standings data from 2/4/2015 to 4/17/2016 and within this time frame there are 606 unique alliances with 200 player members or more at some point during our time frame. On average there were 328 large alliances in play each day, which means there is a lot of turn-over among the alliance with 200+ members. Each alliance can set its standing to every other alliance, but in practice the standings matrix is quite sparse. The alliance matrix also reveals a block structure showing coalitions of alliances: an unofficial collection of alliances that agree to support each other without any mechanism in the game to associate them. Because the standings relationships are nearly perfectly reciprocated, we construct the triad network from a symmetric version of the standings matrix by setting the links to be negative if either direction is negative and positive if both directions are positive.⁶

We primarily make use of a looser variation of SBT for determining frustration in signed social networks that seems more appropriate for EVE. Part of the fun of a multiplayer game like EVE is attacking other players, so the stable outcome of globally friendly relationships is not expected here. Furthermore, in (game and real-world) politics we expect there to be long-standing mutual animosities among more than just two coalitions [17]. These coalitions may form temporary truces with each other to team up against a mutual and otherwise unbeatable enemy, but then go back to being enemies when the immediate threat is over. This is true for world politics [3] and we should expect the same for EVE. Thus in the looser version of SBT we consider the triple negative triads as being weakly frustrated (essentially non-frustrated but non-balanced) compared to strongly frustrated single negative triads [17, 67]. We can also consider triple positive triads as being more strongly balanced than the weaker “mutual enemy” single positive triads; however, in the current

⁵In future work we will compare these results to the subset of sovereign alliances. Because the standings of sovereign alliances have a larger effect on the players, we expect there to be a stricter adherence to structural balance, but here we are primarily interested in whether the temporal web approach can capture and detect frustration propagation.

⁶A more nuanced approach involving continuous-time analyses of frustration dynamics also weights the edges by both the value set and considering both directions. Presenting such an analysis requires details into EVE and into structural balance considerations not pertinent to our goal here of demonstrating the use of temporal webs to track frustration propagation.

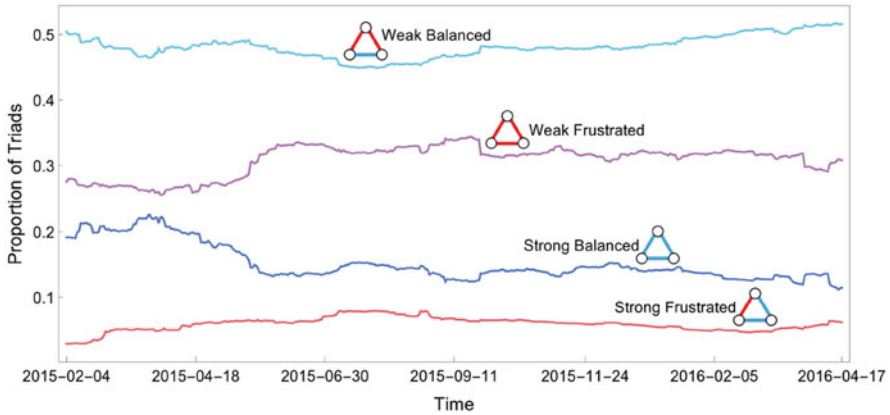






Fig. 4.2 Time series showing the proportions of each state of triad each day. Although the number of triads more than tripled during this period the relative proportions are strongly persistent. Roughly half are balanced “mutual enemy” relations while a third are weakly frustrated triple negative triads. Their consistent presence bolsters the claim that within EVE these triads do not actually cause political frustration. Triple positive triads, which are the norm within coalitions, are overall underrepresented. On average across time less than 6% of the triads are truly frustrated, lending evidence to a loose structural balance mechanism in this context that is consistent with anecdotal accounts within the game

analysis we count them both equally as balanced. As you can see in Fig. 4.2, the triple negative weakly frustrated triads make up roughly a third of the triads across time. Within coalitions everybody is friendly with each other and they all share the same enemies, but nearly everybody in coalition *X* is aggressive to everybody in both coalitions *Y* and *Z*.

4.4.3 Temporal Web Analysis Results

The set of alliances having at least 200 members went from 311 at the beginning, peaked at 349 in the middle of the dataset, and dropped to 312 at the end, but the number of triads steadily (though nonmonotonically) grew from 50,491 to 170,296. The disproportionate increase in the number of triads comes from an increase in edge density in the alliance network. So the network here is dynamic both in the sense that nodes come in and drop out of the system and that the edges among them also form, dissolve, and change sign. This poses no difficulties for a temporal web analysis because each agent at each period is a distinct temporal node object. They are only connected to future selves through a chain of cross-temporal links. And because our temporal nodes are the triads, this opens the possibility to identify cases when ending a relationship that is part of a frustrated triad is used instead of balancing it.

Table 4.1 Summary results showing the proportion of the triad states when they are created, that exist in the system over time, and when they are removed. This only includes adding and removing triads through link creation and destruction; i.e., excluding nodes entering/leaving. Approximately 8% of newly formed triads are strongly frustrated. The type proportions at creation closely match the overall number in the system with a bit less strong frustration ($\sim 5.8\%$) and a bit more weak frustration. The proportions of eliminated triad types show a greater focus on strongly balanced and strongly frustrated triads ($\sim 12\%$), and a tendency against dissolving weakly frustrated triads

Scenario				
Triadic node creation	0.185	0.0799	0.491	0.244
Triadic node persistence	0.146	0.0584	0.484	0.312
Triadic node dissolution	0.228	0.123	0.443	0.206

In order to determine whether alliances use link elimination as a strategy for frustration elimination, we look at the difference in rates of triad dissolution for triads of each of the four kinds of frustration. Because relationship changes may be motivated by a variety of game considerations besides political frustration, there will be a base rate of dissolution. The hypothesis is that dissolution counts as a strategy only if the rate for strongly frustrated triads is significantly greater than the base rate. Although the overall number of triads increases over time, there are still 116,799 cases of standings links being removed. Removing a standings link from the alliance network removes all the triadic nodes and triadic links that utilize it, and doing so cannot affect the state of the remaining triads. Conversely, we can look at how many frustrated triads are generated when (1) a new alliance enters the considered set or (2) a new link is generated between existing alliances.

From the results in Table 4.1 we can see that around 8% of new triads formed through link creation inject strong frustration into the system. This proportion is not much higher than the proportion of strongly frustrated triads across time, meaning both that on average the frustration introduced is partially resolved (possibly through the removal of the links that created the strongly frustrated triads) and that this process is potentially responsible for injecting all of the observed frustration. However, recall that if this is the case then it would also mean that frustration rarely propagates and is instead sequestered to the original frustrated triad until it is dissolved. To determine to what degree frustration propagates we need to look both at state transition behavior and neighbor behavior.

Table 4.2 shows the relative rates of triad state transformations to reveal biases in how the different triads states change their states. Most notably we see how stable the triads' states are: on average more than 99% of all triad states stay the same from day to day. Strongly frustrated triads are the least stable, but only by a small margin. Because the political standings, and therefore triad states, can be long lasting even when there is frustration, we also look at the next state of the triad conditional on some change occurring in Table 4.3.

Table 4.3 shows the same counts as Table 4.2 but renormalized without including the static entries. From this we can more clearly see the changes that occur when they actually occur. The first observation is the large proportions of triads that are

Table 4.2 Summary results of the proportions of triad state changes including though the deletion of edges (but not nodes). Blue edges are positive, red edges are negative, and gray triads are nonexistent. The large proportions along the diagonal indicate that alliance standings are highly stable and therefore from day to day all triad states are likely to persist. Notably the strongly frustrated triads are the least stable while the weakly frustrated (triple negative) are the most stable by tiny margins



















Triad state at time t	Triad state at time $t + 1$				
					
 \rightarrow ?	0.993	0.00251	0.000624	0.00000171	0.00415
 \rightarrow ?	0.00346	0.987	0.00408	0.000119	0.00561
 \rightarrow ?	0.0000480	0.000372	0.996	0.00125	0.00243
 \rightarrow ?	0.000000729	0.00000627	0.00129	0.997	0.00175

Table 4.3 Summary results of the proportions of conditional triad state changes including through the creation and deletion of edges (but not nodes). Blue edges are positive, red edges are negative, and gray triads are nonexistent. Although it is possible for triads to change multiple edge valences in one step because of our use of daily data, we see here that most changes are one edge flip away. However, in the first row we can see that nearly 8.5% of changes from strongly balanced triads go to weakly balanced within a day. This is seven times more frequent than the next largest 2-step change (from weakly balanced straight to strongly balanced). Similarly, weakly balanced triads are more than three times more likely to become weakly frustrated than strongly frustrated. This evidence supports a claim of general avoidance of strong frustration

Triad state at time t	Triad state at time $t + 1$				
					
 \rightarrow ?		0.344	0.0856	0.000235	0.570
 \rightarrow ?	0.261		0.307	0.00895	0.423
 \rightarrow ?	0.0117	0.0907		0.305	0.592
 \rightarrow ?	0.000240	0.00206	0.423		0.575

dissolved through link removal; except for strongly frustrated triads they are more likely to be removed than changed. The second observation is that when a triad does change state it is proportionally more often to be a single valence flip away. Note that because of our daily time resolution, it is possible for many edges to change to occur in one step, but what we see is that this is a rare occurrence. This is consistent with the high level of standing persistence seen in Table 4.2.

Looking in more detail at the differences among triads states, we can see that when single negative (strongly frustrated) triads change they are split similarly between becoming triple positive or weakly balanced triads and the least likely to dissolve. In contrast, the single positive (weakly balanced) triads are three times more likely to switch to weakly frustrated than to strongly frustrated and are the most likely to be dissolved. This may indicate a conscious aversion to making changes that generate strongly frustrated triads, so much so that it is better to

dissolve the relationship than to make it frustrated. All of this helps us understand the dynamics of frustration changes in the dataset, but does not yet address the question of propagation.

We can look more directly at the propagation effects in Fig. 4.3. The cases in which non-existent triads stay non-existent (bottom row) act as baseline rates for the transitions of neighbors because the neighbors are not reacting to anything.⁷

In the row showing proportions of strongly frustrated triads becoming strongly balanced ($\text{⚡} \rightarrow \text{⚡}$) the 14.3% of neighbors also changing from strongly frustrated to strongly balanced (red highlight in Fig. 4.3) is much higher than the baseline (0.02%). These are mostly neighbors sharing the negative edge, so when it becomes positive all triads using it gain an extra positive edge. This change also balances neighboring weakly frustrated triads by converting one negative link to a positive link (13.2% of neighbors). You can also see in that row that 5.34% of neighbors change from weakly balanced to strongly frustrated (green highlight in Fig. 4.3). While this number is small, it is still a considerable number of new strongly frustrated triads and much larger than the base line rate. This is one side of the propagation phenomenon we are looking for – the side of balancing by changing from negative to positive.

Because frustrated triads can also become (weakly) balanced by changing one of the positive links to a negative, there is another side of the propagation story. Specifically, in the row of strongly frustrated changing to weakly balanced ($\text{⚡} \rightarrow \text{⚡}$) we see that 7.6% of the neighboring triads go from strongly balanced to strongly frustrated (blue highlight in Fig. 4.3), while 10.36% change from strongly frustrated to weakly balanced (yellow highlight in Fig. 4.3). So for both directions of edge changes, more neighboring triads become balanced than become frustrated. Together this indicates that whether it is an explicit decision or an implicit pressure, it is the case that changes in standings tend to reduce the overall (strong) frustration of the system. This tentative conclusion stands as evidence in defense of loose structural balance.

Looking at the behaviors of individual triads is probably not insightful, so we focused on characterizing the behavior/influence of triad types. The proportions of conditional reactions in Fig. 4.3 combined with the proportion of behaviors in Tables 4.1 and 4.2 go far in capturing the behavior of the system. These state and rate proportions provide the necessary information to generate simulations with similar behaviors and/or perform a Bayesian-style analysis of the alliances' behavior. However, as stated in Sect. 4.3.3, we are taking a more direct descriptive approach in this work.

⁷One can include all static focal node states, but the number of cases of triads staying non-existent overwhelms the effect of including the others so that the largest differences is one in ten thousand. Furthermore, a comparison of the existent static to the non-existent static cases shows that the neighbor transition proportions are similar to within one in a thousand, bolstering our claim that these static cases can act as a baseline.

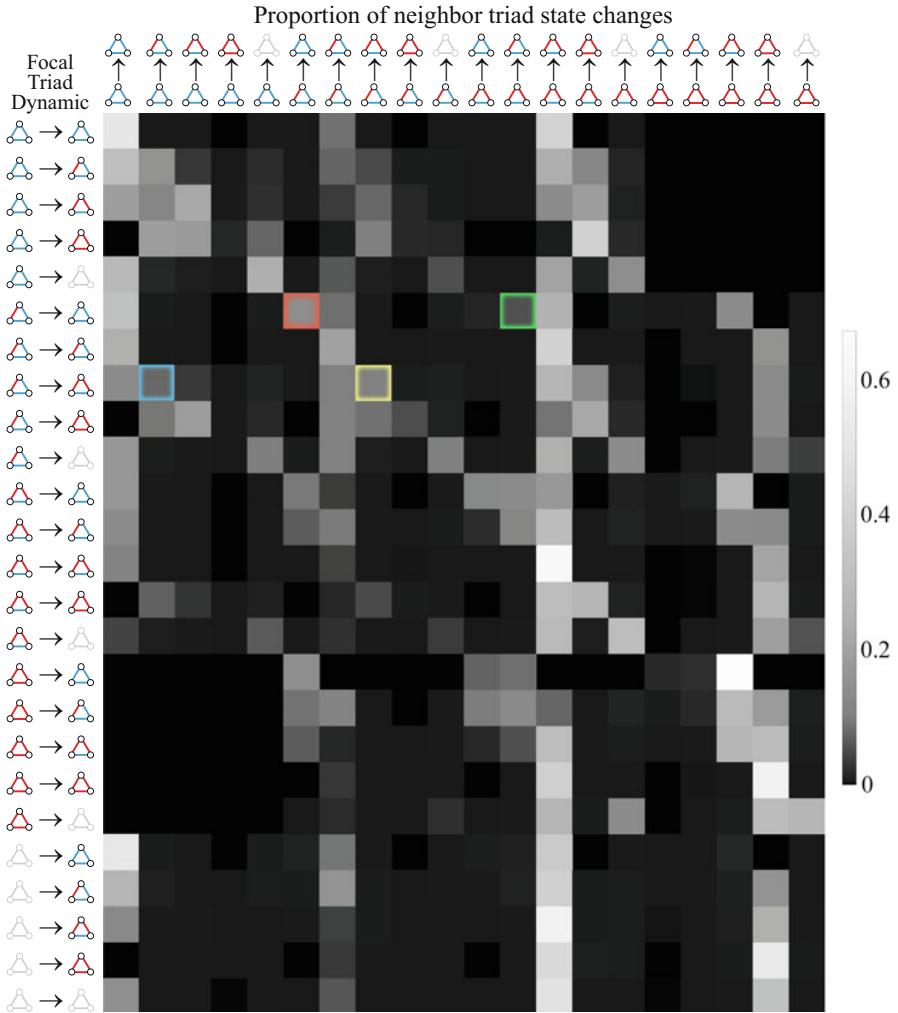


Fig. 4.3 Summary results of the triad states changes among neighbors, contingent on each type of focal node state change (including creation through new links and no change). Specifically, for each focal triad’s change from t to $t + 1$, the figure shows the proportion of each type of triad state changes of those triads that share an edge in the standings data during that same period (i.e. neighbors in the network of triadic nodes). The construction of the triad network requires that when an edge in the standings network changes state, all triads containing (and connected by) that edge also change state. *Boxed cells* are discussed in more detail in the text

Collectively the results show that, based on immediate neighbors, frustration does propagate to some degree, but it loses momentum with each step as more stabilize than become frustrated. These averages across all system dynamics are used to detect global tendencies, but below we use the out components of balancing

triads to track the trajectories of each frustration cascade to see if these conditional neighbor changes chain together. Before moving on to that topic, we make some other conclusions directly related to structural balance theory.

Edge Elimination Strategy. We can discern from the results so far the degree to which edge removal is used by the alliances as an (implicit or explicit) strategy to reduce political frustration. This can be seen both from strongly frustrated triads transitioning into nonexistent ones, and also the relative frequency of transitioning into a nonexistent state instead of a frustrated one. Table 4.2 shows that strongly frustrated triads have the highest rate (by a small margin) of being dissolved (0.00561), indicating that eliminating the triads makes up some of the difference of their lower stability. Table 4.3 shows that conditional on being in the strongly frustrated state, the triads are relatively more likely to switch to a neighboring state (i.e., change one edge valence) than to eliminate the frustrated triad through edge deletion. This result is counter to the hypothesis of an explicit edge elimination strategy.

Now recall that when a triad changes state to balance itself, that edge valence change will unbalance any other balanced triads also using that edge. Table 4.3 shows that these balanced triads tend to dissolve rather than become strongly frustrated, lending evidence to a claim that edge elimination may count as a strategy for frustration *avoidance* rather than frustration removal. One way to think of this is that when a strongly frustrated triad is forced to change it is usually to one form of balanced triad, so there is little pressure to dissolve it unless players were consciously considering the aftershocks it would create. The observed change pattern thus provides evidence that the players commanding alliances in EVE are largely obeying the tenets of structural balance implicitly but not purposefully.

Temporal Influence Abduction. The results described above comprise the basis of the temporal influence abduction analysis described in Sect. 4.3.3. Rather than assessing whether any particular alliance, or any particular triad, is responsible for propagating frustration, we have investigated the behaviors of each type of triad state. We are interested in whether a frustrated triad is more likely than not to cause other triads to become frustrated in an effort to balance itself. To do this we need to look at the neighbors of changing triads to see what effects they have, and specifically we are interested in triads that change from (strongly) frustrated triads to balanced triads. Figure 4.3 shows the proportions of all changes in neighbors immediately effected by changes in (or lack thereof) of each agent at each period. Although standings among persistent alliances are rather stable (indicated by the low variance in proportions for the rows with unchanging focal frustration), when there is a change the nature of structural balance forces a change in the frustration/stability of some neighboring triads. So this reflects less the behavior of the players and more the rules of structural balance. However, we can confirm that certain transitions are more likely than others to shift frustrations to other triads.

A strongly frustrated triad has one negative edge and it can become balanced by either changing that negative one to a positive one (26.1%) or by changing one of the positive edges to another negative one (30.7%). When changing to a positive

one, that would propagate by converting weakly balanced neighboring triads into strongly frustrated ones, but this doesn't happen often (9.1%). Strongly balanced triple positive triads convert to strongly frustrated triads 24.4% of the time, thus they are the main vehicle for frustration propagation. In fact, from Table 4.3 you can see that the strongly balanced triads are 3.8 times more likely to become strongly frustrated, and even then 57% of the time they do change, they are dissolved instead.

Triple positive triads are common among the alliances within a coalition, and when a pair of such alliances have a falling out all of the other alliances in the coalition are still friends with both. This causes an upswell in frustration: 62% of neighbors stay the same (mostly because they weren't using the edge that went negative) but 15% become strongly frustrated. When a triple positive instead skips over the strongly frustrated step and directly becomes weakly balanced (adding two negative), 12% of its coalition partner's triads become strongly frustrated, although 22% also skip the frustration step and pick sides within a day. From this it doesn't seem that balancing triads is the main source of frustration propagation, but we can look from another perspective to make sure.

These probabilities so far have been conditional on the focal triad dynamic, but we get a slightly different view when we normalize by all the events that could directly create a frustrated neighbor (i.e., proportions down the column of all focal triad transitions that result in strongly frustrated neighbors). Frustrated focal agents spreading frustration when they become (either kind of) balanced only make up 13.6% of the frustration injection into the system. 27.3% comes from triple positives gaining a negative edge just mentioned above, 21.5% comes from weakly balanced triads becoming weakly frustrated, and 9.4% comes from when weakly balanced triads become frustrated. All other transitions induce 5% or less of the frustration into the system. From this data we see that changes to balance the network do happen, but they tend to remove frustration rather than spread it. Most frustration injection comes from pairs of alliances in a coalition becoming enemies; this destabilizes both their internal coalition triads and their mutual enemy triads.

Temporal Out Components. The above analysis looks at immediate changes to understand how well the micro-dynamics conform to structural balance, but propagation is a macro-dynamic that can only be discerned by looking at longer-term patterns. This is where we pull in the temporal out component. We want to understand how far the effects of correcting for frustration ripple through the network. There is a trigger event (the reduction in frustration of a triad) that causes immediate flips in the frustration state of some neighboring triads. If any neighboring triads become frustrated from these flips, then that counts as part of the magnitude of the trigger node. We follow all these frustrated triads across time (because they need not react immediately) to see if they balance themselves and push the frustration to their neighbors (potentially back to the original trigger). We count both the number of triads that are frustrated (cumulative cases) and the number of frustrated temporal nodes (magnitude) that could be the result of that trigger.

Of course there are also link deletions that cut off frustration without propagation and multiple trajectories in which changes from triggers effect the same downstream

temporal nodes. For deletions we do not need any adjustment; whether it is a conscious strategy of the alliance leaders or an implicit reaction to their situation, deleting an edge involved in a frustrated triad simply removes the frustration without propagating it. For frustrated triads in overlapping out components (i.e., causal overdetermination) we have three choices: count it for both because either is sufficient (common to cumulative cases conditional on the initial agent), weight the contribution by the amount of inflow redundancy (like in [8]), or count it for neither because neither *uniquely* contributes to the spread (like TKO in [9]). Really, we can parameterize the weighting to run the spectrum from counting none or all of the redundant inflow, but conceptually there is a difference here compared to disease propagation: one edge flip frustrates a balanced triad, but a second one balances it again. Thus redundant paths of frustration propagation combine in structural balance in a way that is very different from most other systems in which it merely accumulates. Because of this a frustrated triad would not be doubly caused by frustration coming in from two paths, the two sources of frustration would instead combine to balance the triad. So we can ignore redundancy here and simply look at the number of strongly frustrated triads in the frustrated subgraph of the temporal out component of each trigger event.

As shown in Fig. 4.4, each cascade event is triggered by a frustrated triad becoming balanced and pushing that frustration to neighboring triads. The duration of a cascade event is the maximal path length between the trigger and all the nodes in its temporal out component (i.e., the longest branch). The cumulative cases measure counts the number of distinct triads that become frustrated as a result of the trigger event, and only counts itself if it again becomes frustrated. Magnitude counts the distinct temporal nodes in the temporal out component that are “infected” by the trigger event.

You can see in Fig. 4.5 the duration (length) and magnitude (color) of each cascade in our time period. If multiple triads trigger the exact same changes in neighboring triads, then that is recorded as a single cascade. The blocks seen in the figure are the result of separate, but related, cascades in which initially different subsets of triads were affected by the initial trigger events (because of slightly different sets of neighboring triads) that typically converge on one chain of propagation causing them to end at the same time.

The duration of the infections is 45% correlated with the magnitude, and the cumulative cases measure is 91.9% correlated. The maximum value for magnitude equals cumulative cases times duration, and indeed that combination is 94.9% correlated with magnitude. In general, the correlation with cumulative cases diminishes as the amount of reinfection increases, thus indicating that in this dataset the reinfection rate is low. We already know that persistence of state is high for triads; however, with frustration lasting as long it does here, there would be ample time for reinfection and we do not see it.

Because the cumulative cases measure correlates much better with magnitude than duration, we can infer that the breadth of the infection makes up the greatest volume of the cascade size despite the apparent long durations. In this case the maximal path length is much longer than the average path length across all the

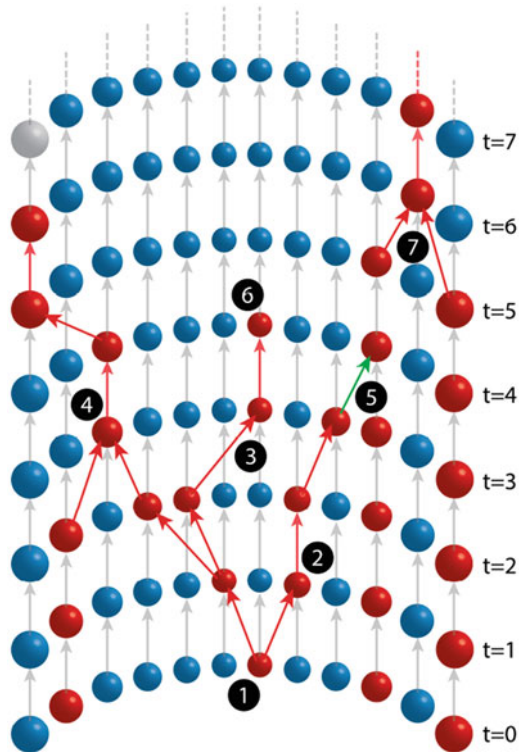


Fig. 4.4 This diagram represents an idealized version of the triad network being analyzed to demonstrate key points in the analysis (non-active triad links and weakly frustration details are left off for clarity). (1) A trigger event occurs whenever a triad converts from strongly frustrated to either kind of balanced triad and that change is not part of a chain of events originating earlier. (2) The frustration may propagate to neighboring triads if they become strongly frustrated while the triggering nodes becomes balanced. (3) It is possible that the frustration will get pushed back onto the originating node. (4) In some cases multiple node balancing events may lead into a new frustrated triad; in such cases both are considered responsible and the propagation calculations are considered independently. (5) If the neighboring node is already frustrated then this does not count as spreading and path ends there. (6) In some cases a triad will balance without spreading frustration at all, which also marks the end of the path. (7) Multiple balancing events can initiate the same series of spread events, in which case they are all considered triggers. Focusing on the trigger event at (1), we can calculate the cumulative cases (8 distinct triads including itself due to reinfection), the longevity (6 time steps for the longest path), and the magnitude (12 frustrated temporal nodes in the frustrated subgraph of its temporal out component)

branches. It could be that weighting the triads’ frustration by their importance will reveal that the propagation pushes the frustration to corners of the systems where it doesn’t interfere with players’ activities (more below).

There are 439 days in the dataset, but because triggers and propagations require changes in triad and neighboring triad states, there are two fewer time steps for

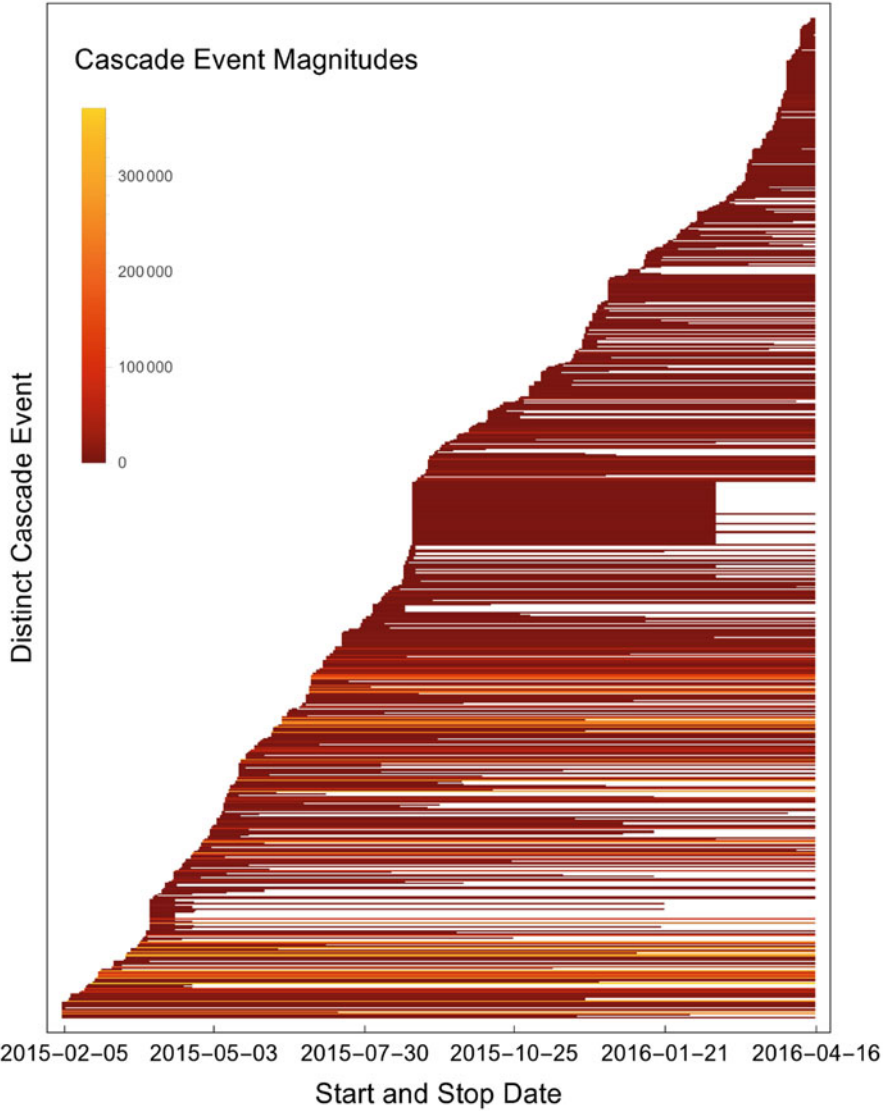


Fig. 4.5 Each cascade event is represented by a *horizontal line* from its trigger day to its end day. Colors represent the eventual magnitude of that event. As mentioned earlier, there is a baseline level of frustration in the system and 98.7% of strongly frustrated triads stay that way; this can be seen from the long durations of the cascades even when the magnitude (and hence the number of cumulative cases) is low

this analysis. For there to be several events with magnitudes reaching past 300,000 temporal nodes, many hundreds or thousands of distinct triads must be involved. Recall that the dense connectivity within a coalition of just a couple dozen alliances is already thousands of triads, and most edges are used by many triads. When one alliance in such a coalition changes its political position towards another, all of those triads become frustrated. Over a few days the other alliances align to either eject the defector or create a schism in the coalition. Some of the frustration may never be ameliorated, but most of it is. Earlier we sought the source of frustration in the system, and it does indeed seem that these events can inject frustration and spread it to other triads, many of which do not become balanced even a year later.

4.4.4 Conclusions on Structural Balance Propagation

We have presented a detailed analysis of the conditional behaviors of alliance standings changes based on the frustration of the triads formed according to an appropriately loose version of structural balance theory. Although only the temporal out component segment explicitly uses the temporal web formulation to measure influence properties of types of triads, the other behavioral measures provides necessary background understanding. Temporal influence abduction contrasts the kinds of results derived from the temporally extruded representation from what can be done using aggregate behavior. By utilizing the contingent behavior proportions we can construct a generative model of triad changes and compare the temporal web results. Such tests are necessary to bridge the knowledge gap between the kinds of analyses we are accustomed to and those enabled by temporal networks.

Among the things we learned is that propagation in structural balance has two components: the first is mechanistic changes in triads that share an edge when that edge changes sign, and the second is how players respond to those changes. Because our empirical dataset came from a virtual online world, we do not have problems of dirty or missing data, but it is still necessary to separate signal from noise. In this analysis we defined our trigger events via an exogenous shock of frustrated triads becoming balanced without being an adaptation to the states of neighboring triads. We then traced the shock through neighbors of the trigger balancing themselves and frustrating their neighbors, and so forth through time and across the network. That is not the only possible trigger event, and not the kind of event that accounts for most frustration injection into the system. By changing the analysis to other triggers we will find different propagation patterns within the same dataset. Although the propagation results are clear, there are competing explanations that can also be explored using the technique demonstrated above.

For now we can tentatively conclude that frustration does in fact propagate through the network, and players do respond to frustration in the system in a way that is consistent with structural balance theory. However, our analysis also revealed that this adherence to SBT is likely to be implicit rather than through the conscious

decisions of players to balance their standings. Furthermore, the short temporal path lengths and the patterns of contingent dynamics indicate that players more strongly work to avoid frustration than they do ameliorate it once it arrives. In a game based on conflict it is not strange to think that some frustration would persist, but the strong role of cooperation and coordination across alliances suffices to pressure players into forming stable and coherent political relationships.

4.4.5 *Other Considerations for Future Work*

As a further refinement we consider a measure of frustration weighted in several ways. As already mentioned, we are extending this analysis to the subset of sovereign alliances to determine whether they more strongly conform to the tenets of structural balance. We can do this as a separate category, and we can also do this by weighting alliances using various functions of the number of systems they hold sovereignty over. The reasoning is that the larger the alliance's territory, the more pressure it would feel from its players to have a consistent political policy. For similar reasons of importance, it is also natural to include all alliances and weight them by their membership.

Another obvious weight is the distance between the alliances. The game universe of EVE is large, and in some cases the territories of aggressive alliances are far away from each other. In such cases there may be little push to adjust the standings because they have little effect on the actions of the players. The *effective frustration* among alliances captures this feature by down-weighting the frustration by the distance between the centroids of their sovereign territory. We are interested in the difference in the amount of frustration, the speed at which it is ameliorated, and any differences in the specifics of the dynamics. Through these and other weightings we can explore whether frustration propagates in such a way that it also minimizes effective frustrations, such as trading frustration with larger sovereign alliances with frustration with smaller landless alliances. That is, even if the number of frustrated triads increases, the total level of frustration may still be decreasing.

Signed social network analysis beyond structural balance has gaining increased interest [13, 15, 20], but it is still not yet a well-developed field. Although we pursue some measures of signed temporal networks in other forthcoming work, here we focused on the propagation of frustration encoded in nodes representing triads, an approach that itself does not require specifically signed network measures. The richness of the EVE dataset will open up more opportunities to develop and refine augmented temporal network measures for multi-graphs as well because alliances have many different relations to each other beyond their political standings.

A major practical consideration here, and one shared by temporal network research more generally, is the time resolution of events. Most of the players who are in charge of large alliances log into the game nearly every day and update their

standings quickly in response to events. In this analysis we do coarse-graining by using values at the time of daily server maintenance, but a perturbation may arise, propagate, and dissolve within a day and therefore not be detected. In future work we explore the use of a continuous time version that incorporates each standing change as it happens.

Finally, here we analyzed a temporal network of the political triads, and showed how frustration propagates across the political network via changes in shared edges. Another way to do the conversion, which we apply elsewhere, is to keep the alliances as the nodes and count the number/proportion of frustrated triads that each alliance is a member of. In this case, rather than tracking which relationships are influential in spreading frustration through the system, this alliance-centric version determines which agents are responsible for pushing frustration to other agents. In order to do this, however, one must have a measure of influence that can handle quantitative changes (rather than just categorical changes), which is reserved for future work.

4.5 Propagation of Risk Factors on Interbank Networks

Our second dataset will showcase the use of the temporal web technique in order to study the propagation of systemic risk in interbank loan networks. During the recent financial crisis, the interbank lending market proved to be one of the most important channels of financial risk contagion and hence of systemic risk. The malfunctioning of this overly interconnected market caused a liquidity drought across financial markets with consequences reverberating throughout the entire economy. Since then, research into interbank markets has proliferated. The dominant subject is to uncover the topology of interbank markets, to understand how they function, and how they could catalyze a systemic meltdown. There are many approaches to understanding the problem and recommending solutions, but the most promising ones are grounded in network science and/or agent-based modeling [10, 23, 26, 34].

In this chapter we approach these matters by analyzing interbank lending as a temporal web. This technique will not only enable us to quantify the extent of cascades of bank troubles but it will also enable us to have a better understanding of the micro dynamics of the spreading process. We will use temporal influence abduction and out components to address questions like: Does lending to an unhealthy bank tend to negatively effect the lender? Do unhealthy banks only interact with other unhealthy banks or not? Are there lending patterns specific to at-risk banks? Are there lending practices that act as firewalls to contain a risk cascade? This section starts with a description of the dataset, then moves on to a discussion of the uncovered micro dynamics and ends with the insights garnered from the temporal web.

4.5.1 Description of Dataset

We use a dataset on the Russian interbank market provided by the private financial information agency Mobile for the period from August 1998 to October 2004. This dataset has two parts; the first part contains monthly bank balances for most Russian banks (described in detail in [36]). From this first part we take two variables: total bank assets and capital. The second part of the dataset contains monthly reports “On Interbank Loans and Deposits” and represents a register of all interbank loans issued in the Russian market. For each loan we know its size, interest rate, issuer, receiver, reporting date, and maturity date.⁸ More details on the dataset can be found in [37] and [69].

Because the balance sheet data is only reported monthly, we aggregate the loans to be on the same time scale. One way to encode this interbank lending scenario as a temporal web is that if bank A lent money to bank B in a given month t there is a directed link from bank B at month t to bank A at month $t + 1$. The link expresses the fact that bank A has an exposure to bank B in month t and hence, for example, a deterioration in the state of bank B at month t might trigger a deterioration in the state of bank A in month $t + 1$. For the time being we only work with unweighted links (instead of weighted by the amount of the loan) to keep the analysis simple.⁹

Figure 4.6 shows the time series of the number of banks active on the interbank market (solid green line) and the number of issued loans (dotted gray line). During the 1998–2002 period the interbank network experiences growth: we observe a steady and comparable increase in the number of active banks and of issued loans. Starting around 2002 the interbank network gradually matures as revealed by the number of active banks flattening out while the number of loans per bank continues to grow. Note, however, the strong variation in the number of issued loans from the second half of 2003 onwards.

As is indicated in Fig. 4.6, our sample period includes two crises: one in August 1998 and one in the summer of 2004. Both crises resulted in a partial meltdown of the Russian interbank market. They coincide with the edges of the sample period and are clearly marked by a reduction in the number of active banks and issued loans. The first crisis got triggered on August 17, 1998 when Russia abandoned its exchange rate regime, defaulted on its domestic public debt and declared a moratorium on all private foreign liabilities. The second crisis was ignited by an

⁸In this chapter, we restrict ourselves to short-term loans, defined as loans with a maturity of less than a week. These account for more than 80% of the transactions both in terms of the number and of the volume. The reasons for this restriction is because the data provide information about the repayment date and not about the issuance date of the loans. This makes it hard to infer the exact duration of the connection between two banks for the long-term loans.

⁹Because the loans we are using have a maturity of less than one week, it may not be the case that A still has an exposure to B in month $t + 1$ if the loan was initiated in t . However, we do not know the conditions of that repayment. The idea is that lending to a bank that is at risk of default does not immediately elevate the lender’s risk; failing to be paid back or having a high-risk asset on the books however may elevate a lender’s risk, and that shows up in the next balance sheet.

Fig. 4.6 The time dependence of the number of active banks (*solid green line*) and the number of interbank loans (*dashed line*) in the Russian interbank network between 1998 and 2005. Data are aggregated over a month. The arrows indicate the start of the two “crises” (Figure reused from [69] with permission)

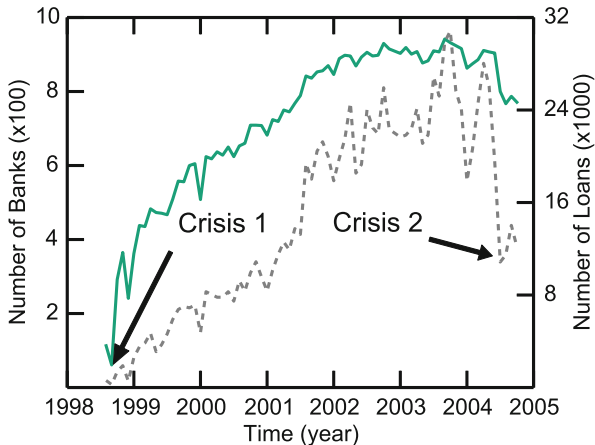


Table 4.4 For the current analysis we apply a coarse-graining of the data into these five categories by their equity ratio

Bank state	Equity ratio	Percent of banks
Healthy+ (+)	$14\% \leq E$	0.743
Healthy (H)	$7 \leq E < 14\%$	0.191
Stressed (S)	$0 \leq E < 7\%$	0.0507
Zombie (Z)	$E < 0\%$	0.0149
Dead (D)	NA	NA

investigation of banks accused of money laundering and sponsorship of terrorism. This gave rise to a wave of distrust among banks and a consequent liquidity drought.

4.5.2 Temporal Web Analysis Results

Before we are able to track the propagation of risk in interbank networks, we first need a measure of a bank’s riskiness. A commonly used measure to express risk is the equity ratio of a bank: the total equity held by a bank divided by its total assets. The higher this ratio, the more a bank will be able to cushion shocks to its balance sheet. A continuous value-based analysis could look at any changes in the banks’ equity ratios, but for the current analysis we apply a coarse-graining of the banks’ equity ratios into the five categories defined in Table 4.4. During most of the period under analysis the Russian banking system had an equity ratio requirement of 7%. Banks above that are considered healthy, but many banks are well above that (up to 100%) and their behavior is distinct from merely healthy banks. The final column in Table 4.4 shows the proportion of banks that are in the corresponding equity ratio category across time. Zombie banks are banks with negative equity, meaning they are past bankrupt, but which still have a license to operate and hence still appear in the dataset. Although the percent of Zombie banks is small, their effect on system

Table 4.5 Summary results of the proportions of bank state changes from t to $t + 1$ compiled across the entire dataset

Bank state at time t	Bank state at time $t + 1$				
	Healthy+	Healthy	Stressed	Zombie	Dead
Healthy+	0.952	0.0419	0.00222	0.000422	0.00376
Healthy	0.145	0.802	0.0482	0.00154	0.00387
Stressed	0.0465	0.155	0.763	0.0221	0.0130
Zombie	0.0273	0.0143	0.0463	0.834	0.0777

risk may not be. Dead banks are the ones that have closed (or not yet opened), and so have neither an equity ratio nor a temporal node.

Having categorized banks by our measure of financial riskiness, we can now look at the aggregate changes in their risk categories. Table 4.5 shows the proportions of month to month bank state transformations. We find a high level of consistency from period to period (76.3–95.2%), with Healthy+ banks as the most stable and Stressed banks the least. Unsurprisingly, Zombie banks have the highest proportions of closures (7.8%), but more than 1.4% of Stressed banks also close without going through the Zombie state first. Also note that a large number (but small proportion) of Healthy and Healthy+ banks also close directly without becoming Stressed or Zombie banks.

Other results gleaned from Table 4.5 include that somewhat surprisingly 8.8% of the banks that are Zombies at t actually recover into positive equity ratios the next month. The Stressed banks improve the following month in 20.2% of cases across time and only 3.5% become Zombies or close. Banks may stay Stressed for a while, but when they transition it is usually for the better. With the exception of Zombie banks becoming Healthy+, we can see that banks are much more likely to change incrementally through the adjacent categories rather than jump. These figures provide a foundation for understanding risk level changes in the system and the base transformation rates needed to create a simulation with similar aggregate behavior.

Temporal Influence Abduction. The next step in the analysis is to investigate whether the interbank lending network actually is a channel of risk propagation by looking at the conditional changes of lenders. Lending money exposes the lender to the situation of the borrower because a (sudden) drop in the health of the borrower might mean that the money will never be returned. This in turn influences the balance sheet of the lender and could result in a drop of the health of the lender too. When a bank lends to an unhealthy bank and then itself becomes less healthy, we can interpret this as the financial risk spreading from the borrower to the lender. Table 4.6 gives an exhaustive overview of the state changes of lenders from t to $t + 1$ conditional on the state of the borrower at t . The results are compiled across the entire dataset and reflect the micro dynamics of possible risk propagation.

The boxed entries in Table 4.6 highlight the cases in which the state of the lending bank dropped after lending to a risky borrower. Comparing values down those

Table 4.6 Summary results showing the proportions of lending bank state changes from t to $t + 1$ (columns) conditional on borrower types (rows) compiled across the entire dataset. This shows the conditional effects of riskiness of the borrower on the stability of the lender. Note that the proportions are normalized across the rows, and the rows are split between the top and bottom subtables

Borrowing bank state at time t		Lending bank state changes from t to $t + 1$									
		$+\rightarrow+$	$+\rightarrow H$	$+\rightarrow S$	$+\rightarrow Z$	$+\rightarrow D$	$H\rightarrow+$	$H\rightarrow H$	$H\rightarrow S$	$H\rightarrow Z$	$H\rightarrow D$
Healthy+	0.589	0.0352	0.000279	0.000010	0.000508	0.0334	0.276	0.0103	0.000034	0.000191	
Healthy	0.504	0.0338	0.000287	0.000009	0.000479	0.0330	0.337	0.0125	0.000009	0.000218	
Stressed	0.472	0.0323	0.000359	0	0.000431	0.0333	0.324	0.0153	0.000180	0.000359	
Zombie	0.310	0.0464	0	0	0	0.0333	0.199	0.0232	0	0	
Borrowing bank state at time t		Lending bank state changes from t to $t + 1$									
		$S\rightarrow+$	$S\rightarrow H$	$S\rightarrow S$	$S\rightarrow Z$	$S\rightarrow D$	$Z\rightarrow+$	$Z\rightarrow H$	$Z\rightarrow S$	$Z\rightarrow Z$	$Z\rightarrow D$
Healthy+	0.00182	0.00950	0.0423	0.000034	0.000117	0.000015	0.000020	0.000064	0.000953	0	
Healthy	0.00167	0.0123	0.0633	0.000070	0.000113	0.000052	0.000009	0.000148	0.00147	0	
Stressed	0.00187	0.0157	0.0977	0.000647	0.000144	0.000144	0.000108	0.000324	0.00528	0	
Zombie	0.00706	0.0151	0.270	0.0101	0	0	0	0.00907	0.0766	0	

Table 4.7 This table focuses on the type of borrowing bank for cases in which the lender becomes more risky. The first data column shows the proportions of lenders having their equity ratios drop at least one category (including death). Banks lending to Zombie banks are the most likely to see a reduction in stability. However also note that because there are so many more Healthy+ and Healthy banks than Stressed and Zombie banks, most decreases in equity ratios happen after borrowing from Healthy+ and Healthy banks. The effect revealed here is that, conditional upon lending to an at-risk bank, a lending bank is marginally more likely to become at risk itself

Borrower type	Got worse	Below 7%
Healthy+	0.0467	0.0106
Healthy	0.0475	0.0129
Stressed	0.0497	0.0165
Zombie	0.0796	0.0333

columns it is clear that lending to a Stressed or Zombie bank has a comparatively higher rate of decreasing the risk status of lending banks, but comparing across rows shows that these are still low proportions. So this finding corroborates the idea that risk can propagate via the interbank lending network. However, we can also see that Stressed and Zombie banks recover proportionately more after borrowing from other Stressed and Zombie banks. This may have more to do with who is willing to lend to these banks than the effect of the loans on equity ratios.

To further test the risk spread hypothesis we can focus on those entries in which the banks' risk status got worse. These figures are summarized in Table 4.7. The first data column shows the proportions of lenders having their equity ratios drop at least one category (including death). Banks lending to Zombie banks are the most likely to see a reduction in stability. Some of those stability changes are from Healthy+ to Healthy, or from Healthy+ to Dead (although presumably they likely died for other reasons). So the second data column shows the proportions of lenders having their equity ratio dropped into the Stressed or Zombie categories, or from the Stressed to Zombie category. This also reveals a slightly larger proportion of banks becoming stressed contingent upon lending to Zombie. From these combined results we tentatively conclude that based on immediate neighbors, financial risk does spread to some degree across the interbank lending network.

Temporal Out Components. Temporal influence abduction indicates that financial risk can spread from a borrowing bank to a lending bank, its "neighbors" in the temporal web of the interbank market. In turn, these neighbors can also affect their neighbors in a cascade of risk propagation. Hence an initial bad loan of a bank can ripple through the bank system to increase overall system risk. In this section, our goal is to see whether the conditional neighbor changes seen above can indeed be chained together into risk-propagating cascades.

First it is important to understand the dynamics of bank lending, bank risk, and how they translate into a temporal web. Figure 4.7 shows an idealized scenario for a temporal web of an interbank loan network. In this case a trigger event is when a non-risky bank borrows from a risky (Stressed or Zombie) bank and then becomes risky itself. The infecting bank is not itself infected because it was already risky. The

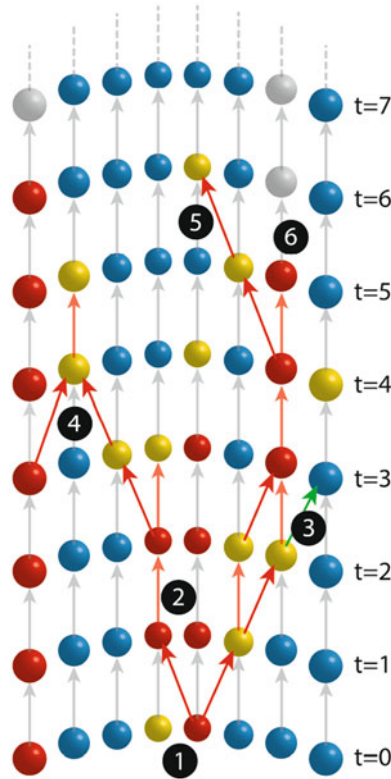


Fig. 4.7 This diagram represents an idealized version of the interbank loan temporal web to demonstrate the events that trigger and propagate financial risk through the system. (1) A trigger event occurs when a risky bank (with equity ratio below 7%) borrows money from another bank and that bank’s equity status becomes worse. (2) The risk injected by that trigger is not counted when maintained by the triggering borrower, but it accumulated through paths of contagion. (3) If a lending bank does not become riskier in the next period it is not counted as part of the cascade, even if it becomes riskier later without additional inputs. (4) A bank may lend to multiple risky banks and turn riskier; this counts in the magnitude of the contagion for each borrower. (5) The trigger node maintaining risk does not add to magnitude, but recovering and then becoming risky again does add to the magnitude if it occurs in the bank’s own temporal out component. In this case the focal bank produces 6 cumulative cases (including itself through reinfection), a duration of 6 periods, and a magnitude of 14 temporal nodes

infected bank is also infectious as long as it stays in one of the risky states; any bank lending to it and becoming risky also becomes infected and infectious and added to the cascade originating from the trigger. A chain ends whenever an infected bank recovers into a healthy state or closes.

In this scenario the cumulative cases measure captures the number of unique banks involved in a cascade (excluding the trigger unless it becomes healthy and then reinfected by lending to a risky bank in the cascade that it started). In the

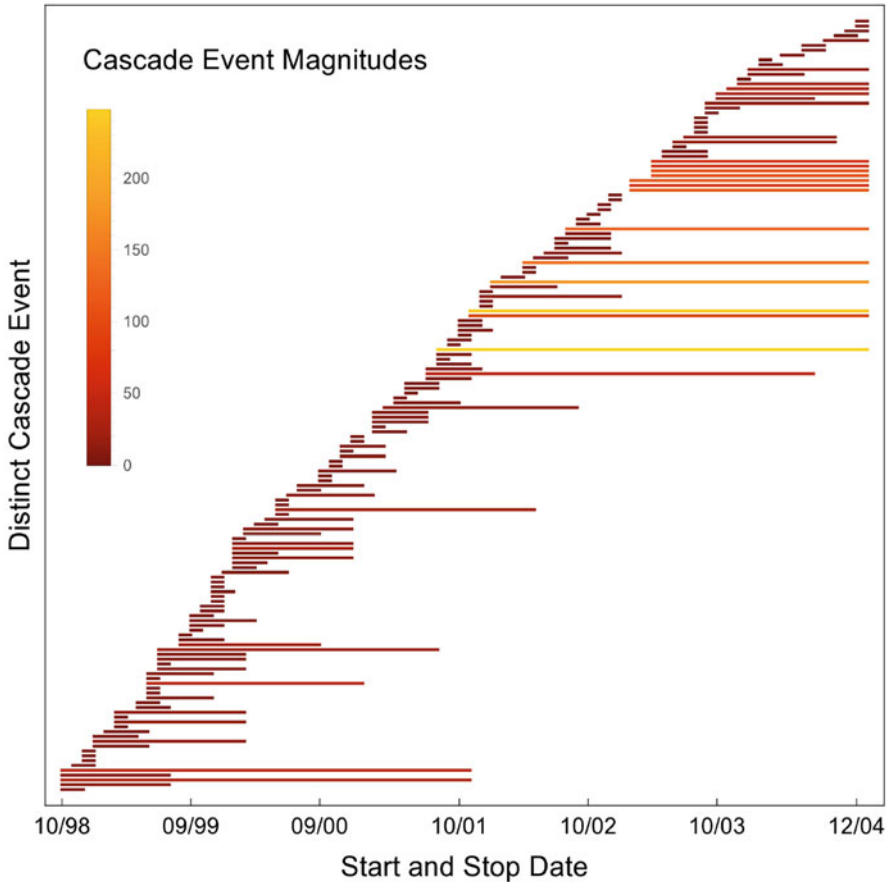


Fig. 4.8 This figure shows each of the 160 cascades from their start date to their end date color coded by cascade magnitude. Unlike the EVE structural balance analysis nearly all the cascades finish within the data time frame because most stressed and Zombie banks either recover or die over several months

widest chain there were 38 unique banks involved, but on average 3.59 banks are involved per cascade with most involving just one or two banks. The longest chain of infections lasted 40 months, but the average was 6.89 months (remembering that our data was in monthly time increments).

The cascade patterns for this temporal web are also distinct from the structural balance data in several key ways as can be seen in Fig. 4.8. There are a few small blocks of related cascades, but most are distinct events with separate subsets of banks involved. The most striking thing about these results is how regular they are. There is no burstiness in cascade creation and long cascades occur throughout the period of analysis. Considering the number of banks and interbank loans in the dataset, the cascade results indicate that they are actually rare events.

Magnitude is the number of infected bank-months (temporal nodes) and so incorporates how long those banks stay in a risky state after infection (and also includes reinfection). For this dataset magnitude and cumulative cases are 96.4% correlated, and magnitude is 97.7% correlated with cumulative cases times max duration. Duration itself is 82.2% correlated with magnitude. These high correlations indicate that the more banks that are infected the more time some bank is infected because the set of infected banks is staggered. It also implies that the reinfection rate is low. There are a few cascades that last a long time (38 months) involving only a few banks, but most larger cascades are ones that are both longer and involve more banks.

4.5.3 Conclusions on Propagation of Risk Factors in Interbank Networks

As many other studies have found before us (see [34] for an excellent review), our temporal web analysis lets us tentatively conclude that interbank lending is a channel of systemic risk. Next to highlighting the micro dynamics, we were able to expose chains of risk propagating throughout the interbank system. We acknowledge the exploratory nature of this analysis and offer this as a demonstration of how to apply temporal webs to a field of increasing importance.

Across all cascades a total of 574 banks were involved with a total magnitude of 2646 temporal nodes. As we saw in Fig. 4.8 most cascades were short lived and involved few banks, and only a few were large-scale events. In some cases individual banks become infected and stay stressed for more than a year, but the longest cascades involve multiple chains in which one bank passes off the infection to another bank that carries it forward. Perhaps counterintuitively, the largest chains originate in and last through the healthiest part of the bank system history. Although not many new cascades start during the second crisis, it is the case that several cascades last until that period, perhaps indicating that it is a build-up effect rather than a spontaneous reaction to a particular trigger.

Of course we are not claiming that the infecting loan was the only, or the primary, source of the increased bank risk among infected banks. Specifically we do not account for the size of the loans in this demonstration. By weighting the edges by the size of the loans we could generate a size-weighted magnitude score that more accurately reflects the spread of financial risk. Such an analysis is a natural pairing to a move to a continuous values of bank risk instead of categories. Furthermore the equity ratio is not the only measure of riskiness, so that is another avenue of expansion. Even with these limitations of the current analysis, there is a clear propagation pattern in the interbank loan network. Risk does seem to spread from risky banks to healthy banks through bad loans at least some of the time. The harm is usually quickly ameliorated, but in some cases (probably in concordance with exogenous factors) the bad loan does in fact trigger a cascade of reduced financial

stability. These cascades are, we argue, best captured and measured with temporal webs because they make explicit the chains of events that constitute such cascades.

4.6 Propagation of Emotional Affect on Twitter Networks

Micro-blogging is an easy way for people to share information and opinions about a variety of subjects. Twitter is currently the largest micro-blogging platform on which millions of people voice their opinions and share information daily using messages (tweets) within the 140 character limit. The content of these tweets creates a massive stream of data with possible uses in subjects such as public opinion [5, 6, 35, 46, 56], information dissemination [18, 59, 65, 74], and even event tracking [25, 42, 45].

To utilize these messages to measure opinion or intention it is essential to know the sentiment of the tweets; this is the first step in transforming tweets into useful data. We will not go into detail about the many techniques that exist for this sentiment extraction as this is not our focus, but instead refer to the large body of work on automated sentiment analysis [50, 62]. Most of these techniques use some sort of natural language recognition, either by the use of dictionaries or trained neural networks, to map words, word combinations, and symbols onto emotions.

The role of sentiment on the probability of online material going viral has gathered much attention in the last years, especially for market research purposes. Various social media platforms play an important role in this spreading of content and every platform has its own characteristics that are used to different ends. By analyzing the sharing of articles in “The New York Times” Berger and Milkman found that content virality is positively correlated to its positivity and emotions linked to activation of arousal (awe, anxiety and anger) and negatively correlated to sadness [4]. However, their dataset might contain only a limited type of content and not be representative of all platforms, especially considering these results seem to be in contradiction with the folk theory that negative news sells.

Hansen et al. looked into this conflict in [27] using retweets in twitter, which is part social media and part news and information dissemination. They found that there was a difference between news content and non-news content. News content’s virality was connected to negative sentiment content, while for non-news content positive sentiments supports virality. Heimbach extended these results and found that the connection between positivity and virality was non-linear and thus interacts in a more complicated way as first suggested by classic theories [30].

Previous analyses have only looked at the conditional behavior of content based on sentiment to make generalization about the effects of sentiment on spreadability. This is similar to aspects of temporal influence abduction, but by using temporal webs, we can follow and study its longer-term propagation through the system and find the most important spreaders (and bottlenecks) of positive (and negative) sentiment. Sentiment is of importance in various subjects because it is an indicator of intention towards acting [5, 44, 63, 64] – people that have a positive sentiment

towards vaccination or a presidential candidate will more likely get vaccinated or vote for this candidate. Understanding the dynamics behind sentiment propagation can thus contribute to the precision of predictions about future behavior.

To uncover features of the propagation of a property like sentiment through a network, it is necessary to include chains through time. This is especially so in the case of social networks wherein the time-order of communication plays an essential role in social contagion. There has been some work on Twitter data using dynamical network techniques and temporal analysis [43, 54, 68], but to our knowledge there has not yet been explicitly temporal network analyses research conducted on it (perhaps for reasons of computational limitations). Below we present a temporal web analysis of one Twitter dataset that includes the network of followers, the tweets sent, and the encoded sentiment of those tweets.

4.6.1 *Description of the Dataset*

The dataset used here was shared with us by Prof. Marcel Salathé who used it in [63, 64]. The dataset contains 411,720 tweets between August 2009 and January 2010 from users based in the United states which contain keywords pertaining to vaccination.¹⁰ The 4,793,160 follower-followee connections between the 101,852 authors of these tweets were also gathered. By combining these sources we have a social network in which the nodes are people tweeting about vaccines and the directed edges are tweets that go from the author to all his or her followers.

In his papers Salathé et al. investigated the characteristics and dynamics of health behavior sentiments towards the then novel influenza A(H1N1) vaccine (the time window of the data coincides with the fall wave of the swine flu pandemic). To obtain the sentiment of the collected tweets they utilized an ensemble method combining a naive Bayes and a maximum entropy classifier. The training set was generated by students that all together rated 88,237 tweets and 47,143 unique tweets. They were presented with four options for every tweet: “positive”, “negative”, “neutral”, and “irrelevant”. Irrelevant tweets were those that were not about the influenza vaccine and the others reflect the emotional valence of the sentiment. They report an accuracy of 84.29% for this ensemble classifier, and while the quality of the sentiment detection effects our results we simply take their results as given to demonstrate the temporal web approach on this kind of dataset. We refer to [63] for the details of their sentiment encoding methodology.

¹⁰This includes retweets in both the old and the current form. The old form of retweet was just copy-pasting the other person’s text and manually adding RT. The current form of retweets was rolled out for everyone on Nov 19, 2009. The keywords included are: vaccine, vaccinated, vaccinate, vaccinating, immunized, immunize, immunization, and immunizing.

It is important to mention that the potential contact network is taken to be static. If at any moment within the dataset user B is a follower of user A , there is a corresponding edge between them in the constructed social network. Changes in followers and followees are thus not taken into account. Furthermore, we do not currently have a measure of the rate of change in followers to judge how much this feature of the data may be affecting our results. The concern is that our method expects the sentiment of tweets by A to effect the sentiment of tweets of A 's followers. If we find that this is not true for some B , we don't know whether that is because B is unaffected or because B wasn't actually a follower for much of the dataset. While acknowledging this weakness in the current dataset we can still assess the qualitative tendency of sender sentiment to effect followers (even if the specific values of our propagation measures are off by some unknown quantity).

In what follows we present an analysis of the data using temporal influence abduction to uncover the sentiment of tweets conditional on the tweets they see from the people they follow. Then, using temporal webs we investigate the propagation of this sentiment within the network of vaccine-related tweets. With this technique, we are able to find longer patterns in the dynamics of sentiment propagation; we can move from "Does sentiment affects immediate virality?" to "Is it really infectious?".

4.6.2 *Constructing the Temporal Web*

Our first move is to cull the data by only including tweets related to the topic of vaccines and thus exclude the tweets tagged as "irrelevant". Because we are leaving a continuous time version of the temporal web technique for future work, we have to choose a coarse-graining of the data to construct a temporal web from the data. To do this we aggregate the tweets by day so that each time step represents all persons active in the network and their tweets within a certain day.

Although there are some alternatives to analyzing the spread of sentiment in this dataset, our goal here is to determine whether a person who is exposed to a lot of negative tweets increases that person's negativity, and whether exposure to positive messages increases the positivity of tweets made. To do this we need to establish the mood of a person based on their tweets. There are three sentiments that can be expressed in a tweet: "positive", "negative", and "neutral". The mood of a person is therefore uniquely represented by two numbers:

$$\text{Mood Positivity} = \frac{\text{number of positive tweets sent}}{\text{total number of tweets sent}} \quad (4.1)$$

$$\text{Mood Negativity} = \frac{\text{number of negative tweets sent}}{\text{total number of tweets sent}} \quad (4.2)$$

One could calculate the ratio of these two to get a single index, but that would hide the proportion of tweets with sentiment compared to all tweets.¹¹ Furthermore, for the purpose of comparing whether negativity or positivity is more contagious, the separate scores are more useful.

Using these equations we calculate a mood for each person at each time step based on their activity. If we look at time step t and a person has not tweeted up to that point, that person is coded as not having a mood (a null value that is different from being neutral). A person who does not tweet in time step t , but has tweeted in a previous time step, is assigned the mood from the previous time step. We call this *temporal inheritance* and reflects a (sometimes explicit, sometimes implicit) connection from an agent to its immediate future self. This convention is common in disease and epistemic temporal networks to reflect that the agent's state stays the same unless acted upon, but is less clearly appropriate for moods of people on Twitter.

The next step is to construct the temporal web from the flow of information in the system. We use the follower network and connect each followee at time t to all of his/her followers at time $t + 1$. The edges are cross-temporal to reflect the effect of the tweets on the calculated moods of the receivers even though the tweets themselves may have been seen immediately. To answer the question of sentiment spread, we calculate the positivity and negativity of a person's feed, which is based on the collection of all tweets a person is exposed to from all the people followed. This aggregation again leads to two numbers that characterize the mood of a person's feed:

$$\text{Feed Positivity} = \frac{\text{number of positive tweets exposed to}}{\text{total number of tweets exposed to}} \quad (4.3)$$

$$\text{Feed Negativity} = \frac{\text{number of negative exposed to}}{\text{total number of tweets exposed to}} \quad (4.4)$$

We generated histograms of the distributions of each person's mood and (rather surprisingly) both the positivity and negativity are distributed almost entirely into three narrow spikes: one near zero, one near the center, and one at the extreme. We repeated this for the feed sentiment values and found a high concentration on and near zero (though more dispersed than for mood), a narrow spike near the center, and a narrow spike on the extreme. Thus both mood and feed can be cleanly broken down into distinct categories according to the scheme in Table 4.8.

¹¹If both positivity and negativity have 5 tweets out of 10, then the sentiment ratio is 1:1. If they both have 5 out of 1000 then again the ratio is 1:1. However, in the former case they both have medium sentiment levels and in the later case they both have low sentiment levels. In other work we provide a combined sentiment measurement, but the added complication is beyond the scope of this work.

Table 4.8 Categorization schemes for both mood and feed positivity and negativity based on the proportion of tweets having emotional affect for that day

Category	Range
Low	$0 \leq m \leq \frac{1}{3}$
Medium	$\frac{1}{3} < m < \frac{2}{3}$
High	$\frac{2}{3} \leq m \leq 1$

Table 4.9 The distributions of both moods and feeds for each category separated into positives and negatives. Most tweets lack sentiment, but there is a notably higher level of highly positive tweet writers despite a lack of highly positive tweet readers. For each group the value for the medium category is the lowest, but especially for the moods

Category	Mood negativity	Feed negativity	Mood positivity	Feed positivity
Low	0.903	0.933	0.853	0.955
Medium	0.0106	0.0324	0.0101	0.0201
High	0.0868	0.0347	0.137	0.0251

In Table 4.9 we show the distribution of the mood and feed negativity and positivity among the three categories of Table 4.8. We thus see that the spikes near zero make the low category by far the largest of the three. That feed negativity has a higher value for the medium category and lower value for the high category compared to mood negativity indicates that most people, even if they have a highly negative mood, do not only follow other people with a highly negative mood, but will also follow people that either send out purely informative tweets (low negativity) or that are more positive on average.

4.6.3 Temporal Web Analysis Results

The first step is to look at the transitions in mood from time step t to time step $t + 1$ by type, shown in Table 4.10. Here we separately analyze the positive and negative moods since there might be an asymmetry in the propagation. We see that there is high stability in moods, with the low level being the most stable. We also see that for both positive and negative moods there is nearly an order of magnitude difference between the probability of going from one extreme to the other than going to an adjacent (medium) level. For medium we see it is much more likely to transition to low than it is to high.

The conditional state changes in Table 4.10 highlight both the similarity of positive and negative mood changes and the pattern of changing directly between high and low instead of through medium. Low sentiment is three times more likely to transition to high than medium levels, and high sentiment is 24 times (positive sentiment) or 15 times (negative sentiment) more likely to transition into low than medium levels. Mediums levels are roughly six times more likely to drop than

Table 4.10 Summary results of the proportions of mood changes from t to $t + 1$ compiled across the entire dataset. Tables (a) and (b) show all states for positivity and negativity respectively. Although all three levels are extremely stable, medium levels are the least stable and low levels are the most stable. Subtables (c) and (d) renormalize the data conditional on there being a change to highlight what those changes are

All states				Conditional on transition			
(a) Negative sentiment				(c) Negative sentiment			
Mood at time t	Mood at $t + 1$			Mood at time t	Mood at $t + 1$		
	Low	Medium	High		Low	Medium	High
Low	0.999	0.000208	0.000674	Low	0.236	0.764	
Medium	0.0198	0.976	0.00373	Medium	0.842	0.158	
High	0.00511	0.000281	0.995	High	0.948	0.0521	

(b) Positive sentiment				(d) Positive sentiment			
Mood at time t	Mood at $t + 1$			Mood at time t	Mood at $t + 1$		
	Low	Medium	High		Low	Medium	High
Low	0.999	0.000236	0.000823	Low	0.223	0.777	
Medium	0.0191	0.978	0.00294	Medium	0.869	0.134	
High	0.00283	0.000108	0.997	High	0.963	0.0368	

to increase. Despite these lower levels, the medium level sentiment holders could play a key role in propagation if they are typically low level sentiment people with temporary spikes of higher sentimentality. To discern whether or not this is the case, we need to look at the conditional changes in sentiment level.

Temporal Influence Abduction. To start looking at the effect of the exposed positivity and negativity on the mood of a person, we present the mood change proportions per feed sentiment level they get exposed to in Table 4.11. As before, we see that most people stay in the low sentiment category (regardless of the feed level) and the next largest group stays in the high category. This raises the idea that there are two dominant types of Twitter users: broadcasters of information and opinion pushers. Their behavior is changed little by the inputs they receive. The feed sentiment level does not have a large influence on these trends on an aggregate level but threads of propagation might be buried in the noise.

By looking deeper at the contingent behaviors we can uncover a few other details that hint at the presence of influence propagation. For example, for the positive posts, people with a medium level are much more likely to switch to a high sentiment level given a high feed sentiment level compared to other feed levels. In the negative sentiment case, people with a low sentiment mood are twice as likely to switch to a high level after receiving a high-level feed than they are to stay low or go to medium. Negative medium level people are also marginally most likely to switch to a high level given a high feed level. Because most people stay in the same category, these small marginal differences may indicate the influence of the feed on one's sentiment level, but it is difficult to perform meaningful statistical tests to check for the significance of these small differences due to the structure of the data across people, their networks, and time.

Table 4.11 Summary results of the proportions of mood changes from t to $t + 1$ compiled across the entire dataset contingent on the mood of the feed. The extreme levels and the non-changing states again dominate. A majority of people stay in the low level, followed by the high level independent of the feed mood

		(a) Negative sentiment							
		Change in mood from t to $t + 1$							
Feed negativity at time t	$l \rightarrow l$	$l \rightarrow m$	$l \rightarrow h$	$m \rightarrow l$	$m \rightarrow m$	$m \rightarrow h$	$h \rightarrow l$	$h \rightarrow m$	$h \rightarrow h$
Low	0.870	0.000181	0.000575	0.000188	0.00929	0.0000351	0.000600	0.0000324	0.119
Medium	0.840	0.000180	0.00125	0.000361	0.0142	0.0000790	0.00143	0.0000677	0.142
High	0.829	0.000127	0.00101	0.000216	0.0125	0.0000636	0.000903	0.000127	0.156

		(b) Positive sentiment							
		Change in mood from t to $t + 1$							
Feed positivity at time t	$l \rightarrow l$	$l \rightarrow m$	$l \rightarrow h$	$m \rightarrow l$	$m \rightarrow m$	$m \rightarrow h$	$h \rightarrow l$	$h \rightarrow m$	$h \rightarrow h$
Low	0.793	0.000189	0.000649	0.000180	0.00913	0.0000268	0.000553	0.0000208	0.196
Medium	0.849	0.0000968	0.00126	0.000221	0.0116	0.0000692	0.000775	0.0000692	0.137
High	0.792	0.0000873	0.000661	0.0000624	0.0111	0.0000749	0.000574	0.0000250	0.195

Temporal Out Component Analysis. As before, to really see whether a property spreads across the network, one must look at the network across time and chain together the changes of interest. Given the large size of the network (101,852 nodes and 4,793,160 edges at each daily time step) the small conditional change probabilities might still constitute cascades of influence across the temporal web. The first step is to refine our definition of what it means for a person to be influenced by another in this context.

We use the following criteria to identify sentiment propagation. If person B is a follower of person A , and person A has an upwards change in sentiment from $t - 1$ to t , then we say there is propagation along the edge from A to B if person B shows a change in sentiment in the same direction as A from t to $t + 1$. One can think of the temporal web as a transformation of the data into a structure in which the temporal nodes are changes in sentiment levels with a property value of ‘increased’, ‘static’, or ‘decreased’. Temporal node α at layer L connects to temporal node β at layer $L + 1$ if and only if β follows α and α tweets something on both times $t - 1$ and t . If A ’s proportion of sentiment-having tweets is higher at t than $t - 1$, then the α node at L has the property ‘increased’ and is considered infectious. If person B sends a larger number of emotional tweets in $t + 1$ compared to t then the temporal node β has the ‘increased’ property at layer $L + 1$ and we say that propagation occurs from A to B between t and $t + 1$.

Unlike the previous two analyses, in the Twitter case there is a separation between being infectious and being infected. Nodes are only infectious on the time steps after an increase in their proportion of sentiment-laden tweets. Agents only become infected when they perceive such an increase, and then increase their sentiment level themselves in response. At that point they are both infected and infectious. If they remain in the elevated state then they remain *infected*, but because their sentiment level is constant they are *not infectious*. Because we have three levels of sentiment, it is possible for a person to go from low to medium, and then from medium to high. Both increases will make them infectious, but after reaching the high state there is nowhere to go except to stay high or drop. Once the level decreases from the elevated state the person is considered recovered and is no longer infected. Recall that states are inherited across times without tweets, this allows us to identify changes from past moods to judge increases and decreases, but their mood can only change if they actively tweet something that day.

We can perform separate analysis for the subset of nodes that are infectious and the ones that are infected. This distinction produces some interesting insights into the flow of sentiment on the Twitter temporal web, but for now we abbreviate these analysis to present only the core results. The main difference is that when all infected nodes are included, the magnitude and duration last as long as somebody stays in a heightened state, and this sometimes lasts until the end of the dataset. By contrast, when only the infectious nodes are included there is a strict limit on the length of time a particular cascade can dwell in a node (one or two days). The difference is just one of bookkeeping and measurement; whether to perform an analysis of the infectiousness of sentiment or of the social impact of sentiment spread.

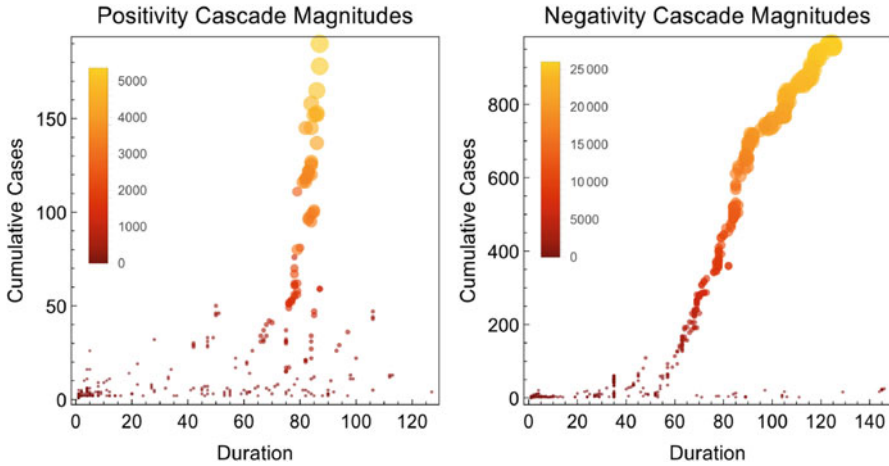


Fig. 4.9 Scatter plots for propagation of positivity (*left*) and negativity (*right*) in which each disk represents a distinct cascade. The disk's location indicates its duration and cumulative cases, while the color and size indicate magnitude. Note the difference in scaling, especially the y-axis

Here we will focus on whether sentiment propagates on the Twitter network and, if it does, whether positivity or negativity propagates better? We found 539 distinct cascades in the positive sentiment temporal web and 653 distinct cascades in the negative sentiment temporal web. As you can see in Fig. 4.9 most of these cascades were small, infecting fewer than a dozen people. In the case of the negativity spread (right scatter plot) there is a large conspicuous series of cascades of increasing magnitude, cumulative cases, and duration. Starting on September 15, 2009 there is a single chain of sentiment spread that on each day infects between one and dozens of people and lasts until November 29, 2009. Although there are three slightly different sets of initially infected agents that form three different triggers (hence distinct cascades), the paths leading from those events quickly converge. As the chain progresses through time there are dozens of other trigger events along the way that converge into this one main stream. It is like many small tributaries feeding a main river. So although each independent trigger counts as a distinct cascade, nearly all the nodes involved in the cascades are shared.

Looking at the timelines for the infectious cascades this is even more conspicuous because all those cascades start at different times but end on the same day. If we count the overlap differently, therefore, we would get very different quantitative results for magnitude and cumulative cases. We revisit this point below. The convergence of chains of propagation is not uncommon, in fact it happens to a lesser scale four other times in the negativity cascades and there are five small cases of convergence in the positivity cascades, but we didn't expect to see any chains this long or broad from this dataset. To discover such a long chain, and one that has so many independent triggers, means that not only does large scale propagation of sentiment occur on the Twitter networks, large scale propagation is inevitable (at least on this subset of Twitter).

Table 4.12 Comparison of the cascade features of positive and negative sentiment propagation. A Kolmogorov-Smirnov two-sample test reveals that these distributions are different with an extremely high significance, which is already clear from these summary statistics

	Positivity cascades	Negativity cascades
Number of cascade events	539	653
Mean duration	25.2	46.6
Max duration	127	146
Mean cumulative cases	14.5	225.7
Max cumulative cases	190	965
Mean magnitude	340.3	5620.1
Max magnitude	5355	25,993

Now we address the question of whether positivity or negativity is more viral. The scatter plots in Fig. 4.9 share some features, but also have some clear differences. The summary statistics of the positivity and negativity cascades presented in Table 4.12 demonstrate clearly that negativity is more successful in spreading in this Twitter data. The cascades of negativity are more frequent, larger, and longer lasting. This is in line with what Salathé et al. found in their papers, namely that negative sentiment spreads much more easily than positive. However, the bulk of the magnitude of negativity is contained in that one huge chain, whereas the chains in positivity are more diverse. If we change the way we account for out component overlap it could drastically effect this result; we revisit this issue in the next section.

Although infectiousness has a very limited time frame, specifically the period after a mood change, the magnitude is calculated throughout the infected period. If people undergo long-term changes in their posting sentiment propensities then the durations and magnitudes will be greater, and magnitude will correlate less with cumulative cases. What we find is that for positivity, magnitude and cumulative cases are 98.2% correlated, while in negativity they are 99.9% correlated. Durations are 59.6% and 82.3% correlated with magnitude for positivity and negativity respectively. This means that spreading to new people dominates the magnitude measure and changes are short-lived. It also means that cumulative cases times duration is actually slightly less correlated with magnitude than cumulative cases alone. This finding is consistent with the earlier claim that people are generally either spreaders of information or of opinion; they may change their style based on a particular issue, but quickly return to their base rate.

4.6.4 *Conclusions on Propagation of Sentiment on a Twitter Network*

Here we showed that propagation of the type similar to sentiment propagation, in which person A changes his/her mind from time $t - 1$ to t , causing person B to

change his/her mind from time t to $t + 1$ (which is a different type of propagation than the last two types), can easily be tracked and quantified within the presented temporal web framework without losing information in aggregation. Although the aggregated change proportions showed little evidence of spread, the temporal web analysis shows that cascades of change actually play a large role in who changes sentiment and when.

The particular chain patterns found in this dataset are quite interesting and unexpected. The single long chain in the negativity propagation brings to the forefront questions about how to count overlapping out components. As mentioned above, in this work we are treating them as distinct cascades, multiply counting each infected temporal node for each independent event that could have infected them. This measures, for each trigger, its potential to spread sentiment; i.e., what sentiment it would have spread even if all other cascade events were eliminated. However, this is a poor measure of the marginal effect on sentiment spread because most of infections are infecting the already infected. To capture marginal effect one needs to identify each cascade's unique influence by identifying temporal nodes that would not have been infected without that event. The intermediate approach of weighting each path from each trigger event node potentially best captures the contribution of each temporal node in each event, but the appropriate weighting may depend on the application and the distribution of events.

The reason this is important ties back to the principal use of temporal webs to measure influence. The next step in such an analysis is to compare the score each trigger node achieves according to various (temporal and static) network measures to the magnitude it generates. Alternate ways of measuring impact on the temporal web will produce different comparisons and highlight different network features. This then feeds back into the role that capturing temporally extruded cascades plays in identifying useful network measures of influence.

Moving forward with the Twitter analysis, a natural addition is to combine the two sides of the sentiment to also analyze the interplay between positive and negative sentiment. For example, here we determined whether having a more positive feed leads to more positive tweets, and we can extend this to include having fewer negative tweets as well. The current dataset on the avian flu is rather limited in its scope and has features that we believe are particular to this topic. By applying this technique to a variety of Twitter subgraphs on a variety of unrelated topics we can make broader claims about general features of propagation on this social network platform.

4.7 Summary

This chapter provided a general description of measuring influence on dynamic social networks using a temporal web structure of the interactions across time. We also proposed a way to derive the rules that people use via a technique called temporal influence abduction. This approach uses aggregated contingent behaviors

to uncover the kinds of information one would need to build a simulation that recreates data like the single observed one. In future work we will use these contingent behavior rules to generate multiple alternate counterfactual histories for each dataset and compare the propagation patterns of the real and simulated temporal web. One motivation to do this is to determine the role of luck (i.e., a convergence of probabilistically rare events) in the appearance of large-scale cascades and/or to determine to what degree some amount of propagation is inevitable in dynamic networked systems.

For each of the datasets analyzed here cumulative cases (and cumulative cases times duration) were very highly correlated with magnitude. This is not generally true based on previous work with disease simulations, and so reflects a substantive feature of spread on these networks. The improved accuracy of the magnitude measure is one of the proposed benefits of the temporal web approach over running dynamics on static networks or analyzing flattened networks. In the three cases presented above, this benefit is limited because the easier and more traditional measures act as reasonable proxies for the temporal web measure. This is generally the case when either cumulative cases or the duration is the main driving factor of total spread size, and less so when both factors play a significant role. There are many techniques useful for studying propagation, studies like this help us home in on the features of network contagion for which the temporal web approach provides unique insights.

Although work on this method is still fresh, it is gaining momentum. Demonstrations of how to use temporal networks (beyond just temporal webs) and the benefits of such applications are critical to them gaining a wider acceptance. Our sincere hope is that this detailed analysis of three applications of temporal webs to empirical data provides such an example. These datasets are already large, and because each agent at each period is encoded as a temporal node, analyzing them requires especially efficient algorithms to run. Although this may act as a barrier to entry for some researchers, we are eager to collaborate with interested parties in extending our applications of temporal webs.

References

1. Abell, P.: Structural balance in dynamic structures. *Sociology* **2**(3), 333–352 (1968)
2. Antal, T., Krapivsky, P.L., Redner, S.: Social balance on networks: the dynamics of friendship and enmity. *Phys. D Nonlinear Phenom.* **224**(1), 130–136 (2006)
3. Axelrod, R., Bennett, D.S.: Landscape theory of aggregation. *Br. J. Polit. Sci.* **23**(02), 211–233 (1993)
4. Berger, J., Milkman, K.L.: What makes online content viral? *J. Mark. Res.* **49**(2), 192–205 (2012)
5. Bermingham, A., Smeaton, A.F.: On using Twitter to monitor political sentiment and predict election results. In: *Sentiment Analysis Where AI Meets Psychology (SAAIP) Workshop at the International Joint Conference for Natural Language Processing (IJCNLP)*, Chiang Mai (2011)
6. Bollen, J., Mao, H., Zeng, X.: Twitter mood predicts the stock market. *J. Comput. Sci.* **2**(1), 1–8 (2011)

7. Braha, D., Bar-Yam, Y.: From centrality to temporary fame: dynamic centrality in complex networks. *Complexity* **12**(2), 59–63 (2006)
8. Bramson, A., Vandermarliere, B.: Dynamical properties of interaction data. *J. Complex Netw.* **4**(1), 87–114 (2015)
9. Bramson, A., Vandermarliere, B.: Benchmarking measures of network influence. *Sci. Rep.* **6**, 34052 (2016)
10. Buchanan, M.: Meltdown modelling. *Nature (London)* **460**(7256), 680–682 (2009)
11. Cartwright, D., Harary, F.: Structural balance: a generalization of Heider's theory. *Psychol. Rev.* **63**(5), 277–293 (1956)
12. Chen, D., Lü, L., Shang, M.S., Zhang, Y.C., Zhou, T.: Identifying influential nodes in complex networks. *Phys. A: Stat. Mech. Appl.* **391**(4), 1777–1787 (2012)
13. Ciotti, V., Bianconi, G., Capocci, A., Colaiori, F., Panzarasa, P.: Degree correlations in signed social networks. *Phys. A* **422**, 25–39 (2015)
14. Colizza, V., Barrat, A., Barthelemy, M., Valleron, A.J., Vespignani, A.: Modeling the worldwide spread of pandemic influenza: baseline case and containment interventions. *PLoS Med.* **4**(1), e13 (2007)
15. Costantini, G., Perugini, M.: Generalization of clustering coefficients to signed correlation networks. *PLoS ONE* **9**(2), e88669 (2014)
16. Cui, J., Zhang, Y.Q., Li, X.: On the clustering coefficients of temporal networks and epidemic dynamics. In: 2013 IEEE International Symposium on Circuits and Systems (ISCAS2013), pp. 2299–2302. IEEE, Beijing (2013)
17. Davis, J.A.: Clustering and structural balance in graphs. *Hum. Relat.* **20**, 181–187 (1967)
18. De Domenico, M., Lima, A., Mougél, P., Musolesi, M.: The anatomy of a scientific rumor. *Sci. Rep.* **3**, 2980 (2013)
19. Dekker, A.H.: Network centrality and super-spreaders in infectious disease epidemiology. In: 20th International Congress on Modelling and Simulation (MODSIM2013), Adelaide (2013)
20. Doreian, P., Mrvar, A.: Partitioning signed social networks. *Soc. Netw.* **31**(1), 1–11 (2009)
21. DuBois, T., Golbeck, J., Srinivasan, A.: Predicting trust and distrust in social networks. In: 2011 IEEE Third International Conference on Privacy, Security, Risk and Trust (PASSAT) and 2011 IEEE Third International Conference on Social Computing (SocialCom), Boston, pp. 418–424 (2011)
22. Facchetti, G., Iacono, G., Altafini, C.: Computing global structural balance in large-scale signed social networks. *PNAS* **108**(52), 20953–20958 (2011)
23. Georg, C.P.: The effect of the interbank network structure on contagion and common shocks. *J. Bank. Financ.* **37**(7), 2216–2228 (2013)
24. Grindrod, P., Higham, D.J.: A matrix iteration for dynamic network summaries. *SIAM Rev.* **55**(1), 118–128 (2013)
25. Guille, A., Favre, C.: Event detection, tracking, and visualization in Twitter: a mention-anomaly-based approach. *Soc. Netw. Anal. Min.* **5**(1), 1–18 (2015)
26. Haldane, A.: Rethinking the financial network. Speech delivered at the Financial Student Association, Amsterdam (2009)
27. Hansen, L.K., Arvidsson, A., Nielsen, F.A., Colleoni, E., Etter, M.: Good friends, bad news. Affect and virality in Twitter. In: *Future Information Technology. Communications in Computer and Information Science*, vol. 185, pp. 34–43. Springer, Berlin (2011)
28. Harary, F.: On the measurement of structural balance. *Behav. Sci.* **4**(4), 306–323 (1959)
29. Heider, F.: Attitudes and cognitive organization. *J. Psychol.* **21**, 107–122 (1946)
30. Heimbach, I., Hinz, O.: The impact of content sentiment and emotionality on content virality. *Int. J. Res. Mark.* **33**(3), 695–701 (2016)
31. Holme, P.: Modern temporal network theory: a colloquium. *Eur. Phys. J. B* **88**(9), 1–30 (2015)
32. Holme, P., Saramäki, J.: Temporal networks. *Phys. Rep.* **519**(3), 97–125 (2012)
33. Hummon, N.P., Doreian, P.: Some dynamics of social balance processes: bringing Heider back into balance theory. *Soc. Netw.* **25**(1), 17–49 (2003)
34. Hüser, A.C.: Too interconnected to fail: a survey of the interbank networks literature. Technical report. <https://ssrn.com/abstract=2577241> (2015)

35. Jahanbakhsh, K., Moon, Y.: The predictive power of social media: on the predictability of U.S. presidential elections using Twitter. In: arXiv preprint arXiv:1407.0622 (2014)
36. Karas, A., Schoors, K.: Heracles or sisyphus? Finding, cleaning and reconstructing a database of Russian banks. Working paper 327, Ugent (2005)
37. Karas, A., Schoors, K.: A guide to Russian banks data. SSRN. <http://ssrn.com/paper-1658468> (2010)
38. Kempe, D., Kleinberg, J., Tardos, É.: Influential nodes in a diffusion model for social networks. In: Automata, Languages and Programming, pp. 1127–1138. Springer, Berlin/Heidelberg (2005)
39. Kim, H., Anderson, R.: Temporal node centrality in complex networks. *Phys. Rev. E* **85**(2), 026107 (2012)
40. Kimura, M., Saito, K., Nakano, R., Motoda, H.: Extracting influential nodes on a social network for information diffusion. *Data Min. Knowl. Discov.* **20**(1), 70–97 (2010)
41. Kitsak, M., Gallos, L.K., Havlin, S., Liljeros, F., Muchnik, L., Stanley, H.E., Makse, H.A.: Identification of influential spreaders in complex networks. *Nat. Phys.* **6**, 888–893 (2010)
42. Kumar, S., Liu, H., Mehta, S., Subramaniam, L.V.: From tweets to events: exploring a scalable solution for twitter streams. arXiv preprint arXiv:1405.1392 (2014)
43. Kwak, H., Lee, C., Park, H., Moon, S.: What is Twitter, a social network or a news media? In: Proceedings of the 19th International Conference on World Wide Web, pp. 591–600. ACM, Raleigh (2010)
44. Lamos, V.: On voting intentions inference from Twitter content: a case study on UK 2010 General Election. Computing Research Repository (CoRR). arXiv:1204.0423 (2012)
45. Lamos, V., De Bie, T., Cristianini, N.: Flu detector – tracking epidemics on twitter. In: ECML PKDD, Barcelona, pp. 599–602. Springer (2010)
46. Lamos, V., Lansdall-Welfare, T., Araya, R., Cristianini, N.: Analysing mood patterns in the United Kingdom through Twitter content. Computing Research Repository (CoRR). arXiv:1304.5507 (2013)
47. Lawyer, G.: Understanding the influence of all nodes in a network. *Sci. Rep.* **5**, 8665 (2015)
48. Lerman, K., Ghosh, R., Kang, J.H.: Centrality metric for dynamic networks. In: Proceedings of the Eighth Workshop on Mining and Learning with Graphs, Washington, DC, pp. 70–77. ACM (2010)
49. Leskovec, J., Huttenlocher, D., Kleinberg, J.: Signed networks and in social and media. In: CHI 2010: Machine Learning and Web Interactions, Atlanta, 10–15 Apr 2010 (2010)
50. Liu, B.: Sentiment Analysis: Mining Opinions, Sentiments, and Emotions. Cambridge University Press, New York (2015)
51. Lü, L., Zhang, Y.C., Yeung, C.H., Zhou, T.: Leaders in social networks, the delicious case. *PLoS ONE* **6**(6), e21202 (2011)
52. Malliaros, F.D., Rossi, M.E.G., Vazirgiannis, M.: Locating influential nodes in complex networks. *Sci. Rep.* **6**, 19307 (2016)
53. Mantzaris, A.V., Higham, D.J.: Dynamic communicability predicts infectiousness. In: Temporal Networks, pp. 283–294. Springer, Heidelberg (2013)
54. Moro, E.: Temporal network of information diffusion in Twitter (2012). <http://estebanmoro.org/2012/10/temporal-network-of-information-diffusion-in-twitter/>
55. Nicosia, V., Tang, J., Mascolo, C., Musolesi, M., Russo, G., Latora, V.: Graph metrics for temporal networks. In: Temporal Networks, pp. 15–40. Springer, Heidelberg (2013)
56. Pagolu, V.S., Challa, K.N.R., Panda, G., Majhi, B.: Sentiment analysis and of twitter and data for and predicting stock and market movements. In: International Conference on Signal Processing, Communication, Power and Embedded System (SCOPEs), Sankt Goar (2016)
57. Pastor-Satorras, R., Vespignani, A.: Immunization of complex networks. *Phys. Rev. E* **65**, 036104 (2002)
58. Pfitzner, R., Scholtes, I., Garas, A., Tessone, C.J., Schweitzer, F.: Betweenness preference: quantifying correlations in the topological dynamics of temporal networks. *Phys. Rev. Lett.* **110**, 198701 (2013)

59. Riquelme, F., González-Cantergiani, P.: Measuring user influence on Twitter: a survey. *Inf. Process. Manag.* **52**(5), 949–975 (2016)
60. Rocha, L.E., Blondel, V.D.: Flow motifs reveal limitations of the static framework to represent human interactions. *Phys. Rev. E* **87**(4), 042814 (2013)
61. Rocha, L.E., Masuda, N.: Random walk centrality for temporal networks. *New J. Phys.* **16**(6), 063023 (2014)
62. Saif, H., Fernández, M., He, Y., Alani, H.: Evaluation datasets for twitter sentiment analysis: a survey and a new dataset, the STS-Gold. In: 1st International Workshop on Emotion and Sentiment in Social and Expressive Media: Approaches and Perspectives from AI (ESSEM 2013), Turin (2013). <http://oro.open.ac.uk/40660/>
63. Salathé, M., Khandelwal, S.: Assessing vaccination sentiments with online social media: implications for infectious disease dynamics and control. *PLoS Comput. Biol.* **7**(10), e1002199 (2011)
64. Salathé, M., Vu, D.Q., Khandelwal, S., Hunter, D.R.: The dynamics of health behavior sentiments on a large online social network. *EPJ Data Sci.* **2**(1), 1–12 (2013)
65. Serrano, E., Iglesias, C.A.: Validating viral marketing strategies in Twitter via agent-based social simulation. *Expert Syst. Appl.* **50**, 140–150 (2016)
66. Sikić, M., Lancić, A., Antulov-Fantulin, N., Stefancić, H.: Epidemic centrality – is there an underestimated epidemic impact of network peripheral nodes? *Eur. Phys. J. B* **86**(10), 1–13 (2013)
67. Szell, M., Lambiotte, R., Thurner, S.: Multirelational organization of large-scale social networks in an online world. *PNAS* **107**(31), 13636–13641 (2010)
68. Taxidou, I., Fischer, P.M.: Online analysis of information diffusion in Twitter. In: Proceedings of the 23rd International Conference on World Wide Web, WWW'14 Companion, pp. 1313–1318. ACM, New York (2014)
69. Vandermarliere, B., Karas, A., Ryckebusch, J., Schoors, K.: Beyond the power law: uncovering stylized facts in interbank networks. *Phys. A* **428**, 443–457 (2015)
70. Viard, J., Latapy, M.: Identifying roles in an IP network with temporal and structural density. In: 2014 IEEE Conference on Computer Communications Workshops (INFOCOM WKSHPS), pp. 801–806. IEEE, New York (2014)
71. Wehmuth, K., Ziviani, A., Fleury, E.: A unifying model for representing time-varying graphs. In: 2015 IEEE International Conference on Data Science and Advanced Analytics (DSAA), pp. 1–10. IEEE (2015). doi:10.1109/DSAA.2015.7344810
72. Xu, S., Wang, P.: Identifying important nodes by adaptive leaderrank. *Phys. A* **469**, 654–664 (2017)
73. Yu, Y., Berger-Wolf, T.Y., Saia, J., et al.: Finding spread blockers in dynamic networks. In: Advances in Social Network Mining and Analysis, pp. 55–76. Springer, Berlin/Heidelberg (2010)
74. Zhao, L., Cui, H., Qiu, X., Wang, X., Wang, J.: Sir rumor spreading model in the new media age. *Phys. A* **392**(4), 995–1003 (2013)

Chapter 5

Mean Field at Distance One

Ka Yin Leung, Mirjam Kretzschmar, and Odo Diekmann

Abstract To be able to understand how infectious diseases spread on networks, it is important to understand the network structure itself in the absence of infection. In this text we consider dynamic network models that are inspired by the (static) configuration network. The networks are described by population-level averages such as the fraction of the population with k partners, $k = 0, 1, 2, \dots$. This means that the bookkeeping contains information about individuals and their partners, but no information about partners of partners. Can we average over the population to obtain information about partners of partners? The answer is ‘it depends’, and this is where the mean field at distance one assumption comes into play. In this text we explain that, yes, we may average over the population (in the right way) in the static network. Moreover, we provide evidence in support of a positive answer for the network model that is dynamic due to partnership changes. If, however, we additionally allow for demographic changes, dependencies between partners arise. In earlier work we used the slogan ‘mean field at distance one’ as a justification of simply ignoring the dependencies. Here we discuss the subtleties that come with the mean field at distance one assumption, especially when demography is involved. Particular attention is given to the accuracy of the approximation in the setting with demography. Next, the mean field at distance one assumption is discussed in the

K. Y. Leung (✉)

Mathematical Institute, Utrecht University, Utrecht, The Netherlands

Julius Center for Primary Care and Health Sciences, University Medical Center Utrecht, Utrecht, The Netherlands

Department of Mathematics, Stockholm University, Stockholm, Sweden

e-mail: kayin.leung@math.su.se

M. Kretzschmar

Julius Center for Primary Care and Health Sciences, University Medical Center Utrecht, Utrecht, The Netherlands

National Institute for Public Health and the Environment, Utrecht, The Netherlands

e-mail: m.e.e.kretzschmar@umcutrecht.nl

O. Diekmann

Mathematical Institute, Utrecht University, Utrecht, The Netherlands

e-mail: o.diekmann@uu.nl

context of an infection superimposed on the network. We end with the conjecture that an extension of the bookkeeping leads to an exact description of the network structure.

5.1 Introduction

Consider a large population of individuals who engage in partnerships. These partnerships make up the network structure of the population. The network evolves over time due to both demographic and partnership changes. Rather than keeping track of all individuals and partnerships over time, we are interested in a statistical description of the network at a particular point in time by characterizing population-level (p-level) quantities of interest, e.g. the fraction of the population having k partners, $k = 0, 1, 2, \dots$, and use these p-level averages to describe the disease dynamics in the population. In general, it is not possible to use such a statistical description to predict the future spread of the disease. Indeed, the precise network structure influences how the disease is transmitted on the network. A statistical description of p-level fractions generally does not provide enough information to recover the structure of the network. But, by making assumptions about the structure of the network, e.g. by assuming a (static) configuration network, such a statistical description may be possible.

The construction of the (static) configuration network guarantees the absence of degree-degree correlation. As a consequence it is easy to describe the transmission dynamics of an infectious disease across the network in the course of time, even for rather general infectivity functions, see [1, Section 2.5] and [2]. The dynamic network models that we consider in this text (and previous work [1]) are inspired by the (static) configuration network.

An essential feature of the network models under consideration are the ‘binding sites’ (in the static setting these are often referred to as half-edges or stubs; these were most cleverly used to describe transmission dynamics of an SIR infection in the static setting by Volz in [3] and in subsequent work by Miller, Volz, and coauthors (e.g. [4] and references therein)): each individual consists of a number of (conditionally) independent binding sites. In the static configuration network, binding sites are paired in a uniform way. Two binding sites that are paired form a partnership between their owners. Note that, while the construction of the network may lead to self-loops and multiple partnerships between the same individuals, the proportions are such that we may ignore these in the infinite population limit, see e.g. [5, 6] for precise statements and proofs.

We distinguish three different levels in the network: (i) binding sites, (ii) individuals, and (iii) the population. Systematic model formulation relates the three levels to each other. At the binding-site and individual level (i-level) we have a Markov chain description with p-level influences captured by environmental variables. We work in the large population limit, so the description at the p-level is deterministic. The binding sites are the essential building blocks of the model and allow us to understand the dynamics at the p-level.

In [1] we formulated models for the spread of an infectious disease over two dynamic variants of the static configuration network. Here we reconsider these dynamic networks while focusing on the mean field at distance one assumption. First, in Sect. 5.2, we allow for partnership formation and separation. Next, in Sect. 5.3, we also incorporate demographic turnover. The key question, central to the mean field at distance one assumption, is: what information about partners of partners can we recover from a bookkeeping scheme that only contains information about individuals and their partners?

In the case of a static configuration network this question is readily answered. There is *independence* in the degrees of partners. Therefore, the probability that a partner has k partners is simply obtained from the size-biased degree distribution, i.e. if P_k is the probability that a randomly chosen individual has k partners, then $kP_k / \sum_l lP_l$ is the probability that a randomly chosen partner has k partners (where $\sum_l lP_l$ serves as a normalization constant). We show in Sect. 5.2 that this property is also shared by the dynamic network without demography, but, as we show in Sect. 5.3, things are more subtle in the dynamic network with demography. In fact, in Sect. 5.3, we show that degree dependencies arise as a result of age dependencies, and we quantify the dependency between the degrees of partners by the correlation coefficient. In Sect. 5.4 we discuss the mean field at distance one assumption in the context of an infectious disease superimposed on the network, and we explain where additional complications arise. Finally, in Sect. 5.5, we end with a discussion and some conclusions. We conjecture that changing the bookkeeping of partners to include age allows for an exact description of the dynamic network with demography.

5.2 Dynamic Network Without Demography

5.2.1 Model Formulation

To obtain a first dynamic configuration network we assume:

- occupied binding sites become free at rate σ
- free binding sites form partnerships at rate ρF where F is the fraction of binding sites that are free (mass action / supply and demand)

cf. [1, Section 3]. Let the partnership capacity n of an individual be the maximum number of partners it *may* have at any given time. The actual number of partners (a.k.a. the degree) of the individual changes over time according to the per-binding-site rules specified in the two bullets above. In principle, the partnership capacity n is a random variable with a specified distribution (with finite first and second moments). Here, for the sake of exposition, we assume that the distribution is concentrated in one point (also denoted by n). In other words, all individuals have exactly the same partnership capacity n . As a consequence, the degree of an individual follows a binomial distribution, see Eq. (5.2) below.

The network dynamics entail that binding sites of an individual behave independently of one another in partnership changes. One can describe the dynamics of the fraction F of free binding sites with the following ordinary differential equation (ODE):

$$\frac{dF}{dt} = -\rho F^2 + \sigma(1 - F).$$

As a consequence, we find that F stabilizes at a value characterized by the identity

$$F = \frac{\sigma}{\rho F + \sigma}. \quad (5.1)$$

Solving for F in terms of σ and ρ yields

$$F = \frac{\sqrt{\sigma(4\rho + \sigma)} - \sigma}{2\rho}.$$

Therefore, we assume that F is constant and satisfies Eq. (5.1). This assumption for F ensures that the network structure is stationary even though the network itself is changing over time due to partnership dynamics. As a matter of fact, we assume that we start in stationarity.

5.2.2 Independence in the Degrees of Partners

We adopt the convention that the joint degree of two partners refers to the total number of partners of each of the individuals (including their known partner). We calculate the joint degree distribution $\pi_{k,l}(\xi)$ of two partners at partnership duration ξ , given that they remain partners for this period of time; see Table 5.1 for an overview. If our derivations seem overly detailed, please bear in mind that these details serve to prepare for the analysis in Sect. 5.3 of a more subtle situation.

Table 5.1 Overview of distributions that are used in Sect. 5.2

Variable	Description
$(P_k)_{k=0}^n$	Degree distribution for a randomly chosen individual, $\sum_{k=0}^n P_k = 1$
$(q_k)_{k=1}^n$	Degree distribution for a newly acquired partner, $\sum_{k=1}^n q_k = 1$
$\varphi(\xi) = F$	Probability that a binding site is free at time ξ after its owner acquired a partner at a different binding site
$(\pi_{k,l}(\xi))_{k,l=1}^n$	Joint degree distribution of two partners at time ξ after partnership formation, $\sum_{k,l=1}^n \pi_{k,l} = 1$

First, by combinatorics, we find that the probability P_k that a randomly chosen individual in the population has k partners is simply

$$P_k = \binom{n}{k} F^{n-k} (1-F)^k, \quad (5.2)$$

i.e. the degree distribution (P_k) is a binomial distribution with parameters n and $1-F$.

The probability q_k that a newly acquired partner has k partners (in total) is $(n-k+1)P_{k-1} / \sum_l (n-l)P_l$ (a potential partner in state $k-1$ has $(n-k+1)$ free binding sites; immediately after partner formation, it will be in state k). Here the sum serves to renormalize into a probability distribution. Working this out, we find that

$$\begin{aligned} q_k &= (n-k+1) \binom{n}{k-1} F^{n-k+1} (1-F)^{k-1} \bigg/ \sum_l (n-l)P_l \\ &= n \binom{n-1}{k-1} F^{n-k+1} (1-F)^{k-1} \bigg/ nF \\ &= \binom{n-1}{k-1} F^{n-k} (1-F)^{k-1}. \end{aligned} \quad (5.3)$$

So, we find that a newly acquired partner has at least one occupied binding site and the other $n-1$ binding sites are free with probability F and occupied with probability $1-F$. Hence, q_k is equal to the probability that a randomly chosen *partner* has k partners.

Next, let φ denote the probability that a binding site is free at time ξ after partner acquisition at another binding site of the same owner. Then $\varphi(\xi) = F$, since binding sites behave independently of one another. On the other hand, φ satisfies

$$\begin{aligned} \frac{d\varphi}{d\xi} &= -\rho F \varphi + \sigma(1-\varphi), \\ \varphi(0) &= F. \end{aligned} \quad (5.4)$$

Solving for φ we find that

$$\varphi(\xi) = \frac{\sigma}{\rho F + \sigma} + \frac{\rho F^2 - \sigma(1-F)}{\rho F + \sigma} e^{-(\rho F + \sigma)\xi} = F, \quad (5.5)$$

where we used identity (5.1) for F in the second equality. In particular, this confirms our intuition that partnership duration ξ is not relevant.

We are now ready to consider the probability $\pi_{k,l}(\xi)$ that u and v have k and l partners in total at time ξ after they formed a partnership, given that u and v remain partners in the period under consideration. First of all, note that

$$\pi_{k,l}(0) = q_k q_l, \quad (5.6)$$

with q_j given by Eq. (5.3) (partnerships are formed at random between free binding sites in the population), i.e. there is independence in the degrees of the individuals in a newly formed partnership. Furthermore, both u and v have exactly one binding site occupied by their known partner and $n - 1$ other binding sites at which partnership formation and separation can take place. Taking into account partnership-formation and -separation at the other binding sites, and conditioning on the existence of partnership uv in the period under consideration, we find that $\pi_{k,l}$ satisfies

$$\begin{aligned} \frac{d\pi_{k,l}}{d\xi} = & -\rho F(n-k)\pi_{k,l} - \rho F(n-l)\pi_{k,l} - \sigma(k-1)\pi_{k,l} - \sigma(l-1)\pi_{k,l} \\ & + \rho F(n-k+1)\pi_{k-1,l} + \rho F(n-l+1)\pi_{k,l-1} + \sigma k\pi_{k+1,l} + \sigma l\pi_{k,l+1}, \end{aligned} \quad (5.7)$$

with initial condition (5.6). Let

$$p_{k,l}(\xi) := \binom{n-1}{k-1} \varphi(\xi)^{n-k} (1-\varphi(\xi))^{k-1} \binom{n-1}{l-1} \varphi(\xi)^{n-l} (1-\varphi(\xi))^{l-1}. \quad (5.8)$$

We claim that $\pi_{k,l}(\xi) = p_{k,l}(\xi)$. Indeed, differentiating $p_{k,l}(\xi)$ with respect to ξ and using Eq. (5.4), we find that the ODE (5.7) for $\pi_{k,l}$ is indeed satisfied. Since these are straightforward calculations, we omit the details, and only note that the relations $(n-k)\binom{n-1}{k-1} = k\binom{n-1}{k}$ and $(k-1)\binom{n-1}{k-1} = (n-k+1)\binom{n-1}{k-2}$ yield the desired result.

On the other hand, since $\varphi(\xi) = F$ (see Eq. (5.5)), from Eq. (5.8), we find that $p_{k,l}(\xi) = q_k q_l$. Hence the joint degree distribution of two partners at time ξ after partnership formation is given by

$$\pi_{k,l}(\xi) = q_k q_l.$$

In particular, we find that there is independence in the degrees of two partners. Moreover, the joint degree of two individuals in a partnership is the same (i) at partnership formation, (ii) at a specific partnership duration ξ of their partnership, and (iii) at a randomly chosen time in their partnership. The only information that such a partnership gives us about the degree of the partners is that both partners have at least one occupied binding site.

5.3 Dynamic Network with Demography

5.3.1 Model Formulation

A next dynamic variant of the static configuration network model is obtained by adding demographic turnover to the partnership changes of Sect. 5.2, cf. [7] and [1, Section 4]. We additionally assume that

- life length is exponentially distributed with parameter μ
- newborn individuals appear at a constant rate (which is equal to μ if we consider fractions, i.e. normalize the total population size to 1)
- at birth, individuals enter the population without any partners

In other words, we assume a stationary age distribution with density $a \mapsto \mu e^{-\mu a}$. Note that our assumptions on demography imply that the rate at which occupied binding sites become free is $\sigma + \mu$ where σ corresponds to ‘separation’ and μ to ‘death of the partner’. The fraction F of binding sites that are free now satisfies

$$\frac{dF}{dt} = \mu - \mu F - \rho F^2 + (\sigma + \mu)(1 - F).$$

Again, as in Sect. 5.2, F stabilizes to a constant that satisfies

$$\rho F^2 - (\sigma + 2\mu)(1 - F) = 0. \quad (5.9)$$

Therefore, we assume that F is constant. In terms of the model parameters this constant F equals

$$F = \frac{\sqrt{(\sigma + 2\mu)(4\rho + \sigma + 2\mu)} - (\sigma + 2\mu)}{2\rho}. \quad (5.10)$$

As a consequence, although the network itself changes due to partnership dynamics and demographic turnover, the population structure is statistically stable. In particular, the degree distribution does not change with time. We assume that the network starts in stationarity.

In subsequent subsections we show that, contrary to the static network and the dynamic network without demography, there is no longer independence in degrees in the dynamic network with demography. We do so by showing that age-age dependence and age-degree dependence exist, leading to the conjecture that demographic turnover causes degree-degree dependence. We verify the conjecture, and compute the correlation coefficient and study how it depends on the parameters. For convenience an overview of the probabilities and distributions relevant to Sect. 5.3 are given in Table 5.2. A related dynamic network incorporating demography (in a growing population) is considered in [8, 9], where also the degree-degree correlation is determined.

Table 5.2 Overview of probabilities and densities that are used in Sect. 5.3. By assumption, whenever we write ‘at age a ’ (or just ‘age a ’), the individual under consideration remains alive in the period between being born and reaching age a

Variable	Description
$\varphi(a)$	Probability that a binding site is free given that its owner has age a
$\pi_0(a)$	Density function for the age of the owner of a randomly chosen free binding site
$\pi_1(a)$	Density function for the age of the owner of a randomly chosen occupied binding site
$H(a, \alpha)$	Density function for the ages of two partners in a randomly chosen partnership
$p_k(a)$	Probability that an individual has k partners at age a , $k = 0, \dots, n$
$q_k(a)$	Probability that a partner of age a has k partners in total, $k = 1, \dots, n$
$P(k, l)$	Probability that the joint degree of a randomly chosen partnership is (k, l) , $k, l = 1, \dots, n$

Finally, as always, the assumptions matter. Here we model demography so that individuals enter the population without any partners. After its birth, an individual may acquire and lose partners according to the rules assumed in Sect. 5.2. Therefore, the number of partners of an individual contains information about the age of that individual. One may think of different ways of modelling demography that may not necessarily lead to age dependencies. Indeed, an assumption for the numbers of partners of newborn individuals made in [10] achieves that age dependencies are absent.

5.3.2 Age-Age and Age-Degree Dependencies

We show that there is dependence between the ages of partners by reasoning at the binding site and partnership level (compare with the derivation of the correlation coefficient for the related model in [9, Section 3.3]). Whenever we write ‘at age a ’ (or just ‘age a ’), the individual under consideration has, by assumption, survived until that age. First, consider a binding site (see also [1, Section 4]). Let $\varphi(a)$ denote the probability that a binding site is free at age a . Then φ satisfies the ODE

$$\frac{d\varphi}{da} = -\rho F \varphi + (\sigma + \mu)(1 - \varphi),$$

with birth condition $\varphi(0) = 1$, so

$$\varphi(a) = \frac{\sigma + \mu}{\rho F + \sigma + \mu} + \frac{\rho F}{\rho F + \sigma + \mu} e^{-(\rho F + \sigma + \mu)a}. \quad (5.11)$$

We have the identity

$$F = \int_0^{\infty} \mu e^{-\mu a} \varphi(a) da$$

for the fraction of free binding sites (one can use Eq. (5.9) to check that this identity holds). Then the probability density function of the age of (the owner of) a free binding site is given by

$$\pi_0(a) = \frac{\mu e^{-\mu a} \varphi(a)}{F}. \quad (5.12)$$

Similarly, the probability density function for the age of a randomly chosen occupied binding site is

$$\pi_1(a) = \frac{\mu e^{-\mu a} (1 - \varphi(a))}{1 - F}. \quad (5.13)$$

Next, observe that, due to independence at partner formation, the joint age density function of two partners at partner formation is the product $\pi_0(a)\pi_0(\alpha)$ of age density functions of free binding sites. Two free binding sites are paired at rate ρF^2 , and a partnership dissolves at rate $\sigma + 2\mu$. Furthermore, newborn individuals (at age 0) have no partners. Therefore, the density function for the ages of two partners in a randomly chosen partnership satisfies

$$\begin{aligned} \frac{\partial p}{\partial a} + \frac{\partial p}{\partial \alpha} &= \rho F^2 \pi_0(a) \pi_0(\alpha) - (\sigma + 2\mu)p, \\ p(0, \alpha) &= 0 = p(a, 0). \end{aligned}$$

Solving for p and normalizing into a probability density function $H(a, \alpha)$ for the ages of two partners in a randomly chosen partnership yields

$$\begin{aligned} H(a, \alpha) &= \frac{p(a, \alpha)}{\int_0^{\infty} \int_0^{\infty} p(b, \beta) db d\beta} \\ &= \frac{\int_0^{\min(a, \alpha)} \rho F^2 \pi_0(a - \xi) \pi_0(\alpha - \xi) e^{-(\sigma + 2\mu)\xi} d\xi}{1 - F}. \end{aligned} \quad (5.14)$$

Here we used that $\int_{a=0}^{\infty} \int_{\alpha=0}^{\infty} p(a, \alpha) da d\alpha = 1 - F$ in the second equality (use Eq. (5.20) in Lemma A.1 of “[Appendix 1: Relationship Between \$\pi_1\(a\)\$ and \$H\$](#) ”).

Note that we can also reason directly from the interpretation of the model to obtain Eq. (5.14). Consider a randomly chosen partnership of duration ξ with partners of age a and α , then at partnership formation these individuals had ages $a - \xi$ and $\alpha - \xi$. At partnership formation, their ages are independent and the densities are $\pi_0(a - \xi)$ and $\pi_0(\alpha - \xi)$. The rate at which a partnership is formed is ρF^2 . Next,

the probability that a partnership has duration of at least ξ is $e^{-(\sigma+2\mu)\xi}$. Obviously, the partnership duration ξ satisfies $0 \leq \xi \leq \min(a, \alpha)$. Finally, the probability that a binding site is occupied is $1 - F$, yielding the normalizing constant. By combining these elements we obtain Eq. (5.14).

Finally, the expression for $H(a, \alpha)$ allows us to conclude that there is dependence in the ages of two partners. Indeed, if these were independent of one another, then the probability density function for the ages of two partners in a randomly chosen partnership would be the product of the probability density functions for the age of a randomly chosen occupied binding site, i.e. $\pi_1(a)\pi_1(\alpha)$ with π_1 given by Eq. (5.13). Since $H(a, \alpha) \neq \pi_1(a)\pi_1(\alpha)$, we conclude that demographic turnover (in the way that we have modelled it) induces age dependence.

In order to show that the age and degree of an individual are correlated, we relate the binding site level to the i -level. Let $p_k(a)$ denote the probability that an individual has k partners at age a . Then, by the independence assumption for binding sites, combinatorics yields

$$p_k(a) = \binom{n}{k} \varphi(a)^{n-k} (1 - \varphi(a))^k.$$

In particular, we find that information about the age of an individual helps to predict its degree. Since we also have dependence in the ages of two partners, we expect that there is dependence in the degrees of two partners. This dependence is quantified by means of the degree correlation coefficient in the next subsection.

5.3.3 Quantifying the Degree-Degree Dependence

5.3.3.1 Joint Degree Distribution

Let $P(k, l)$ denote the probability that a randomly chosen partnership has joint degree (k, l) , $1 \leq k, l \leq n$, i.e. the probability that two individuals have degrees k and l given that they are partners.

Next, we consider the probability that an individual u has k partners at age a , given that it is a partner of an individual v with age α . By assumption, given the age of the owner, the binding sites of an individual are independent of one another as long as the owner does not die. Therefore, the fact that u of age a is in a partnership with individual v simply means that one of the n binding sites of u is already occupied. The probability that any other binding site of u is free is $\varphi(a)$ with $\varphi(a)$ given by Eq. (5.11). Combinatorics yields that the probability that u has, at age a , k partners in total, given partner v with age α , is equal to

$$q_k(a) = \binom{n-1}{k-1} \varphi(a)^{n-k} (1 - \varphi(a))^{k-1}, \quad (5.15)$$

where $1 \leq k \leq n$, $a > 0$. Conditioning on u having age a and v having age α , the probability that the joint degree of u and v is (k, l) is simply

$$q_k(a)q_l(\alpha). \quad (5.16)$$

The probability density function for the ages of the partners in a randomly chosen partnership is $H(a, \alpha)$ (see Eq. (5.14)). By integrating over all possible ages a and α we obtain the probability $P(k, l)$ that two individuals u and v in a randomly chosen partnership have k and l partners:

$$P(k, l) = \int_{\alpha=0}^{\infty} \int_{a=0}^{\infty} q_k(a)q_l(\alpha)H(a, \alpha)dada\alpha \quad (5.17)$$

Note that two individuals in a randomly chosen partnership are identically distributed (with respect to age as well as with respect to number of partners) so P is symmetric in k and l , i.e. $P(k, l) = P(l, k)$. Furthermore, note that both the $q_k(a)$ and $\pi_0(a)$ are functions of $\varphi(a)$ with $\varphi(a)$ given by Eq. (5.11). By algebraic expansion of the powers of the form $(x + y)^m$ one can rewrite these probabilities q_k as

$$q_k(a) = \binom{n-1}{k-1} \sum_{j=0}^{n-k} \sum_{i=0}^{k-1} \binom{n-k}{j} \binom{k-1}{i} (-1)^i \left(\frac{\sigma + \mu}{\rho F + \sigma + \mu} \right)^{k-1+j} \left(\frac{\rho F}{\rho F + \sigma + \mu} \right)^{n-k-j} e^{-(\rho F + \sigma + \mu)(i+j)a}.$$

So Eq. (5.17) can be written as the sum of integrals over exponential functions. By working out these integrals one obtains an explicit expression for $P(k, l)$ in terms of the model parameters. In this paper, our aim is to quantify the dependence between the degrees of partners by means of the correlation coefficient, and we are not that much interested in the specific probabilities $P(k, l)$ for specific k and l . Therefore, we do not write down the explicit expression for $P(k, l)$. Rather, when considering the correlation coefficient in Sect. 5.3.3.2, the sum $\sum k l P(k, l)$ plays an important role, which, among other sums, is worked out in “[Appendix 3: The Correlation Coefficient as a Function of Model Parameters](#)”. Finally, we can obtain the marginal degree distribution (Q_k) from the joint degree distribution $P(k, l)$, and this leads to the same expression for Q_k as the one derived from the degree distribution in the population (see our previous work [7]); see “[Appendix 2: The Marginal Degree Distribution \$Q_k = \sum_l P\(k, l\)\$](#) ” for details.

Remark 1 (Binding site or i -level perspective) Note that one could also obtain the probability $P(k, l)$ by taking the perspective of individuals in a partnership rather than binding sites. This is exactly what we have done in [11, Appendix B] for $n = 2$. We calculated probability (5.17) for $n = 2$ using the number of partners of two individuals in a partnership without taking into account their ages. While in principle

this is not more difficult than the reasoning in this section, generalizing to $n > 2$ quickly becomes quite involved as the number of possible (k, l) pairs grows quickly with n . This is also the reason that we only worked out $n = 2$ in the appendix of [11]: for $n = 2$ only the inverse of a 3×3 matrix is needed, but the size of this matrix quickly grows with n . Nevertheless, one can check that Eq. (5.17) coincides with Eq. (51) of [11] for $n = 2$ (e.g. by using Mathematica and identity (20) in [7] for F).

5.3.3.2 Correlation Coefficient

Choose a partnership at random and consider one of the partners. The probability that this individual has k partners is Q_k where Q_k is given by Eq. (5.22). On the other hand, the probability that the randomly chosen partnership has joint degree (k, l) is $P(k, l)$ with $P(k, l)$ given by Eq. (5.17). In [1, 11] we approximated the network structure by pretending that there is independence between partners of two individuals that are in a partnership, i.e. we approximated $P(k, l)$ by $Q_k Q_l$. That this is really an approximation, i.e. that $P(k, l) \neq Q_k Q_l$, was shown by way of explicit calculations for $n = 2$ in [11, Appendix B]. In this section we investigate the approximation in more detail.

We use the correlation coefficient to quantify the dependence (this coefficient is often denoted by ρ but since we have already reserved this symbol for the partnership formation rate we will simply write *corr*). Let D_u and D_v be the random variables denoting the degrees of the individuals u and v in a randomly chosen partnership. Then the joint probability distribution of D_u and D_v is $(P(k, l))$. The degree correlation coefficient is given by

$$\text{corr} = \frac{E(D_u D_v) - E(D_u)E(D_v)}{\sqrt{\text{Var}(D_u)\text{Var}(D_v)}} = \frac{\text{Cov}(D_u, D_v)}{\text{Var}(D_u)} = \frac{A - B^2}{C - B^2}. \quad (5.18)$$

where $\text{Cov}(D_u, D_v)$ is the covariance of D_u and D_v , and

$$A = \sum_{k,l} klP(k, l), \quad B = \sum_k kQ_k, \quad \text{and} \quad C = \sum_k k^2 Q_k. \quad (5.19)$$

The correlation coefficient satisfies $-1 \leq \text{corr} \leq 1$, where $\text{corr} = -1$ corresponds to fully disassortative mixing in the degrees of partners and $\text{corr} = 1$ corresponds to fully assortative mixing. In case the degrees of partners are independent of one another, the correlation coefficient is zero. Note that for $n = 1$, i.e. in the case of monogamous pair formation, the degree of a partner is always 1, i.e. $Q_1 = 1$ and $P(1, 1) = 1$. The correlation coefficient is not defined for this case. We are only interested in $n = 2, 3, \dots$

We are interested in the behaviour of *corr* as a function of the four model parameters n (partnership capacity), σ (partnership separation rate), ρ (partnership formation rate), and μ (death rate). An explicit expression for *corr* in terms of the

model parameters is found by working out A , B , and C (defined by Eq. (5.19)) at the right-hand side of Eq. (5.18). These can all be expressed as integrals of simple functions of $\varphi(a)$, which we then can evaluate (note that F is also a function of model parameters σ , ρ , and μ ; see Eq. (5.10)). We work this out in “[Appendix 3: The Correlation Coefficient as a Function of Model Parameters](#)”.

The calculations in [11, Appendix B] already showed that there is dependence for $n = 2$ with $corr > 0$. So for $n = 2$ there is assortativity with respect to the degrees of partners. For general n , the expression (5.27) in “[Appendix 3: The Correlation Coefficient as a Function of Model Parameters](#)” in this text shows that $corr > 0$. So, in accordance with our expectation in Sect. 5.3.2, there is dependence in the degrees of partners. Moreover, $corr > 0$ for all $\rho, \sigma, \mu > 0$, and $n > 1$. In other words, for all $n > 1$, the network is assortative in the degree: partners tend to have similar degrees. We study how $corr$ depends on the model parameters in the next subsection.

Remark 2 (Limiting behaviour $\mu \rightarrow 0$) Note that $\lim_{\mu \rightarrow 0} corr = 0$ (use the explicit expression for $corr$ calculated in “[Appendix 3: The Correlation Coefficient as a Function of Model Parameters](#)”), in complete accordance with the independence in degrees in the dynamic network model without demography of Sect. 5.2.

Remark 3 (Degree-degree correlation) Degree correlation does occur in some real world networks and constructive procedures to generate networks with prescribed degree-degree correlation have been devised, see [12–14] and references therein. As has been shown here, a dynamic network model incorporating demographic turnover can exhibit degree-degree correlation as a consequence of age-age correlation. This provides a possible mechanistic interpretation of emergent assortative mixing.

5.3.3.3 The Effect of Demographic Changes on the Correlation Coefficient

Now that we have an explicit expression for $corr$, we can ask how it depends on the model parameters. Our main interest is in the relative time scales of demographic changes compared to partnership changes. Therefore, we are interested in $\mu/\sigma \in (0, 1]$. In particular, we are interested in the limit $\mu/\sigma \rightarrow 0$, i.e. in the limit that partnership changes are much faster than any demographic changes, while at the same time ρ/σ remains constant, i.e. the partnership formation rate ρ and the separation rate σ are on the same time scale.

The formula (5.18) for $corr$ and the expressions (5.24), (5.25), and (5.26) allow for an explicit expression of $corr$ in terms of model parameters n , σ , ρ , and μ . To eliminate one parameter, we rewrite the correlation coefficient $corr$ as a function of n , $\tilde{\rho} = \rho/\sigma$, and $\tilde{\mu} = \mu/\sigma$:

$$corr = \frac{a}{b},$$

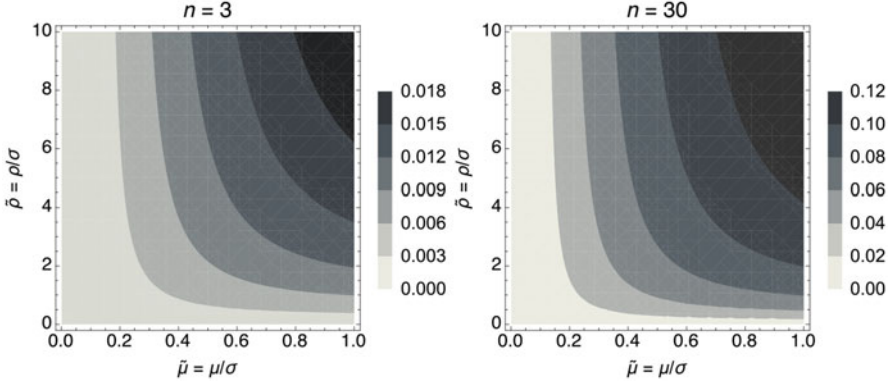


Fig. 5.1 Correlation coefficient as a function of $\tilde{\mu}$ (x-axis) and $\tilde{\rho}$ (y-axis) for $n = 3$ and $n = 30$. Note that the colour scales are different in the two figures: for $n = 3$ the scale is between 0 and 0.018 and for $n = 30$ the scale is between 0 and 0.12

with

$$\begin{aligned}
 a &= \tilde{\mu}^2(n-1)(2\tilde{\mu} + 3x + 3) (4\tilde{\mu}^2 + 2\tilde{\rho}^2 + \tilde{\mu}(8\tilde{\rho} - 2x + 4) - 2\tilde{\rho}(x-2) - x + 1), \\
 b &= 2(-2\tilde{\mu} + x - 1)(2\tilde{\mu} + x + 2) \{ -4\tilde{\mu}^3(n+1) + 2\tilde{\mu}^2(n(-3\tilde{\rho} + x - 2) \\
 &\quad - 9\tilde{\rho} + x - 3) + \tilde{\mu}(n(\tilde{\rho}(x-3) + x - 1) - 23\tilde{\rho} + 7\tilde{\rho}x + 2x - 2) + 6\tilde{\rho}(x-1) \}, \\
 x &= \sqrt{(1 + 2\tilde{\mu})(4\tilde{\rho} + 1 + 2\tilde{\mu})}.
 \end{aligned}$$

Next, by considering the derivative of *corr* with respect to the parameters n , $\tilde{\rho}$, and $\tilde{\mu}$, we find that *corr* is strictly increasing in n and $\tilde{\rho}$, and $\tilde{\mu}$. In Sect. 5.3.3.2 we also observed that *corr* > 0 so the network is assortative in degree. Furthermore, since *corr* is strictly increasing in n , $\tilde{\rho}$, and $\tilde{\mu}$, by considering the limit $\lim_{n \rightarrow \infty, \tilde{\rho} \rightarrow \infty, \tilde{\mu} \rightarrow 1} \text{corr} = 1/4$, we find that the correlation coefficient is at most 1/4, for all $n \geq 2$, $\tilde{\rho} > 0$, and $\tilde{\mu} \in (0, 1]$.

Finally, we investigate *corr* numerically. For fixed n , we investigate the correlation coefficient as a function of $\tilde{\mu}$ and $\tilde{\rho}$. As we are interested in the relative time scales of demographic changes compared to partnership changes, we consider $\tilde{\mu} \in (0, 1]$ and $\tilde{\rho} \in (0, \infty)$. In general, we find that the correlation coefficient is close to zero; see Fig. 5.1 for $n = 3$ and $n = 30$. So, although there is dependence, the dependence is generally not very strong. The correlation coefficient *corr* is largest when the time scales of demographic and partnership changes are close to each other. Moreover, the higher the partnership formation rate is compared to the separation rate, the larger *corr* is.

Next, we compare the effect of different n values while keeping $\tilde{\rho}$ fixed in Fig. 5.2. While the correlation coefficient increases as a function of n , for relatively small values of n , *corr* remains relatively close to 0 (compared to the supremum

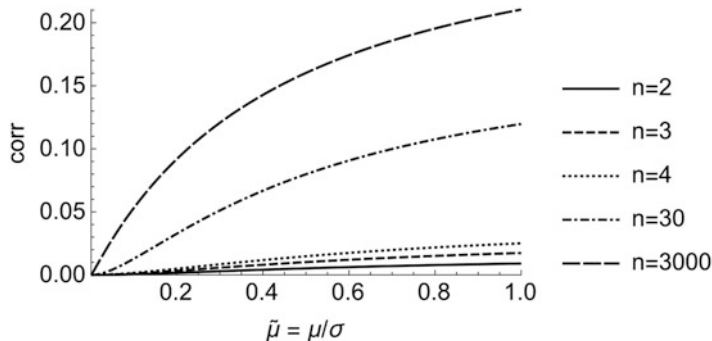


Fig. 5.2 Correlation coefficient as a function of the ratio $\tilde{\mu}$ for $n = 2, 3, 4, n = 30$, and $n = 3000$ and $\tilde{\rho} = 10$. The corresponding fraction F of free binding sites is monotonically decreasing from ~ 0.41 for $\tilde{\mu}=1$ to ~ 0.27 for $\tilde{\mu} = 0$

value of $1/4$). For all n , it holds that the faster partnership changes are compared to demographic changes, i.e. the smaller $\tilde{\mu}$ is, the smaller $corr$ is. We find that $corr$ tends to zero quite rapidly as $\tilde{\mu} \rightarrow 0$.

5.4 The Mean Field at Distance One Assumption and the Spread of an SIR Infectious Disease on the Network

In this text we have so far considered the static configuration network and two dynamic variants, one without and one with demographic turnover (Sects. 5.2 and 5.3, respectively). If we describe the network by only labelling individuals by their degree, i.e. by their numbers of partners, then no information about the partners of partners is included in the bookkeeping. However, in both the static network and the dynamic network without demography, we know that there is independence in the degrees of partners. Therefore, although not explicitly included in our bookkeeping, statistical information about the number of partners of partners of an individual with k partners is readily available in the form of the size-biased degree distribution.

This is not the case for the dynamic network model with demographic turnover. We have seen in Sect. 5.3 that in this dynamic network model there is dependence in degrees of partners. Therefore, the degree of the individual under consideration cannot be ignored when considering the degree of the partner. But in previous work [1, 11] we did exactly that. We pretended that the degree of the partner was independent of the degree of the focus individual, and we termed the approximation the ‘mean field at distance one assumption’ (more appropriately we should have called it the mean field at distance one *approximation*). This mean field at distance one assumption allowed us to formulate a model for the spread of infection on

the dynamic network with demography. It enabled us to write down a closed system of equations that is analytically tractable. Therefore, while we were well aware that an approximation was made by this assumption, it was very convenient to do so.

Information about partners of partners of an individual is crucial in describing the disease dynamics on the network. In the remainder of this section we elaborate on this point. Consider the spread of an SIR (Susceptible→Infectious→Recovered) infection superimposed on the network. We label each individual by (i) its disease status, (ii) the number of partners it has, and (iii) the disease status of each of these partners. Then, in order to describe the disease dynamics in the population, we need to make statements about partners of partners of an individual. Indeed, suppose we have an individual with a susceptible partner, then the rate at which this susceptible partner becomes infected depends on the total number of infectious partners it has. However, this kind of information is exactly what we do not have in our description. In fact, such information would only be available if we have a complete description of the entire network. Indeed, suppose we would incorporate partners of partners in our description. Then we would also need to know about the number of infectious partners of susceptible partners of partners, etcetera. This is where the mean field at distance one assumption comes into play. This is the assumption that we may average over the population in a certain way and consider the *expected* number of infectious partners of a susceptible partner instead.

In the static network and the dynamic network without demography, with independence in degrees, averaging is done as follows. Consider an individual u with disease status d (either susceptible, infectious, or recovered), and consider a susceptible partner v of u . Then we take into account that u has disease status d but not the degree of u (here we use independence of degrees): the expected number of infectious partners of v is the expected number of infectious partners of a susceptible partner of an individual with disease status d . The latter is the expected number at the p-level. In fact, we can apply the mean field at distance one assumption purely at the binding site level. The probability that v has k partners is given by the size-biased degree distribution. Individual v has one special binding site for which the transmission rate along this binding site is determined by the disease status of u . The $k - 1$ other binding sites of v are indistinguishable. The transmission rate along each of these other $k - 1$ binding sites is determined by the probability that a binding site of v is occupied by an infectious partner.

In the static network case one can prove that the mean field at distance one description is exact: the deterministic description can be obtained as the large population limit of a stochastic model (under suitable technical conditions), see [2, 15, 16]. For the dynamic network without demography we conjecture that this is also true and we pose this as an open problem in [1]. In Sect. 5.2 we provided evidence in support of this conjecture by showing that, as in the static setting, there is independence in the degrees of partners. In the dynamic network with demography we *know* that we need to take into account the dependence in degrees.

In Sect. 5.3.3 we quantified the dependence between degrees through the correlation coefficient that we subsequently studied numerically. While the degree correlation is always larger than zero in case of demographic turnover, in general, we

found the correlation coefficient to be quite small. So, even though an approximation is made by ignoring knowledge about the degree of an individual u when considering the degree of a partner v , this approximation may not be that bad. Yet, we wonder whether it is possible to give an exact statistical description of the disease dynamics on the network. We conjecture that this is in fact possible and that the key to this is age.

As we have seen in Sect. 5.3, degree-degree correlation can be deduced from age-age correlation. If we incorporate the age of partners in the bookkeeping of individuals, we can use that age to predict the number of partners of those partners. More concretely, consider a binding site belonging to an individual with age a . This binding site is either free or occupied by a partner *with age* α . If the binding site is, at age a , occupied by a partner with age α , then this partner has k partners with probability $q_k(\alpha)$, where $q_k(\alpha)$ is given by Eq. (5.15). In particular, no approximation needs to be made. We conjecture that this carries over to the setting with an infectious disease superimposed on the network: by including in our bookkeeping not only the disease status and age of the binding site under consideration and the disease status of any partner, but also the ages of these partners, one can again employ the mean field at distance one assumption without making an approximation, i.e. average over the population in the correct way: we may consider the *expected number* of infectious partners of a susceptible partner *of age* α of an individual with disease status d and age a (which is part of the description of the model if the bookkeeping includes age of partners).

Proving this claim about the bookkeeping with the age of partners included is both outside the scope of this text and outside our area of expertise. Rather we conclude this section by highlighting some aspects of the mean field at distance one assumption by considering the basic reproduction number R_0 . The traditional perspective that one takes for R_0 is that of an infectious case: R_0 can be interpreted as the expected number of secondary cases generated by one typical newly infected case at the beginning of an epidemic. As we explained in [1], it can be advantageous to take the different perspective of ‘reproduction opportunities’ (where ‘reproduction’ corresponds to transmission of the infectious agent to another host). In this context reproduction opportunities consist of $-+$ links, i.e. partnerships between susceptible ($-$) and infectious ($+$) individuals. This different perspective does not change the expression that one obtains for R_0 . So we can interpret R_0 as the expected number of $-+$ links generated by one typical newly formed $-+$ link at the beginning of an epidemic.

The reasoning in [1, Section 4.3] was as follows. At the beginning of an epidemic, for an SIR infection, there are two birth-types of $-+$ links:

- Type 0 the $-+$ link was formed when a $-$ binding site and a $+$ binding site got connected
- Type 1 the $-+$ link is a transformed $--$ link (one of the two owners got infected by one of its other partners)

Note that the density of the age distribution of the owner of a binding site is π_0 upon partner formation (see Eq. (5.12)). Therefore, the density of the age distribution of the $-$ binding site of Type 0 $-+$ links is π_0 . However, the age of the $-$ binding site of Type-1 $-+$ links is correlated to the age of its $+$ partner. In [1], we approximated the age of the $-$ binding site in the Type-1 link by ignoring the correlation with the age of its $+$ partner. We approximated the density of the age distribution of the $-$ binding site in the Type-1 link by π_1 where π_1 is given by Eq. (5.13) (see [1, Section 4.3] for details). These densities π_0 and π_1 for the ages of binding sites are key in characterizing R_0 . One ends up with a characterization of R_0 as the dominant eigenvalue of a 2×2 next-generation matrix K where entry K_{ij} of K can be interpreted as the expected number of secondary cases with state-at-infection i caused by one newly infected individual with state-at-infection j at the beginning of an epidemic [17, Chapter 7].

However, if we include the age of partners in our bookkeeping, then this also needs to be included in our characterization of R_0 . While nothing changes for the $-$ binding sites in the Type-0 links in terms of the density of the age distribution, we can no longer simply consider Type-1 links. Rather, one needs to keep track of age at the moment that the Type-1 $-+$ link is born. This leads to an infinite-dimensional problem rather than the simple setting of two types that arise from the approximation. Clearly from the point of view of the characterization of R_0 it is attractive to make an approximation by ignoring age correlation i.e. assuming independence. One only deals with two types (and the dominant eigenvalue of a 2×2 next-generation matrix) rather than infinitely many types (and a corresponding next-generation operator and its spectral radius).

Is the mathematical tractability then lost by including ages of partners in the bookkeeping? No, not necessarily. But the R_0 -characterization does illustrate that including the age of partners in the bookkeeping will make the model formulation and analysis far less straightforward than in the static network or the dynamic network without demography.

5.5 Conclusion

In this text we discussed the mean field at distance one assumption for two dynamic network models of [1] that are inspired by the (static) configuration network. The first dynamic network model includes partnership formation and separation, while the second dynamic network model additionally includes demographic turnover. We concerned ourselves with a description that only includes individuals and their partners, without any information about partners of partners in the bookkeeping. The mean field at distance one assumption concerns itself with these partners of partners. It states that one can average over the population in a well-defined way to obtain the relevant information. In case of a static configuration network the mean field at

distance one assumption holds as there is independence in the degrees of partners. This independence in degrees of partners is shared by the dynamic network model without demography; see Sect. 5.2. This independence result suggests that we can describe the spread of infection on the dynamic network without demography using the mean field at distance one approach (as indeed conjectured in [1]).

However, degree dependence between partners arises in the dynamic network model with demography. We showed this via the existing age dependence between partners in Sect. 5.3.2. As discussed in Sect. 5.4, in previous work we ignored these dependencies between the partners [1, 11]. In the current text we investigated the dependency between partners by means of the degree correlation coefficient. In general this degree correlation coefficient is positive but reasonably small. This is especially the case if demographic and partnership changes are on somewhat different time scales, and partnership formation and separation are on comparable time scales, and partnership capacity n is not too large, which are quite reasonable assumptions to make.

Clearly there are advantages to approximating the true process by ignoring these dependencies between partners. Especially if the degree correlation is rather small, then it is attractive to do so. The goal of this text is not to advocate that one should never concern oneself with approximations (clearly not as this is exactly what we have done in previous work). Rather, our point is that it is important to be aware of the assumptions that one makes when formulating models and the limitations and consequences of the assumptions.

Ideally, one can provide a statistical description for transmission dynamics on a network without making approximations (whether it is desirable to still make approximations, e.g. for computational convenience, is a different issue). In Sect. 5.4, we speculated that by incorporating age of partners in the dynamic network with demography, one can avoid making approximations. But, as we also outlined in the same section, this probably comes at a price. It may be that the analysis of the model becomes much harder. How to formulate and analyse the model that includes ages of partners is outside of the scope of this text and is left for future work. Here we end with the conjecture that bookkeeping that takes the age of partners into account allows for an exact description of the spread of infectious diseases on the dynamic network with demography. We hope that this text motivates some probabilists to take up the challenge of proving (or, unexpectedly, disproving) the conjecture.

Acknowledgements We would like to thank Pieter Trapman for opening our eyes during the Infectious Disease Dynamics meeting at the Isaac Newton Institute in Cambridge in 2013 as well as the members of the infectious disease dynamics journal clubs in Utrecht and Stockholm, and two anonymous reviewers for helpful comments.

K.Y. Leung is supported by the Netherlands Organisation for Scientific Research (NWO) [grant Mozaïek 017.009.082] and the Swedish Research Council [grant number 2015-05015_3].

Appendix 1: Relationship Between $\pi_1(a)$ and H

The probability density function $\pi_1(a)$ for the age of an occupied binding site (see Eq. (5.13)) is related to the probability density function $H(a, \alpha)$ for the ages of two partners u and v in a randomly chosen partnership. This relation is formulated in Eq. (5.20).

Lemma A.1

$$\int_{\alpha=0}^{\infty} H(a, \alpha) d\alpha = \pi_1(a). \quad (5.20)$$

Proof First note that we can rewrite $H(a, \alpha)$ as

$$H(a, \alpha) = \frac{\mu e^{-\mu a}}{1 - F} \int_{\xi=0}^{\min(a, \alpha)} \rho F \varphi(a - \xi) \pi_0(\alpha - \xi) e^{-(\sigma + \mu)\xi} d\xi.$$

Next, one finds that

$$\int_{\alpha=0}^{\infty} \int_{\xi=0}^{\min(a, \alpha)} \rho F \varphi(a - \xi) \pi_0(\alpha - \xi) e^{-(\sigma + \mu)\xi} d\xi d\alpha = 1 - \varphi(a), \quad (5.21)$$

by direct calculations using Eqs. (5.11) and (5.13) for φ and π_0 , and we conclude that Eq. (5.20) holds. One can also reason as follows for Eq. (5.21): $\rho F \varphi(a - \xi) \pi_0(\alpha - \xi) e^{-(\sigma + \mu)\xi}$ is the probability that a binding site with age a has a partner with age α and partnership duration ξ given that the owner of the binding site under consideration does not die. By integrating over all possible partnership durations $0 \leq \xi \leq \min(a, \alpha)$, we obtain the probability that a binding site with age a has a partner with age α (given that the owner does not die): $\int_0^{\min(a, \alpha)} \rho F \varphi(a - \xi) \pi_0(\alpha - \xi) e^{-(\sigma + \mu)\xi} d\xi$. Then finally, by integrating over all possible $\alpha \geq 0$ we obtain the probability $1 - \varphi(a)$ that a binding site with age a is occupied.

Appendix 2: The Marginal Degree Distribution

$$Q_k = \sum_l P(k, l)$$

We obtain the probability Q_k that an individual involved in a randomly chosen partnership has degree k from the joint probability distribution $P(k, l)$, cf. (5.17), by summing over all $l = 1, \dots, n$, i.e. $Q_k = \sum_{l=1}^n P(k, l)$. On the other hand, in previous work [7] we have derived an expression for Q_k from the stable degree distribution $(P_k)_k$ in the population: $Q_k = kP_k/n(1 - F)$. We show that both ways of arriving at Q_k yield the same expression, i.e.

$$Q_k = \sum_{l=1}^n P(k, l) = kP_k/n(1-F). \quad (5.22)$$

First, we work out the right-hand side. P_k is expressed in terms of the probability $\varphi(a)$ as follows:

$$P_k = \binom{n}{k} \int_0^\infty \mu e^{-\mu a} \varphi(a)^{n-k} (1 - \varphi(a))^k da.$$

On the other hand, we can simplify $\sum_{l=1}^n P(k, l)$. First of all, note that since $q_l(a)$ is a probability distribution, $\sum_{l=1}^n q_l(\alpha) = 1$. Therefore

$$\begin{aligned} & \sum_{l=1}^n P(k, l) \\ &= \sum_{l=1}^n \int_{a=0}^\infty \int_{\alpha=0}^\infty \int_0^{\min(a,\alpha)} q_k(a) q_l(\alpha) \frac{\rho F^2 \pi_0(a - \xi) \pi_0(\alpha - \xi) e^{-(\sigma+2\mu)\xi}}{1-F} d\xi d\alpha da \\ &= \int_{a=0}^\infty \int_{\alpha=0}^\infty \int_0^{\min(a,\alpha)} q_k(a) \frac{\rho F^2 \pi_0(a - \xi) \pi_0(\alpha - \xi) e^{-(\sigma+2\mu)\xi}}{1-F} d\xi d\alpha da. \end{aligned} \quad (5.23)$$

Next, note that we can simplify Eq. (5.23) as follows:

$$\begin{aligned} & \sum_{l=1}^n P(k, l) \\ &= \frac{k \binom{n}{k}}{n(1-F)} \int_{a=0}^\infty \mu e^{-\mu a} \varphi(a)^{n-k} (1 - \varphi(a))^k (1 - \varphi(a))^{-1} \\ & \quad \int_{\alpha=0}^\infty \int_{\xi=0}^{\min(a,\alpha)} \rho F^2 e^{\mu\xi} \frac{\varphi(a - \xi)}{F} \frac{\mu e^{-\mu(\alpha - \xi)} \varphi(\alpha - \xi)}{F} e^{-(\sigma+2\mu)\xi} d\xi d\alpha da \\ &= \frac{k \binom{n}{k}}{n(1-F)} \int_{a=0}^\infty \mu e^{-\mu a} \varphi(a)^{n-k} (1 - \varphi(a))^k (1 - \varphi(a))^{-1} \\ & \quad \int_{\alpha=0}^\infty \int_0^{\min(a,\alpha)} \rho F \varphi(a - \xi) \pi_0(\alpha - \xi) e^{-(\sigma+\mu)\xi} d\xi d\alpha da \\ &= \frac{k \binom{n}{k}}{n(1-F)} \int_{a=0}^\infty \mu e^{-\mu a} \varphi(a)^{n-k} (1 - \varphi(a))^k (1 - \varphi(a))^{-1} (1 - \varphi(a)) da. \end{aligned}$$

Here we used Eq. (5.20) in the third equality. So we find that Eq. (5.22) indeed holds.

Appendix 3: The Correlation Coefficient as a Function of Model Parameters

We work out Eq. (5.18) by computing A , B , and C , defined by Eq. (5.19).

$$\begin{aligned}
 A &= \sum_{k=1}^n \sum_{l=1}^n k l P(k, l) = \int_{a=0}^{\infty} \int_{\alpha=0}^{\infty} \sum_{k=1}^n k q_k(a) \sum_{l=1}^n l q_l(\alpha) H(a, \alpha) d a d \alpha \\
 &= \int_{a=0}^{\infty} \int_{\alpha=0}^{\infty} (n(1 - \varphi(a)) + \varphi(a))(n(1 - \varphi(\alpha)) + \varphi(\alpha)) H(a, \alpha) d a d \alpha \\
 &= \frac{1}{(1 - F)(\rho F + \sigma + 2\mu)^2(2\rho F + 3\sigma + 4\mu)(2(\rho F + \sigma + \mu) + \mu)^2} \\
 &\quad \left\{ \rho(\mu^2(\rho^2 F^2(n(33n + 46) + 1) + 2\rho F\sigma(92n + 33) + 179\sigma^2) \right. \\
 &\quad \quad + 4\mu(\rho F n + \sigma)(4\rho^2 F^2 n + 10\rho F\sigma(n + 1) + 19\sigma^2) \\
 &\quad \quad \left. + 6\mu^3(2\rho F(8n + 3) + 31\sigma) + 4\sigma(2\rho F + 3\sigma)(\rho F n + \sigma)^2 + 72\mu^4 \right\}, \tag{5.24}
 \end{aligned}$$

where the last equality is calculated using Mathematica.

We already calculated the mean $B = \sum_{k=1}^n k Q_k$ in [7, eq. (23)]. For completeness, we work it out using the probability distribution $(P(k, l))$.

$$\begin{aligned}
 B &= \sum_{k=1}^n k Q_k = \sum_{k=1}^n k \sum_{l=1}^n P(k, l) \\
 &= \int_{a=0}^{\infty} \sum_{k=1}^n k q_k(a) \int_{\alpha=0}^{\infty} \sum_{l=1}^n q_l(\alpha) H(a, \alpha) d \alpha d a \\
 &= \int_{a=0}^{\infty} (n(1 - \varphi(a)) + \varphi(a)) \int_{\alpha=0}^{\infty} H(a, \alpha) d \alpha d a \\
 &= \int_{a=0}^{\infty} (n(1 - \varphi(a)) + \varphi(a)) \pi_1(a) d a \\
 &= 1 + \frac{2\rho F(n - 1)}{2(\rho F + \sigma + \mu) + \mu}. \tag{5.25}
 \end{aligned}$$

In the first equality we used that (Q_k) is the marginal distribution of $(P(k, l))$, and in the fifth equality we used identity (5.20).

Finally, we consider the second moment $C = \sum_{k=1}^n k^2 Q_k$:

$$\begin{aligned}
 C &= \sum_{k=1}^n k^2 Q_k = \sum_{k=1}^n k^2 \sum_{l=1}^n P(k, l) \\
 &= \int_{a=0}^{\infty} \sum_{k=1}^n k^2 q_k(a) \int_{\alpha=0}^{\infty} \sum_{l=1}^n q_l(\alpha) H(a, \alpha) d\alpha da \\
 &= \int_{a=0}^{\infty} (n^2(1 - \varphi(a))^2 + \varphi(a)((3n - 1)(1 - \varphi(a)) + \varphi(a))) \int_{\alpha=0}^{\infty} H(a, \alpha) d\alpha da \\
 &= \int_{a=0}^{\infty} (n^2(1 - \varphi(a))^2 + \varphi(a)((3n - 1)(1 - \varphi(a)) + \varphi(a))\pi_1(a) da \\
 &= \frac{\rho F(\mu(12\mu + \rho F(24n - 7) + 17\sigma) + 6(\rho^2 F^2 n^2 + \rho F(3n - 1)\sigma + \sigma^2))}{(1 - F)(\rho F + \sigma + 2\mu)(2(\rho F + \sigma + \mu) + \mu)(3(\rho F + \sigma + \mu) + \mu)}. \tag{5.26}
 \end{aligned}$$

Inserting Eqs. (5.24), (5.25), and (5.26) together in Eq. (5.18), we find an explicit expression for the correlation coefficient $corr$. Note that the variance of a random variable is always nonnegative (and nonzero if the random variable is not equal to a constant). Therefore, we find that the sign of $Cov(D_u, D_v) = A - B^2$ determines the sign of the correlation coefficient $corr$ in Eq. (5.18). Note that identity (5.9) for F allows us to express σ in terms of the other parameters: $\sigma = \rho F^2 / (1 - F) - 2\mu$. For clarity, we use this identity for σ in the numerator (but not in the denominator) in the simplification of $Cov(D_u, D_v)$. We find that

$$A - B^2 = \frac{\mu^2 \rho^3 F^2 (1 - F)(n - 1)^2}{(1 - F)^2 (\rho F + \sigma + 2\mu)^2 (2\rho F + 3\sigma + 4\mu)(2\rho F + 2\sigma + 3\mu)^2}. \tag{5.27}$$

In particular, the covariance (and therefore the correlation coefficient $corr$) is strictly larger than zero if $\rho > 0$, $\sigma > 0$, $\mu > 0$, and $n > 1$.

References

1. Leung, K.Y., Diekmann, O.: Dangerous connections: on binding site models of infectious disease dynamics. *J. Math. Biol.* **74**, 619–671 (2017)
2. Barbour, A.D., Reinert, G.: Approximating the epidemic curve. *Electron. J. Probab.* **18**(54), 1–30 (2013)
3. Volz, E.M.: IR dynamics in random networks with heterogeneous connectivity. *J. Math. Biol.* **56**, 293–310 (2008)
4. Kiss, I.Z., Miller, J.C., Simon, O.: *Mathematics of Epidemics on Networks: From Exact to Approximate Models*. Springer, Cham (2017)
5. Durrett, R.: *Random Graph Dynamics*. Cambridge University Press, Cambridge (2006)

6. Van der Hofstad, R.: Random Graphs and Complex Networks, vol. I. Cambridge University Press, Cambridge (2016)
7. Leung, K.Y., Kretzschmar, M.E.E., Diekmann, O.: Dynamic concurrent partnership networks incorporating demography. *Theor. Popul. Biol.* **82**, 229–239 (2012)
8. Britton, T., Lindholm, M.: Dynamic random networks in dynamic populations. *J. Stat. Phys.* **139**, 518–535 (2010)
9. Britton, T., Lindholm, M., Turova, T.: A dynamic network in a dynamic population: asymptotic properties. *J. Appl. Prob.* **48**, 1163–1178 (2011)
10. Lashari, A.A., Trapman, P.: Branching process approach for epidemics in dynamic partnership network. *J. Math. Biol.* (2017). doi:10.1007/s00285-017-1147-0
11. Leung, K.Y., Kretzschmar, M.E.E., Diekmann, O.: *SI* infection of a dynamic partnership network: characterization of R_0 . *J. Math. Biol.* **71**, 1–56 (2015)
12. Newman, M.E.J.: Assortative mixing in networks. *Phys. Rev. Lett.* **89**(20), 208701 (2002)
13. Newman, M.E.J.: The structure and function of complex networks. *SIAM Rev.* **45**(2), 167–256 (2003)
14. Ball, F., Britton, T., Sirl, D.: A network with tunable clustering, degree correlation and degree distribution, and an epidemic thereon. *J. Math. Biol.* **66**, 979–1019 (2013)
15. Decreusefond, L., Dhersin, J.-S., Moyal, P., Tran, V.C.: Large graph limit for an SIR process in random network with heterogeneous connectivity. *Ann. Appl. Probab.* **22**, 541–575 (2012)
16. Janson, S., Luczak, M., Windridge, P.: Law of large numbers for the SIR epidemic on a random graph with given degrees. *Random Struct. Algor.* **45**(4), 724–761 (2014)
17. Diekmann, O., Heesterbeek, J.A.P., Britton, T.: *Mathematical Tools for Understanding Infectious Disease Dynamics*. Princeton University Press, Princeton (2013)

Chapter 6

Towards Identifying and Predicting Spatial Epidemics on Complex Meta-population Networks

Xiang Li, Jian-Bo Wang, and Cong Li

Abstract In the past decade, the network science community has witnessed huge advances in the threshold theory, prediction and control of epidemic dynamics on complex networks. While along with the understanding of spatial epidemics on meta-population networks achieved so far, more challenges have opened the door to identify, retrospect, and predict the epidemic invasion process. This chapter reviews the recent progress towards identifying susceptible-infected compartment parameters and spatial invasion pathways on a meta-population network as well as the minimal case of two-subpopulation version, which may also extend to the prediction of spatial epidemics as well. The artificial and empirical meta-population networks verify the effectiveness of our proposed solutions to the concerned problems. Finally, the whole chapter concludes with the outlook of future research.

6.1 Introduction

After around 70 years of the seminal work of Norbert Wiener “Cybernetics: or the Control and Communication in the Animal and the Machine” [1], Wiener’s great thinking still presents fundamental impacts to many folds of the human society in the era of networking world and Big Data today, ranging from modelling and

A part of this chapter has been contributed to the 2016 IEEE Conference on Norbert Wiener in the twenty-first century (21CW) to memorize Dr. Norbert Wiener. This work was partly supported by the Natural Science Fund for Distinguished Young Scholar of China (No. 61425019), the National Natural Science Foundation (Nos. 61273223, 61603097), the Key Project of National Social Science Fund (No. 12&ZD218) of China, Shanghai SMEC-EDF Shuguang Project (No. 14SG03), and Natural Science Foundation of Shanghai (No. 16ZR1446400).

X. Li (✉) • J.-B. Wang • C. Li

Adaptive Networks and Control Lab, Department of Electronic Engineering and Research Center of Smart Networks & Systems, School of Information Science & Engineering, Fudan University, 200433, Shanghai, People’s Republic of China

e-mail: lix@fudan.edu.cn

feedback-loop analysis to stability and control of categories of systems and subjects, whatever large-scale or simply structured, linear or nonlinear, low dimensional or extremely high dimensional. The communications among humans and machines in the eyes of Norbert Wiener in 1950s were generally assumed as point-to-point or neglected as regularly structured in the scope of classic graph theory [2, 3]. Afterwards, Erdős and Rényi extended the graph description with uncertainty and randomness, and proposed the random graph theory in 1960s [4]. In the following decades the flourishing information and communication techniques have pushed the whole human society to a networking village of today, while the understanding of dominant yet hidden connectivity patterns of the communications among humans and machines were not revisited until recently.

The discovery of small-world and scale-free features in 1998–1999 has been verified in ubiquitous complex networks [5, 6], which have attracted the world-wide attention to the new emergence of network science. The popular concerns cover not only the topological complexity of a large-scale complex network system but also the interdependence between the infrastructure and the collective performance of such networks [7–10]. Typically, from the viewpoint of system and control, the precise mathematic description and appropriate models of a complex network play a significant role to achieve the desirable performance in return. However, in the situations of large-scale spatial prevalence of diseases in human populations, for example, such a solution may be infeasible if the availability of accurate data collections is far from sufficiently satisfactory.

Nevertheless the global outbreaks of prevalent infectious diseases in recent decades have led to great social, economic, and public health loss [11–14], which is partially due to the urbanization process and, in particular, the wide-establishment of long-distance public transportation networks (e.g., world-wide air-line web) and urban public commuting systems (e.g., subway and metro networks) to facilitate the dissemination of pathogens accompanied with passengers [15, 16]. Academia has witnessed that prediction and control of epidemic dynamics in networks as a flourishing research topic with interdisciplinary approaches [17–20]. However, more challenging problems arising from the epidemic prevalence on a meta-population network have not received adequate attentions, such as identifying the parameters of epidemic network systems and the epidemic invasion pathways on a meta-population network, which, ignored previously, certainly play important roles in evaluating the intensity of outbreak of epidemics among human patches/populations.

Assume the seed of a disease/virus as the input signal to the whole human population system, and the observed patient samples as the system output. Then, the spatial invasion of the disease inside the human population is obscure as a black box to be identified, and this system combines many factors such as human mobility patterns (commuting and long-distance traveling) and mathematical epidemiology as well. Therefore, identifying such an epidemic process with the interplay of complex networks and the human population is a challenge to public health-care administrative agency when predicting the large-scale spatial prevalence of a disease and announcing counter strategies.

The theory of system identification has been used to estimate the epidemic parameters of a complex system which are described by ordinary differential equations (ODE) such as HIV/AIDS epidemic dynamics [21]. Another related topic is inferring network topology by utilizing the information about a dynamics process on networks [22, 23]. Note that system identification and network inference techniques are not fit to handle the epidemic process on meta-population networks which are stochastic, high-dimensional, and multi-scale. Besides, source identification on complex networks is a close and popular topic. Some source identification algorithms [24, 25] have been designed for information/contact networks, but they are not feasible in identifying the invasion processes on meta-population networks.

Many instructive methods have also been proposed to explore the spatial spread of an epidemic process on meta-population networks. Maeno [26] inferred the epidemic network between eleven countries and areas during SARS in 2003 by analysing the epidemic time series. Reference [27] extracted the most likely epidemic transmission trees of the 1918 influenza pandemic in England, Wales and the United States. Some methods based on machine learning were also proposed to infer the epidemic networks from surveillance data [28–30]. Gautreau et al. presented a measure of the average arrival time to characterize the minimum-distance path from subpopulation i to subpopulation j over all possible paths [31], and the average arrival time-based shortest path tree is constructed by assembling all the shortest paths from the seed subpopulation to any other subpopulation in a networked meta-population. Balcan et al. proposed a Monte Carlo maximum likelihood method to produce a most likely infection tree [32]. They constructed the minimum spanning tree from the seed subpopulation to minimize the distance. Recently, Brockmann and Helbing [15] proposed a new concept called “effective distance” to predict the disease arrival time. From node/location i to node/location j , the effective distance D_{ij} is defined as the minimum sum of effective lengths over all reachable branches along this path. The set of shortest paths to all other nodes from seed node i constitutes a shortest path tree, illustrating the most probable paths from the root to other nodes. On the other hand, approaches based on machine learning such as genetic algorithm [28–30] has been used to extract epidemic transmission networks.

Note that some of the above works didn’t distinguish epidemic transmission network and invasion pathways/trees. In fact, these two concepts are a bit different, and very few work has discussed the parameter identification of a meta-population network system. Here a natural problem poses itself that whether the parameters and epidemic invasion process can be identified from the infection data of populations and network topology? To get a better understanding of how the contagion diffuses via an invasion process on network, more topics deserve further efforts: (i) So far, there are few works on identification of parameters of a meta-population network which an epidemic is occurring on. New questions such as the following ones are raised: How to use the data from the limited epidemic realizations to infer the system parameters as accurate as possible? Does a more appropriate model of individual mobility exist? (ii) Identification of spatial invasion pathways is to uncover the channels by which the hosts transmit viruses in a spatially structured population with

the infection data. In a large-scale meta-population network, the complex pattern of pathways challenges the methodology to identify the epidemic invasion pathways in a meta-population network.

In this chapter, we review our series of work in recent years [33–37] on identifying parameters of the susceptible-infected model and spatial invasion pathways on a meta-population network as well as the minimal case of two-subpopulation version, which may also extend to the prediction of spatial epidemics as well. The remainder of this chapter is arranged as follows. Section 6.2 gives the detailed description of preliminaries. Section 6.3 introduces the parameter identification of epidemic models on a meta-population network. Section 6.4 contributes the inference of epidemic invasion pathways in a meta-population network with both methodologically and example verifications. In Sect. 6.5, extending the steps of the previous sections, the prediction of spatial epidemic transmission comes with several feasible methods. Finally, Sect. 6.6 concludes the whole chapter with outlook in future research.

6.2 Preliminary

A meta-population network, which was originated from the meta-population model proposed by Richard Levins [38] to explore spatial ecology, embeds public transportation networking systems to model and uncover nontrivial patterns of spatial prevalence of global infectious diseases in the past years [15, 31, 32, 39, 40]. In this section, we introduce the meta-population network model and the susceptible-infected (SI) compartment epidemic dynamic as well. In this chapter, we consider the discrete-time dynamics.

6.2.1 The Compartment Model with SI Reaction Dynamics

The well-known susceptible-infected (SI) compartment model (Fig. 6.1), which is the simplest version in the epidemic compartment family, generally describes the early stage of prevalence of viruses/pathogen [24, 25, 41], especially in the situation of non-recovery. In such a population, the states of individuals are stratified into two compartments (classes): susceptible to the infection of the pathogen; and infected by the pathogen. Generally, we assume that all individuals are homogeneously mixing in the population. The state transition of an individual between two compartments

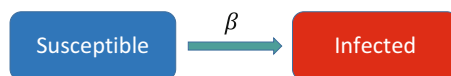


Fig. 6.1 Schematic illustration of the SI compartment model, where β denotes the infection rate

is governed by the following reaction process: When a susceptible individual meets (i.e., has the contacts) with an infected individual in a unit time, the susceptible individual will be infected with an infection rate β .

6.2.2 The Two-Subpopulation Version of a Meta-population Network

Before describing a general meta-population network, we first introduce a minimal meta-population network containing two subpopulations (labelled as 1 and 2 as shown in Fig. 6.2) with SI epidemic compartments. We assume the infection process evolves as a discrete-time system, and subpopulation 1 is infected initially (In this case of simulation, we assume 1 individual is infected among all 10,000 individuals in subpopulation 1). During each time step, the reaction takes place in each subpopulation if it contains two classes of individuals (susceptible and infected). Denote p_{12} (p_{21}) the diffusion rate of individuals transferring from subpopulation 1 to 2 (2 to 1), which are often not symmetric, i.e., $p_{12} \neq p_{21}$. Besides, an individual in subpopulation 1 (2) chooses jumping to subpopulation 2 (1) at diffusion rate p_{12} (p_{21}), i.e., the so-called diffusion process. Therefore, the probability an individual stays in subpopulation 1 (2) is $1 - p_{12}$ ($1 - p_{21}$).

Therefore, without considering the diffusion of new increment of infected individuals after reaction, the whole evolution dynamics is described as

$$\begin{cases} \langle I_1(t + 1) - I_1(t) \rangle = \beta I_1(t) \frac{S_1(t)}{N_1(t)} + p_{21} I_2(t) - p_{12} I_1(t), \\ \langle I_2(t + 1) - I_2(t) \rangle = \beta I_2(t) \frac{S_2(t)}{N_2(t)} + p_{12} I_1(t) - p_{21} I_2(t), \end{cases} \quad (6.1)$$

where $\langle \cdot \rangle$ represents the expectation of the corresponding terms, $N_1(t)$ ($N_2(t)$) denotes the number of individuals in subpopulation 1 (2) at time t , $I_1(t)$ ($I_2(t)$) denotes the number of infected individuals in subpopulation 1 (2), $S_1(t)$ ($S_2(t)$)

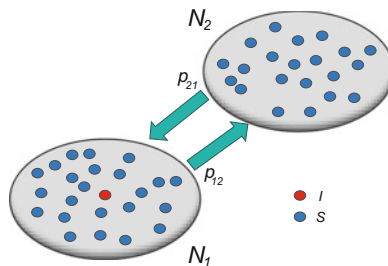


Fig. 6.2 Schematic representation of a minimal meta-population network with the SI model. At initial time, subpopulation 1 is infected (containing at least one infected individual (red)), and subpopulation 2 is susceptible (all are susceptible individuals (blue)) (From Wang et al. [33])

denotes the number of susceptible individuals in subpopulation 1 (2). The first term of the right-hand side (RHS) in Eq. (6.1) represents the new increment of infected individuals $\langle \Delta_R I_i(t) \rangle = \beta I_i(t) \frac{S_i(t)}{N_i(t)}$, $i = 1, 2$, after reaction from t to $t+1$. The second and third terms of RHS in Eq. (6.1) represent the diffusion of infected individuals in the diffusion process. As mentioned above, we do not consider the diffusion of new increment of infected individuals after reaction in this case. Besides, the evolution of susceptible individuals is similar with the infected individuals.

6.2.3 The General Description of a Meta-population Network

Extending the minimal version as two subpopulations to the general case of a meta-population network, we divide the whole population (generally, such a population covers a large-scale spatial region of a country or the whole world) into a number of subpopulations. In a meta-population network, a subpopulation is connected with others via a public transportation network, e.g., the air-line web, the high-way web to form the backbone of such a meta-population network. A subpopulation as a node in the network contains a number of individuals homogeneously mixed, and individuals travel between two subpopulations (nodes) via the public transportation means (edge) with some (fixed) diffusion rate. All edges are directed.

With the SI dynamics, the disease propagates in subpopulations and spreads among neighbouring subpopulations via the reaction-diffusion process in a unit time, as illustrated in Fig. 6.3. Denote N the number of subpopulations (nodes) of a meta-population network, and $N_i(t) = S_i(t) + I_i(t)$ is the population size of

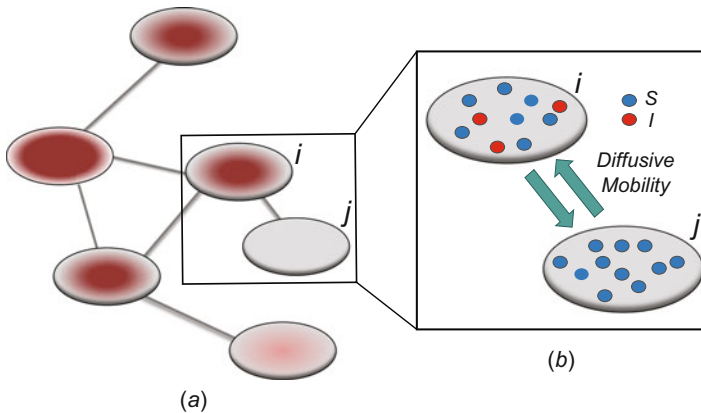


Fig. 6.3 Illustration of a networked meta-population model, which comprises six subpopulations that are coupled by the mobility of individuals. In each subpopulation, each individual can be in one of the two states (susceptible, infected), as shown in different colours. Grey ones represent susceptible subpopulations. Red ones represent infected subpopulations. Light red subpopulations denote less number of infected individuals than the dark red ones. Each individual can travel between the connected subpopulations. (a) A networked meta-population. (b) Two subpopulations (From Wang et al. [35])

subpopulation i at time t , where $S_i(t)$ is the number of susceptible individuals, and $I_i(t)$ is the number of infected individuals of subpopulation i at time t , respectively. Therefore, the intra-population epidemic dynamics in subpopulation i is governed by the SI model. Per unit time, the risk of infection of a susceptible individual within subpopulation i is characterized by $\lambda_i(t) = \beta I_i(t)/N_i(t)$ during the reaction process. Denote the probability that an individual (S or I) of subpopulation i moves to its neighbouring subpopulation j as diffusion rate p_{ij} , which describes the inter-population mobility dynamics. The symbol of diffusion rate $0 \leq p_{ij} = \frac{\langle w_{ij} \rangle}{\langle N_i \rangle} < 1$, where w_{ij} is the number of individuals moving from subpopulation i to j per unit time ($0 \leq \langle w_{ij} \rangle < \langle N_i \rangle$).

Therefore, if we do not consider the diffusion of new increment of infected individuals after the reaction process, the evolution of an infected subpopulation i is described as follows:

$$\langle I_i(t+1) - I_i(t) \rangle = \beta I_i(t) \frac{S_i(t)}{N_i(t)} + \sum_{j=1, j \neq i}^N p_{ji} I_j(t) - \sum_{j=1, j \neq i}^N p_{ij} I_i(t), \quad (6.2)$$

which is investigated in Sect. 6.4.

When we consider the diffusion of new increment of infected individuals after the reaction, the evolution is described by

$$\langle I_i(t+1) - I_i(t) \rangle = \beta I_i(t) S_i(t) / N_i(t) + \sum_{j \neq i} \{ p_{ji} [I_j(t) + \langle \Delta_R I_j(t) \rangle] - p_{ij} [I_i(t) + \langle \Delta_R I_i(t) \rangle] \}, \quad (6.3)$$

where $\Delta_R I_j(t)$ is the increment of $I_j(t)$ after the reaction from t to $t+1$. We give the extensive investigation of the dynamics given by Eq. (6.3) in Sect. 6.5.

We now discuss the individual *mobility operator* to handle the presence of stochasticity and independence of individual mobility, where the number of successful migration of individuals between adjacent subpopulations is quantified by a binomial or a multinomial process, respectively. If the focal subpopulation i only has one neighbouring subpopulation j , the number of individuals in a given compartment \mathcal{X} ($\mathcal{X} \in \{S, I\}$ and $\sum_{\mathcal{X}} \mathcal{X}_i = N_i$) transferred from i to j per unit time, $\mathcal{T}_{ij}(\mathcal{X}_i)$, is generated from a binomial distribution with probability p_{ij} representing the diffusion rate and the number of trials \mathcal{X}_i , i.e.,

$$\text{Binomial}(\mathcal{T}_{ij}, \mathcal{X}_i, p_{ij}) = \frac{\mathcal{X}_i!}{\mathcal{T}_{ij}! (\mathcal{X}_i - \mathcal{T}_{ij})!} p_{ij}^{\mathcal{T}_{ij}} (1 - p_{ij})^{(\mathcal{X}_i - \mathcal{T}_{ij})}, \quad (6.4)$$

where $1 - p_{ij}$ denotes the probability of an individual staying in subpopulation i .

If the focal subpopulation i has multiple neighbouring subpopulations j_1, j_2, \dots, j_k , with k representing i 's degree, the numbers of individuals in a given compartment \mathcal{X} moving from i to j_1, j_2, \dots, j_k are generated from a multinomial

distribution with probabilities $p_{ij_1}, p_{ij_2}, \dots, p_{ij_k}$ representing the diffusion rates on the edges emanated from subpopulation i and the number of trails \mathcal{X}_i , i.e.,

$$\begin{aligned} & \text{Multinomial}(\{\mathcal{T}_{ij_\ell}\}, \mathcal{X}_i, \{p_{ij_\ell}\}) \\ &= \frac{\mathcal{X}_i!}{\prod_\ell \mathcal{T}_{ij_\ell}! (\mathcal{X}_i - \sum_\ell \mathcal{T}_{ij_\ell})!} \left(\prod_\ell p_{ij_\ell}^{\mathcal{T}_{ij_\ell}} \right) (1 - \sum_\ell p_{ij_\ell})^{(\mathcal{X}_i - \sum_\ell \mathcal{T}_{ij_\ell})}, \end{aligned} \quad (6.5)$$

where integer $\ell \in [1, k]$, term $1 - \sum_\ell p_{ij_\ell}$ denotes the probability of an individual staying in subpopulation i .

6.3 Epidemic Parameter Identification

The epidemic parameters of a networked meta-population include the infection rate and diffusion rate, which play an important role in the SI dynamics, while the stochastic epidemic dynamics and the limit of available data make such an identification task more difficult. In this section, we review the method to identify both parameters for a two-subpopulation network and an estimation of infection rate for a general network version.

6.3.1 The Case of Two-Subpopulation Model

We first describe one realization of the invasion process evolving as follows. At the beginning, subpopulation 1 has been initialized with one infected individual in this case. When time evolves, the number of infected individuals $I_1(t)$ of subpopulation 1 increases due to the SI reaction dynamics in this subpopulation. The epidemic arrival time (EAT) is defined as the first arrival time of infected individuals from an infected subpopulation moving to a neighbouring susceptible subpopulation. To address the EAT, some infected individual(s) will move (diffuse) to subpopulation 2, which finally succeed in infecting subpopulation 2. Therefore, recording the infection data (the number of infected individuals in subpopulation i at time t , i.e., $I_i(t)$, $i = 1, 2$) of each subpopulation as the available data, we need to identify the unknown infection rate β and diffusion rate p_{12} .

At the early stage of epidemic dynamics, we can approximate $S_i(t) \approx N_i(t)$, $i = 1, 2$ ($I_i(0) \ll N_i(0)$) and therefore simplify Eq. (6.1) as

$$\langle I_1(t+1) - I_1(t) \rangle + \langle I_2(t+1) - I_2(t) \rangle \approx \beta(I_1(t) + I_2(t)). \quad (6.6)$$

Denote $I(t)$ the number of infected individuals in all subpopulations at time t , i.e., $I(t) = I_1(t) + I_2(t)$. Traditionally, the RHS of the above equation accounts for an exponential growth of the number of infected individuals, and β is regarded

as the Malthusian growth rate. Thus, we rewrite Eq. (6.6) in the compact form as $I(t) \approx e^{\beta(t-0)}I(0)$. Considering $\ln[I(0)] \ll \ln[I(t)]$, ($0 \ll t$), we have $\beta \sim \frac{\ln[I(t)]}{t}$. Therefore, we estimate the infection rate β by fitting the slope of $\ln[I(t)]$.

We now discuss how to identify diffusion rate p_{12} . Repeat the invasion of subpopulation 2 from subpopulation 1 until we record the epidemic arrival time to subpopulation 2, i.e., the disease/virus finally lands in subpopulation 2 and starts the local infection. We investigate the period from the initial time ($t = 0$) to the epidemic arrival time (t_{EAT}) that the first \mathcal{H} individuals from subpopulation 1 invade subpopulation 2. From $t_{EAT} - 1$ to t_{EAT} , we get

$$\begin{cases} \langle I_1(t_{EAT}) - I_1(t_{EAT} - 1) \rangle = \beta I_1(t_{EAT} - 1) - p_{12} I_1(t_{EAT} - 1), \\ \langle I_2(t_{EAT}) - I_2(t_{EAT} - 1) \rangle = p_{12} I_1(t_{EAT} - 1). \end{cases} \quad (6.7)$$

The likelihood function about the first \mathcal{H} infected individuals from subpopulation 1 traveling to subpopulation 2 at time t_{EAT} is

$$P(\mathcal{H}, t_{EAT} - 1) = C_{I_1(t_{EAT}-1)}^{\mathcal{H}} (1 - p_{12})^{I_1(t_{EAT}-1) - \mathcal{H}} p_{12}^{\mathcal{H}} \times \prod_{i=1}^{\eta-1} (1 - p_{12})^{I_1^{(i)}}, \quad (6.8)$$

where $t_{EAT} - 1 = \eta$, η ($\eta \geq 1$) is an integer. If there are s ($s \geq 1$) rounds of repeated realizations of invasion processes, the joint likelihood function is given by

$$\begin{aligned} P(\mathcal{H}^{\{1\}}, t_1; \mathcal{H}^{\{2\}}, t_2; \dots; \mathcal{H}^{\{s\}}, t_s) \\ = P(\mathcal{H}^{\{1\}}, t_1) \times P(\mathcal{H}^{\{2\}}, t_2) \times \dots \times P(\mathcal{H}^{\{s\}}, t_s), \end{aligned} \quad (6.9)$$

where s is the number of rounds of repeated simulation realizations of epidemic invasion processes. Take the logarithm of Eq. (6.9), the joint likelihood function yields $L(P) = \ln(P(\mathcal{H}^{\{1\}}, t_1; \mathcal{H}^{\{2\}}, t_2; \dots; \mathcal{H}^{\{s\}}, t_s))$.

Therefore, by means of the maximum likelihood estimation, we have $\frac{dL(P)}{dp_{12}} = \frac{1}{p_{12}-1} (\sum_{i=1}^s (I_1^{\{i\}}(\eta_i) - \mathcal{H}^{\{i\}}) + \sum_{i=1}^s \sum_{j=1}^{\eta_i-1} I_1^{\{i\}}(j)) + \frac{1}{p_{12}} \sum_{i=1}^s \mathcal{H}^{\{i\}}$. Letting $\frac{dL(P)}{dp_{12}} = 0$, we finally have

$$\hat{p}_{12} = \frac{\sum_{i=1}^s \mathcal{H}^{\{i\}}}{\sum_{i=1}^s [I_1^{\{i\}}(\eta_i) - \mathcal{H}^{\{i\}} + \mathcal{H}^{\{i\}} + \sum_{j=1}^{\eta_i-1} I_1^{\{i\}}(j)]} = \frac{\sum_{i=1}^s \mathcal{H}^{\{i\}}}{\sum_{i=1}^s \sum_{j=1}^{\eta_i} I_1^{\{i\}}(j)}, \quad (6.10)$$

where \hat{p}_{12} represents the estimation of diffusion rate p_{12} .

6.3.2 The Case of a Meta-population Network

Mathematically, the estimation of diffusion rates requires the availability of a large number of epidemic realizations for a given meta-population network. However, the availability of such repeated data for emergent infectious diseases is rather limited in reality. Therefore, the estimation of diffusion rates in the general case of a meta-population network is infeasible due to the computational complexity and the limit of available data, which generally can be alternatively obtained from the statistics of public transportation section. The estimation of infection rate β in the general case of a meta-population network is addressed here.

Summing the number of infected individuals in Eq. (6.3) over all subpopulations i , we have $\sum_i \langle I_i(t+1) - I_i(t) \rangle = \sum_{i=1}^N \beta I_i(t) S_i(t) / N_i(t)$. Since $I_i(t) \ll N_i(t)$ at the early epidemic stage, it is simplified as $\sum_i \langle I_i(t+1) - I_i(t) \rangle \approx \beta \sum_i I_i(t)$. The term $I_i(t+1) - I_i(t)$ fluctuates around its mathematical expectation, and we have the approximation as

$$\beta \sim \frac{\sum_i (I_i(t+1) - I_i(t))}{\sum_i I_i(t)}. \quad (6.11)$$

Thus, given all recorded times $t_1, t_2, \dots, t_{m'}$, the infection rate $\hat{\beta}$ is estimated as

$$\hat{\beta} = \arg \min_{\beta^*} \sum_{t=t_1}^{t_{m'}} |(I(t+1) - I(t)) - \beta^* I(t)|^2 = (X^\top X)^{-1} X^\top Y, \quad (6.12)$$

where X^\top represents the transposition of X , and $X = [I(t_1), I(t_2), \dots, I(t_{m'})]^{-1}$, $Y = [(I(t_1+1) - I(t_1)), (I(t_2+1) - I(t_2)), \dots, (I(t_{m'+1}) - I(t_{m'}))]^{-1}$.

6.3.3 Example: Identifying the Diffusion Rate p_{12}

In this subsection, we only illustrate the identification performance of estimating diffusion rate p_{12} on a two-subpopulation SI model as an example. A more general case (in the sense of an arbitrary number of subpopulations) of example of identification performance of infection rate β will be investigated in Sect. 6.5. In the two-subpopulation case, statistic information of p_{12} is embedded in the surveillance infection data of the two subpopulations during the epidemic invasion process. As shown in Fig. 6.4, the estimation of p_{12} approaches the real value if the number of realizations increase, and the estimation error $|\hat{p}_{12} - p_{12}|$ is less than 5% of p_{12} . Finally the estimation of p_{12} as \hat{p}_{12} tends to the real value.

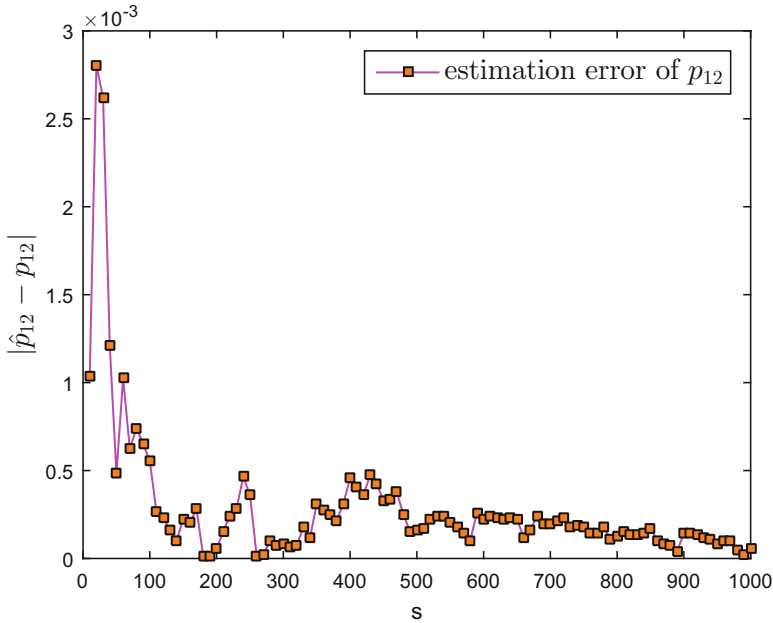


Fig. 6.4 The estimation error of diffusion rate p_{12} versus the number of realizations of the invasion process, and the error finally converges to zero. \hat{p}_{12} is the estimated value of p_{12} . The actual value of diffusion rate p_{12} is 0.01

6.4 Identification of Invasion Pathways

During a real spatial cascade of an infectious disease, the spatial invasion pathways are the collection of directed transmission paths of an infectious disease rooted in the infected source subpopulation invading their susceptible neighbouring subpopulations. Actually, no one can predict such spatial invasion pathways to suppress the spreading processes at its infant prevalence. With the data availability of epidemic arrival time (EAT), i.e., the first invasion time discussed in the previous section, we may infer the patterns of invasion pathways.

Suppose one subpopulation is initially infected containing several infected individuals. As time evolves, the infected individuals of the seed subpopulation travel to the neighbouring subpopulations and try to infect their individuals. The successful invasion brings more invaded subpopulations with the cascade of infections. Therefore, the focus of interest is that when a subpopulation is invaded/infected by its $m(m \geq 2)$ infected neighbours with the available EAT data, how can we infer the culprit(s) and identify the invasion pathways in such a cascade infection? In the concerned situation, we assume that the surveillance infection data (the number of infected individuals of each subpopulation at each time t) is available as well as the topology of the meta-population network (including diffusion rates).

6.4.1 Invasion Partition and Types of Invasion Cases

We categorize all candidates of invasion pathways via the so-called invasion partition (INP) into four types of invasion cases (INCs), as shown in Fig. 6.5. An invasion case contains two sets, i.e., \mathbb{S} and \mathbb{I} . Subpopulations which are not infected at $t_{EAT} - 1$ but infected at t_{EAT} are put in set \mathbb{S} , and their neighbours which are infected at $t_{EAT} - 1$ are put in set \mathbb{I} . All four types of invasion cases are defined.

- (i) $I \mapsto S$: In this case, both \mathbb{I} and \mathbb{S} only have one subpopulation. That is to say, a susceptible subpopulation is infected at t_{EAT} by the first arrival of infected individual(s) from its unique neighbouring infected subpopulation at $t_{EAT} - 1$, and this infected subpopulation has no other newly infected neighbours at t_{EAT} .
- (ii) $I \mapsto nS (n > 1)$: In this case, \mathbb{I} contains one infected subpopulation, and \mathbb{S} contains $n (n > 1)$ subpopulations. That is to say, an infected subpopulation

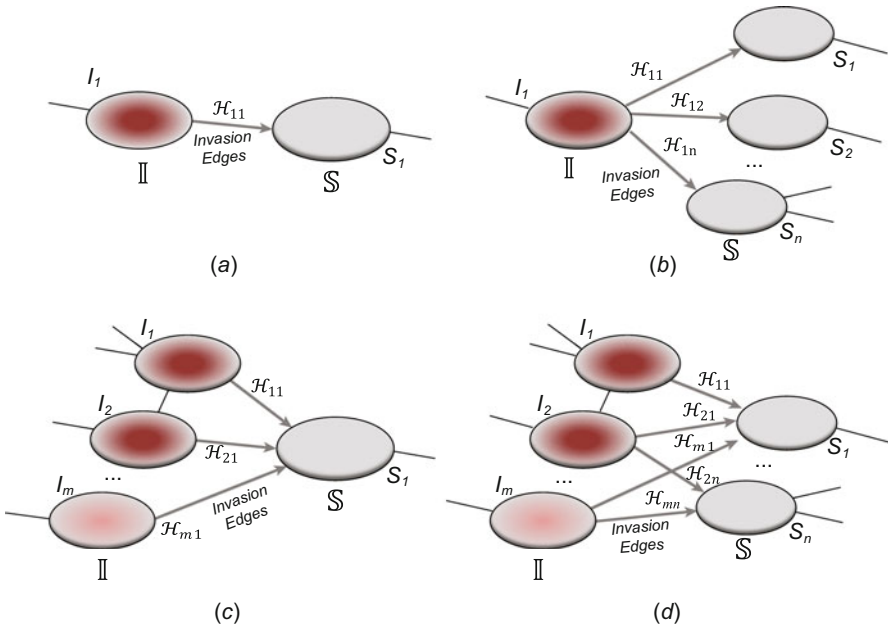


Fig. 6.5 (a) Example of $I \mapsto S$ INC, in which the infected individuals of only one infected subpopulation invades one susceptible subpopulation. The infected subpopulation is represented in red, while the plain patch is the subpopulation that remains susceptible before time t_{EAT} but will be infected between $t_{EAT} - 1$ to t_{EAT} due to the arrival of infected individuals from the upstream infected subpopulation. (b) Example of $I \mapsto nS$ INC, in which the infected individuals of only one infected subpopulation invades $n (n \geq 2)$ susceptible subpopulations. (c) Example of $mI \mapsto S$ INC, in which the infected individuals of m infected subpopulations invade one susceptible subpopulation. (d) Example of $mI \mapsto nS$ INC, in which the infected individuals of $m (m \geq 2)$ infected subpopulations invade $n (n \geq 2)$ susceptible subpopulations (From Wang et al. [35])

- simultaneously infects its $n(n > 1)$ susceptible neighbours, each of which has only one infected neighbouring subpopulation.
- (iii) $mI \mapsto S(m > 1)$: In this case, \mathbb{I} consists of $m(m > 1)$ subpopulations, and \mathbb{S} only contains one single subpopulation. That is to say, a susceptible subpopulation is infected by the first arrival of infected individual(s) coming from its $m(m > 1)$ infected neighbouring subpopulation, which has no other newly infected neighbours at this time.
 - (iv) $mI \mapsto nS(m, n > 1)$: In this case, sets \mathbb{S} and \mathbb{I} both contain more than one subpopulation. The edges from \mathbb{I} to \mathbb{S} form a connected subgraph. Each previously susceptible subpopulation in \mathbb{S} is infected by the new arrival of infected individual(s) from at least one of the m infected subpopulations in \mathbb{I} . Each subpopulation in \mathbb{I} has no other newly infected neighbours except the subpopulations in \mathbb{S} at this time.

Figure 6.5 illustrates such four types of invasion cases as $I \mapsto S$, $mI \mapsto nS(n > 1)$, $mI \mapsto S(m > 1)$ and $mI \mapsto nS(m, n > 1)$. Besides, we define the directed edges from infected subpopulation i in \mathbb{I} to susceptible subpopulations in \mathbb{S} as invasion edges, which are the candidates of invasion pathways. Therefore, we define a decomposition procedure *invasion partition* (INP) to achieve the task of dividing subpopulations and edges into such invasion cases. As summarized in Algorithm 1, we propose a heuristic algorithm to achieve the INP task.

Algorithm 1 Invasion Partition (INP)

- 1: At an epidemic arrival time, collect all newly infected subpopulations as initial \mathbb{S} and their previously infected neighbours as \mathbb{I} ;
 - 2: Start with an arbitrary element S_i in set \mathbb{S} , to compose the initial \mathbb{S}^* ;
 - 3: Find all neighbors of S_i in set \mathbb{I} to compose the set \mathbb{I}^* ;
 - 4: For each new member in \mathbb{I}^* , find its new neighbours in the \mathbb{S} to update \mathbb{S}^* if any;
 - 5: For each new member in \mathbb{S}^* , find its new neighbours in the \mathbb{I} to update \mathbb{I}^* if any;
 - 6: Repeat the above two steps until we cannot find any new neighbours in \mathbb{S} and \mathbb{I} , we get an invasion case consisting of \mathbb{I}^* and \mathbb{S}^* , then update the \mathbb{S} and \mathbb{I} ;
 - 7: Repeat steps 2–6 to get new invasion cases until there are no elements in \mathbb{S} .
-

6.4.2 Observability of a Subpopulation and an Edge

We further classify the observability of a subpopulation and an edge. Observability of a subpopulation is defined by comparing the number of infected individuals of subpopulation i at time $t_{EAT} - 1$ and t_{EAT} , which reflects the information held for the inference of relevant invasion pathway. Observability of an directed edge emanated from an infected subpopulation can be defined by the types of subpopulations it connects to.

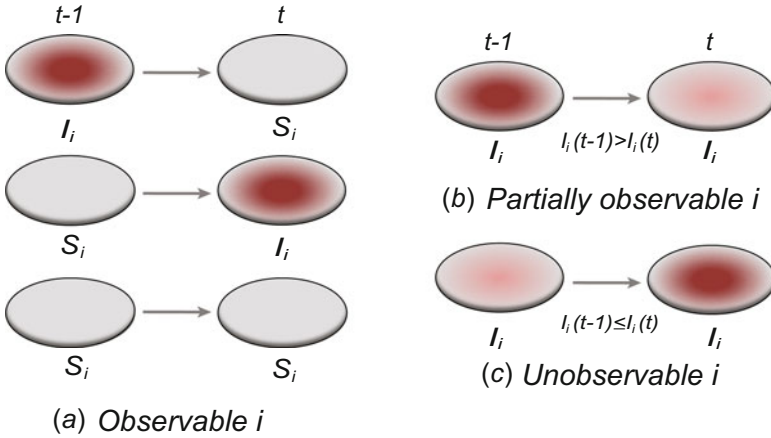


Fig. 6.6 Illustration of subpopulation observability: (a) observable subpopulations, (b) partially observable subpopulation, and (c) unobservable subpopulation. Here time t is t_{EAT} (From Wang et al. [35])

- (i) *Observable Subpopulation*: From $t_{EAT} - 1$ to t_{EAT} , subpopulation i is an observable subpopulation if it experiences one of the following three state transitions. The first is $S_i \rightarrow I_i$, which indicates that this subpopulation has been infected (for the first time) during this period by infected individuals (because $I_i(t)$ is available). The second is $I_i \rightarrow S_i$. We know how many infected individuals diffused from this subpopulation in this case. The third is $S_i \rightarrow S_i$. This case represents subpopulation i keeps its susceptible status.
- (ii) *Partially Observable Subpopulation*: The number of infected individuals of an infected subpopulation may decrease, that is to say $I_i(t_{EAT}) < I_i(t_{EAT} - 1)$ and $I_i(t_{EAT}) > 0$. We call subpopulation i is a partially observable subpopulation, because we know at least $\Delta I_i(t_{EAT}) = |I_i(t_{EAT}) - I_i(t_{EAT} - 1)|$ infected individuals leave i .
- (iii) *Unobservable Subpopulation*: If the number of infected individuals does not decrease, i.e., $I_i(t_{EAT}) \geq I_i(t_{EAT} - 1)$, it is difficult to judge whether and how many infected hosts leave subpopulation i . We call it unobservable subpopulation.

Here the observability of a subpopulation indicates the diffusion information of this subpopulation. Figure 6.6a–c illustrate the above cases. Together with the observability of a subpopulation, the directed edges emanated from an infected subpopulation (here denoted i) in set \mathbb{I} can be classified into three types, i.e., observable edges, partially observable edges and unobservable edges:

- (i) *Observable Edges*: Any directed edge from i to observable subpopulation j whose transition is $S_j \rightarrow S_j$ or $I_j \rightarrow S_j$ from $t_{EAT} - 1$ to t_{EAT} . This edge implies no infected hosts move from i .

- (ii) *Partially Observable Edges*: If an directed edge emanated from infected subpopulation i to a partially observable subpopulation, the edge is partially observable.
- (iii) *Unobservable Edges*: If infected subpopulation i connects with an unobservable subpopulation, this directed edge from i is an unobservable edge.

6.4.3 Accurate Identification of Invasion Pathways

We now consider to accurately identify the invasion pathways. Among the four types of invasion cases (INCs), since the two types of INCs ($I \mapsto S$ and $I \mapsto nS$, $n \geq 2$) have the unique invasion edge(s) from the neighboring infected subpopulation, the invasion pathways therefore are easy to identify accurately. We only need concern the other two types of INCs, i.e., $mI \mapsto S$ and $mI \mapsto nS$.

6.4.3.1 The Case of $mI \mapsto S$ ($m > 1$)

A representative $mI \mapsto S$ ($m > 1$) INC (Fig. 6.5c) consists of two sets. Set $\mathbb{I} = \{I_1, I_2, \dots, I_m\}$ is composed of the infected subpopulations at $t_{EAT} - 1$, and set $\mathbb{S} = \{S_1\}$ is composed of the susceptible subpopulation(s) at $t_{EAT} - 1$ which are infected at t_{EAT} . Assume subpopulation S_1 is infected at t_{EAT} by the first arrival of \mathcal{H} infected individuals coming from some of the infected subpopulations in \mathbb{I} , where \mathcal{H} is a positive integer.

Suppose \mathcal{H}_{i1} is the actual number of infected individuals travelling from an infected subpopulation I_i in set \mathbb{I} , and we have

$$\sum_{i=1}^m \mathcal{H}_{i1} = \mathcal{H}, \quad (6.13)$$

where $0 \leq \mathcal{H}_{i1} \leq \mathcal{H}$, $\mathcal{H}_{i1} \leq I_i(t_{EAT} - 1)$, and $0 \leq i \leq m$. \mathcal{H} is available from the infection data, while we do not know \mathcal{H}_{i1} . To reach the unique solution of Eq. (6.13) which corresponds to a set of invasion pathways of $mI \mapsto S$ ($m > 1$), we give Theorem 1 to accurately identify the invasion pathways of INC $mI \mapsto S$ ($m > 1$).

Theorem 1 *The invasion pathways of the invasion case $mI \mapsto S$ ($m > 1$) can be accurately identified, given the following two conditions are satisfied: (1) among m possible sources illustrated in set \mathbb{I} , there are only m' ($m' \leq m$) partially observable subpopulations \mathbb{I}' , whose neighbouring subpopulations j (excluding the invasion destination S_1) only experience the transition $S_j \rightarrow S_j$ or $I_j \rightarrow S_j$ at that EAT, (2) $\sum_{i \in \mathbb{I}'} [I_i(t_{EAT} - 1) - I_i(t_{EAT})] = \mathcal{H}$.*

Proof According to the definition of observability, in an INC, the number of local infected individuals in an partially observable source i will be decreased by

$[I_i(t_{EAT} - 1) - I_i(t_{EAT})]$ due to the movement of infected individuals. If the subpopulations j in the neighbourhood of i only experience the transition of $S_j \rightarrow S_j$ or $I_j \rightarrow S_j$ from $t_{EAT} - 1$ to t_{EAT} , they do not receive the infected individuals from subpopulation i . Therefore, the newly infected subpopulation S_1 is the only destination for those infected individuals departing from the partially observable sources. Since $m' \leq m$, the second condition guarantees that Eq. (6.13) only has a unique solution, which corresponds to the accurate identification of invasion pathways of this invasion case. \square

6.4.3.2 The Case of $mI \mapsto nS(m > 1, n > 1)$

The final typical INC $mI \mapsto nS$ as shown in Fig. 6.5d includes set $\mathbb{I} = \{I_i | i = 1, 2, \dots, m\}$ and $\mathbb{S} = \{S_i | i = 1, 2, \dots, n\}$. Denote $\{\mathcal{H}_i | i = 1, 2, \dots, n\}$ the number of the first arrival of infected individuals to susceptible subpopulation S_i in set \mathbb{S} , and $U_i (i = 1, 2, \dots, m)$ the subset of susceptible neighbouring subpopulations in set \mathbb{S} of infected subpopulation I_i , and $Y_j (j = 1, 2, \dots, n)$ the subset of infected neighbouring subpopulations in set \mathbb{I} of susceptible subpopulation S_j .

Define $\sigma = \{\{\mathcal{H}_{i1} | i \in Y_1\}, \dots, \{\mathcal{H}_{in} | i \in Y_n\}\}$ as a potential solution for the $mI \mapsto nS$, if σ is subject to the following two conditions: (i)

$$\sum_{i \in Y_k} \mathcal{H}_{ik} = \mathcal{H}_k, \quad (6.14)$$

where $\mathcal{H}_{ik} (\geq 0)$ is the number of infected hosts invading subpopulation S_k from I_i at t_{EAT} ; (ii) For any \mathcal{H}_{ik} , we have $\sum_{k \in U_i} \mathcal{H}_{ik} \leq I_i(t_{EAT} - 1)$, where $1 \leq i \leq m, 1 \leq k \leq n$.

Suppose an $mI \mapsto nS$ has M potential solutions, and $\sigma_j = \{\{\mathcal{H}_{i1}^{(j)} | i \in Y_1\}, \dots, \{\mathcal{H}_{in}^{(j)} | i \in Y_n\}\}$ ($1 \leq j \leq M$) represents one of the solutions.

Given some specific prerequisites (as the conditions of Theorem 2), Eq. (6.14) has a unique solution, which implies that the invasion pathway(s) can be identified accurately. Theorem 2 elucidates this scenario.

Theorem 2 *The invasion pathway(s) of the invasion case $mI \mapsto nS(m, n > 1)$ can be identified accurately, given the following three conditions are satisfied: (1) the number of invasion edges $E_{in} \leq n + m$, (2) the neighbouring subpopulations j of each subpopulation in set \mathbb{I} are with the transition $S_j \rightarrow S_j$ or $I_j \rightarrow S_j$ except their neighbouring subpopulations in set \mathbb{S} during $t_{EAT} - 1$ to t_{EAT} , (3) $\sum_{i=1}^m \Delta I_i(t_{EAT}) = \sum_{k=1}^n \mathcal{H}_k$.*

Proof Since the number of infected individuals in the partially observable subpopulation i reduces at time t_{EAT} , i.e., $I_i(t_{EAT}) < I_i(t_{EAT} - 1)$, $I_i(t_{EAT}) > 0$, it is inevitable that a few infected individuals diffuse away from subpopulation i . Occurring the state transitions of $S_j \rightarrow S_j$ or $I_j \rightarrow S_j$ from $t_{EAT} - 1$ to t_{EAT} , subpopulations j in the neighbourhood of i (excluding the new infected subpopulation j) cannot receive

infected individuals. Therefore, the only possible destination for those infected individuals is subpopulation S_k in \mathbb{S} .

The conditions $E_{in} \leq n + m$ and $\sum_{i=1}^m \Delta I_i(t_{EAT}) = \sum_{k=1}^n \mathcal{H}_k$ make the equations $\sum_{i \in Y_k} \mathcal{H}_{ik} = \mathcal{H}_k$ and $\sum_{k \in U_i} \mathcal{H}_{ik} = \Delta I_i(t_{EAT})$ have the unique solution $\sigma = \{\{\mathcal{H}_{i1} | i \in Y_1\}, \dots, \{\mathcal{H}_{in} | i \in Y_n\}\}$. The reason is that $\text{rank}(A_{coef}) = E_{in}$, where A_{coef} is the coefficient matrix of equations $\sum_{i \in Y_k} \mathcal{H}_{ik} = \mathcal{H}_k$ and $\sum_{k \in U_i} \mathcal{H}_{ik} = \Delta I_i(t_{EAT})$. Thus the invasion pathway(s) of this $mI \mapsto nS (m, n > 1)$ can be identified accurately. \square

6.4.4 Identification for Potential Invasion Pathways

Now we are in the position to construct the whole framework of identifying invasion pathways, namely, the invasion pathways identification (IPI) algorithm as summarized as below.

- (i) Invasion partition: $T_{\text{whole invasion pathways}}$ is defined as the whole invasion pathways of an invasion process. At each EAT, we get four types of invasion cases (i.e. $I \mapsto S, I \mapsto nS, mI \mapsto S, mI \mapsto nS (m > 1, n > 1)$). Suppose $T_{\text{whole invasion pathways}}$ is contained in all Λ INCs. Denote by \hat{a}_i the identified invasion pathways of INC_i , which can be optimally solved by (stochastic) dynamic programming as

$$T_{\text{whole invasion pathways}} = \text{opt} \sum_{i=1}^{\Lambda} \hat{a}_i, \quad (6.15)$$

where “opt” represents the optimal solution via dynamic programming.

- (ii) Accurate identification: For the two cases of $I \mapsto S, I \mapsto nS$, it is easy to reach the accurate identification of invasion pathways. In the other two cases of $mI \mapsto S, mI \mapsto nS$, we first evaluate whether $mI \mapsto S$ or $mI \mapsto nS$ can be accurately identified or not. If yes, Theorems 1 and 2 work out the accurate identification.
- (iii) Identification of potential invasion pathways: If accurate identification is not feasible, we propose an efficient optimization method based on the maximum likelihood estimation to identify the most likely invasion pathways. We define the maximum likelihood (ML) estimator as

$$\hat{a}_i = \arg \max_{a_i \in INC_i} P(a_i | INC_i), \quad (6.16)$$

where $P(a_i | INC_i)$ is the likelihood of uncovering the potential pathway a_i , supposing the actual pathway is a_i^* . Therefore, we evaluate $P(a_i | INC_i)$ and choose the maximal likelihood one as a_i^* from all potential pathways $a_i \in INC_i$.

- (iv) The whole spatial invasion pathways can be reconstructed by assembling all invasion cases chronologically.

Therefore, in the situations where accurate identification of invasion pathways is not feasible, e.g., the conditions of Theorems 1 and 2 are not satisfied, Eqs. (6.13) and (6.14) may have a number of potential solutions which correspond to a set of potential invasion pathways. Therefore, we propose the identification algorithm to infer the most likely pathways among all potential invasion pathways. Herein we unify $mI \mapsto S(m > 1)$ and $mI \mapsto nS(m > 1, n > 1)$ as $mI \mapsto nS(m > 1, n \geq 1)$.

Denote $\Omega(\mathcal{H}_{kk\bar{h}}^{(j)})$ the transfer estimator of infected subpopulation I_k in \mathbb{I} , $k, \bar{h} \in Y_k$. Here the transfer estimator is used to estimate the diffusion likelihood if I_k diffuses $\mathcal{H}_{kk\bar{h}}^{(j)}$ infected individuals to $S_{k\bar{h}}$. Thus, the likelihood of potential solution σ_j of an INC $mI \mapsto nS(m > 1, n \geq 1)$ is presented by

$$P(\sigma_j | INC_{mInS}) = \prod_{k=1}^m \Omega(\mathcal{H}_{kk\bar{h}}^{(j)}) / \sum_{i=1}^M \prod_{k=1}^m \Omega(\mathcal{H}_{kk\bar{h}}^{(i)}), \quad (6.17)$$

where M represents the number of solution σ_j .

We now consider the events from $t_{EAT} - 1$ to t_{EAT} , and give some definitions. We assume an infected subpopulation I_i in \mathbb{I} emanates k_i edges in total, among which there are $\rho_i (1 \leq \rho_i \leq n)$ invasion edge(s) labeled as $1, 2, \dots, \rho_i$ with the corresponding diffusion rates $p_{\bar{h}}, \bar{h} \in [1, \rho_i]$, \bar{h} is an integer. We suppose $\mathcal{H}_{i\bar{h}}$ infected hosts invade its neighbouring subpopulations in the subset $\{Y_i = i_{\bar{h}}\}$ at t_{EAT} . Assume there are ℓ_i unobservable and partially observable edges, labelled as $1 + \rho_i, \dots, \ell_i + \rho_i$. Along each unobservable or partially observable edge, the traveling rate is $p_{\ell}, \ell \in [1, \ell_i]$, and x_{ℓ} infected hosts leave I_i . Accordingly, in total $\eta_i = \sum_{\ell} x_{\ell}$ infected individuals leave I_i through the unobservable and partially observable edges. Now there remain $k_i - \ell_i - \rho_i$ observable edges, labelled as $\ell_i + \rho_i + 1, \dots, k_i$. Along each observable edge, the diffusion rate is $p_{\mathfrak{N}}$, integer $\mathfrak{N} \in [\ell_i + \rho_i + 1, k_i]$, and $x_{\mathfrak{N}}$ infected individuals leave I_i . With probability $\bar{p}_i = 1 - \sum_{\bar{h}} p_{\bar{h}} - \sum_{\ell} p_{\ell} - \sum_{\mathfrak{N}} p_{\mathfrak{N}}$, an infected individual keeps staying at subpopulation I_i . There are \bar{x}_i infected individuals staying in subpopulation I_i with probability \bar{p}_i . Because I_i connects the unobservable and partially observable infected subpopulations, we obtain $\sum_{\ell} x_{\ell} + \bar{x}_i = \eta'_i$.

Therefore, we have the transfer likelihood estimator Ω of I_i in the following three parts.

(a) *Unobservable Subpopulation I_i* : It is difficult to estimate whether and how many infected hosts move to which neighbours due to $\Delta I_i(t_{EAT}) = I_i(t_{EAT} - 1) - I_i(t_{EAT}) \leq 0$ (we have $I_i(t_{EAT} - 1) \leq I_i(t_{EAT})$ because unobservable subpopulation I_i). We write the transfer likelihood estimator of I_i as

$$\begin{aligned} \Omega_u(\mathcal{H}_{i\bar{h}}) = & P(\mathcal{H}_{i\bar{h}}, p_{\bar{h}}, \bar{h} = [1, 2, \dots, \rho]; x_{\ell}, p_{\ell}, \ell = [1 + \rho, 2 + \rho, \\ & \dots, l + \rho]; x_{\mathfrak{N}}, p_{\mathfrak{N}}, \mathfrak{N} = [l + \rho + 1, l + \rho + 2, \dots, k]; \bar{x}_i, \bar{p}_i). \end{aligned} \quad (6.18)$$

With the definition of observable edges, the transfer likelihood estimator is simplified as

$$\Omega_u = \frac{I_i(t-1)!}{\prod_{\bar{h}} \mathcal{H}_{i\bar{h}}! \eta_i'} \prod_{\bar{h}} p_{\bar{h}}^{H_{i\bar{h}}} \left[\sum_{\ell} p_{\ell} + \bar{p}_i \right]^{\eta_i'}. \quad (6.19)$$

(b) *Observable Subpopulation I_i ($I_i \rightarrow S_i$):* Given an $I \rightarrow S$ observable subpopulation I_i , the infected individuals $H_i = \{\mathcal{H}_{i\bar{h}} | \bar{h} = 1, 2, \dots, \rho\}$ moved out of subpopulation I_i to $S_{i\bar{h}}$ are all from the term of $\Delta I_i(t_{EAT})$. Therefore, its transfer likelihood estimator is derived as

$$\Omega_{ob} = \frac{\Delta I_i(t)!}{\prod_{\bar{h}} \mathcal{H}_{i\bar{h}}! (\Delta I_i(t) - \sum_{\bar{h}} \mathcal{H}_{i\bar{h}})!} \prod_{\bar{h}} \left(\frac{p_{\bar{h}}}{\sum_{k=1}^{l+\rho} p_k} \right)^{\mathcal{H}_{i\bar{h}}''} \left(\frac{\sum_{\ell} p_{\ell}}{\sum_{j=1}^{l+\rho} p_j} \right)^{\Delta I_i(t) - \sum_{\bar{h}} \mathcal{H}_{i\bar{h}}}, \quad (6.20)$$

where $\Delta I_i(t_{EAT}) = I_i(t_{EAT} - 1) - I_i(t_{EAT}) = I_i(t_{EAT} - 1)$ (we have $I_i(t_{EAT}) = 0$ because observable subpopulation I_i ($I_i \rightarrow S_i$)).

(c) *Partially Observable Subpopulation I_i :* Because $\Delta I_i(t_{EAT}) = I_i(t_{EAT} - 1) - I_i(t_{EAT}) > 0$, at least $\Delta I_i(t_{EAT})$ infected individuals leave subpopulation I_i from $t_{EAT} - 1$ to t_{EAT} according to the definition of partially observable subpopulation. $H_i = \{\mathcal{H}_{i\bar{h}} | \bar{h} = 1, \dots, \rho\}$ is decomposed into two subsets: $H_i' = \{\mathcal{H}_{i\bar{h}}' | \bar{h} = 1, \dots, \rho\}$ and $H_i'' = \{\mathcal{H}_{i\bar{h}}'' | \bar{h} = 1, 2, \dots, \rho\}$, $\mathcal{H}_{i\bar{h}}' + \mathcal{H}_{i\bar{h}}'' = \mathcal{H}_{i\bar{h}}$, where $\mathcal{H}_{i\bar{h}}' \geq 0$, $\mathcal{H}_{i\bar{h}}'' \geq 0$. $H_i' = \{\mathcal{H}_{i\bar{h}}' | \bar{h} = 1, \dots, \rho\}$ represents the set of infected individuals departing from $I_i(t_{EAT} - \Delta t) - \Delta I_i(t_{EAT})$, and $H_i'' = \{\mathcal{H}_{i\bar{h}}'' | \bar{h} = 1, \dots, \rho\}$ denote the infected individuals departing from $\Delta I_i(t_{EAT})$. We then have the transfer likelihood estimator in the following two cases.

Case 1: $\sum_{\bar{h}} \mathcal{H}_{i\bar{h}} \geq \Delta I_i(t_{EAT})$

The transfer likelihood estimator is

$$\Omega_{pu} = \sum_{\phi=0}^{\Delta I_i(t_{EAT})} \sum_{\sum \mathcal{H}_{i\bar{h}}'' = \phi} P_1 P_2, \quad (6.21)$$

where

$$P_1 = \frac{\Delta I_i(t_{EAT})!}{\prod_{\bar{h}} \mathcal{H}_{i\bar{h}}''! (\Delta I_i(t_{EAT}) - \phi)!} \prod_{\bar{h}} \left(\frac{p_{\bar{h}}}{\sum_{k=1}^{l+\rho} p_k} \right)^{\mathcal{H}_{i\bar{h}}''} \left(\frac{\sum_{\ell} p_{\ell}}{\sum_{j=1}^{l+\rho} p_j} \right)^{\Delta I_i(t_{EAT}) - \phi},$$

$$P_2 = \frac{(I_i(t_{EAT} - \Delta t) - \Delta I_i(t_{EAT}))!}{\prod_{\bar{h}} \mathcal{H}_{i\bar{h}}'! (I_i(t_{EAT} - \Delta t) - \Delta I_i(t_{EAT}) - \sum_{\bar{h}} \mathcal{H}_{i\bar{h}}' + \phi)!} \prod_{\bar{h}} p_{\bar{h}}^{\mathcal{H}_{i\bar{h}}'} \times (\sum_{\ell} p_{\ell} + \bar{p}_i)^{I_i(t_{EAT} - \Delta t) - \Delta I_i(t_{EAT}) - \sum_{\bar{h}} \mathcal{H}_{i\bar{h}}' + \phi}.$$

Here, $\phi = \sum_{\bar{h}} \mathcal{H}''_{i\bar{h}} (0 \leq \phi \leq \Delta I_i(t_{EAT}))$, which represents the sum of infected individuals travelling from subpopulation I_i to $S_{i\bar{h}}$. For a given ϕ , we need to enumerate all possible sets $H_i'' = \{\mathcal{H}''_{ij} | j = 1, \dots, \rho\}$ to calculate the Ω_{pu} .

Case 2: $\sum_{\bar{h}} \mathcal{H}''_{i\bar{h}} < \Delta I_i(t)$

Denote $\phi = \sum_{\bar{h}} \mathcal{H}''_{i\bar{h}} (0 \leq \phi \leq \sum_{\bar{h}} \mathcal{H}''_{i\bar{h}})$. Similar to Case 1, we should enumerate all possible permutations of $H_i'' = \{\mathcal{H}''_{ij} | j = 1, \dots, \rho\}$ for a fixed ϕ . Therefore, in this case we have the transfer likelihood estimator of I_i as

$$\Omega_{pu} = \sum_{\phi=0}^{\sum_{\bar{h}} \mathcal{H}''_{i\bar{h}}} \sum_{\sum \mathcal{H}''_{ij}=\phi} P_1 P_2, \quad (6.22)$$

where P_1 and P_2 are the same as those in Eq. (6.21).

According to Eq. (6.17), the most likely invasion pathways for an INC $ml \mapsto nS (m > 1, n \geq 1)$ are identified as

$$\hat{a}^{ml \mapsto nS} = \arg \max_{\sigma_i} P(\sigma_i | INC_{ml \mapsto nS}) = \arg \max_{a_i} P(a_i | INC_{ml \mapsto nS}). \quad (6.23)$$

If the number of the first arrival infected individuals $\mathcal{H}_{ij} \geq 3$, multiple potential solutions may correspond to the same set of potential pathway(s). In this case, we merge the transfer likelihood of all potential solutions of this INC if they belong to the same invasion pathways. Then we find out the most likely invasion pathways corresponding to the maximum likelihood.

After identifying the potential invasion pathways, the whole invasion pathway $T_{\text{whole invasion pathways}}$ can be reconstructed chronologically by assembling all INCs. Finally, we depict the IPI algorithm explicitly with the pseudocodes as outlined in Algorithm 2.

Algorithm 2 Invasion Pathways Identification (IPI)

- 1: Inputs: the time series of infection data $I_i(t)$ and topology of network G
 - 2: Find all EAT data
 - 3: **for** each EAT
 - 4: Invasion partition to find out the $I \mapsto S$, $I \mapsto nS$, $ml \mapsto S$ and $ml \mapsto nS$.
 - 5: **for** each $ml \mapsto S$ or $ml \mapsto nS$
 - 6: **if** it satisfies conditions of Th 1 or Th 2
 - 7: Compute the unique invasion pathway
 - 8: **else** It does not satisfy conditions of Th 1 or Th 2
 - 9: Find all M potential solutions σ_j
 - 10: Compute the $P(\sigma_j | INC_{ml \mapsto S})$ or $P(\sigma_j | INC_{ml \mapsto nS})$
 - 11: Merge the $P(\sigma_j | INC_{ml \mapsto S})$ or $P(\sigma_j | INC_{ml \mapsto nS})$ of σ_j corresponding to same pathway(s)
 - 12: **end if**
 - 13: **end for**
 - 14: Find invasion pathway $a^{ml \mapsto S}$ or $a^{ml \mapsto nS}$ that maximize $P(\sigma_j | INC_{ml \mapsto S})$ or $P(\sigma_j | INC_{ml \mapsto nS})$
 - 15: **end for**
 - 16: Reconstruct the whole invasion pathways (T) by assembling each invasion case chronologically
-

6.4.5 Identifiability of Invasion Pathways

We now evaluate the identifiability of invasion pathways of all invasion cases. Denote π the likelihood corresponding to the most likely pathways for a given invasion case. Therefore we have

$$\pi(\sigma) = \sup_{\sigma_i} \{P(\sigma_i|INC)\}. \quad (6.24)$$

Property 1 Given an invasion case ' $mI \mapsto S$ ' or ' $mI \mapsto nS$ ', $P(\sigma_j|INC) = \frac{\prod_{k=1}^m \Omega}{\sum_{i=1}^M \prod_{k=1}^m \Omega}$, there must exist P_{min} and P_{max} satisfying

$$P_{min} \leq \pi(\sigma) \leq P_{max}. \quad (6.25)$$

Proof Suppose that $P(\sigma_1|INC) \leq \dots \leq P(\sigma_M|INC)$, where M is the number of potential solutions. Thus $P_{max} = (P(\sigma_M|INC)/P(\sigma_2|INC) + \dots + P(\sigma_M|INC))$; Because $\pi(\sigma) \geq 1/M$, let $P_{min} = \max\{1/M, P(\sigma_M|INC)/(P(\sigma_1|INC) + \sum_{j=1}^M P(\sigma_j|INC))\}$. We have $P_{min} \leq \pi(\sigma) \leq P_{max}$. \square

We define an entropy to characterize the likelihood vector of M potential pathways of an INC.

Definition 1 (Entropy of Likelihoods of M Potential Solutions) Define the normalized entropy of transfer likelihood $P(\sigma_1|INC), \dots, P(\sigma_M|INC)$ as

$$\mathcal{S} = -\frac{1}{\log M} \sum_{i=1}^M P(\sigma_i|INC) \log P(\sigma_i|INC). \quad (6.26)$$

This likelihood entropy \mathcal{S} tells the information embedded in the likelihood vector of the potential solutions of a given INC.

Definition 2 (Identifiability of Invasion Pathways) Define the identifiability of invasion pathways to characterize the feasibility to identify an invasion case as

$$\Pi = \pi(\sigma)(1 - \mathcal{S}). \quad (6.27)$$

Definition 2 tells that the bigger $\pi(\sigma)$ and the smaller entropy \mathcal{S} , the easier to identify the epidemic invasion pathways for an invasion case.

6.4.6 Examples

We illustrate the performance of our proposed IPI algorithm to identify the invasion pathways, with the maximal connected component of the American airports network (AAN, Fig. 6.7) to form a meta-population network. Note that the data to construct



Fig. 6.7 Illustration of an American airports network (From Brockmann et al. [42])

the AAN was collected from the U.S. demographic statistical data and domestic air transportation [35, 43]. Here, the AAN is a weighted and directed graph having $V = 404$ nodes (airports) and $E = 6480$ weighted and directed edges representing flight routes. The weight of edge E_{ij} is defined as diffusion rate $p_{ij} = \frac{\langle w_{ij} \rangle}{\langle N_i \rangle}$, where $\langle w_{ij} \rangle$ is the daily amount of passengers of the flight from i to j , $\langle N_i \rangle$ is the population of serving areas [43] of airport i . The average degree of the AAN is $\langle k \rangle \approx 16$, and the range of degree k is [1,158]. The range of distributions of $\langle w_{ij} \rangle$ and p_{ij} is [1, 9100] and $[7.4 \times 10^{-8}, 0.03]$, respectively. The range of distribution of $\langle N_i \rangle$ is [6100, 1.907×10^7], and the total population of the AAN is $N_{total} \approx 0.243 \times 10^9$, i.e., approximately the whole population of the United States of America. Therefore, the AAN as the sample of a meta-population network shows high heterogeneity of connectivity patterns, traffic capacities as well as the population distribution [43].

To verify the performance of the proposed IPI algorithm, we select three methods [15, 31, 32] as the benchmark for comparison, which generate the shortest path trees or minimum spanning trees of a meta-population network. In more detail, [31] generates the average-arrival-time-based (ARR) shortest path tree, and [15] generates the effective-distance-based (EFF) most probable paths, and [32] generates the Monte-Carlo-Maximum-Likelihood-based (MCML) most likely epidemic invasion tree.

We define the identifying accuracy as the ratio of the number of correctly identified invasion pathways by each method to the number of true invasion pathways. We also compute the accuracy of accumulative INCs of $mI \mapsto S$ and $mI \mapsto nS$, which is defined as the ratio of the number of correctly identified invasion pathways by each method to the number of true invasion pathways in this INC. Besides, we also make the comparison of the identification accuracy at the

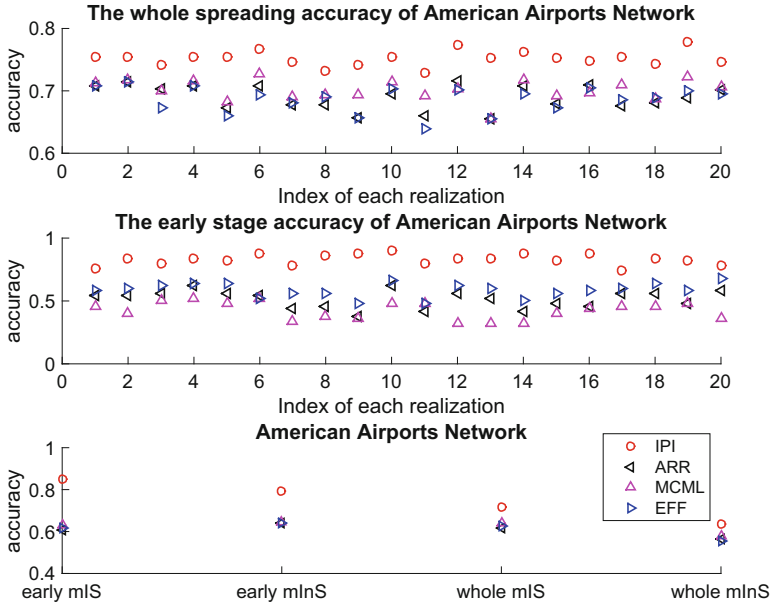


Fig. 6.8 (Top) The wholly identifying accuracy of the invasion pathways on the AAN with 20 rounds of independent realizations. (Middle) The identifying accuracy of the invasion pathways for the early stage (before infecting 50 subpopulations) on the AAN with 20 rounds of independent realizations. (Bottom) The accumulative identifying accuracy of invasion cases ($mI \mapsto S$ and $mI \mapsto nS$) for the early stage and the whole invasion pathways on the AAN. Here “mIS” and “mInS” stand for $mI \mapsto S$ and $mI \mapsto nS$, respectively (From Wang et al. [35])

early stage of epidemic dynamics, which is defined as the period when the first 50 subpopulation have been infected. In the top and middle panels of Fig. 6.8, we observe the whole identification accuracy and the early-stage identification accuracy, while the bottom panel of Fig. 6.8 presents the early and whole accumulative identification accuracy of $mI \mapsto S$ and $mI \mapsto nS$ through 20 independent realizations on the AAN, respectively. Here the whole identification accuracy means the identification accuracy of whole meta-population network has been infected. The seed subpopulation in all such independent realizations is set as the Sun Valley Airport in Bullhead City, Arizona. We clearly observe that the IPI algorithm is more accurate at identifying the invasion pathways than other benchmark methods.

We then visualize the identified invasion pathways (the lower panel of Fig. 6.9) during the early stage of a realization compared with the actual invasion pathways (the upper panel of Fig. 6.9). The weights (diffusion rates) of invasion edges are shown by the thicknesses of lines, and arrows represent the directions of invasions. We observe that most of the invasion pathways are correctly identified to form the invasive backbone of this realization of an epidemic dynamics, while there still exist some wrongly identified pathways in some INCs, indicating the necessity of defining the identifiability of an INC.

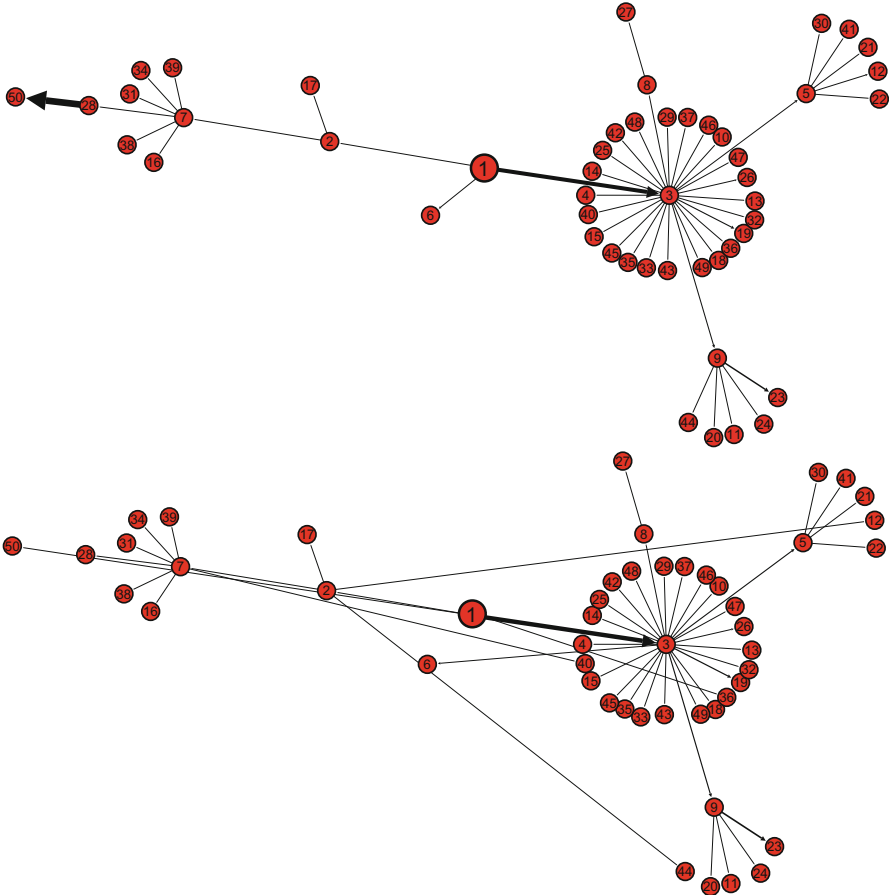


Fig. 6.9 Illustration of the actual invasion pathways (the *upper panel*) and the identified invasion pathways (the *lower panel*), during the early stage of a realization (before the appearance of 50 infected subpopulations) on the AAN. Subpopulation 1 is the seed (Sun Valley Airport in Bullhead City, Arizona) (From Wang et al. [35])

We finally examine the identifiability of an invasion case. Figure 6.10 shows the entropy and identifiability of wrongly identified $mI \mapsto S$ of 20 independent realizations on the AAN. The smaller the identifiability of an invasion case is, the more prone it is to be wrongly identified. The identifiability depicts the wrongly identified $mI \mapsto S$ more reasonably than the likelihoods entropy. The frequency of identifiability of INCs descends obviously, but that of the likelihood entropy of INCs does not clearly ascend. This statistical result indicates that the identifiability Π has a better performance to distinguish whether an invasion case is difficult to identify or not than the distinction performance of the likelihood entropy, and also tells that why some invasion cases are easy to identify, whose Π are more than 0.5,

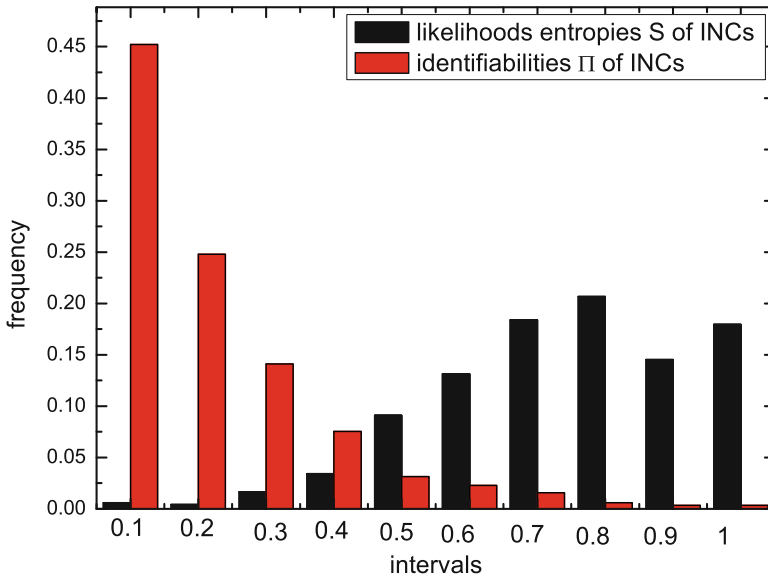


Fig. 6.10 Statistical analysis of the likelihoods entropy and identifiability of wrongly identified $mI \mapsto S$ in 20 realizations of epidemic spreading on the AAN (From Wang et al. [35])

and why some invasion cases are difficult to identify, whose Π are much less than 0.5. Here 0.5 is an empirical value.

6.5 Predicting the Epidemic Transmission

As the final part of this chapter, we now move a step further to predict the early stage of an epidemic transmission. Suppose the epidemic process starts from the patient 0 subpopulation. This subpopulation invades and infects its neighbours, and the cascading transmission proceeds. At the early epidemic stage, the time series of the number of infected individuals in each subpopulation $I_i(t)$ (i.e., the infection data) is recorded. Assume the topology of the meta-population network (including population sizes and diffusion rates, as Sect. 6.4) and the time series of the recorded infection data $I_i(t)$ until time t are available, and the focus of interest in this section is to predict which subpopulations will be infected at time step $t+1$. We consider the SI model with the diffusion of new increment of infected individuals after reaction (see Sect. 6.2 Eq. (6.3)).

6.5.1 A Prediction Algorithm

The growth of infected individuals in an infected subpopulation is governed by the infected rate β , while the diffusion process is ruled by the parameters of multinomial distribution. We first identify the infection rate β by using the method in Sect. 6.3.2, then estimate the increment $\Delta_R I_i(t)$ of $I_i(t)$ of subpopulation i after the reaction from t to $t + 1$. Statistically, $\langle \Delta_R I_i(t) \rangle = \beta I_i(t) S_i(t) / N_i(t)$. To keep the population balance of each subpopulation, we assume $\langle w_{ij} \rangle = \langle w_{ji} \rangle$, i.e., $\langle N_i(t) p_{ij} \rangle = \langle N_j(t) p_{ji} \rangle$, where w_{ij} is the number of individuals that have moved from subpopulation i to subpopulation j in a unit time (e.g., a day). Thus we have $\langle N_j(t) \rangle = \langle N_j(t + 1) \rangle$. At the early stage, $N_j(t) \approx S_j(t)$, and $N_j(t)$ is included in the population information of each subpopulation of meta-population network. Therefore, we estimate $\Delta_R I_j(t)$ by $\Delta_R I_j(t) \approx \beta I_j(t) / N_j(t)$.

Next we give the algorithm predicting n ($n \geq 1$) subpopulations infected from t to $t + 1$ during the diffusion process. At time step t , all susceptible subpopulations having at least one infected neighbouring subpopulation comprise set \mathbf{S} . We discuss the two cases of $n = 1$ and $n > 1$ in the following, and Algorithm 3 presents the pseudocode for the prediction algorithm.

(i) $n = 1$;

In this case, there is only one susceptible subpopulation infected at time $t + 1$. The likelihood $\mathcal{L}_i(t + 1)$ that subpopulation i in set \mathbf{S} is infected at time $t + 1$ is derived as

$$\begin{aligned} \mathcal{L}_i(t + 1) = & 1 - (1 - p_{1i})^{I_1(t) + \Delta_R I_1(t)} (1 - p_{2i})^{I_2(t) + \Delta_R I_2(t)} \\ & \dots (1 - p_{mi})^{I_m(t) + \Delta_R I_m(t)}, \end{aligned} \quad (6.28)$$

where m is the number of infected neighbouring subpopulations of i at time step t . We label infected neighbouring subpopulations of i as $1, 2, \dots, m$.

Accordingly, the most likely infected subpopulation \hat{v} is predicted as

$$\hat{v} = \arg \max_i \mathcal{L}_i \prod_{j \neq i, j \in \mathbf{S}} \overline{\mathcal{L}}_j, \quad (6.29)$$

where $\overline{\mathcal{L}}_j = 1 - \mathcal{L}_j$.

(ii) $n \geq 2$;

The most likely n ($n \geq 2$) infected subpopulations in \mathbf{S} can be predicted as

$$\hat{v}_n = \arg \max_{i_k} \mathcal{L}_{i_1} \mathcal{L}_{i_2} \dots \mathcal{L}_{i_n} \prod_{j \neq i_k, k=1,2,\dots,n, j \in \mathbf{S}} \overline{\mathcal{L}}_j. \quad (6.30)$$

Algorithm 3 Prediction Algorithm

-
- 1: Inputs: time series of infection data $I_i(t)$ and topology of network G
 - 2: Estimate the infection rate β
 - 3: **for** each time step t
 - 4: find all possible candidate subpopulations (set \mathbf{S})
 - 5: compute the likelihood $\mathcal{L}_i(t+1)$ of each subpopulation $i \in \mathbf{S}$
 - 6: rank all subpopulations i by their likelihoods $\mathcal{L}_i(t+1)$
 - 7: **end for**
 - 8: Choose the subpopulation i corresponding to the maximal likelihood $\mathcal{L}_i(t+1)$ as the most likely infected i in the next time step
-

Note that the above method only presents the most likely infected subpopulations at the next time step. Generally, the number of possibly infected subpopulations increases sharply during the epidemic dynamics. In this case, the likelihood of the most likely infected subpopulation may be very small. Therefore, we shall rank the likelihoods and investigate the top ranking subpopulations, which help us to judge which subpopulations are prone to be infected. Let $\mathcal{P}_i = \mathcal{L}_i \prod_{j \neq i, j \in \mathbf{S}} \overline{\mathcal{L}_j}$ in Eq. (6.29). We define the infected likelihood vector $\{\mathcal{P}_1, \mathcal{P}_2, \dots, \mathcal{P}_Z\}$ of all Z candidate subpopulations in set \mathbf{S} , where \mathcal{P}_i is the likelihood the susceptible subpopulation i gets infected in the next time step as Eq. (6.29), $i = 1, 2, \dots, Z$. Then we define the infected likelihood entropy \mathcal{E} as

$$\mathcal{E} = -\frac{1}{\log M} \sum_{i=1}^M \mathcal{P}_i \log \mathcal{P}_i. \quad (6.31)$$

This entropy tells the extent of prediction difficulty at each time step. The smaller \mathcal{E} , the easier the prediction.

6.5.2 Examples

This time we select an artificial meta-population network as the simulation example of spatial epidemic prediction. We generate a scale-free network with the BA model [6], then design the diffusion rate of each edge. Note that empirically the diffusion rates [44] of air transportation networks depend on the degree of the nodes. We define the diffusion rate from node i to node j as

$$p_{ij} = \frac{b_{ij} k_j^{\hat{\theta}}}{\sum_l b_{il} k_l^{\hat{\theta}}} C, \quad (6.32)$$

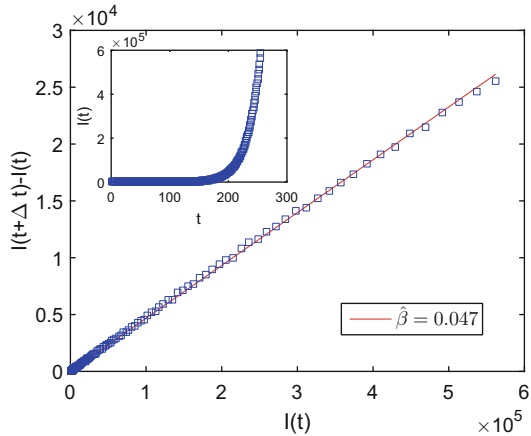
where b_{ij} stands for the elements of the adjacency matrix ($b_{ij} = 1$ if i connects to j , and $b_{ij} = 0$ otherwise), C is a constant (C is assumed as available, and set as 0.005), and $\hat{\theta}$ is a parameter. We assume that parameter θ follows the Gaussian distribution

$\theta \sim N(\hat{\theta}, \delta^2) = \frac{1}{\sqrt{2\pi\delta}} \exp(-\frac{(\hat{\theta}-\theta)^2}{2\delta^2})$ for each subpopulation. By setting constant C and computing the population of each subpopulation at equilibrium, the polynomial regression is employed to evaluate parameters $\hat{\theta}$ and δ^2 based on the empirical rule of $T' \sim k^{\beta'}$, $\beta' \simeq 1.5 \pm 0.1$, (where $T' = \sum_l w_{jl}$, and β' is approximately linear with $\hat{\theta}$ (observed in simulations). Assume $\hat{\theta} = a'\beta' + b'$, we can obtain $\hat{\theta}$, where a', b' are parameters). Therefore we can determine the diffusion rate p_{ij} along each edge. We set the whole BA meta-population network having 404 nodes (subpopulation), and fix $\langle k \rangle = 16$ ($m'_0 = 9, m' = 8$) as the average degree of the BA meta-population network. The initial size of each subpopulation is $N_1 = N_2 = \dots = N_N = 6 \times 10^5$, and the total population of the whole meta-population network is $N_{total} = 6 \times 10^5 \times 404 = 2.424 \times 10^8$.

As illustrated in Fig. 6.11, the estimation of β is close to the actual infection rate. We compare our prediction algorithm with the randomization prediction, i.e., we randomly choose a susceptible subpopulation in \mathbf{S} as the most likely infected subpopulation at the next time step. Ranking distance is defined as the difference of rank of likelihood $\mathcal{L}(t + 1)$ between the investigated two subpopulations i and j . In Fig. 6.12, “RankError” means the ranking distance of the corresponding infected likelihood between the predicted candidate and the actual infected subpopulation. “RandError” means the ranking distance of the corresponding infected likelihood between the randomly selected candidate and the actual infected subpopulation. As shown in Fig. 6.12, the subpopulations predicted by our algorithm are closer to the actual infected subpopulations at the next time step compared with those randomly selected subpopulations.

We further investigate why the accurate prediction of the infected subpopulation is difficult to achieve. At time step t , if any new subpopulation(s) will be infected in this realization at the next time step, $t + 1$ is called the prediction time. As shown in Fig. 6.13, we observe that the number of possible infected candidates Z increases sharply, and the infected likelihood entropy also increases (generally

Fig. 6.11 The estimation of the infection rate β on a BA meta-population network with 404 subpopulations. The actual value of $\beta = 0.05$. Inset: The evolution of $I(t)$ in a linear scale (From Wang et al. [36])



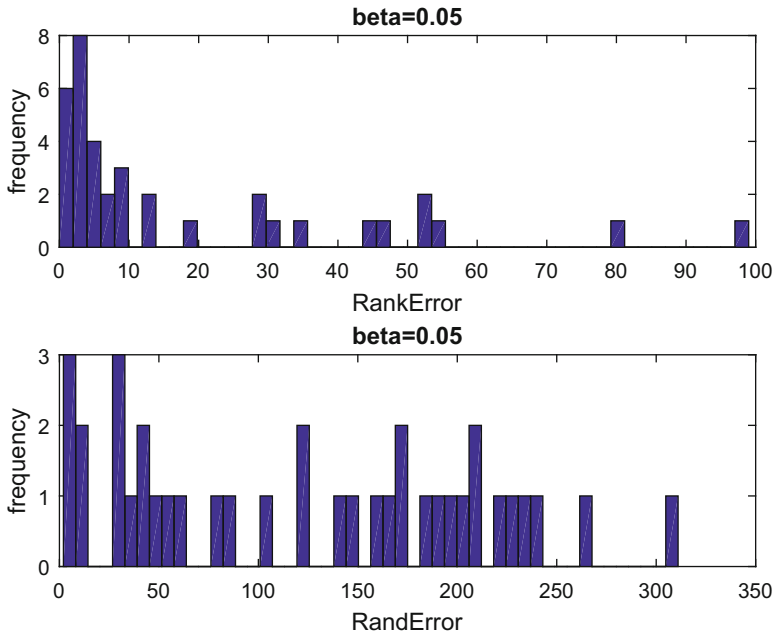


Fig. 6.12 (Top) The distribution of the RankError from t to $t + 1$ at the early stage of a realization (one run) of epidemic dynamics. (Bottom) The distribution of the RandError from t to $t + 1$ at the early stage of the same realization of epidemic dynamics. Here $t + 1$ is each time of prediction. In the realization, the infection rate $\beta = 0.05$ (From Wang et al. [36])

$\mathcal{E} > 0.5$) during the time evolution. Because the likelihoods of possibly infected subpopulations become more homogeneous as the infection prevails, indicating the infected likelihoods in the likelihood vector are not significantly different from each other, the infected likelihood entropy herein becomes large, suggesting the difficulty of accurately predicting the next infected subpopulation.

6.6 Outlook

As only a snapshot of the emergent frontier in the exciting network science, some latest advances on identification and prediction of epidemic meta-population networks have been introduced in this chapter. The future steps along this line may involve the following aspects: (1) The adaptiveness of humans deserves sufficient respect when facing the modelling, analyses and prediction of a large-scale spatial pandemic situation, and an appropriately designed role with the feedback-loop of human adaptiveness into such a complex networking system will be much appreciated. (2) The power of Big Data and cloud computing may help embed high-resolution records of human behavioural dynamics (including mobility, interaction

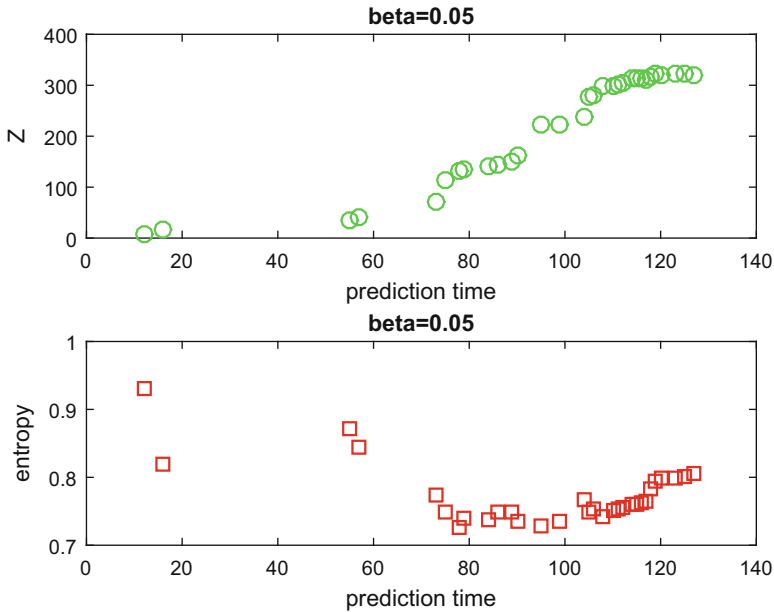


Fig. 6.13 (Top) The evolution of the number of possibly infected candidates Z with each prediction time. (Bottom) The entropy of likelihoods vector. The epidemic realization is run on a BA meta-population network with 404 subpopulations with the infection rate $\beta = 0.05$ (From Wang et al. [36])

and other non-private profiles) into the study. Nevertheless, abuse of data should be carefully avoided. (3) The verification even for the prediction of an infectious process requires the precise control means and public strategy in the viewpoints of not only mathematical results but also implementations in practice. Finally comes the end of this chapter, which may still stands at the beginning of the long journey in this exciting and challenging direction.

References

1. Wiener, N.: *Cybernetics: or Control and Communication in the Animal and the Machine*. MIT Press, Cambridge, MA (1961)
2. Bondy, J.A., Murty, U.S.R.: *Graph Theory with Applications*. Macmillan, London (1976)
3. West, D.B.: *Introduction to Graph Theory*. Prentice Hall, Upper Saddle River (2001)
4. Erdős, P., Rényi, A.: On the evolution of random graphs. *Publ. Math. Inst. Hungar. Acad. Sci.* **5**, 17–61 (1960)
5. Watts, D.J., Strogatz, S.H.: Collective dynamics of ‘small-world’ networks. *Nature* **393**, 440–442 (1998)
6. Barabási, A.-L., Albert, R.: Emergence of scaling in random networks. *Science* **286**, 509–512 (1999)

7. Albert, R., Barabási, A.-L.: Statistical mechanics of complex networks. *Rev. Mod. Phys.* **74**, 47–97 (2002)
8. Wang, X., Li, X., Chen, G.: *Complex Networks: Theories and Applications*. Tsinghua University Press, Beijing (2006, in Chinese)
9. Newman, M.E.J.: *Networks: An Introduction*. Oxford University Press, New York (2010)
10. Chen, G., Wang, X., Li, X.: *Introduction to Complex Networks: Models, Structures and Dynamics*. Higher Education Press, Beijing (2012)
11. Keeling, M.J., Rohani, P.: *Modeling Infectious Diseases in Humans and Animals*. Princeton University Press, Princeton/Oxford (2008)
12. Anderson, R.M., May, R.M.: *Infectious Diseases of Humans: Dynamics and Control*. Oxford University Press, Oxford (1991)
13. Heesterbeek, H., Anderson, R.M., Andreasen, V., et al.: Modeling infectious disease dynamics in the complex landscape of global health. *Science* **347**, aaa4339 (2015)
14. Fitch, J.P.: Engineering a global response to infectious diseases. *Proc. IEEE* **103**, 263–272 (2015)
15. Brockmann, D., Helbing, D.: The hidden geometry of complex, network-driven contagion phenomena. *Science* **342**, 1337–1342 (2013)
16. McMichael, A. J.: Globalization, climate change, and human health. *N. Engl. J. Med.* **368**, 1335–1343 (2013)
17. Pastor-Satorras, R., Castellano, C., Van Mieghem, P., Vespignani, A.: Epidemic processes in complex networks. *Rev. Mod. Phys.* **87**, 925–979 (2015)
18. Fu, X., Small, M., Chen, G.: *Propagation Dynamics on Complex Networks: Models, Methods and Stability Analysis*. Higher Education Press, Beijing (2014)
19. Li, X., Li, X.: A Data-driven inference algorithm for epidemic pathways using surveillance reports in 2009 outbreak of influenza A (H1N1). In: *Proceedings of 51st IEEE Conference on Decision and Control (CDC)*, pp. 2840–2845 (2012)
20. Hufnagel, L., Brockmann, D., Geisel, T.: Forecast and control of epidemics in a globalized world. *Proc. Natl. Acad. Sci. U. S. A.* **101**, 15124–15129 (2004)
21. Miao, H., Xia, X., Perelson, A.S., et al.: On identifiability of nonlinear ODE models and applications in viral dynamics. *SIAM Rev.* **53**, 3–39 (2011)
22. Gomez-Rodriguez, M., Leskovec, J., Krause, A.: Inferring networks of diffusion and influence. In: *Proceedings of 16th ACM SIGKDD Conference on Knowledge Discovery and Data Mining (KDD)*, pp. 1019–1028 (2010)
23. Han, X., Shen, Z., Wang, W.-X., Di, Z.: Robust reconstruction of complex networks from sparse data. *Phys. Rev. Lett.* **114**, 028701 (2015)
24. Shah, D., Zaman, T.: Rumors in a network: who's the culprit? *IEEE Trans. Inf. Theory* **57**, 5163–5181 (2011)
25. Wang, Z., Dong, W., Zhang, W., Tan, C.-W.: Rumor source detection with multiple observations: fundamental limits and algorithms. In: *Proceedings of the ACM Sigmetrics 2014*, pp. 1–13 (2014)
26. Maeno, Y.: Discovering network behind infectious disease outbreak. *Phys. A* **389**, 4755–4768 (2010)
27. Eggo, R.-M., Cauchemez, S., Ferguson, N.M.: Spatial dynamics of the 1918 influenza pandemic in England, Wales and the United States. *J. R. Soc. Interface* **8**, 233–243 (2011)
28. Wan, X., Liu, J., Cheung, W.K., Tong, T.: Inferring epidemic network topology from surveillance data. *PLoS One* **9**, e100661 (2014)
29. Shi, B., Liu, J., Zhou, X.-N., Yang, G.-J.: Inferring plasmodium vivax transmission networks from tempo-spatial surveillance data. *PLoS Negl. Trop. Dis.* **8**, e2682 (2014)
30. Yang, X., Liu, J., Zhou, X.-N., Cheung, W.-K.: Inferring disease transmission networks at a metapopulation level. *Health Inf. Sci. Syst.* **17**, 8 (2014)
31. Gautreau, A., Barrat, A., Barthelemy, M.: Global disease spread: statistics and estimation of arrival times. *J. Theor. Biol.* **251**, 509–522 (2008)
32. Balcan, D., Colizza, V., Gonçalves, B., Hu, H., Ramasco, J.J., Vespignani, A.: Multiscale mobility networks and the spatial spreading of infectious diseases. *Proc. Natl. Acad. Sci. U. S. A.* **106**, 21484–21489 (2009)

33. Wang, J.-B., Cao, L., Li X.: On estimating spatial epidemic parameters of a simplified metapopulation model. In: Proceedings of 13th IFAC Symposium on Large Scale Complex Systems: Theory and Applications, pp. 383–388 (2013)
34. Wang, J.-B., Li, X., Wang, L.: Inferring spatial transmission of epidemics in networked metapopulations. In: Proceedings of 2015 IEEE International Symposium on Circuits and Systems (ISCAS), pp. 906–909 (2015)
35. Wang, J.-B., Wang, L., Li, X.: Identifying spatial invasion of pandemics on metapopulation networks via anatomizing arrival history. *IEEE Trans. Cybern.* **46**, 2782–2795 (2016)
36. Wang, J.-B., Li, C., Li, X.: Predicting spatial transmission at the early stage of epidemics on a networked metapopulation. In: Proceedings of 12th IEEE International Conference on Control & Automation (ICCA), pp. 116–121 (2016)
37. Li, X., Wang, J.-B., Li, C.: Towards identifying epidemic processes with interplay between complex networks and human populations. In: Proceedings of 2016 IEEE Conference on Norbert Wiener in the 21st Century (21CW), pp. 67–71 (2016)
38. Levins, R.: Some demographic and genetic consequences of environmental heterogeneity for biological control. *Bull. Entomol. Soc. Am.* **15**, 237–240 (1969)
39. Rvachev, L.A., Longini, I.M.: A mathematical model for the global spread of influenza. *Math. Biosci.* **75**, 3–22 (1985)
40. Wang, L., Li, X.: Spatial epidemiology of networked metapopulation: an overview. *Chin. Sci. Bull.* **59**, 3511–3522 (2014)
41. Brooks-Pollock, E., Roberts, G.O., Keeling, M.J.: A dynamic model of bovine tuberculosis spread and control in Great Britain. *Nature* **511**, 228–231 (2014)
42. Brockmann, D., Theis, F.: Money circulation, trackable items, and the emergence of universal human mobility patterns. *IEEE Pervasive Comput.* **7**, 28–35 (2008)
43. Wang, L., Li, X., Zhang, Y.-Q., Zhang, Y., Zhang, K.: Evolution of scaling emergence in large-scale spatial epidemic spreading. *PLoS One* **6**, e21197 (2011)
44. Barrat, A., Barthélemy, M., Pastor-Satorras, R., Vespignani, A.: The architecture of complex weighted networks. *Proc. Natl. Acad. Sci. U. S. A.* **101**, 3747–3752 (2004)

Chapter 7

Epidemic Threshold in Temporally-Switching Networks

Leo Speidel, Konstantin Klemm, Víctor M. Eguíluz, and Naoki Masuda

Abstract Infectious diseases have been modelled on networks that summarise physical contacts or close proximity of individuals. These networks are known to be complex in both their structure and how they change over time. We present an overview of recent progress in numerically determining the epidemic threshold in temporally-switching networks, and illustrate that slower switching of snapshots relative to epidemic dynamics lowers the epidemic threshold. Therefore, ignoring the temporally-varying nature of networks may underestimate endemicity. We also identify a predictor for the magnitude of this shift which is based on the commutator norm of snapshot adjacency matrices.

7.1 Introduction

Mathematical models of epidemics on networks describe transmission of infectious diseases through dyadic connections between individuals [2, 21, 31]. Depending on the disease, individuals may assume different states, such as being susceptible, infected, recovered or immune. A common assumption is that infected individuals

L. Speidel

Department of Statistics, University of Oxford, 24–29 St Giles, OX1 3LB, Oxford, UK

Doctoral Training Centre in Systems Biology, University of Oxford, Rex Richards Building, South Parks Road, OX1 3QU, Oxford, UK

K. Klemm

School of Science and Technology, Nazarbayev University, Qabanbay Batyr Ave 53, 010000, Astana, Kazakhstan

Instituto de Física Interdisciplinar y Sistemas Complejos IFISC (CSIC-UIB), E07122, Palma de Mallorca, Spain

V.M. Eguíluz

Instituto de Física Interdisciplinar y Sistemas Complejos IFISC (CSIC-UIB), E07122, Palma de Mallorca, Spain

N. Masuda (✉)

Department of Engineering Mathematics, University of Bristol, Merchant Venturers Building, Woodland Road, BS8 1UB, Clifton, Bristol, UK
e-mail: naoki.masuda@bristol.ac.uk

transmit the disease to adjacent susceptible individuals at some constant infection rate β . For many epidemic models, increasing the infection rate relative to other parameters results in a phase transition from a disease-free state to an epidemic (i.e., a macroscopic number of nodes can be eventually infected) or an endemic (i.e., a macroscopic number of nodes is infected in the equilibrium) phase. The critical infection rate β_c is called the epidemic threshold. Efficiently realising $\beta < \beta_c$ to prevent a large-scale outbreak by immunising networks or engineering network structure has received substantial attention over the years [2, 22, 28, 31]. A prerequisite for such studies is a good understanding for what influences β_c . For instance, network properties such as the degree distribution have been shown to influence the value of β_c [31].

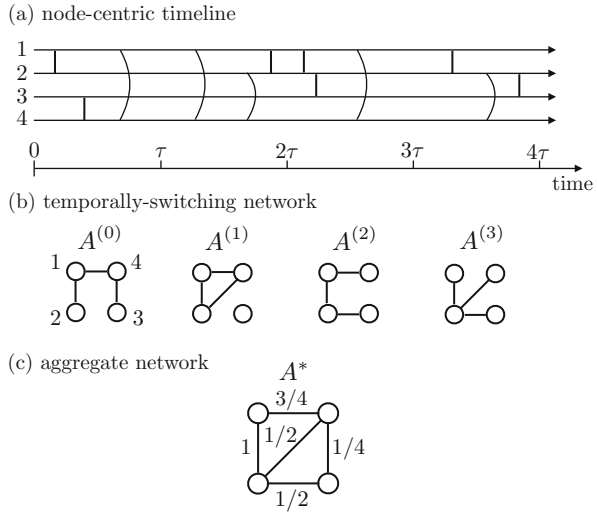
Epidemics spread on networks of communication, physical contacts, or close proximity between humans or animals. These networks vary over time on different time scales, forming temporal networks, which can alter the effect of networks on epidemic processes [1, 18, 19, 25, 27]. Valdano and colleagues presented a theory to calculate the epidemic threshold in temporal networks for the discrete-time susceptible-infected-susceptible (SIS) epidemic model in which each node is either in the susceptible or infected state [40]. In Ref. [36], we adapted their theory to the continuous-time SIS model. We found that the epidemic threshold in temporal networks is smaller compared to the corresponding value in the time-aggregated static network. Therefore, ignoring the time-varying nature of networks would lead to underestimation of endemicity. In this chapter, we will summarise these recent findings in a pedagogical manner and provide further numerical evidence.

7.2 Representations of Temporal Networks

There are several ways to represent temporal networks and which representation is preferable over others depends on a number of factors. For instance, to adapt techniques of static networks, temporal networks are represented as a sequence of static networks; alternatively, to borrow techniques from time series analysis, node or link activities are represented as time series. Computational advantages of one representation over another are also worth considering. We point to review articles for more detailed discussion [18, 19].

Data of temporal networks quite often come in the form of time-stamped links. Time stamps indicate the time of appearance (and disappearance) of a link. An example in terms of a node-centric time line is visualised in Fig. 7.1a. To investigate epidemic spreading on temporal networks, let us aggregate links over intervals of length τ . We refer to each network representing a time interval as a snapshot and call the sequence of snapshots a temporally-switching network. For empirical temporal networks, the sequence of snapshots is finite. One technique to elongate the sequence of snapshots is to periodically repeat the empirical sequence, where the first snapshot follows the last snapshot. Temporally-switching networks are common for studying synchronization processes [23, 26, 29]. The

Fig. 7.1 Different representations of temporal networks. (a) Schematic of a node-centric time line of time stamped links. Nodes 1 and 2 interact first, then nodes 3 and 4, nodes 1 and 4, and so forth. (b) A temporally-switching network obtained by the aggregation of the temporal network shown in (a) over time windows of size τ . (c) The aggregate network corresponding to (b). The link weight in the aggregate adjacency matrix, A^* , is equal to the sum of the link weight over the four snapshots divided by four



temporally-switching network constructed by the aggregation of the links in Fig. 7.1a is shown in Fig. 7.1b. It should be noted that some of the information contained in the data is lost in the process of creating a temporally-switching network from the list of time-stamped links, unless we choose τ to be equal to the temporal resolution of the data. Non-constant τ is discussed in Sect. 7.6.

7.3 Epidemic Threshold of the SIS Model in Static Networks

Before we start investigating the epidemic threshold in temporal networks, we recapture how to calculate the epidemic threshold in static networks. We denote the epidemic threshold of the discrete-time and continuous-time models by β_c^{disc} and β_c^{cont} , respectively. Already for static networks, exact estimates of β_c^{disc} and β_c^{cont} are not known for general network structures and one has to rely on approximations. Different approximation schemes have been developed [4, 31, 33]. Here, we calculate β_c^{cont} using the so-called individual-based approximation (IBA) [5, 7]. One can verify that for the SIS model the IBA leads to $\beta_c^{disc} = \beta_c^{cont}$.

In the continuous-time SIS model, an infected node transmits the disease to a susceptible node at rate β , and it recovers to the susceptible state at rate γ . A proxy to this continuous time version is the discrete-time SIS model, in which infection and recovery happens in synchronised time steps of duration Δt with probabilities $\beta\Delta t$ and $\gamma\Delta t$ for some $\Delta t > 0$, respectively.

We assign each node i a variable $X_i(t)$ indicating its state at time t . In the SIS model, $X_i(t)$ assumes values S and I for the susceptible and infected states, respectively. We denote the probability that node i is infected at time t by $x_i(t) =$

$P(X_i = I)$. On a static network defined by the adjacency matrix A , the time evolution of $x_i(t)$ is described by a system of ordinary differential equations (ODEs) given by

$$\frac{dx_i(t)}{dt} = \beta \sum_{j=1}^N A_{ij} P(X_i(t) = S, X_j(t) = I) - \gamma x_i(t). \quad (7.1)$$

An exact solution for $x_i(t)$ is practically unavailable for general A . Therefore, different approximation schemes have been developed [31, 33]. The IBA assumes independence between the events $X_i(t) = S$ and $X_j(t) = I$ such that

$$P(X_i(t) = S, X_j(t) = I) \approx [1 - x_i(t)] x_j(t). \quad (7.2)$$

Substitution of Eq. (7.2) in Eq. (7.1) yields

$$\frac{dx_i(t)}{dt} = \beta \sum_{j=1}^N A_{ij} [1 - x_i(t)] x_j(t) - \gamma x_i(t), \quad (7.3)$$

which is now a system of ODEs that is closed in terms of $\mathbf{x}(t) = (x_1(t), \dots, x_N(t))^T$, where \top is the transposition.

The IBA leads to $\beta_c^{\text{cont}} = \gamma/\alpha_{\max}$, where α_{\max} is the largest eigenvalue of A [5, 7, 31]. This result is obtained by linearising Eq. (7.3) around the disease-free state given by $x_i(t) = 0$ ($i = 1, \dots, N$), which yields

$$\frac{d\mathbf{x}(t)}{dt} \approx (\beta A - \gamma I)\mathbf{x}(t) + o(\mathbf{x}(t)), \quad (7.4)$$

where I is the identity matrix. The largest eigenvalue of $\beta A - \gamma I$ equals 0 at $\beta = \beta_c^{\text{cont}}$. Equation (7.4) indicates that $\mathbf{x}(t)$ exponentially decays in time if $\beta < \beta_c^{\text{cont}}$. If $\beta > \beta_c^{\text{cont}}$, $\mathbf{x}(t)$ exponentially grows in time as long as the initial condition is not orthogonal to the eigenvector corresponding to the largest eigenvalue of A . Therefore, one obtains $\beta_c^{\text{cont}} = \gamma/\alpha_{\max}$. The epidemic threshold β_c^{cont} depends on α_{\max} , which is determined by the structure of the network.

7.4 Epidemic Threshold of the SIS Model in Temporally-Switching Networks

We show how one can use the IBA to calculate the epidemic threshold in temporally-switching networks. This approach for temporal networks was pioneered by Valdano and colleagues for the discrete-time SIS model [40]. We developed a similar approach for the continuous-time SIS model [36].

We are given a temporally-switching network defined by an infinite sequence of snapshot adjacency matrices $\{A^{(0)}, A^{(1)}, \dots\}$ (see Sect. 7.2). We sequentially apply each snapshot for time τ . Within these intervals of length τ , the network is static and we run an epidemic process on top of it. We regard τ as a free parameter that controls the relative time scale between epidemic dynamics and temporal switching of the network. If we decrease τ , snapshots change faster relative to epidemic dynamics, and vice versa if we increase τ .

7.4.1 Continuous Time

In continuous time, we apply snapshot $A^{(\ell')}$ for $t \in [\ell'\tau, (\ell' + 1)\tau)$. As before, the infection rate is given by β and the recovery rate by γ . Because changing (τ, β, γ) to $(c\tau, \beta/c, \gamma/c)$ for any $c > 0$ does not change the dynamics, we assume that $\gamma = 1$ without loss of generality.

The probabilities $x_i(t)$ ($1 \leq i \leq N$) evolve according to the following dynamics:

$$\frac{dx_i(t)}{dt} = \beta \sum_{j=1}^N A_{ij}^{(\ell')} P(X_i(t) = S, X_j(t) = I) - x_i(t), \quad (7.5)$$

where ℓ' is such that $\ell'\tau \leq t \leq (\ell' + 1)\tau$. To obtain a closed system, we use the IBA and obtain

$$\frac{dx_i(t)}{dt} \approx \beta \sum_{j=1}^N A_{ij}^{(\ell')} [1 - x_i(t)] x_j(t) - x_i(t). \quad (7.6)$$

To find the epidemic threshold, we linearise Eq. (7.6) around the disease-free state, which is given by $x_i = 0$ ($i = 1, \dots, N$), and obtain

$$\frac{d\mathbf{x}(t)}{dt} = (\beta A^{(\ell')} - I)\mathbf{x}(t) + o(\mathbf{x}(t)). \quad (7.7)$$

The solution of Eq. (7.7) is given by

$$\mathbf{x}(\ell\tau) \approx T_{\text{cont}}(\tau)\mathbf{x}(0), \quad (7.8)$$

where

$$T_{\text{cont}}(\tau) = \prod_{\ell'=\ell-1, \dots, 0} \exp \left[(\beta A^{(\ell')} - I)\tau \right]. \quad (7.9)$$

The product of matrices is evaluated in the indicated order, i.e., in descending order from $\ell' = \ell$ to $\ell' = 0$. The disease-free state is stable as long as the largest

eigenvalue of $T_{\text{cont}}(\tau)$, which we denote by μ_c^{cont} , is less than 1. The epidemic threshold β_c^{cont} satisfies $\mu_c^{\text{cont}} = 1$.

If the network does not change in time, Eq. (7.8) is reduced to

$$T_{\text{cont}}(\tau) = \exp[(\beta A - I)\ell\tau], \quad (7.10)$$

where A is the adjacency matrix of the static network. The largest eigenvalue of $T_{\text{cont}}(\tau)$ is given by $\mu_c^{\text{cont}} = \exp[(\beta\alpha_{\text{max}} - 1)\ell\tau]$. Therefore, we reproduce $\beta_c^{\text{cont}} = 1/\alpha_{\text{max}}$ derived in Sect. 7.3 for static networks.

Decreasing τ makes switching of snapshots faster compared to epidemic dynamics. In the limit $\tau \rightarrow 0$, the dynamics are effectively the same as those on the aggregate network defined by adjacency matrix $A^* = \lim_{\ell \rightarrow \infty} 1/\ell \sum_{\ell'=0}^{\ell-1} A^{(\ell')}$ (see Fig. 7.1c) [26, 36]. It follows that $\lim_{\tau \rightarrow 0} \beta_c^{\text{cont}} = 1/\alpha_{\text{max}}^*$, where $1/\alpha_{\text{max}}^*$ is the epidemic threshold of the aggregate network with α_{max}^* being the largest eigenvalue of A^* .

In Fig. 7.2a, we compare stochastic simulations of the continuous-time SIS model (solid lines) and the theoretical epidemic threshold β_c^{cont} (arrows) on an empirical temporal network. For the numerical results, we estimated the position of the epidemic threshold as the peak of the susceptibility defined by $\chi \equiv N((\rho^2) - \langle \rho \rangle^2) / \langle \rho \rangle$, where ρ was the fraction of infected nodes in the equilibrium [12]. We measured ρ at the end of each cycle (i.e., right after the ℓ snapshots had been applied). The dashed lines in Fig. 7.2a represent χ . The figure suggests that the epidemic threshold is roughly given by the peak of χ unless τ is too small.

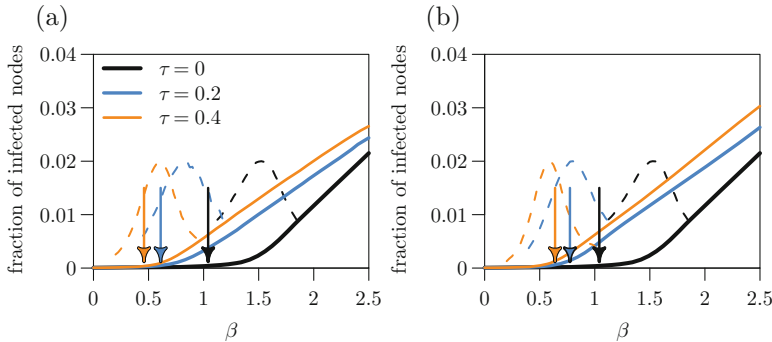


Fig. 7.2 Stochastic simulations of (a) the continuous-time SIS model and (b) the discrete-time SIS model on the sexual contact data set [34]. We imposed periodic boundary conditions. *Solid lines* show the mean fraction of infected nodes, $\langle \rho \rangle$. *Dashed lines* show $\chi \equiv N((\rho^2) - \langle \rho \rangle^2) / \langle \rho \rangle$ [12], normalised such that the peaks are at 0.02 in the plot. The epidemic threshold obtained using a bisection method on the largest eigenvalue of $T_{\text{cont}}(\tau)$ and $T_{\text{disc}}(\tau)$ is indicated by the *arrows*. To obtain the β_c^{cont} value in (a), we expanded each matrix exponential in $T_{\text{cont}}(\tau)$ up to the term of the order of $O(\tau^{10})$. The largest eigenvalue was calculated using the power method

7.4.2 Discrete Time

In discrete time, we apply a new snapshot from an infinite sequence $\{A^{(0)}, A^{(1)}, \dots\}$ in each time step. The probability that an infected node infects an adjacent susceptible node in a time step is set to $\beta\tau$, and the probability that an infected node recovers in a time step to τ .

The probabilities $x_i(t)$ ($i = 1, \dots, N$) obey the following dynamics:

$$x_i(t+1) = x_i(t) + \beta\tau \sum_{j=1}^N A_{ij}^{(t)} P(X_i(t) = \text{S}, X_j(t) = \text{I}) - \tau x_i(t). \quad (7.11)$$

By using the IBA, we obtain

$$x_i(t+1) = x_i(t) + \beta\tau \sum_{j=1}^N A_{ij}^{(t)} [1 - x_i(t)] x_j(t) - \tau x_i(t). \quad (7.12)$$

To find the epidemic threshold, we linearise Eq. (7.12) around the disease-free state and obtain

$$\mathbf{x}(t+1) = [(1-\tau)I + \beta\tau A^{(t)}] \mathbf{x}(t) + o(\mathbf{x}(t)). \quad (7.13)$$

The solution of Eq. (7.13) is given by

$$\mathbf{x}(t) \approx T_{\text{disc}}(\tau) \mathbf{x}(0), \quad (7.14)$$

where

$$T_{\text{disc}}(\tau) = \prod_{t'=t-1, \dots, 0} [(1-\tau)I + \beta\tau A^{(t')}]. \quad (7.15)$$

The disease-free state is stable if the largest eigenvalue of $T_{\text{disc}}(\tau)$, which we denote by μ_c^{disc} , is less than one. The epidemic threshold β_c^{disc} satisfies $\mu_c^{\text{disc}} = 1$.

One obtains Eq. (7.11) by approximating the derivative in Eq. (7.5) as $dx_i(t)/dt \approx [x_i(t+\tau) - x_i(t)]/\tau$. This approximation is exact as $\tau \rightarrow 0$. Therefore, the limit $\tau \rightarrow 0$ in the discrete-time SIS model corresponds to epidemic spreading on the aggregate network, and we obtain $\lim_{\tau \rightarrow 0} \beta_c^{\text{disc}} = 1/\alpha_{\text{max}}^*$. Usually, we consider the discrete-time SIS model as a proxy to the continuous-time counterpart which is sometimes more realistic. For instance, the discrete-time SIS model implicitly assumes that, for time τ , each node is allowed to make at most one transition between the susceptible and infected states. This is not the case in the continuous-time framework.

In Fig. 7.2b, we compare stochastic simulations of the discrete-time SIS model and the β_c^{disc} values predicted by the IBA. The figure shows that the prediction is again reasonably accurate unless τ is too small.

7.5 Epidemic Threshold as a Function of τ

In Sect. 7.4, we presented a numerical scheme to calculate, respectively, β_c^{cont} and β_c^{disc} for the continuous-time and discrete-time SIS models in temporally-switching networks. We have seen that the dynamics in the limit $\tau \rightarrow 0$ are effectively the same as those on the aggregate network, yielding $\lim_{\tau \rightarrow 0} \beta_c^{\text{cont}} = \lim_{\tau \rightarrow 0} \beta_c^{\text{disc}} = 1/\alpha_{\text{max}}^*$. Focussing on continuous-time dynamics, we now study the dependency of β_c^{cont} on τ .

7.5.1 General Networks

In Fig. 7.2a, the arrows indicate β_c^{cont} for $\tau = 0, 0.2$, and 0.4 in the sexual contact temporal network data set. These numerical results and those on nine other temporal network data sets [36] indicate that the epidemic threshold decreases as τ increases in the continuous-time SIS model, i.e.,

$$\beta_c^{\text{cont}} \leq \beta_c^{\text{cont}}(\tau = 0) = 1/\alpha_{\text{max}}^*. \quad (7.16)$$

So far, we have not encountered any counterexample for Eq. (7.16). However, a mathematical proof is still missing.

Equation (7.16) has the following theoretical supports. First, Eq. (7.16) is true for two solvable temporal network models (Sect. 7.5.2). Second, Eq. (7.16) holds for two snapshots $A^{(0)}$ and $A^{(1)}$ applied alternatingly. A theorem (theorem 1 in Ref. [8]) states that any real-valued, continuous spectral function ϕ that acts on the spectrum of its matrix argument and only attains finite values satisfies $\phi(e^{M_1} e^{M_2}) \geq \phi(e^{M_1 + M_2})$ for arbitrary symmetric matrices M_1 and M_2 . We let $M_1 = \tau\beta A^{(0)}$ and $M_2 = \tau\beta A^{(1)}$, and let ϕ be the spectral radius. By applying the theorem, we obtain

$$\phi(e^{\tau\beta A^{(0)}} e^{\tau\beta A^{(1)}}) \geq \phi(e^{2\tau\beta A^*}), \quad (7.17)$$

where $A^* = (A^{(0)} + A^{(1)})/2$ is the adjacency matrix of the aggregate network. By multiplying both sides of Eq. (7.17) with $e^{-2\tau}$, we obtain

$$\mu_c^{\text{cont}} = \phi(e^{(\beta A^{(0)} - I)\tau} e^{(\beta A^{(1)} - I)\tau}) \geq \phi(e^{(\beta A^* - I)2\tau}). \quad (7.18)$$

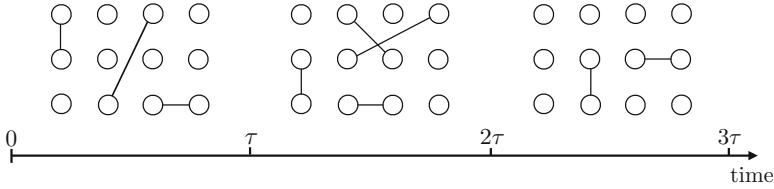


Fig. 7.3 Schematic showing a temporally-switching network composed of disjoint links

Equation (7.18) implies that $\mu_c^{\text{cont}} \geq 1$ at $\beta = 1/\alpha_{\text{max}}^*$ and therefore Eq. (7.16) holds true. To generalise the above argument to more than two snapshots, we require the inequality $\phi(\prod_{i=1}^{\ell} e^{M_i}) \geq \phi(e^{\sum_{i=1}^{\ell} M_i})$ to be valid for $\ell > 2$. When matrices M_i have negative entries, counterexamples exist for $\ell > 2$ [39]. However, it seems that, up to our numerical efforts, the inequality holds true for general ℓ if each M_i permits only non-negative entries.

If the IBA is not accurate, the epidemic threshold in temporal networks may not be smaller than in the aggregate network. One such example is the case in which snapshots are composed of disjoint links, such that every node has either degree zero or one (Fig. 7.3). In this case, the epidemic threshold is larger in temporal than aggregate networks [36]. The deterministic approximation using the IBA is inaccurate in this situation because the probability that the epidemic is extinguished by stochastic effects is not negligible. We developed a theory that accounts for this stochasticity for the case of a single link and $N = 2$ nodes (Appendix B of Ref. [36]). As $\tau \rightarrow \infty$, stochastic effects become relevant also in snapshots with larger connected components. If τ exceeds the typical time of reaching the absorbing state for a connected component, the epidemic dynamics would be absorbed to the disease-free state due to stochasticity. Our theory therefore requires that connected components contained in snapshots are large enough and that τ is not too large so that stochastic effects play negligible roles.

7.5.2 Epidemic Threshold in Model Temporal Networks

We previously derived expressions for the epidemic threshold for two model temporal networks [36]. Here we elaborate on how the epidemic threshold depends on parameters that influence the aggregate network or composition of snapshots. We find that the epidemic threshold decreases with variance in the number of links of the snapshots.

In these network models, we assume that snapshots are drawn uniformly and independently with replacement from a set of possible snapshots. To derive expressions for the epidemic threshold, we approximate T_{cont} by its expectation to obtain

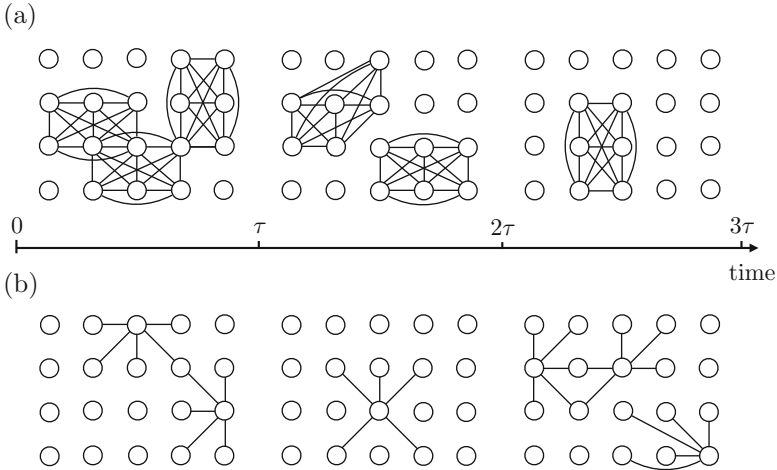


Fig. 7.4 Schematic showing temporally-switching networks with **(a)** clique snapshots ($d_{cl} = 5$) and **(b)** the activity driven model ($d_{hub} = 5$)

$$\hat{T}_{\text{cont}}(\tau) = \frac{1}{r} \sum_A \exp [(\beta A - I)\tau], \quad (7.19)$$

where the summation runs over all possible snapshots and r is the number of possible snapshots. We denote the leading eigenvalue of $\hat{T}_{\text{cont}}(\tau)$ by $\hat{\mu}_c$ and by $\hat{\beta}_c^{\text{cont}}$ the value of β that satisfies $\hat{\mu}_c = 1$. In Ref. [36], we showed that $\hat{\beta}_c^{\text{cont}} \leq \beta_c^{\text{cont}}$ and verified numerically that $\hat{\beta}_c^{\text{cont}} \approx \beta_c^{\text{cont}}$.

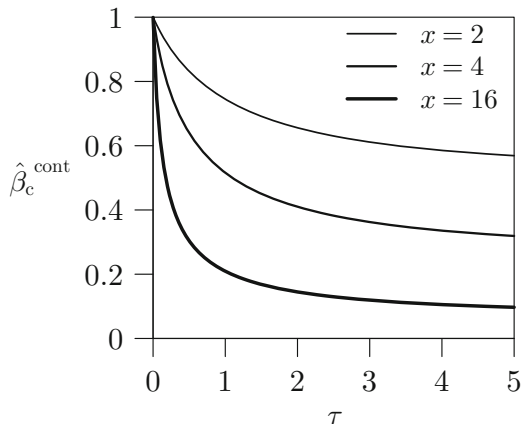
7.5.2.1 Networks with Clique Snapshots

In the first model, each snapshot consists of a union of cliques and isolated nodes. Each clique has $d_{cl} + 1$ nodes, where the size of a clique remains the same across different cliques and snapshots. The number of cliques may depend on a snapshot. It should be noted that cliques in a snapshot may overlap and that a snapshot may contain multiedges. An example of a temporally-switching network generated from this model is shown in Fig. 7.4a. We obtain

$$\hat{\beta}_c^{\text{cont}} \approx \frac{1}{\tau d_{cl}} \ln \left[1 + \frac{d_{cl}}{\alpha_{\max}^*} (e^\tau - 1) \right], \quad (7.20)$$

whose accuracy when overlaps of cliques are sufficiently rare has been verified by numerical simulations [36].

Fig. 7.5 Epidemic threshold, $\hat{\beta}_c^{\text{cont}}$, as a function of τ for networks with clique snapshots and the activity driven model. Plotted is Eq. (7.21) for $x = 2, 4, 16$ and $\alpha_{\max}^* = 1$



We rewrite Eq. (7.20) as

$$\hat{\beta}_c^{\text{cont}} \approx \frac{\alpha_{\max}^*}{\tau x} \ln [1 + x(e^\tau - 1)], \quad (7.21)$$

where $x = d_{\text{cl}}/\alpha_{\max}^*$, and plot Eq. (7.21) in Fig. 7.5. The figure indicates that the epidemic threshold decreases as τ increases, verifying that temporality of the networks as modelled by switching networks decreases the epidemic threshold. Figure 7.5 also indicates that the epidemic threshold decreases as d_{cl} or x increases when the aggregate network, and therefore α_{\max}^* , is kept fixed.

This result suggests that it is not sufficient to measure the aggregate network to predict the epidemic threshold. Rather, one needs to account for the composition of snapshots. In Fig. 7.6a, we show that a larger value of d_{cl} makes snapshots more variable in the sense that some snapshots have many links and others have only few links. Higher variability of snapshots may be one contributing factor for a smaller epidemic threshold.

7.5.2.2 Activity Driven Model

In the second model, each snapshot consists of a union of stars. We assume that each star has one hub node connected to d_{hub} leaves. We assume that the size of the stars is the same for different stars and snapshots. The number of stars may vary across different snapshots. An example of a temporally-switching network generated from this model is shown in Fig. 7.4b. As compared to the previous model, the present model allows snapshots to be more heterogeneous in terms of the node's degree.

As a special case, we study the discrete-time version of the activity driven model [24, 32]. We assign a probability a_i to each node which plays a similar role to that in the previous model but is distinct from it. In each snapshot, node i is

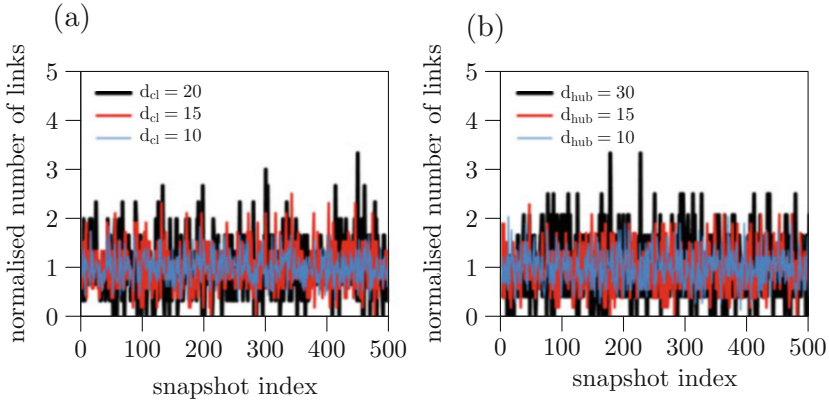


Fig. 7.6 Number of links in each snapshot normalised by the mean number of links across all snapshots for **(a)** the clique network model with $d_{cl} = 10, 15,$ and 20 and **(b)** the activity driven model with $d_{hub} = 10, 15,$ and 30 . In the clique network model, we assign every node i a probability a_i that i is activated in a snapshot. We assume that every node is activated independently of other nodes. Once activated, a node triggers a clique of size $d_{cl} + 1$ by involving d_{cl} other nodes selected uniformly at random. For all networks generated by either of the two models, we set $N = 2000$, $r = 500$, and let each a_i obey the power-law distribution with the probability density function $(1 - \eta)a_i^{-\eta}/(1 - \varepsilon^{1-\eta})$, where $\varepsilon \leq a_i \leq 1$. We set $\eta = 3$ and adjusted ε to ensure $\langle a \rangle = 0.0025$

activated with probability a_i independently of other nodes. If activated, i connects to d_{hub} other nodes that are drawn with equal probability.

The epidemic threshold for the activity driven model is approximately given by [36]

$$\hat{\beta}_c^{\text{cont}} \approx \frac{1}{\tau \sqrt{d_{hub}}} \ln \left[1 + \frac{\sqrt{d_{hub}}}{\alpha_{\max}^*} (e^\tau - 1) \right]. \quad (7.22)$$

Equation (7.22) is remarkably similar to Eq. (7.20). In fact, Eq. (7.22) is equivalent to Eq. (7.21) with $x = \sqrt{d_{hub}}/\alpha_{\max}^*$. Therefore, the epidemic threshold depends on the composition of snapshots in a similar way to the case of clique snapshots. A larger d_{hub} decreases the epidemic threshold if the aggregate network is kept fixed. Figure 7.6b suggests that a larger d_{hub} value makes snapshots temporally more variable. This result is consistent with the results for the previous model with clique snapshots (Fig. 7.6a).

7.5.3 Non-commutativity of Snapshot Adjacency Matrices

In the continuous-time SIS model, increasing τ lowered the epidemic threshold in all instances that we considered [36]. In fact, the magnitude of the shift in the

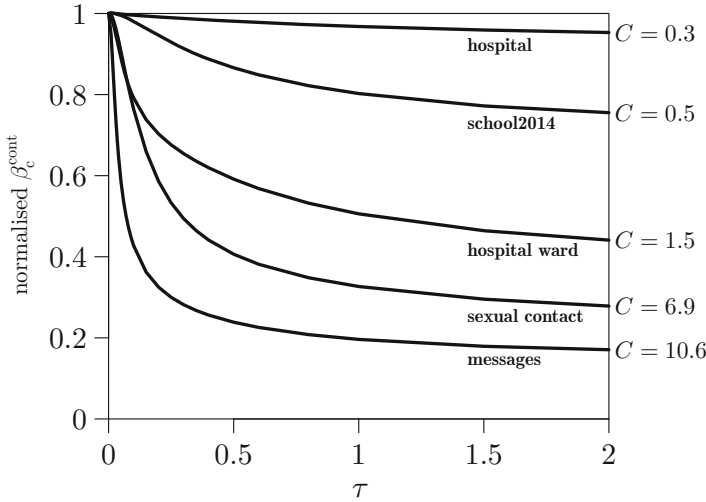


Fig. 7.7 Normalised epidemic threshold $\alpha_{\max}^* \beta_c^{\text{cont}}$ as a function of τ for empirical temporal networks whose properties are summarised in Table 7.1. The C value for each network is shown to the right. We used periodic boundary conditions

epidemic threshold is dependent on the data set, as shown in Fig. 7.7. In Ref. [36], we proposed a quantity C to predict the magnitude of this shift when the temporal rather than aggregate network is considered. Firstly, we introduce the degree of non-commutativity of snapshot adjacency matrices by using the commutator bracket as follows:

$$[M_1, M_2] \equiv M_1 M_2 - M_2 M_1, \tag{7.23}$$

where M_1 and M_2 are two matrices. Then, to summarise the degree of non-commutativity between all snapshot pairs, we define

$$C \equiv \frac{1}{(\ell \alpha_{\max}^*)^2} \sum_{\ell'=1}^{\ell-1} \sum_{\ell''=0}^{\ell'-1} \left\| [A^{(\ell')}, A^{(\ell'')}] \right\|_2, \tag{7.24}$$

where $\| \cdot \|_2$ is the spectral norm given by $\|M\|_2 = \sqrt{\phi(MM^T)}$. The multiplicative constant $(1/\alpha_{\max}^*)^2$ in Eq. (7.24) normalises the leading eigenvalue of the aggregate network to unity.

Commutator brackets between snapshot adjacency matrices appear when we expand $T_{\text{cont}}(\tau)$ using Zassenhaus' formula as follows:

Table 7.1 Properties of empirical temporal networks used for Figs. 7.2 and 7.7. The number of nodes (N), that of links (M), that of events (M_{event}), that of snapshots (r), and the length of the aggregating time window are shown. We used the largest connected component of the aggregate undirected network for each data set

Data	N	M	M_{event}	r	Aggregating window
Hospital ward [41]	75	1,139	32,424	97	1 h
School2014 [14, 37]	242	8,317	125,773	33	1 h
Online message [30]	1,892	13,835	59,831	195	1 day
Hospital [11]	5,607	60,177	936,101	105	7 days
Sexual contact [34]	15,810	38,540	50,116	75	30 days

$$\exp[(\beta A^* - I)\ell\tau] = T_{\text{cont}}(\tau) \prod_{\ell'=1}^{\ell-1} \prod_{n \geq 2} \exp\left[(\tau\beta)^n C_n \left(A^{(\ell')}, \sum_{\ell''=0}^{\ell'-1} A^{(\ell'')}\right)\right], \quad (7.25)$$

where $s = \tau\beta$ and matrices $C_n(M_1, M_2)$ ($n \geq 2$) are given by linear combinations of nested commutator brackets of M_1 and M_2 . For instance, we obtain

$$C_2(M_1, M_2) = -\frac{1}{2}[M_1, M_2] \quad (7.26)$$

and

$$C_3(M_1, M_2) = \frac{1}{6}(2[M_2, [M_1, M_2]] + [M_1, [M_1, M_2]]). \quad (7.27)$$

When all pairs of snapshot adjacency matrices commute, $C_n \equiv 0$ for all $n \geq 2$, implying $C = 0$. In this case, we obtain $T_{\text{cont}}(\tau) = \exp[(\beta A^* - I)\ell\tau]$ and therefore $\beta_c^{\text{cont}} = 1/\alpha_{\text{max}}^*$, irrespectively of τ . If $C > 0$, some pairs of snapshot adjacency matrices do not commute and we expect a gap between $1/\alpha_{\text{max}}^*$ and β_c^{cont} .

The values of C for the data sets summarised in Table 7.1 are shown in Fig. 7.7. We observe that the magnitude in the shift of the epidemic threshold is larger for data sets with larger C as well as for larger τ .

7.6 Discussion

In this chapter, we explained recent progresses in determining the epidemic threshold in the susceptible-infected-susceptible (SIS) model on temporally-switching networks. In particular, we presented evidence that the epidemic threshold for temporal networks is smaller than that for the corresponding aggregate networks. We then introduced quantity C as a measure of non-commutativity of snapshots in

a sequence. Quantity C is strongly correlated with the magnitude in the shift of the epidemic threshold induced by temporality of networks.

The individual-based approximation (IBA) can in principle be applied to any epidemic model. However, the IBA neglects correlations between the states of nodes. Although dynamics of networks may decrease the correlation, the IBA may yield inaccurate results. More sophisticated approximation schemes, such as the pair approximations (e.g., [9]) or the approximate master equation approach [15] may be useful for more accurately describing epidemic dynamics on temporal networks. How to compute the epidemic threshold in epidemic models other than the SIS model also needs further investigation (e.g., [35]).

In this contribution we have addressed the dependence of the critical threshold in epidemic spreading on the temporality of the link sequence. To obtain analytical results we have considered the case where links last for the same time τ , each of them starting at a given time t and ending at $t + \tau$. Empirical evidence shows that the duration of the interactions and/or the time between interactions do not follow such a regular pattern; both quantities in general obey broad distributions [6]. A more general framework is needed to account for these properties of data [20, 42]. In addition, consecutive τ values are often positively correlated [16, 27]. To address these issues, a common practice would be to compare dynamics on real sequences of pairwise interaction and time-shuffled sequences [18, 20]. It may also be useful to consider generative models of temporal networks with which effects of different distributions of τ on dynamics can be tested [3, 10, 17, 38]. Real systems are generically construed as a sequence of diverse interactions. Thus, understanding of epidemic processes in real systems will require the combination of temporal and multilayer networks. Data in this direction starts to be available [13].

Acknowledgements LS acknowledges the support provided through the Engineering and Physical Sciences Research Council (EPSRC) [grant number EP/G03706X/1]. LS and NM acknowledge the support provided through JST, ERATO, Kawarabayashi Large Graph Project. KK acknowledges funding from the Ramón y Cajal program of MINECO. KK and VME acknowledge support from projects SPASIMM (FIS2016-80067-P AEI/FEDER, UE) and NOMAQ (FIS2014-60343-P). NM acknowledges the support provided through JST, CREST.

References

1. Bansal, S., Read, J., Pourbohloul, B., Meyers, L.A.: The dynamic nature of contact networks in infectious disease epidemiology. *J. Biol. Dyn.* **4**, 478–489 (2010)
2. Barrat, A., Barthélemy, M., Vespignani, A.: *Dynamical Processes on Complex Networks*. Cambridge University Press, Cambridge, UK (2008)
3. Baxter, G.J.: A voter model with time dependent flip rates. *J. Stat. Mech. Theor. Exp.* **2011**, P09005 (2011)
4. Cai, C.R., Wu, Z.X., Chen, M.Z.Q., Holme, P., Guan, J.Y.: Solving the dynamic correlation problem of the susceptible-infected-susceptible model on networks. *Phys. Rev. Lett.* **116**, 258301 (2016)

5. Castellano, C., Pastor-Satorras, R.: Thresholds for epidemic spreading in networks. *Phys. Rev. Lett.* **105**, 218701 (2010)
6. Cattuto, C., Van den Broeck, W., Barrat, A., Colizza, V., Pinton, J.F., Vespignani, A.: Dynamics of person-to-person interactions from distributed RFID sensor networks. *PLoS One* **5**, e11596 (2010)
7. Chakrabarti, D., Wang, Y., Wang, C., Leskovec, J., Faloutsos, C.: Epidemic thresholds in real networks. *ACM Trans. Inf. Syst. Secur.* **10**, 1:26 (2008)
8. Cohen, J.E., Friedland, S., Kato, T., Kelly, F.P.: Eigenvalue inequalities for products of matrix exponentials. *Linear Algebra Appl.* **45**, 55–95 (1982)
9. Eames, K.T.D., Keeling, M.J.: Modeling dynamic and network heterogeneities in the spread of sexually transmitted diseases. *Proc. Natl. Acad. Sci. U. S. A.* **99**, 13330–13335 (2002)
10. Fernández-Gracia, J., Eguíluz, V.M., San Miguel, M.: Update rules and interevent time distributions: slow ordering versus no ordering in the voter model. *Phys. Rev. E* **84**, 015103 (2011)
11. Fernández-Gracia, J., Onnela, J.P., Barnett, M.L., Eguíluz, V.M., Christakis, N.A.: Influence of a patient transfer network of US inpatient facilities on the incidence of nosocomial infections. *Sci. Rep.* **7**, 2930 (2017). <http://www.nature.com/articles/s41598-017-02245-7>
12. Ferreira, S.C., Castellano, C., Pastor-Satorras, R.: Epidemic thresholds of the susceptible-infected-susceptible model on networks: a comparison of numerical and theoretical results. *Phys. Rev. E* **86**, 041125 (2012)
13. Gallotti, R., Barthelemy, M.: The multilayer temporal network of public transport in Great Britain. *Sci. Data* **2**, 140056 (2015)
14. Gemmetto, V., Barrat, A., Cattuto, C.: Mitigation of infectious disease at school: targeted class closure vs school closure. *BMC Infect. Dis.* **14**, 695 (2014)
15. Gleeson, J.P.: High-accuracy approximation of binary-state dynamics on networks. *Phys. Rev. Lett.* **107**, 068701 (2011)
16. Goh, K.I., Barabási, A.L.: Burstiness and memory in complex systems. *EPL* **81**, 48002 (2008)
17. Hoffmann, T., Porter, M.A., Lambiotte, R.: Generalized master equations for non-poisson dynamics on networks. *Phys. Rev. E* **86**, 046102 (2012)
18. Holme, P.: Modern temporal network theory: a colloquium. *Eur. Phys. J. B* **88**, 234 (2015)
19. Holme, P., Saramäki, J.: Temporal networks. *Phys. Rep.* **519**, 97–125 (2012)
20. Karsai, M., Kivela, M., Pan, R.K., Kaski, K., Kertész, J., Barabási, A.L., Saramäki, J.: Small but slow world: how network topology and burstiness slow down spreading. *Phys. Rev. E* **83**, 025102 (2011)
21. Keeling, M.J., Eames, K.T.D.: Networks and epidemic models. *J. R. Soc. Interface* **2**, 295–307 (2005)
22. Keeling, M.J., Rohani, P.: *Modeling Infectious Diseases in Humans and Animals*. Princeton University Press, Princeton (2008)
23. Liberzon, D.: *Switching in Systems and Control*. Springer Science + Business Media, New York (2003)
24. Liu, S., Perra, N., Karsai, M., Vespignani, A.: Controlling contagion processes in activity driven networks. *Phys. Rev. Lett.* **112**, 118702 (2014)
25. Masuda, N., Holme, P.: Predicting and controlling infectious disease epidemics using temporal networks. *F1000Prime Rep.* **5**, 6 (2013)
26. Masuda, N., Klemm, K., Eguíluz, V.M.: Temporal networks: slowing down diffusion by long lasting interactions. *Phys. Rev. Lett.* **111**, 188701 (2013)
27. Masuda, N., Lambiotte, R.: *A Guide to Temporal Networks*. World Scientific, Singapore (2016)
28. Newman, M.E.J.: The structure and function of complex networks. *SIAM Rev.* **45**, 167–256 (2003)
29. Olfati-Saber, R., Fax, J.A., Murray, R.M.: Consensus and cooperation in networked multi-agent systems. *Proc. IEEE* **95**, 215–233 (2007)
30. Opsahl, T., Panzarasa, P.: Clustering in weighted networks. *Soc. Netw.* **31**, 155–163 (2009)
31. Pastor-Satorras, R., Castellano, C., Van Mieghem, P., Vespignani, A.: Epidemic processes in complex networks. *Rev. Mod. Phys.* **87**, 925–979 (2015)

32. Perra, N., Gonçalves, B., Pastor-Satorras, R., Vespignani, A.: Activity driven modeling of time varying networks. *Sci. Rep.* **2**, 469 (2012)
33. Porter, M.A., Gleeson, J.P.: *Dynamical Systems on Networks - A Tutorial*. Springer, Berlin/Heidelberg (2016)
34. Rocha, L.E.C., Liljeros, F., Holme, P.: Information dynamics shape the sexual networks of internet-mediated prostitution. *Proc. Natl. Acad. Sci. USA* **107**, 5706–5711 (2010)
35. Rocha, L.E.C., Masuda, N.: Individual-based approach to epidemic processes on arbitrary dynamic contact networks. *Sci. Rep.* **6**, 31456 (2016)
36. Speidel, L., Klemm, K., Eguíluz, V.M., Masuda, N.: Temporal interactions facilitate endemicity in the susceptible-infected-susceptible epidemic model. *New J. Phys.* **18**, 073013 (2016)
37. Stehlé, J., Voirin, N., Barrat, A., Cattuto, C., Isella, L., Pinton, J., Quaghiotto, M., Van den Broeck, W., Régis, C., Lina, B., Vanhems, P.: High-resolution measurements of face-to-face contact patterns in a primary school. *PLoS One* **6**, e23176 (2011)
38. Takaguchi, T., Masuda, N.: Voter model with non-poissonian interevent intervals. *Phys. Rev. E* **84**, 036115 (2011)
39. Thompson, C.J.: Inequality with applications in statistical mechanics. *J. Math. Phys.* **6**, 1812–1813 (1965)
40. Valdano, E., Ferreri, L., Poletto, C., Colizza, V.: Analytical computation of the epidemic threshold on temporal networks. *Phys. Rev. X* **5**, 021005 (2015)
41. Vanhems, P., Barrat, A., Cattuto, C., Pinton, J.F., Khanafer, N., Régis, C., Kim, B., Comte, B., Voirin, N.: Estimating potential infection transmission routes in hospital wards using wearable proximity sensors. *PLoS One* **8**, e73970 (2013)
42. Vazquez, A., Rácz, B., Lukács, A., Barabási, A.L.: Impact of non-poissonian activity patterns on spreading processes. *Phys. Rev. Lett.* **98**, 158702 (2007)

Chapter 8

Control Strategies of Contagion Processes in Time-Varying Networks

Márton Karsai and Nicola Perra

Abstract The vast majority of strategies aimed at controlling contagion processes on networks consider a timescale separation between the evolution of the system and the unfolding of the process. However, in the real world, many networks are highly dynamical and evolve, in time, concurrently to the contagion phenomena. Here, we review the most commonly used immunization strategies on networks. In the first part of the chapter, we focus on controlling strategies in the limit of timescale separation. In the second part instead, we introduce results and methods that relax this approximation. In doing so, we summarize the main findings considering both numerical and analytically approaches in real as well as synthetic time-varying networks.

8.1 Introduction

A wide range of real-world phenomena such as the spreading of ideas, memes, infectious diseases, and malwares can be effectively modeled as contagion processes on networks [1–5]. An intense research on the subject allowed to identify a set of network features that affect such processes. In particular, two properties have been thoroughly investigated. The first is the heterogeneity observed in the distribution of networks' metrics. Examples are the number of connections per node, degree, and the intensity of contacts, weight. These quantities follow distributions characterized by heavy-tails, which imply the absence of characteristic scales and the presence of large fluctuations with respect to the average [6]. The second is the higher-order organization of connectivity patterns associated to the presence of clusters/communities or to the correlation between node's features [2, 7].

M. Karsai (✉)

Univ de Lyon, ENS de Lyon, INRIA, CNRS, UMR 5668, IXXI, 69364, Lyon, France
e-mail: marton.karsai@ens-lyon.fr

N. Perra

Centre for Business Network Analysis, University of Greenwich, Park Row, London, SE10 9LS, UK
e-mail: n.perra@greenwich.ac.uk

The understanding of these properties and their effects on spreading phenomena has spurred the creation of strategies aimed at controlling or promoting diffusion processes. These can be classified in two main categories [8]. In the first, we find *global* strategies that rely on the full knowledge of the network structure. In the second instead, we find *local* strategies which relax this, often unrealistic, assumption. In order to better understand the problem set-up, let us imagine that we want to protect a network of computers against the spreading of malwares. The trivial solution is clearly to immunize all computers. However, this strategy is very costly and often impractical. The problem then is finding a way to immunize just a fraction p of nodes and still effectively protect the entire network. Each prescription for the selection of this fraction constitutes what we call a strategy. To this end, global strategies use centrality measures such as degree, k-core, betweenness and PageRank to rank the importance of each node [1, 2, 9, 10]. Local strategies instead infer the role of nodes by local explorations and samples [11].

One common assumption in the majority of related works is to consider a timescale separation between the changes in network structures, τ_G , and the contagion process τ_P . Indeed, spreading processes have been typically considered to take place in either static ($\tau_P \ll \tau_G$) or annealed ($\tau_P \gg \tau_G$) networks. While these approximations can be used to study a range of processes such as the spreading of some diseases in contact networks or the propagation of energy in power grids it fails to describe many other phenomena in which the two timescales are comparable [12–40]. In these cases, such as the spreading of ideas, memes, information and some type of diseases the diffusion processes take place in time-varying networks [41–43]. Thus their study and modeling needs to consider the interplay between the two simultaneously unfolding dynamics.

In this chapter, we will first review the main strategies to control contagion processes in static and annealed networks. We will then focus on time-varying graphs and discuss the recent body of research based on numerical simulations of contagious processes on real and synthetic temporal networks. Finally, we will consider spreading processes unfolding on a particular class of time-varying networks called activity-driven networks which allows the analytical study of different global and local strategies of immunization. As prototypical example of contagion processes we will consider the Susceptible-Infected-Susceptible (SIS) model [1, 44, 45]. SIS dynamics are characterized by two transitions between the two different mutually exclusive states of nodes $S + I \xrightarrow{\beta} 2I, I \xrightarrow{\mu} S$. The stationary state of the process is described by two different behaviors. Above the epidemic threshold an endemic state is reached where the density of nodes in the class I reaches a balance, I_∞ , determined by the balance of the spreading and recovery rates. Below the threshold the spreading is not able to sustain itself and dies out, thus in the stationary state of the process the number of nodes in the class I is zero.

8.2 Controlling Contagion Processes in Static/Annealed Networks

How can we protect a network from the spreading of an infectious disease? While this is the underlying question of the chapter, in this section we will first focus on two timescale separation limits. In order to devise effective control strategies it is crucial to understand how contagion processes spread on networks. In particular, it is important to determine how the properties of networks affect such phenomena. As mentioned above, the topology of real-world networks is typically characterized by broad degree distributions often approximated by power laws i.e. $P(k) \sim k^{-\gamma}$. The heterogeneities that these distributions have genuine effects on the unfolding of contagion processes. Indeed, it has been shown [46] that the epidemic threshold of a SIS process spreading on uncorrelated annealed networks is:

$$\frac{\beta}{\mu} > \frac{\langle k \rangle}{\langle k^2 \rangle}, \quad (8.1)$$

thus it vanishes as the second moment of the degree distribution $\langle k^2 \rangle \rightarrow \infty$. The derivation of the threshold is performed by means of heterogeneous mean-field (HMF) theory which assumes that nodes with the same degree are statistically equivalent. In this perspective connections between nodes are continuously reshuffled such that the degree distribution $P(k)$ and the probability of having connections between nodes with degree k and k' , $P(k'|k)$, are kept constant [15]. The timescale describing this shuffling is much faster than the timescale describing the spreading process. Consequently, the disease spreads in an effective network where all these connections are available routes of contagion. Interestingly, in the case of networks with exponent $2 < \gamma < 3$ the second moment of the degree distribution diverges as $N \rightarrow \infty$, which implies a vanishing epidemic threshold: any virus with a spreading rate larger than zero will be able to affect a macroscopic fraction of the network. In finite networks where only finite fluctuations are possible, none of the moments diverge thus the threshold is larger than zero. However, the presence of nodes with degree much larger than the average, hubs, pushes the threshold to values much smaller than in the case of corresponding homogeneous networks with the same size (number of nodes) and average connectivity. Indeed, among other effects, hubs decrease the shortest paths between any pair of nodes in the network and once infected, they dramatically accelerate the diffusion by virtue of their large number of connections.

In case of static networks the timescale describing the evolution of the contagion process is much faster than the timescale of the network, thus the contagion phenomena evolves in a frozen, quenched structure. The threshold of an SIS model in this case is tied to the spectral properties of the adjacency matrix A_{ij} coding the static network structure. Indeed, for an arbitrary network the epidemic threshold is inversely proportional to the largest eigenvalue λ_1 [47–49] of the matrix. In case of uncorrelated networks, we have $\lambda_1 \sim \sqrt{k_{max}}$, thus the threshold is associated

to the largest degree in the system. It is interesting to notice that the analytical results for uncorrelated annealed and static scale-free graphs are equivalent if the degree exponent $\gamma < 2.5$, while for $\gamma > 2.5$, the results obtained with the HMF theory deviate from those obtained in static networks. Although the study of such deviation is fascinating, it is beyond the scope of this chapter, and we refer the interested reader to the following recent papers on the subject [50–53].

Now that we understand in some details how contagion processes spread on networks we can shift the attention towards controlling/vaccination strategies. Interestingly, this problem is closely related to the robustness of a network structure against attacks [54], which further maps to a site percolation in networks [3]. In both cases the objective is to identify a critical fraction of nodes which removal would decouple the network structure and thus disrupt the spreading of a contagion process. In case of vaccination this translates to the identification of a critical p_c fraction of nodes to immunize in order to push the epidemics to an inactive phase i.e. below the threshold. Studies discussed above suggest that nodes in heterogeneous networks have very different roles in sustaining spreading processes and have indisputable effects on the epidemic threshold. In order to demonstrate this observation, let us consider the simplest vaccination strategy which involves a fraction p of randomly selected nodes. This strategy is agnostic to the features of the networks and has been shown to simply re-scale the effective spreading rate $\beta \rightarrow \beta(1-p)$ [10, 55]. For uncorrelated annealed networks, the threshold becomes:

$$\frac{\beta}{\mu}(1-p_c) = \frac{\langle k \rangle}{\langle k^2 \rangle}. \quad (8.2)$$

In this case, the large fluctuations typical of heavy-tailed degree distributions push the critical immunization fraction p_c to values close to one as $N \rightarrow \infty$. In other words, in order to protect heterogeneous networks against infectious diseases a random immunization strategy is inefficient as it requires a large fraction of nodes to be vaccinated.

Can we do better, and if yes, how? The answer to this question depends on the amount of information available about the network structure. Let us first consider a scenario in which we have full access to the structure and features of the nodes. In this case, we can implement *targeted immunization* strategies based on global knowledge. These rely on different centrality measures which have been developed to characterize and rank the importance of nodes in a network [1, 2]. Interestingly, many of these are defined via diffusion processes [56], thus the importance of nodes is explicitly associated to their role in sustaining spreading phenomena.

One of the simplest centrality measure is the degree centrality, which indicates hubs in the network. By removing nodes with the highest degree it is possible to reduce degree fluctuations which in turn increases the epidemic threshold. Here the critical fraction p_c to arrest the epidemic spreading is determined by a critical $k_c(p)$ degree, which corresponds (for annealed uncorrelated networks) to the critical point $\langle k \rangle_{p_c}^2 / \langle k^2 \rangle_{p_c} = \beta / \mu$. For graphs with degree exponent $\gamma = 3$ the critical fraction p_c of immunization to arrest epidemics appears as

$$p_c \sim e^{-2\mu/k_{min}\beta}, \quad (8.3)$$

where k_{min} assigns the smallest degree in the network [10, 55]. As clear from the exponential dependence on the k_{min} and β , targeted vaccination strategy based on degree centrality provides a very efficient way to control epidemic spreading. Similar conclusions can be drawn by applying other centrality measures, such as betweenness and k-core centrality, or memberships, for the selection of immunized nodes [9, 57–61].

Let us consider now the case in which we do not have access to the global structure of the network and to the features of all nodes. Immunization strategies developed under this very realistic assumption are typically called local strategies as they are based on local exploration and sampling of the network structure.

One of the most notable local methods is the *acquaintance vaccination* [11]. This relies on the so called “friendship paradox”: *your friends on average have more friends that you do*. In the case of uncorrelated heterogeneous networks it is very easy to prove that this counterintuitive fact holds true [1, 2]. Several studies performed in real-world networks confirm the paradox as a genuine feature tied to the large fluctuations in degree observed across a wide range of graphs [62–64].

Cohen et al. realized how this feature can be used to find highly connected nodes in the system via a local exploration. In the acquaintance strategy we first select randomly an f fraction of probe nodes. However, instead of vaccinating them, we choose randomly one of their neighbors as target of our vaccination. Note that the local search from different probes can lead to the same neighbor i.e. $p \leq f$. The critical fraction of nodes is:

$$p_c = 1 - \sum_k P(k) v_{f_c}^k, \quad (8.4)$$

where $v_f = \langle e^{-f/k} \rangle_k$ is the probability that an acquaintance is not selected in a single attempt, while f_c denotes the critical fraction of random probes which can be determined numerically as shown in [3, 11, 65, 66]. The critical immunization fraction of this method is always $p_c < 1$ and considerably smaller for scale-free networks with any degree exponent as compared to the random vaccination strategy [11].

Note that other variations of the acquaintance vaccination strategy were proposed by optimizing the neighbor selection [67]. At the same time immunization was also studied on meta-population networks [68]. In other studies, it has been argued that efficient immunization strategies can be developed by considering the higher-order organization of connectivity patterns [57, 69–74]. Further studies proposed vaccination strategies using evolutionary games [75], or considering complex contagion processes [76]. For a recent review on the subject we refer the readers to Ref. [8].

8.3 Controlling Contagion Processes in Time-Varying Networks

We now move away from the limits of timescale separation and study spreading processes and immunization strategies on time-varying networks in which the timescales driving the evolution of the system and of the spreading process are comparable. As done before for annealed and static networks, we will first study the epidemic threshold. We will then use this knowledge to present and better understand immunization strategies aimed at controlling contagion phenomena.

A closed formula for the epidemic threshold of a SIS epidemic process unfolding on *any* time-varying has been derived [77]. In this approach the time-varying network is considered as a sequence of adjacency matrices A_1, A_2, \dots, A_T which describe the evolution of the network in time. Prakash et al. showed that the disease will not be able to spread in the system if

$$\lambda_{\prod_i \mathbf{S}_i} < 1, \quad (8.5)$$

where $\mathbf{S}_i = (1 - \mu)\mathbf{I} + \alpha\mathbf{A}_i$, and α is the transmission rate per contact. In other words, the disease will die out if the largest eigenvalue of the system-matrix $\mathbf{S} = \prod_i \mathbf{S}_i$ is smaller than one. This result have been recently confirmed with a different approach [78]. It is interesting to note that in both static and time-varying networks the largest eigenvalue, of the adjacency matrix in one case and of the system matrix in the other, determines the unfolding of the disease. Despite the generality and the practical importance of this result, the computation of the threshold needs to be done numerically. Also, the condition obtained hinders the effects of temporal connectivity patterns on spreading processes. For this reason, in the next subsections we will consider SIS processes unfolding on a particular type of time-varying networks. In doing so, we will be able to derive a more explicit condition for the spreading and thus better understand the efficiency of different immunization strategies.

8.3.1 Epidemic Threshold on Activity-Driven Networks

In activity-driven networks, each node i is characterized by an activity rate a_i . This quantity encodes the probability per unit time to establish contacts with other nodes. The activity rates are assigned according to a given probability distribution $F(a)$. Observations in a wide range of different real-world networks show that activities follow heavy-tailed distributions [29, 32, 33, 79, 80]. We approximate such distributions as power laws, i.e., $F(a) = Ba^{-\gamma}$ with activities restricted in the region $a \in [\epsilon, 1]$ to avoid divergences for $a \rightarrow 0$. In these settings, the generative network evolution process is defined according to the following rules (see Fig. 8.1a, b):

- At each discrete time step t , the network G_t starts with N disconnected vertices;

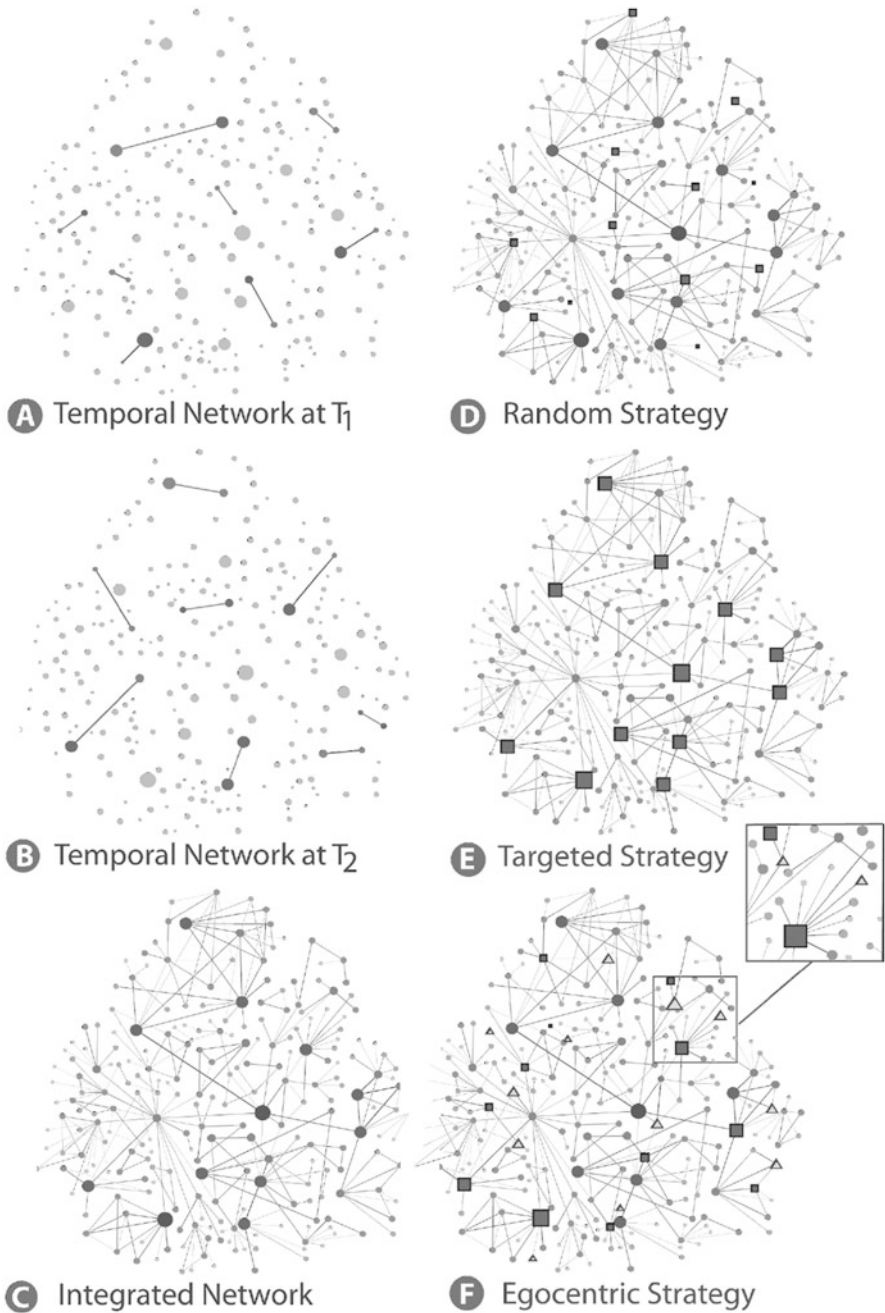


Fig. 8.1 Schematic representation of activity driven model and control strategies. (a), (b) Temporal network at two different time steps T_1 and T_2 . (c) Integrated network over a certain period of time. The size of each node describes its activity, while the width of each link describes the weight. (d)–(f) Random, targeted, and egocentric control strategy respectively. Immunized nodes are plotted as *squares*; probes as *triangles*

- With probability $a_i \Delta t$, each vertex i becomes active and generates m links that are connected to m other randomly selected vertices;
- At the next time step $t + \Delta t$, all the edges in the network G_t are deleted.

All interactions have a constant duration Δt . In the following, without loss of generality, we will set $\Delta t = 1$. Activity-driven networks in their simplest form are random and memoryless. We refer the reader interested in more realistic extensions of the model to the following references [29, 79–82]. The full dynamics of the network and its ensuing structure are driven by the activity distribution $F(a)$. Moreover, it is possible to prove that integrating activity-driven networks in finite time windows such that $T \ll N$ and $k \ll N$ (where T is the size of the time window and k the degree) yield graphs characterized by degree distributions following the functional form $F(a)$ [32, 83].

Let us now consider a SIS model unfolding on activity-driven networks. Using the HMF theory we group nodes according to their activity assuming that nodes in the same class are statistically equivalent. At the mean-field level, the spreading process can be described by the number of infected individuals in the class of activity a at time t , i.e., I_a^t [32]. Following Ref. [32], the number of infected individuals of class a at time $t + 1$ given by:

$$I_a^{t+1} = I_a^t - \mu I_a^t + \alpha m (N_a - I_a^t) a \int da' \frac{I_{a'}^t}{N} + \alpha m (N_a - I_a^t) \int da' \frac{I_{a'}^t a'}{N}, \quad (8.6)$$

where N_a is the total number of individuals with activity rate a (which is constant over time). Each term in the Eq. (8.6) has a clear physical interpretation. In fact, the number of infected nodes in the class a at time $t + 1$ is given by: the number of infected nodes in this class at time t (first term), minus the number of nodes that recover and going back to the class S_a (second term), plus the number of infected individuals generated when nodes in the class $S_a^t = N_a - I_a^t$ are active and connect with infected nodes in the other activity classes (third term), plus the number of infected nodes generated when nodes in the class S_a^t are linked by active infected nodes in other activity classes.

Summing on all of the classes and ignoring the second order terms we can write:

$$\int da I_a^{t+1} = I^{t+1} = I^t - \mu I^t + \alpha m \langle a \rangle I^t + \alpha m \theta^t, \quad (8.7)$$

where $\theta^t = \int da' I_{a'}^t a'$. Multiplying both sides of Eq. (8.6) by a and integrating we obtain:

$$\theta^{t+1} = \theta^t - \mu \theta^t + \alpha m \langle a^2 \rangle I^t + \alpha m \langle a \rangle \theta^t. \quad (8.8)$$

In the continuous time limit, we can write Eqs. (8.6) and (8.8) in a differential form:

$$\partial_t I = -\mu I + \alpha m \langle a \rangle I + \alpha m \theta, \quad (8.9)$$

$$\partial_t \theta = -\mu \theta + \alpha m \langle a^2 \rangle I + \alpha m \langle a \rangle \theta. \quad (8.10)$$

The Jacobian matrix of this set of linear differential equations takes the form

$$J = \begin{pmatrix} -\mu + \alpha m \langle a \rangle & \alpha m \\ \alpha m \langle a^2 \rangle & -\mu + \alpha m \langle a \rangle \end{pmatrix},$$

and has eigenvalues

$$\Lambda_{(1,2)} = \langle a \rangle \alpha m - \mu \pm \alpha m \sqrt{\langle a^2 \rangle}. \quad (8.11)$$

The threshold is obtained by requiring the largest eigenvalue to be larger than 0, which leads to:

$$\frac{\alpha}{\mu} \geq \frac{1}{m} \frac{1}{\langle a \rangle + \sqrt{\langle a^2 \rangle}}. \quad (8.12)$$

Considering the per capita spreading rate $\beta = \alpha \langle k \rangle$ we can write the threshold for the *SIS* process, ξ^{SIS} , as:

$$\frac{\beta}{\mu} \geq \xi^{SIS} \equiv \frac{2 \langle a \rangle}{\langle a \rangle + \sqrt{\langle a^2 \rangle}}. \quad (8.13)$$

In words, the epidemic threshold is a function of the first and second moment of the activity distribution. Due to the co-evolution of the network structure and the spreading processes the threshold is not dependent on time-aggregated metrics such as the degree. It is defined by the interplay between the timescale of the contagion process and the convolution of the network timescales encoded in the moments of the activity distribution.

8.3.2 Controlling Contagion Processes in Activity-Driven Networks

We can now study different immunization strategies. Following Ref. [84] and what has been presented above for annealed and static networks we will consider three main strategies: random, global and local. In all the cases, we introduce a fraction p of nodes as immunized. To account for this new class of nodes, we introduce a new compartment, R , in the classic *SIS* scheme. Thus, the Eq. (8.6) becomes:

$$\begin{aligned} I_a^{t+1} &= I_a^t - \mu I_a^t + \alpha m (N_a - I_a^t - R_a^t) a \int da' \frac{I_{a'}^t}{N} + \\ &+ \alpha m (N_a - I_a^t - R_a^t) \int da' \frac{I_{a'}^t a'}{N}, \end{aligned} \quad (8.14)$$

First, let us consider the random strategy (RS) in which a fraction p of nodes is immunized with an uniform probability (see Fig. 8.1d) [84]. In this case, the system of equations describing the dynamic process in activity-driven networks can be obtained by setting $R_a = pN_a$. The epidemic threshold condition changes as

$$\frac{\beta}{\mu} \geq \xi^{RS} \equiv \frac{1}{1-p} \frac{2\langle a \rangle}{\langle a \rangle + \sqrt{\langle a^2 \rangle}} = \frac{\xi^{SIS}}{1-p}. \quad (8.15)$$

Consistently with what we found for annealed and static networks, when a fraction p of nodes is randomly immunized, the epidemic threshold can be written as the threshold with no intervention, ξ^{SIS} , rescaled by the number of nodes still available to the spreading process. Indeed, immunizing random nodes is equivalent to rescaling the per capita spreading rate by the fraction of available nodes $\beta \rightarrow \beta(1-p)$. Another important quantity is the critical value of immunized nodes, p_c , necessary to halt the contagion process. This quantity is a function of network's structure and the specific features of the contagion process. The explicit value of p_c can be obtained by inverting Eq. (8.15). In Fig. 8.2a, we show p_c as a function of β/μ . The values on the heat map are the average asymptotic density of infected nodes, I_∞^p . The phase space of the diffusion process is divided into two different regions separated by the black solid line that represents p_c as derived by Eq. (8.15). In the region below the curve, the spreading process will take over, $p < p_c$. However, in the region above the curve, the fraction of removed/immunized nodes is large enough to completely stop the spreading process, $p \geq p_c$. To assess the efficiency of the immunization strategy in Fig. 8.2d (triangles) we plot, as a function of the density of removed nodes p , the ratio I_∞^p/I_∞^0 where I_∞^0 is the asymptotic density of infected nodes when no-intervention is implemented. As shown clearly in the figure, the random strategy allows a reduction in the fraction of infected nodes just for large values of p .

In activity-driven networks a natural way to implement a global immunization strategy is to target high-activity nodes. Indeed, from the study of the epidemic threshold without intervention, we saw the importance of the moments of the activity distribution. By targeting high-activity nodes we can reduce the average and the fluctuations of activity and thus move the threshold to higher values. Following this strategy we rank nodes in decreasing order of activity, immunizing the top ranking pN nodes (see Fig. 8.1e). This method is equivalent to fix a value a_c so that any node with activity $a \geq a_c$ is immune to the contagion process.¹ Also, for this scheme, it is possible to derive the analytic expression for the epidemic threshold [84]:

$$\frac{\beta}{\mu} \geq \xi^{TS} \equiv \frac{2\langle a \rangle}{\langle a \rangle^c + \sqrt{(1-p)\langle a^2 \rangle^c}}, \quad (8.16)$$

¹The value of p and a_c are linked by the relation $p = \int_{a_c}^1 F(a)da$.

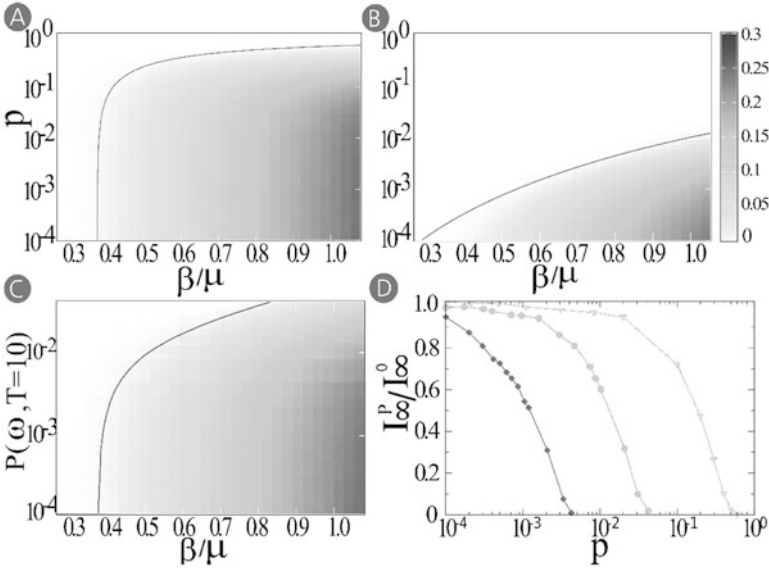


Fig. 8.2 Panels (a), (b), and (c) show the phase space of an SIS process under random, targeted, and egocentric control strategy, respectively. Considering $N = 10^4$, $m = 3$, $\epsilon = 10^{-3}$, activity distributed as $F(a) \sim a^{-2.2}$, we plot I_∞ as a function of β/μ and p . Black curves represent the critical value p_c . Panel (d) shows the comparison of the stationary state of a SIS model with and without control strategy, I_∞^p/I_∞^0 , as a function of p when $\beta/\mu = 0.81$. Using triangles, we consider the random strategy, with diamonds the targeted strategy, and with circles the egocentric strategy. Each plot is made by averaging 10^2 independent simulations started with 1% of random seeds

where ξ^{TS} indicates the threshold in the case of the targeted control strategy. In the above expression, we define $\langle a^n \rangle^c = \int_\epsilon^{a_c} a^n F(a) da$ as the moments of the activity distribution discounting the immunized nodes. Consistently to what has been found for annealed and static networks, Eq. (8.16) is not a simple rescaling of the expression of the original threshold and implies a drastic change in the behavior of the contagion process. In order to define the critical value of p necessary to completely stop the spreading, we have to invert Eq. (8.16). The moments of the distribution of the remaining nodes are a function of p through a_c thus it is not possible to derive explicitly p_c . However, it can be easily evaluated numerically by solving the equation $\xi^{TS} - \beta/\mu = 0$ for different values of β/μ . In Fig. 8.2b, we show p_c (black line) as a function of β/μ . The efficiency of the targeted strategy is clear, which is also confirmed in Fig. 8.2d (diamonds) where we plot the ratio I_∞^p/I_∞^0 . Immunizing a very small fraction of the most active nodes is enough to stop the contagion process. Indeed, by immunizing just the top 1% of nodes is enough to halt the disease.

As discussed above, the network-wide knowledge required to implement targeted control strategies is generally not available [11]. In the case of evolving networks, this issue is even more pronounced as node’s characterization depends on how

long it is possible to observe the network dynamics. It is possible to generalize the acquaintance immunization strategy to activity-driven networks. A fraction f of randomly selected nodes act as “probes”. During an observation time T , we monitor their egocentric network generated by their interactions in the network. After the observation window, we select randomly a node in the egocentric network of each probe and immunizing it (as shown in Fig. 8.1f). For the sake of comparison with the previous control strategies, we define the fraction of actual immunized nodes as p (in general $f \neq p^2$), and the epidemic starts after nodes have been immunized. In this scheme, the probability of immunization for one node with activity a after a time step is:

$$P_a = af \int da' \frac{mN_{a'}}{N} + f \int da' a' \frac{mN_{a'}}{N} \frac{1}{m}. \quad (8.17)$$

The first term on the r.h.s. considers the probability that a node of class a is active and reaches one of the probes; the second term, instead, takes into account the probability that one node of class a gets a connection from one active probe. Solving the integrals in Eq. (8.17), we can write $P_a = f(am + \langle a \rangle)$. Thus, the probability of immunization of one node in the activity class a after t time steps is $P_a^t = 1 - (1 - P_a)^t$, and therefore, summing over all the activity classes, we can estimate the total number of immunized individuals as $R^T = \sum_a N_a P_a^T = \sum_a N_a [1 - (1 - P_a)^T]$. The equation for P_a does not consider the depletion of nodes in each class due to the immunization process. The formulation is then a good approximation for small f and T , when the probability that a probe is selected more than once is very small. In these settings, the epidemic threshold for the egocentric sampling strategy (ESS) can be written [84] as:

$$\frac{\beta}{\mu} \geq \xi^{ESS} \equiv \frac{2\langle a \rangle}{\Psi_1^T + \sqrt{\Psi_0^T \Psi_2^T}}, \quad (8.18)$$

where we define $\Psi_n^T = \int da a^n (1 - P_a)^T F(a)$. This last integral is a function of the observation time window T , the probability of immunization of each class and the activity distribution. We evaluate each Ψ term through numerical integration. As done for the other two cases, we define the critical value of p by solving numerically the equation $\xi^{ESS} - \beta/\mu = 0$ for different values of β/μ . In Fig. 8.2c, we show p_c (black line) as a function of β/μ , and in Fig. 8.2d we plot the ratio I_∞^p/I_∞^0 (dots). From these figures it is clear how this strategy is much more efficient than the random one, although not as performant as the targeted scheme. The efficiency of this strategy is due to the ability to reach active nodes by a local exploration done observing the systems for few time steps.

²In order to guarantee that a fraction f of nodes is immunized the systems need to be observed for more than one time step. We define T^* as the average time needed for all the probes to have at least one interaction with other nodes. For any observation time $T < T^*$ the fraction of immunized nodes will be in general $p < f$.

8.3.3 *Controlling Contagion Processes in Real Temporal Networks*

Real-world time-varying networks are characterized by a range of complex features such as heterogeneous activity patterns, correlations among nodes, persistence of links, and burstiness just to cite a few. For detailed reviews on the topic we refer the reader to Refs. [41–43]. Over the last years an increasing body of literature has been focused on the study of such properties and their relation to effective controlling strategies. Here, we will summarize some of the main results.

In their work, Prakash et al. [77] used their analytical derivation of the epidemic threshold in a general time-varying network mentioned above, to study the efficiency of different controlling strategies in a real network obtained from the MIT Reality Mining project [85]. This dataset describes the interactions of 104 students recorded via Bluetooth. The authors consider several global and local strategies immunizing: (1) the top ranked nodes for degree in each temporal snapshot of the network, (2) the top ranked nodes for degree in the average adjacency matrix defined as $A_{average} = T^{-1} \sum_{i=1, T} \mathbf{A}_i$, (3) nodes selected via the acquaintance method applied to the average adjacency matrix, (4) the nodes that sequentially (greedy method) induce the largest drop to the largest eigenvalue of the system's adjacency matrix, (5) nodes in a sequence that provide the largest (optimal method) reduction to the largest eigenvalue of the system matrix. Interestingly, they found strategies 1, 2 and 4 to have similar performance with respect to the optimal strategy. Instead, the acquaintance strategy was found, not surprisingly, to perform significantly worst. It is important to notice that they used as objective metric to benchmark each strategy the change in the largest eigenvalue of the system matrix.

Lee et al. [86] compared the acquaintance strategy against two proposed variations of it, which include the temporal dynamics on the networks. In particular, they considered strategies in which either the most recent or the most frequent contacts of randomly selected nodes are immunized. They studied the efficiency of each method in four different datasets: an online forum describing sexual interactions with prostitutes [87], proximity interactions in hospital wards [88], email exchanges [89], and online dating [90]. They considered scenarios in which an immunization campaign can be applied in an initial time window of size ΔT . Interestingly, they found that the two extensions of the acquaintance method have a larger impact on the disease spreading as the original strategy. Furthermore, in three of the four datasets the strategy based on the most recent contacts outperforms the method based on the most frequent contacts. As an objective measure of performance they used was “the average upper bound of outbreak size” obtained by running epidemic spreading with $\alpha = 1$ i.e. where the probability of infection per contact is one.

Starnini et al. [91] studied several immunization strategies in different face-to-face networks obtained via RFID tags in the SocioPatterns collaboration [92]. As done by Lee et al. [86] they introduced an immunization campaign in the first ΔT time steps. They considered strategies in which the nodes to be

immunized are selected considering: (1) the degree, (2) the betweenness, (3) the acquaintance method, (4) the frequency of activation of each link,³ (5) the latest activated contacts in the time window,³ and (6) randomly selected nodes. It is important to notice how this study contrasts global and local strategies considering both structural and temporal features. In the comparisons, the authors considered as objective metrics the speed of the spreading and the final number of infected nodes. Overall they found strategies that target nodes according to their degree and betweenness centrality to be more efficient. Furthermore, the authors observed a saturation effect for increasing sizes of the time window ΔT . In principle, longer time windows should allow to gather more information and thus should be linked to better immunization performances. However, the observations showed that this is true only up to a certain point. The authors linked such unexpected behavior to the emergence of central nodes at early stages in the system's dynamics. It is important to notice that even the considered datasets provide a very high temporal resolution, 20 s, they were recorded over typically a few days, thus they do not provide observations of long temporal trends of contact networks.

Tang et al. [93] studied the spreading of malwares via bluetooth and efficient way to contain them. They considered three different datasets: the MIT reality mining project mentioned before, the interaction between researchers at the University of Cambridge [94], and those between participants in a conference [95]. Interestingly, they found that strategies based on temporal betweenness centrality do not perform as expected. Although this metric provides the quantitative measure of the number of diffusion routes between nodes, the immunization of top ranked nodes does not necessarily stop the spreading as many alternative routes might exist. They proposed an immunization strategy in which the patch necessary to protect phones in the network is in competition with the malware. In their approach, the selection of nodes to immunize is done via the temporal closeness centrality measure which ranks node considering the speed at which each node can disseminate a message in the network. They showed how such strategy is efficient in terms of the consumption of network resources and time necessary to protect the system.

Liu et al. [84] studied the efficiency of the three different strategies introduced in Sect. 8.3.2 in a mobile phone call data network. Interestingly, the numerical simulations confirm qualitatively the analytical results obtained in activity-driven networks. In particular, the strategy that targets high-active nodes is the most efficient, followed by the generalization of the acquaintance methods: the egocentric sampling strategy. The objective measure adopted to judge the efficiency of each strategy is the ratio between the stationary state of a SIS model with and without control strategy, i.e. $I_{\infty}^p/I_{\infty}^0$.

³As proposed by Lee et al. [86].

8.4 Conclusions and Outlook

We presented a summary of strategies to control contagion processes in annealed, static, and time-varying networks. In doing so, we considered a range of different analytical and numerical results. We observed how heterogeneities that characterize many features of real-world networks make targeted global strategies extremely efficient. However, these strategies assume complete knowledge of the networks' topology and their dynamical evolution. Local strategies based on local exploration and sampling of the networks are in general less efficient than global methods but are more realistic and provide a higher performance with respect to random strategies.

We considered scenarios where the dynamics *of* networks (temporal evolution of networks' structure) affect the dynamics *on* networks (contagion processes). In general also the opposite is true. For example, the spreading of an infectious disease might induce changes in the evolution of a contact network [96, 97] or the spreading of information on an online social network might affect its structure and evolution [98]. In this case the dynamics *on* the networks affect the dynamics *of* the network. In the literature the study of this reverse problem (with respect to what we considered here) is found under the umbrella of *adaptive networks*. We invite the interested reader to several other chapters of this book for details.

Generally speaking, the dynamics of and on networks are intertwined. Networks are subject to natural temporal dynamics which are perturbed by contagion processes. In turn, contagion processes are subject to the natural evolution of networks and are affected by the changes they induce. The understanding of these intricacies is still very limited and requires the development of methods to model and mathematically describe complex coupled dynamics, possibly acting at different timescales. Furthermore, it requires the availability of high resolution data that capture all these processes and their interplay. Despite the unprecedented access to large-scale datasets of human interactions in recent times, the observation of the feedback loop between the dynamics of and on networks is typically indirect and thus the casual link between the two, necessary to inform or test models, is often missing.

We believe that addressing all these challenges is of extreme importance to better understand the spreading of contagion processes on real networks and to develop efficient methods to control them. Doing so will require an interdisciplinary effort from a set of disciplines ranging from network and data science to sociology and applied mathematics.

Acknowledgements The results presented in Sect. 8.3.2 are adapted from Ref. [84] and obtained in collaboration with S. Liu and A. Vespignani.

References

1. Barrat, A., Barthélemy, M., Vespignani, A.: *Dynamical Processes on Complex Networks*. Cambridge University Press, Cambridge (2008)
2. Newman, M.E.J.: *Networks. An Introduction*. Oxford University Press, Oxford (2010)
3. Cohen, R., Havlin, S.: *Complex Networks: Structure, Robustness and Function*. Cambridge University Press, Cambridge (2010)
4. Butts, C.T.: Revisiting the foundations of network analysis. *Science* **325**, 414–416 (2009)
5. Gonçalves, B., Perra, N.: *Social Phenomena: From Data Analysis to Models*. Springer, Cham/New York (2015)
6. Vespignani, A.: Predicting the behavior of techno-social systems. *Science* **325**, 425–428 (2009)
7. Fortunato, S.: Community detection in graphs. *Phys. Rep.* **486**, 75–174 (2010)
8. Wang, Z., Bauch, C.T., Bhattacharyya, S., d’Onofrio, A., Manfredi, P., Perc, M., Perra, N., Salathé, M., Zhao, D.: Statistical physics of vaccination. *Phys. Rep.* **664**, 1–113 (2016)
9. Kitsak, M., Gallos, L.K., Havlin, S., Makse, H.A.: Identification of influential spreaders in complex networks. *Nat. Phys.* **6**, 888 (2010)
10. Pastor-Satorras, R., Vespignani, A.: Immunization of complex networks. *Phys. Rev. E* **63**, 036104 (2002)
11. Cohen, R., Havlin, S., and ben-Avraham, D.: Efficient immunization strategies for computer networks and populations. *Phys. Rev. Lett.* **91**, 247901 (2003)
12. Morris, M.: Telling tails explain the discrepancy in sexual partner reports. *Nature* **365**, 437 (1993)
13. Morris, M., Goodreau, S., Moody, J.: Sexual networks, concurrency, and STD/HIV, Ch. 7. In: Holmes, K.K. et al. (eds.) *Sexually Transmitted Diseases*. McGraw-Hill, New York, USA (2007)
14. Clauset, A., Eagle, N.: Persistence and periodicity in a dynamic proximity network. In: *DIMACS Workshop on Computational Methods for Dynamic Interaction Networks*, pp. 1–5 (2007)
15. Vespignani, A.: Modeling dynamical processes in complex socio-technical systems. *Nat. Phys.* **8**, 32–30 (2012)
16. Rocha, L.E.C., Liljeros, F., Holme, P.: Simulated epidemics in an empirical spatiotemporal network of 50,185 sexual contacts. *PLoS Comput. Biol.* **7**(3), e1001109, 03 (2011)
17. Isella, L., Stehlé, J., Barrat, A., Cattuto, C., Pinton, J.-F., Van den Broeck, W.: What’s in a crowd? analysis of face-to-face behavioral networks. *J. Theor. Biol.* **271**, 166 (2011)
18. Stehlé, J., Voirin, N., Barrat, A., Cattuto, C., Colizza, V., Isella, L., Régis, C., Pinton, J.-F., Khanafer, N., Van den Broeck, W., Vanhems, P.: Simulation of an SEIR infectious disease model on the dynamic contact network of conference attendees. *BMC Med.* **9**(87) (2011)
19. Karsai, M., Kivela, M., Pan, R.K., Kaski, K., Kertész, J., Barabási, A.-L., Saramäki, J.: Small but slow world: how network topology and burstiness slow down spreading. *Phys. Rev. E* **83**, 025102 (2011)
20. Miritello, G., Moro, E., Lara, R.: Dynamical strength of social ties in information spreading. *Phys. Rev. E* **83**, 045102 (2011)
21. Kivela, M., Pan, R., Kaski, K., Kertész, J., Saramäki, J., Karsai, M.: Multiscale analysis of spreading in a large communication network. *J. Stat. Mech.* **2012**(3), P03005 (2012)
22. Fujiwara, N., Kurths, J., Díaz-Guilera, A.: Synchronization in networks of mobile oscillators. *Phys. Rev. E* **83**(2), 025101 (2011)
23. Parshani, R., Dickison, M., Cohen, R., Stanley, H. E., Havlin, S.: Dynamic networks and directed percolation. *EPL (Europhys. Lett.)* **90**(3), 38004 (2010)
24. Bajardi, P., Barrat, A., Natale, F., Savini, L., Colizza, V.: Dynamical patterns of cattle trade movements. *PLoS One* **6**(5), e19869, 05 (2011)
25. Panisson, A., Barrat, A., Cattuto, C., Van den Broeck, W., Ruffo, G., Schifanella, R.: On the dynamics of human proximity for data diffusion in ad-hoc networks. *Ad Hoc Netw.* **10**, 1532–1543 (2011)

26. Baronchelli, A., Díaz-Guilera, A.: Consensus in networks of mobile communicating agents. *Phys. Rev. E* **85**, 016113 (2012)
27. Starnini, M., Baronchelli, A., Barrat, A., Pastor-Satorras, R.: Random walks on temporal networks. *Phys. Rev. E* **85**, 056115 (2012)
28. Pfitzner, R., Scholtes, I., Garas, A., Tessone, C.J., Schweitzer, F.: Betweenness preference: quantifying correlations in the topological dynamics of temporal networks. *Phys. Rev. Lett.* **110**, 19 (2013)
29. Karsai, M., Perra, N., Vespignani, A.: Time varying networks and the weakness of strong ties. *Sci. Rep.* **4**, 4001 (2014)
30. Hoffmann, T., Porter, M.A., Lambiotte, R.: Generalized master equations for non-poisson dynamics on networks. *Phys. Rev. E* **86**, 046102 (2012)
31. Toroczkai, Z., Guclu, H.: Proximity networks and epidemics. *Phys. A* **378**(1), 68–75 (2007)
32. Perra, N., Gonçalves, B., Pastor-Satorras, R., Vespignani, A.: Time scales and dynamical processes in activity driven networks. *Sci. Rep.* **2**, 469 (2012)
33. Ribeiro, B., Perra, N., Baronchelli, A.: Quantifying the effect of temporal resolution on time-varying networks. *Sci. Rep.* **3**, 3006 (2013)
34. Perra, N., Baronchelli, A., Mocanu, D., Gonçalves, B., Pastor-Satorras, R., Vespignani, A.: Random walks and search in time varying networks. *Phys. Rev. Lett.* **109**, 238701 (2012)
35. Liu, S., Baronchelli, A., Perra, N.: Contagion dynamics in time-varying metapopulations networks. *Phys. Rev. E* **87**(032805) (2013)
36. Starnini, M., Pastor-Satorras, R.: Topological properties of a time-integrated activity-driven network. *Phys. Rev. E* **87**, 062807 (2013)
37. Takaguchi, T., Sato, N., Yano, K., Masuda, N.: Importance of individual events in temporal networks. *New J. Phys.* **14**, 093003 (2012)
38. Takaguchi, T., Masuda, N., Holme, P.: Bursty communication patterns facilitate spreading in a threshold-based epidemic dynamics. *PLoS One* **8**(7), e68629 (2013)
39. Holme, P., Liljeros, F.: Birth and death of links control disease spreading in empirical contact networks. *Sci. Rep.* **4**, 4999 (2014)
40. Holme, P., Masuda, N.: The basic reproduction number as a predictor for epidemic outbreaks in temporal networks. *PLoS One* **10**(3), e0120567 (2015)
41. Holme, P., Saramäki, J.: Temporal networks. *Phys. Rep.* **519**, 97 (2012)
42. Holme, P.: Modern temporal network theory: a colloquium. *Eur. Phys. J. B* **88**(9), 1–30 (2015)
43. Masuda, N., Lambiotte, R.: *A Guide to Temporal Networks*. World Scientific, New Jersey (2016)
44. Kermack, W.O., McKendrick, A.G.: A contribution to the mathematical theory of epidemics. *Proc. R. Soc. A* **115**, 700 (1927)
45. Keeling, M.J., Rohani, P.: *Modeling Infectious Disease in Humans and Animals*. Princeton University Press, Princeton (2008)
46. Pastor-Satorras, R., Vespignani, A.: Epidemic spreading in scale-free networks. *Phys. Rev. Lett.* **86**, 3200 (2001)
47. Wang, Y., Chakrabarti, D., Wang, G., Faloutsos, C.: Epidemic spreading in real networks: an eigenvalue viewpoint. In: *Proceedings of 22nd International Symposium on Reliable Distributed Systems*, pp. 25–34 (2003)
48. Castellano, C., Pastor-Satorras, R.: Thresholds for epidemic spreading in networks. *Phys. Rev. Lett.* **105**, 218701 (2010)
49. Durrett, R.: Some features of the spread of epidemics and information on a random graph. *Proc. Natl. Acad. Sci.* **107**, 4491–4498 (2010)
50. Goltsev, A.V., Dorogovtsev, S.N., Oliveira, J.G., Mendes, J.F.F.: Localization and spreading of diseases in complex networks. *Phys. Rev. Lett.* **109**(12), 128702 (2012)
51. Boguñá, M., Castellano, C., Pastor-Satorras, R.: Nature of the epidemic threshold for the susceptible-infected-susceptible dynamics in networks. *Phys. Rev. Lett.* **111**(6), 068701 (2013)
52. Castellano, C., Pastor-Satorras, R.: Thresholds for epidemic spreading in networks. *Phys. Rev. Lett.* **105**(21), 218701 (2010)

53. Lee, H.K., Shim, P.S., Noh, J.D.: Epidemic threshold of the susceptible-infected-susceptible model on complex networks. *Phys. Rev. E* **87**(6), 062812 (2013)
54. Albert, R., Jeong, H., Barabási, A.L.: Error and attack tolerance of complex networks. *Nature* **406**, 378 (2000)
55. Pastor-Satorras, R., Vespignani, A.: Epidemics and Immunization in Scale-Free Networks. In: Bornholdt, S., Schuster, H.G. (eds.) *Handbook of Graphs and Networks: From the Genome to the Internet*, pp. 111–130. Wiley-VCH Verlag GmbH Co/KGaA, Weinheim (2005)
56. Perra, N., Fortunato, S.: Spectral centrality measures in complex networks. *Phys. Rev. E* **78**(3), 036107 (2008)
57. Hébert-Dufresne, L., Allard, A., Young, J.-G., Dubé, L.J.: Global efficiency of local immunization on complex networks. *Sci. Rep.* **3**, 2171 (2013)
58. Thechanamoorthy, G., Piraveenan, M., Uddin, S., Senanayake, U.: Influence of vaccination strategies and topology on the herd immunity of complex networks. *Soc. Netw. Anal. Min.* **4**(1), 213 (2014)
59. Chen, Y., Paul, G., Havlin, S., Liljeros, F., Eugene Stanley, H.: Finding a better immunization strategy. *Phys. Rev. Lett.* **101**, 058701 (2008)
60. Holme, P., Kim, B.J., Yoon, C.N., Han, S.K.: Attack vulnerability of complex networks. *Phys. Rev. E* **65**(5), 056109+ (2002)
61. Schneider, C.M., Mihaljev, T., Herrmann, H.J.: Inverse targeting – an effective immunization strategy. *EPL (Europhys. Lett.)* **98**(4), 46002+ (2012)
62. Feld, S.L.: Why your friends have more friends than you do. *Am. J. Sociol.* **96**(6), 1464–1477 (1991)
63. Hodas, N.O., Kooti, F., Lerman, K.: Friendship paradox redux: your friends are more interesting than you. In: *Proceedings of 7th International Conference on Weblogs and Social Media*, Apr (2013)
64. Lattanzi, S., Singer, Y.: The power of random neighbors in social networks. In: *Proceedings of the Eighth ACM International Conference on Web Search and Data Mining, WSDM '15*. ACM, New York, pp. 77–86 (2015)
65. Madar, N., Kalisky, T., Cohen, R., ben Avraham, D., Havlin, S.: Immunization and epidemic dynamics in complex networks. *Eur. Phys. J. B* **38**(2), 269–276 (2004)
66. Dezső, Z., Barabási, A.: Halting viruses in scale-free networks. *Phys. Rev. E* **65**, 055103 (2002)
67. Gallos, L.K., Liljeros, F., Argyrakis, P., Bunde, A., Havlin, S.: Improving immunization strategies. *Phys. Rev. E* **75**, 045104(R) (2007)
68. Tanaka, G., Urabe, C., Aihara, K.: Random and targeted interventions for epidemic control in metapopulation models. *Sci. Rep.* **4**, 5522 EP–07 (2014)
69. Gong, K., Tang, M., Hui, P.M., Zhang, H.F., Younghae, D., Lai, Y.-C.: An efficient immunization strategy for community networks. *PLoS One* **8**(12), 1–11 (2013)
70. Salathé, M., Jones, J.H.: Dynamics and control of diseases in networks with community structure. *PLoS Comput. Biol.* **6**(4), e1000736 (2010)
71. Eames, K.T.D.: Modelling disease spread through random and regular contacts in clustered populations. *Theor. Popul. Biol.* **73**(1), 104–111 (2008)
72. Smieszek, T., Fiebig, L., Scholz, R.W.: Models of epidemics: when contact repetition and clustering should be included. *Theor. Biol. Med. Model.* **6**(1), 1 (2009)
73. Miller, J.C.: Spread of infectious disease through clustered populations. *J. R. Soc. Interface* **6**, 1121–1134 (2009)
74. Britton, T., Deijfen, M., Lagerås, A.N., Lindholm, M., et al.: Epidemics on random graphs with tunable clustering. *J. Appl. Probab.* **45**(3), 743–756 (2008)
75. Cardillo, A., Reyes-Suárez, C., Naranjo, F., Gómez-Gardeñes, J.: Evolutionary vaccination dilemma in complex networks. *Phys. Rev. E* **88**, 032803 (2013)
76. Campbell E., Salathé, M.: Complex social contagion makes networks more vulnerable to disease outbreaks. *Sci. Rep.* **3**, 1905 EP–05 (2013)
77. Prakash, B.A., Tong, H., Valler, N., Faloutsos, M., Faloutsos, C.: Virus propagation on time-varying networks: theory and immunization algorithms. In: *Joint European Conference on Machine Learning and Knowledge Discovery in Databases*. Springer, pp. 99–114 (2010)

78. Valdano, E., Ferreri, L., Poletto, C., Colizza, V.: Analytical computation of the epidemic threshold on temporal networks. *Phys. Rev. X* **5**(2), 021005 (2015)
79. Tomasello, M.V., Perra, N., Tessone, C.J., Karsai, M., Schweitzer, F.: The role of endogenous and exogenous mechanisms in the formation of R&D networks. *Sci. Rep.* **4**, 5679 (2014)
80. Ubaldi, E., Perra, N., Karsai, M., Vezzani, A., Burioni, R., Vespignani, A.: Asymptotic theory of time-varying social networks with heterogeneous activity and tie allocation. *Sci. Rep.* **6**, 35724 (2016)
81. Ubaldi, E., Vezzani, A., Karsai, M., Perra, N., Burioni, R.: Burstiness and tie activation strategies in time-varying social networks. *Sci. Rep.* **7**, 46225 (2017)
82. Alessandretti, L., Sun, K., Baronchelli, A., Perra, N.: Random walks on activity-driven networks with attractiveness. *Phys. Rev. E* **95**, 052318 (2017)
83. Starnini, M., Pastor-Satorras, R.: Topological properties of a time-integrated activity-driven network. *Phys. Rev. E* **87**(6), 062807 (2013)
84. Liu, S., Perra, N., Karsai, M., Vespignani, A.: Controlling contagion processes in activity driven networks. *Phys. Rev. Lett.* **112**(11), 118702 (2014)
85. Pentland, A., Eagle, N., Lazer, D.: Inferring social network structure using mobile phone data. *Proc. Natl. Acad. Sci. (PNAS)* **106**(36), 15274–15278 (2009)
86. Lee, S., Rocha, L.E.C., Liljeros, F., Holme, P.: Exploiting temporal network structures of human interaction to effectively immunize populations. *PLoS One* **7**, e36439 (2012)
87. Rocha, L., Liljeros, F., Holme, P.: Information dynamics shape the sexual networks of internet-mediated prostitution. *Proc. Natl. Acad. Sci.* **107**(13), 5706–5711 (2010)
88. Liljeros, F., Giesecke, J., Holme, P.: The contact network of inpatients in a regional healthcare system. a longitudinal case study. *Math. Popul. Stud.* **14**(4), 269–284 (2007)
89. Eckmann, J.-P., Moses, E., Sergi, D.: Entropy of dialogues creates coherent structures in e-mail traffic. *Proc. Natl. Acad. Sci. U. S. A.* **101**(40), 14333–14337 (2004)
90. Holme, P., Edling, C.R., Liljeros, F.: Structure and time evolution of an internet dating community. *Soc. Netw.* **26**(2), 155–174 (2004)
91. Starnini, M., Machens, A., Cattuto, C., Barrat, A., Pastor-Satorras, R.: Immunization strategies for epidemic processes in time-varying contact networks. *J. Theor. Biol.* **337**, 89–100 (2013)
92. Sociopatterns. <http://www.sociopatterns.org/>.
93. Tang, J., Mascolo, C., Musolesi, M., Latora, V.: Exploiting temporal complex network metrics in mobile malware containment. In: 2011 IEEE International Symposium on a World of Wireless, Mobile and Multimedia Networks (WoWMoM), IEEE, pp. 1–9 (2011)
94. Rachuri, K.K., Musolesi, M., Mascolo, C., Rentfrow, P.J., Longworth, C., Aucinas, A.: Emotionsense: a mobile phones based adaptive platform for experimental social psychology research. In: Proceedings of the 12th ACM International Conference on Ubiquitous Computing. ACM, pp. 281–290 (2010)
95. Scott, J., Gass, R., Crowcroft, J., Hui, P., Diot, C., Chaintreau, A.: CRAWDAD dataset Cambridge/haggle (v. 2009-05-29). Downloaded from <http://crawdad.org/cambridge/haggle/20090529>, May 2009
96. Funk, S., Salathé, M., Jansen, V.A.A.: Modelling the influence of human behaviour on the spread of infectious diseases: a review. *J. R. Soc. Interface* **7**(50), 1247–1256 (2010)
97. Wang, Z., Andrews, M.A., Wu, Z.X., Wang, L., Bauch, C.T.: Coupled disease–behavior dynamics on complex networks: a review. *Phys. Life Rev.* **15**, 1–29 (2015)
98. Weng, L., Ratkiewicz, J., Perra, N., Gonçalves, B., Castillo, C., Bonchi, F., Schifanella, R., Menczer, F., Flammini, A.: The role of information diffusion in the evolution of social networks. In: Proceedings of the 19th ACM SIGKDD International Conference on Knowledge Discovery and Data Mining. ACM, pp. 356–364 (2013)

Chapter 9

Leveraging Topological and Temporal Structure of Hospital Referral Networks for Epidemic Control

Vitaly Belik, André Karch, Philipp Hövel, and Rafael Mikolajczyk

Abstract Antimicrobial-resistant pathogens constitute a major threat for health care systems worldwide. The hospital-related pathway is a key mechanism of their spread. Contrary to intra-hospital transmission data that requires sophisticated contact tracing technologies, data on inter-hospital transmission is collected on a regular basis. We investigate the dataset of patient referrals between hospitals in a large region of Germany. This dataset contains approximately one million patients over a 3-year period. The dataset is used to build a dynamic network of hospitals where nodes are hospitals and edges represent movements of patients between them. We consider the worst-case scenario of a highly contagious disease corresponding to deterministic infection dynamics. Furthermore, we investigate the impact on epidemic processes of the correction to the temporal network due to home (or community) visits of possibly contagious patients returning to hospitals. Moreover, we implement an extensive stochastic agent-based computational model of epidemics on this network. By leveraging the topological and temporal network structure for epidemic control, we propose intervention schemes able to hinder spread. Our approach can be used to design optimal control strategies for containment of nosocomial diseases in health-care networks.

V. Belik (✉)

System Modeling Group, Institute for Veterinary Epidemiology and Biostatistics, Freie Universität Berlin, Königsberg 67, 14163, Berlin, Germany
e-mail: vitaly.belik@fu-berlin.de

A. Karch • R. Mikolajczyk

Helmholtz Center for Infection Research, Inhoffenstraße 7, 38124, Braunschweig, Germany
e-mail: andre.karch@helmholtz-hzi.de; rafael.mikolajczyk@helmholtz-hzi.de

P. Hövel

Institut für Theoretische Physik, Technische Universität Berlin, Hardenbergstraße 36, 10623, Berlin, Germany
e-mail: phoewel@physik.tu-berlin.de

9.1 Introduction

Nosocomial or healthcare-associated infections are a significant mortality and morbidity factor in Europe and across the globe [1, 2]. As an additional challenge, many of these are caused by pathogens which are drug-resistant. Annually, up to 700.000 deaths worldwide can be attributed to antimicrobial resistances [2]. The administrative data on patient hospital admission and discharge constitute referral patterns and is routinely collected by healthcare providers. This data could be used to identify factors facilitating the spread of nosocomial diseases in a healthcare system. For this purpose it is important to consider patient-resolved data, because the identity and causal order of movement events have significant implications for the spreading dynamics [3–6]. From the data the underlying hospital referral network could be reconstructed, with vertices being hospitals and edges being movements of patients between hospitals. The patient movements occur only on some days and thus the edges of the referral network appear and disappear on daily basis. Such networks changing form one time instance to another are known as temporal or dynamic [7, 8].

Note that some aspects of epidemics on hospital referral networks from different countries were considered in Refs. [9–13]. One crucial assumption in such models concerns the disease-free status of patients discharged from hospitals, which may not hold. If such patients return to hospitals, still carrying the pathogen, they may facilitate the further spread of pathogens. Another frequently neglected aspect are temporal and topological correlations [14–16]. In Germany only one small regional network of hospitals was considered on a descriptive level without modeling epidemic spread on it [17]. In the present study we consider referral patterns in a big region in Germany with almost one million patients over 3 years and investigate epidemics on the corresponding network.

In this chapter, we begin by discussing structural properties of the static and the temporal representations of the referral network of hospitals. Then, we present results on the analysis of generic deterministic worst-case spreading phenomena (SI and SIR epidemics) in the static and the temporal frameworks. Finally, we present results of extensive numeric simulations of an endemic disease (modeled as SIS epidemics) and evaluate the effect of various control measures.

9.2 Dataset on Hospital Referrals

From patient referral data we extract a network with vertices being hospitals and edges between hospitals corresponding to direct relocations of patients between two hospitals. One should note, that direct relocations between hospitals correspond only to approximately 3% of referrals in the system. The rest are relocations from or into the community (non hospital whereabouts of patients). We consider only relocations

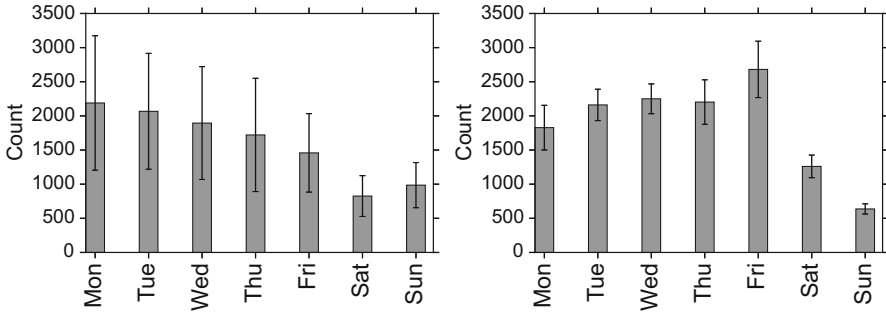


Fig. 9.1 The average number of referral events for every day of the week. *Left panel*: admission frequency. *Right panel*: discharge frequency. Error bars correspond to the standard deviation

between two hospitals on a single day, which is the majority of cases.¹ The dataset was preprocessed to exclude overlapping stays in different hospitals and overlapping stays in a single hospitals were merged together.

9.2.1 Referral Patterns

The dataset spans from the 1st of January 2009 until the 31st of December 2011. Each data record corresponds to a hospital stay and includes the day of admission t^{in} , the day of discharge t^{out} , the anonymized hospital ID and the anonymized patient ID. In our dataset we have 2,037,460 records for 917,834 individuals. The dataset contains patients that were in the system on the 1st of January 2009 (9,874 individuals). The first admission date mentioned in the dataset is the 30th of November 2005. Admission patterns manifest strong temporal regularities (Fig. 9.1). The number of admissions is maximal on Monday (around 2200) and continuously decreases until it reaches a minimum around 700 on Saturday. The number of discharges is minimal on Sunday (around 600), increases until Wednesday, has a small decrease on Thursday and reaches a maximum on Friday (around 2500).²

There were 1654 hospital IDs in the data. However because the data comes from a major insurance provider of the federal state under consideration (Lower Saxony) it makes sense to restrict ourselves only to hospitals located in Lower Saxony. This is done by considering only hospitals with a maximal number of patients per hospital per day larger than 30 (as estimated from the data). This results in 185 vertices (Fig. 9.2, see also Ref. [18] for justification of the procedure).

¹However there were around 300 patients which were apparently transferred between 3 hospitals in one single day. We exclude those from the network reconstruction.

²This weekly dynamics will be also reflected in the epidemic dynamics (Fig. 9.6).

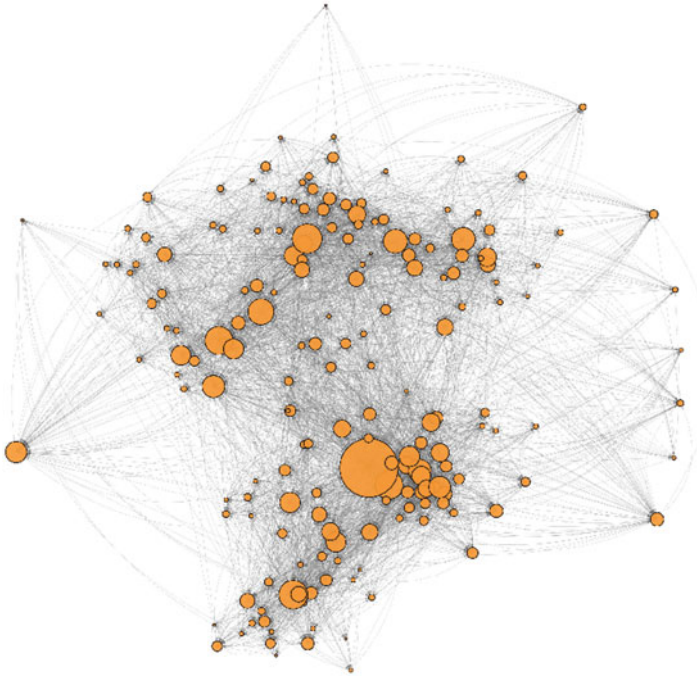


Fig. 9.2 Visualization of the aggregated network of hospitals obtained by considering direct movements of patients between hospitals as edges. The size of vertices is proportional to their in-degree

9.2.2 Network Properties

If we consider the whole available time span and aggregate the temporal edges, we obtain an unweighted static network. In this case, a static edge between two vertices is present, if a temporal edge occurred at least once. In the resulting static network there are 4,949 directed edges. The average in/out-degree is 27 (± 17 and ± 13 respectively, \pm denotes standard deviation) with the diameter equal to 3. In Fig. 9.3 the distributions of in- and out-degrees are presented. Note that the in-degrees show a less heterogeneous distribution, than the out-degrees. The chance to be taken out of a hospital into another one is more less heterogeneously distributed than the chance of being admitted to a hospital from another hospital – there are just a few major hospitals admitting patients from other hospitals. Note that degree distributions resemble an exponential distribution characteristic of random Erdős-Rényi networks (in the limit of a large network size).

So far we considered the aggregated network of hospitals, where we were not concerned with the temporal order of edges. Now we consider a temporal network and review its basic temporal properties.

Fig. 9.3 The complementary cumulative probability distribution function of in-degrees (*circles*) and out-degrees (*squares*). Note that the in-degrees are more broadly distributed than the out-degrees. This reveals a hierarchy of hospitals in the healthcare network with a few large broadly specialized clinics receiving the majority of patients

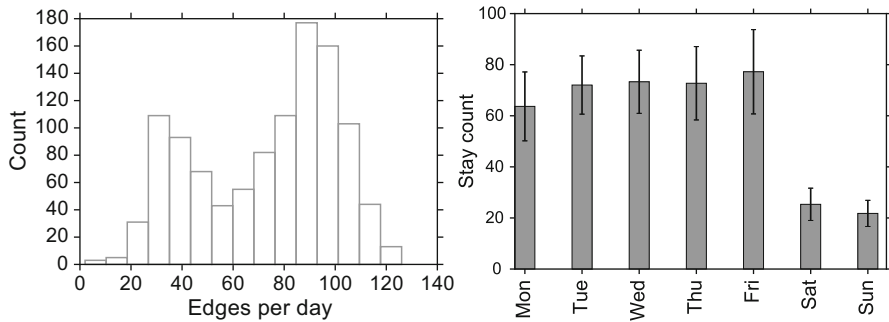
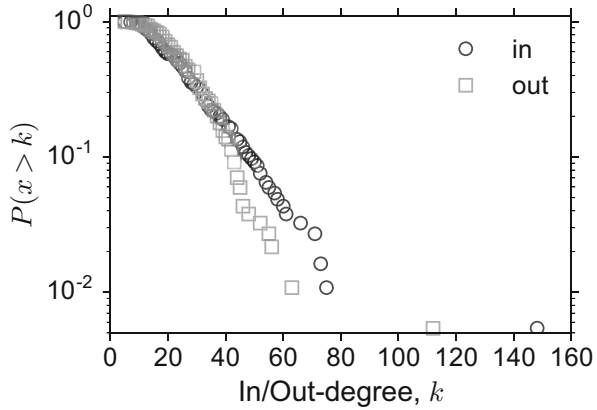


Fig. 9.4 Daily properties of the temporal referral network of hospitals. Histogram of the number of edges per day (*left*). The bimodal distribution corresponds to the small number of edges (around 30) on weekends and large number of edges (around 90) during the rest of the week. This becomes clear from the plot of the average number of edges versus day of the week (*right*). Error bars correspond to standard deviations

After data preprocessing we obtain about 67,000 temporal edges (edges with the corresponding timestamps of their occurrence) for 1,099 days. On average there were 61 ± 22 edges per day. However, in the distribution of the daily number of edges there are two peaks attributable to particular week days (Fig. 9.4).

We define the activity of an edge $j \rightarrow i$ as the number of its occurrences ω_{ij} in a temporal network. In a directed graph an edge could be an incoming edge for a recipient node or an outgoing edge for a donor node. The number of occurrences (or activity) of incoming/outgoing edges for a node reads $a_i^{\text{in}} = \sum_j \omega_{ij}$ and $a_i^{\text{out}} = \sum_j \omega_{ji}$ respectively. Distributions of ω_{ij} , a_i^{in} , and a_i^{out} over the whole time span are presented in Fig. 9.5. Concerning activity of incoming/outgoing edges, we see the picture similar to the in/out-degree distribution (Fig. 9.3) – there are less vertices (hospitals) with the high recipient activity. Activity of outgoing edges is distributed more homogeneously. As it could be seen from the semi-logarithmic plot, the activity distributions resemble the exponential distribution.

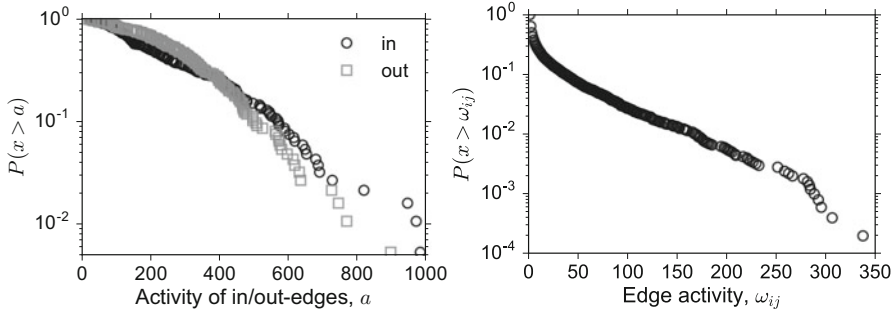


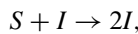
Fig. 9.5 *Left:* The complementary cumulative distribution of the node activity a_i^{in} and a_i^{out} over the whole time span of outgoing (“out”) and incoming (“in”) edges of a node respectively. *Right:* The complementary cumulative distribution of the activity of directed edges ω_{ij} over the whole time span of a node

9.3 Epidemic Dynamics

In the next sections we investigate on epidemic dynamics on the network of hospitals. First, we examine the network of hospitals as a directed contact network, considering a hospital as a single unit being in one of the susceptible, infected or recovered states. Second, we take into account the detailed referral patterns of single individuals, but assume the well-mixed approximation for the stochastic infection dynamics within a single hospital.

9.3.1 Deterministic SI Model

First of all we consider a deterministic (corresponding to the worst-case scenario) disease with no recovery or an infinite infectious period. Such an SI (susceptible-infected) process has the kinetics



where a susceptible node becomes immediately infected upon contact (via temporal edge) with an infectious node.

The spread of a deterministic SI process during t days in a static network could be described by the reachability or accessibility matrix

$$P_t = \bigcup_{n=1}^t A^n, \tag{9.1}$$

where A denotes the adjacency matrix³ of the static network and \cup denotes the Boolean operator OR (a Boolean analog of the matrix multiplication). Elements of this matrix are non zero if there is a path from the vertex i to the vertex j — a connected sequence of edges, where the target vertex of the previous edge ($i \rightarrow j$, $i \neq j$) is the start vertex of the next one ($j \rightarrow k$, $j \neq k$). Equation (9.1) is easy to understand if we recall, that all possible paths up to the length t are given by $\sum_{n=1}^t A^n$. Equation (9.1) is just the Boolean version of the last relation. Analogously the spread of a deterministic SI process on a temporal network could be described by the temporal accessibility matrix

$$\mathcal{P}_t = \bigcap_{n=1}^t (\mathbb{1} \cup A_n),$$

where \cup is the Boolean operator AND (a Boolean analog of the matrix addition), $\mathbb{1}$ is the identity matrix and A_n is the adjacency matrix for the n -th snapshot (on the n -th day) of the temporal network [19]. The temporal accessibility contains all possible spreading paths of duration less or equal to t of a deterministic infection with the infinite infectious period started at all vertices. The elements of the temporal accessibility matrix are non-zero, when there is a time respecting path from the vertex i to the vertex j — a connected sequence of temporal edges, where the target vertex of the previous edge ($n : i \rightarrow j$, $i \neq j$) is the start vertex of the next one ($n + \tau : j \rightarrow k$, $j \neq k$, $0 < \tau \leq t$).

The density $\rho(\mathcal{P}_t)$ (fraction of non-zero elements) of the accessibility matrix gives a cumulative distribution F_t of the number of shortest paths of duration less or equal than t between any two nodes [19]. Thus the difference between two successive values of the cumulative distribution $F_t - F_{t-1}$, $F_0 \equiv 0$ gives us the probability distribution of shortest paths of duration t . It is shown in Fig. 9.6. As it is clear from Fig. 9.6, the characteristic time scale of the spread in this network is around 80 day (corresponding to the peak position). The total duration of the spreading activity is around 100 days.

Not all paths possible in a static aggregated network are present in the temporal one. The causal fidelity gives the fraction of paths present in the temporal network relative to the paths in the corresponding static (aggregated) network [19]

$$c(t) = \rho(\mathcal{P}_t) / \rho(\mathbf{P}_t), \quad (9.2)$$

where \mathbf{P}_t is the accessibility in the static aggregated case with all daily network snapshots being the same. It tells us how important the temporal resolution is compared with the aggregated network. The dependence of the causal fidelity on time is depicted in Fig. 9.7. As it can be clearly seen, if the time scale (e.g. infectious period) of a dynamic process on the network is larger than approximately 300 days, we can consider the aggregated network as a static network.

³Its element $a_{ij} = 1$ if there is the edge $j \rightarrow i$ and zero otherwise.

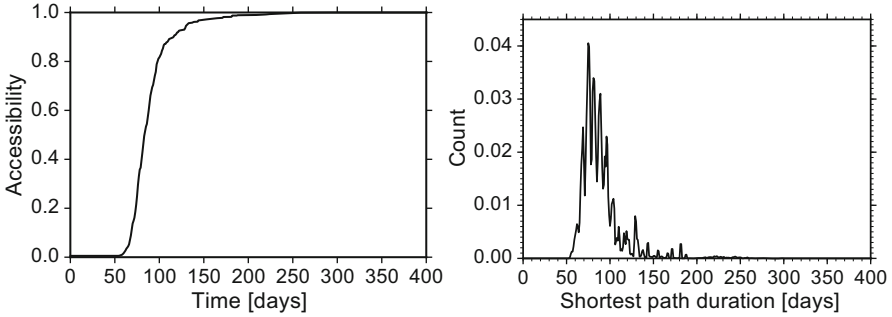
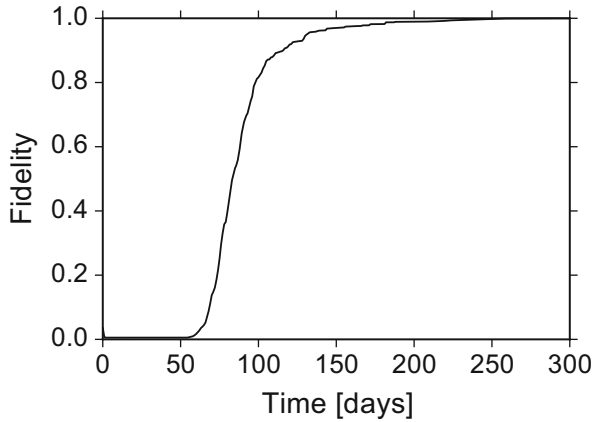


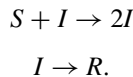
Fig. 9.6 *Left*: the density (fraction of non-zero elements) of the accessibility matrix $\rho(\mathcal{P}_t)$ of the temporal referral network of hospitals. *Right*: the difference between successive values of the accessibility density $\rho(\mathcal{P}_t)$ corresponding to the distribution of shortest path durations [19]

Fig. 9.7 The causal fidelity is given by the fraction of time respecting causal paths present in the aggregated static network, Eq. (9.2)



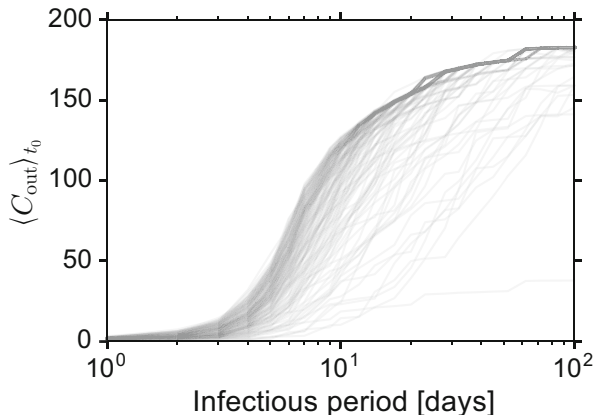
9.3.2 Deterministic SIR Model

So far we considered a deterministic infection without recovery. However the causal chain of contacts of a temporal network manifests itself even stronger in the case of a disease with a finite fixed infectious period. If vertices become immune to the disease after infection, the following kinetics can be used



Note that we again consider the deterministic case, and thus upon contact with an infected, a susceptible individual becomes infected for sure. For a general analysis of deterministic SIR epidemics on temporal networks see [20]. As a quantity of interest we consider an out-component of the vertex i – a set of vertices which

Fig. 9.8 Sizes of the out-components $\langle C_{out} \rangle_{t_0}$ for all of the 185 nodes in the referral network of hospitals in dependence on the infectious period k . Averaging was performed over initial time of infection t_0



could be reached by an epidemic with the infectious period k started from the given node i at the initial time t_0 by following all temporal edges respecting their time order [21]. We denote the size of the out-component by $C_{out}(i, k, t_0)$ which can be also considered as an upper bound for the number of infected nodes in the case of a stochastic disease transmission.

In Fig. 9.8 the out-components sizes averaged over initial times t_0 are presented for all nodes in the referral network of hospitals in dependence on the infectious period. We observe, that except for a few nodes, the majority of out-components reaches the size of the whole network for a disease with the infectious period of $k \sim 100$ days. Note that in the case of MRSA (Methicillin-resistant *Staphylococcus aureus*), the carriage of the pathogens could be even longer than 100 days. Figure 9.8 could not immediately reveal how long it would take to actually reach all the nodes in the out-component. Furthermore, we rank 185 hospitals according to their out-component size (Fig. 9.9, left panel) for different infectious periods. We observe a strong heterogeneity in the rank due to changes in tied values of the out-components for small (for $k \sim 3$ days there is a maximum number of ranks) and intermediate values of the infectious period. For high values of the infectious period the rank becomes very similar for all nodes. Small values of infectious period lead to highly fluctuating rank due to the high importance of the precise timing of outgoing links from the given node and small sizes of the resulting out-components.

We also average the ranks over all considered infectious periods (Fig. 9.9, right panel) and observe a strongly heterogeneous distribution – only a few nodes have a small rank, the majority has high rank values.

To analyze the robustness of the rank we considered the entropy of the rank distribution values for different infectious periods

$$\mathcal{H} = \sum_i p_i \ln p_i, \quad (9.3)$$

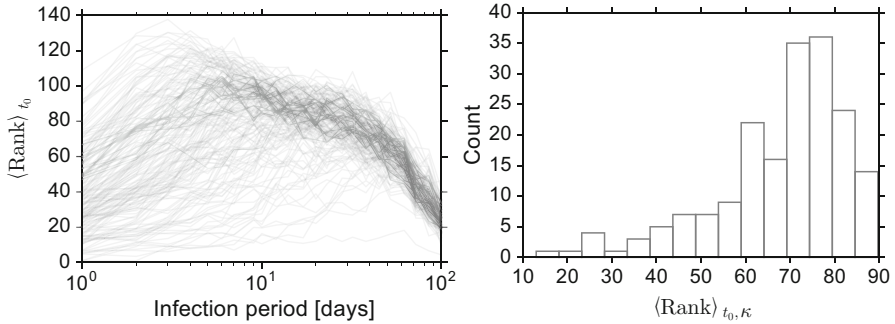
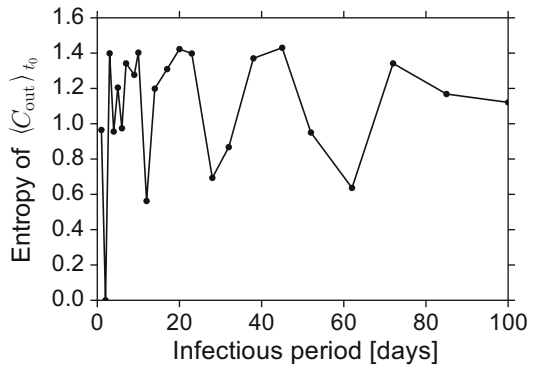


Fig. 9.9 *Left:* The node ranking according to the size of their out-component, averaged over initial times t_0 . In the case of tied values the minimal rank values are taken. *Right:* Node ranks averaged over both initial time t_0 and infectious period κ

Fig. 9.10 The entropy Eq.(9.3) of the out-component rank distribution averaged over initial time t_0 versus the infectious period



where p_i is the probability of the out-component $\langle C_{out} \rangle_{t_0}$ to have rank i (Fig. 9.10). High entropy values correspond to strong heterogeneity. We observe a peculiar behavior – the entropy oscillates with the infectious period, especially for very low and very high values of k . It may be due to some “resonance” effect. Some values of the infectious period lead to similar out-components corresponding to the low entropy.

9.3.3 Network Correction Due to Community Stays

Until now we neglected the community stays and considered only direct transfers of patients between hospitals as edges in a dynamic network. This holds under the assumption of the complete recovery of a patient after a hospital visit. This approach was also adopted e.g. in Ref. [10]. If patients are not pathogen-free upon discharge from the hospital n , they could still carry pathogens when they return to the hospital m from the community. This happens, if the time spent in the community

is less than the infectious period of the pathogen: $t_m^{\text{in}} - t_n^{\text{out}} < k$, where subscripts of discharge and admission times denote the corresponding hospital. Now we relax this assumption and allow patients to carry the pathogens also in the community (without transmission) and adjust the corresponding effective dynamic network and quantify the impact of the pathogen carriage during community stays.

We call the network of direct patients transfers between two hospitals considered above an H-network. The H-network with additional edges due to possible transmission events after stays in the community is a C-network. In the C-network we include the edge between a hospital visited before the community stay and a hospital visited afterwards, if the duration of the community stay is less than the infectious period. Out-components \tilde{C}_{out} in the C-network are larger than the out-components C_{out} in the H-network, because the H-network is a subset of the C-network (Fig. 9.11), left panel). In Fig. 9.11, right panel, the difference between $\langle \tilde{C}_{\text{out}} \rangle_{t_0, h}$ and $\langle C_{\text{out}} \rangle_{t_0, h}$ is shown. We see a pronounced peak around the infectious period of $k \approx 7$ days. For this infectious period, using only the H-network we underestimate the actual out-component by 20%.

This difference could be clarified if we look on the Jaccard coefficient $\Theta(k)$ between the edges of H- and C-networks given by

$$\Theta(k) = \frac{|E_H \cap E_C|}{|E_H \cup E_C|}, \quad (9.4)$$

where $|\cdot|$ denotes the cardinality of a set (number of its elements) and E_H and E_C are set of edges in H- and C-networks respectively. The Jaccard coefficient quantifies the relative overlap of two sets. It is maximal (equal to one), if two sets coincide and is zero if two sets are disjoint. In Fig. 9.12, left panel, we observe that maximal overlap is reached at the value of the infectious period $k \sim 7$ days. Additional increase of the infectious period does not lead to higher Jaccard index. This effect could be explained if we look on the denominator and the numerator in Eq. (9.4) separately (Fig. 9.12, right panel). Both the total number of edges in the C-network $|E_H \cap E_C|$ and the number of edges common in both C- and H-networks $|E_H \cup E_C|$ increases with the infectious period k . However, the former increases first sub-linearly but after the value of $k \sim 7$ days it increases in a super-linear manner. The latter increases first in a super-linear way but after the value of $k \sim 7$ days it increases sub-linearly. Together this leads to the peak in the Jaccard coefficient.

So far, in the epidemic analysis we considered the network extracted from the available dataset as a ground truth. However, we actually observe only around 50% of individuals [18] due to the market share limitations. This could lead to the underestimation of epidemic effects, such as timescales of the spread and the number of affected nodes. On the other hand, because we considered deterministic epidemics, we overestimated the epidemic effects. To account for both deficiencies – missing data and stochasticity of the transmission events, in the next section we consider a fully stochastic, discrete-event, and agent-based computational model of a disease with total recovery but no immunity and implement control measures.

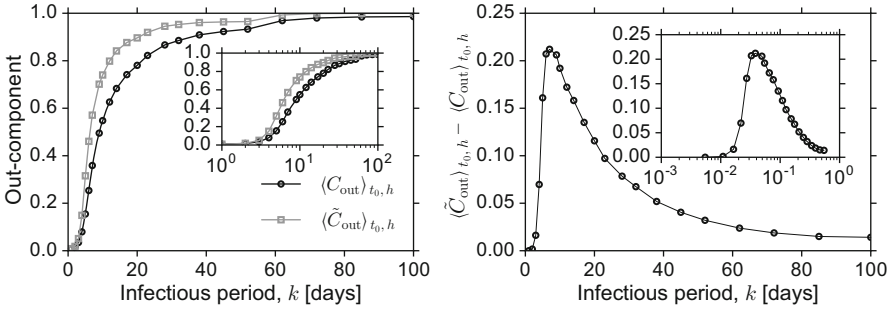


Fig. 9.11 *Left*: The effect of community stays on the out-component averaged over different initial times t_0 and over different hospitals h . \tilde{C}_{out} and C_{out} denote the out-components of the C and H-network respectively. *Right*: The difference between $(\tilde{C}_{\text{out}})_{t_0, h}$ and the out-component $(C_{\text{out}})_{t_0, h}$. Note that we consider the whole dataset (with initial time starting from the beginning of the data). *Insets* show the same dependences as the main plot in semi-logarithmic coordinates

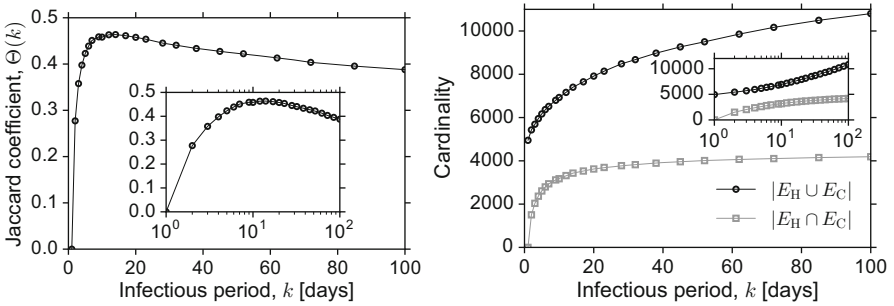


Fig. 9.12 The effect of community stays. *Left*: The relative overlap of the aggregated network is measured by the Jaccard coefficient $\Theta(k)$, Eq. (9.4) versus the infectious period k . *Right*: the total number of edges in C-network and the number of edges common in both C- and H-networks versus the infectious period k . *Insets* show the same dependences as the main plots in semi-logarithmic coordinates

9.3.4 Agent-Based Computational Model

In this section we introduce the computational framework for modeling the disease spread in a network of hospitals. In a single hospital we assume a randomly mixed situation, i.e. every patient could encounter every other patient. Information on healthcare workers was not available and they are assumed not to contribute to epidemic dynamics. We consider an endemic disease modeled by the standard SIS kinetics



Here the number of infected individuals I in a single hospital increases due to encounters with susceptibles S at the per capita rate α . The infecteds could become susceptible again at the rate β . The spread of some nosocomial diseases such as resistant pathogens reached an extent of an endemic with the prevalence for the MRSA around 4% in hospitals [22]. To ensure the prevalence of 4%, we use the following parameter values: $\alpha = 0.023 \text{ day}^{-1}$ and $\beta = 0.0027 \text{ day}^{-1}$ corresponding to half a year of carriage of the pathogens before recovery.

For our computational model, we need an artificial or a surrogate population due to the incompleteness of the data (only around 50% of the total population is included in the data), privacy reasons and to make projection into the future. Generation of a surrogate population is a non-trivial task, because the data is highly spatially and temporally correlated which is usually neglected. E.g. in the study by Donker and colleagues [10], hospital stays, separated by a community stay, were considered uncorrelated which makes sense only for patients healthy at discharge from a hospital. See also Ref. [23] for related issues in intra-hospital contact tracing. To produce the surrogate population and to keep the correlations present in the original dataset, we use the following bootstrapping procedure.

For every surrogate patient, we randomly choose a patient from the original dataset considering only the middle year $[T, 2T]$ (out of three) for bootstrapping, where $T = 365$ days as counted from the beginning of the dataset (the 1st of January 2009). We randomly from a uniform distribution choose the day $t \in (T, 2T]$ of the first appearance of the surrogate patient within the interval $(T, 2T]$ and replicate individual referral history periodically, n times.⁴ To account for vital (birth/death) dynamics we need M – the total number of patients staying in hospitals during the year – for every annual period $[(k-1)T, kT]$, $k \leq n$. We choose randomly μM patients at a random time point within the current k -th time interval $[(k-1)T, kT]$, exchange their IDs by new ones and reset their infection status to susceptible for the next hospital stay in the future. Here $\mu = 0.25$ is the turnover rate of the population (disappearance and appearance of patients) in the censored period of time.

The simulation was implemented using a modified stochastic Gillespie algorithm [24] for epidemic dynamics within a hospital, combined together with explicitly scheduled patient transfer events. All relevant events were implemented as a priority queue data structure [25]. The health status of all the patients in the system was tracked. We let the system equilibrate to a stationary level before starting the epidemic simulation.

Using the above computational model we can easily access the effect of different intervention measures based on the topological and temporal properties of the patient referral network. We choose two exemplary intervention scenarios. In both of them the resources for random screening of 50% of incoming patients and subsequent decolonization (this reduces the rest recovery time 3-fold) and isolation were allocated to the selected 10% of hospitals with the highest ranks. The ranking

⁴Since hospital stays could fall outside the interval $(T, 2T]$, we choose to cut the stays to fit into the interval.

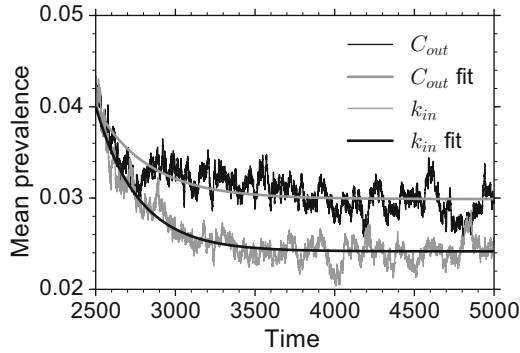


Fig. 9.13 Impact of interventions. Results of the numerical simulations of an agent based model, Eq. (9.5) with interventions – allocation of resources for screening and subsequent decontamination and isolation to 10% of hospitals (prioritized according to the out-component $\langle C_{out} \rangle_{t_0, k}$ of nodes (blue) and according to the aggregated in-degree k_{in} of a node (red)). For the fit an exponential function Eq. (9.6) was chosen. The in-degree ranking seems to be more efficient to reduce the prevalence than the time-averaged out-component ranking

was performed (i) according to the deterministic out-component $\langle C_{out} \rangle_{t_0}$ of a node and (ii) according to the in-degree of a node in the aggregated network. In Fig. 9.13 the time course of the prevalence, averaged over all hospitals, after intervention were applied, is presented for both scenarios. The comparison shows, that the in-degree ranking is more appropriate for the prevalence reduction than the out-component. The deviation in the final prevalences is up to $20\% \pm 10\%$. As an estimate for the final prevalence y_0 we took the limit $t \rightarrow \infty$ of the fit function to the prevalence time series $y(t)$ of the form

$$y = y_0 - (\pi^* - y_0) e^{-a(t-t_0)}, \quad (9.6)$$

where $\pi^* = 0.4$ is the baseline prevalence. This curve describes an abrupt prevalence decrease after intervention, afterwards slowly approaching the endemic prevalence level. We obtain for the ranking by the out-component $y_0 = 0.30$ and for the in-degree $y_0 = 0.24$. Note also that allocation of limited resources only to some hospitals usually leads to reduction of the prevalence but not to (almost) eradication of the disease, which could be achieved if the intervention measures were applied at all the hospitals. This supports the hypothesis, that in the network of hospitals the prevalence reduction is achieved immediately in the hospitals where control measures are implemented (high in-degree selects hospitals with a lot of incoming patients) and not due to the indirect effects of the reduction of disease transmission to other hospitals (which corresponds to the high out-component).

9.4 Conclusion

We have investigated patient referral patterns in a large federal state in Germany. We extracted the underlying network of hospitals and investigated its properties with respect to pathogen spread. For the worst case scenario of a highly contagious pathogen with and without recovery we examined the time scales and, in the presence of recovery, sizes of an outbreak dependent on the infectious period. We investigated the role of patients returning to hospitals but still carrying the pathogen acquired during previous hospital visits. We showed that this results in a deviation (underestimate) of the size of the out-components (or outbreak size) up to 20% for the values of the infectious period of one week without patient returns. By deploying an agent- and discrete event-based computational model of an endemic disease (MRSA), we assessed the impact of intervention strategies based on the out-component size and the in-degree resource allocation. Our analysis showed the advantage of the in-degree based allocation.

There is still the need for generic models of contacts patterns, to account for the missing data as well as to project the results into the future. Recently some additional epidemic control strategies based on the temporal aspects of the network were proposed as a promising direction for the future research [26, 27]. Prioritization scheme according to the risk of disease introduction should be used based on novel network distance measures [28, 29]. Our approach helps to understand the spread of infections in a network of hospitals and could be used to plan preventive measures as well as to design informed clinical studies.

Acknowledgements All the authors acknowledge the courtesy of the AOK Niedersachsen for providing the anonymized data on patient referrals. VB and PH acknowledge funding by the Deutsche Forschungsgemeinschaft in the framework of Collaborative Research Center 910. At the early stage of this study VB was financially supported by the fellowship “Computational Sciences” of the VolkswagenStiftung.

References

1. Cassini, A., Plachouras, D., Eckmanns, T., Sin, M.A., Blank, H.P., Ducomble, T., Haller, S., Harder, T., Klingeberg, A., Sixtensson, M., et al.: PLoS Med. **13**(10), e1002150 (2016)
2. O’Neill, J.: The review on antimicrobial resistance. Tackling drug-resistant infections globally: final report and recommendations. <http://amr-review.org> [WebCite Cache ID 6jI5znBnd] (2016). Accessed 26 July 2016
3. Keeling, M.J., Danon, L., Vernon, M.C., House, T.A.: Proc. Natl. Acad. Sci. **107**(19), 8866 (2010)
4. Belik, V., Geisel, T., Brockmann, D.: Phys. Rev. X **1**(1), 011001 (2011)
5. Rosvall, M., Esquivel, A.V., Lancichinetti, A., West, J.D., Lambiotte, R.: Nat. Commun. **5**, 4630 (2014)
6. Scholtes, I., Wider, N., Pfitzner, R., Garas, A., Tessone, C.J., Schweitzer, F.: Nat. Commun. **5**, 5024 (2014)
7. Holme, P., Saramäki, J.: Phys. Rep. **519**(3), 97 (2012)

8. Casteigts, A., Flocchini, P., Quattrociochi, W., Santoro, N.: *Int. J. Parallel Emergent Distrib. Syst.* **27**(5), 387 (2012)
9. Fernandez-Gracia, J., Onnela, J.P., Barnett, M., Eguiluz, V.M., Christakis, N.A.: Spread of pathogens in the patient transfer network of US hospitals. arXiv preprint arXiv:1504.08343 (2015)
10. Donker, T., Wallinga, J., Slack, R., Grundmann, H.: *PLoS One* **7**(4), 1 (2012)
11. Ohst, J., Liljeros, F., Stenhem, M., Holme, P.: *EPJ Data Sci.* **3**(1), 1 (2014)
12. Rocha, L.E., Singh, V., Esch, M., Lenaerts, T., Stenhem, M., Liljeros, F., Thorson, A.: arXiv preprint arXiv:1611.06784 (2016)
13. Karkada, U.H., Adamic, L., Kahn, J.M., Iwashyna, T.J.: *Intensive Care Med.* **37**(10), 1633 (2011)
14. Schneider, C.M., Belik, V., Couronné, T., Smoreda, Z., González, M.C.: *J. R. Soc. Interface* **10**(84), 20130246 (2013)
15. Kovanen, L., Karsai, M., Kaski, K., Kertész, J., Saramäki, J.: Temporal motifs. In: *Temporal Networks*, pp. 119–133. Springer, Berlin/Heidelberg (2013)
16. Lentz, H.H.K., Koher, A., Hövel, P., Sokolov, I., Gethmann, J., Sauter-Louis, C., Selhorst, T., Conraths, F.: *PLoS One* **11**(5), e0155196 (2016)
17. Wieler, L.H., Ewers, C., Guenther, S., Walther, B., Lübke-Becker, A.: *Int. J. Med. Microbiol.* **303**(6–7), 380 (2013)
18. Belik, V., Hövel, P., Mikolajczyk, R.: Control of epidemics on hospital networks. In: *Control of Self-Organizing Nonlinear Systems*, pp. 431–440. Springer International Publishing, Cham (2016)
19. Lentz, H., Selhorst, T., Sokolov, I.M.: *Phys. Rev. Lett.* **110**(11), 118701 (2013)
20. Koher, A., Lentz, H.H.K., Hövel, P., Sokolov, I.: *PLoS One* **11**(4), e0151209 (2016)
21. Korschake, M., Lentz, H.H.K., Conraths, F.J., Hövel, P., Selhorst, T.: *PLoS One* **8**(2), e55223 (2013)
22. Marschall, J., Mühlemann, K.: *Infect. Control* **27**(11), 1206 (2006)
23. Génois, M., Vestergaard, C.L., Cattuto, C., Barrat, A.: *Nat. Commun.* **6**, 8860 (2015)
24. Gillespie, D.T.: *J. Phys. Chem.* **81**(25), 2340 (1977)
25. Cormen, T.H.: *Introduction to Algorithms*. MIT Press, Cambridge (2009)
26. Liu, S., Perra, N., Karsai, M., Vespignani, A.: *Phys. Rev. Lett.* **112**(11), 118702 (2014)
27. Belik, V., Fengler, A., Fiebig, F., Lentz, H.H.K., Hövel, P.: arXiv preprint arXiv:1509.04054 (2016)
28. Brockmann, D., Helbing, D.: *Science* **342**(6164), 1337 (2013)
29. Iannelli, F., Koher, A., Brockmann, D., Hövel, P., Sokolov, I.M.: *Phys. Rev. E* **97**, 012313 (2017)

Chapter 10

Surveillance for Outbreak Detection in Livestock-Trade Networks

Frederik Schirdewahn, Vittoria Colizza, Hartmut H. K. Lentz,
Andreas Koher, Vitaly Belik, and Philipp Hövel

Abstract We analyze an empirical, temporal network of livestock trade and present numerical results of epidemiological dynamics. The considered network is the backbone of the pig trade in Germany, which forms a major route of disease spreading between agricultural premises. The network is comprised of farms that are connected by a link, if animals are traded between them. We propose a concept for epidemic surveillance, which is generally performed on a subset of the system due to limited resources. The goal is to identify agricultural holdings that are more likely to be infected during the early phase of an epidemic outbreak. These farms, which we call *sentinels*, are excellent candidates to monitor the whole network. To identify potential sentinel nodes, we determine most probable transmission routes by calculating functional clusters. These clusters are formed by nodes that – chosen as seed for an outbreak – have similar invasion paths. We find that it is indeed possible to group the German pig-trade network in such clusters. Furthermore, we select sentinels by choosing nodes out of every cluster. We argue that any epidemic outbreak can be reliably detected at an early stage by monitoring a small number

F. Schirdewahn (✉) • A. Koher • P. Hövel
Institute of Theoretical Physics, Technische Universität Berlin, Hardenbergstr. 36,
10623, Berlin, Germany
e-mail: frederik.schirdewahn@t-online.de; andreas.koher@campus.tu-berlin.de;
phoevel@physik.tu-berlin.de

V. Colizza
Sorbonne Universités, UPMC Univ Paris 06, INSERM, Institut Pierre Louis d'épidémiologie
et de Santé Publique (IPLESP UMRS 1136), 75012, Paris, France
e-mail: vittoria.colizza@inserm.fr

H.H.K. Lentz
Institute of Epidemiology, Friedrich-Loeffler-Institut, Südufer 10, 17493, Greifswald, Insel
Riems, Germany
e-mail: hartmut.lentz@fli.de

V. Belik
System Modeling Group, Institute for Veterinary Epidemiology and Biostatistics,
Freie Universität Berlin, Königsweg 67, 14163, Berlin, Germany
e-mail: vitaly.belik@fu-berlin.de

of those sentinels. Considering a susceptible-infected-recovered model, we show that an outbreak can be detected with only 18 sentinels out of almost 100,000 farms with a probability of 65% in approximately 13 days after first infection. This finding can be further improved by including nodes with the largest in-component (highest vulnerability), which increases the detection probability to 86% within 8 days after first occurrence of the disease.

10.1 Introduction

Diseases in livestock holdings have been a major challenge in the industrial meat production and related economy in the last decades. For example, the foot-and-mouth disease (FMD), which broke out in Great Britain in 2001 in herds of cloven hoofed animals, caused estimated costs of 8 billion British Pound [1]. In rare occasions FMD could even pose a health risk to humans, which means that it becomes zoonotic, that is, it can be transferred from animals to humans. In general, outbreaks of animal-related diseases should be prevented for multiple reasons: They diminish animal well-being, reduce productivity, cause great economic losses, and might be transferable to human.

The study of spreading livestock diseases contributes to a better understanding of contagion processes in general [2]. To model an infection many mathematical models have been successfully investigated such as the SIR (susceptible-infected-recovered), SIS (susceptible-infected-susceptible) or SI (susceptible-infected) model [1, 3–5]. Major transmission routes of disease spread may be geographical proximity, where aerial transmission is the main carrier. In addition, arthropods (mosquitoes or ticks) can be vectors. We will focus on the trade of livestock, which was the main route due to direct transmission between animals, for instance, during a swine-fever outbreak in Germany in the 1990s [6]. The disease transmission between animal holdings takes place, if an infected animal is transported from one farm to the next. To model and analyze the impact of disease spread due to livestock trade, we use concepts from network science [7].

Since livestock-trade networks span tens of thousands of agricultural holdings, it is not possible to examine every single farm for an infection due to limited resources. Examinations should therefore focus on some premises with a high probability of being infected in case of an outbreak. In Ref. [8], Bajardi et al. analyzed the Italian cattle-trade network and presented a novel surveillance concept. We will apply the same framework to identify special nodes, the so called *sentinels*, that may be affected by a potential outbreak occurring in the system with a high probability. We will demonstrate that the number of sentinel nodes is several orders of magnitude smaller than the total number of animal holdings. For this purpose, we consider different selection protocols and show that surveillance can be made much more efficient by concentrating resources on a few nodes.

This chapter focuses on the data of the German pork industry, which is one of the largest in the world. Every year, five million tons of pork meat are produced and the rate is increasing.¹ Therefore, investigating efficient detection schemes on the underlying network is of great relevance.

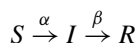
The rest of this chapter is organized as follows: In Sect. 10.2, we will introduce the susceptible-infected-recovered model and some concepts from network science. We will show how an invasion path evolves on a temporal network allowing to define functional clusters. In Sect. 10.3, we describe the data under consideration and summarize the steps taken to analyze the network on a temporal basis. Furthermore, we apply strategies proposed in Ref. [8] to the network and discuss the possibility to identify sentinel nodes. Finally, we conclude with a summary in Sect. 10.4.

10.2 Theory

In the following, we will review basic aspects of the susceptible-infected-recovered (SIR) model (Sect. 10.2.1) and discuss how an epidemic can spread in a network via invasion paths (Sect. 10.2.2). We provide details on our numerical simulation in Sect. 10.2.3. The characterization of different nodes in the network according to their in- and out-components will be the topic of Sect. 10.2.4 and we will elaborate how clusters evolve from different invasion paths in Sect. 10.2.5.

10.2.1 Deterministic Susceptible-Infected-Recovered-Model

To describe the spreading of an infectious disease in a population, we need a model for its progression [1]. Let us assume that size of the population is constant and that it can be divided in susceptible (or healthy) S , infected (and therefore infectious) I and recovered (and hence immunized) individuals R . Following the transition scheme



a susceptible individual becomes infected with a probability α upon contact with an infected. After an infectious period of β^{-1} , where β denotes the recovery rate, an infected individual turns into a recovered one. Note that this scheme does not account for births, deaths, or migration. In our study, we consider a deterministic version of the SIR model with a fixed recovery time and guaranteed infection upon

¹*Agrarpolitischer Bericht der Bundesregierung* (2015). *Bundesministerium für Ernährung und Landwirtschaft* (BMEL), available as <http://www.bmel.de/SharedDocs/Downloads/Broschueren/Agrarbericht2015.html>

contact, that is, $\alpha = 1$ [8, 9]. Alternatively, the SIR dynamics can also be written as a set of differential equations [10].

Livestock diseases may spread directly between animals. Here, we model a corresponding contagion process on a broader perspective by considering the agricultural holding as epidemiological unit. Our main goal is not to investigate a detailed model for the local disease dynamics within a farm. Instead, we assume that every infected animal will transmit the disease immediately to the whole population, when it arrives at another farm. In the beginning of each simulation, all premises are considered as susceptible or disease free except for a single node [8, 11], which we call the *seed*. The infection is transmitted in each time step along outgoing links connected to susceptible neighbors, which then transmit the disease in the following time step further in the network via their susceptible neighbors and so on. In short, the considered model consists of two dynamical mechanisms [8]:

1. A susceptible farm will be infected with a probability $\alpha = 1$, if it receives an animal from an infected farm.
2. A farm stays infected for a duration of τ days, which we call the *infectious period*. We set this value to $\tau = \beta^{-1} = 7$ days. Afterwards, the farm recovers and cannot be infected again.

Note that the first mechanism implicitly accounts for directionality. Opposed to other mobility scenarios such as commuting, only the node at the end of an edge is at risk to become infected in a production chain. If a susceptible farm sells an animal to an infected one, it still maintains its disease-free status. The advantage of such a deterministic model is a significant reduction of computational effort. It allows us to consider all nodes as a possible starting point of an outbreak. In short, our numerical findings provide information in terms of a worst-case scenario. Bajardi et al. also obtained similar results using a stochastic modeling approach [8].

The next sections describe how an infection takes place on a temporal network and how the algorithm used in this study is implemented.

10.2.2 Temporal Networks

As Vernon and Keeling pointed out in Ref. [12], the spread of infectious diseases is only predicted correctly, if the chronology of contacts is accurately accounted for. For a realistic model of disease transmission, we therefore consider a directed temporal network, because typical trade connections take place on different timescales and a disease can only be transmitted along time-respecting paths.

Next, we will give a short introduction into the mathematical description of temporal networks [13–15]. We define $G = (V, E)$ as a directed, temporal graph consisting of a set of nodes V and time-stamped edges E connecting these nodes. For further reading, in particular connected to livestock-trade networks, we refer to [8, 9, 12, 16, 11, 17, 18].

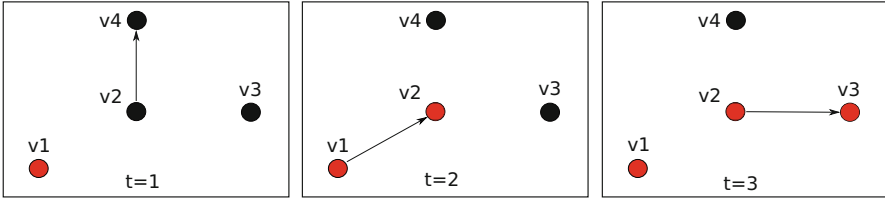


Fig. 10.1 Snapshot of a schematic network for three different times. Initially node v_1 is infected (indicated by the red dot) and the disease can spread to node v_3 , which is susceptible (indicated by the black dot), via v_2

If an outbreak at a node v_i can reach a node v_j , there has to be either a direct link, that is, an edge, or an indirect connection. The latter case is described by a path from one to the other. Such a path P_{ij} consists of a sequence of edges via intermediate nodes v_k , where no node is visited twice. Therefore, a path is given by:

$$P_{ij} = [(v_i, v_1, t_0), (v_1, v_2, t_1), \dots, (v_{n-1}, v_j, t_{n-1})].$$

The length of the path is the number of edges n . Note that we introduce a time stamp to each edge of the path. Hence, a time-respecting path satisfies: $t_0 < t_1 < \dots < t_{n-1}$. Between a pair of nodes, there might be a large number of paths of different lengths [19]. We stress that a path with the smallest number of edges might not be the fastest depending on the specific timing of its edges [20]. For a disease spread between two nodes, the earliest arrival time is of particular importance. We call the set of directed, time-respecting edges starting at a particular seed node *invasion path* Γ . In the considered deterministic SIR model, just the first contact with the disease infects the node. Recurrent infections will have no effect as repeated infections are not possible.

Figures 10.1, 10.2 and 10.3 provide different perspectives of a spreading process on a temporal network. The disease starts at a single infected node v_1 . While Fig. 10.1 depicts a series of snapshots at different times, Fig. 10.2 shows an overlay of the snapshots, where the times, when an edge is active, are explicitly given. In this schematic example, an invasion path $\Gamma_{13} = [(v_1, v_2, t = 2), (v_2, v_3, t = 3)]$ exists between the initially infected seed node v_1 and node v_3 via v_2 . Node v_4 , however, cannot be infected, because the connection P_{24} takes place, before the outbreak reaches v_2 . Hence, the path $P_{14} = [(v_1, v_2, t = 2), (v_2, v_4, t = 1)]$ is not time-respecting and violates causality. The notion of an invasion path includes the possibility of branching into tree-like transmission routes. A time-layered aspect is depicted in Fig. 10.3. Here, the number of nodes that are going to be infected in every time step, so called *incidences*, is easy to see.

Fig. 10.2 Overlay of snapshots of a temporal network (cf. Fig. 10.1). A time-respecting path leads from node v_1 to v_3 . If one aggregates the network over all times, however, a path between v_1 and v_4 emerges that does not exist in the temporal case

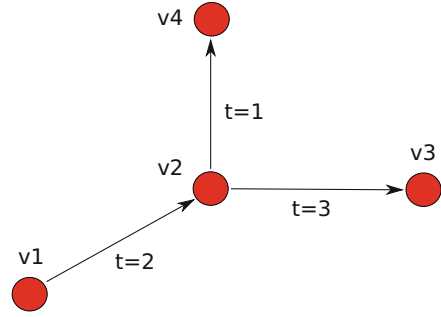
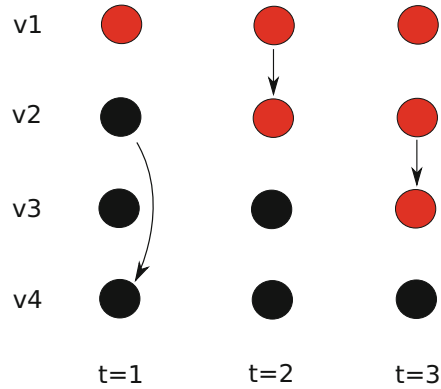


Fig. 10.3 The same temporal network as in Figs. 10.1 and 10.2, but in a layered representation. In time step $t=1$ two susceptible nodes have contact. Only in step $t=2$ and $t=3$ the disease can be transmitted



10.2.3 Modelling an Infection on the Network

To model the spread of an infectious disease on the network, we use an algorithm of breadth-first-search type to iteratively simulate the deterministic SIR dynamics introduced in Sect. 10.2.1. The main steps are the following: We start at a seed node $v_i \in V$ and mark it as infected at time t_0 . In every time step t_n , we identify all edges (v_i, v_j, t_n) that start at the initially infected node v_i (or in further steps at nodes along the production chain originating from v_i) and lead to a susceptible node v_j . All nodes that can be reached this way are marked as infected, that is, we assume a transmissibility of 100%. A node can transmit the disease as long as it is infected. After having acquired an infection, the node stays infected and infectious for a fixed period, which we choose as $\tau = 7$ days. Subsequently, we iterate over all infected nodes v_i and mark those, which have recovered, as removed. In the next step the time t_n is incremented by one corresponding to the temporal resolution of the available data and the process will be repeated, until no more infected nodes are present. The time that it takes from the beginning of the outbreak to its termination is called the *outbreak duration*.

In the next section, we will summarize some measures of a temporal network, which help to characterize its structure.

10.2.4 Measure of Centrality

There is a large number of measures that quantify the centrality of nodes in a network [21–23]. For epidemiological purposes, central nodes may have a high chance to become infected or may transmit a disease to large parts of the network. In this section, we will focus on some of those measures that have a direct epidemiological relevance.

In network terminology, the *out-component* $c_{\text{out}}(v_i, \tau, t_0)$ of a node v_i is given by a set of nodes that can be reached from a primary infected node $v_i \in V$. The parameter τ is the finite infectious period introduced in Sect. 10.2.1 and t_0 denotes the starting time of the epidemic. In general, a large infectious period τ produces more secondary outbreaks and leads therefore to a greater probability to reach more nodes in the network [11]. $c_{\text{out}}(v_i, \tau, t_0)$ can be calculated as the union of the sets of nodes along all possible invasion paths originating from v_i at time t_0 . This out-component corresponds to the final size of an epidemic, which is an important quantity in epidemiology. It indicates the accumulated number of all infected individuals during an epidemic. The impact of a node in terms of the size of its out-component can be interpreted as a measure of centrality.

Another important network property is the set of nodes, from which a particular node $v_j, \in V$ can be infected. This is called *in-component* $c_{\text{in}}(v_j, \tau, t_0)$. The size of the in-component can be used as a measure for the *vulnerability* of a node [11]. Furthermore, we define the *out-degree* k_i^{out} and *in-degree* k_i^{in} of node v_i as the number of edges, which leave a node (selling events) or arrive at a node (buying events) aggregated over the whole observation time, respectively.

After this brief excursion to notions from network science connected to epidemiology, we will introduce additional aspects such as seed clusters, which contain nodes with similar invasion paths and spreading behavior, in the next section.

10.2.5 Invasion Path and Seed Clusters

If we consider a node v as infectious and if it has contact with susceptible nodes during its infectious period over some directed links e , the disease will be transmitted in the framework of the considered deterministic SIR model. If this node is the origin of the disease, we call it a seed. All nodes, which will be infected as time goes on, are part of one of its invasion paths at least. As defined in Sect. 10.2.2, an invasion path of length $n \in \mathbb{N}$ consists of a set of directed edges $\{e_0, \dots, e_{n-1}\} \subseteq E$ connecting a set of nodes $\{v_0, \dots, v_n\} \subseteq V$ at times $t_0 < \dots < t_{n-1}$.

The invasion paths depend strongly on the initial conditions given by the starting time t_0 and seeding node v_i . To explore the dependence of the spreading process on the initial conditions, we aim to identify similar spreading patterns. For this purpose, we use the unions Γ_1 and Γ_2 of invasion paths of two seeds at a fixed starting time t_0 to compute the similarity between them. We define the *Jaccard index* Θ_{12} as the relative overlap of the two sets measured by the number of their common nodes:

$$\Theta_{12} = \frac{|\Gamma_1 \cap \Gamma_2|}{|\Gamma_1 \cup \Gamma_2|}, \tag{10.1}$$

where $|\Gamma|$ denotes the number of nodes. In words, we calculate the fraction of the sizes of the intersection between the two node sets and their union. Consider Fig. 10.4, where a schematic example of two invasion paths $\Gamma_1 = [(v_1, v_3), (v_3, v_4), (v_4, v_6), (v_6, v_8)]$ and $\Gamma_2 = [(v_2, v_3), (v_3, v_4), (v_4, v_6), (v_6, v_9)]$ is shown in blue and red, respectively. We find a Jaccard index of $\Theta_{12} = |\Gamma_1 \cap \Gamma_2|/|\Gamma_1 \cup \Gamma_2| = 3/7$ as the relative overlap of the two paths.

Since the disease can in principle start from any node, we need to consider every node pair at a fixed starting time t_0 and evaluate the similarity of their invasion paths. If we calculate this overlap Θ_{ij} between every pair of potential seeds (v_i, v_j) , it is possible to construct a weighted and undirected network, which is called the *initial-condition similarity network* (see Fig. 10.5). In that network, nodes refer to invasion paths, which are determined by their seed. The strength of a link between two invasion paths Γ_i and Γ_j is given by the overlap $\Theta_{ij} \in [0, 1]$. This gives rise to

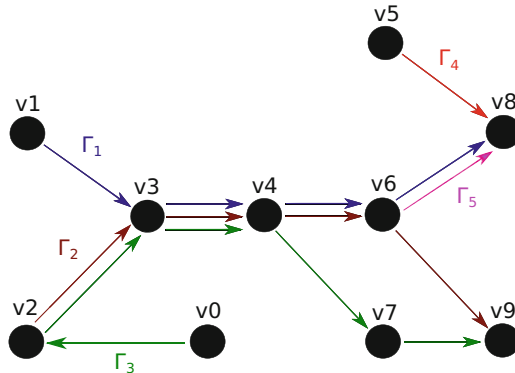
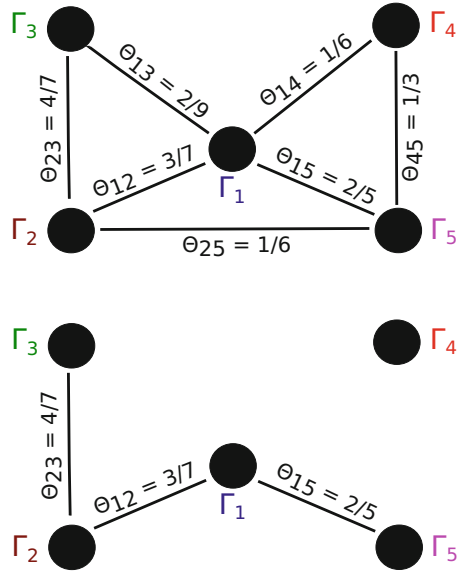


Fig. 10.4 Overlap between invasion paths $\Gamma_1 = [(v_1, v_3), (v_3, v_4), (v_4, v_6), (v_6, v_8)]$ (blue), $\Gamma_2 = [(v_2, v_3), (v_3, v_4), (v_4, v_6), (v_6, v_9)]$ (red), $\Gamma_3 = [(v_0, v_2), (v_2, v_3), (v_3, v_4), (v_4, v_7), (v_7, v_9)]$ (green), $\Gamma_4 = [(v_5, v_8)]$ (orange), and $\Gamma_5 = [(v_6, v_8)]$ (pink). The paths Γ_1 and Γ_2 have nodes $v_3, v_4,$ and v_6 in common, which results in a Jaccard index $\Theta_{12} = 3/7$. The value $\Theta_{23} = 4/7$ is found for Γ_2 and Γ_3 , but not for Γ_1 and Γ_3 , which is $\Theta_{13} = 2/9$. The connection of two nodes v_5 and v_6 to the same final node v_8 with the paths Γ_4 and Γ_5 can be seen as a triadic motif for a relatively high Jaccard index of $\Theta_{45} = 1/3$. The Jaccard index between Γ_1 and Γ_4 is $\Theta_{14} = 1/6$

Fig. 10.5 *Top*: the undirected and weighted similarity network according Fig. 10.4 based on different initial conditions emerges out of the overlap of the respective invasion paths (only non-zero overlap shown). The network is weighted by the overlap (Jaccard index). *Bottom*: exemplary depiction of the emergence of cluster if a threshold of $\Theta_{th} \in (1/3, 2/5]$ is applied. In this example one cluster contains the seeding nodes $v_1, v_2,$ and v_6 of the invasion paths $\Gamma_1, \Gamma_2, \Gamma_3,$ and Γ_5 . A second cluster refers to just one seeding node v_5 of the invasion path Γ_4



an all-to-all connected network. If we apply a threshold Θ_{th} to the edge weights in that network and disregard smaller ones, the resulting network disintegrates and we obtain subsets of nodes with similar invasion paths Γ . This thresholding can lead to disconnected subgraphs and we call their connected components *clusters*. The bottom panel of Fig. 10.5 depicts the two clusters obtained for invasions paths of Fig. 10.4 for a threshold of $1/3 < \Theta_{th} \leq 2/5$. We define the size of a cluster by the number of seed nodes at the origin of the invasion paths that lead to the formation of that cluster.

Note that it is not required that all nodes in the same cluster are connected with each other by an invasion path. If two nodes $v_i \subseteq V$ and $v_j \subseteq V$ belong to the same cluster, it simply means that there is a set of other nodes $\{v_1, v_2, \dots, v_p\} \subseteq V$ that have an overlap $\Theta_{i1}, \Theta_{i2}, \dots, \Theta_{pj}$ greater than the threshold, but not necessarily that the overlap Θ_{ij} is greater than Θ_{th} . See, for instance, the Jaccard index for the two pairs of invasion paths (Γ_1, Γ_2) and (Γ_2, Γ_3) in Fig. 10.4. The respective overlaps are $\Theta_{12} = 3/7$ and $\Theta_{23} = 2/3$, although the Jaccard index between Γ_1 and Γ_3 is smaller: $\Theta_{13} = 1/4$. It is also important to note that these different clusters evolve over time. Invasion paths, from which clusters are computed, refer to the same starting time t_0 . Since an invasion path depends on t_0 , the clusters are time dependent, too. The robustness of the clusters will be the topic of Sect. 10.3.6.

Based on our numerical simulations, we measure the overlap of every possible pair of seeds to group nodes in clusters. Note that geographical proximity is not a necessary initial condition for this network-based procedure. Therefore, two nodes that have a great geographical distance can be part of the same cluster because of their similar invasion paths.

Many nodes considered as seeds for an outbreak lead to short infection paths [8, 19], but high Jaccard indexes. See, for instance, the triadic motif depicted in Fig. 10.4. Two premises (node v_5 and v_6) are just connected to the same dead end (node v_8), that is most likely, a slaughterhouse, which yields an overlap of $1/3$. To avoid these misleading high values, we consider only infection paths that contain at least 10 nodes. Both of these restrictions still lead to the emergence of non-trivial clusters of initial conditions, that is, other than single, isolated nodes. Nodes with an out-component $|c_{\text{out}}| \geq 10$ nodes have a high spreading potential and usually belong to a part of the network that is called *giant in-component* (GIC) or *giant strongly connected component* (GSCC) [19]. The latter is defined as a set of nodes, in which any pair of nodes is connected by a directed, time-respecting path. The GIC consists of an additional set of nodes that are not part of the GSCC, but are connected to the GSCC via time-respecting paths.

In the next section, we will present the methodology to compare clusters obtained for different starting times. This will lead to the analysis of the robustness of the clusters.

10.2.6 Measurement of the Robustness of the Clusters Over Time

The method described in the last section leads to a partition $\{C_1(t_0), C_2(t_0), \dots\}$ of different clusters based on the similarity of invasion paths with starting time t_0 [8]. We will consider only the M largest clusters in the following. To measure the robustness of a cluster $C_i(t_0)$ at a later time t , we compute the relative change of the cluster size in comparison to any of the M largest clusters:

$$\rho_{ij}(t_0, t) = \frac{|C_i(t_0) \cap C_j(t)|}{|C_i(t_0)|}. \quad (10.2)$$

This $M \times M$ matrix $\{\rho_{ij}\}$ represents in every row $\rho_i(t_0, t)$ the fraction of nodes of $C_i(t_0)$ present in the cluster $C_j(t)$, which is computed according to invasion paths starting at time t . If the cluster $C_i(t_0)$ persists or becomes part of one larger cluster, the row $\rho_i(t_0, t)$ will have one entry equal to 1, and all others will be zero. Similarly, when all nodes of $C_i(t_0)$ are redistributed over the M largest clusters, the sum over the i -th row will be unity. Following this intuition, we define a robustness measure by $\sigma_i(t_0, t) = \sum_{j=1}^M \rho_{ij}(t_0, t)$. This quantity will be smaller than 1, if some nodes of cluster $C_i(t_0)$ are not present in any of the M largest clusters at time t . Note that for $t_0 \neq t$, the matrix $\{\rho_{ij}\}$ does not need to be symmetric, because the M largest clusters might differ considerably in size and node set for different times.

For further quantitative analysis, we compute the conditional entropy of the i -th cluster defined as

$$H_i(t_0, t) = \frac{\sum_{j=1}^M \rho_{ij}(t_0, t) \log[\rho_{ij}(t_0, t)]}{\sigma_i(t_0, t) \log \frac{\sigma_i(t_0, t)}{M}}. \quad (10.3)$$

The entropy quantifies the redistribution among the M largest clusters at time t in comparison to an earlier time t_0 . The entropy vanishes ($H_i = 0$), if $C_i(t_0)$ is also a cluster at time t . Apart from this extreme case of stationary clusters, the minimum entropy is given by $H_{\min, i}(t_0, t) = [1 - \log(M)/\log(\sigma_i)]^{-1}$, if all nodes of $C_i(t_0)$ are found in exactly one cluster $C_k(t)$ at time t except a fraction $(1 - \sigma_i)$ of them that do not belong to any of the M largest clusters anymore. This configuration yields: $\rho_{ik}(t_0, t) = \sigma_i(t_0, t)$ and $\rho_{ij}(t_0, t) = 0$ for $j \neq k$ and we find indeed

$$H_i(t_0, t) = \frac{1}{1 - \frac{\log(M)}{\log[\sigma_i(t_0, t)]}}. \quad (10.4)$$

In case that all nodes of $C_i(t_0)$ are equally distributed over the M largest clusters or if no node of $C_i(t_0)$ is anymore found in one of them, i.e., $\rho_{ij}(t_0, t) = 0$ and thus $\sigma_i(t_0, t) = 0$, we have $H_i = 1$ [8].

10.3 Results for the German Pig-Trade Network

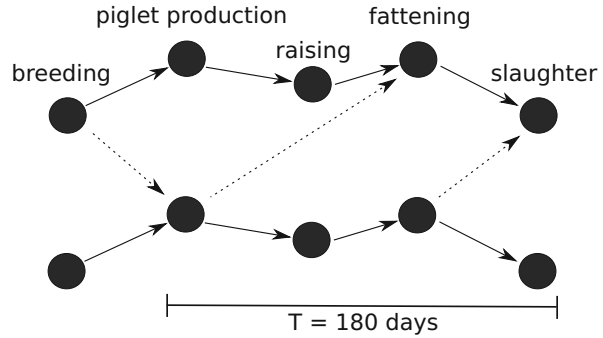
This section provides an overview of the characteristics of the considered livestock-trade network in Sect. 10.3.1. Then, we will apply the deterministic SIR model to this particular time-varying network (cf. Sects. 10.2.1 and 10.2.3) and thereby calculate different seed clusters (Sect. 10.3.3). In Sect. 10.3.4, we present different ways to identify sentinel nodes and finally, we will exploit the underlying mechanism to design a detection scheme for possible outbreaks in Sect. 10.3.5.

10.3.1 From Data to Network

In the present study, anonymized data on pig-trade movements are analyzed in collaboration with the Friedrich-Loeffler-Institut. The dataset spans the period from January 1, 2011 to December 31, 2014 and is extracted from the *HI-Tier* database.² Within this 4-year period, each German pig holding recorded the number

²Bayerisches Staatsministerium für Ernährung, Landwirtschaft und Forsten (StMELF). *Herkunftssicherungs- und Informationssystem für Tiere*, available from: www.hi-tier.de

Fig. 10.6 Schematics of the production chain forming the pig trade [19]. The *dashed arrows* refer to deviations from this chain, which are present in the data, because the network contains more edges than the minimal production-chain forest



of pigs of every purchase so that we can infer the corresponding movements of livestock within Germany from the dataset. Note that only the aggregated trading volume (batches) is recorded in the database. The available resolution for this time-dependent network is 1 day. Farmers are required to register each transaction within 7 days, which sets the upper bound for the uncertainty of data accuracy. Every trade record includes the premises of origin and destination via anonymized IDs, the date, and the number of delivered pigs. From a graph-theoretical perspective, the dataset can be interpreted as a dynamical network, where nodes, directed edges, and edge weights correspond to farms, trading events, and the number of traded animals, respectively. For a detailed, time-resolved analysis of this dataset, see Ref. [19].

Figure 10.6 depicts an illustration of the production chain of the underlying farming system, which is composed of different farm types. Different stages of the production chain refer to breeding, piglet production, raising, fattening, and slaughter. In addition, trades can also be mediated by brokers. These are part of the recorded transaction in the database, but do not own a farm themselves. The lifetime of a pig is 180 days, which sets the timescale of the total production chain. Each farm has an anonymized ID from 0 to 97,980. The considered period of 4 years contains more than 6.3 million movements with a total trade volume of 615 million pigs. In the year 2014, 28 million pigs have been bred. This implies that each animal is traded roughly five times along the product chain indicating a high specialization and different farm types. Some basic characteristics of the time-aggregated network are summarized in Table 10.1.

Next, we will present the main results of our numerical simulations.

10.3.2 Outbreak Duration and Size

In our simulations, we consider all nodes as seed and choose the first Monday in each month as starting time t_0 or, if it is a holiday, we use the following working day. In previous studies, these days have been found to show the highest trade activity in the network and are therefore the days for which the largest outbreak size can be

Table 10.1 Standard network properties of the static, i.e., time-aggregated, German pig-trade network

Property	Value
Number of nodes	97,980
Number of edges	315,333
Edge density	3.2×10^{-5}
Size of GSCC	28 %
Diameter	18
Average shortest path length	5.5
Path density	0.24
Median and average trade volume of a premises	
on a day	32.0, 113.4
in a month	88.0, 355.0
in a year	280.0, 2587.6

Diameter and shortest path length are computed for the giant strongly connected component (GSCC)

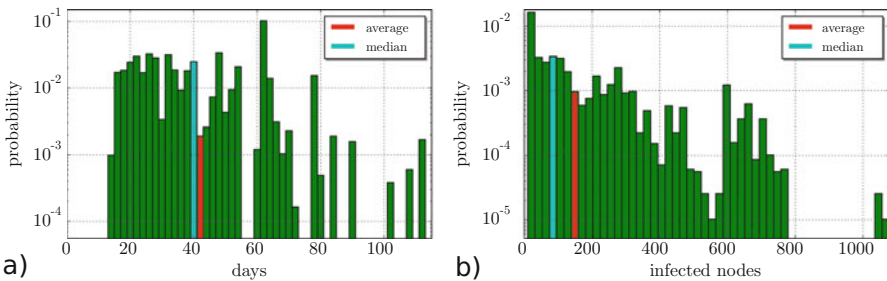


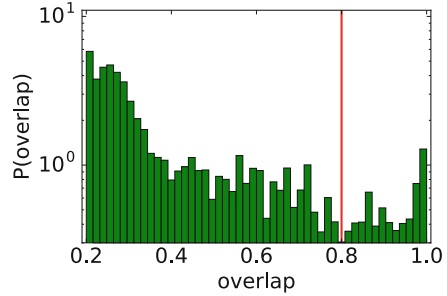
Fig. 10.7 Panel (a): Normalized distribution for the outbreak duration. Duration for a fixed starting time averaged over all possible seed nodes (red): 41.6 days; median (cyan) 40 days. Panel (b): Normalized distribution of outbreak size. Average size (red): 149 nodes; median (cyan): 84 nodes. All nodes with an out-component $|c_{\text{out}}| \geq 10$ are considered as seed. The starting times t_0 are chosen as the first Monday in each month or, if it is a holiday, we use the following working day

expected. In this sense, they cause the most harm to the network [19]. Since we are interested in nodes that can trigger outbreaks of a considerable size, we restrict the pool of potential sentinels to nodes with an out-component $|c_{\text{out}}| \geq 10$.

In Fig. 10.7a, one can see the normalized distribution that an outbreak lasts a certain number of days in the network. Panel (b) shows the normalized distribution of the size of an outbreak. Average and mean values are also indicated by red and cyan bars, respectively. We find that the average outbreak lasts 41.6 days, during which 149 nodes are infected.

Using a deterministic SIR model on a network to explore a worst-case scenario (cf. Sects. 10.2.1 and 10.2.3), we find that all outbreaks eventually come to an end in our simulations. As we show later in Sect. 10.3.3 we observe outbreak durations of around 60 days for the considered infectious period of 7 days. This

Fig. 10.8 Distribution of overlap of invasion paths calculated based on the Jaccard index. A minimum is found at a value of $\Theta = 0.8$ (red line), which we choose as a threshold to define clusters



is much shorter than the 4 years observation time of the network. In other words, we measure the complete out-components. Therefore, we conclude that we capture the entire dynamical process by the proposed modelling framework. See Ref. [13] for a discussion of finite observation periods for a temporal network.

In the next section, we demonstrate how clusters introduced in Sect. 10.2.5 can be constructed from the numerical results.

10.3.3 Seed Clusters

Our aim is to design a surveillance scheme that requires only a small number of nodes. For this purpose, we identify similar spreading patterns and partition the network in functional clusters. In our simulations, we consider every node in the network with $|c_{\text{out}}| \geq 10$ as starting point of an outbreak and consider different starting times as well. Next, however, we discuss the results obtained for the starting time $t_0 = \text{January 3, 2011}$, as an example.

Figure 10.8 shows the distribution of the Jaccard index. As mentioned above, it describes the overlap of different invasion paths. Therefore, a matrix Θ with elements Θ_{ij} will be calculated out of invasion paths i and j . For the cluster calculation, we consider just overlaps greater than the threshold value $\Theta_{\text{th}} = 0.8$, which corresponds to the minimum in the distribution of overlaps (red line). Therefore, all overlaps with a larger Jaccard index are considered in the following. For further information on this subject see Refs. [19, 24]. This choice coincides with the threshold reported in Ref. [8].

Figure 10.9 shows a ranking of cluster sizes for this threshold (red dots) and the cumulative cluster-size distribution (blue triangles). We find that there are many small clusters. More than half of the clusters consist of at most ten seed nodes. The largest cluster is formed by 284 seed nodes. In the following, we consider only the largest 18 clusters. They contain at least 79 seed nodes (red horizontal line) and together cover 31.7% of all seed nodes that can be grouped in clusters (blue horizontal line).

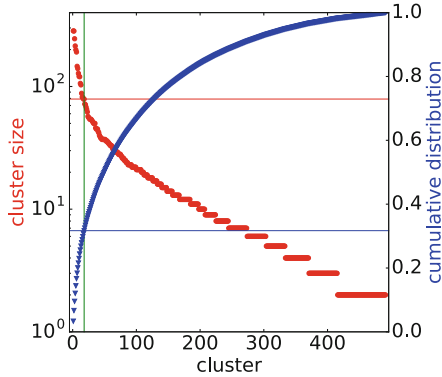


Fig. 10.9 Ranking of cluster size (*red dots*). For the initial time $t_0 = \text{January 3, 2011}$ and the threshold $\Theta_{th} = 0.8$, we find 491 clusters. The *blue triangles* refer to the cumulative distribution of cluster sizes. The *green line* marks the 18 largest clusters. The *blue line* marks the cumulative cluster distribution of the 18 largest cluster (*green vertical line*). The size of the 18th largest cluster is indicated by the *red line*. There are in total 8490 seed nodes in the observed 491 clusters

Next, we compute the outbreak size triggered from each cluster. It is given by the number of nodes, which can be reached by an infection starting at the seed nodes that form the respective cluster. We call the corresponding percentage *network coverage*. Furthermore, we calculate the power of each cluster to detect an outbreak. This is quantified by the percentage of outbreaks (*detection probability*) that involve any node of the respective cluster. Table 10.2 shows the cluster size, the network coverage (in %), and the detection probability (in %). In general, we find that the numbers fluctuate in both the network coverage and detection probability. For example, there are clusters whose invasion paths appear to be rather isolated in the network, which results in a small detection probability. Other clusters that do not necessarily consist of a large number of seed nodes have a much higher probability to detect an outbreak. For comparison to our findings, consider the results on the 18 largest cluster of the Italian cattle-trade network presented in Ref. [8].

Figure 10.10 depicts numerical results for the 18 largest clusters, which are computed via the Jaccard coefficient of all invasion paths starting at $t_0 = \text{January 3, 2011}$. For each cluster, the time series of the prevalence is shown for every node of the cluster considered as seed (*red curves*). The black curve refers to the average of all prevalence curves originating from the cluster. The blue curves correspond to the size of the epidemic measured by the number of recovered nodes and the black curve shows again the average.

In general, all time series exhibit a qualitatively similar behavior: an increasing number of infections leading to a peak, beyond which the curve decreases again and the outbreak eventually terminates. These qualitative features are in line with the expected dynamics of the SIR model. All premises within one cluster show a similar spreading pattern, which means that for a given initial condition of seed

Table 10.2 Cluster size, network coverage (in %), and detection probability (in %) of the 18 largest clusters

Cluster	Size	Network coverage	Network coverage of nodes with $ c_{\text{out}} \geq 10$	Detection probability	Cumulative detection probability
1	284	0.5	3.2	38.2	38.2
2	283	0.9	5.8	3.4	38.7
3	245	1.6	9.9	13.8	43.9
4	214	1.3	8.1	10.8	47.7
5	199	0.7	4.4	10.0	49.6
6	191	0.4	2.8	4.0	50.2
7	146	0.6	3.9	4.5	50.5
8	140	0.5	3.0	25.2	53.7
9	128	0.7	4.7	19.1	56.0
10	121	0.8	4.9	25.4	57.9
11	120	0.4	2.8	23.2	58.4
12	106	0.8	5.0	14.7	59.1
13	103	0.3	1.8	0.9	59.2
14	88	0.2	1.2	43.4	61.2
15	82	0.2	0.9	26.0	65.0
16	81	0.2	1.1	0.5	65.1
17	79	0.2	1.0	0.2	65.1
18	79	0.3	1.7	0.001	65.1

Starting time $t_0 = \text{January 3, 2011}$

and time (v_i, t_0) the number of infected premises is roughly the same. We also find that the timing of the peak does not vary much between the different clusters. There are, however, considerable quantitative differences between prevalence curves of different clusters. Consider, for instance, the duration of an outbreak, the peak number of infected nodes (maximum prevalence), or the total number of infected nodes. The mean outbreak duration $\langle \delta_i \rangle$ in the i -th cluster and we obtain that it varies between 30 and 76 days. The average duration of infection for all 18 largest clusters is 55 days.

Recall that each cluster refers to a set of seed nodes. Since the out-component of a cluster is given by the nodes in the network that can be infected from its seeds, the out-component can be larger than the size of the cluster itself, that is, the number of its seed nodes. For some clusters (cf. cluster 3 or 4), even the peak of the prevalence is larger. In order to design an efficient surveillance protocol, we have to make sure that the infection will be detected very early before the outbreak reaches large parts of the potential out-component.

After the construction of clusters of similar invasion paths, we will show in the next section, how this can be used to select a small number of sentinel nodes for surveillance of the whole network.

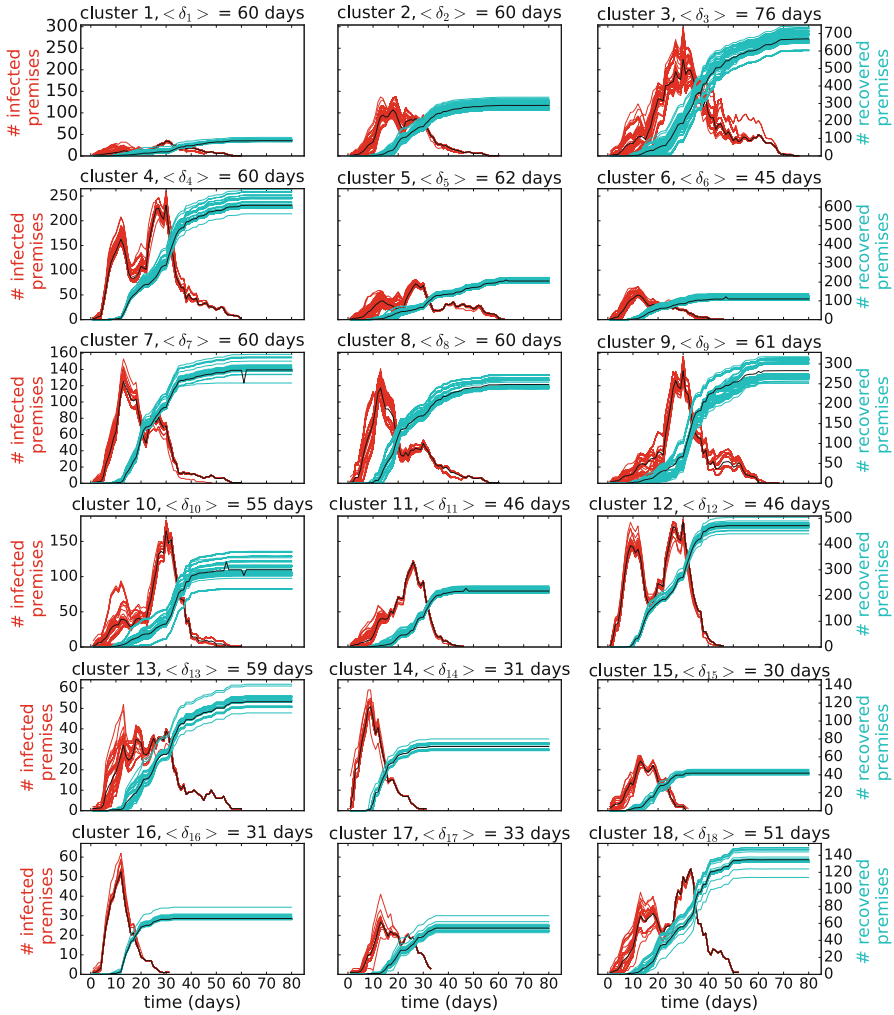


Fig. 10.10 SIR dynamics on the German pig-trade network for the 18 largest clusters. The *red* curves refer to the time series of the number of infected nodes for all nodes in the respective cluster taken as seed. The *blue* curves represent the number of recovered nodes over time. The *black* curves show their average of each cluster. δ_i is the mean duration of outbreaks in the i -th cluster. For the starting time $t_0 =$ January 3, 2011, the mean outbreak mean duration of all nodes in the 18 largest clusters is $\delta = 55$ days. Parameter: infectious period $\tau = 7$ days

10.3.4 Sentinel Nodes

For an identification of potential sentinel nodes, we propose two approaches and evaluate them in terms of detection probability, fast detection, and minimum number of infected nodes until detection. The selection of an optimal, that is, minimum, set is an open question related to set cover problems in combinatorial geometry and has recently been linked to optimal percolation. See Ref. [26] and references therein. This family of problems is known to be NP hard. The methods used here serve as heuristics for the exact problem.

The first protocol consists of the following strategy: Choose the node of largest or second-largest sum of in- and out-degree of each cluster. This results in 18 or 36 sentinel nodes, respectively. We conjecture that these hubs are good candidates for the following reason: Hubs are known to be infected at an early stage of outbreaks on scale-free networks and thus key players for the spreading [25]. The set of sentinel nodes will be most likely part of the GSCC, because they need to receive and send livestock from/to many different nodes to meet the selection criterion. Therefore, they are expected to have a large out-component.

Figure 10.11 shows, how in- and out-degree varies in the two largest clusters. Nodes with the largest sum of in- and out-degree can be found on the *upper, right side* in the figures. The candidate nodes to serve as sentinels (*red square and diamond*) are well separated from the rest of the seed nodes that form the respective cluster (*green dots*).

As a second approach, we apply the algorithm introduced in Sect. 10.2.3 to infect all nodes of the network at the starting time t_0 and then rank them according to how often each node appears in an invasion paths. This way, we exploit the size $|c_{in}|$ of the in-component, which is equivalent to the vulnerability of a node. The set of sentinel nodes is given by the top ranked nodes.

Following Ref. [8], we are interested in the nodes that are part of the outcomponent of a large number of nodes. These nodes will be hit by many epidemics

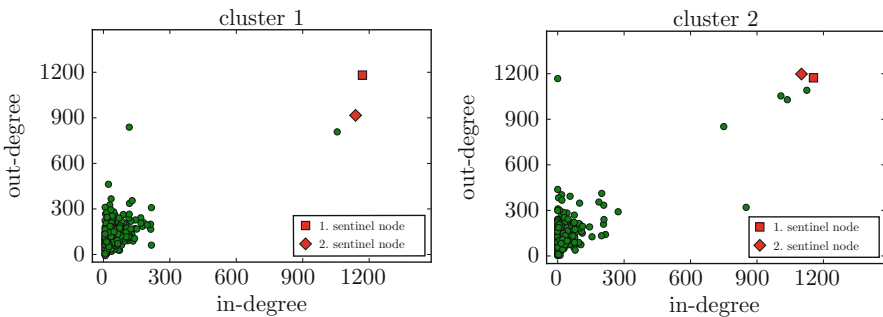


Fig. 10.11 In- and out-degree for all seed nodes of the two largest clusters. We choose sentinel nodes based on the largest sum of in- and out-degree. These nodes can be found in the upper, right part of the panels

starting at different nodes. Therefore, nodes that have a high $|c_{in}|$ are more vulnerable than nodes with smaller in-component. Some of these nodes, however, are slaughterhouses and are found at the end of the production chain. They are not suitable as sentinel nodes for early disease detection, because the damage of an outbreak would have been done already and could not be contained. These nodes can easily be excluded, because they have an out-degree $k_i^{out} = 0$. In addition, sentinel nodes should have a significant spreading potential. Therefore, we consider only nodes as sentinels that at the same time have an out-degree of $k_i^{out} \geq 5$. We choose 18 of these, which we call most infected nodes, and take those 18 most infected nodes together with the 18 nodes of the largest sum of in- and out-degree in each cluster to define the set of sentinel nodes. In an additional protocol, we also consider the 36 nodes with the largest in-component for comparison.

Next, we will investigate, how the different protocols to select sentinel nodes perform in terms of detection probability, detection time and how many nodes become infected until detection.

10.3.5 Disease Detection with Sentinel Nodes and Results

Applying different protocols to select sentinel nodes as introduced in Sect. 10.3.4, we calculate the probability to detect an outbreak for every starting day. See Fig. 10.12, where panel (a) depicts this detection probability based on 18 (blue

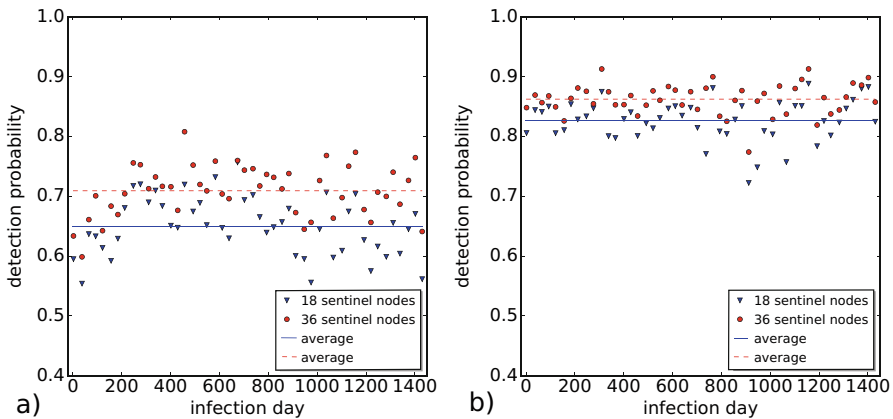


Fig. 10.12 Detection probability of 18 (blue triangles) and 36 (red dots) sentinel nodes based on (a) largest and second-largest sum of in- and out-degree out of each cluster, (b) 18 nodes based on highest vulnerability (blue triangles) and additionally 18 nodes out of each cluster with the largest sum of in- and out-degree (red dots). The mean value is depicted by the solid and dashed lines, respectively: (a) 65% and 70.9%; (b) 82.7% and 86.2%. Each dot refers to the starting time t_0 (day of initial infection), which is chosen as the first Monday in each month or, if it is a holiday, we use the following working day. All nodes with an out-component $|c_{out}| \geq 10$ are considered as seed

Table 10.3 Detection probability, time until detection, and number of infected nodes until detection for the considered selection protocols to determine the set of sentinel nodes

Protocol	Detection probability	Detection time / days	Outbreak size
18 nodes based on sum of in- and out-degree	65.1%	12.5	43.6
36 nodes based on sum of in- and out-degree	71.0%	10.5	31.2
18 nodes based on highest vulnerability	82.7%	9.0	22.2
36 nodes based on highest vulnerability	83.1%	8.9	21.4
18 nodes based on highest vulnerability and 18 nodes based on in- and out-degree	86.2%	7.8	15.4

triangles) and 36 (red dots) sentinel nodes with the largest sum of in- and out-degree in each cluster, respectively. The blue solid and red dashed lines represent the average probability of a disease detection, which is 65% and 70.9%, respectively. Similarly, Fig. 10.12b depicts the protocol, where 18 sentinel nodes are selected based on the highest vulnerability (blue triangles) or additional 18 nodes with the largest sum of in- and out-degree for each cluster (red dots). This results in average detection probabilities of 82.7% and 86.2%, respectively.

Table 10.3 provides an overview of the obtained results for all proposed selection schemes. Considering twice as many sentinel nodes improves all considered quantities: a higher detection probability, a shorter detection time, and a smaller number of infections until detection. An earlier detection by 2 days results in a reduction of the epidemiological impact by about 25%. This is in agreement with findings of Ref. [8]: The information provided by the sentinel nodes is meaningful as long as the detection occurs rather early during an outbreak. This result is not only important for surveillance, but also for identifying the initial outbreak location, because it enhances the chances to trace the invasion path back to the seed. An even stronger improvement can be obtained, if the selection of sentinels is based on the highest vulnerability. This advantage can be further improved in combination with nodes of largest in- and out-degree. Then, the detection probability is larger than 86% with an average detection time of 7.8 days and an average outbreak size of 15.4 nodes. This gives a larger benefit than choosing 36 nodes with highest vulnerability, for example.

10.3.6 Cluster Development in Time

In this section, we will investigate the temporal stability of the clusters given their importance in the identification of sentinel nodes. Consider a pair of seed nodes, which are a part of the same cluster at one instance in time. They might, however, not belong to the same or any other cluster at a later time. In detail, we consider the development of the 18 largest clusters. Based on two partitions of clusters at different times, that is, $P(t_0) = \{C_1(t_0), C_2(t_0), \dots, C_{18}(t_0)\}$ and $P(t) = \{C_1(t), C_2(t), \dots, C_{18}(t)\}$, we calculate the relative overlap via $\rho_{ij} = |C_i(t_0) \cap C_j(t)|/|C_i(t_0)| \in [0, 1]$. We expect $\rho_{ij} = 0$, if the clusters $C_i(t_0)$ and $C_j(t)$ do not have a single node in common, and unity, if clusters persist or expand.

Figure 10.13 shows the matrix $\{\rho_{ij}\}$ for different times. Trivially, we find the identity matrix for $t = t_0$ due to disjoint clusters corresponding to disconnected subgraphs. The clusters evolve and change their nodes over time. For subsequent times t , nodes belonging at t_0 to the same cluster can be redistributed in multiple clusters, which might consist of additional nodes, or might not be a part of any other subsequent cluster. One can see that for times $t = 7, t = 14$, and $t = 21$, there is no significant overlap anymore. This can also be seen in the bottom panels, which show a distribution of the overlap between the 18 initial clusters and the 18 subsequent clusters.

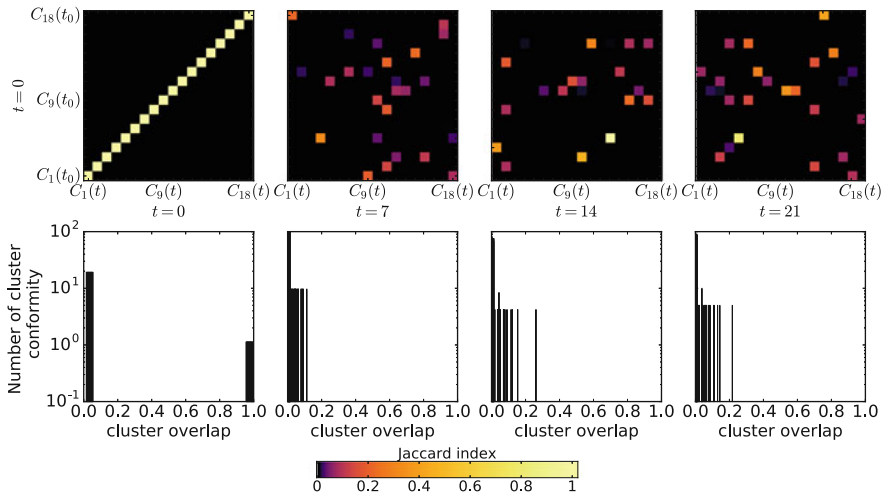


Fig. 10.13 Change of the cluster partitions. The color code refers to the relative overlap of the 18 largest clusters at different times in comparison with $t_0 = 0$ corresponding to January 3, 2011. The top left figure shows the comparison from the cluster $t_0 = 0$ with itself, that is, a trivial perfect overlap along the diagonal. The lower four figures show the distribution of the cluster overlap at respective times

How rapidly and to which extent the node set of the clusters changes can be calculated with the entropy function (cf. Sect. 10.2.6), which will be the topic of the next section.

10.3.7 Entropy of Clusters

In order to quantify the robustness of a cluster, we compute the conditional entropy $H_i(t_0, t)$ of each cluster $C_i(t_0)$ given by Eq. (10.3) comparing different times. This provides insight, how much the nodes of a cluster of time t_0 are redistributed among the M largest clusters at a later time t . Recall that $H_i(t_0, t)$ vanishes, if the set of seed nodes forming a cluster does not change over time. We have $H_i(t_0, t) = 1$, if no node is part of any of the M largest clusters at time t . For comparison, we also calculate the minimum entropy H_{\min} , which corresponds to the case that a fraction of nodes of a cluster still form a cluster and the rest does not belong to any of the M largest clusters.

Figure 10.14 depicts the entropy $H(t_0, t)$ (red dots), the minimum entropy H_{\min} (blue circles), and the difference between them (yellow bar) for exemplary clusters 4 and 15. The difference $H(t_0, t) - H_{\min}$ can be interpreted as the robustness of the cluster. A cluster is more robust, if that difference is smaller (and the entropy is not equal to one as in cluster 15), because many nodes from the starting time are still found in one of the 18 largest clusters. Cluster 4, for instance, remains stable over the first 30 weeks.

In cluster 15 we can see that $H = 1$ at 11 different times due to the peculiarities of the cluster development. Cluster 15 has such a high entropy for many weeks, because its nodes do not belong to any of the 18 largest clusters at these times. In

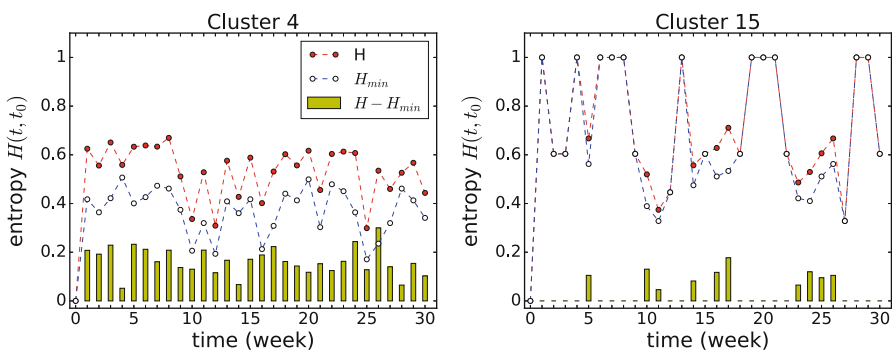


Fig. 10.14 Entropy $H(t_0, t)$ of cluster 4 and 15 over time (red dots), minimum entropy (blue empty dots), and their difference (yellow bars)

contrast to the fluctuating entropy of cluster 15, cluster 4 is quite stable over the first 30 weeks. The time-resolved entropy of the 16 largest clusters is added in the appendix as Figs. 10.15 and 10.16 for comparison.

10.4 Conclusion and Outlook

We have applied the concept of sentinel nodes proposed in Ref. [8] to the German pig-trade network. For this purpose, we have implemented a deterministic susceptible-infected-recovered model and computed invasion paths for different seed nodes and starting times. Our results have shown that the approach of seed clusters, which was initially applied to the Italian cattle-trade network, can indeed be transferred to the considered dataset. The clustering method can be used to design an optimized surveillance system and allows for rapid and efficient containment strategies.

Large delays between the start of the outbreak and its detection results in larger outbreak sizes. After a few days, the outbreak often reaches a number of nodes far greater than the size of the cluster (number of seed nodes identified to yield a similar outbreak pattern), where it started. Then, the disease is able to infect large fractions of the network. In addition, high temporal variability and the complex nature of the network make identification of the possible origin of the outbreak a particularly difficult task. Recently, some approaches using the concept of effective distance have been proposed [27, 28].

Following a network-based analysis, we have identified farms that are at a high risk of becoming infected and subsequently promote the spreading the disease further. We have conjectured that these farms are good candidates to detect an outbreak early in its evolution. Therefore, we have chosen one or two nodes with the largest sum of in- and out-degree for each cluster. In addition, we have also considered farms that have the largest in-component in the network. These nodes are very vulnerable, because they can be infected from a large number of outbreak origins. We have found out that these farms, when considered as sentinel nodes, have the highest detection probability and the shortest detection time. As a consequence, the outbreak size before detection can be considerably reduced. This can be further improved by combining both selection protocols.

Acknowledgements This work was supported by *Deutscher Akademischer Austauschdienst (DAAD)* within the PPP-PROCOPE scheme. FS, AK, and PH acknowledge funding by *Deutsche Forschungs- gemeinschaft* in the framework of Collaborative Research Center 910. The work is partially funded by the EC-ANIHWA Contract No. ANR-13-ANWA-0007-03 (LIVEepi) to VC.

A.1 Appendix

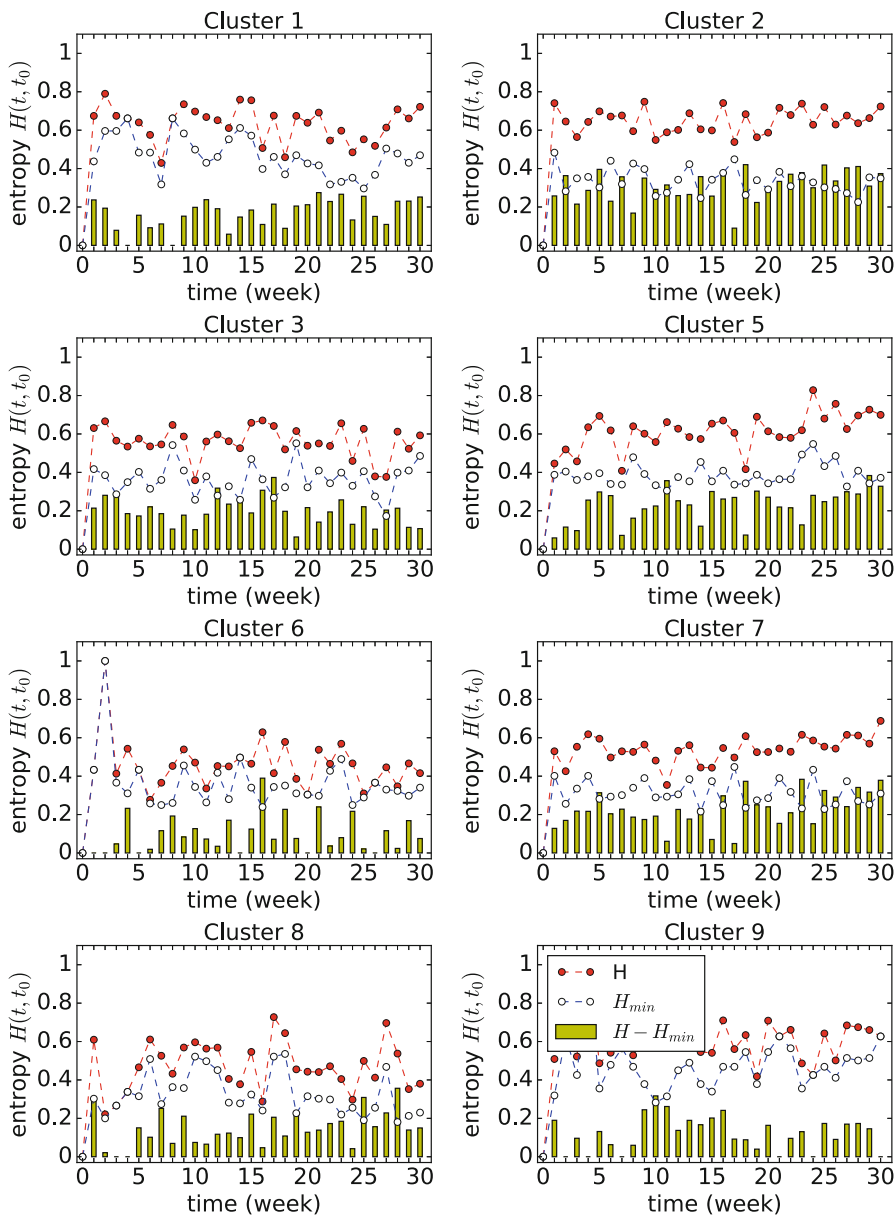


Fig. 10.15 Entropy $H(t_0, t)$ of the eight largest clusters not mentioned in the main text (for cluster 4 see Fig. 10.14) over time (red dots), minimum entropy (blue empty dots), and their difference (yellow bars)

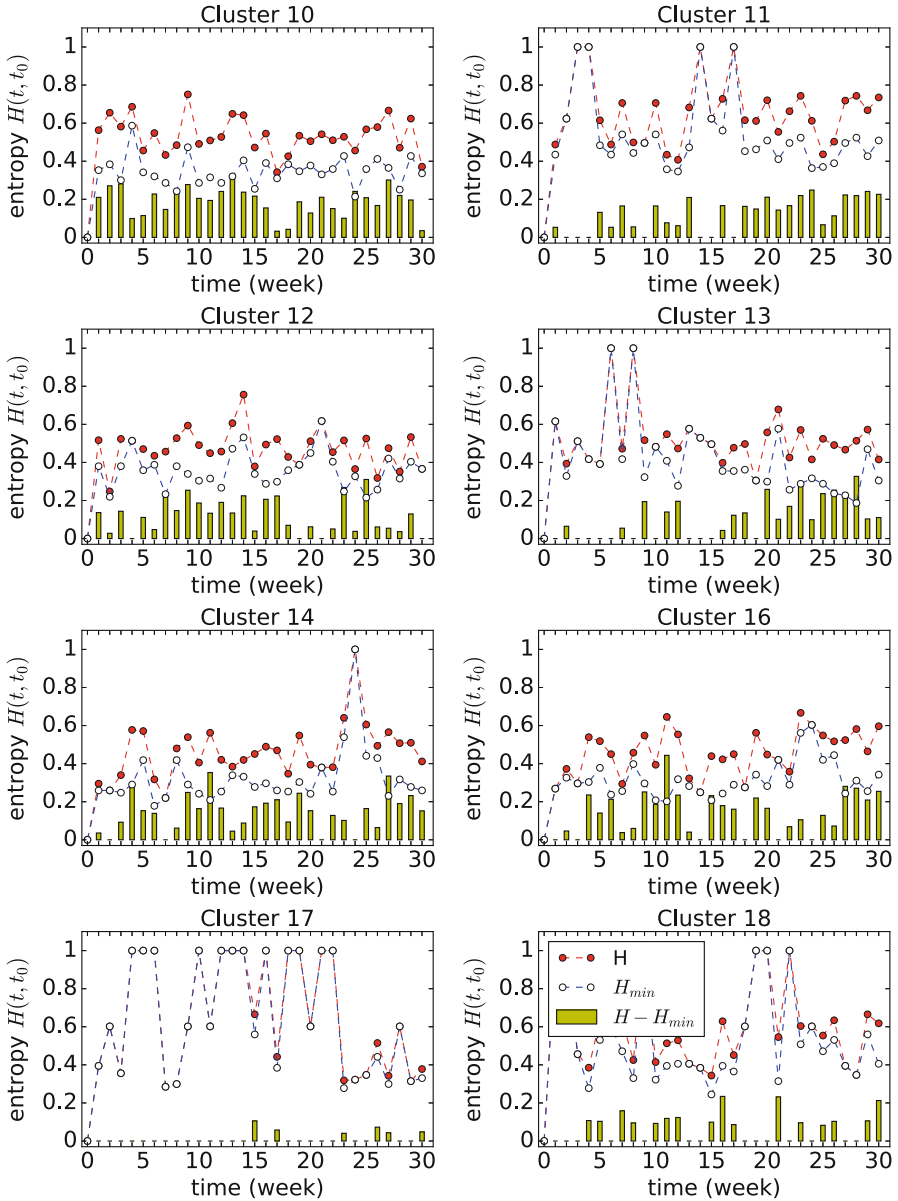


Fig. 10.16 Entropy $H(t_0, t)$ of the clusters 9–18 except for cluster 15, which is shown in Fig. 10.14, over time (red dots), minimum entropy (blue empty dots), and their difference (yellow bars)

References

1. Keeling, M.J., Rohani, P.: *Modeling Infectious Diseases in Humans and Animals*. Princeton University Press, Princeton (2008)
2. Funk, S., Gilad, E., Watkins, C., Jansen, V.A.: *Proc. Natl. Acad. Sci.* **106**, 6872 (2009)
3. Anderson, R.H., May, R.M.: *Infectious Diseases of Humans: Dynamics and Control*. Oxford University Press, Oxford/New York (1992)
4. Murray, J.D.: *Mathematical Biology: I. An Introduction Interdisciplinary Applied Mathematics*. Springer, New York (2002)
5. Diekmann, O., Heesterbeek, H., Britton, T.: *Mathematical Tools for Understanding Infectious Disease Dynamics*. Princeton University Press, Princeton (2013)
6. Fritzsche, J., Teuffert, J., Greiser-Wilke, I., Staubach, C., Schlüter, H., Moennig, V.: *Vet. Microbiol.* **77**, 29 (2000)
7. Hethcote, H.W.: *SIAM Rev.* **42**, 599 (2000)
8. Bajardi, P., Barrat, A., Savini, L., Colizza, V.: *J. Roy. Soc. Interface.* **9**, 2814 (2012)
9. Koher, A., Lentz, H.H.K., Hövel, P., Sokolov, I.: *PLoS One.* **11**, e0151209 (2016)
10. Newman, M.E.J.: *Phys. Rev. E.* **66**, 016128 (2002)
11. Korschake, M., Lentz, H.H.K., Conraths, F., Hövel, P., Selhorst, T.: *PLoS One.* **8**, e55223 (2013)
12. Vernon, M.C., Keeling, M.J.: *Proc. R. Soc. Lond. B. Biol. Sci.* **276**, 469 (2009)
13. Holme, P., Saramäki, J.: *Phys. Rep.* **519**, 97 (2012)
14. Casteigts, A., Flocchini, P., Quattrocioni, W., Santoro, N.: *Int. J. Parallel Emergent Distrib. Syst.* **27**, 387 (2012)
15. Holme, P.: *EPJ B.* **88**, 1 (2015)
16. Bajardi, P., Barrat, A., Natale, F., Savini, L., Colizza, V.: *PLoS One.* **6**, e19869 (2011)
17. Rocha, L.E., Liljeros, F., Holme, P.: *PLoS Comput. Biol.* **7**, e1001109 (2011)
18. Valdano, E., Ferreri, L., Poletto, C., Colizza, V.: *Phys. Rev. X.* **5**, 021005 (2015)
19. Lentz, H.H.K., Koher, A., Hövel, P., Gethmann, J., Sauter-Louis, C., Selhorst, T., Conraths, F.: *PLoS One.* **11**, e0155196 (2016)
20. Wu, H., Cheng, J., Huang, S., Ke, Y., Lu, Y., Xu, Y.: *Proc. VLDB Endowment.* **7**, 721 (2014)
21. Newman, M.E.J.: *Networks: An Introduction*. Oxford University Press, Inc., New York (2010)
22. Barabasi, A.L.: *Network Science*. Cambridge University Press, Cambridge (2016)
23. Lü, L., Chen, D., Ren, X.-L., Zhang, Q.-M., Zhang, Y.-C., Zhou, T.: *Phys. Rep.* **650**, 1 (2016)
24. Dorogovtsev, S.N., Mendes, J.F.F., Samukhin, A.N.: *Phys. Rev. E.* **64**, 025101 (2001)
25. Pastor-Satorras, R., Vespignani, A.: *Phys. Rev. Lett.* **86**, 3200 (2001)
26. Morone, F., Makse, H.A.: *Nature.* **524**, 65 (2015)
27. Brockmann, D., Helbing, D.: *Science.* **342**, 1337–1342 (2013)
28. Iannelli, F., Koher, A., Brockmann, D., Hövel, P., Sokolov, I.M.: *Phys. Rev. E.* **95**, 012313 (2017)

Chapter 11

Optimal Containment of Epidemics in Temporal and Adaptive Networks

Masaki Ogura and Victor M. Preciado

Abstract In this chapter, we focus on the problem of containing the spread of diseases taking place on both *temporal* and *adaptive* networks (i.e., networks whose structure changes as a result of the epidemic). We specifically focus on the problem of finding the optimal allocation of containment resources (e.g., vaccines, medical personnel, traffic control resources, etc.) to eradicate epidemic outbreaks over the following three models of temporal and adaptive networks: (i) Markovian temporal networks, (ii) aggregated-Markovian temporal networks, and (iii) stochastically adaptive network models. For each model, we present a rigorous and tractable mathematical framework to efficiently find the optimal distribution of control resources to eliminate the disease. In contrast with other existing results, our results are not based on heuristic control strategies, but on a disciplined analysis using tools from dynamical systems and convex optimization.

11.1 Introduction

The containment of spreading processes taking place on complex networks is a major research area with applications in social, biological, and technological systems [3, 31, 71]. The spread of information in on-line social networks, the evolution of epidemic outbreaks in human contact networks, and the dynamics of cascading failures in the electrical grid are relevant examples of these processes. While major advances have been made in this field (see, for example, [34, 42] and references therein), most current results are specifically tailored to study spreading processes taking place on *static* networks. Cohen et al. [13] proposed a heuristic

M. Ogura (✉)

Nara Institute of Science and Technology, 8916-5 Takayama, 630-0192, Ikoma, Nara, Japan
e-mail: oguram@is.naist.jp

V.M. Preciado

University of Pennsylvania, 3330 Walnut Street, 19104, Philadelphia, PA, USA
e-mail: preciado@seas.upenn.edu

vaccination strategy called acquaintance immunization policy and proved it to be much more efficient than random vaccine allocation. In [5], Borgs et al. studied theoretical limits in the control of spreading processes in undirected network with a non-homogeneous distribution of antidotes. Chung et al. [11] studied a heuristic immunization strategy based on the PageRank vector of the contact graph. Preciado et al. [44, 47] studied the problem of determining the optimal allocation of control resources over static networks to efficiently eradicate epidemics described by the networked SIS (Susceptible-Infected-Susceptible) model. This work was later extended in [10, 32, 35, 38, 45, 46, 69, 70] by considering more general epidemic models. Wan et al. developed in [67] a control theoretic framework for disease spreading, which has been recently extended to the case of sparse control strategies in [58]. Optimal control problems over networks have also been considered in [25, 26]. Drakopoulos et al. proposed in [14] an efficient curing policy based on graph cuts. Decentralized algorithms for epidemic control have been proposed in [48, 59] using a game-theoretic framework to evaluate the effectiveness of protection strategies against SIS virus spreads. An optimization framework to achieve resource allocations that are robust to stochastic uncertainties in nodal activities was proposed in [40].

Most epidemic processes of practical interest take place on *temporal networks* [29], having time-varying topologies [20]. In the context of temporal networks, we are interested in the interplay between the epidemiological dynamics on networks (i.e., the dynamics of epidemic processes taking place on the network) and the dynamics of networks (i.e., the temporal evolution of the network structure). Although the dynamics on and of networks are usually studied separately, there are many cases in which the evolution of the network structure is heavily influenced by the dynamics of epidemic processes taking place on the network. This can be illustrated by a phenomenon called social distancing [4, 16], where healthy individuals avoid contact with infected individuals in order to protect themselves against the disease. As a consequence of social distancing, the structure of the network adapts to the dynamics of the epidemics taking place on the network. Similar adaptation mechanisms have been studied in the context of the power grid [53], biological systems [51] and on-line social networks [2].

We can find a plethora of studies dedicated to the *analysis* of epidemic spreading processes over temporal networks based on either extensive numerical simulations [21, 23, 30, 49, 63, 64] or rigorous theoretical analyses [43, 52, 57, 65]. However, there is a lack of methodologies for *containing* epidemic outbreaks on temporal networks (except the work [28] for activity driven networks). This is also the case for adaptive networks. In this latter case, various methods for the analysis of the behavior of spreading processes evolving over adaptively changing temporal networks [17, 18, 50, 56, 60, 61, 68] exist. However, these heavily rely on extensive numerical simulations (except the work [54] based on a compartmental model). This suggests a lack of rigorous analytical tools for working out effective control strategies in the context of temporal or adaptive networks.

Nevertheless, in recent years, we have witnessed an emerging effort towards the efficient containment of epidemic processes in temporal and adaptive networks using tools from the field of control theory. The aim of this chapter is to give an overview of this research thrust by focusing on optimal resource allocation problems for efficient eradication of epidemic outbreaks. We specifically focus the scope of this chapter on the following three classes of temporal and adaptive networks: (1) Markovian temporal networks [37], (2) aggregated-Markovian edge-independent temporal networks [33, 41], and (3) SIS models on adaptive networks [18, 39]. We see that the optimal resource allocation problem in these three cases can be reduced to an efficiently solvable class of optimization problems called convex programming [7] (more precisely, geometric programming [6]).

This chapter is organized as follows. In Sect. 11.2, we study the optimal resource allocation problem in Markovian temporal networks. We then focus our exposition on a specific class of Markovian temporal networks, called aggregated-Markovian edge-independent temporal networks, in Sect. 11.3. We finally present recent results in the context of SIS models on adaptive network models in Sect. 11.4.

Notation We denote the identity matrix by I . The maximum real part of the eigenvalues of a square matrix A is denoted by $\lambda_{\max}(A)$. For matrices A_1, \dots, A_m , we denote by $\bigoplus_{i=1}^m A_i$ the block-diagonal matrix containing A_1, \dots, A_m as its diagonal blocks. If the matrices A_1, \dots, A_m have the same number of columns, then the matrix obtained by vertically stacking A_1, \dots, A_m is denoted by $\text{col}_{i=1}^m A_i$. An undirected graph is defined as the pair $\mathcal{G} = (\mathcal{V}, \mathcal{E})$, where $\mathcal{V} = \{1, \dots, n\}$ is a set of nodes and \mathcal{E} is a set of edges, defined as unordered pairs of nodes. The adjacency matrix $A = [a_{ij}]_{i,j}$ of \mathcal{G} is defined as the $n \times n$ matrix such that $a_{ij} = a_{ji} = 1$ if $\{i, j\} \in \mathcal{E}$, and $a_{ij} = 0$ otherwise.

11.2 Markovian Temporal Networks

Since the dynamics of realistic temporal networks has intrinsic uncertainties in, for example, the appearance or disappearance of edges, the durations of temporal interactions, and inter-event times, most mathematical models of temporal networks in the literature have been written in terms of stochastic processes. In particular, many stochastic models of temporal networks (see, e.g., [12, 24, 43, 65]) employ *Markov processes* due to their simplicity, including time-homogeneity and memoryless properties. The aim of this section is to present a rigorous and tractable framework for the analysis and control of epidemics taking place in Markovian temporal networks. We remark that, throughout this chapter, we shall focus on the specific type of spreading processes described by the SIS epidemic model, among other epidemic models (see, e.g., [42]).

11.2.1 Model

In this subsection, we present the model of disease spread and temporal networks studied in this section. We start our exposition from reviewing a model of spreading processes over static networks called the *Heterogeneous Networked SIS* (HeNeSIS) model [47], which is an extension of the popular *N*-intertwined SIS model [62] to the case of nodes with heterogeneous spreading rates. Let \mathcal{G} be an undirected graph having n nodes, where nodes in \mathcal{G} represent individuals and edges represent interactions between them. At a given time $t \geq 0$, each node can be in one of two possible states: *susceptible* or *infected*. In the HeNeSIS model, when a node i is infected, it can randomly transition to the susceptible state with an instantaneous rate $\delta_i > 0$, called the *recovery rate* of node i . On the other hand, if a neighbor of node i is in the infected state, then the neighbor can infect node i with the instantaneous rate β_i , where $\beta_i > 0$ is called the *infection rate* of node i . We define the variable $x_i(t)$ as $x_i(t) = 1$ if node i is infected at time t , and $x_i(t) = 0$ if i is susceptible; then, the transition probabilities of the HeNeSIS model in the time window $[t, t + h]$ can be written as

$$\Pr(x_i(t+h) = 1 \mid x_i(t) = 0) = \beta_i \sum_{j \in \mathcal{N}_i} x_j(t)h + o(h), \quad (11.1)$$

$$\Pr(x_i(t+h) = 0 \mid x_i(t) = 1) = \delta_i h + o(h),$$

where \mathcal{N}_i is the set of neighbors of node i and $o(h)/h \rightarrow 0$ as $h \rightarrow 0$.

Although the collection of variables (x_1, \dots, x_n) is simply a Markov process, this process presents a total of 2^n possible states (two states per node). Therefore, its analysis is very hard for arbitrary contact networks of large size. A popular approach to simplify the analysis of this type of Markov processes is to consider upper-bounding linear models, as described below. Let A denote the adjacency matrix of \mathcal{G} . Define the vector $p = (p_1, \dots, p_n)^\top$ and the diagonal matrices $B = \bigoplus(\beta_1, \dots, \beta_n)$ and $D = \bigoplus(\delta_1, \dots, \delta_n)$. Then, it is known [47] that the solutions $p_i(t)$ ($i = 1, \dots, n$) of the vectorial linear differential equation

$$dp/dt = (BA - D)p \quad (11.2)$$

upper-bound the evolution of the infection probabilities $\Pr(i \text{ is infected at time } t)$ from the exact Markov process with 2^n states. Thus, if the solution of (11.2) satisfies $p(t) \rightarrow 0$ exponentially fast as $t \rightarrow \infty$, then the infection dies out in the exact Markov process exponentially fast as well. Since the differential equation (11.2) is a linear system, the maximum real eigenvalue $\lambda_{\max}(BA - D)$ of the matrix $BA - D$ determines the asymptotic behavior of the solution. The above considerations show that the spreading process dies out exponentially fast if

$$\lambda_{\max}(BA - D) < 0. \quad (11.3)$$

In the special case of homogeneous infection and recovery rates, i.e., $\beta_i = \beta$ and $\delta_i = \delta$ for all nodes i , condition (11.3) yields the following well-known extinction condition (see, e.g., [1, 27])

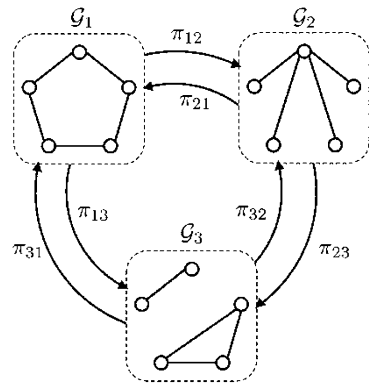
$$\frac{\beta}{\delta} < \frac{1}{\lambda_{\max}(A)}. \tag{11.4}$$

However, conditions (11.3) and (11.4) are not applicable to the case of temporal networks having time-varying adjacency matrices. In this section, we focus on the case where the dynamics of the temporal network is modeled by a Markov process. In order to specify a Markovian temporal network, we need the following two ingredients. The first one is the set of ‘graph configurations’ that can be achieved by the temporal network. Let those configurations (static and undirected networks) be $\mathcal{G}_1, \dots, \mathcal{G}_L$. This implies that, at each time $t \geq 0$, the temporal network always takes one of the configurations $\mathcal{G}_1, \dots, \mathcal{G}_L$. The other ingredient is the set of stochastic transition rates between graph configurations. Specifically, we let $\pi_{k\ell}$ denote the stochastic transition rate from configuration \mathcal{G}_k to \mathcal{G}_ℓ . This implies that, if the configuration of the temporal network at time t is \mathcal{G}_k , then the probability of the temporal network having another configuration \mathcal{G}_ℓ at time $t + h$ equals $\pi_{k\ell}h + o(h)$, independent of t . A schematic diagram of a Markovian temporal network is shown in Fig. 11.1.

We now describe the model of disease spread considered in this section. Let $\mathcal{G}(t)$ be a Markovian temporal network (as a continuous-time function of $t \geq 0$). Let $\mathcal{N}_i(t)$ be the set of neighbors of node i at time t in graph $\mathcal{G}(t)$. Then, we can reformulate the transition probabilities (11.1) of the HeNeSIS model as

$$\begin{aligned} \Pr(x_i(t+h) = 1 \mid x_i(t) = 0) &= \beta_i \sum_{j \in \mathcal{N}_i(t)} x_j(t)h + o(h), \\ \Pr(x_i(t+h) = 0 \mid x_i(t) = 1) &= \delta_i h + o(h). \end{aligned} \tag{11.5}$$

Fig. 11.1 Markovian temporal network having three possible configurations (\mathcal{G}_1 , \mathcal{G}_2 , and \mathcal{G}_3), and the corresponding stochastic transition rates



Notice that, in the first equation, the infection probability is dependent not only on the infection states of the other nodes but also the connectivity of the network, i.e., \mathcal{N}_i in (11.1) changes to $\mathcal{N}_i(t)$. Then, we can formulate an upper-bounding model for the HeNeSIS model over the Markovian temporal network $\mathcal{G}(t)$ as

$$dp/dt = (BA(t) - D)p(t),$$

where $A(t)$ denotes the adjacency matrix of $\mathcal{G}(t)$.

11.2.2 Optimal Resource Distribution

Let us consider the following epidemiological problem [47]: Assume that we have access to vaccines that can be used to reduce the infection rates of individuals in the network, as well as antidotes that can be used to increase their recovery rates. Assuming that both vaccines and antidotes have an associated cost and that we are given a fixed budget, how should we distribute vaccines and antidotes throughout the individuals in the network in order to eradicate an epidemic outbreak at the maximum decay rate? In what follows, we state this question in rigorous terms and present an optimal solution using an efficient optimization framework called geometric programming [6].

Assume that we have to pay $f(\beta_i)$ unit of cost to tune the infection rate of node i to β_i . Likewise, we assume that the cost for tuning the recovery rate of node i to δ_i equals $g(\delta_i)$. Notice that the total cost of tuning the collection of infection rates $(\beta_1, \dots, \beta_n)$ and recovery rates $(\delta_1, \dots, \delta_n)$ in the network is given by

$$R = \sum_{i=1}^n (f(\beta_i) + g(\delta_i)).$$

We further assume that these rates can be tuned within the following feasibility intervals:

$$0 < \underline{\beta} \leq \beta_i \leq \bar{\beta}, \quad 0 < \underline{\delta} \leq \delta_i \leq \bar{\delta}. \quad (11.6)$$

We can now state our optimal resource allocation problem as follows:

Problem 1 Consider a HeNeSIS spreading process over a Markovian temporal network. Given a budget $\bar{R} > 0$, tune the infection and recovery rates β_i and δ_i in the network in such a way that the exponential decay rate of the infection probabilities is maximized while satisfying the budget constraint $R \leq \bar{R}$ and the box constraints (11.6).

In order to solve this problem, we first present an analytical framework for quantifying the decay rate of the infection probabilities, given the parameters in the HeNeSIS model and the Markovian temporal network. In fact, using tools from control theory [36], it is possible to prove the following upper-bound on the decay rate of infection probabilities in the HeNeSIS model:

Proposition 1 *Consider the HeNeSIS spreading process over a Markovian temporal network. Let $\pi_{\ell\ell} = -\sum_{\ell \neq k} \pi_{\ell k}$. If*

$$\lambda_{\max}(\mathcal{A}_1) < 0$$

for the matrix

$$\mathcal{A}_1 = \begin{bmatrix} BA_1 - D + \pi_{11}I & \pi_{21}I & \cdots & \pi_{L1}I \\ \pi_{12}I & \ddots & \ddots & \vdots \\ \vdots & \ddots & \ddots & \pi_{L,L-1}I \\ \pi_{1L}I & \cdots & \pi_{L-1,L}I & BA_L - D + \pi_{LL}I \end{bmatrix},$$

then the infection probabilities of nodes converge to zero exponentially fast with an exponential decay rate of $|\lambda_{\max}(\mathcal{A}_1)|$.

Besides providing an analytical method for quantifying the rate of convergence to the disease-free state, this proposition allows us to optimally minimize the decay rate of the epidemic by minimizing the maximum real eigenvalue $\lambda_{\max}(\mathcal{A}_1)$ of the Metzler matrix \mathcal{A}_1 . In fact, by employing the celebrated Perron-Frobenius theory [22] for nonnegative matrices, we are able to solve Problem 1 via a class of optimization problems called geometric programming [47, Proposition 10], briefly reviewed below [6]. Let x_1, \dots, x_n denote positive variables and define $x = (x_1, \dots, x_n)$. In the context of geometric programming, a real function $g(x)$ is a *monomial* if there exist a $c \geq 0$ and $a_1, \dots, a_n \in \mathbb{R}$ such that $g(x) = cx_1^{a_1} \cdots x_n^{a_n}$. Also, we say that a function $f(x)$ is a *posynomial* if it is a sum of monomials of x (we point the readers to [6] for more details). Given a collection of posynomials $f_0(x), \dots, f_p(x)$ and monomials $g_1(x), \dots, g_q(x)$, the optimization problem

$$\begin{aligned} & \underset{x > 0}{\text{minimize}} && f_0(x) \\ & \text{subject to} && f_i(x) \leq 1, \quad i = 1, \dots, p, \\ & && g_j(x) = 1, \quad j = 1, \dots, q, \end{aligned}$$

is called a *geometric program*. A constraint of the form $f(x) \leq 1$ with $f(x)$ being a posynomial is called a posynomial constraint. It is known [6] that a geometric

program can be efficiently converted into an equivalent convex optimization problem, which can be solved in polynomial time [7].

We can now state the first main result of this chapter:

Theorem 1 ([37, Section VI]) *Assume that the cost function f is a posynomial and, also, there exists $\hat{\delta} > \bar{\delta}$ such that the function $\tilde{g}(\tilde{\delta}) = g(\hat{\delta} - \tilde{\delta})$ is a posynomial in $\tilde{\delta}$. Then, the infection and recovery rates that solve Problem 1 are given by $\{\beta_i^*\}_{i=1}^n$ and $\{\hat{\delta} - \tilde{\delta}_i^*\}_{i=1}^n$, where the starred variables solve the optimization problem*

$$\begin{aligned}
 & \underset{\beta_i, \tilde{\delta}_i, v > 0, \lambda > 0}{\text{minimize}} && 1/\lambda \\
 & \text{subject to} && \mathcal{A}_1 v \leq -\lambda v, \\
 & && \sum_{i=1}^n (f(\beta_i) + \tilde{g}(\tilde{\delta}_i)) \leq \bar{R}, \\
 & && \underline{\beta} \leq \beta_i \leq \bar{\beta}, \\
 & && \hat{\delta} - \bar{\delta} \leq \tilde{\delta}_i \leq \hat{\delta} - \underline{\delta}.
 \end{aligned} \tag{11.7}$$

Moreover, this optimization problem can be equivalently converted to a geometric program.

In the optimization problem (11.7), the variable λ becomes equal to $-\lambda_{\max}(\mathcal{A}_1)$ at optimality by Perron-Frobenius theory. It is rather straightforward to verify that the optimization problem (11.7) can be converted to a geometric program. For example, one can easily confirm that the vectorial constraint $\mathcal{A}_1 v \leq -\lambda v$ is equivalent to the following set of posynomial constraints

$$\frac{(\sum_{k \neq \ell} \pi_{k\ell} v_{ki}) + \beta_i \sum_{j=1}^n [A_\ell]_{ij} v_{\ell j} + \tilde{\delta}_i v_{\ell i} + \lambda v_{\ell i}}{(\hat{\delta}_i - \pi_\ell) v_{\ell i}} \leq 1,$$

for all $i = 1, \dots, n$ and $\ell = 1, \dots, L$. We refer the interested readers to the references [37, 47] for details.

11.2.3 Numerical Simulations

To illustrate the results presented in this section, we consider the HeNeSIS model over a Markovian temporal network based on the well-known Zachary Karate Club [72]. In order to construct a Markovian temporal network from this static network, we first identify two clusters (i.e., a division of the set of nodes into two disjoint subsets) in the network using the spectral clustering technique (see, e.g., [66]). We then classify the edges in the static network into the following three classes: edges within the first cluster ($\mathcal{E}^{(1)}$), within the second cluster ($\mathcal{E}^{(2)}$), and

between distinct clusters ($\mathcal{E}^{(3)}$). We then consider the following stochastic temporal behavior for the network structure: edges in each class $\mathcal{E}^{(i)}$ ($i = 1, 2, 3$) appear or disappear simultaneously, with an activation rate p_i and a deactivation rate q_i , respectively. Notice that, in this setting, the temporal network has a total of $2^3 = 8$ configurations $\mathcal{G}_\ell = (\mathcal{V}, \mathcal{E}_\ell)$ ($\ell = 1, \dots, 8$) having the sets of edges listed below:

$$\begin{aligned} \mathcal{E}_1 &= \mathcal{E}^{(1)} \cup \mathcal{E}^{(2)} \cup \mathcal{E}^{(3)}, \\ \mathcal{E}_2 &= \mathcal{E}^{(1)} \cup \mathcal{E}^{(2)}, & \mathcal{E}_3 &= \mathcal{E}^{(2)} \cup \mathcal{E}^{(3)}, & \mathcal{E}_4 &= \mathcal{E}^{(1)} \cup \mathcal{E}^{(3)}, \\ \mathcal{E}_5 &= \mathcal{E}^{(1)}, & \mathcal{E}_6 &= \mathcal{E}^{(2)}, & \mathcal{E}_7 &= \mathcal{E}^{(3)}, \\ \mathcal{E}_8 &= \emptyset. \end{aligned}$$

We show the transition diagram of the resulting Markovian temporal network (called the Markovian Karate network) in Fig. 11.2, where solid (dashed) arrows indicate transitions involving the activation (deactivation) of edges.

Using Proposition 1, we first illustrate how the time-variability of the Markovian Karate network affects the behavior of the epidemic threshold. We let the activation and deactivation rates of the edges be

$$p_1 = p_2 = 0.1, q_1 = q_2 = 1, p_3 = 0.02, \text{ and } q_3 = 5. \tag{11.8}$$

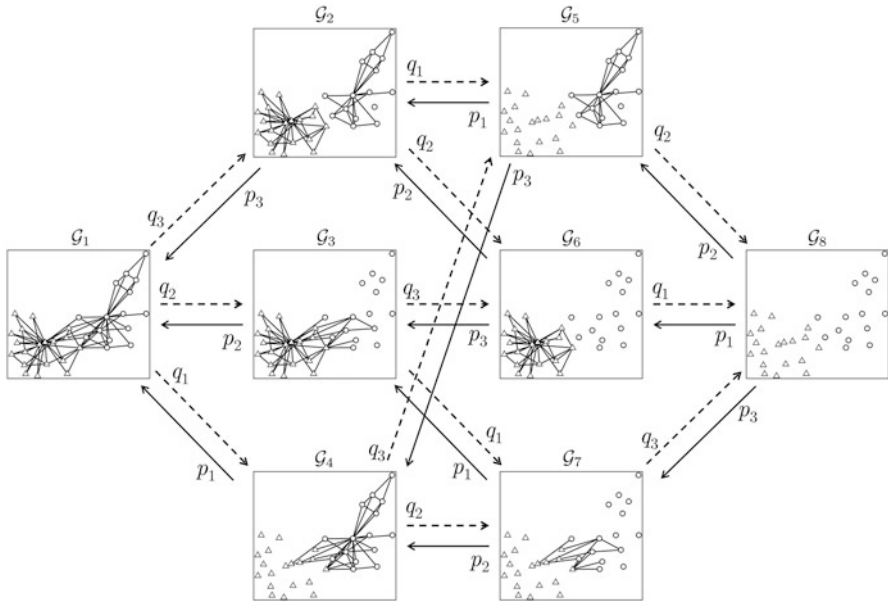
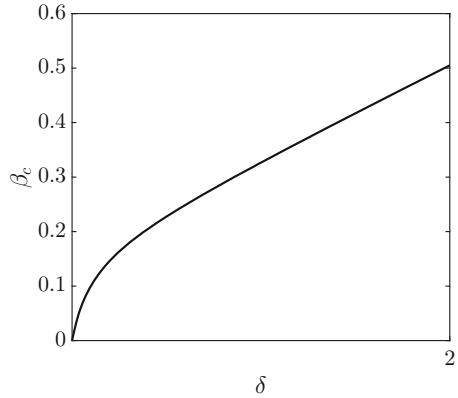


Fig. 11.2 Transition diagram of the Markovian Karate Club network. Circles and triangles represent nodes belonging to the first and second clusters, respectively

Fig. 11.3 The epidemic threshold β_c of the Markovian Karate Club network versus the recovery rate δ



As for the HeNeSIS model, we first assume that all the nodes have the same transmission rate β and the recovery rate δ . For each value of $\delta \in [0, 2]$, we use a bisection search to find the supremum β_c of the transmission rate β that guarantees the exponentially fast extinction of the disease spread (i.e., $\lambda_{\max}(\mathcal{A}_1) < 0$). We show the obtained values of β_c versus δ in Fig. 11.3. We can observe that, unlike in the case of static network, the threshold value β_c in our case exhibits a nonlinear dependence on δ .

We then move to the cost-optimal eradication of epidemic outbreaks over the Markovian Karate network. Let us fix $\underline{\delta} = p_1/2 = 0.05$ and $\bar{\beta} = \beta_c$, which are considered to be the ‘natural’ recovery and infection rates of the nodes. We then assume that a full dose of vaccinations and antidotes can improve these rates at most 20%, i.e., we let

$$\underline{\beta} = (0.8)\bar{\beta}, \quad \bar{\delta} = (1.2)\underline{\delta}.$$

The cost functions for tuning the rates are set to be

$$f(\beta) = c_1 + c_2/\beta^q, \quad g(\delta) = c_3 + c_4/(\hat{\delta} - \delta)^r, \tag{11.9}$$

where q and r are positive parameters that allow us to tune the shape of the cost functions; c_1, \dots, c_4 are constants to normalize the cost functions in such a way that $f(\underline{\beta}) = 1/2, f(\bar{\beta}) = 0, g(\underline{\delta}) = 0$, and $g(\bar{\delta}) = 1/2$. Notice that, with this choice of the normalization constants, we have $R = 0$ if $(\beta_i, \delta_i) = (\bar{\beta}, \underline{\delta})$ for every node i (i.e., all nodes keep their natural infection and transmission rates), while $R = n$ (full protection) if $(\beta_i, \delta_i) = (\underline{\beta}, \bar{\delta})$ for every i (i.e., all nodes receive the full amount of vaccinations and antidotes). Plots of the cost defined above are shown for various values of q and r in Fig. 11.4, when $\hat{\delta} = 2\bar{\delta}$. In our numerical simulation, we use the values $q = r = 0.1$, in which case the cost functions become almost linear (solid lines in Fig. 11.4). Setting the available budget as $\bar{R} = n/2$, we solve the optimization problem in Theorem 1 and numerically obtain the optimal

Fig. 11.4 *Left:* Cost function (f) for transmission rates. *Solid:* $q = 0.1$, *dashed:* $q = 10$, *dotted:* $q = 50$. *Right:* Cost function (g) for recovery rates. *Solid:* $r = 0.1$, *dashed:* $r = 10$, *dotted:* $r = 50$

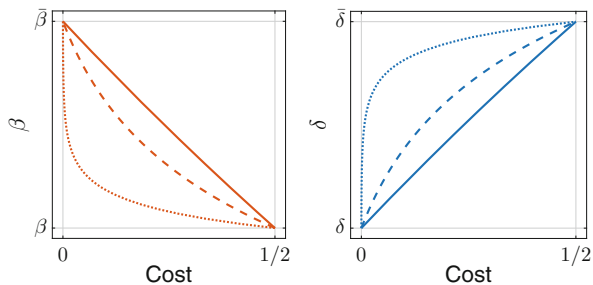


Table 11.1 Optimal investments for (a) infection rates and (b) recovery rates in the case of (1) the Markovian network and (2) time-aggregated network, respectively. Darker node colors represent heavier investments (i.e., either $f(\beta_i^*)$ or $g(\delta_i^*)$) to vaccinate/antidote the node, while white nodes do not receive any investment. The ‘boundary’ nodes receiving no investment in the Markovian case, as well as those nodes receiving full investment in the time-aggregated case, are emphasized with circles

	(a) Infection rates	(b) Recovery rates
(1) Markovian network		
(2) Time-aggregated network		

resource allocation over the Markovian Karate network (illustrated in the first row of Table 11.1). We can observe that the nodes at the ‘boundaries’ of clusters do not receive much investment. This is reasonable because the first and second clusters are effectively disconnected (due to the low activation rate p_3 and the high deactivation rate q_3 of edges between clusters) and, therefore, the risk of infection across different clusters is low.

For the sake of comparison, we solve the same resource allocation problem for the original (static) Karate Club network using the framework presented in [47] and obtain another allocation of vaccines and antidotes over the network (shown in the second row of Table 11.1). We can see that, in the latter allocation of resources, some of the nodes (the circled nodes) at the boundaries of the clusters receive a full investment, unlike in the Markovian case. This observation shows that, by taking into account the time-variability of temporal networks, we are able to distribute resources in a more efficient manner.

11.3 Edge-Independent Networks

Although the framework presented in the previous section can theoretically deal with epidemic control on temporal networks presenting the Markovian property, the framework is not necessarily applicable to some realistic temporal networks having a large number of graph configurations (i.e., when the number L is large under the notation in Sect. 11.2.1). For example, in the situation studied in Sect. 11.2.3, it would be more realistic to assume that the activations and deactivations of edges within a cluster or between clusters occur not simultaneously (as assumed in the example) but rather *respectively* (or, *independently* of each other). However, if we allow independent edge activations and deactivations for all the 78 edges in the network, we would end up obtaining a Markovian temporal network having $L = 2^{78} > 10^{23}$ possible graph configurations, which makes the optimization problem (11.7) computationally untractable to solve.

The aim of this section is to present an optimization framework to contain epidemic outbreaks over temporal networks where edges are allowed to activate and deactivate independently of each other. We specifically focus on the HeNeSIS model evolving over *aggregated-Markovian edge-independent (AMEI)* temporal networks introduced in [41]. We present an efficient method for tuning the infection and recovery rates of the nodes in the network for containing epidemic outbreak in AMEI temporal networks. Unlike the optimization problem (11.7), the computational complexity for solving the optimization problem presented in this section *does not* grow with respect to the number L of graph configurations. We also remark that another advantage of the AMEI temporal networks is its ability of modeling non-exponential, heavy-tail distributions of inter-event times found in several experimental studies [9, 55].

11.3.1 Model

We start by presenting the definition of the aggregated-Markovian edge-independent (AMEI) temporal network model [41]. For simplicity in our exposition, we shall adopt a formulation slightly simpler than the original one in [41].

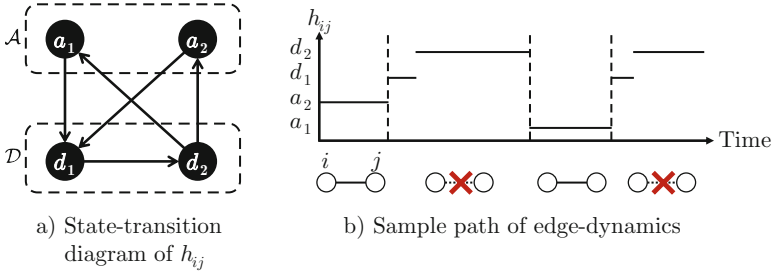


Fig. 11.5 Example of the stochastic transitions of a particular edge $\{i, j\}$ in an AMEI model with the active set $\mathcal{A} = \{a_1, a_2\}$ and the inactive set $\mathcal{D} = \{d_1, d_2\}$. *Left:* State-transition diagram of the Markov process h_{ij} . *Right:* a sample path of the time-evolution of the edge $\{i, j\}$

Definition 1 ([41]) We say that a random and undirected temporal network $\mathcal{G}(t)$ is an *aggregated-Markovian edge-independent (AMEI for short)* temporal network if there exist

- disjoint and finite sets \mathcal{A} and \mathcal{D} , and
- stochastically independent $(\mathcal{A} \cup \mathcal{D})$ -valued Markov processes h_{ij} for each distinct and unordered pair $\{i, j\}$ of nodes,

such that

$$\begin{cases} \text{edge } \{i, j\} \text{ is present at time } t, & \text{if } h_{ij}(t) \in \mathcal{A}, \\ \text{edge } \{i, j\} \text{ is not present at time } t, & \text{if } h_{ij}(t) \in \mathcal{D}. \end{cases}$$

We call \mathcal{A} and \mathcal{D} the *active set* and *inactive set*, respectively (see Fig. 11.5 for an illustration).

A few remarks on the AMEI temporal networks are in order. First, the independence of the Markov processes h_{ij} for all pairs of nodes ensures the independent dynamics of the connectivity of any node-pairs, unlike in the example presented in Sect. 11.2.3. Secondly, in the special case where both \mathcal{A} and \mathcal{D} consist of a single element, AMEI temporal networks reduce to the well-known model of temporal networks called the edge-Markovian model [12]. Thirdly, AMEI temporal networks in fact allow us to model a wider class of temporal networks. For example, in an edge-Markovian graph, the time it takes for an edge to switch from connected to disconnected (or vice versa) must follow an exponential distribution. In contrast, in an AMEI temporal network, we can *design* the active and inactive sets \mathcal{A}, \mathcal{D} as well as the Markov process h_{ij} to fit any desired distribution for the contact durations with an arbitrary precision [41, Example 1]. Finally, since all the processes h_{ij} are Markovian, the dynamics of an AMEI temporal network can be described by the collection $h = (h_{ij})_{i,j}$, which is again a Markov process.

11.3.2 Optimal Resource Allocation

In this section, we consider the same epidemiological problem as Problem 1:

Problem 2 ([33]) Consider a HeNeSIS model over an AMEI temporal network. Given a budget $\bar{R} > 0$, tune the infection and recovery rates β_i and δ_i in the network in such a way that the exponential decay rate of the infection probabilities is minimized while satisfying the budget constraint $R \leq \bar{R}$ and the box constraints (11.6).

Although Problem 2 is a particular case of Problem 1 for general Markovian temporal networks since an AMEI temporal network is Markovian, we cannot necessarily apply the optimization framework presented in Theorem 1 to the current case for the following reason. Notice that an AMEI temporal network allows a total of 2^m graph configurations, where $m = 2^{n(n-1)/2}$ is the number of the undirected edges that can exist in the network. This implies that the dimension of the vector-valued decision variable v in the optimization problem (11.7), $nL = n2^m$, grows exponentially fast with respect to n , making it very hard to efficiently solve the optimization problem (11.7) even for small-scale networks. We further emphasize that this difficulty cannot be relaxed as long as we rely on the estimate on the decay rate of infection probabilities presented in Proposition 1, because the estimate already relies on a matrix of dimensions $(nL) \times (nL)$. This observation motivates us to derive an alternative, computationally efficient method for estimating the decay rate of infection probabilities. In this direction, using tools from random matrix theory, we are able to derive an alternative, tractable extinction condition for spreading processes over AMEI temporal networks [41]:

Proposition 2 ([41, Theorem 3.4]) For positive constants b and d , define the decreasing function $\kappa(s) = n \exp(s/b)[(bs + d)/d]^{-(bs+d)/b^2}$ for $s \geq 0$. Let us consider the HeNeSIS spreading process over an AMEI temporal network. Define the $n \times n$ matrix $\bar{A} = [\bar{a}_{ij}]_{i,j}$ by

$$\bar{a}_{ij} = \lim_{t \rightarrow \infty} \Pr(a_{ij}(t) = 1). \tag{11.10}$$

Let $\Delta = \max_{1 \leq i \leq n} \sum_{j=1}^n (\beta_i \beta_j \bar{A}_{ij} (1 - \bar{A}_{ij}))$ and $c = \lambda_{\max}(B(\text{sgn} \bar{A}) - D) - \kappa_{\beta_{\max}, \Delta}^{-1}(1)$, where $\text{sgn}(\cdot)$ denotes the entry-wise application of the sign function and $\beta_{\max} = \max_{1 \leq i \leq n} \beta_i$. If

$$\lambda_{\max}(\mathcal{A}_2) < \tau, \tag{11.11}$$

where

$$\mathcal{A}_2 = B\bar{A} - D$$

and

$$\tau = \max_{s \in (\kappa_{\beta_{\max}, \Delta}^{-1}(1), \bar{\delta} + (|c| - c)/2]} \left(\frac{s + c\kappa_{\beta_{\max}, \Delta}(s)}{1 - \kappa_{\beta_{\max}, \Delta}(s)} \right),$$

then the infection probabilities converge to zero exponentially fast, almost surely.

The extinction condition (11.11) is comparable with the condition in (11.3) for static networks. Roughly speaking, we can understand \bar{A} defined in (11.10) as the adjacency matrix of a weighted *static* network $\bar{\mathcal{G}}$ ‘representing’ the original AMEI temporal network, while τ can be regarded as a safety margin we have to impose as a penalty for the simplification. We further notice that the static network $\bar{\mathcal{G}}$ arises by taking a long-time limit of the original AMEI temporal network [41]. We finally remark that it is possible to upper-bound the decay rate of the convergence of infection probabilities using the maximum real eigenvalue of \mathcal{A}_2 (for details, see [41]).

Proposition 2 gives us the following two alternative options to solve Problem 2 for a given HeNeSIS spreading process over an AMEI temporal network: (1) to increase τ or (2) to decrease $\lambda_{\max}(\mathcal{A}_2)$. Among these two options, the former is not realistic because τ has a complicated expression and depends on relevant parameters in a highly complex manner. On the other hand, the maximum real eigenvalue $\lambda_{\max}(\mathcal{A}_2)$ is easily tractable by the framework used in Sect. 11.2.2. This consideration leads us to the following solution to Problem 2:

Theorem 2 ([37, Section VI]) *Assume that the cost function f is a posynomial and, also, there exists $\hat{\delta} > \bar{\delta}$ such that the function $\tilde{g}(\tilde{\delta}) = g(\hat{\delta} - \tilde{\delta})$ is a posynomial in $\tilde{\delta}$. Then, the infection and recovery rates that optimally solve Problem 2 are given by $\{\beta_i^*\}_{i=1}^n$ and $\{\hat{\delta} - \tilde{\delta}_i^*\}_{i=1}^n$, where the starred variables solve the optimization problem*

$$\begin{aligned}
 & \underset{\beta_i, \tilde{\delta}_i, v > 0, \lambda > 0}{\text{minimize}} && 1/\lambda \\
 & \text{subject to} && \mathcal{A}_2 v \leq -\lambda v, \\
 & && \sum_{i=1}^n (f(\beta_i) + \tilde{g}(\tilde{\delta}_i)) \leq \bar{R}, \\
 & && \underline{\beta} \leq \beta_i \leq \bar{\beta}, \\
 & && \hat{\delta} - \bar{\delta} \leq \tilde{\delta}_i \leq \hat{\delta} - \underline{\delta}.
 \end{aligned}$$

Moreover, this optimization problem can be equivalently converted to a geometric program.

11.3.3 Numerical Simulation

In this subsection, we illustrate the optimization framework for the optimal resource allocation over AMEI temporal networks presented in Theorem 2. For simplicity in the presentation, and to be consistent with the Markovian case in the previous

section, we focus on the case where \mathcal{A} and \mathcal{D} are singletons (although the following analysis can be applied to the general non-Markovian case where the edge-dynamics is explained by Markov processes h_{ij}). In this subsection, we consider the HeNeSIS spreading model over an AMEI temporal network based on the static Karate network. Recall that, in the Markovian Karate network, the activations and deactivations of edges within a cluster (or between clusters) must occur simultaneously. In this numerical simulation, we assume that these activations and deactivations occur independently of other edges. We specifically construct our AMEI temporal network as follows. For an edge $\{i, j\}$ between the nodes belonging to the first (or second) cluster, we let h_{ij} be the two-state Markov process whose activation and deactivation rates are given by p_1 and q_1 (p_2 and q_2 , respectively). Also, we let the activation and deactivation rates of edges between different clusters to be p_3 and q_3 . The values of these activation and deactivation rates are the same as in (11.8). Finally, for a pair $\{i, j\}$ of nodes not connected in the static Karate Club network, we let their activation and deactivation rates to be 0 and 1, respectively. This choice guarantees that edges not present in the static network do not appear in our AMEI Karate network.

Using the cost function in (11.9), as well as the box constraints (11.6) and budget $\bar{R} = n/2$ used in Sect. 11.2.3, we numerically solve Problem 2 by using Theorem 2. The obtained resource distribution is illustrated in Fig. 11.6. As for the infection rates, we observe that nodes at the ‘boundaries’ of the clusters receive small investments, as already observed in the Markovian case. On the other hand, we cannot clearly observe this phenomenon for recovery rates. We finally notice that, in this specific numerical simulation, the resulting investment heavily leans towards increasing recovery rates, not decreasing infection rates.

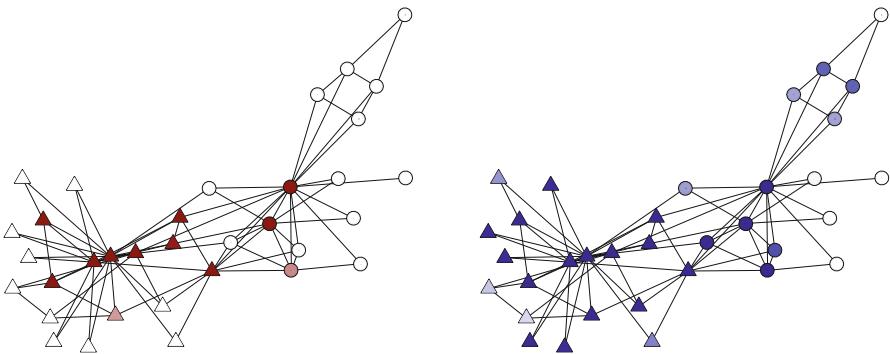


Fig. 11.6 Optimal resource allocation for the AMEI Karate Club network. *Circles and triangles* represent different clusters. *Left*: costs for transmission rates. *Right*: costs for recovery rates. Darker colors represent heavier investments, while white nodes do not receive any investment

11.4 Adaptive Networks

In the case of epidemic outbreaks, it is commonly observed that the connectivity of human networks is significantly influenced by the progress of the disease spread. This phenomenon, called *social distancing* [4, 16], is known to help societies cope with epidemics. A key feature of temporal networks of this type is their dependence on the nodal infection states. However, this structural dependence (or adaptation) cannot be well captured by the Markovian temporal networks because, in those networks, the dynamics of the network structure is assumed to be independent of the nodal states. In this direction, the aim of the current section is to present the so-called *Adaptive SIS* (ASIS) model [18, 39], which is able to replicate adaptation mechanisms found in realistic networks. We first present a tight extinction condition of epidemic outbreaks evolving in the ASIS model. Based on this extinction condition, we then illustrate how one can tune the adaptation rates of networks to eradicate epidemic outbreaks over the ASIS model.

11.4.1 Model

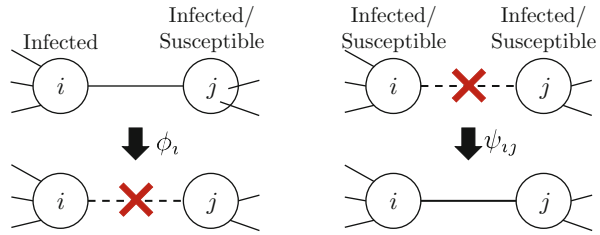
In this section, we first describe the heterogeneous ASIS model [39]. As in the HeNeSIS model over Markovian temporal networks (studied in the previous two sections), the ASIS model consists of the following two components: the $\{0, 1\}$ -valued nodal states $x_i(t)$ and a temporal network $\mathcal{G}(t)$. While the nodal states in the ASIS model have the same transition probabilities as in (11.5), the transition probabilities of the network $\mathcal{G}(t)$ in the ASIS model are quite different from Markovian temporal networks because the probabilities depend on the states of the nodes, as described below. Let $\mathcal{G}(0) = (\mathcal{V}, \mathcal{E}(0))$ be an initial connected contact graph with adjacency matrix $A(0) = [a_{ij}(0)]_{i,j}$. Then, edges in the initial graph $\mathcal{G}(0)$ appear and disappear over time according to the following transition probabilities:

$$\Pr(a_{ij}(t+h) = 0 \mid a_{ij}(t) = 1) = \phi_i x_i(t)h + \phi_j x_j(t)h + o(h), \quad (11.12)$$

$$\Pr(a_{ij}(t+h) = 1 \mid a_{ij}(t) = 0) = a_{ij}(0)\psi_{ij}h + o(h), \quad (11.13)$$

where the parameters $\phi_i > 0$ and $\psi_{ij} = \psi_{ji} > 0$ are called the *cutting* and *reconnecting* rates, respectively. Notice that the transition rate in (11.12) depends on the nodal states x_i and x_j , inducing an adaptation mechanism of the network structure to the state of the epidemics. The transition probability in (11.12) can be interpreted as a protection mechanism in which edge $\{i, j\}$ is stochastically removed from the network if either node i or j is infected. More specifically, because of the first summand (respectively, the second summand) in (11.12), whenever node i (respectively, node j) is infected, edge $\{i, j\}$ is removed from the network according to a Poisson process with rate ϕ_i (respectively, rate ϕ_j). On the other hand, the transition probability in (11.13) describes a mechanism for which a ‘cut’ edge $\{i, j\}$ is ‘reconnected’ into the network according to a Poisson process with rate

Fig. 11.7 Adaptation mechanisms in the Adaptive SIS model



ψ_{ij} (see Fig. 11.7). Notice that we include the term $a_{ij}(0)$ in (11.13) to guarantee that only edges present in the initial contact graph $\mathcal{G}(0)$ can be added later on by the reconnecting process. In other words, we constrain the set of edges in the adaptive network to be a part of the arbitrary contact graph $\mathcal{G}(0)$.

11.4.2 Optimal Resource Allocation

In this section, we consider the situation in which we can tune the values of the cutting rates in the network by incurring a cost. In particular, we can tune the value of the cutting rate of node i to ϕ_i by incurring a cost of $h(\phi_i)$. The total tuning cost is therefore given by

$$R = \sum_{i=1}^n h(\phi_i).$$

Although the problem of tuning the reconnection rates ψ_{ij} for keeping the connectivity of the whole network is another important problem [54], in this chapter we focus on the eradication of epidemics. In this setup, we can state the following optimal resource allocation problem:

Problem 3 Consider a heterogeneous ASIS model. Given a budget \bar{R} , tune the cutting rates ϕ_i in the network in such a way that the exponential decay rate of the infection probabilities is maximized while satisfying the budget constraint $R \leq \bar{R}$ and the box-constraint $0 < \phi \leq \phi_i \leq \bar{\phi}$.

In order to solve this problem, we shall follow the same path as we did in the previous sections: we first find an analytical estimate of the decay rate of the infection probabilities in the ASIS model. For this purpose, we first represent the ASIS model by a set of stochastic differential equations described below (see [39] for details). For $\gamma > 0$, let N_γ denote a Poisson counter with rate γ [15]. Then, from the two equations in (11.5), the evolution of the nodal states can be exactly described by the following stochastic differential equation:

$$dx_i = -x_i dN_{\delta_i} + (1 - x_i) \sum_{j \in \mathcal{N}_i(0)} a_{ij} x_j dN_{\beta_i}, \tag{11.14}$$

for all nodes i . Similarly, from (11.12) and (11.13), the evolution of the edges can be exactly described by

$$da_{ij} = -a_{ij}(x_i dN_{\phi_i} + x_j dN_{\psi_j}) + (1 - a_{ij}) dN_{\psi_{ij}}, \quad (11.15)$$

for all $\{i, j\} \in \mathcal{E}(0)$. Then, by (11.14), the expectation $E[x_i]$ obeys the differential equation $(d/dt)E[x_i] = -\delta_i E[x_i] + \beta_i \sum_{k \in \mathcal{N}_i(0)} E[(1 - x_i)a_{ik}x_k]$. Let $p_i(t) = E[x_i(t)]$ and $q_{ij}(t) = E[a_{ij}(t)x_i(t)]$. Then, it follows that

$$\frac{dp_i}{dt} = -\delta_i p_i + \beta_i \sum_{j \in \mathcal{N}_i(0)} q_{ji} - f_i, \quad (11.16)$$

where $f_i = \beta_i \sum_{k \in \mathcal{N}_i(0)} E[x_i x_k a_{ik}]$ contains positive higher-order terms. Similarly, from (11.14) and (11.15), the Ito formula for stochastic differential equations (see, e.g., [19]) shows that

$$\frac{dq_{ij}}{dt} = -\phi_i p_{ij} + \psi_{ij}(p_i - q_{ij}) - \delta_i q_{ij} + \beta_i \sum_{k \in \mathcal{N}_i(0)} q_{ki} - g_{ij}, \quad (11.17)$$

where $g_{ij} = \phi_j E[x_i x_j a_{ij}] + \beta_i \sum_{k \in \mathcal{N}_i(0)} E[x_i x_k a_{ik} + (1 - a_{ij})a_{ik}x_k]$ contains positive higher-order terms. We remark that the differential equations (11.16) and (11.17) *exactly* describe the joint evolution of the spreading process and the network structure without relying on mean-field approximations.

Based on the above derivation, we are able to prove the following proposition:

Proposition 3 ([39]) *Let T_i be the unique row-vector satisfying $T_i q = \sum_{k \in \mathcal{N}_i(0)} q_{ki}$. Define the matrices*

$$\begin{aligned} B_1 &= \text{col}_{1 \leq i \leq n} (\beta_i T_i), & B_2 &= \text{col}_{1 \leq i \leq n} (\beta_i \mathbb{1}_{d_i} \otimes T_i), & D_1 &= \bigoplus_{i=1}^n \delta_i, & D_2 &= \bigoplus_{i=1}^n (\delta_i I_{d_i}), \\ \Phi &= \bigoplus_{i=1}^n (\phi_i I_{d_i}), & \Psi_1 &= \bigoplus_{i=1}^n \left(\text{col}_{j \in \mathcal{N}_i(0)} \psi_{ij} \right), & \Psi_2 &= \bigoplus_{i=1}^n \bigoplus_{j \in \mathcal{N}_i(0)} \psi_{ij}, \end{aligned}$$

where d_i denotes the degree of node i in the initial graph $\mathcal{G}(0)$, \otimes denotes the Kronecker product [8] of matrices, and $\mathbb{1}_n$ denotes the all-one vector of length n . If the matrix

$$\mathcal{A}_3 = \begin{bmatrix} -D_1 & B_1 \\ \Psi_1 & B_2 - D_2 - \Phi - \Psi_2 \end{bmatrix}$$

satisfies

$$\lambda_{\max}(\mathcal{A}_3) < 0, \tag{11.18}$$

then the infection probabilities in the heterogeneous ASIS model converge to zero exponentially fast with an exponential decay rate $|\lambda_{\max}(\mathcal{A}_3)|$.

We remark that, in the homogeneous case, where all the nodes share the same infection rate $\beta > 0$ and recovery rate $\delta > 0$, and all the edges share the same cutting rate $\phi > 0$ and reconnecting rate $\psi > 0$, the condition in (11.18) reduces [39] to the following simple inequality:

$$\frac{\beta}{\delta} < \frac{1 + \omega}{\lambda_{\max}(A(0))}, \tag{11.19}$$

where $\omega = \phi/(\delta + \psi)$ is called the *effective cutting rate*. The proof of this reduction can be found in [39, Appendix B]. We remark that, in the special case when the network does not adapt to the prevalence of infection, i.e., when $\phi = 0$, we have that $\omega = 0$ and, therefore, the condition in (11.19) is identical to the extinction condition (11.4) corresponding to the homogeneous networked SIS model over a static network [62].

Now, based on Proposition 3, one can give the following solution to Problem 3 based on geometric programming:

Theorem 3 ([39, Section IV]) *Assume that there exists $\hat{\phi} > \bar{\phi}$ such that the function $\tilde{h}(\tilde{\phi}) = h(\hat{\phi} - \tilde{\phi})$ is a posynomial in $\tilde{\phi}$. Then, the cutting rates that solve Problem 3 are given by $\{\hat{\phi} - \tilde{\phi}_i^*\}_{i=1}^n$, where the starred variables solve the optimization problem:*

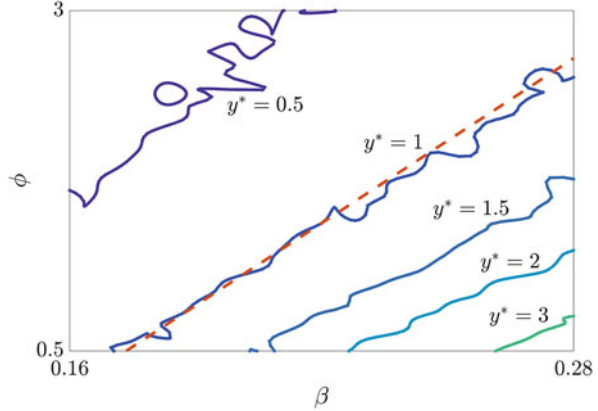
$$\begin{aligned} & \underset{\tilde{\phi}_i, v > 0, \lambda > 0}{\text{minimize}} && 1/\lambda \\ & \text{subject to} && \mathcal{A}_3 v \leq -\lambda v, \\ & && \sum_{i=1}^n \tilde{h}(\tilde{\phi}_i) \leq \bar{R}, \\ & && \hat{\phi} - \bar{\phi} \leq \tilde{\phi}_i \leq \hat{\phi} - \phi. \end{aligned}$$

Moreover, this optimization problem can be equivalently converted to a geometric programming.

11.4.3 Numerical Simulations

In this section, we illustrate the results presented in this section. Let the initial graph $\mathcal{G}(0)$ be the Zachary Karate Club. We first consider the homogeneous case, and fix the recovery rate and the reconnecting rate in the network to be $\delta = 1$ and

Fig. 11.8 The meta-stable (quasi-stationary) number of the infected nodes y^* versus β and ϕ , with $\delta = 1$ and $\psi = 2$. The dashed straight lines show the analytically derived lower bound $(1 + \omega)/\lambda_{\max}(A(0)) = \beta$ on the epidemic threshold



$\psi = 2$ for all nodes in the graph, for the purpose of illustration. We then compute the meta-stable (i.e., quasi-stationary) value y^* of the infected nodes in the network for various values of β and ϕ (for the details of this simulation and its parameters, see [39]). The obtained numbers are shown as a contour plot in Fig. 11.8. We see how the analytical threshold $\beta/\delta = (1 + \omega)/\lambda_{\max}(A(0))$ from (11.19) (represented as a dashed straight line in Fig. 11.8) is in good agreement with the numerically found threshold $y^* = 1$.

We then consider the optimal resource distribution stated in Problem 3. We assume that all the nodes share the same infection rate β_c and recovery rate 0.05 that were used in the previous examples. We also assume that the reconnection rates are given by

$$\psi_{ij} = \begin{cases} p_1, & \text{if } i \text{ and } j \text{ belong to the first cluster,} \\ p_2, & \text{if } i \text{ and } j \text{ belong to the second cluster,} \\ p_3, & \text{otherwise,} \end{cases}$$

for the values given in (11.8). In this simulation, we use the cost function $h(\phi) = c_5 + c_6/(\hat{\phi} - \phi)^s$ similar to the one used in (11.9), where s is a positive parameter for tuning the shape of the cost function, $\hat{\phi}$ is a constant larger than $\bar{\phi}$, and c_5 and c_6 are constants such that $h(\phi) = 0$ and $h(\hat{\phi}) = 1$. We let $\bar{\phi} = 0.5$, $\hat{\phi} = 100\bar{\phi}$, and $s = 1$, for which the resulting cost function resembles a linear function as in the case of Markovian temporal networks. Using these cost functions and the budget $\bar{R} = n/2$, we numerically solve the optimization problem in Theorem 3 to find the optimal distribution of resource over the network (illustrated in Fig. 11.9). Interestingly, unlike in the Markovian cases in Sects. 11.2 and 11.3, we cannot clearly observe the phenomenon where nodes at the boundaries of the clusters receive relatively less investments.

Finally, in Fig. 11.10, we summarize the amount of optimal resource distributions obtained for the Markovian, AMEI, and ASIS Karate Club networks. We see that,

Fig. 11.9 The distribution of the resource for tuning the cutting rates in the ASIS Karate network. Darker colors represent heavier investments, while white nodes do not receive any investment

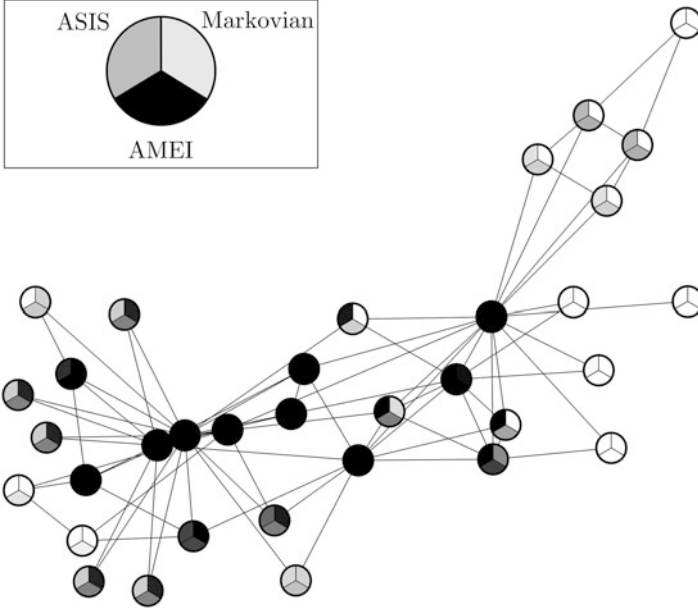
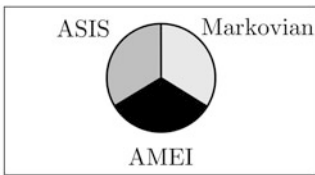
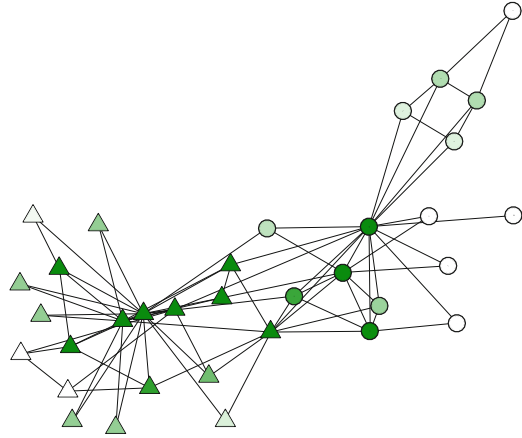


Fig. 11.10 Optimal intervention on nodes. In each circle (node), the upper-right, lower, and upper-left colors indicate the investments according to the Markovian, AMEI, and ASIS formulations, respectively. Darker colors represent heavier investments, while white color indicates no investment

although the three allocations share a certain tendency such as concentration of resource on high-degree nodes, they are not necessarily qualitatively equal. This observation confirms the necessity of appropriately incorporating the characteristics of temporal/adaptive networks into our mechanism of resource distributions.

11.5 Conclusion

In this chapter, we have given an overview of recent progress on the problem of containing epidemics taking place on temporal and adaptive complex networks. Specifically, we have presented analytical frameworks for finding the optimal distribution of resources over Markovian temporal networks, aggregated-Markovian edge-independent temporal networks, and in the Adaptive SIS model. For each of the cases, we have seen that the optimal resource distribution problems can be reduced to an efficiently solvable class of convex optimization problems called geometric programming. We have illustrated the results with several numerical simulations based on the well-studied Zachary Karate Club.

Acknowledgements This work has been supported in part by the National Science Foundation under grants IIS-1447470 and ECCS-1651433.

References

1. Ahn, H.J., Hassibi, B.: Global dynamics of epidemic spread over complex networks. In: 52nd IEEE Conference on Decision and Control, pp. 4579–4585 (2013)
2. Antoniadou, D., Drovolis, C.: Co-evolutionary dynamics in social networks: a case study of Twitter. *Comput. Soc. Netw.* **2**, 14 (2015)
3. Barrat, A., Barthelemy, M., Vespignani, A.: *Dynamical Processes on Complex Networks*. Cambridge University Press, Cambridge (2008)
4. Bell, D., Nicoll, A., Fukuda, K., Horby, P., Monto, A., Hayden, F., Wylks, C., Sanders, L., Van Tam, J.: Nonpharmaceutical interventions for pandemic influenza, national and community measures. *Emerg. Infect. Dis.* **12**(1), 88–94 (2006)
5. Borgs, C., Chayes, J., Ganesh, A., Saberi, A.: How to distribute antidote to control epidemics. *Random Struct. Algorith.* **37**(2), 204–222 (2010)
6. Boyd, S., Kim, S.J., Vandenberghe, L., Hassibi, A.: A tutorial on geometric programming. *Optim. Eng.* **8**(1), 67–127 (2007)
7. Boyd, S., Vandenberghe, L.: *Convex Optimization*. Cambridge University Press, New York (2004)
8. Brewer, J.: Kronecker products and matrix calculus in system theory. *IEEE Trans. Circuits Syst.* **25**(9), 772–781 (1978)
9. Cattuto, C., van den Broeck, W., Barrat, A., Colizza, V., Pinton, J.F., Vespignani, A.: Dynamics of person-to-person interactions from distributed RFID sensor networks. *PLoS One* **5**(7), 1–9 (2010)
10. Chen, X., Preciado, V.M.: Optimal coinfection control of competitive epidemics in multi-layer networks. In: 53rd IEEE Conference on Decision and Control, pp. 6209–6214 (2014)
11. Chung, F., Horn, P., Tsiatas, A.: Distributing antidote using pagerank vectors. *Internet Math.* **6**(2), 237–254 (2009)
12. Clementi, A.E., Macci, C., Monti, A., Pasquale, F., Silvestri, R.: Flooding time in edge-Markovian dynamic graphs. In: 27th ACM Symposium on Principles of Distributed Computing, pp. 213–222 (2008)
13. Cohen, R., Havlin, S., Ben-Avraham, D.: Efficient immunization strategies for computer networks and populations. *Phys. Rev. Lett.* **91**, 247901 (2003)
14. Drakopoulos, K., Ozdaglar, A., Tsitsiklis, J.N.: An efficient curing policy for epidemics on graphs. *IEEE Trans. Netw. Sci. Eng.* **1**(2), 67–75 (2014)

15. Feller, W.: *An Introduction to Probability Theory and Its Applications*. John Wiley & Sons, New York (1956)
16. Funk, S., Salathé, M., Jansen, V.A.A.: Modelling the influence of human behaviour on the spread of infectious diseases: a review. *J. R. Soc. Interface* **7**, 1247–1256 (2010)
17. Gross, T., Blasius, B.: Adaptive coevolutionary networks: a review. *J. R. Soc. Interface* **5**, 259–271 (2008)
18. Guo, D., Trajanovski, S., van de Bovenkamp, R., Wang, H., Van Mieghem, P.: Epidemic threshold and topological structure of susceptible-infectious-susceptible epidemics in adaptive networks. *Phys. Rev. E* **88**, 042802 (2013)
19. Hanson, F.B.: *Applied Stochastic Processes and Control for Jump-Diffusions: Modeling, Analysis and Computation*. Society for Industrial and Applied Mathematics, Philadelphia (2007)
20. Holme, P.: Modern temporal network theory: a colloquium. *Eur. Phys. J. B* **88**, 234 (2015)
21. Holme, P., Liljeros, F.: Birth and death of links control disease spreading in empirical contact networks. *Sci. Rep.* **4**, 4999 (2014)
22. Horn, R., Johnson, C.: *Matrix Analysis*. Cambridge University Press, Cambridge (1990)
23. Karsai, M., Kivela, M., Pan, R.K., Kaski, K., Kertész, J., Barabasi, A.L., Saramäki, J.: Small but slow world: how network topology and burstiness slow down spreading. *Phys. Rev. E* **83**, 025102 (2011)
24. Karsai, M., Perra, N., Vespignani, A.: Time varying networks and the weakness of strong ties. *Sci. Rep.* **4**, 4001 (2014)
25. Khanafer, A., Basar, T.: An optimal control problem over infected networks. In: *1st International Conference on Control, Dynamic Systems, and Robotics*, 125 (2014)
26. Khouzani, M. H. R., Sarkar, S., Altman, E.: Optimal control of epidemic evolution. In: *2011 IEEE International Conference on Computer Communications*, pp. 1683–1691 (2011)
27. Lajmanovich, A., Yorke, J.A.: A deterministic model for gonorrhea in a nonhomogeneous population. *Math. Biosci.* **28**(1976), 221–236 (1976)
28. Liu, S., Perra, N., Karsai, M., Vespignani, A.: Controlling contagion processes in activity driven networks. *Phys. Rev. Lett.* **112**, 118702 (2014)
29. Masuda, N., Holme, P.: Predicting and controlling infectious disease epidemics using temporal networks. *FI000prime Rep.* **5**, 6 (2013)
30. Masuda, N., Klemm, K., Eguíluz, V.M.: Temporal networks: slowing down diffusion by long lasting interactions. *Phys. Rev. Lett.* **111**, 188701 (2013)
31. Newman, M., Barabási, A.L., Watts, D.J.: *The Structure and Dynamics of Networks*. Princeton University Press, Princeton (2006)
32. Nowzari, C., Ogura, M., Preciado, V.M., Pappas, G.J.: A general class of spreading processes with non-Markovian dynamics. In: *54th IEEE Conference on Decision and Control*, pp. 5073–5078 (2015)
33. Nowzari, C., Ogura, M., Preciado, V.M., Pappas, G.J.: Optimal resource allocation for containing epidemics on time-varying networks. In: *49th Asilomar Conference on Signals, Systems and Computers*, pp. 1333–1337 (2015)
34. Nowzari, C., Preciado, V.M., Pappas, G.J.: Analysis and control of epidemics: a survey of spreading processes on complex networks. *IEEE Control Syst.* **36**(1), 26–46 (2016)
35. Nowzari, C., Preciado, V.M., Pappas, G.J.: Stability analysis of generalized epidemic models over directed networks. In: *53rd IEEE Conference on Decision and Control*, pp. 6197–6202 (2014)
36. Ogura, M., Martin, C.F.: Stability analysis of positive semi-Markovian jump linear systems with state resets. *SIAM J. Control. Optim.* **52**, 1809–1831 (2014)
37. Ogura, M., Preciado, V.M.: Optimal design of switched networks of positive linear systems via geometric programming. *IEEE Trans. Control Netw. Syst.* (accepted) (2015)
38. Ogura, M., Preciado, V.M.: Efficient containment of exact SIR Markovian processes on networks. In: *55th IEEE Conference on Decision and Control*, pp. 967–972 (2016)
39. Ogura, M., Preciado, V.M.: Epidemic processes over adaptive state-dependent networks. *Phys. Rev. E* **93**, 062316 (2016)

40. Ogura, M., Preciado, V.M.: Optimal design of networks of positive linear systems under stochastic uncertainty. In: 2016 American Control Conference, pp. 2930–2935 (2016)
41. Ogura, M., Preciado, V.M.: Stability of spreading processes over time-varying large-scale networks. *IEEE Trans. Netw. Sci. Eng.* **3**(1), 44–57 (2016)
42. Pastor-Satorras, R., Castellano, C., Van Mieghem, P., Vespignani, A.: Epidemic processes in complex networks. *Rev. Mod. Phys.* **87**(3), 925–979 (2015)
43. Perra, N., Gonçalves, B., Pastor-Satorras, R., Vespignani, A.: Activity driven modeling of time varying networks. *Sci. Rep.* **2**, 469 (2012)
44. Preciado, V.M., Zargham, M., Enyioha, C., Jadbabaie, A., Pappas, G.J.: Optimal vaccine allocation to control epidemic outbreaks in arbitrary networks. In: 52nd IEEE Conference on Decision and Control, pp. 7486–7491 (2013)
45. Preciado, V.M., Sahneh, F.D., Scoglio, C.: A convex framework for optimal investment on disease awareness in social networks. In: 2013 Global Conference on Signal and Information Processing, pp. 851–854 (2013)
46. Preciado, V.M., Jadbabaie, A.: Spectral analysis of virus spreading in random geometric networks. In: 48th IEEE Conference on Decision and Control, pp. 4802–4807 (2009)
47. Preciado, V.M., Zargham, M., Enyioha, C., Jadbabaie, A., Pappas, G.J.: Optimal resource allocation for network protection against spreading processes. *IEEE Trans. Control Netw. Syst.* **1**(1), 99–108 (2014)
48. Ramirez-Llanos, E., Martinez, S.: Distributed and robust fair resource allocation applied to virus spread minimization. In: 2015 American Control Conference, pp. 1065–1070 (2015)
49. Rocha, L.E.C., Blondel, V.D.: Bursts of vertex activation and epidemics in evolving networks. *PLoS Comput. Biol.* **9**(3), e1002974 (2013)
50. Rogers, T., Clifford-Brown, W., Mills, C., Galla, T.: Stochastic oscillations of adaptive networks: application to epidemic modelling. *J. Stat. Mech: Theory Exp.* **2012**(08), P08018 (2012)
51. Schaper, W., Scholz, D.: Factors regulating arteriogenesis. *Arterioscler. Thromb. Vasc. Biol.* **23**(7), 1143–1151 (2003)
52. Schwarzkopf, Y., Rákos, A., Mukamel, D.: Epidemic spreading in evolving networks. *Phys. Rev. E* **82**, 036112 (2010)
53. Scirè, A., Tuval, I., Eguíluz, V.M.: Dynamic modeling of the electric transportation network. *Europhys. Lett.* **71**(2), 318–324 (2005)
54. Sélley, F., Besenyi, Á., Kiss, I.Z., Simon, P.L.: Dynamic control of modern, network-based epidemic models. *SIAM J. Appl. Dyn. Syst.* **14**(1), 168–187 (2015)
55. Stehlé, J., Voirin, N., Barrat, A., Cattuto, C., Isella, L., Pinton, J.F., Quaghiotto, M., van den Broeck, W., Régis, C., Lina, B., Vanhems, P.: High-resolution measurements of face-to-face contact patterns in a primary school. *PLoS One* **6**(8), e23176 (2011)
56. Szabó-Solticzky, A., Berthouze, L., Kiss, I.Z., Simon, P.L.: Oscillating epidemics in a dynamic network model: stochastic and mean-field analysis. *J. Math. Biol.* **72**(5), 1153–1176 (2016)
57. Taylor, M., Taylor, T.J., Kiss, I.Z.: Epidemic threshold and control in a dynamic network. *Phys. Rev. E* **85**, 016103 (2012)
58. Torres, J.A., Roy, S., Wan, Y.: Sparse allocation of resources in dynamical networks with application to spread control. In: 2015 American Control Conference, pp. 1873–1878 (2015)
59. Trajanovski, S., Hayel, Y., Altman, E., Wang, H., Van Mieghem, P.: Decentralized protection strategies against SIS epidemics in networks. *IEEE Trans. Control Netw. Syst.* **2**(4), 406–419 (2015)
60. Tunc, I., Shaw, L.B.: Effects of community structure on epidemic spread in an adaptive network. *Phys. Rev. E* **90**, 022801 (2014)
61. Valdez, L.D., Macri, P.A., Braunstein, L.A.: Intermittent social distancing strategy for epidemic control. *Phys. Rev. E* **85**, 036108 (2012)
62. Van Mieghem, P., Omic, J., Kooij, R.: Virus spread in networks. *IEEE/ACM Trans. Netw.* **17**(1), 1–14 (2009)
63. Vazquez, A., Rácz, B., Lukács, A., Barabasi, A.L.: Impact of non-Poissonian activity patterns on spreading processes. *Phys. Rev. Lett.* **98**, 158702 (2007)

64. Vestergaard, C.L., Génois, M., Barrat, A.: How memory generates heterogeneous dynamics in temporal networks. *Phys. Rev. E* **90**, 042805 (2014)
65. Volz, E., Meyers, L.A.: Epidemic thresholds in dynamic contact networks. *J. R. Soc. Interface* **6**(32), 233–241 (2009)
66. Von Luxburg, U.: A tutorial on spectral clustering. *Stat. Comput.* **17**(4), 395–416 (2007)
67. Wan, Y., Roy, S., Saberi, A.: Designing spatially heterogeneous strategies for control of virus spread. *IET Syst. Biol.* **2**(4), 184–201 (2008)
68. Wang, B., Cao, L., Suzuki, H., Aihara, K.: Epidemic spread in adaptive networks with multitype agents. *J. Phys. A Math. Theor.* **44**(3), 035101 (2011)
69. Watkins, N.J., Nowzari, C., Preciado, V.M., Pappas, G.J.: Optimal resource allocation for competitive spreading processes on bilayer networks. *IEEE Trans. Control Netw. Syst.* (accepted) (2016)
70. Watkins, N.J., Nowzari, C., Preciado, V.M., Pappas, G.J.: Optimal resource allocation for competing epidemics over arbitrary networks. In: 2015 American Control Conference, pp. 1381–1386 (2015)
71. Watts, D.J., Strogatz, S.H.: Collective dynamics of ‘small-world’ networks. *Nature* **393**(6684), 440–442 (1998)
72. Zachary, W.W.: An information flow model for conflict and fission in small groups. *J. Anthropol. Res.* **33**(4), 452–473 (1977)

Chapter 12

Mapping Out Emerging Network Structures in Dynamic Network Models Coupled with Epidemics

István Z. Kiss, Luc Berthouze, Joel C. Miller, and Péter L. Simon

Abstract We consider the susceptible – infected – susceptible (SIS) epidemic on a dynamic network model with addition and deletion of links depending on node status. We analyse the resulting pairwise model using classical bifurcation theory to map out the spectrum of all possible epidemic behaviours. However, the major focus of the chapter is on the evolution and possible equilibria of the resulting networks. Whereas most studies are driven by determining system-level outcomes, e.g., whether the epidemic dies out or becomes endemic, with little regard for the emerging network structure, here, we want to buck this trend by augmenting the system-level results with mapping out of the structure and properties of the resulting networks. We find that depending on parameter values the network can become disconnected and show bistable-like behaviour whereas the endemic steady state sees the emergence of networks with qualitatively different degree distributions. In particular, we observe de-phased oscillations of both prevalence and network degree

I.Z. Kiss (✉)

Department of Mathematics, School of Mathematical and Physical Sciences,
University of Sussex, BN1 9QH, Falmer, Brighton, UK
e-mail: i.z.kiss@sussex.ac.uk

L. Berthouze

Centre for Computational Neuroscience and Robotics, University of Sussex,
BN1 9QH, Falmer, Brighton, UK
e-mail: l.berthouze@sussex.ac.uk

J.C. Miller

School of Mathematical Sciences, School of Biological Sciences and Monash Academy
for Cross and Interdisciplinary Mathematics, Monash University, Clayton, VIC, Australia

Institute for Disease Modeling, Bellevue, WA, USA

e-mail: joel.c.miller.research@gmail.com

P.L. Simon

Institute of Mathematics, Eötvös Loránd University Budapest, and Numerical Analysis,
and Large Networks Research Group, Hungarian Academy of Sciences, Budapest, Hungary
e-mail: simonp@cs.elte.hu

during which there is role reversal between the level and nature of the connectivity of susceptible and infected nodes. We conclude with an attempt at describing what a potential bifurcation theory for networks would look like.

12.1 Introduction

Networks have been and remain extremely useful in modelling complex systems. Their use has led to rapid progress in the study of stochastic spreading processes such as information, rumour and epidemics. The role of contact heterogeneity, preferential mixing and (to a lesser extent) of clustering is now well understood [3, 11, 17]. Mean-field models ranging from heterogenous mean-field [17], pairwise [5, 9, 10] and effective-degree [1, 13] to edge-based compartmental models [15, 16] have proved crucial in circumventing the technical analysis of the underlying stochastic process. This shifts the focus onto the analysis of low-dimensional systems of ordinary differential equations, where variables are system-level expected values such as the the number of nodes and edges of different statuses.

Attempting to account for more realistic features of spreading processes (e.g., non-exponentially-distributed waiting times) or networks (e.g., clustered and/or with higher-order structure, time-varying or embedded in some space) leads to models that are more complex, harder to analyse and less transparent. Indeed, this typically requires (i) more complex network models, including a better understanding of the properties of empirical networks, or (ii) the derivation of new or refined mean-field models which may require sophisticated mathematical tools or techniques.

In this chapter we focus on the latter and consider a model where the epidemic dynamics on the network is coupled with a network which evolves in time. Several studies have already made important observations regarding how coupling the dynamics on the network with that of the network may change or enrich the outcome of the epidemic. For example, [7] showed that for a rewiring process that preserved the number of links (“link number-preserving”) where susceptible nodes cut links to infected nodes and instantaneously reconnect to a random susceptible node, can lead to oscillations, albeit over a very narrow area of the parameter space [8]. This model was later refined and extended either by considering a different rewiring mechanism (e.g., non link-preserving rewiring but still dependent on link status [19, 22, 24, 25]) or by modelling the same process but with more sophisticated models such as the effective degree [14]. For reviews on this topic, we refer the reader to [6, 20].

Such dynamic or adaptive networks present several challenges in that usually the resulting mean-field models are of a higher dimension than the static network equivalent. In many cases, this is explained by the fact that closures now involve dynamic or time-varying quantities (e.g., the average degree of the network) that need to be tracked via their own equations. But perhaps more important is the fact such coupled dynamics lead to correlations that usually violate the assumptions behind even the more complex closures. Still, mean-field models have an important role to play in providing a qualitative picture of the different behaviours of the system, and to guide a more rigorous analysis.

Despite ongoing progress in model refinement and accounting for more realistic scenarios of dynamic contact structures, very few studies focus on understanding and mapping out the structure of the emerging networks. While there is detailed information about when an epidemic dies out, there is value in knowing whether the epidemic died out due to the network being poorly connected or due to an unfavourable ratio of infection to recovery rates despite the network being well connected. Other important insights may come from knowing whether the fluctuations in prevalence can lead to fluctuation in average degree of the network, whether the network can fall apart into disjointed components isolating the infection; or, finally, what the degree distribution will be at the endemic equilibrium or during oscillations in prevalence. In this chapter we set out to map out the structure of the emerging networks for an SIS epidemic coupled with a link status-dependent link addition and deletion model, where existing links are deleted and new links are created depending on the disease status of the nodes that these links connect.

The chapter is structured as follows. After formulating the model in Sect. 12.2, we provide a bifurcation analysis of the simple pairwise model describing the coupled epidemic and dynamic network model in Sect. 12.3. Section 12.4 is dedicated to mapping out the emerging network structure by using the compact pairwise model which tracks the degree of the nodes and by relying on explicit stochastic network simulations. We conclude with a discussion of our results identifying open questions and new directions for further research.

12.2 Model Formulation

This chapter considers *SIS* (susceptible-infected-susceptible) epidemic propagation on an adaptive network with link status-dependent link activation and deletion. Specifically, the model incorporates the following independent Poisson processes:

- **Infection:** Infection is transmitted across each contact between an I and an S node, or $(I - S)$ link, at rate τ ,
- **Recovery:** Each I node recovers (becoming an S node) at rate γ independently of the network,
- **Link activation:** A non-existing link between a node of status A and another of status B is activated at rate α_{AB} , with $A, B \in \{S, I\}$,
- **Link deletion:** An existing link between a node of status A and another of status B is terminated at rate ω_{AB} , with $A, B \in \{S, I\}$.

This model is significantly different from ‘smart’ rewiring [6], where S nodes have full knowledge of the status of all other nodes and choose to minimise their exposure to infection by cutting links to I neighbours and immediately rewiring to a randomly chosen S node. This latter approach conserves the number of links in the network and simplifies the analysis of the resulting system, by not having to consider an evolving average degree.

Here, we set out to explore and explain the spectrum of system behaviours with special focus on understanding and mapping the evolution of the network structure and attainable network equilibria. The first task is carried out via classical bifurcation analysis at system level and focuses on identifying regimes such as die-out, endemic equilibria and oscillations.

In order to do this, we will employ a number of approaches including: (i) two different types of pairwise or pair-based mean-field ODE models, and (ii) full network-based stochastic simulation. Regarding the rewiring parameters we focus on two scenarios, namely:

- A.** $\alpha_{SI} = \alpha_{II} = \alpha_{SS} = \alpha$ and $\omega_{SI} = \omega_{II} = \omega_{SS} = \omega$, and
- B.** $\alpha_{SI} = \alpha_{II} = 0$ and $\alpha_{SS} \neq 0$, and $\omega_{II} = \omega_{SS} = 0$ and $\omega_{SI} \neq 0$.

While the first is link status-independent and leads to simpler and more tractable models, the second is motivated by practical considerations, such as those used in the ‘smart’ rewiring – where nodes aim to minimise the risk of becoming infected while maintaining their connectivity to the network.

We start by formulating the pairwise model for the expected number of nodes and pairs of different statuses. As was shown in [12], this gives rise to

$$\dot{[I]} = \tau[SI] - \gamma[I], \quad (12.1a)$$

$$\dot{[SI]} = \gamma([II] - [SI]) + \tau([SSI] - [ISI] - [SI]) + \alpha_{SI}([S][I] - [SI]) - \omega_{SI}[SI], \quad (12.1b)$$

$$\dot{[II]} = -2\gamma[II] + 2\tau([ISI] + [SI]) + \alpha_{II}([I]([I] - 1) - [II]) - \omega_{II}[II], \quad (12.1c)$$

$$\dot{[SS]} = 2\gamma[SI] - 2\tau[SSI] + \alpha_{SS}([S]([S] - 1) - [SS]) - \omega_{SS}[SS]. \quad (12.1d)$$

These equations can be interpreted using Fig. 12.1. The basic idea of pairwise models is to derive evolution equations for the expected number of nodes of different statuses, i.e., $[X]$ where $X \in \{S, I\}$. However, looking at the evolution equation of $[I]$, see equation (12.1a), we note that this depends on the expected number of $[SI]$ pairs, and hence equations for this and other pairs, e.g., $[SS]$ and $[II]$, are also needed. The evolution equations of pairs will then depend on the expected number of triples with nodes of certain statuses, i.e., $[SSI]$ and $[ISI]$. This leads to a hierarchical dependence of pairs on triples and then of triples on quadruples, and so on. This is obviously not practical due to the combinatorial explosion in number of equations. Hence, a closure is needed which in this case approximates triples in terms of singles and pairs. From the model it follows that $[S] + [I] = N$, and that the closure requires the time-dependent expected average degree of S nodes. This is given by

$$k_S(t) = \frac{[SS] + [SI]}{[S]}. \quad (12.2)$$

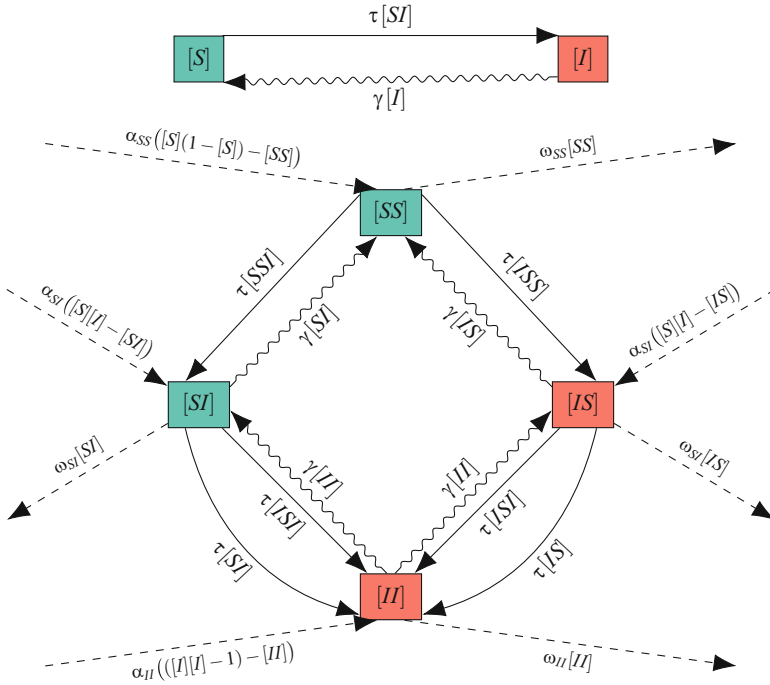


Fig. 12.1 A flow diagram leading to system (12.1). (top) The relevant flows for the individual-level variables. The *solid line* denotes an infection, while the *sinuous line* denotes a recovery. The rate of new infecteds depends on $[SI]$, and so we require pair-level variables. (bottom) The relevant flows for the pair-level variables. The colours denote the status of the “first” node in the edge. The *solid lines* denote infections, the *sinuous lines* denote recoveries, and the *dashed lines* denote addition or removal of edges. Some of the infection events involve triples, and so we need triple-level variables or a closure

The well-known closure [10] is used, namely

$$[SSI] = \frac{(k_S - 1)[SS][SI]}{k_S[S]} \quad \text{and} \quad [ISI] = \frac{(k_S - 1)[SI][SI]}{k_S[S]}. \tag{12.3}$$

Upon applying these closures, a self-consistent system with 4 ODEs is obtained. This can be analysed using classical bifurcation theory techniques.

It is worth noting that the pairwise model above makes some implicit assumptions. First, it assumes that pairs and triples are counted multiple times. This for example implies that $[SI] = [IS]$ and that $[SS]$ stands for twice the number of singly counted edges connecting susceptible nodes. Similarly, $[ISI]$ is a multiple count of arrangements such as nodes i, j and k , with susceptible node j being connected to infected nodes i and k . Second, our model does not explicitly account for the degree of nodes and thus degree-degree correlations are omitted. Finally, we note that closures use the time-dependent excess degree of susceptible nodes, $k_S(t)$, rather than the average degree of the network, $\langle k \rangle$, as it is done for static network models.

12.3 Bifurcation Analysis of the Epidemic

12.3.1 Bifurcation Analysis of the System Behaviour for Scenario A

Turning to scenario A, i.e., the case in which edges are added or removed independently of node status ($\alpha_{SS} = \alpha_{SI} = \alpha_{II} := \alpha$ and $\omega_{SS} = \omega_{SI} = \omega_{II} := \omega$), we determine the steady states and the local behaviour around them. In [12] it was shown that the network becomes an Erdős-Rényi type random graph at the steady state and the probability an edge is active is $p = \frac{\alpha}{\alpha + \omega}$. So the average degree at equilibrium is

$$\langle k \rangle = (N - 1) \frac{\alpha}{\alpha + \omega}$$

In this case the coordinates of the disease-free steady state are $[I] = 0$, $[SI] = 0$, $[II] = 0$ and $[SS] = \frac{N(N-1)\alpha}{\omega + \alpha}$. The Jacobian matrix corresponding to this steady state is

$$J = \begin{pmatrix} -\gamma & \tau & 0 & 0 \\ \alpha N & \tau(\langle k \rangle - 2) - \alpha - \gamma - \omega & \gamma & 0 \\ -\alpha & 2\tau & -2\gamma - \alpha - \omega & 0 \\ \alpha(-2N + 1) & 2\gamma - 2\tau(\langle k \rangle - 1) & 0 & -\alpha - \omega \end{pmatrix},$$

Solving the equation $\det J = 0$ for τ shows that a transcritical bifurcation occurs at

$$\tau_c = \frac{\gamma(2\gamma + \alpha + \omega)}{\alpha N + 2\gamma(\langle k \rangle - 1)}, \quad (12.4)$$

which is derived in [23]. Numerical investigation shows that for $\tau < \tau_c$ the solutions of the system tend to the disease-free steady state, while for $\tau > \tau_c$ the solutions converge to the endemic steady state. Oscillations were not observed in this case, see [23].

An approximation to this bifurcation curve can be determined by theoretical considerations. The simplest way of approximating the transcritical bifurcation curve, which separates the endemic and disease-free regions, is to start from the steady state equation $\tau[SI] = \gamma[I]$ and make an additional assumption (the pair closure) $[SI] \approx \frac{\langle k \rangle}{N-1}[S][I]$. Substituting this into the steady state equation with $\langle k \rangle = N\alpha/(\alpha + \omega)$, then dividing by $[I]$ and substituting $[S] = N$, which holds at the boundary of the endemic region, we arrive at

$$\tau_{pc} = \gamma \frac{\alpha + \omega}{N\alpha},$$

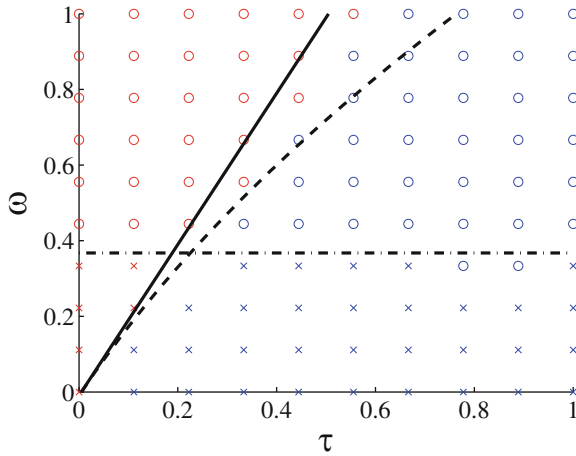


Fig. 12.2 Four behaviours observed in simulations of scenario **A** in the (τ, ω) parameter space and the theoretical bifurcation curves for $\alpha = 0.01, N = 200, \gamma = 1$. The *horizontal (dash-dotted line)* represents the boundary of the parameter domain where the graph transitions from connected to disconnected. In the simulation, networks which on average had at least 3 disjointed components were considered disconnected. The other two curves are the transcendental bifurcation curves obtained from the mean-field approximation (*continuous diagonal line*) and from the pairwise approximation (12.4) (*dashed line*). The markers are as follows: \times – connected, epidemic, \times – connected, no epidemic, \circ – disconnected, epidemic, and \circ – disconnected, no epidemic

where the subscript ‘pc’ denotes pairwise closure. This bifurcation curve and that given by the pairwise model, see (12.4), are shown in Fig. 12.2. As expected the agreement is only partial since the pairwise model provides a more accurate approximation of the true stochastic model.

12.3.2 Bifurcation Analysis of the System Behaviour for Scenario B

Focusing on scenario **B**, the system admits two equilibria: (a) a disease-free equilibrium $([S], [I], [SI], [II], [SS]) = (N, 0, 0, 0, N(N - 1))$ and (ii) an endemic equilibrium which emerges from the solution of a quartic equation.

The linearisation around the disease-free steady state gives rise to a 4×4 Jacobian, the eigenvalues of which can be determined explicitly, see Appendix A in [24]. As shown, two of the eigenvalues are always negative and the remaining two have negative real part if and only if

$$\omega_{SI} > \tau(N - 2) - \gamma, \tag{12.5}$$

which gives rise to a transcritical bifurcation where $\omega_{SI} = \tau(N - 2) - \gamma$, see Fig. 12.3. Thus the following Proposition holds.

Proposition 1 *The disease-free steady state is stable if and only if $\omega_{SI} > \tau(N - 2) - \gamma$.*

As mentioned above the endemic steady state is the solution of a quartic equation, see [24] for its detailed derivation. The analysis of this equation leads to the following proposition concerning the existence of the endemic steady state.

Proposition 2 *If $[S] = x \in (0, N)$ is a root of polynomial*

$$x^4 + A_3x^3 + A_2x^2 + A_1x + A_0 = 0, \tag{12.6}$$

with

$$A_3 = 4ab - 3 - 2b - c,$$

$$A_2 = 2 + 2b + c + b^2 + bc - 6ab - 4ab^2 - 2abc + 4a^2b^2 + Nb(1 - 4a),$$

$$A_1 = Nb(-1 + 6a - b - c + 6ab + 2ac - 8a^2b),$$

$$A_0 = 2N^2ab^2(1 - 2a),$$

where $a = \frac{\omega_{SI}}{\alpha_{SS}}$, $b = \frac{\gamma}{\tau}$ and $c = \frac{\omega_{SI}}{\tau}$, then the system has an endemic steady state, the coordinates of which can be given as

$$[S]_{ss} = x, \quad [I]_{ss} = N - x, \quad [SI]_{ss} = \frac{\gamma}{\tau}(N - x),$$

$$[SS]_{ss} = x(x - 1) - 2\frac{\omega_{SI}\gamma}{\alpha_{SS}\tau}(N - x), \quad [II]_{ss} = \frac{\gamma(N - x)^2}{\tau x} + \frac{(N - x)[SS]_{ss}}{[SS]_{ss} + [SI]_{ss}}.$$

Extensive numerical tests suggest that the quartic polynomial has a single root providing a biologically plausible steady state. This means that below the transcritical bifurcation there is a unique endemic steady state. That is for a fixed value of τ , there is a critical cutting rate ω_{SI}^{crit} such that the unique endemic steady state exists if and only if $\omega_{SI} < \omega_{SI}^{crit} = \tau(N - 2) - \gamma$.

Similarly, the stability of the endemic steady state can only be computed numerically by evaluating the coefficients of the characteristic polynomial. However, this does not prevent us from mapping out where the Hopf bifurcation arises (see Appendix A in [24] for details). It has been shown that the Hopf bifurcation points carve out an island from the parameter space, as shown in Fig. 12.3, within which the prevalence exhibits stable oscillations. Hence, the region below the transcritical bifurcation line and outside the Hopf island is where the endemic equilibrium is stable. It is important to note that the system-level analysis can be complemented by the observation that the expected average degree displays a behaviour similar to that of the expected number of infected nodes, as illustrated by the top panel of Fig. 12.6 but produced using the compact pairwise model.

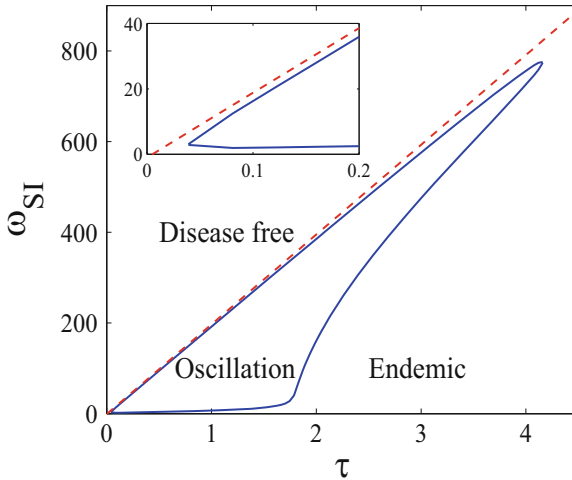


Fig. 12.3 Bifurcation diagram for the pairwise ODE model for scenario **B** in the (τ, ω_{SI}) parameter space for $N = 200$, $\gamma = 1$ and $\alpha_{SS} = 0.04$. The transcritical bifurcation occurs along the *dashed line*, and the Hopf bifurcation occurs along the perimeter of the island

12.4 Network Bifurcation

While some studies of adaptive or dynamic networks do consider and analyse changes in network structure [7, 14, 25], there are many papers which only focus on disease-related quantities such as the prevalence of infection with the aim to characterise those via bifurcation analysis.

However, it has been observed that the networks themselves can also undergo significant changes in time depending on parameters. For example, Gross et al. [7] reported segregation of networks into different components, see Fig. 12.7 also. Such analysis can reveal important network features which can invalidate the use of mean-field or pairwise models and, more importantly, may reveal the true impact of the interplay between dynamics on and of the network on changes in the underlying networks and the range of emerging networks.

Emergence of network structure from such dynamic network models could also be interpreted as a more natural or organic form of emergence of structure, compared to that observed in artificial or synthetic network models. In what follows we aim to couple the analysis of system- and network-level changes, in order to concurrently reveal the spectrum of behaviours at all levels, i.e., both system and network.

12.4.1 Mapping the Emerging Network Structure onto the System-Level Bifurcation Picture for Scenario A

In the case of scenario **A**, that is, when $\alpha_{SI} = \alpha_{II} = \alpha_{SS} := \alpha$, and $\omega_{II} = \omega_{SS} = \omega_{SI} := \omega$ a more complete characterisation of network bifurcations can be achieved. As suggested by the pairwise model, two behaviours may occur according to the long time prevalence level, namely disease-free or endemic steady state. As regards the network structure we studied the connectivity (through determining the type and number of connected components) of the network and its degree distribution. Our goal here is to map out system and network behaviour over the (τ, ω) parameter space. We consider several stochastic simulations at each lattice point in the (τ, ω) parameter plane. The average epidemic level and network connectivity are then determined at the steady state (after a sufficiently long time). The different system and network level outcomes yield four different behaviours shown in Fig 12.2. The most interesting observation is that epidemics can be curtailed either because the network gets disconnected or because the epidemic is sub-threshold even though the network could theoretically support an epidemic.

The bifurcation curve separating the connected and disconnected regions can be derived analytically as follows. We have noted that at the steady-state this network is an Erdős–Rényi graph, with $p = \frac{\alpha}{\alpha + \omega}$, and we know that the threshold for an Erdős–Rényi graph being disconnected is $p = \frac{\ln N}{N}$ [2, 4], where N denotes the number of nodes. Taking into account these two formulas we get the following equation,

$$p = \frac{\alpha}{\alpha + \omega} = \frac{\ln N}{N}.$$

Thus the critical threshold for connectivity is,

$$\omega^* = \alpha \left(\frac{N}{\ln N} - 1 \right). \quad (12.7)$$

The horizontal line in Fig. 12.2 is drawn at this value of ω , see also [23]. There is good agreement with the connectivity results obtained from simulation. Moreover, as expected, the degree distribution of networks during and at the end of simulations is well described by the binomial distribution and for fixed values of α , the number of components increases sharply with larger values of ω . This is natural since in the high deletion and low activation regime the networks become sparse with higher values of ω leading to networks with several disjointed components.

From system (12.1) and using scenario A it also follows that the number of (doubly-counted) edges in the network, $E(t) = [SS](t) + [II](t) + 2[SI](t)$, satisfies

$$\dot{E} = \alpha(N(N - 1) - E) - \omega E \quad (12.8)$$

with its steady state being given by

$$E_{eq} = \frac{\alpha N(N-1)}{\alpha + \omega} \quad (12.9)$$

and with the average degree at equilibrium being $k_{eq} = \frac{E}{N} = \frac{\alpha(N-1)}{\alpha + \omega}$. This also follows from the simple heuristic argument that at equilibrium the rate at which edges are cut is equal to the rate at which edges are created, i.e., $\omega E_{eq} = \alpha(N(N-1) - E_{eq})$.

12.4.2 Mapping the Emerging Network Structure onto the System-Level Bifurcation Picture for Scenario B

We now consider the more realistic case of a link status-dependent link addition and deletion model. While the system-level characterisation (i.e. focusing on the analysis of the pairwise model from the viewpoint of the outcome of the epidemic, without explicitly considering the underlying dynamic network) is not trivial, one can use classical bifurcation theory techniques even if some calculations can only be performed numerically. In [24] it was shown that the agreement between the pairwise model and simulation is mainly qualitative, insofar as the pairwise model predicts the observed outcomes but the size and boundaries of the different regimes in the parameter space differ between pairwise and simulation-based models. This is the result of the sub-optimal performance of closures which fail to capture the heterogeneity in degree distribution as well as, and perhaps more importantly, the presence of correlations introduced by the link status-dependent creation and deletion. These factors lead to the breakdown of closures. In addition, we shall show that the underlying network can become disconnected which further degrades the performance of the closures.

A detailed analysis of emerging network structures is made even more challenging by the need to rely on (i) different variants of pairwise models (tracking versus not tracking the degree of nodes), and (ii) explicit stochastic network-based simulation, sometimes on small networks to gain intuition. The former is useful to provide a rough guide of the possible behaviours and to identify broad parameter regions leading to networks of different type, such as connected versus disconnected, degree distributions that change throughout the oscillation cycle.

12.4.2.1 Analysing Emerging Networks Using Mean-Field Models

Let us progressively move from the simplest towards the most complex mean-field model and explore what information we can gain about the structure of the emerging networks. Starting with the pairwise model (12.1) one can ascertain at

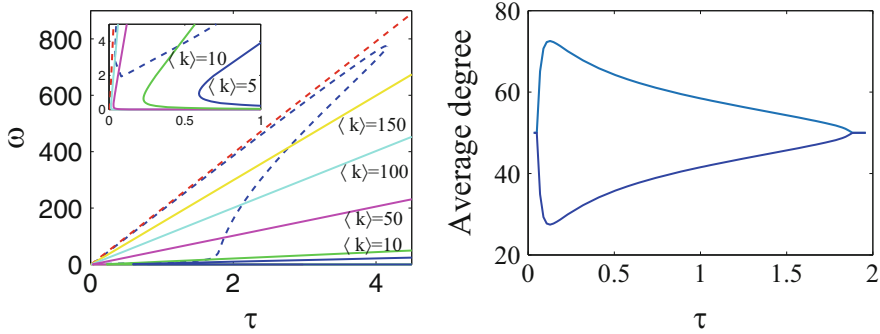


Fig. 12.4 (Left-panel) Contour plot of the average degree (or mean average degree over one cycle of oscillation when oscillations are stable) overlaid on the system-level bifurcation diagram. The inset provides a zoomed-in version of the bottom-left corner of the main plot to reveal the fine structure at low ω and τ values. (Right-panel) The amplitude of the oscillations of the average degree when travelling through the Hopf island along the isoline where the mean average degree is $\langle k \rangle = 50$. Parameter values are $N = 200$, $\gamma = 1$, $\alpha_{SS} = 0.04$

least the behaviour of the average degree over time. Thus, we can explore whether the average degree will stabilise or oscillate, and determine how these two regimes will partition the parameter space considered in the bifurcation diagram at system-level shown in Fig. 12.3.

In Fig. 12.4 we show a contour plot of the average degree and we track the amplitude of oscillations of the average degree along an isoline where the mean average degree over an oscillatory cycle is constant. This figure reveals that the resulting networks exhibit a wide range of average degree values. Two important observations can be made. First, we note that for a fixed value of τ and as the cutting rate increases, the average degree at equilibrium (or its mean over one cycle) tends to higher values. This is due to the cutting of $S - I$ links which reduces the impact of the epidemic and leads to fewer infected nodes. This in turn leads to more susceptible nodes such that the addition of new $S - S$ links is fast and increases the average degree. Second, we note regions in which a form of bistability exists (see inset in the left panel of Fig. 12.4). Namely, the same average degree can be achieved for the same value of the transmission rate τ but two distinct values of ω_{SI} . This can be explained by considering the prevalence level (not shown) which, as intuition suggests, will be lower for higher values of the cutting rate and much higher for smaller values of ω_{SI} . Thus, networks with the same average degree and transmission rate can sustain either higher prevalence with a lower cutting rate or lower prevalence with a higher cutting rate.

The amplitude of the oscillations of the average degree in Fig. 12.4 confirms our expectations by showing that the amplitude tends to zero at the boundaries of the Hopf island and grows considerably when moving away from the boundary separating the stable endemic equilibrium and the oscillatory regime.

It is obvious that the previous model offers no information about how links are distributed over nodes, and thus about the degree distribution. To improve on this and get a basic description of the behaviour of the degree distribution one can write down a more complete set of pairwise equations that track the degree of nodes. Epidemics on networks with heterogeneous degrees can be described by heterogeneous mean-field models [5]. However, the number of equations in such models is of order $O(N^2)$ since the degree in a dynamic network can, in principle, vary between 0 and $N - 1$, where N is the number of nodes in the network. As a trade-off between keeping degree heterogeneity and having a tractable system of ODEs, so-called compact pairwise models have been introduced [9]. The variables of this model are $[S_k]$ and $[I_k]$ representing the average number of susceptible and infected nodes of degree k , respectively, and the average number of pairs $[SI]$, $[SS]$ and $[II]$. We make use of the approximation

$$[A_k B] = [AB] \frac{k[A_k]}{\sum_j j[A_j]}, \quad (12.10)$$

where $[A_k B] = \sum_j [A_k B_j]$. In fact, the pairs $[A_k B_j]$ are not needed in the compact pairwise model, and only pairs of the form $[A_k B]$ are used, significantly reducing the number of equations. We extend this model with terms accounting for link addition/creation and deletion as follows. The deletion of links connecting an infected to a susceptible node with degree k at rate ω_{SI} contributes positively to $[S_{k-1}]$ and negatively to $[S_k]$. The creation of links connecting a susceptible to another susceptible node with degree k contributes negatively to $[S_k]$ with rate $\alpha_{SS}([S_k]([S] - 1) - [S_k S])$ because the total number of such possible links is $[S_k]([S] - 1)$ and the number of existing links is $[S_k S]$. The same process contributes positively to $[S_{k+1}]$. Using similar arguments we arrive at the following system,

$$[\dot{S}_k] = -\tau[S_k I] + \gamma[I_k] + \omega_{SI}([S_{k+1} I] - [S_k I]) \quad (12.11a)$$

$$+ \alpha_{SS}([S_{k-1}]([S] - 1) - [S_{k-1} S]) - \alpha_{SS}([S_k]([S] - 1) - [S_k S]),$$

$$[\dot{I}_k] = \tau[S_k I] - \gamma[I_k] + \omega_{SI}([I_{k+1} S] - [I_k S]), \quad (12.11b)$$

$$[\dot{S}I] = \gamma([II] - [SI]) + \tau([SSI] - [ISI] - [SI]) - \omega_{SI}[SI], \quad (12.11c)$$

$$[\dot{I}I] = -2\gamma[II] + 2\tau([ISI] + [SI]), \quad (12.11d)$$

$$[\dot{S}S] = 2\gamma[SI] - 2\tau[SSI] + \alpha_{SS}([S]([S] - 1) - [SS]), \quad (12.11e)$$

where $[S] = \sum_k [S_k]$. The approximation in Eq. (12.10) is used to compute the pairs $[S_k I]$ and $[I_k S]$ for $k = 0, 1, \dots, N - 1$, and according to [9], the triples are closed by

$$[AS I] = \frac{[AS][SI]}{([SS] + [SI])^2} \sum_k k(k-1)[S_k].$$

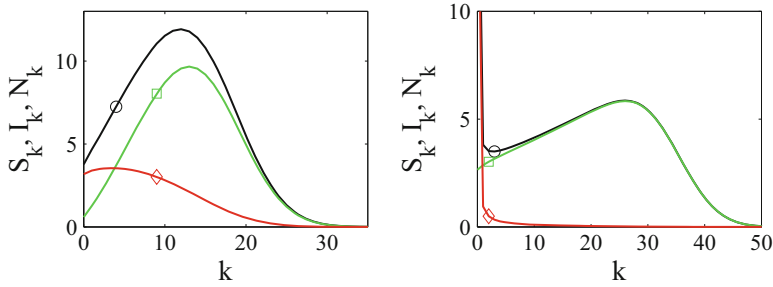


Fig. 12.5 Degree distributions (shown as a non-normalised degree histogram here and in all subsequent figures) of the susceptible (\square), infected (\diamond), and the whole network (\circ) at the endemic steady state using the compact pairwise model (12.11). The parameter values are $N = 200$, $\gamma = 1$, and $\alpha_{SS} = 0.04$ with (left-panel) $\tau = 0.2$ and $\omega_{SI} = 1.5$, and (right-panel) $\tau = 4$ and $\omega_{SI} = 100$

Preliminary numerical investigations reveal that this compact model produces better qualitative agreement with results from simulation than the standard pairwise model. And although this agreement is not optimal, the model offers further value through providing qualitative insights into the behaviour of the degree distribution in time or at equilibrium. A detailed study of the compact pairwise model is beyond the scope of the present paper, but below we present some output from this model with special focus on elucidating the types of networks that are likely to emerge.

We start by reporting on the behaviour of networks when the endemic steady state is stable. In Fig. 12.5 the degree distributions (shown as a non-normalised degree histogram here and in all subsequent figures) of the whole network and those of susceptible and infected nodes separately are plotted. This reveals that the emerging networks can vary both in their degree distribution and average degree. The most striking difference is the propensity of the infected nodes to become isolated compared to susceptible nodes. This effect is exacerbated in the left panel of Fig. 12.5. On the one hand, the network dynamics removes $S-I$ links thus reducing the number of edges originating from infected nodes. On the other hand, the network is replenished with $S-S$ links and these nodes enjoy and share more links compared to infected ones. In the true network-based stochastic simulation model this effect, for the right parameter combinations, can lead to complete isolation of the infected nodes through being cut off from the rest of the network, leading to the whole process being eventually attracted to the absorbing state with no infected nodes and all possible links present.

Let us now focus on the oscillatory regime within the Hopf island. In the top panel of Fig. 12.6 we show a typical plot of the time evolution of both prevalence and average degree. We note that these oscillations go hand in hand but are out of phase. At high average degree the prevalence is typically small meaning that the network has many susceptible nodes that become more and more densely connected. However, as soon as infection manages to invade from the fringe of this tightly connected cluster of susceptible nodes, the epidemic spreads and the prevalence

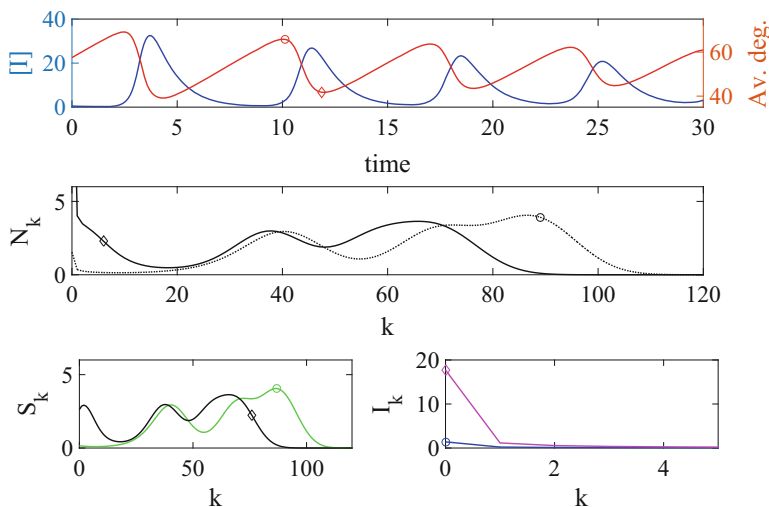


Fig. 12.6 Illustration of the oscillatory behaviour in the expected prevalence and average degree (the curve with the markers) based on the compact pairwise model (12.11) (*top panel*). Prevalence and average degree are out of phase with the network being most densely connected when the prevalence of infection is low and vice-versa. The degree distribution at the peak (\circ) and trough (\diamond) of the oscillatory cycle of the average degree (*middle panel*) shows that the network loses links and more poorly connected nodes emerge with the entire degree distribution moving towards lower degrees. The degree distribution of susceptible and infected nodes (*bottom panel*) reveal that infected nodes are in general poorly connected due to the cutting of $S-I$ links. Parameter values are: $N = 200$, $\tau = 0.4$, $\gamma = 1$, $\alpha_{SS} = 0.04$ and $\omega_{SI} = 25$. We note that the oscillations eventually stabilise with a well defined amplitude and cycle duration

grows. As the number of infected nodes increases so does that of the $S-I$ links. The link removal becomes significant and slows the epidemic due to fewer links being available for transmission.

The middle panel of Fig. 12.6 shows the typical degree distribution at the peak and trough of the degree oscillation. Again, as explained above, we notice that at the trough, when the average degree attains its minimum, the number of nodes with no or few connections increases significantly. As shown in the bottom two panels of the same figure, it is mainly the infected nodes that suffer the consequences of the link cutting process and these nodes lose many of their links leaving them with no or very few connections. In contrast, the susceptible nodes are more resilient and their degree distribution shows less dramatic change between peak and trough.

12.4.2.2 Analysing Emerging Networks Using Simulation

Finally, we present some results from rigorous network-based stochastic simulations using a Gillespie algorithm. Before we turn to the analysis of the output we recall some of the nuances of the comparison between mean-field and simulation models.

First, it is well known that the worst performance of the mean-field models is usually when the system operates close to threshold, i.e., at the point separating die-out from an epidemic. Moreover, during oscillations that come close to extinction (i.e., a system with a small number of infected nodes), agreement with the mean-field models is also expected to break down. Typically in such cases, the stochastic process can be absorbed by the all-susceptible state, while the mean-field models will indicate oscillations.

In what follows we focus on the oscillatory regime and map out how both system and network behave during one cycle of oscillation. First, we note that the de-phasing between prevalence and average degree is not as clear as for the deterministic model, see Fig. 12.7. However, the trend is similar in that the average degree peaks before the epidemic peaks. Our analysis here is based on peaks and troughs in prevalence rather than average degree, as per the mean-field case. This is purely because oscillations in prevalence had a bigger amplitude and thus were easier to capture. However, we shall show this complements the results thus far. We also note that the parameter values for the simulation were chosen based on a simulation-based bifurcation diagram in [24]. This was necessary because the agreement between bifurcation boundaries in the mean-field and simulation models is qualitative rather than quantitative.

There is an interesting contrast between the four competing processes: (a) link creation, (b) link deletion, (c) transmission, and (d) recovery. These processes compete and balance out in order to give rise to oscillatory behaviour both in the prevalence and degree. This is illustrated in Fig. 12.7 where we also show a few explicit network snapshots during the main phases of a full cycle, including the trough and peak of the oscillation in prevalence. The main phases of the oscillation cycle are:

1. **Phase A:** $[I]$ decreasing, $\langle k \rangle$ decreasing with recovery and link cutting dominating transmission and link creation, respectively;
2. **Phase B:** $[I]$ decreasing, $\langle k \rangle$ increasing with recovery dominating transmission but link creation dominating link cutting;
3. **Phase C:** $[I]$ increasing, $\langle k \rangle$ increasing with transmission and link creation dominating recovery and link cutting, respectively;
4. **Phase D:** $[I]$ increasing, $\langle k \rangle$ decreasing with transmission dominating recovery but link cutting dominating link creation.

Several important observations can be made. The simulation captures different phases of the cycle. At peak prevalence the cutting of $S - I$ links has the biggest impact on the remaining few susceptible nodes. These become disconnected from the cluster of tightly connected infected nodes. Here, the S nodes are poorly connected while the I nodes share many links with other I nodes; see Fig. 12.7 and the corresponding degree distributions in Fig. 12.8. However, when the prevalence is low, the infected nodes become isolated and the network is dominated by the cluster of susceptible nodes. Table 12.1 shows clearly that the average degree of infected nodes is small when the prevalence is at its trough, while the average degree of susceptible nodes attains its minimum when prevalence peaks.

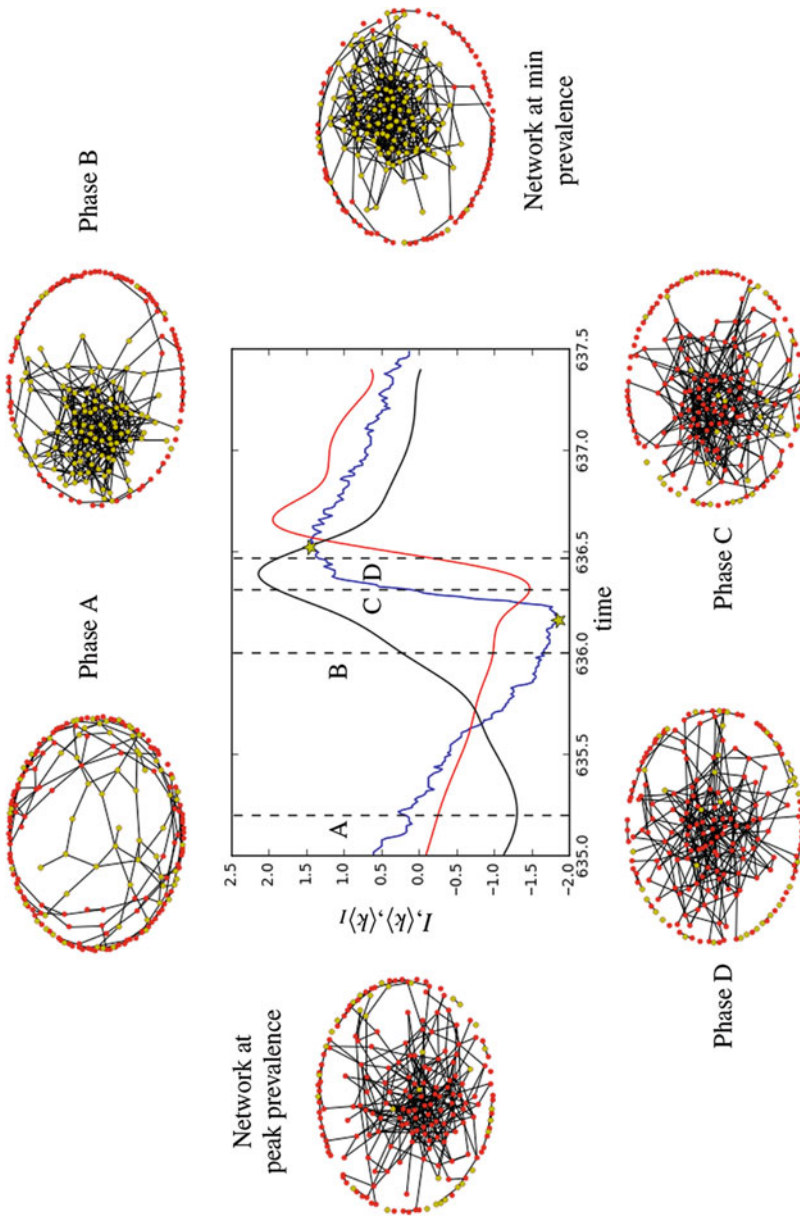


Fig. 12.7 A full cycle of oscillation of prevalence (*blue, I*), average degree of the whole network (*black, $\langle k \rangle$*) and of infected nodes (*red, $\langle k \rangle_I$*) based on a single realisation of the stochastic simulation (printed in portrait mode for clarity). All data series have been normalised as $\frac{Y-\nu}{\sigma}$, where ν and σ are the mean and standard deviation of the data series taken over the time interval shown in the figure. The *dashed lines* denote the time points when the networks have been plotted and, more importantly correspond to the four Phases A, B, C and D of the oscillation cycle. The peak and trough of prevalence are highlighted by star symbols and the networks corresponding to these turning points are given at the bottom and top, respectively. Parameter values are $N = 200$, $\gamma = 1$, $\alpha_{SS} = 0.04$, $\tau = 6$ and $\omega_{ST} = 4$

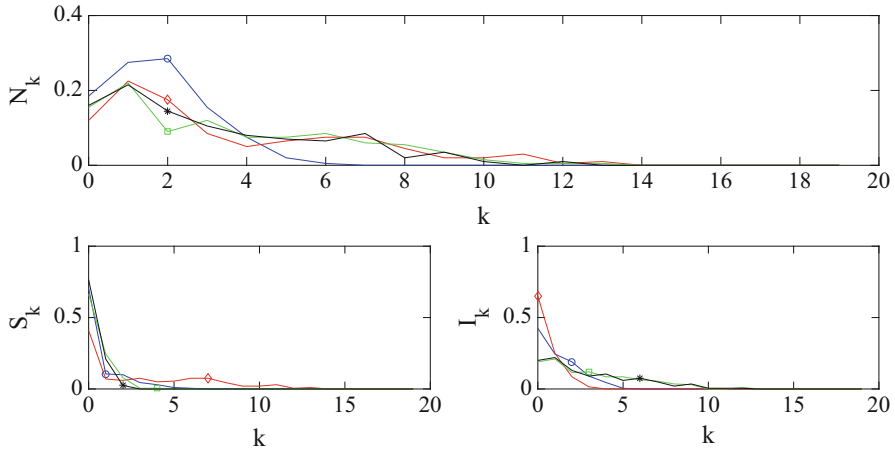


Fig. 12.8 Degree distributions of networks in Phase A (\circ), B (\diamond), C (\square) and D ($*$). In the *top panel* the degree distribution of the entire network is plotted independently of the status of the nodes. The *bottom left and right panels* focus on the degree distributions of susceptible and infected nodes, respectively. Parameter values are: $N = 200$, $\tau = 6$, $\gamma = 1$, $\alpha_{SS} = 0.04$ and $\omega_{SI} = 4$

Focusing on the case when prevalence is small, it is evident from Fig. 12.7 that the creation of $S - S$ links floods the subset of S nodes, making this part of the network well connected. At this point, the very few infected nodes that may still share links with the susceptible cluster can trigger a sizeable increase in infection prevalence. Of course, at this critical point, the epidemic may die out with some non-negligible probability if enough I nodes are isolated from the susceptible cluster.

To complement the heuristic network plots, the degree distributions of networks at Phases A, B, C and D are shown in Fig. 12.8. In contrast to the analysis based on the compact pairwise models, the simulation shows that the role reversal between the degree of S and I nodes, when going from peak to minimum prevalence, is more balanced and the number of poorly connected S and I nodes is comparable between Phases B and D. This of course may be parameter-specific and these regimes may be present in both models.

Looking at Tables 12.1 and 12.2 we note that the network undergoes significant changes and these are summarised below. The average degree achieves its highest value when the prevalence is at its minimum. The networks are sparsest in Phase A, when following a major increase in the prevalence level the network is thinned, and both the cutting of links and recovery dominate. Overall the observed networks remain fairly sparse and, as expected, the level of clustering is low. Table 12.2 shows the unique counts of a few chosen subgraphs for all six networks. Again, as expected, subgraphs are more numerous at the time point when prevalence is at its minimum.

Table 12.1 Summary network characteristics for the 6 networks considered in Fig. 12.7. Given the large number of components in the network, the table provides information both for the entire network and the giant component. The global clustering coefficient denoted by C in the Table was calculated using the formula proposed in [10]. The number of components (not shown) is fairly constant across networks (average of 43, min=37 at min prevalence, max=47 in network A). Network A has the largest number of nodes with degree 0 (37) and degree 1 (55). The network at min prevalence has the smallest number of nodes with degree 0 (21) and degree 1 (43)

	Entire network						Giant component						
	[I]	[S]	n	n_I	n_S	C	[N]	[I]	[S]	n	n_I	n_S	C
A	132	68	1.74	1.67	1.88	0.02	134	84	50	2.28	2.15	2.50	0.02
B	83	117	3.59	1.12	5.34	0.08	128	18	110	5.11	1.72	5.66	0.08
Min	77	123	4.22	1.09	6.18	0.07	137	17	120	5.77	1.88	6.32	0.07
C	158	42	3.45	3.81	2.10	0.05	144	117	27	4.60	4.93	3.15	0.05
D	164	36	3.17	3.55	1.44	0.05	143	125	18	4.24	4.46	2.67	0.05
Max	166	34	3.13	3.51	1.26	0.05	142	127	15	4.20	4.40	2.47	0.05

Table 12.2 Number of uniquely counted subgraphs for each network as calculated by the subgraph counting algorithm described in [18]. It should be noted that the number of Δ corresponds to Δ not involved in either \boxtimes or \boxminus

	\boxtimes	\boxminus	\square	Δ	\diamond	\circ
A	0	0	5	2	6	3
B	3	37	143	9	544	2056
Min	3	51	289	7	1143	4558
C	0	8	117	14	331	1156
D	0	7	101	11	256	803
Max	0	6	95	12	230	771

12.4.3 Towards a Bifurcation Theory of Dynamic Networks

In formulating this problem, we restrict ourselves to undirected, unweighted networks with N nodes, where links are binary (i.e., either present or not). In this case the state space of all such networks \mathcal{G} has cardinality $2^{N(N-1)/2}$. The body of work concerning the properties and the dynamics of and on such networks indicates that certain sub-sets of the whole state space are more likely to arise in applications and in theoretical work. Hence, considering subsets $\mathcal{G}_i \in \mathcal{G}$, where \mathcal{G}_i correspond to classes of well-known networks (e.g., Erdős-Rényi random, lattice-type, clustered, scale-free etc) is a widely used approach.

This setup is particularly useful when considering dynamical processes evolving on a fixed network specified on the basis of empirical observations or a network model. However, when considering adaptive or evolving networks, i.e., when the dynamics on the network and that of the network are coupled, this approach needs to be made more rigorous. Let us first assume that we have a dynamics on the network where nodes can achieve a discrete number of possible states (i.e., a_1, a_2, \dots, a_m) with transition rules and rates stored in an operator \mathcal{D} (dynamic on the network). This operator is in fact of the form $\mathcal{D} = (D_{i,j})_{i,j=1,2,\dots,m}$, where $D_{ij} = D_{ij}(r_{ij}, \mathcal{G})$ with r_{ij} describing the transition rate of a node in state a_j to state a_i , where this transition may or may not involve knowledge about the network (i.e., \mathcal{G} – the network’s adjacency matrix).

Another operator \mathcal{H} specifies the dynamics of the network which may be vertex type-dependent (e.g., link activation and cutting, nodes birth and death and instant partner exchange). For link activation and deletion alone, this operator can be written as

$$\mathcal{H} = (H_{ij})_{i=1,2,\dots,M,j=1,2},$$

where $M = m(m + 1)/2$, $H_{i,1} = H_{i,1}(\alpha_{se(i)}, \mathcal{G})$ and $H_{i,2} = H_{i,2}(\omega_{se(i)}, \mathcal{G})$, where $se(i)$ is the i th element of the set describing all potential edge statuses

$$SE = \{a_1a_1, a_1a_2, \dots, a_1a_m, a_2a_2, a_2a_3, \dots, a_2a_m, a_3a_3, \dots, a_ma_m\}.$$

If, for example, instant partner switching is to be implemented, \mathcal{H} can be augmented by $\mathcal{L} = (L_{ij})_{i,j=1,2,\dots,m^2}$, where L_{ij} is simply the rate at which edges of type $se(j)$ switch to edges of type $se(i)$. Particular interest is paid to understanding how the topology of the network changes under the action of different dynamics on and of the network and how these are coupled. This naturally leads to the question of how to translate the mathematical concepts and tools from the *bifurcation theory of dynamical systems* to a *bifurcation theory of dynamical networks*.

For example, in the case of a simple epidemic model such as *SIS* (susceptible-infected/infectious-susceptible, where τ is the per-contact infection rate and γ is the recovery rate), coupled with the activation and deletion of links of different statuses (i.e., $SE = \{SS, SI, II\}$) and with partner switching or smart rewiring, where the *S* node in an *S–I* rewires to a randomly chosen other susceptible, the entire dynamics can be captured by the following operators,

$$\mathcal{D} = \begin{pmatrix} 0 & \gamma \\ \tau & \tau_G 0 \end{pmatrix}, \quad \mathcal{H} = \begin{pmatrix} \alpha_{SS} & \omega_{SS} \\ \alpha_{SI} & \omega_{SI} \\ \alpha_{II} & \omega_{II} \end{pmatrix} \quad \text{and} \quad \mathcal{L} = \begin{matrix} & SS & SI & IS & II \\ \begin{matrix} SS \\ SI \\ IS \\ II \end{matrix} & \begin{pmatrix} 0 & \omega & 0 & 0 \\ 0 & 0 & 0 & 0 \\ 0 & 0 & 0 & 0 \\ 0 & 0 & 0 & 0 \end{pmatrix} \end{matrix}.$$

In this relatively well-studied case [7, 12, 24] and given the results in this chapter, the following observations can be made:

1. if link activation and deletion are link status-independent (i.e., Scenario A and $\omega = 0$ in \mathcal{L}), then at equilibrium the resulting network will be an Erdős-Rényi random network;
2. if link activation and deletion are link status-independent (i.e., Scenario A and $\omega = 0$ in \mathcal{L}) then at the critical cutting rate α^* , see Eq. (12.7) and Fig. 12.2, the network will transition from being connected to disconnected, or vice-versa;
3. in Scenario B (and $\omega = 0$ in \mathcal{L}) and at the endemic equilibrium, depending on the precise parameter values, the network at equilibrium may or may not have a high density of poorly connected nodes, see Fig. 12.5;

4. in [7], for smart rewiring, it was shown that when $\mathcal{H} = 0$ then depending on the rewiring or partner switching rate ω the network transitions from being connected to disconnected, or vice-versa.

The interplay between \mathcal{D} , \mathcal{H} and \mathcal{L} leads to a *bifurcation in the network topology*, where under the action and interaction of dynamical processes, the network can evolve towards different topologies/structures. This type of parameter-dependent change or evolution in network structure is analogous to bifurcations in dynamical systems, and we can interpret the change in network topology as certain network steady states losing or gaining stability at the cost of other network steady states gaining or losing stability.

As seen in the results section above, there is a subtlety as to what can be regarded as a significant enough difference between two networks in order to be classified as a different behaviour type. For example using the simple pairwise model we have seen that the average degree can vary significantly, see Fig. 12.4, but this may not be regarded as a sufficiently different outcome. In general, we believe that the partitioning of the graph state space \mathcal{G} in terms of known network types may not be the ideal resolution. Nevertheless, we conjecture that it will be possible to give results such as the one below.

Conjecture *Given a spreading process defined by \mathcal{D} , and a dynamic network given by \mathcal{H} and \mathcal{L} , with the respective set of transition rates, $\mathcal{TR} \in \mathbb{R}^d$ (d – total number of parameters), one can determine a mapping $\mathcal{M} : \mathbb{R}^d \rightarrow \cup_i \mathcal{G}_i$ which identifies the bifurcation manifolds, whereby given a fixed set of parameters, the asymptotic behaviour (e.g., steady-state, quasi steady state and limit cycle) of the network structure can be specified.*

12.5 Discussion

In this chapter we set out to redress the balance between analysis at system level and analysis of the emerging network structures by focusing on the latter. Starting from the simplest pairwise model and guided by its bifurcation analysis we showed that when the epidemic is at the endemic equilibrium, the average degree of the network attains a wide range of values and bistable-like behaviour is observed, where the same average degree is achieved at the same value of the transmission rate, τ , but different cutting rates, ω .

Recognising the importance of the degree distribution as defining a network, we moved to the compact pairwise model which apart from the status of the nodes also tracks their degree. This model allowed us to show that the emerging networks can be significantly different at the peak and trough of the oscillations, and that at equilibrium and depending on the parameter values, networks with significantly different degree distributions emerge. The analysis of the stochastic model via simulation revealed a range of networks during the oscillatory cycle and highlighted a role reversal between susceptible and infected nodes when going from high to low prevalence. We also speculated mathematically about the shape a bifurcation theory for networks may take.

Several important questions remain. First of all, the bifurcation analysis of the compact pairwise model needs to be completed as this may reveal additional features or richer model behaviour. This may be challenging as the system is high-dimensional so the analysis may be restricted to numerical investigations alone. A big open question remains about the validity of such mean-field models for systems where dynamics on and of the network are coupled. As explained above, this may lead to networks becoming disconnected as well as excessive correlations between nodes of different status, all being factors that may invalidate mean-field models. Nevertheless, there is some evidence that mean-field models still play an important role in getting an initial insight into analysing such models.

The numerical investigation of the phases of the oscillatory cycle needs to be extended to include many different parameter values and assess how the resulting networks change. In addition, a similar type of numerical investigation or simulation should be carried out when the epidemic stabilises to the endemic state. Perhaps more importantly, different dynamics should be considered which may lead to even richer network-level behaviour. Such dynamics may include voter model, complex contagion, neuronal dynamics with homeostatic plasticity.

Mathematically, the problem of characterising the emerging network structure in a bifurcation theory-like fashion may prove to be challenging, partly due to the mean-field systems being high-dimensional. Overlooking the problem of whether mean-field models agree well with the average behaviour of the exact stochastic process, the analysis of such mean-field models may be best considered like a discretisation of a partial differential equation, thus allowing us to derive a more compact model which is amenable to analysis. Examples of this type can be found in [21].

Finally, given that it is reasonable to expect that many real-world networks are in fact time-frozen snapshots of an otherwise evolving system, we argue that such a network-focused view is not only desirable but could stimulate the development or design of more natural network-generating algorithms with stronger direct links to realistic processes.

Acknowledgements Joel C. Miller was funded by the Global Good Fund through the Institute for Disease Modeling and by a Larkins Fellowship from Monash University. Péter L. Simon acknowledges support from Hungarian Scientific Research Fund, OTKA, (grant no. 115926).

References

1. Ball, F., Neal, P.: Network epidemic models with two levels of mixing. *Math. Biol.* **212**(1), 69–87 (2008)
2. Chung, F.R., Lu, L.: *Complex Graphs and Networks*, vol. 107. American Mathematical Society Providence, Providence (2006)
3. Danon, L., Ford, A.P., House, T., Jewell, C.P., Keeling, M.J., Roberts, G.O., Ross, J.V., Vernon, M.C.: Networks and the epidemiology of infectious disease. *Interdisciplinary Perspectives on Infectious Diseases* **2011** (2011)

4. Durrett, R.: *Random Graph Dynamics*. Cambridge University Press, Cambridge (2007)
5. Eames, K., Keeling, M.: Modeling dynamic and network heterogeneities in the spread of sexually transmitted diseases. *Proc. Natl. Acad. Sci. USA* **99**(20), 13330–13335 (2002)
6. Gross, T., Blasius, B.: Adaptive coevolutionary networks: a review. *J. R. Soc. Interface* **5**(20), 259–271 (2008)
7. Gross, T., D’Lima, C.J.D., Blasius, B.: Epidemic dynamics on an adaptive network. *Phys. Rev. Lett.* **96**(20), 208701 (2006)
8. Gross, T., Kevrekidis, I.G.: Robust oscillations in sis epidemics on adaptive networks: coarse graining by automated moment closure. *Europhys. Lett.* **82**(3), 38004 (2008)
9. House, T., Keeling, M.: Insights from unifying modern approximations to infections on networks. *J. R. Soc. Interface* **8**(54), 67–73 (2011)
10. Keeling, M.J.: The effects of local spatial structure on epidemiological invasions. *Proc. R. Soc. B Biol. Sci.* **266**(1421), 859–867 (1999)
11. Kiss, I.Z., Miller, J.C., Simon, P.L.: *Mathematics of Epidemics on Networks: From Exact to Approximate Models*. IAM. Springer (2017)
12. Kiss, I.Z., Berthouze, L., Taylor, T.J., Simon, P.L.: Modelling approaches for simple dynamic networks and applications to disease transmission models. *Proc. R. Soc. A* **468**(2141), 1332–1355 (2012)
13. Lindquist, J., Ma, J., van den Driessche, P., Willeboordse, F.: Effective degree network disease models. *J. Math. Biol.* **62**(2), 143–164 (2011). doi:10.1007/s00285-010-0331-2
14. Marceau, V., Noël, P.A., Hébert-Dufresne, L., Allard, A., Dubé, L.J.: Adaptive networks: coevolution of disease and topology. *Phys. Rev. E* **82**(3), 036116 (2010)
15. Miller, J.C., Kiss, I.Z.: Epidemic spread in networks: existing methods and current challenges. *Math. Model. Nat. Phenom.* **9**(02), 4–42 (2014)
16. Miller, J.C., Slim, A.C., Volz, E.M.: Edge-based compartmental modelling for infectious disease spread. *J. R. Soc. Interface* **9**(70), 890–906 (2012). doi:10.1098/rsif.2011.0403
17. Pastor-Satorras, R., Castellano, C., Van Mieghem, P., Vespignani, A.: Epidemic processes in complex networks. *Rev. Mod. Phys.* **87**(3), 925–979 (2015)
18. Ritchie, M., Berthouze, L., House, T., Kiss, I.Z.: Higher-order structure and epidemic dynamics in clustered networks. *J. Theor. Biol.* **348**, 21–32 (2014)
19. Rogers, T., Clifford-Brown, W., Mills, C., Galla, T.: Stochastic oscillations of adaptive networks: application to epidemic modelling. *J. Stat. Mech: Theory Exp.* **2012**(08), P08018 (2012)
20. Sayama, H., Pestov, I., Schmidt, J., Bush, B.J., Wong, C., Yamanoi, J., Gross, T.: Modeling complex systems with adaptive networks. *Comput. Math. Appl.* **65**(10), 1645–1664 (2013)
21. Silk, H., Demirel, G., Homer, M., Gross, T.: Exploring the adaptive voter model dynamics with a mathematical triple jump. *New J. Phys.* **16**(9), 093051 (2014)
22. Szabó, A., Simon, P.L., Kiss, I.Z.: Detailed study of bifurcations in an epidemic model on a dynamic network. *Differ. Equ. Appl.* **4**, 277–296 (2012)
23. Szabó-Solticzky, A.: Dynamics of a link-type independent adaptive epidemic model. *Differ. Equ. Appl.* **9**, 105–122 (2017)
24. Szabó-Solticzky, A., Berthouze, L., Kiss, I.Z., Simon, P.L.: Oscillating epidemics in a dynamic network model: stochastic and mean-field analysis. *J. Math. Biol.* **72**(5), 1153–1176 (2016)
25. Taylor, M., Taylor, T.J., Kiss, I.Z.: Epidemic threshold and control in a dynamic network. *Phys. Rev. E* **85**(1), 016103 (2012)

Chapter 13

Disease Spreading in Time-Evolving Networked Communities

Jorge M. Pacheco, Sven Van Segbroeck, and Francisco C. Santos

Abstract Human communities are organized in complex webs of contacts that may be represented by a graph or network. In this graph, vertices identify individuals and edges establish the existence of some type of relations between them. In real communities, the possible edges may be active or not for variable periods of time. These so-called temporal networks typically result from an endogenous social dynamics, usually coupled to the process under study taking place in the community. For instance, disease spreading may be affected by local information that makes individuals aware of the health status of their social contacts, allowing them to reconsider maintaining or not their social contacts. Here we investigate the impact of such a dynamical network structure on disease dynamics, where infection occurs along the edges of the network. To this end, we define an endogenous network dynamics coupled with disease spreading. We show that the effective infectiousness of a disease taking place along the edges of this temporal network depends on the population size, the number of infected individuals in the population and the capacity of healthy individuals to sever contacts with the infected, ultimately dictated by availability of information regarding each individual's health status. Importantly, we also show how dynamical networks strongly decrease the average time required to eradicate a disease.

J.M. Pacheco (✉)

Centro de Biologia Molecular e Ambiental, Universidade do Minho, 4710 - 057, Braga, Portugal

Departamento de Matemática e Aplicações, Universidade do Minho, 4710 - 057, Braga, Portugal

ATP-group, P-2744-016, Porto Salvo, Portugal

e-mail: jmpacheco@math.uminho.pt

S. Van Segbroeck

ATP-group, P-2744-016, Porto Salvo, Portugal

F.C. Santos

ATP-group, P-2744-016, Porto Salvo, Portugal

INESC-ID & Instituto Superior Técnico, Universidade de Lisboa, 2744-016, Porto Salvo, Portugal

© Springer Nature Singapore Pte Ltd. 2017

N. Masuda, P. Holme (eds.), *Temporal Network Epidemiology*,
Theoretical Biology, DOI 10.1007/978-981-10-5287-3_13

13.1 Introduction

Understanding disease spreading and evolution involves overcoming a multitude of complex, multi-scale challenges of mathematical and biological nature [1, 2]. Traditionally, the contact process between an infected individual and the susceptible ones was assumed to affect equally any susceptible in a population (mean-field approximation, well-mixed population approximation) or, alternatively, all those susceptible living in the physical neighborhood of the infected individual (spatial transmission). During recent years, however, it has become clear that disease spreading [2–5] transcends geography: the contact process is no longer restricted to the immediate geographical neighbors, but exhibits the stereotypical small-world phenomenon [6–9], as testified by recent global pandemics (together with the impressive amount of research that has been carried out to investigate them) or, equally revealing, the dynamics associated with the spreading of computer viruses [5, 10–23]. Recent advances in the science of networks [3, 4, 19, 24, 25] also provided compelling evidence of the role that the networks of contacts between individuals or computers play in the dynamics of infectious diseases [4, 7]. In the majority of cases in which complex networks of disease spreading have been considered [9], they were taken to be a single, static entity. However, contact networks are intrinsically temporal entities and, in general, one expects the contact process to proceed along the lines of several networks simultaneously [11, 13–16, 18, 23, 24, 26–36]. In fact, modern societies have developed rapid means of information dissemination, both at local and at centralized levels, which one naturally expects to alter individuals' response to vaccination policies, their behavior with respect to other individuals and their perception of likelihood and risk of infection [37]. In some cases one may even witness the adoption of centralized measures, such as travel restrictions [38, 39] or the imposition of quarantine spanning parts of the population [40], which may induce abrupt dynamical features onto the structure of the contact networks. In other cases, social media can play a determinant role in defining the contact network, providing crucial information on the dynamical patterns of disease spreading [41]. Furthermore, the knowledge an individual has (based on local and/or social media information) about the health status of acquaintances, partners, relatives, etc., combined with individual preventive strategies [42–50] (such as condoms, vaccination, the use of face masks or prophylactic drugs, avoidance of visiting specific web-pages, staying away from public places, etc.), also leads to changes in the structure and shape of the contact networks that naturally acquire a temporal dimension that one should not overlook.

Naturally, the temporal dimension and multitude of contact networks involved in the process of disease spreading render this problem intractable from an analytic standpoint. Recently, sophisticated computational platforms have been developed to deal with disease prevention and forecast [5, 10, 11, 18, 27, 29–36, 51–55]. The computational complexity of these models reflects the intrinsic complexity of the problem at stake, and their success relies on careful calibration and validation procedures requiring biological and socio-geographic knowledge of the process at stake.

Our goal here, instead, will be to answer the following question: What is the impact of a temporal contact network structure in the overall dynamics of disease progression? Does one expect that it will lead to a rigid shift of the critical parameters driving disease evolution, as one witnesses whenever one includes spatial transmission patterns? Or even to an evanescence of their values whenever one models the contact network as a (static and infinite) scale-free network, such that the variance of the network degree distribution becomes arbitrarily large? Or will the temporal nature of the contact network lead to new dynamical features? And, if so, which features will emerge from the inclusion of this temporal dimension?

To answer this question computationally constitutes, in general, a formidable challenge. We shall attempt to address the problem analytically, and to this end some simplifications will be required. However, the simplifications we shall introduce become plausible taking into consideration recent results (*i*) in the evolutionary dynamics of social dilemmas of cooperation, (*ii*) in the dynamics of peer-influence, and even (*iii*) in the investigation of how individual behavior determines and is determined by the global, population wide behavior. All these recent studies point out to the fact that the impact of temporal networks in the population dynamics stems mostly from the temporal part itself, and not so much from the detailed shape and structure of the network [56–63]. Indeed, we now know that (*i*) different models of adaptive network dynamics lead to similar qualitative features regarding their impact in what concerns the evolution of cooperation [56–63], (*ii*) the degree of peer-influence is robust to the structural patterns associated with the underlying social networks [62], and (*iii*) the impact of temporal networks in connecting individual to collective behavior in the evolution of cooperation is very robust and related to a problem of N-body coordination [61, 63]. Altogether, these features justify that we model the temporal nature of the contact network in terms of a simple, adaptive network, the dynamics of which can be approximately described in terms a coupled system of ODEs. This “adaptive-linking” dynamics, as it was coined [28, 57–59], leads to network snapshot structures that do not replicate what one observes in real-life, in the same sense that the small-world model of Watts and Strogatz does not lead to the heterogeneous and diverse patterns observed in data snapshots of social networks. Notwithstanding, the active-linking dynamics allows us to include, analytically, the temporal dimension into the problem of disease dynamics. The results [28], as we elaborate in Sects. 3 and 4, prove rewarding, showing that the temporal dimension of a contact network leads to a shift of the critical parameters (defined below) which is no longer rigid but, instead, becomes dependent on the frequency of infected individuals in the population. This, we believe, constitutes a very strong message with a profound impact whenever one tries to incorporate the temporal dimension into computational models of disease forecast.

This chapter is organized as follows. In the following Sect. 2, we introduce the standard disease models we shall employ, as well as the details of the temporal contact network model. Section 3 is devoted to present and discuss the results, and Sect. 4 contains a summary of the main conclusions of this work.

13.2 Models and Methods

In this section, we introduce the disease models we shall employ which, although well-known and widely studied already, are here introduced in the context of stochastic dynamics in finite populations, a formulation that has received less attention than the standard continuous model formulation in terms of coupled Ordinary Differential Equations (ODEs). Furthermore, we introduce and discuss in detail the temporal contact network model.

13.2.1 Disease Spreading Models in Finite Populations

Here we introduce three standard models of disease transmission that we shall employ throughout the manuscript, using this section at profit to introduce also the appropriate notation associated with stochastic dynamics of finite populations and the Markov chain techniques that we shall also employ in the remainder of this chapter. We shall start by discussing the models in the context of well-mixed populations, which will serve as a reference scenario for the disease dynamics, leaving for the next section the coupling of these disease models with the temporal network model described below. We investigate the popular Susceptible-Infected-Susceptible (**SIS**) model [2, 4], the Susceptible-Infected (**SI**) model [2] used to study, e.g., **AIDS** [2, 64], and the Susceptible-Infected-Recovered (**SIR**) model [2, 65], more appropriate to model, for instance, single season flu outbreaks [2] or computer virus spreading [7]. It is also worth pointing out that variations of these models have been used to successfully model virus dynamics and the interplay between virus dynamics and the response of the immune system [66].

13.2.1.1 The SIS Model

In the **SIS** model individuals can be in one of two epidemiological states: Infected (I) or Susceptible (S). Each disease is characterized by a recovery rate (δ) and an infection rate (λ). In an *infinite*, well-mixed population, the fraction of infected individuals (x) changes in time according to the following differential equation

$$\dot{x} = \lambda \langle k \rangle xy - \delta x,$$

where $y = 1 - x$ is the fraction of susceptible individuals and $\langle k \rangle$ the average number of contacts of each individual [4]. There are two possible *equilibria* ($\dot{x} = 0$): $x = 0$ and $x = 1 - R_0^{-1}$, where $R_0 = \lambda \langle k \rangle / \delta$ denotes the basic reproductive ratio. The value of R_0 determines the stability of these two equilibria: $x = 1 - R_0^{-1}$ is stable when $R_0 > 1$ and unstable when $R_0 < 1$.

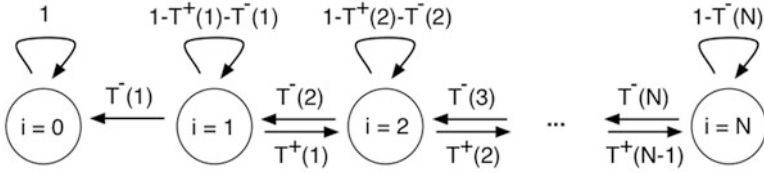


Fig. 13.1 Schematic representation of the Markov Chain associated with the stochastic **SIS** dynamics

Let us now move to finite populations, and consider the well-mixed case where the population size is fixed and equal to N . We define a discrete stochastic Markov process describing the disease dynamics associated with the **SIS** model. Each configuration of the population, which is defined by the number of infected individuals i , corresponds to one state of the Markov chain. Time evolves in discrete steps and two types of events may occur which change the composition of the population: *infection* events and *recovery* events. This means that, similar to computer simulations of the **SIS** model on networked populations, at most one infection or recovery event will take place in each (discrete) time step. Thus, the dynamics can be represented as a Markov chain \mathbf{M} with $N+1$ states [67, 68] — as many as the number of possible configurations — illustrated in the following Fig. 13.1.

In a finite, well-mixed population, the number i of infected will decrease at a rate given by

$$T^-(i, r) = \frac{1}{\tau_0} \frac{i}{N} \delta, \tag{13.1}$$

where τ_0 denotes the recovery time scale, $\frac{i}{N}$ the probability that a randomly selected individual is infected and δ the probability that this individual recovers. Adopting τ_0 as a reference, we assume that the higher the average number of contacts $\langle k \rangle$, the smaller the time scale τ_{INF} at which infection update events occur ($\tau_{INF} = \tau_0 / \langle k \rangle$) [4]. Consequently, the number of infected will also increase at a rate given by

$$T^+(i, r) = \frac{\langle k \rangle}{\tau_0} \frac{N-i}{N} \frac{i}{N-1} \lambda. \tag{13.2}$$

Equations (13.1) and (13.2) define the transitions between different states. This way, we obtain the following transition matrix for \mathbf{M} :

$$P = \begin{bmatrix} 1 & 0 & 0 & \dots & 0 & 0 & 0 \\ T_1^- & 1 - T_1^+ - T_1^- & T_1^+ & \dots & 0 & 0 & 0 \\ \vdots & \vdots & \vdots & \ddots & \vdots & \vdots & \vdots \\ 0 & 0 & 0 & \dots & T_{N-1}^- & 1 - T_{N-1}^+ - T_{N-1}^- & T_{N-1}^+ \\ 0 & 0 & 0 & \dots & 0 & T_N^- & 1 - T_N^- \end{bmatrix}, \tag{13.3}$$

where each element p_{kj} of P represents the probability of moving from state k to state j during one time step. The state without any infected individual ($i=0$) is an absorbing state of M . In other words, the disease always dies out and will never re-appear, once this happens.

Average Times to Absorption

At this level of approximation, it is possible to derive an analytical expression for the average time t_i it takes to reach the single absorbing state of the **SIS** Markov chain (i.e., the average *time to absorption*) starting from a configuration in which there are i infected **individuals**. Denoting by $P_i(t)$ the probability that the disease disappears at time t when starting with i infected individuals at time 0 , we may write [69]

$$t_i \equiv \sum_{t=0}^{\infty} tP_i(t). \tag{13.4}$$

Using the properties of $P_i(t)$ we obtain the following recurrence relation for t_i

$$t_i = (1 - T_i^+) t_i + T_i^+ t_{i+1} + 1, \tag{13.5}$$

whereas for t_N we may write

$$t_N = T_N^- t_{N-1} + (1 - T_N^-) t_N + 1. \tag{13.6}$$

Defining the auxiliary variables $\gamma_i = \frac{T_i^-}{T_i^+}$ and $q_i = \prod_{l=1}^i \gamma_l$, a little algebra allows us to write, for t_1

$$t_1 = \frac{1}{q_{N-1} T_N^-} + \sum_{k=1}^{N-1} \frac{1}{T_k^+ q_k}, \tag{13.7}$$

such that t_i can be written as a function of t_1 as follows

$$t_i = \sum_{k=1}^i s_k = t_1 \sum_{k=0}^{i-1} q_k - \sum_{k=0}^{i-1} q_k \sum_{j=0}^{i-1} \frac{1}{T_j^+ q_j}. \tag{13.8}$$

The intrinsic stochasticity of the model, resulting from the finiteness of the population, makes the disease disappear from the population after a certain amount of time. As such, the population size plays an important role in the average time to absorption associated with a certain disease, a feature we shall return to below.

Quasi-Stationary Distributions in Finite Populations

Equations (13.1) and (13.2) define the Markov chain \mathbf{M} just characterized. The fraction of time the population spends in each state is given by the stationary distribution of \mathbf{M} , which is defined as the eigenvector associated with eigenvalue 1 of the transition matrix of \mathbf{M} [67, 68]. The fact that in the **SIS** model the state without infected ($i=0$) is an absorbing state of the Markov chain, implies that the standard stationary distribution will be completely dominated by this absorbing state, which precludes one to gather information on the relative importance of other configurations. This makes the so-called quasi-stationary distribution of \mathbf{M} [70] the quantity of interest. This quantity allows us to estimate the relative prevalence of the population in configurations other than the absorbing state, by computing the stationary distribution of the Markov chain obtained from \mathbf{M} by excluding the absorbing state $i=0$ [70]. It provides information on the fraction of time the population spends in each state, assuming the disease does not go extinct.

The Infinite, Well-Mixed Populations as a Limiting Case

The Markov process \mathbf{M} defined before provides a finite population analogue of the well-known mean-field equations written at the beginning of Sect. 2.1.1. Indeed, in the limit of large populations, $\tau_0 G(i) = T^+(i) - T^-(i)$ provides the rate of change of infected individuals. For large N , replacing $\frac{i}{N}$ by x and $\frac{N-i}{N}$ by y , the *gradients of infection* which characterize the rate at which the number of infected are changing in the population, are given by

$$\tau_0 G(i) = \langle k \rangle \frac{N-i}{N} \frac{i}{N-1} \lambda - \frac{i}{N} \delta \xrightarrow{N \rightarrow \infty} \langle k \rangle \lambda xy - \delta x.$$

Again, we obtain two roots: $\tau_0 G(i) = 0$ for $i = 0$ and $i_{r_0}^* = N - \frac{(N-1)\delta}{\langle k \rangle \lambda}$. Moreover, $i_{r_0}^*$ becomes the finite population equivalent of an interior equilibrium for $R_0 \equiv \frac{\lambda}{\delta} \langle k \rangle \frac{N}{N-1} > 1$ (note that, for large N we have that $\frac{N}{N-1} \approx 1$). The disease will most likely expand whenever $i < i_{r_0}^*$, the opposite happening otherwise.

13.2.1.2 The SI Model

The **SI** model is mathematically equivalent to the **SIS** model with $\delta = 0$, and has been employed to study for instance the dynamics of AIDS. The Markov Chain representing the disease dynamics is therefore defined by transition matrix Eq. (13.3), with $T_i^- = 0$ for all i . The remaining transition probabilities T_i^+ ($0 < i < N$) are exactly the same as for the **SIS** model. Since all T_i^- equal zero, the Markov Chain has two absorbing states: the canonical one without any infected ($i=0$) and the one without any susceptible ($i=N$). The disease will expand monotonically as soon as one individual in the population gets infected, ultimately leading to a fully infected population. The average amount of time after which this happens, which

we refer to as the *average infection time*, constitutes the main quantity of interest. This quantity can be calculated analytically [28]: The average number of time steps needed to reach 100% infection, starting from i infected individuals is given by

$$t_i = \sum_{j=i}^{N-1} \frac{1}{T_j^+}. \quad (13.9)$$

13.2.1.3 The SIR Model

With **SIR** one models diseases in which individuals acquire immunity after recovering from infection. We distinguish three epidemiological states to model the dynamics of such diseases: susceptible (S), infected (I) and recovered (R), indicating those who have become immune to further infection.

The **SIR** model in infinite, well-mixed populations is defined by a recovery rate δ and an infection rate λ . The fraction of infected individuals x changes in time according to the following differential equation

$$\dot{x} = \langle k \rangle \lambda xy - \delta x, \quad (13.10)$$

where y denotes the fraction of susceptible individuals, which in turn changes according to

$$\dot{y} = -\langle k \rangle \lambda xy. \quad (13.11)$$

Finally, the fraction of individuals z in the recovered class changes according to

$$\dot{z} = \delta x. \quad (13.12)$$

To address the **SIR** model in finite, well-mixed populations, we proceed in a way similar to what we have done so far with **SIS** and **SI** models. The Markov Chain describing the disease dynamics becomes slightly more complicated and has states (i, r) , where i is the number of infected individuals in the population and r the number of recovered (and immune) individuals ($i + r \leq N$). A schematic representation of the Markov Chain is given in Fig. 13.2.

Note that the states $(0, r)$, with $0 \leq r \leq N$, are absorbing states. Each of these states corresponds to the number of individuals that are (or have become) immune at the time the disease goes extinct.

Consider a population of size N with average degree $\langle k \rangle$. The number of infected will increase with a rate

$$T^+(i, r) = \frac{\langle k \rangle N - i - r}{\tau_0} \frac{i}{N - 1} \lambda \quad (13.13)$$

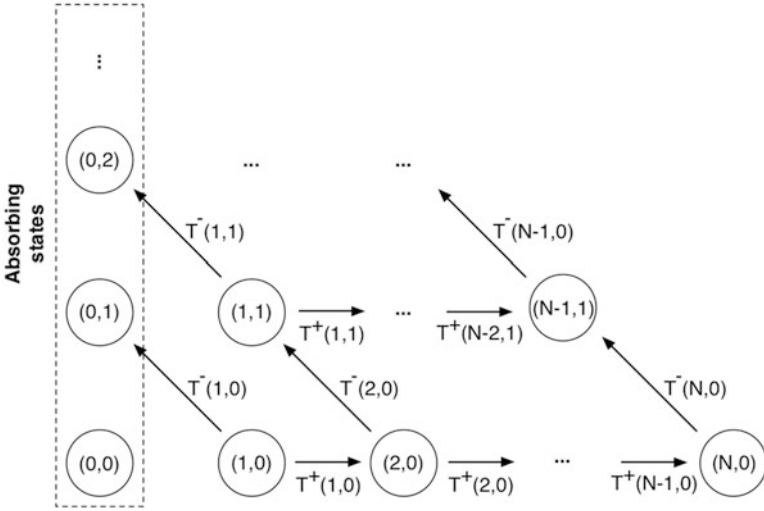


Fig. 13.2 Schematic representation of the Markov Chain associated with the stochastic **SIR** dynamics

and decrease with a rate

$$T^-(i, r) = \frac{1}{\tau_0} \frac{i}{N} \delta, \tag{13.14}$$

where τ_0 denotes the recovery time scale. As before, the gradient of infection $G(i)$, such that $\tau_0 G(i) = T^+(i) - T^-(i)$, measures the likelihood for the disease to either expand or shrink in a given state, and is given by

$$\tau_0 G(i, r) = \langle k \rangle \frac{N-i-r}{N} \frac{i}{N-1} \lambda - \frac{i}{N} \delta \xrightarrow{N \rightarrow \infty} \langle k \rangle \lambda xy - \delta x. \tag{13.15}$$

Note that we recover Eq. (13.10) in the limit $N \rightarrow \infty$. For a fixed number of recovered individuals r_0 , we have that $\tau_0 G(i, r_0) = 0$ for $i = 0$ and for $i^*_r = N - \frac{(N-1)\delta}{\langle k \rangle \lambda} - r_0$. For $R_0^{r_0} = \langle k \rangle \frac{\lambda}{\delta} \frac{N-r_0}{N-1} > 1$, i^*_r becomes the finite population analogue of an interior equilibrium. Furthermore, one can show that the partial derivative $\frac{\partial G(i, r)}{\partial i}$ has at most one single root in $(0, 1)$, possibly located at $\bar{i}_{r_0} = \frac{i^*_r}{2} \leq i^*_r$. Hence, $G(i, r_0)$ reaches a local maximum at \bar{i}_{r_0} (given that at that point $\frac{\partial^2 G(i, r)}{\partial i^2} \Big|_{\bar{i}_{r_0}} = -\frac{2\langle k \rangle \lambda}{N(N-1)} < 0$). The number of infected will therefore most likely increase for $i < \bar{i}_{r_0}$ (assuming r_0 immune individuals), and most likely decrease otherwise.

The gradient of infection also determines the probability to end up in each of the different absorbing states of the Markov chain. These probabilities can be calculated analytically [28]. To this end, let us use $y_{i, r}^a$ to denote the probability that the population ends up in the absorbing state with a recovered individuals, starting

from a state with i infected and r recovered. We obtain the following recurrence relationship for $y_{i,r}^a$

$$y_{i,r}^a = T^-(i, r) y_{i-1, r+1}^a + T^+(i, r) y_{i+1, r}^a + (1 - T^-(i, r) - T^+(i, r)) y_{i,r}^a, \quad (13.16)$$

which reduces to

$$y_{i,r}^a = \left(T^-(i, r) + T^+(i, r) \right)^{-1} \left(T^-(i, r) y_{i-1, r+1}^a + T^+(i, r) y_{i+1, r}^a \right). \quad (13.17)$$

The following boundary conditions

$$\begin{aligned} y_{0,r}^a &= 1, \\ y_{0,r}^a &= 0 \quad \text{if } r \neq a, \\ y_{i,r}^a &= 0 \quad \text{if } r > a, \end{aligned} \quad (13.18)$$

allow us to compute $y_{i,r}^a$ for every a, i and r .

13.2.2 Network Model

Our network model explicitly considers a finite and constant population of N individuals. Its temporal contact structure allows, however, for a variable number of overall links between individuals, which in turn will depend on the incidence of disease in the population. This way, infection proceeds along the links of a contact network whose structure may change based on each individual's health status and the availability of information regarding the health status of others. We shall assume the existence of some form of local information about the health status of social contacts. Information is local, in the sense that individual behavior will rely on the nature of their links in the contact network. Moreover, this will influence the way in which individuals may be more or less effective in avoiding contact with those infected while remaining in touch with the healthy.

Suppose all individuals seek to establish links at the same rate c . For simplicity, we assume that new links are established and removed randomly, a feature which usually does not always apply in real cases, where the limited social horizon of individuals or the nature of their social ties may constrain part of their neighborhood structure (see below). Let us further assume that links may be broken off at different rates, based on the nature of the links and the information available about the individuals they connect: Let us denote these rates by b_{pq} for links of type pq ($p, q \in \{S, I, R\}$). We assume that links are bidirectional, which means that we have links of pq types SI , SR , and IR . Let L_{pq} denote the number of links of type pq and L_{pq}^M the maximum possible number of links of that type, given the number of individuals of type S , I and R in the population. This allows us to write down (at a

mean-field level) a system of ODEs [57, 58] for the time evolution of the number of links of pq -type (L_{pq}) [57, 58]

$$\dot{L}_{pq} = c (L_{pq}^M - L_{pq}) - b_{pq}L_{pq}$$

which depends on the number of individuals in states p and q ($L_{pp}^M = p(p-1)/2$ and $L_{pq}^M = pq$ for $p \neq q$) and thereby couples the network dynamics to the disease dynamics. In the steady state of the linking dynamics ($\dot{L}_{pq} = 0$), the number of links of each type is given by $L_{pq}^* = \varphi_{pq}L_{pq}^M$, with $\varphi_{pq} = c/(c + b_{pq})$ the fractions of active pq -links, compared to the maximum possible number of links L_{pq}^M , for a given number of S , I and R . In the absence of disease only SS links exist, and hence ϕ_{SS} determines the average connectivity of the network under disease free conditions, which one can use to characterize the type of the population under study. In the presence of I individuals, to the extent that S individuals manage to avoid contact with I , they succeed in escaping infection. Thus, to the extent that individuals are capable of reshaping the contact network based on available information of the health status of other individuals, disease progression will be inhibited. In the extreme limit of perfect information and individual capacity to immediately break up contacts with infected, we are isolating all infected, and as such containing disease progression. Our goal here, however, is to understand how and in which way local information, leading to a temporal reshaping of the network structure, affects overall disease dynamics.

13.2.3 Computer Simulations

We investigate the validity of the approximations made to derive analytical results as well as their robustness by means of computer simulations. All individual-based simulations start from a complete network of size $N=100$. Disease spreading and network evolution proceed together under asynchronous updating. Disease update events take place with probability $(1 + \tau)^{-1}$, where $\tau = \tau_{NET}/\tau_{DIS}$. We define τ_{DIS} as the time-scale of disease progression, whereas τ_{NET} is the time scale of network change. The parameter $\tau = \tau_{NET}/\tau_{DIS}$ provides the relative time scale in terms of which we may interpolate between the limits when network adaptation is much slower than disease progression ($\tau \rightarrow 0$) and the opposite limit when network adaptation is much faster than disease progression ($\tau \rightarrow \infty$). Since $\tau = \tau_{NET}/\tau_{DIS}$ is the only relevant parameter, we can make, without loss of generality, $\tau_{DIS} = 1$. For network update events, we randomly draw two nodes from the population. If connected, then the link disappears with probability given by the respective b_{pq} . Otherwise, a new link appears with probability c . When a disease update event occurs, a recovery event takes place with probability $(1 + \langle k \rangle)^{-1}$, an infection event otherwise. In both cases, an individual j is drawn randomly from the population. If j is infected and a recovery event has been selected then j will become susceptible

(or recovered, model dependent) with probability δ . If j is susceptible and an infection event occurs, then j will get infected with probability λ if a randomly chosen neighbor of j is infected. The quasi-stationary distributions are computed (in the case of the **SIS** model) as the fraction of time the population spends in each configuration (i.e., number of infected individuals) during 10^9 disease event updates (10^7 generations; under asynchronous updating, one generation corresponds to N update events, where N is the population size; this means that in one generation, every individual has one chance, on average, to update her epidemic state). The average number of infected $\langle I \rangle$ and the mean average degree of the network $\langle k \rangle^*$ observed during these 10^7 generations are kept for further plotting. We have checked that the results reported are independent of the initial number of infected in the network. Finally, for the **SIR** and **SI** models, the disease progression in time, shown in the following sections, is calculated from 10^4 independent simulations, each simulation starting with 1 infected individual. The reported results correspond to the average amount of time at which i individuals become infected.

13.3 Results and Discussion

In this section we start by (i) showing that a quickly adapting community induces profound changes in the dynamics of disease spreading, irrespective of the underlying epidemic model; then, (ii) we resort to computer simulations to study the robustness of these results for intermediate time-scales of network adaptation; finally, (iii) we profit from the framework introduced above to analyze the impact of information on average time for absorption and disease progression in adaptive networks.

13.3.1 *Disease Spreading in a Quickly Adaptive Network Structure*

Empirically, it is well-known that often individuals prevent infection by avoiding contact with infected once they know the state of their contacts or are aware of the potential risks of such infection [31, 33, 42–50]: such is the case of many sexually transmitted diseases [42, 71–73], for example, and, more recently, the voluntary use of face masks and the associated campaigns adopted by local authorities in response to the SARS outbreak [40, 43–45] or even the choice of contacting or not other individuals based on information on their health status gathered from social media [41, 74, 75]. In the present study, individual decision is based on available local information about the health state of one's contacts. Thus, we can study analytically the limit in which the network dynamics — resulting from adaptation to the flow of local information — is much faster than disease dynamics, as in this case, one

may separate the time scales between network adaptation and contact (disease) dynamics: The network has time to reach a steady state before the next contact takes place. Consequently, the probability of having an infected neighbor is modified by a neighborhood structure which will change in time depending on the impact of the disease in the population and the overall rates of severing links with infected.

Let us start with the **SIR** model. The amount of information available translates into differences mostly between the break-up rates of links that may involve a potential risk for further infection (b_{SI} , b_{IR} , b_{II}), and those that do not (b_{SS} , b_{SR} , b_{RR}). Therefore, we consider one particular rate b_I for links involving infected individuals ($b_I \equiv b_{SI} = b_{IR} = b_{II}$), and another one, b_H , for links connecting healthy individuals ($b_H \equiv b_{SS} = b_{SR} = b_{RR}$). In general, one expects b_I to be maximal when each individual has perfect information about the state of her neighbors and to be (minimal and) equal to b_H when no information is available, turning the ratio between these two rates into a quantitative measure of the efficiency with which links to infected are severed compared to other links. Note that we reduce the model to two break-up rates in order to facilitate the discussion of the results. Numerical simulations show that the general principles and conclusions remain valid when all break-up rates are incorporated explicitly. It is worth noticing that three out of these six rates are of particular importance for the overall disease dynamics: b_{SS} , b_{SR} and b_{SI} . These three rates, combined with the rate c of creating new links, define the fraction of active SS , SR and SI links, and subsequent correlations between individuals [76], and therefore determine the probability for a susceptible to become infected (see Models and Methods). This probability will increase when considering higher values of c (assuming $b_I > b_H$). In other words, when individuals create new links more often, therefore increasing the likelihood of establishing connections to infected individuals (when present), they need to be better informed about the health state of their contacts in order to escape infection. In the fast linking limit, the other three break-up rates (b_{II} , b_{IR} and b_{RR}) will also influence disease progression since they contribute to changing the average degree of the network.

When the time scale for network update (τ_{NET}) is much smaller than the one for disease spreading (τ_{DIS}), we can proceed analytically using at profit the separation of times scales. In practice, this means that the network has time to reach a steady state before the next disease event takes place. Consequently, the probability of having an infected neighbor is modified by a neighborhood structure which will change in time depending on the impact of the disease in the population and the overall rates of severing links with infected individuals. For a given configuration (i, r) of the population, the stationary state of the network is characterized by the parameters φ_{SS} , φ_{SI} and φ_{SR} . Consequently, the number of infected increases at a rate [28]

$$T^+(i, r) = \langle k \rangle \frac{N - i - r}{N} \frac{\phi_{SI} i}{\phi_{SS} (N - i - r - 1) + \phi_{SI} i + \phi_{SR} r} \lambda, \quad (13.19)$$

where we made $\tau_0 = 1$. The effect of the network dynamics becomes apparent in the third factor, which represents the probability that a randomly selected neighbor of a susceptible is infected. In addition, Eq. (13.14) remains valid, as the linking

dynamics does not affect the rate at which the number of infected decreases. It is noteworthy that we can write Eq. (13.19) in the form

$$T^+(i, r) = \langle k \rangle \frac{N-i-r}{N} \frac{i}{N-1} \lambda^A, \quad (13.20)$$

which is formally equivalent to Eq. (13.13) and shows that disease spreading in a temporal adaptive network is equivalent to that in a well-mixed population with (i) a frequency dependent average degree $\langle k \rangle$ and (ii) a transmission probability that is rescaled compared to the original λ according to $\lambda^A = \eta^{-1} \lambda$, where

$$\eta = \frac{\phi_{SS}}{\phi_{SI}} + \left(1 - \frac{\phi_{SS}}{\phi_{SI}}\right) \frac{i}{N-1} + \left(\frac{\phi_{SR} - \phi_{SS}}{\phi_{SI}}\right) \frac{r}{N-1}. \quad (13.21)$$

Note that this expression remains valid for both **SIR**, **SIS** ($r = 0$) and **SI** ($\delta = 0$, $r = 0$) models. Since the lifetime of a link depends on its type, the average degree $\langle k \rangle$ of the network depends on *the number of infected in the population*, and hence becomes frequency (and time) dependent, as $\langle k \rangle$ depends on the number of infected (through L_{pq}^M) and changes in time. Note that η scales linearly with the frequency of infected in the population, decreasing as the number of infected increases (assuming $\phi_{SS}/\phi_{SI} > 1$); moreover, it depends implicitly (via the ratio ϕ_{SS}/ϕ_{SI}) on the amount of information available.

It is important to stress the distinction between the description of the disease dynamics at the local level (in the vicinity of an infected individual) and that at the population wide level. Strictly speaking, a dynamical network does not change the disease dynamics at the local level, meaning that infected individuals pass the disease to their neighbors with probability intrinsic to the disease itself. At the population level, on the other hand, disease progression proceeds as if the infectiousness of the disease effectively changes, as a result of the network dynamics. Consequently, analyzing a temporal network scenario at a population level can be achieved via a renormalization of the transmission probability, keeping the (mathematically more attractive) well-mixed scenario. In this sense, from a well-mixed perspective, dynamical networks contribute to changing the effective infectiousness of the disease, which becomes *frequency* and *information* dependent. Note further that this information dependence is a consequence of using a single temporal network for spreading the disease and information. Interestingly, adaptive networks have been shown to have a similar impact in social dilemmas [63]. From a global, population-wide perspective, it is as if the social dilemma at stake differs from the one every individual actually plays.

As in Sect. 2, one can define a gradient of infection G , which measures the tendency of the disease to either expand or shrink in a population with given configuration (defined by the number of individuals in each of the states S , I and R). To do so, we study the partial derivative $\frac{\partial G(i,r)}{\partial i}$ at $i = 0$

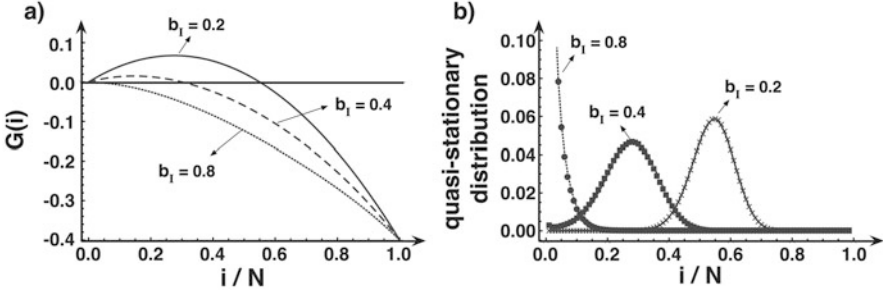


Fig. 13.3 Disease spreading under fast linking dynamics in the **SIS** model. The *left* panel shows the gradient of infection G as a function of the fraction of infected for different values of the rate b_I at which links with infected disappear ($b_I \equiv b_{SI} = b_{II}$): $b_I = 0.8$ (dotted line), $b_I = 0.4$ (dashed line) and $b_I = 0.2$ (solid line). The *right* panel shows the corresponding quasi-stationary distributions, obtained analytically (lines) and via individual-based computer simulations (circles for $b_I = 0.8$, squares for $b_I = 0.4$ and crosses for $b_I = 0.2$). We use $b_H \equiv b_{SS} = 0.2$, $c = 0.25$, $N = 100$, $N\lambda/\delta = 4$ and $\tau = 10^{-2}$

$$\left. \frac{\partial G(i, r)}{\partial i} \right|_{i=0} = -\frac{\delta}{N} + \frac{N-r}{N^2} \lambda \phi_{SI} \left[2(N-r) + \frac{r(r-1)\phi_{RR} - (N-r)(N-r-1)\phi_{SS}}{r\phi_{SR} + (N-r-1)\phi_{SS}} \right]. \quad (13.22)$$

This quantity exceeds zero whenever

$$\phi_{SI} \frac{\lambda}{\delta} \frac{N-r}{N} \left[2(N-r) + \frac{r(r-1)\phi_{RR} - (N-r)(N-r-1)\phi_{SS}}{r\phi_{SR} + (N-r-1)\phi_{SS}} \right] > 1. \quad (13.23)$$

Note that taking $r = 0$ yields the basic reproductive ratio R_0^A for both **SIR** and **SIS**: $R_0^A \equiv N\phi_{SI} \frac{\lambda}{\delta} > 1$. On the other hand, whenever $R_0^A < 1$, eradication of the disease is favored in the **SIS** model ($G(i) < 0$), *irrespective of the fraction of infected*, indicating how the presence of information ($b_H < b_I$) changes the basic reproductive ratio.

In Fig. 13.3 we illustrate the role of information in the **SIS** model by plotting G for different values of b_I (assuming $b_H < b_I$) and a fixed transmission probability λ . The corresponding quasi-stationary distributions are shown in the right panel and clearly reflect the sign of G . Whenever $G(i)$ is positive (negative), the dynamics will act to increase (decrease), on average, the number of infected. Figure 13.3 indicates how the availability of local information hinders disease progression: For $b_I = 0.75$ the interior root of $G(i)$ disappears, making disease expansion unlikely in any configuration of the population.

The analysis of the gradient of infection of the **SIS** model has the advantage of showing the effect of adaptive networks in a one-dimensional simplex (the fraction of infected). Yet, an analogous result holds for the **SIR** model. The gradient of infection now also depends on the number of recovered (r) individuals in the

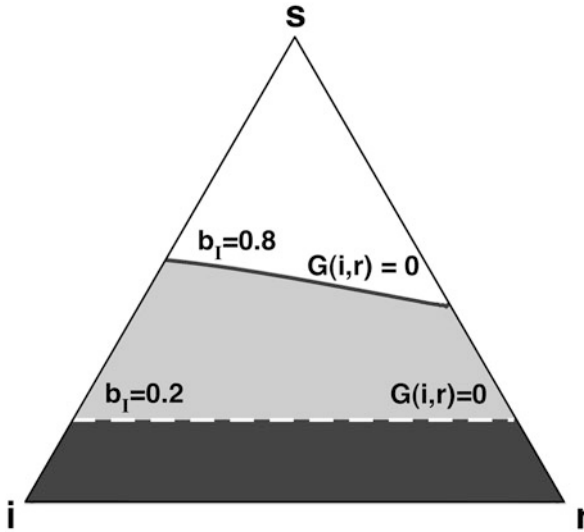


Fig. 13.4 Gradient of infection in the **SIR** model in a network with information (*solid black line*, $b_I = 0.8$, $b_H = 0.2$), and without information (*dashed white line*, $b_I = b_H = 0.2$). Each point in the triangle (the so-called *simplex*) satisfies that population size is conserved, i.e., $i+r+s=N$. Vertices of the simplex represent populations with only one class of individuals present. Lines in the interior of the simplex indicate configurations in which $G(i, r) = 0$. For each case, disease expansion is more likely than disease contraction in configurations above the line, and less likely otherwise, showing that availability of information greatly reduces the regions of state space in which disease may progress. We use the following parameter values: ($c = 0.25$, $N = 100$, $N\lambda/\delta = 10$)

population and, once again, allows us to identify when disease expansion will be favored or not. Figure 13.4 gives a complete picture of the gradient of infection, using the appropriate simplex structure in which all points satisfy the relation $i+r+s=N$. The dashed line indicates the boundary $G(i, r) = 0$ in case individuals do not have any information about the health status of their contacts, i.e., links that involve infected individuals disappear at the same rate as those that do not ($b_I = b_H$). Disease expansion is more likely than disease contraction ($G(i, r) > 0$) when the population is in a configuration above the line, and less likely otherwise. Similarly, the solid line indicates the boundary $G(i, r) = 0$ when individuals share information about their health status, and use it to avoid contact with infected. Once again, the availability of information modifies the disease dynamics, inhibiting disease progression for a broad range of configurations.

13.3.2 Analysis of Intermediate Time-Scales Through Computer Simulations

Up to now we have assumed that the network dynamics proceeds much faster than disease spreading (the limit $\tau \rightarrow 0$). This may not always be the case, and hence it is important to assess the domain of validity of this limit. In the following, we use computer simulations to verify to which extent these results, obtained analytically via time scale separation, remain valid for intermediate values of the relative timescale τ for the linking dynamics. We start with a complete network of size N , in which initially one individual is infected, the rest being susceptible. As stated before, disease spreading and network evolution proceed simultaneously under asynchronous updating. Network update events take place with probability $(1 + \tau)^{-1}$, whereas a disease model (**SI**, **SIS** or **SIR**) state update event occurs otherwise. For each value of τ , we run 10^4 simulations. For the **SI** model, the quantity of interest to calculate is the average number of generations after which the population becomes completely infected. These values are depicted in Fig. 13.5.

The lower dashed line indicates the analytical prediction of the infection time in the limit $\tau \rightarrow \infty$ (the limit when networks remain static), which we already recover in the simulations for $\tau > 10^2$. When τ is smaller than 10^2 , the average infection time significantly increases, and already reaches the analytical prediction for the limit $\tau \rightarrow 0$ (indicated by the upper dashed line) when $\tau < 1$. Hence, the validity of the time scale separation does again extend well beyond the limits one might expect.

For the **SIR** model, we let the simulations run until the disease goes extinct, and computed the average final fraction of individuals that have been affected by

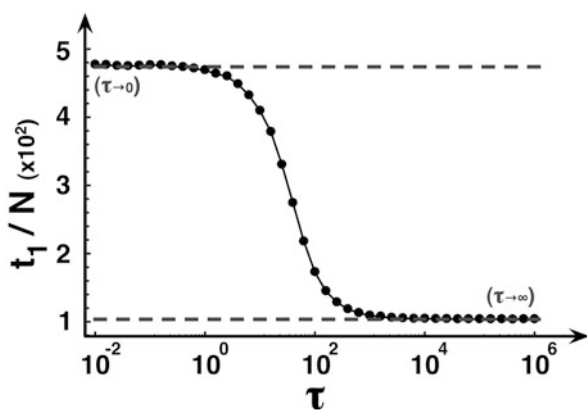


Fig. 13.5 Disease spreading in the **SI** model for variable time scales τ of the linking dynamics. Solid circles show the average number of generations to reach a fully infected population, starting from one single infected individual, obtained in simulation. *Dashed lines* indicate the analytical predictions for these values, either in the limit $\tau \rightarrow 0$ (*upper dashed line*), or in the limit $\tau \rightarrow \infty$ (*lower dashed line*). We use the following parameter values: $b_I = 0.8$, $b_H = 0.2$, $c = 0.25$, $N = 100$ and $\lambda = 0.001$

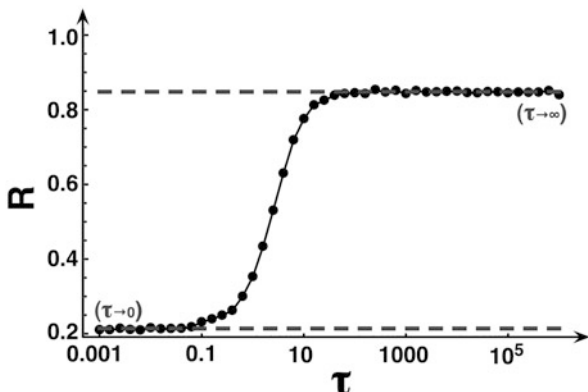


Fig. 13.6 Disease spreading in the **SIR** model for variable time scales τ of the linking dynamics. Solid circles show the final fraction of recovered individuals as a function of τ in populations with initially one infected. The upper (*lower*) dashed line shows the corresponding analytical prediction in the limit $\tau \rightarrow \infty$ ($\tau \rightarrow 0$). We use the following parameter values: $b_I = 0.8$, $b_H = 0.2$, $c = 0.25$, $\lambda = 0.01$, $\delta = 0.15$ and $N = 100$

the disease, which corresponds to the final fraction of individuals in the recovered class. These results are depicted in Fig. 13.6.

The upper dashed line indicates the expected fraction of recovered individuals in a static network ($\tau \rightarrow \infty$). This value is obtained by calculating $\sum_{i=0}^N i y_{1,0}^i$, where $y_{1,0}^i$ is given by Eqs. (13.17) and (13.18). One observes that linking dynamics does not affect disease dynamics for $\tau > 10$. Once τ drops below ten, a significantly smaller fraction of individuals is affected by the disease. This fraction reaches the analytical prediction for $\tau \rightarrow 0$ as soon as $\tau < 0.1$. Hence, and again, results obtained via separation of time scales remain valid for a wide range of intermediate time scales.

We finally investigate the role of intermediate time scales in the **SIS** model. We performed computer simulations in the conditions discussed already, and computed several quantities that we plot in Fig. 13.7.

Figure 13.7 shows the average $\langle I \rangle$ of the quasi-stationary distributions obtained via computer simulations (circles) as a function of the relative time scale τ of network update. Whenever $\tau \rightarrow \infty$, we can characterize the disease dynamics analytically, assuming a well-mixed population (complete graph), whereas for $\tau \rightarrow 0$ we recover the analytical results obtained in the fast linking limit. At intermediate time scales, Fig. 13.7 shows that as long as τ is smaller than ten, network dynamics contributes to inhibit disease spreading by effectively increasing the critical infection rate. Overall, the validity of the time scale separation extends well beyond the limits one might anticipate based solely on the time separation ansatz. As long as the time scale for network update is smaller than the one for disease spreading ($\tau < 1$), the analytical prediction for the limit $\tau \rightarrow 0$, indicated by the lower dashed line in Fig. 13.7, remains valid. The analytical result in the extreme opposite limit ($\tau \rightarrow \infty$), indicated by the upper dashed line in Fig. 13.7,

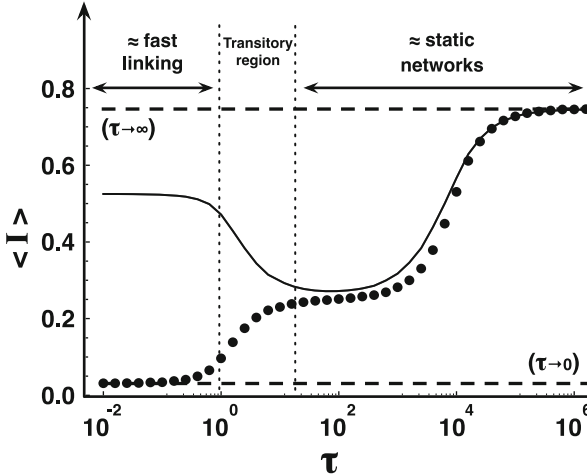
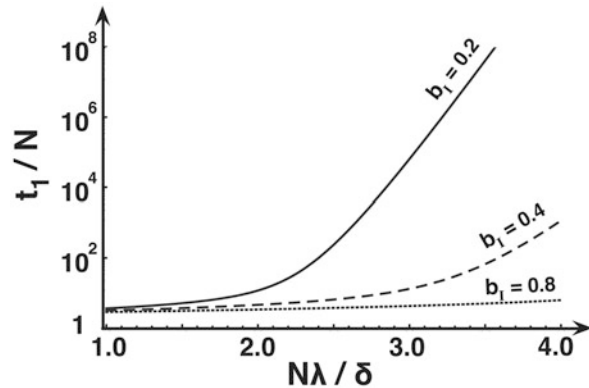


Fig. 13.7 Disease spreading under linking dynamics in the SIS model. Circles show results of individual-based simulations for the quasi-stationary average fraction of infected ($\langle I \rangle$) as function of τ . The lower (upper) dashed line shows the analytical prediction of $\langle I \rangle$ for $\tau \rightarrow 0$ ($\tau \rightarrow \infty$), calculated as the average of the quasi-stationary distribution. The analytical prediction in the fast linking limit ($\tau \rightarrow 0$) remains valid as long as $\tau < 1$, whereas the prediction in the limit of static networks ($\tau \rightarrow \infty$) remains valid as long as $\tau > 10^5$. The solid line depicts the analytical prediction of $\langle I \rangle$ in static networks whose average degree equals the value obtained computationally for the average connectivity of the network at each given τ . Results show that for $\tau > 10^2$, the network dynamics influences disease progression only by controlling $\langle k \rangle^*$. We use $b_I = 0.8$, $b_H = 0.2$, $c = 0.25$, $N = 100$ and $N\lambda/\delta = 4$

holds as long as $\tau > 10^5$. Moreover, it is noteworthy that the network dynamics influences the disease dynamics both by *reducing the frequency of interactions between susceptible and infected*, and by *reducing the average degree of the network*. These complementary effects are disentangled in intermediate regimes, in which the network dynamics is too slow to warrant sustained protection of susceptible individuals from contacts with infected, despite managing to reduce the average degree (not shown). In fact, for $\tau > 10$ the disease dynamics is mostly controlled by the average degree, as shown by the solid lines in Fig. 13.7. Here, the average stationary distribution was determined by replacing, in the analytic expression for static networks, $\langle k \rangle$ by the time-dependent average connectivity $\langle k \rangle^*$ computed numerically. This, in turn, results from the frequency dependence of $\langle k \rangle$. When $b_I > b_H$, the network will reshape into a configuration with smaller $\langle k \rangle$ as soon as the disease expansion occurs. For $\tau < 1$, $\langle k \rangle^*$ reflects the lifetime of SS links, as there are hardly any infected in the population. For $10^0 < \tau < 10^3$, the network dynamics proceeds fast enough to reduce $\langle k \rangle$, but too slowly to reach its full potential in hindering disease progression. Given the higher fraction of infected, and the fact that SI and II links have a shorter lifetime than SS links, the average degree drops when increasing τ from 1 to 10^3 . Any further increase in τ leads to a higher average degree, as the network approaches its static limit.

Fig. 13.8 Impact of information on times to absorption. Average number of generations required for disease eradication in an adaptive contact network for different rates b_I , using the SIS model. The remaining parameters are $b_H = 0.2$, $c = 0.25$ and $N = 100$. The availability of information drastically reduces the time for disease eradication



13.3.3 Average Time to Absorption in Adaptive Networks

Contrary to the deterministic SIS model, the stochastic nature of disease spreading in finite populations ensures that the disease disappears after some time. However, this result is of little relevance given the times required to reach the absorbing state (except, possibly, in very small communities). Indeed, the characteristic time scale of the dynamics plays a determinant role in the overall epidemiological process and constitutes a central issue in disease spreading.

Figure 13.8 shows the average time to absorption t_I in adaptive networks for different levels of information, illustrating the spectacular effect brought about by the network dynamics on t_I . While on networks without information ($b_I = b_H$) t_I rapidly increases with the rate of infection λ , adding information moves the fraction of infected individuals rapidly to the absorbing state, and, therefore, to the disappearance of the disease.

Moreover, the size of the population can have a profound effect on t_I . With increasing population size, the population spends most of the time in the vicinity of the state associated with the interior root of $G(i)$. For large populations, this acts to reduce the intrinsic stochasticity of the dynamics, dictating a very slow extinction of the disease, as shown in Fig. 13.9.

When recovery from the disease is impossible, a situation captured by the SI model, the population will never become disease-free again once it acquires at least one infected individual. The time to reach absorbing state in which all individuals are infected, again depends on the presence of information. When information prevails, susceptible individuals manage to resist infection for a long time, thereby delaying the rapid progression of the disease, as shown in the inset of Fig. 13.10. Naturally, the average number of generations needed to reach a fully infected population increases with the availability of information, as illustrated in the main panel of Fig. 13.10.

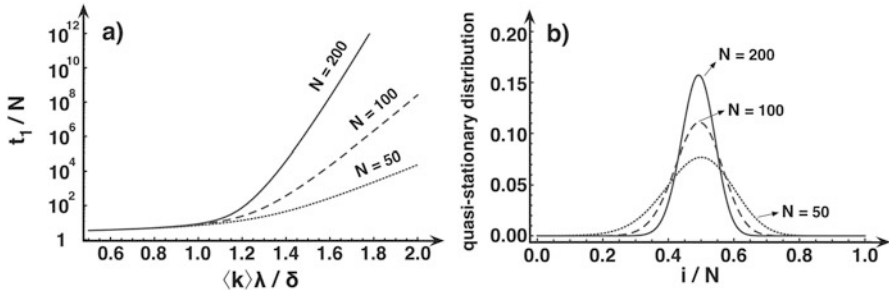


Fig. 13.9 Impact of population size on the average times to absorption t_1 . (a) Average number of generations required for disease eradication in the SIS model in static networks of different size N , while keeping the average degree $\langle k \rangle$ constant ($\langle k \rangle = 49$). (b) Quasi-stationary distribution of the number of infected for the same values of N and $\langle k \rangle$. The disease parameters satisfy $\langle k \rangle \lambda / \delta = 2$

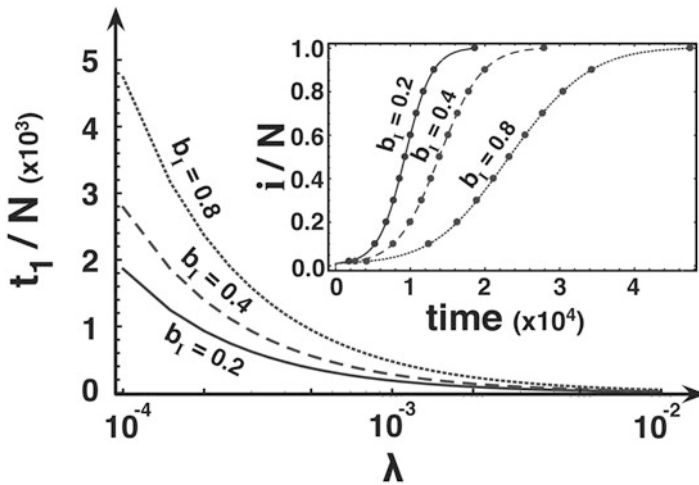


Fig. 13.10 Impact of information on infection times. The main plot shows the average number of generations after which a disease infects the entire population in the SI model, using the same parameters as in Fig. 13.8. The inset shows how, starting from one infected individual, the fraction of infected changes in time for the same rates b_I and $\lambda = 10^{-3}$. The results obtained via individual-based computer simulations (circles, $\tau = 10^{-1}$) fit perfectly with those calculated analytically (lines)

13.4 Conclusions

Making use of three standard models of epidemics involving a finite population in which infection takes place along the links of a temporal graph, the nodes of which are occupied by individuals, we have shown analytically that the bias introduced into the graph dynamics resulting from the availability of information about the

health status of others in the population induces fundamental changes in the overall dynamics of disease progression.

The network dynamics employed here differs from those used in most other studies [29, 32–36, 51–55]. We argue, however, that the differences obtained stem mostly from the temporal aspect of the network, and not so much from the detailed dynamics that is implemented. Importantly, temporal network dynamics leads to additional changes in R_0 compared to those already obtained when moving from the well-mixed assumption to static networks [77]. An important ingredient of our model, however, is that the average degree of the network results from the self-organization of the network structure, and co-evolves with the disease dynamics. A population suffering from high disease prevalence where individuals avoid contact in order to escape infection will therefore exhibit a lower average degree than a population with hardly any infected individuals. Such a frequency-dependent average degree further prevents that containment of infected individuals would result in the formation of cliques of susceptible individuals, which are extremely vulnerable to future infection, as reported before [36, 51, 54].

The description of disease spreading as a stochastic contact process embedded in a Markov chain constitutes a second important ingredient of the present model. This approach allows for a direct comparison between analytical predictions and individual-based computer simulations, and for a detailed analysis of finite-size effects and convergence times, whose exponential growth will signal possible bistable disease scenarios. In such a framework, we were able to show that temporal adaptive networks in which individuals may be informed about the health status of others lead to a disease whose effective infectiousness depends on the overall number of infected in the population. In other words, disease propagation on temporal adaptive networks can be seen as mathematically equivalent to disease spreading on a well-mixed population, but with a rescaled effective infectiousness. In accord with the intuition advanced in the introduction, as long as individuals react promptly and consistently to accurate available information on whether their acquaintances are infected or not, network dynamics effectively weakens the disease burden the population suffers. Last but not least, if recovery from the disease is possible, the time for disease eradication drastically reduces whenever individuals have access to accurate information about the health state of their acquaintances and use it to avoid contact with those infected. If recovery or immunity is impossible, the average time needed for a disease to spread increases significantly when such information is being used. In both cases, our model clearly shows how availability of information hinders disease progression (by means of quick action on infected, e.g., their containment via link removal), which constitutes a crucial factor to control the development of global pandemics.

Finally, it is also worth mentioning that knowledge about the health state of others may not always be accurate or available in time. This is for instance the case for diseases where recently infected individuals remain asymptomatic for a substantial period. The longer the incubation period associated with the disease, the less successful individuals will be in escaping infection, which in our model translates into a lower effective rate of breaking SI links, with the above mentioned

consequences. Moreover, different (social) networks through which awareness of the health status of others proceeds may lead to different rates of information spread. One may take these features into account by modeling explicitly the spread of information through a coupled dynamics between disease expansion and individuals' awareness of the disease [31, 33].

Creation and destruction of links may for instance not always occur randomly, as we assumed here, but in a way that is biased by a variety of factors such as social and genetic distance, geographical proximity, family ties, etc. The resulting contact network may therefore become organized in a specific way, promoting the formation of particular structures, such as networks characterized by long-tailed degree distributions or with strong topological correlations among nodes [3, 78–80] which, in turn, may influence the disease dynamics. The impact of combining such effects, resulting from specific disease scenarios, with those reported here will depend on the prevalence of such additional effects when compared to link-rewiring dynamics. A small fraction of non-random links, or of ties which cannot be broken, will likely induce small modifications on the average connectivity of the contact network, which can be incorporated in our analytic expressions without compromising their validity regarding population wide dynamics. On the other hand, when the contact network is highly heterogeneous (e.g., exhibiting pervasive long-tail degree distributions), non-random events may have very distinct effects, from being almost irrelevant (and hence can be ignored) to inducing hierarchical cascades of infection [81], in which case our results will not apply.

Acknowledgements This research was supported by FCT-Portugal through grants PTDC/EEI-SII/5081/2014, PTDC/MAT/STA/3358/2014, UID/BIA/04050/2013 and UID/CEC/50021/2013.

References

1. Keeling, M.J., Rohani, P.: *Modeling Infectious Diseases in Humans and Animals*. Princeton University Press, Princeton (2008)
2. Anderson, R.M., May, R.M.: *Infectious Diseases in Humans*. Oxford University Press, Oxford (1992)
3. Dorogovtsev, S.N., Mendes, J.F.F.: *Evolution of Networks: From Biological Nets to the Internet and WWW*. Oxford University Press, Oxford (2003)
4. Barrat, A., Barthelemy, M., Vespignani, A.: *Dynamical Processes in Complex Networks*. Cambridge University Press, Cambridge (2008)
5. Pastor-Satorras, R., Castellano, C., Van Mieghem, P., Vespignani, A.: Epidemic processes in complex networks. *Rev. Mod. Phys.* **87**(3), 925–979 (2015)
6. Watts, D.J.: *Small Worlds: The Dynamics of Networks Between Order and Randomness*. Princeton University Press, Princeton/Oxford (1999)
7. Lloyd, A.L., May, R.M.: Epidemiology. How viruses spread among computers and people. *Science*. **292**(5520), 1316–1317 (2001)
8. Santos, F.C., Rodrigues, J.F., Pacheco, J.M.: Epidemic spreading and cooperation dynamics on homogeneous small-world networks. *Phys. Rev. E*. **72**(5 Pt 2), 056128 (2005)
9. May, R.M.: Network structure and the biology of populations. *Trends Ecol. Evol.* **21**(7), 394–399 (2006)

10. Mastrandrea, R., Barrat, A.: How to estimate epidemic risk from incomplete contact diaries data? *PLoS Comput. Biol.* **12**(6), e1005002 (2016)
11. Kiti, M.C., Tizzoni, M., Kinyanjui, T.M., Koech, D.C., Munywoki, P.K., Meriac, M., Cappa, L., Panisson, A., Barrat, A., Cattuto, C.: Quantifying social contacts in a household setting of rural Kenya using wearable proximity sensors. *EPJ Data Sci.* **5**(1), 21 (2016)
12. Fournet, J., Barrat, A.: Epidemic risk from friendship network data: an equivalence with a non-uniform sampling of contact networks. *Sci. Rep.* **6**, 24593 (2016)
13. Merler, S., Ajelli, M., Fumanelli, L., Gomes, M.F., Piontti, A.P., Rossi, L., Chao, D.L., Longini, I.M., Halloran, M.E., Vespignani, A.: Spatiotemporal spread of the 2014 outbreak of Ebola virus disease in Liberia and the effectiveness of non-pharmaceutical interventions: a computational modelling analysis. *Lancet Infect. Dis.* **15**(2), 204–211 (2015)
14. Holme, P., Masuda, N.: The basic reproduction number as a predictor for epidemic outbreaks in temporal networks. *PLoS One.* **10**(3), e0120567 (2015)
15. Holme, P.: Information content of contact-pattern representations and predictability of epidemic outbreaks. *Sci. Rep.* **5**, 14462 (2015)
16. Holme, P., Liljeros, F.: Birth and death of links control disease spreading in empirical contact networks. *Sci. Rep.* **4**, 4999 (2014)
17. Salathé, M., Freifeld, C.C., Mearu, S.R., Tomasulo, A.F., Brownstein, J.S.: Influenza A (H7N9) and the importance of digital epidemiology. *N. Engl. J. Med.* **369**(5), 401 (2013)
18. Masuda, N., Holme, P.: Predicting and controlling infectious disease epidemics using temporal networks. *F1000 prime reports.* **5**, 6 (2013)
19. Goltsev, A.V., Dorogovtsev, S.N., Oliveira, J.G., Mendes, J.F.F.: Localization and spreading of diseases in complex networks. *Phys. Rev. Lett.* **109**(12), 128702 (2012)
20. Swinburn, B.A., Sacks, G., Hall, K.D., McPherson, K., Finegood, D.T., Moodie, M.L., Gortmaker, S.L.: The global obesity pandemic: shaped by global drivers and local environments. *Lancet.* **378**(9793), 804–814 (2011)
21. Salathé, M., Kazandjieva, M., Lee, J.W., Levis, P., Feldman, M.W., Jones, J.H.: A high-resolution human contact network for infectious disease transmission. *Proc. Natl. Acad. Sci. U. S. A.* **107**(51), 22020–22025 (2010)
22. Salathé, M., Jones, J.H.: Dynamics and control of diseases in networks with community structure. *PLoS Comput. Biol.* **6**(4), e1000736 (2010)
23. Funk, S., Salathé, M., Jansen, V.A.: Modelling the influence of human behaviour on the spread of infectious diseases: a review. *J. R. Soc. Interface.* **7**(50), 1247–1256 (2010)
24. Masuda, N., Lambiotte, R.: *A Guide to Temporal Networks*, vol. 4. World Scientific, London (2016)
25. Holme, P., Saramäki, J.: Temporal networks. *Phys. Rep.* **519**(3), 97–125 (2012)
26. Barrat, A., Cattuto, C., Colizza, V., Gesualdo, F., Isella, L., Pandolfi, E., Pinton, J.-F., Ravà, L., Rizzo, C., Romano, M.: Empirical temporal networks of face-to-face human interactions. *EPJ ST.* **222**(6), 1295–1309 (2013)
27. Lee, S., Rocha, L.E., Liljeros, F., Holme, P.: Exploiting temporal network structures of human interaction to effectively immunize populations. *PLoS One.* **7**(5), e36439 (2012)
28. Van Segbroeck, S., Santos, F.C., Pacheco, J.M.: Adaptive contact networks change effective disease infectiousness and dynamics. *PLoS Comput. Biol.* **6**(8), e1000895 (2010)
29. Schwartz, I.B., Shaw, L.B.: Rewiring for adaptation. *Physics.* **3**(17), (2010)
30. Marceau, V., Noël, P.-A., Hébert-Dufresne, L., Allard, A., Dubé, L.J.: Adaptive networks: coevolution of disease and topology. *Phys. Rev. E.* **82**(3), (2010)
31. Funk, S., Gilad, E., Jansen, V.A.A.: Endemic disease, awareness, and local behavioural response. *J. Theor. Biol.* **264**, 501–509 (2010)
32. Risau-Gusman, S., Zanette, D.H.: Contact switching as a control strategy for epidemic outbreaks. *J. Theor. Biol.* **257**, 52–60 (2009)
33. Funk, S., Gilad, E., Watkins, C., Jansen, V.A.: The spread of awareness and its impact on epidemic outbreaks. *Proc. Natl. Acad. Sci. U. S. A.* **106**(16), 6872–6877 (2009)
34. Zanette, D.H., Risau-Gusman, S.: Infection spreading in a population with evolving contacts. *J. Biol. Phys.* **34**, 135–148 (2008)

35. Shaw, L.B., Schwartz, I.B.: Fluctuating epidemics on adaptive networks. *Phys. Rev. E.* **77**, 066101 (2008)
36. Gross, T., Blasius, B.: Adaptive coevolutionary networks: a review. *J. R. Soc. Interface.* **5**(20), 259–271 (2008)
37. Galvani, A.P., Reluga, T.C., Chapman, G.B.: Long-standing influenza vaccination policy is in accord with individual self-interest but not with the utilitarian optimum. *Proc. Natl. Acad. Sci. U. S. A.* **104**(13), 5692–5697 (2007)
38. Colizza, V., Barrat, A., Barthelemy, M., Valleron, A.J., Vespignani, A.: Modeling the worldwide spread of pandemic Influenza: baseline case and containment interventions. *PLoS Med.* **4**(1), e13 (2007)
39. Hufnagel, L., Brockmann, D., Geisel, T.: Forecast and control of epidemics in a globalized world. *Proc. Natl. Acad. Sci. U. S. A.* **101**(42), 15124–15129 (2004)
40. Svoboda, T., Henry, B., Shulman, L., Kennedy, E., Rea, E., Ng, W., Wallington, T., Yaffe, B., Gourmis, E., Vicencio, E., Basrur, S., Glazier, R.H.: Public health measures to control the spread of the severe acute respiratory syndrome during the outbreak in Toronto. *N. Engl. J. Med.* **350**(23), 2352–2361 (2004)
41. Salathé, M., Bengtsson, L., Bodnar, T.J., Brewer, D.D., Brownstein, J.S., Buckee, C., Campbell, E.M., Cattuto, C., Khandelwal, S., Mabry, P.L.: Digital epidemiology. *PLoS Comput. Biol.* **8**(7), e1002616 (2012)
42. Ahituv, A., Hotz, V.J., Philipson, V.J.: The responsiveness of the demand for condoms to the local prevalence of AIDS. *J. Hum. Resour.* **31**(4), 869–897 (1996)
43. Kristiansen, I.S., Halvorsen, P.A., Gyrd-Hansen, D.: Influenza pandemic: perception of risk and individual precautions in a general population. *BMC Public Health.* **7**(48), (2007)
44. Lau, J.T., Yang, X., Tsui, H., Kim, J.H.: Impacts of SARS on health-seeking behaviors in general population in Hong Kong. *Prev. Med.* **41**(2), 454–462 (2005)
45. Ferguson, N.: Capturing human behaviour. *Nature.* **446**(7137), 733 (2007)
46. Laver, S.M., Wetzels, J., Behrens, R.H.: Knowledge of malaria, risk perception, and compliance with prophylaxis and personal and environmental preventive measures in travelers exiting Zimbabwe from Harare and Victoria Falls International Airport. *J. Travel Med.* **8**(6), 298–303 (2001)
47. Brewer, N.T., Chapman, G.B., Gibbons, F.X., Gerrard, M., McCaul, K.D., Weinstein, N.D.: Meta-analysis of the relationship between risk perception and health behavior: the example of vaccination. *Health Psychol.* **26**(2), 136–145 (2007)
48. Brewer, N.T., Cuite, C.L., Herrington, J.E., Weinstein, N.D.: Risk compensation and vaccination: can getting vaccinated cause people to engage in risky behaviors? *Ann. Behav. Med.* **34**(1), 95–99 (2007)
49. Rubin, G.J., Amlot, R., Page, L., Wessely, S.: Public perceptions, anxiety, and behaviour change in relation to the swine flu outbreak: cross sectional telephone survey. *BMJ.* **339**, b2651 (2009)
50. Jones, J.H., Salathe, M.: Early assessment of anxiety and behavioral response to novel swine-origin influenza A(H1N1). *PLoS One.* **4**(12), e8032 (2009)
51. Gross, T., D’Lima, C.J., Blasius, B.: Epidemic dynamics on an adaptive network. *Phys. Rev. Lett.* **96**(20), 208701 (2006)
52. Volz, E., Meyers, L.A.: Susceptible-infected-recovered epidemics in dynamic contact networks. *Proc. R. Soc. B.* **274**, 2925–2933 (2007)
53. Han, X.-P.: Disease spreading with epidemic alert on small-world networks. *Phys. Lett. A.* **365**, 1–5 (2008)
54. Gross, T., Kevrekidis, I.G.: Robust oscillations in SIS epidemics on adaptive networks: coarse graining by automated moment closure. *Europhys. Lett.* **82**, 38004–38006 (2008)
55. Prado, F., Sheih, A., West, J.D., Kerr, B.: Coevolutionary cycling of host sociality and pathogen virulence in contact networks. *J. Theor. Biol.* **261**(4), 561–569 (2009)
56. Santos, F.C., Pacheco, J.M., Lenaerts, T.: Cooperation prevails when individuals adjust their social ties. *PLoS Comput. Biol.* **2**(10), e140 (2006)

57. Pacheco, J.M., Traulsen, A., Nowak, M.A.: Coevolution of strategy and structure in complex networks with dynamical linking. *Phys. Rev. Lett.* **97**(25), 258103 (2006)
58. Pacheco, J.M., Traulsen, A., Nowak, M.A.: Active linking in evolutionary games. *J. Theor. Biol.* **243**, 437–443 (2006)
59. Pacheco, J.M., Traulsen, A., Ohtsuki, H., Nowak, M.A.: Repeated games and direct reciprocity under active linking. *J. Theor. Biol.* **250**(4), 723–731 (2008)
60. Van Segbroeck, S., Santos, F.C., Lenaerts, T., Pacheco, J.M.: Reacting differently to adverse ties promotes cooperation in social networks. *Phys. Rev. Lett.* **102**, 058105 (2009)
61. Van Segbroeck, S., Santos, F.C., Lenaerts, T., Pacheco, J.M.: Selection pressure transforms the nature of social dilemmas in adaptive networks. *New J. Phys.* **13**(1), 013007 (2011)
62. Pinheiro, F.L., Santos, M.D., Santos, F.C., Pacheco, J.M.: Origin of peer influence in social networks. *Phys. Rev. Lett.* **112**(9), 098702 (2014)
63. Pinheiro, F.L., Santos, F.C., Pacheco, J.M.: Linking individual and collective behavior in adaptive social networks. *Phys. Rev. Lett.* **116**(12), 128702 (2016)
64. May, R.M.: Uses and abuses of mathematics in biology. *Science*. **303**, 790–793 (2004)
65. Kermack, W.O., McKendrick, A.G.: A contribution to the mathematical theory of epidemics. *Proc. Roy. Soc. Lond. A*. **115**, 700–721 (1927)
66. Ribeiro, R.M., Bonhoeffer, S.: Production of resistant HIV mutants during antiretroviral therapy. *Proc. Natl. Acad. Sci. U. S. A.* **97**(14), 7681–7686 (2000)
67. Karlin, S., Taylor, H.E.: *A First Course in Stochastic Processes*. Academic Press, New York (1975)
68. Van Kampen, N.G.: *Stochastic Processes in Physics and Chemistry*, 3rd edn. North Holland, Amsterdam (2007)
69. Antal, T., Scheuring, I.: Fixation of strategies for an evolutionary game in finite populations. *Bull. Math. Biol.* **68**(8), 1923–1944 (2006)
70. Nåsel, I.: On the quasi-stationary distribution of the stochastic logistic epidemic. *Math. Biosci.* **156**(1-2), 21–40 (1999)
71. Payn, B., Tanfer, K., Billy, J.O.G., Grady, W.R.: Men’s behavior change following infection with a sexually transmitted disease. *Fam. Plan. Perspect.* **29**(4), 152–157 (1997)
72. Emlet, C.A.: An examination of the social networks and social isolation in older and younger adults living with HIV/AIDS. *Health Soc. Work.* **31**(4), 299–308 (2006)
73. Zacks, S., Beavers, K., Theodore, D., Dougherty, K., Batey, B., Shumaker, J., Galanko, J., Shrestha, R., Fried, M.W.: Social stigmatization and Hepatitis C virus infection. *J. Clin. Gastroenterol.* **40**(3), 220–224 (2006)
74. Salathé, M., Khandelwal, S.: Assessing vaccination sentiments with online social media: implications for infectious disease dynamics and control. *PLoS Comput. Biol.* **7**(10), e1002199 (2011)
75. Chunara, R., Andrews, J.R., Brownstein, J.S.: Social and news media enable estimation of epidemiological patterns early in the 2010 Haitian cholera outbreak. *Am.J.Trop. Med. Hyg.* **86**(1), 39–45 (2012)
76. Keeling, M.J.: The effects of local spatial structure on epidemiological invasions. *Proc. Biol. Sci.* **266**(1421), 859–867 (1999)
77. Ogura, M., Preciado, V.M.: Epidemic processes over adaptive state-dependent networks. *Phys. Rev. E*. **93**(6), 062316 (2016)
78. Amaral, L.A., Scala, A., Barthélemy, M., Stanley, H.E.: Classes of small-world networks. *Proc. Natl. Acad. Sci. U. S. A.* **97**(21), 11149–11152 (2000)
79. Albert, R., Barabási, A.L.: Statistical mechanics of complex networks. *Rev. Mod. Phys.* **74**, 47–98 (2002)
80. Newman, M.E.J.: The structure and function of complex networks. *SIAM Rev.* **45**(2), 167–256 (2003)
81. Barthélemy, M., Barrat, A., Pastor-Satorras, R., Vespignani, A.: Velocity and hierarchical spread of epidemic outbreaks in scale-free networks. *Phys. Rev. Lett.* **92**(17), 178701 (2004)

Chapter 14

Toward a Realistic Modeling of Epidemic Spreading with Activity Driven Networks

Alessandro Rizzo and Maurizio Porfiri

Abstract Models of epidemic spreading are widely used to predict the evolution of an outbreak, test specific intervention scenarios, and steer interventions in the field. Compartmental models are the most common class of models. They are very effective for qualitative analysis, but they rely on simplifying assumptions, such as homogeneous mixing and time scale separation. On the other end of the spectrum, detailed agent-based models, based on realistic mobility pattern models, provide extremely accurate predictions. However, these models require significant computing power and are not suitable for analytical treatment. Our research aims at bridging the gap between these two approaches, toward time-varying network models that are sufficiently accurate to make predictions for real-world applications, while being computationally affordable and amenable to analytical treatment. We leverage the novel paradigm of activity driven networks (ADNs), a particular type of time-varying network that accounts for inherent inhomogeneities within a population. Starting from the basic incarnation of ADNs, we expand on the framework to include behavioral factors triggered by health status and spreading awareness. The enriched paradigm is then utilized to model the 2014–2015 Ebola Virus Disease (EVD) spreading in Liberia, and perform a what-if analysis on the timely application of sanitary interventions in the field. Finally, we propose a new formulation, which is amenable to analytical treatment, beyond the mere computation of the epidemic threshold.

A. Rizzo (✉)

Dipartimento di Elettronica e Telecomunicazioni, Politecnico di Torino, Torino, Italy
Office of Innovation, New York University Tandon School of Engineering, Brooklyn, NY, USA
e-mail: alessandro.rizzo@polito.it

M. Porfiri (✉)

Department of Mechanical and Aerospace Engineering, New York University Tandon School of Engineering, Brooklyn, NY, USA
e-mail: mporfiri@nyu.edu

14.1 Introduction

Models for the spreading of infectious diseases have opened unprecedented scenarios in management and containment of epidemics. The assessment of the effect of vaccination campaigns, travel bans, and prophylaxis campaigns is now possible, partly due to the availability of such models. Models are also effective in providing valuable information to steer interventions in the field, when therapeutical protocols might not be available [1].

The most common and valuable modeling tools are mean-field compartmental [2–4] and agent-based models [5]. Even though such models are widely used and effective under several aspects, they suffer from a number of key limitations that may hamper their effectiveness in forecasting epidemics dynamics and assessing the effect of intervention policies.

Mean-field compartmental models are based on deterministic or stochastic differential equations, in which relevant variables, called compartments, evolve in time to describe the fraction of the population in a given state of the epidemic model [2, 4]. These models are usually calibrated through least-squares optimization on available epidemic data [6]. Then, several instances of the model are studied, varying one or more parameters, to anticipate plausible scenarios for the evolution of the outbreak in terms of the total number of infections and casualties. Mean-field approximations are effective to enable a first, mathematically rigorous understanding of epidemic spreading, but suffer from several limitations.

While these models are computationally simple and theoretically tractable, they do not take into account the inherently time-varying nature of human behavior, which is influenced by several factors, such as health status or risk perception [7–9]. In their basic incarnation, they rely on the assumption of homogeneous mixing, whereby each individual contacts every other. This assumption typically yields an overestimation of cases [10, 11], since social interactions in populations are heterogeneous both in number and intensity [12–14]. Although heterogeneities could be included by refining and increasing the spectrum of compartments [15, 16], such an approach may challenge rigorous analytical treatment and parameter identification.

In terms of complexity, agent-based models are located at the opposite side of the spectrum from mean-field compartmental models. Stochastic simulation of individuals' motion and interaction is the basic component of such models. Several spatial constraints and specific mobility patterns are contemplated to reproduce realistic conditions in the model simulations [17]. The Global Epidemic and Mobility Model (GLEAMviz) [5] is a comprehensive agent-based framework for worldwide simulation. Several infectious outbreaks have been simulated through this model, assessing related risks in a systematic manner [18, 19]. Although very refined, agent-based models require extensive simulation campaigns based on a detailed knowledge of human behavior, and their structure and working principle do not allow any analytical treatment to be carried out.

The present lifestyle, with frequent and fast short- and long-haul travels, yields a reconsideration of typical time scales of the progress of infectious diseases and the dynamics of human contact patterns. Thus, the assumption of homogeneous mixing, according to which every individual contacts everyone else in a population, should be overcome toward approaches that explicitly account for the concurrent evolution of the diseases dynamics and the time-varying formation of the network of contacts.

To enable the study of diffusion models on time-varying networks, it is very often assumed that links between nodes have a much longer or much shorter life span than the epidemic dynamics [20–24], resulting in the separation between the time scales of the dynamics of the network and the process evolution. On the other hand, activity driven networks (ADNs) describe contact processes that evolve over time-varying networks [25], when timing and duration of connections happen over short time scales [14, 26–29], comparable with the dynamics of the process running on the network nodes.

Disease spreading in susceptible-infected-susceptible (SIS) and susceptible-infected-removed (SIR) models has been recently studied through ADNs [30], and spreading and immunization thresholds have been computed using a heterogeneous mean-field approach [25, 30]. The substantial difference in these thresholds compared to those on static networks calls for further investigations on epidemic spreading over time-varying networks. ADNs seem a viable tool, providing accurate and mathematically tractable models of epidemic spreading, which overcome key limitations of mean-field compartmental and agent-based models. Although promising, research on ADNs is in its early stages, and several efforts are being conducted to advance the state of knowledge [31–34].

In this chapter, we describe our research effort to improve the ADN paradigm toward a more realistic modeling of epidemic spreading, with the objective to achieve realistic models that remain computationally affordable and analytically tractable. The chapter is organized as follows. In Sect. 14.2, we offer a review of the working principles of the original ADN formulation. Toward a more realistic treatment of behavioral factors, in Sect. 14.3 we study the effect of individual behavior on the spreading of the epidemic in an SIS process, summarizing our published work [35]. Our findings are then successfully applied in Sect. 14.4 to model the 2014–2015 outbreak of Ebola Virus Disease (EVD) in Liberia. After a calibration phase, the model is used to offer a one-year prediction of the case count, which is confirmed by field data. A what-if analysis on the effect of timely sanitary intervention is also presented, borrowing from our published work [36]. In Sect. 14.5, we examine a mathematical framework that we recently established in [37] for the analytical treatment of ADNs, which enables the analysis of the network dynamics beyond the computation of the epidemic threshold. Finally, conclusions and potential lines of future work are presented in Sect. 14.6.

14.2 Activity Driven Networks: The Original Formulation

ADNs have originally been introduced to model spreading phenomena where the time scales of the epidemic dynamics and of connection formation are comparable, and to simulate such phenomena without relying to the time scale separation hypothesis [25, 30, 38].

The approach is based on an activity potential, which is the probability per unit time that a node will establish contacts with other nodes in the network. We consider a network with N nodes. Each individual is associated with a network node i that is characterized by its activity potential x_i , with $i = 1, \dots, N$. In the original formulation in [25], the x_i s do not change in time and are independent and identically distributed realizations of a random variable x , with a probability density function $F(x)$. The selection of $F(x)$ is a crucial point of the approach, since it determines the interactions within the network. In [25], an analysis of three large, time-resolved datasets of contacts in social networks suggests the use of heavy-tail density functions of the form $F(x) \propto x^{-\gamma}$, with $2 \leq \gamma \leq 3$.

In its original incarnation [25], an activity firing rate $a_i = \eta x_i$ is assigned to each individual, where η is a constant scaling factor that regulates the average number of active nodes in the network in a unit time. Starting from a disconnected network of N nodes, in a time increment Δt , the epidemic model evolves as follows (see Fig. 14.1):

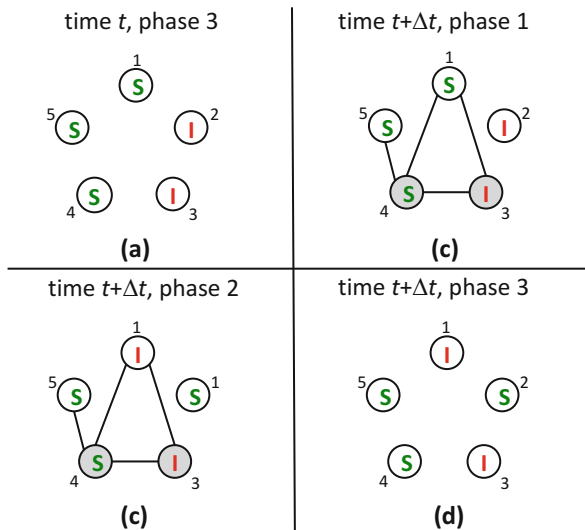


Fig. 14.1 (From [36]) An SIS epidemic model evolving on an ADN with $N = 5$ nodes and $m = 2$ links per active node. Nodes' health states are encircled, and active nodes are shaded. (a) At the last phase of time t , the ADN is disconnected and nodes 2 and 3 are infected. Between t and $t + \Delta t$: (b) nodes 3 and 4 become active and contact nodes 4 and 1, and 5 and 1, respectively; (c) the epidemic process evolves, so that node 3 infects node 1, nodes 2, 4, and 5 remain in the susceptible state, and node 2 recovers; and (d) time Δt has elapsed and all the links are removed before a new time increment is initiated

1. Node i , with $i = 1, \dots, N$ becomes active with probability $a_i \Delta t$. If the node is active, it contacts m other nodes drawn at random from a uniform distribution, creating undirected links. If it is not active, no connections are created. At the end of this step, an undirected graph is assembled;
2. The algorithmic rules of the epidemic model are run on the obtained graph. For example, for an SIS model: (i) each infected node can infect its susceptible neighbors with a per-contact transmission probability λ , and (ii) each infected node recovers to the susceptible state with probability per unit time μ ; and
3. At the next time step $t + \Delta t$, all the network links are removed and the process resumes.

In [25, 30], SIS and SIR processes on ADNs are studied and the epidemic threshold is computed through a heterogeneous mean-field approach [39, 40]. In particular, for the SIS model the epidemic threshold for λ/μ beyond which there is an epidemic is

$$\sigma^0 \equiv \frac{1}{m \langle a \rangle + \sqrt{\langle a^2 \rangle}}, \quad (14.1)$$

where $a = \eta x$ is the random variable whose realizations define the probabilities of activation; $\langle \cdot \rangle$ denotes statistical expectation; and the superscript “0” refers to this baseline formulation. In addition, control strategies for selective immunization have been implemented in [30] and assessed via a mean-field approach.

14.3 Behavioral Epidemic Models on Activity Driven Networks

The role of individual behavior on the spreading of epidemic diseases is becoming increasingly important due to increased travel activity, both on short (commuting) and long (leisure or business trips) space and time scales [41–48]. Moreover, the wide availability of data through mass media grants people access to information that could influence their behavior in response to an epidemic outbreak. For example, individuals may modify travel plans, opt for self-quarantine, decide to avoid infected individuals, or get vaccinated. The search of disease-related information on the Internet is so widespread that search engine query data have been utilized to detect the spreading of influenza [49]. Finally, the behavior of individuals is very often modified by their health status, which may reduce or even prevent their ability to move and, consequently, contact and infect others.

Different approaches have been used to model behavioral changes in epidemic models, namely: introducing changes in the contact rates as a function of health status [50–53]; considering additional compartments or classes in compartmental models [54–57]; and suitably coupling models of the disease and information spreading [58]. Surprising, counter-intuitive phenomena may emerge when

behavioral changes are considered. An important example is the increase in the likely of a global spreading when introducing travel restrictions to locations with a high prevalence of the infection [46].

Here, we focus on the effects of changes of individual behavior in an SIS epidemic model [35]. We consider two salient instances of behavioral modification. The former instance deals with the reduction of activity of infected individuals due to the contraction of the infection. This behavior includes the cases of quarantine, as well as the natural reduction in activity of infected individuals, caused by the illness. This activity limitation is common in the cases of MERS-CoV [59] or SARS [41, 60, 61].

The second instance deals with changes in the activity of susceptible individuals, on the basis of their risk perception. Susceptible individuals tend to avoid contacts with others when they perceive a risk of infection; yet upon contracting the infection, they resume their usual behavior, contacting, and possibly infecting, susceptible individuals. This “selfish” behavior is typical of infections that do not prevent daily habits, such as syphilis, HIV, or gonorrhoea [62–67]. We assume that risk perception is based on the knowledge of two different pieces of information, namely, the prevalence of the epidemic and its rate of growth.

Using ADNs, our results confirm that individual behavior may drastically affect the epidemic spreading both in terms of the epidemic threshold and of the steady state fraction of infected individuals. Specifically, we find that a reduction in the activity rate of either susceptible or infected individuals yields a higher epidemic threshold and a lower steady state fraction of infected individuals. Nevertheless, the reduction of activity of the infected individuals seems to be a more relevant factor, confirming the effectiveness of quarantine-like policies.

In particular, in the case of a reduction of activity of the infected individuals, the relative activity of infected individuals with respect to susceptible ones is a key predictor of the epidemic spreading. We consistently observe that the epidemic threshold benefits from differences in the activity of susceptible and infected individuals. Finally, when the activity of the infected individuals is drastically reduced, we find that the epidemic threshold depends only on the activity of the susceptible individuals and on the network characteristics. On the other hand, in the case of a reduction of activity of the susceptible individuals, the possibility of susceptible individuals spontaneously reducing their activity yields an increase in the epidemic threshold and a decrease in the steady state infected fraction. Nevertheless, such a modulation is more effective when the risk perception is related to the prevalence of the epidemic, rather than to its rate of growth.

14.3.1 Behavioral Changes of Infected Individuals Due to Their Health Status

To model behavioral changes in individuals due to their health status, we change the activity potential x_i of each individual through two different scaling constants, according to their health status [35]. To this aim, the parameter η defined in Sect. 14.2 is replaced with two different scaling factors: η_S , for individuals in the susceptible state; and η_I , for those in the infected state. Thus, two different activity firing rates are assigned to individuals: $a_i = \eta_S x_i$, if individual i is in the susceptible state, and $a_i = \eta_I x_i$, if it is in the infected state. Apart from this operation, the ADN works exactly as in its original incarnation described in Sect. 14.2. We consider the case in which individuals reduce activity as they contract the infection, as a consequence of a self-initiated behavior, or due to a health condition. Thus, we assume that the activity rate parameters of susceptible and infected individuals differ, and, specifically, that $\eta_I < \eta_S$.

The epidemic threshold can be computed analytically through a heterogeneous mean-field approach inspired by [30] and detailed in [35]. The threshold is

$$\sigma^{\text{AR}} \equiv \frac{1}{m} \frac{2}{(\eta_S + \eta_I)\langle x \rangle + \sqrt{(\eta_S - \eta_I)^2 \langle x \rangle^2 + 4\eta_S \eta_I \langle x^2 \rangle}}, \quad (14.2)$$

where the superscript ‘‘AR’’ stands for activity reduction. From Eq. (14.2), we note that the epidemic threshold depends on the interplay between the activity rates of susceptible and infected individuals, and on the first and second statistical moments of the activity potential distribution. Moreover, similar to [25, 30], the epidemic threshold does not depend on any parameter that is representative of the time-aggregated network of contacts.

Two limit cases are of particular interest. When the activity rates are homogeneous, that is, $\eta_S = \eta_I = \eta$, the threshold coincides with that found in [30] and reported in Eq. (14.1). On the other hand, when $\eta_I \ll \eta_S$, the threshold is

$$\sigma^{\text{SAR}} \equiv \frac{1}{m\eta_S \langle x \rangle}, \quad (14.3)$$

where the superscript ‘‘SAR’’ stands for strong activity reduction of the infected individuals. Thus, when the infection severely limits the individual activity, the epidemic threshold depends only on the activity of the susceptible individuals and on the first statistical moment of the activity potential distribution. In this case, activity fluctuations have no effect on the threshold value, and the spreading is independent of the activity of the infected individuals. The ratio η_I/η_S should be considered as a valid indicator of the process heterogeneity. Figure 14.2 displays the threshold σ^{AR} in Eq. (14.2) as a function of the ratio η_I/η_S , for $\eta_S = 15$, $\mu = 0.1$, and a network of $N = 10,000$ nodes with $m = 5$. A distribution $F(x) \propto x^{-\gamma}$, with $\gamma = 2.1$ is selected for the activity potentials and a lower cutoff $\epsilon = 10^{-3}$ on the x variable is adopted to avoid the singularity of $F(x)$ for x close to zero. Such parameter values are maintained along the rest of this section, unless otherwise specified.

Fig. 14.2 (From [35])
Epidemic threshold σ^{AR} as a
function of the activity ratio
 η_I/η_S from Eq. (14.2)

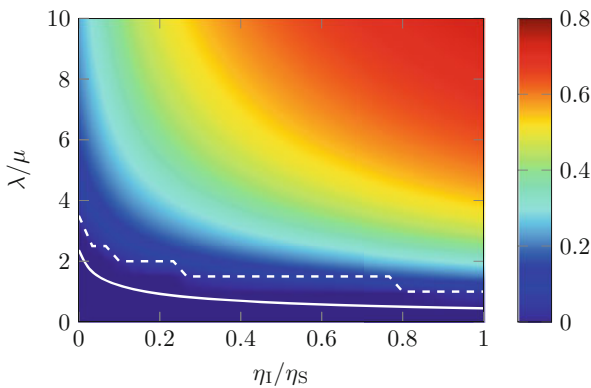
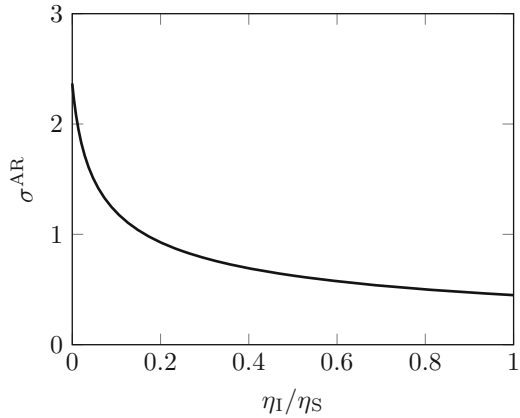


Fig. 14.3 (From [35]) Steady state fraction I^∞/N of infected individuals (*color-coded*) as a function of λ/μ and η_I/η_S . The *white solid line* defines the theoretical threshold computed according to Eq. (14.2), and the *white dashed line* offers a conservative estimate of the epidemic threshold computed on the steady state data, by setting the fraction of infected individuals to 0.001. Results are averaged over 50 independent trials with an initial infected number of $0.01N$ random individuals

The trend of the steady state fraction of infected individuals exhibits a pattern that is consistent with that of the epidemic threshold. Figure 14.3 displays the steady state fraction of infected individuals, I^∞/N , for the same network described above, as a function of λ/μ and η_I/η_S . We find that the level curves show a trend that is similar to that of the threshold, superimposed on the plot with a white solid line. We comment that a higher value of λ/μ is required to obtain a given steady state ratio I^∞/N , when the ratio η_I/η_S is small; conversely, a smaller value of λ/μ suffices for a large value of η_I/η_S .

14.3.2 Behavioral Changes of Susceptible Individuals Due to Risk Perception

A further source of behavioral change may be offered by the risk perception about the epidemic propagation. In this case, individuals may try to protect themselves by reducing their activity, aiming at reducing the chances of contact with others, irrespective of their health status.

We assume that individuals have access to global information about the disease spreading [53] and, to this aim, we contemplate two modeling strategies for risk perception: the former is informed by the epidemic prevalence, that is the number of infected individuals in the population; and the latter is informed by the growth of the epidemic. When no risk is perceived, all the susceptible individuals have the same activity parameter $\bar{\eta}_S$. When the epidemic starts to spread, the activity parameter of susceptible individuals is modulated in time as a function of their perceived risk of infection. We denote such a time-varying activity parameter with η_S^t . To simplify the analysis, we assume that individuals act egoistically, by not reducing their activity when infected, only seeking to minimize their chance to contract the infection. As a consequence, the activity parameter for infected individuals is held fixed at the same value of the disease-free parameter of susceptible individuals, that is $\eta_I = \bar{\eta}_S$.

To model risk perception as a function of the prevalence of the epidemic, we posit the following behavioral rule

$$\eta_S^t = \begin{cases} \bar{\eta}_S(1 - I^t/\bar{I}), & \text{if } I^t \leq \bar{I} \\ 0, & \text{if } I^t > \bar{I} \end{cases}, \quad (14.4)$$

where I^t is the number of infected individuals at time t . In Eq. (14.4), \bar{I} regulates the intensity of the reduction in activity related to risk perception, so that $\eta_S^t = \bar{\eta}_S$ when $I^t = 0$, and $\eta_S^t = 0$ when $I^t = \bar{I}$. In particular, the smaller \bar{I} is, the more intense the activity reduction is (a few infected individuals are sufficient to drop the activity of susceptible individuals to zero).

Figure 14.4 illustrates the steady state fraction I^∞/N of infected individuals in the case of a risk perception behavior based on Eq. (14.4), as a function of $1/\bar{I}$ and λ/μ . Importantly, the epidemic threshold is higher than in the case where susceptible individuals do not change their behavior as in Eq. (14.1). Also, this threshold tends to increase with $1/\bar{I}$, even though for wide ranges of \bar{I} , the epidemic threshold is largely independent of its value. The steady state value of the infected fraction decreases as $1/\bar{I}$ increases, even though such a variation is quite secondary.

These findings suggest that the adoption of a self-protective behavior related to risk perception is beneficial both to the individual and to the community. Indeed, even in the examined case in which individuals resume their usual activity once infected, this behavior still benefits the whole population, in terms both of increasing the epidemic threshold and decreasing the steady state value of the infected fraction.

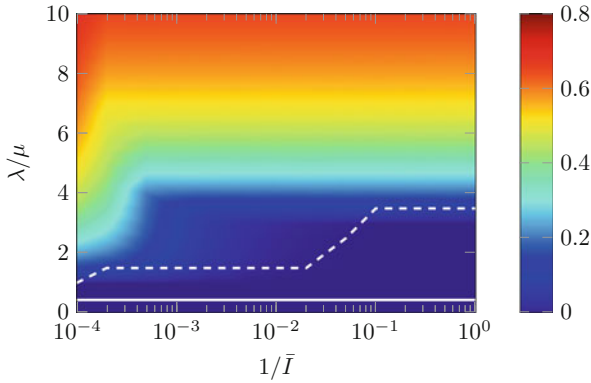


Fig. 14.4 (From [35]) Steady state fraction I^∞/N of infected individuals (*color-coded*) with a risk perception behavior as in Eq. (14.4), as a function of $1/\bar{I}$ and λ/μ , for $\bar{\eta}_S = \eta_I = 15$. The *white solid line* defines the epidemic threshold for uniform and constant activity $\eta_S = \eta_I = 15$, computed according to Eq. (14.1), and the *white dashed line* offers a conservative estimate of the epidemic threshold with the inclusion of risk perception behavior, computed by setting the fraction of infected individuals to 0.001. Results are averaged over 50 independent trials with an initial infected number of $0.01N$ random individuals

The second behavioral strategy is based on the assumption that risk perception is related to the rate of growth of the infection in time. We introduce $\Delta_I^t = I^t - I^{t-\Delta t}$ as the time difference of the number of infected individuals between two consecutive iterations and $\bar{\Delta}$ as a select threshold for such a time difference. Our behavioral rule for the parameter η_S^t is as follows:

$$\eta_S^t = \begin{cases} \bar{\eta}_S, & \text{if } \Delta_I^t \leq 0 \\ \bar{\eta}_S(1 - \Delta_I^t/\bar{\Delta}), & \text{if } 0 < \Delta_I^t < \bar{\Delta} . \\ 0, & \text{if } \Delta_I^t \geq \bar{\Delta} \end{cases} \quad (14.5)$$

Thus, $\bar{\Delta}$ regulates the intensity of the behavioral change with respect to the risk perception (the lower $\bar{\Delta}$ is, the stronger the action in response to a growth in the epidemic spreading is).

Figure 14.5 illustrates the steady state fraction I^∞/N of infected individuals as a function of $1/\bar{\Delta}$ and λ/μ , with the same parameters used to assess the previous behavioral strategy. As expected, a more severe activity reduction (lower $\bar{\Delta}$) yields a higher epidemic threshold together with a lower steady state fraction of infected individuals. Comparing the two risk perception models, we note that variations of \bar{I} have a more significant role on the first behavioral strategy than $\bar{\Delta}$ has on the second behavioral strategy.

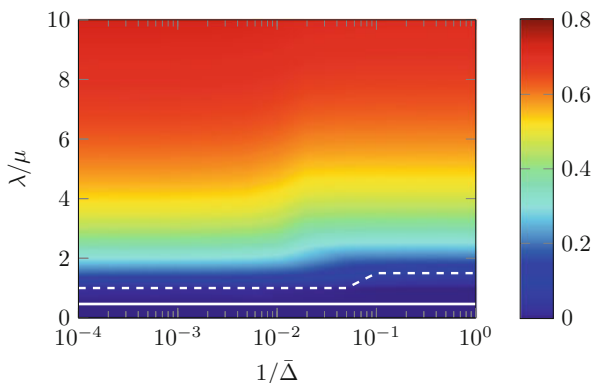


Fig. 14.5 (From [35]) Steady state fraction I^∞/N of infected individuals (*color-coded*) with a risk perception behavior as in Eq. (14.5), as a function of $1/\bar{\Delta}$ and λ/μ , for $\bar{\eta}_S = \eta_I = 15$. The *white solid line* defines the epidemic threshold for uniform and constant activity $\eta_S = \eta_I = 15$, computed according to Eq. (14.1), and the *white dashed line* offers a conservative estimate of the epidemic threshold with the inclusion of risk perception behavior, computed by setting the fraction of infected individuals to 0.001. Network and simulation parameters are the same as in Fig. 14.4

14.4 Modeling the 2014–2015 Ebola Virus Disease (EVD) Spreading in Liberia

The introduction of behavioral phenomena has been of fundamental importance for the development of realistic epidemic models. In this section, we present a model of the 2014–2015 spreading of EVD in Liberia [36]. Behavioral phenomena are of fundamental importance to account for the reduced activity of infected and hospitalized individuals, as well as the zero activity of dead yet extremely infectious corpses that are not safely buried. We calibrate the model from field data of the 2014 April-to-December spreading in Liberia and use the model as a predictive tool, to emulate the dynamics of EVD in Liberia and offer a one year projection, until December 2015. Also, we perform a what-if analysis to assess the efficacy of timely intervention policies. In particular, we show that an earlier application of the same intervention policy would have greatly reduced the number of EVD cases, the duration of the outbreak, and the infrastructures needed for the implementation of the intervention.

The motivation for the selection of ADNs to model EVD is twofold. First, the incubation time of EVD, with a minimum of 2 and a maximum of 21 days [68], is compatible with the time scale of individual mobility patterns [69, 70]. This implies that time scale separation assumptions may yield incorrect predictions on the spread of the epidemic [11]. Second, ADNs can be adapted to account for realistic phenomena that may be critical to the assessment of the severity and duration of an EVD outbreak. The epidemic model used in this work is based on the seminal Legrand’s model for EVD spreading [71], on which most of the recent research body on EVD rests [10, 18, 19, 72–76].

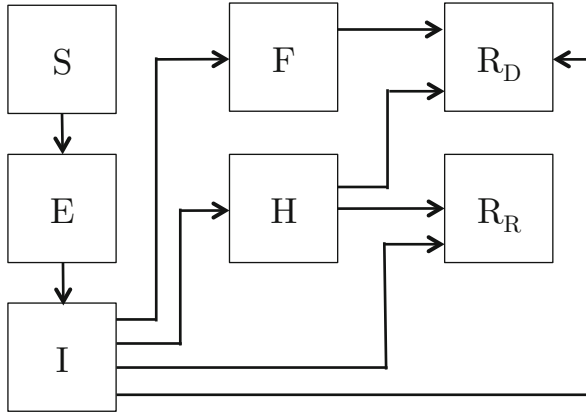


Fig. 14.6 (From [36]) State transitions in a seven-state EVD model. The states are: S , susceptible; E , exposed (infected, non-symptomatic); I , infected (symptomatic); H , hospitalized; F , dead but not buried; R_R , recovered; and R_D , dead and safely buried

Legrand's model is a variant of the Susceptible-Exposed-Infected-Recovered model, which accounts for additional states to describe the specific dynamics of EVD. These additional states include hospitalized individuals and individuals who are dead but unsafely buried. In line with previous works, model parameters have been in part hypothesized from the existing literature [11, 18, 71, 74, 77–79], and in part identified through a least square technique on the available dataset of the case count provided by the World Health Organization (WHO) [79–81].

14.4.1 The ADN-Based EVD Model

Figure 14.6 illustrates the dynamics of the state transition of the proposed model. According to [71], two states related to hospitalization (H) and death followed by a traditional funeral, without immediate safe burial (F) are added. The removed state (R) indicates individuals that cannot contribute any more to the dynamics of the epidemic spreading. This state contains individuals who have recovered and are immune, and those who have died and have been safely buried. In our EVD model, we partition the removed state into two states: recovered (R_R); and dead and safely buried (R_D). Similar to [35], we assume that people infected with EVD and not hospitalized have a lower probability to come in contact with other individuals, as they will move less due to their debilitated health. Yet, such probability is non-zero, as they may infect those who take care of them, that is, friends, parents, and relatives. Thus, we differentiate the activity of susceptible and exposed individuals from that of infected ones, using two different activity rates, namely, η_{SE} and η_I .

Table 14.1 (From [36]) Parameters of the activity driven EVD model

Parameter	Meaning
η_{SE}, η_I	Activity rate
$\lambda_I, \lambda_H, \lambda_F$	Probability of infection
$\mu_{EI}, \mu_{IH}, \mu_{IF}, \mu_{IR_R}, \mu_{IR_D}, \mu_{HR_R}, \mu_{HR_D}, \mu_{FR_D}$	Transition rate
$\delta_{IH}, \delta_{IF}, \delta_{IR_R}, \delta_{IR_D}, \delta_{HR_R}, \delta_{HR_D}$	Transition fraction

Model parameters belong to three categories: probabilities of infection, transition rates, and transition fractions. Probabilities of infection are indicated with λ_{\bullet} , where the subscript identifies (I), (H), or (F) states. These parameters indicate the per-contact probability of a susceptible individual to contract the epidemic by contacting an infected (I), hospitalized (H), or a dead and not safely buried (F) individual. Transition rates are indicated with $\mu_{\bullet \times}$, where subscripts indicate any two different states of the epidemic model. The inverse of a transition rate $1/\mu_{\bullet \times}$ quantifies the average time for an individual to transition from state \bullet to state \times . Similarly, a transition fraction is denoted with $\delta_{\bullet \times}$ and quantifies the fraction of individuals in state \bullet that transition to state \times . Table 14.1 summarizes the parameters of the model.

The state transitions of our ADN-based model, describing the dynamics of EVD spreading, are:

1. If a susceptible (S) individual is in contact with an infected (I), hospitalized (H), or dead and not safely buried (F) individual, he/she will contract the infection and transition to the exposed (E) state with per-contact transmission probability $\lambda_I, \lambda_H,$ and $\lambda_F,$ respectively;
2. An exposed individual (E) transitions to the infected and symptomatic (I) state with rate μ_I ;
3. An infected and symptomatic individual (I) transitions to one of the three states: hospitalized (H), dead and not safely buried (F), recovered (R_R), and dead and safely buried (R_D). A fraction δ_{IH} of infected individuals is hospitalized with rate μ_{IH} ; a fraction δ_{IF} remains in the community, eventually dies, and receives traditional funeral rituals, without safe burial, with rate μ_{IF} ; a fraction δ_{IR_R} recovers with rate μ_{IR_R} ; and a fraction δ_{IR_D} dies in the community and is safely buried by a burial team with a rate μ_{IR_D} . The constraint $\delta_{IH} + \delta_{IF} + \delta_{IR_R} + \delta_{IR_D} = 1$ holds;
4. A hospitalized individual (H) transitions to the recovered (R_R) or the dead and safely buried (R_D) state. A fraction δ_{HR_R} will recover with rate μ_{HR_R} , whereas a fraction δ_{HR_D} will die with rate μ_{HR_D} and then is safely buried. The constraint $\delta_{HR_R} + \delta_{HR_D} = 1$ holds; and
5. Dead people who have not been handled by a burial team will remain infectious until burial. Individuals in the dead and not safely buried (F) state will be buried with a rate μ_{FR_D} and transition to the dead and buried (R_D) state.

Table 14.2 (From [36]) Time-invariant parameters of the activity driven EVD model.

Parameter	Value
λ_I	0.16
λ_F	0.49
μ_{EI}	0.09 days ⁻¹
μ_{IF}	0.13 days ⁻¹
μ_{IR_R}	0.13 days ⁻¹
μ_{IR_D}	0.13 days ⁻¹
μ_{HR_R}	0.22 days ⁻¹
μ_{HR_D}	0.24 days ⁻¹
μ_{FR_D}	0.5 days ⁻¹
δ_{IR_R}	0
δ_{HR_R}	0.46
δ_{HR_D}	0.54

Table 14.3 (From [36]) Time-varying parameters of the activity driven EVD model. Phase 1: before mid-August 2014 (day 0 to 130); Phase 2: between mid-August and mid-October 2014 (day 131 to 180); and Phase3: after mid-October 2014 (from day 181 onward)

Parameter	Phase 1	Phase 2	Phase 3
λ_H	0.33	0.02	0.02
μ_{IH}	0.1 days ⁻¹	0.2 days ⁻¹	0.43 days ⁻¹
δ_{IH}	0.51	0.80	0.89
δ_{IF}	0.1	0.05	0.01
δ_{IR_D}	0.39	0.15	0.10

14.4.2 Model Calibration

The WHO count of confirmed EVD cases in Liberia, from April 8, 2014 to December 31, 2014, has been used to calibrate our model. The data utilized cover a time span of 268 days [79–81]. Literature on the 2014–2015 EVD outbreak and field reports are utilized to set epidemic-specific parameters, while those related to the network activity are obtained through an identification strategy. Three different approaches have been considered to calibrate the model parameters.

Table 14.2 lists a set of parameters that are independent of the application of intervention measurements and are, therefore, considered constant in time. Their values are obtained from the literature on the EVD outbreak [11, 74, 79]. On the other hand, parameters listed in Table 14.3 are regarded as time-varying, since they depend on the level of intervention. The literature reports that such a level has constantly increased from mid-August 2014 [11]. Interventions can be summarized as: (i) an increase in the number of hospital beds for EVD patients; (ii) the exclusive admission of patients in symptomatic states to Ebola treatment units, with

a consequent reduction of the probability of infection; (iii) an increase in the number of safe burial procedures; and (iv) improvements in the implementation of contact tracing procedures [11].

In an effort to minimize the complexity of the model, time-varying parameters are set to different constant values, changing in a step-like manner. The time instants at which such changes occur are: before mid-August (day 0 to 120), between mid-August and mid-October (day 121 to 180), and after mid-October (day 181 onward). The parameters for the first two phases are selected from the available literature [11, 74, 79], while those in the third phase reflect the further increase in the efficiency of the intervention level, which we know has occurred in many districts of Liberia, especially in Montserrado (the Capital County), where a strong improvement in hospitalization, laboratory testing and body collection in October has been reported by the Centers for Disease Control and Prevention (CDC) [82]. Although the parameter set for the third phase has not been confirmed in the literature, our selection reflects the application of an almost ideal intervention in the field confirmed by relevant WHO statements [83].

The remaining ADN-related parameters, that is, the number of contacts per unit time of active nodes, m , the scaling factor of the activity of susceptible and exposed individuals, η_{SE} , and that of infected and symptomatic individuals, η_I , have been identified using a least square optimization technique on the epidemic curve of cumulative WHO-confirmed EVD cases in Liberia [80] from April 8, 2014 to December 31, 2014 (268 days). The identified parameter values are $m = 7$, $\eta_{SE} = 4.5$, and $\eta_I = 3.2$. These parameters have been then used to validate the model on a further portion of the epidemic curve, related to confirmed cases from January 1, 2015, to December 2, 2015. Additional simulations have been performed to assess the role of the exponent of the activity distribution, γ , on the evolution of the epidemic. A good fit has been found by setting $\gamma = 2.1$. This value is consistent with other findings in the literature, which posit that social interactions follow heavy-tailed or skewed statistical distributions [84–87].

14.4.3 Model Validation, Predictions, and What-If Analysis

A validation phase has been run on the model through Monte Carlo simulations over 50 randomized trials. While model parameters and the size of the initial seed of infected individuals are held constant to the values determined by the identification phase, the trials are randomized over the initial locations of the infectious seed cases. The averaged epidemic curve is then compared with the WHO-confirmed cumulative curve of EVD cases [80], and results are illustrated in Fig. 14.7. As anticipated, the model replicates with good accuracy the epidemic curve during the first 268 days used for calibration, while predicting a modest increase in the case count for the remaining 337 days, until December 2, 2015.

The model can be effectively used to estimate the efficacy of timely intervention policies. To this aim, we contemplate the possibility of shifting the time when we have seen an increase in the level of field interventions (day 121 in Table 14.3) to an

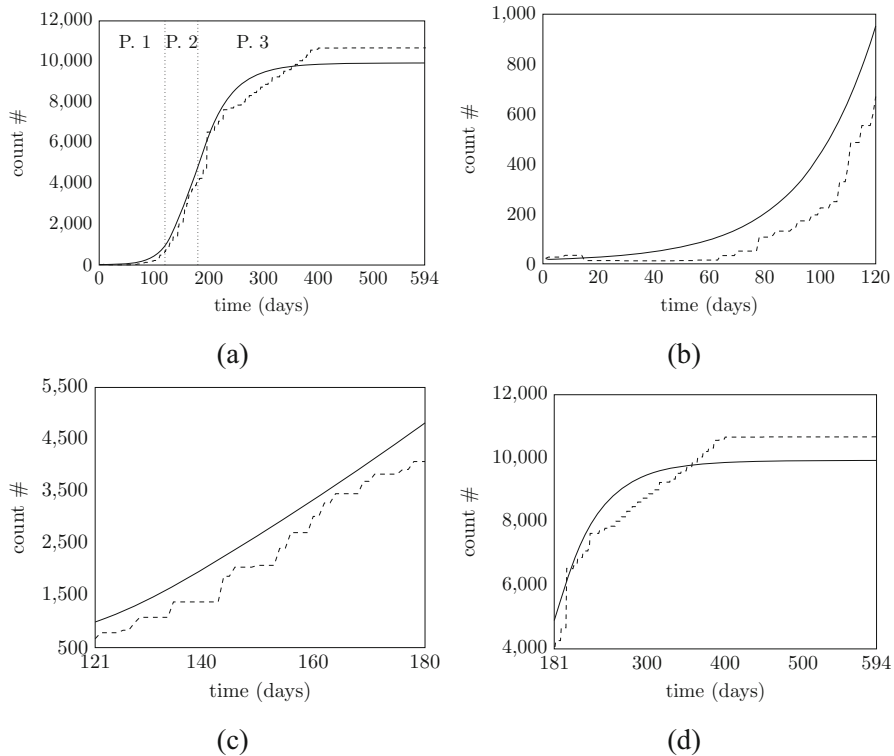


Fig. 14.7 (From [36]) Calibration of the model on real data and model predictions. In (a), the comparison between model predictions and field data involved the entire duration of the spreading from 4/8/2014 to 12/2/2015. The *solid line* shows model results in terms of the cumulative number of cases, and the *dashed line* shows the cumulative case count reported by WHO and CDC in Liberia [80]. The three regions in (a) identify the three phases of the intervention policy hypothesized in Table 14.3. The step-like discontinuity in the case count around sample 200 is likely due to data corruption. This observation is supported by the corresponding death count, which decreases correspondingly (while it should always increase) [88]. In (b)–(d), the three phases of the intervention policies are separately illustrated. Model predictions are illustrated in (d), from day 268 onwards

earlier day. In other words, we run our EVD model by only changing the time when the transition between Phase 1 and Phase 2 takes place. We consider the following possible dates: early July (day 76), early June (day 46), and early May (day 16). Figure 14.8a displays the forecasted cumulative case counts associated with the selected times. As expected, anticipating the implementation of more effective intervention policies drastically reduces the epidemic spreading. For example, the outbreak would have ended with a 72% reduction of the total Ebola cases (i.e., 2,830 rather than 9,922) by anticipating the increase in the level of interventions to day 76.

The beneficial effect of an earlier implementation of superior intervention policies is also noted in the timing of the epidemic peak. Figure 14.8b displays

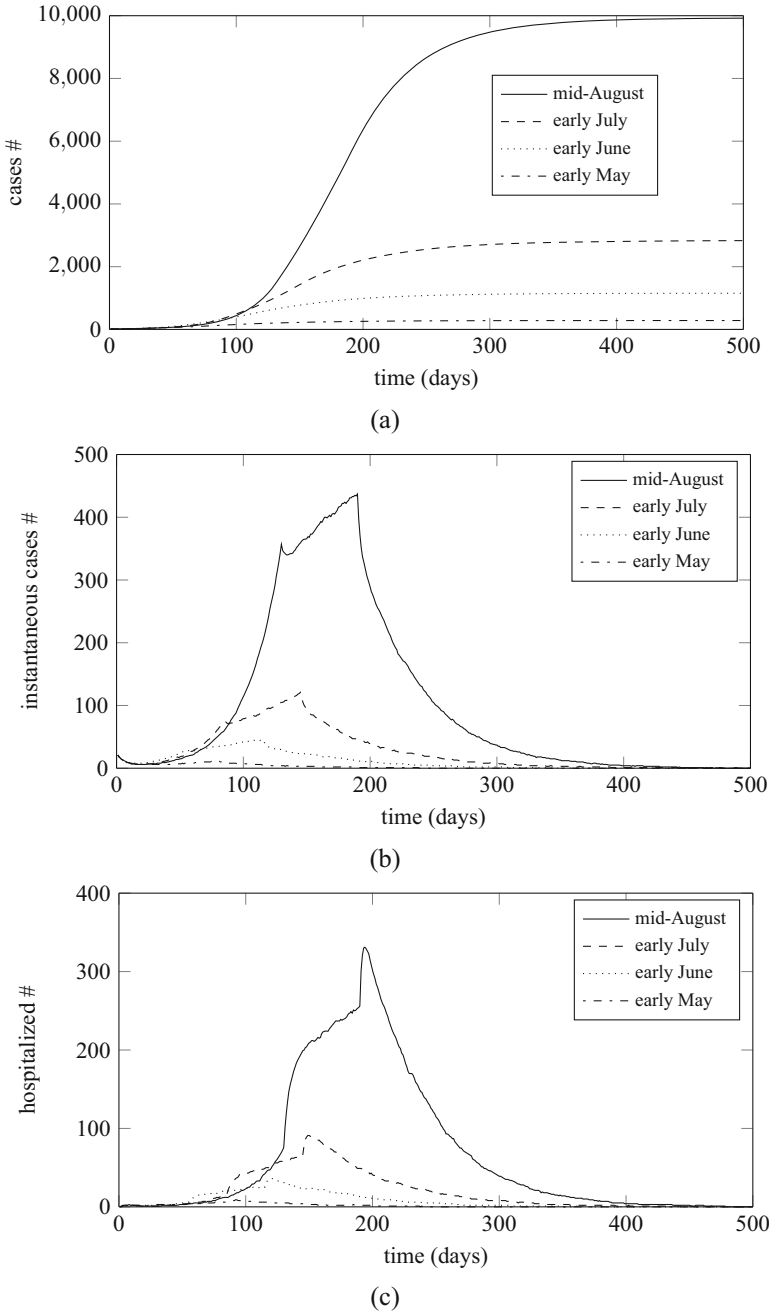


Fig. 14.8 (From [36]) Prediction of the (a) cumulative number of cases; (b) instantaneous number of cases; and (c) instantaneous number of hospitalized patients in Liberia between 4/8/2014 and 8/20/2015, by varying the time of the transition between Phase 1 and Phase 2, defining when the level of interventions is increased. The dates of such transitions are detailed in the legend. Simulations are averaged over 50 independent trials

the trend of the instantaneous number of infected individuals for the same instances considered in Fig. 14.8a. We observe that the occurrence of the peak recedes when these superior intervention policies are applied earlier. A timely implementation would thus also be beneficial to a faster resolution of the outbreak.

The model can also be used to estimate the needed infrastructure to face the outbreak, in the form of the number of beds available for EVD patients. Figure 14.8c shows the number of hospitalized persons as a function of time for the same instances considered in Figs. 14.8a,b. To implement a desired intervention policy at a given time, the number of available hospital beds must be larger than or equal to the number of persons that should be theoretically hospitalized. Therefore, the peak value of the number of hospitalized persons predicted by the model can be used to estimate the numbers of beds that should be made available in the country. Figure 14.8c suggests that anticipating the implementation of more effective intervention policies reduces the size of the infrastructure that should be available. While the mid-August timing is estimated to require 331 beds, anticipating it to early in July would have only required 91 beds.

14.5 Toward Analytical Treatment of ADNs: A Continuous-Time, Discrete-Distribution Theory

Apart from the computation of the epidemic threshold [25, 30, 35, 38], previous studies on ADNs largely carry out their analysis based on extensive Monte Carlo simulations [25, 30, 31, 35, 36, 38, 89–94]. In this section, we establish an analytical framework to study the entire dynamics of the epidemic spreading at the population level (from the zero-infected condition to the endemic equilibrium) [37]. Differently from the original ADN formulation, where a discrete-time epidemic model is implemented with a continuous probability distribution for the nodes' activities, we formulate a continuous-time model with a discrete distribution.

The advantages of our approach are manifold. First, it does not rely on extensive Monte Carlo simulations, but requires the integration of simple ordinary differential equations (ODEs). Second, it is not necessary to select a time step, a required procedure for discrete-time models that can lead to confounds in the correct reproduction of the system dynamics [95]. Third, it is based on a reduced number of parameters with respect to traditional instances of ADNs [25, 30, 31, 35, 36, 38, 89–93].

In our new framework, we consider a (large) population of N individuals, each associated with a node of a time-varying undirected graph $\mathcal{G}(t) = (\mathcal{V}, \mathcal{E}(t))$, with $t \in \mathbb{R}^+$. $\mathcal{V} = \{1, \dots, N\}$ is the node set and $\mathcal{E}(t)$ is the time-varying link set. We focus on an SIS process [4]. Each node $v \in \mathcal{V}$ is assigned a time-invariant activity rate a_v , which represents the expected number of contacts that node v generates in a unit time interval. Starting from $t = 0$, node v becomes active after a time that is sampled from an exponentially distributed random variable with parameter a_v [96].

When a node activates, it contacts exactly one node uniformly at random in \mathcal{V} , generating a single link. If this link connects an infected node with a susceptible one, then the epidemic propagates with a fixed probability λ , otherwise nothing happens. We suppose that the duration of the contact is instantaneous, so that λ is considered a per-contact infection probability. The link is instantaneously removed, and the node may activate again according to the same rule. Each infected node recovers after a time that is drawn from an exponentially distributed random variable with parameter μ , becoming susceptible again. Thus, μ^{-1} is the expected time needed by a individual to recover.

The relationship with discrete-time ADN models is straightforward. In a time step Δt , the continuous-time model establishes as many links as in a realization of the discrete-time model. The activity rate of a node in continuous-time corresponds to the product of its activity potential and the number of contacts it can establish in the time step. The probability that an infected node recovers in a discrete-time step is $1 - e^{-\mu\Delta t}$. The per-contact infection probability does not change between continuous- and discrete-time.

The proposed discrete activity distribution follows a power-law with k equidistant activation classes, each characterized by an activity rate a_i ($a_1 < \dots < a_k$). For the generic i -th class, we denote with n_i its number of nodes and we let $n_i \propto a_i^{-\gamma}$. The parameter γ controls the heterogeneity among individuals, similar to the classical ADN paradigm with a continuous distribution of activity potentials.

With reference to an SIS epidemic process, $Y_v(t) \in \{S, I\}$ denotes the susceptible (S) or infected (I) state of node v at time t . All the states are encapsulated in a vector $Y(t) \in \{S, I\}^{\mathcal{V}}$. The analysis is executed by mapping $Y(t)$ to a k -dimensional stochastic process $Z(t) := Z[Y(t)]$, comprising the fraction of infected nodes in each activation class. Variable $Z_i(t)$ indicates the fraction of infected nodes with activity rate a_i , at time t .

In the thermodynamic limit $N \rightarrow \infty$, the fraction of nodes ($n_1/N, \dots, n_k/N$) in each of the activation classes converges to (η_1, \dots, η_k) , independent of N , due to the central limit theorem. Then, Kurtz' theorem [97] ensures that for every finite time horizon, the stochastic process $Z(t)$ is close to a deterministic dynamical system with vector variable $\zeta(t)$, solution of the following set of ODEs:

$$\dot{\zeta}_i = -\mu\zeta_i + \lambda(1 - \zeta_i)(a_i x_1 + x_2), \quad (14.6)$$

with $i = 1, \dots, k$ and $\zeta_i(0) = Z_i(0)$. Here, the macroscopic variable $x_1 = \sum \eta_h \zeta_h$ represents the fraction of infected individuals across all classes, which is the main observable in the study of epidemic spreading. The macroscopic variable $x_2 = \sum \eta_h a_h \zeta_h$ takes into consideration the fraction of infected nodes weighted by their individual activity rates. In general, we define $x_j = \sum \eta_h a_h^{j-1} \zeta_h$.

From Eq. (14.6), we appreciate that the drift in the fraction of infected nodes in each class is determined by three effects: the recovery of infected nodes ($-\mu\zeta_i$); the spreading associated with active nodes in the i -th class generating contacts toward infected nodes ($\lambda(1 - \zeta_i)a_i x_1$); and the spreading related to active infected nodes generating contacts with the nodes of the i -th class ($\lambda(1 - \zeta_i)x_2$).

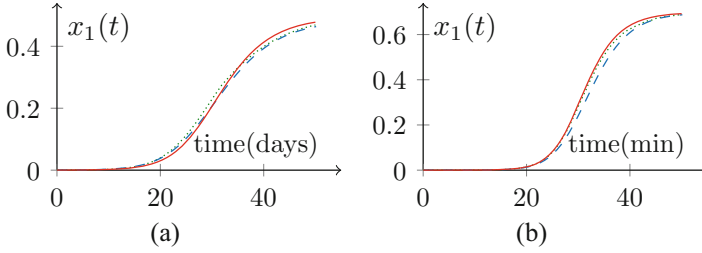


Fig. 14.9 (From [37]) Time evolution of the fraction of infected nodes for the flu **(a)** and Twitter **(b)** case studies. Comparison between discrete-time continuous-distribution ADN process (blue, dashed), our continuous-time discrete-distribution approach (green, dotted) model, and theoretical predictions (red, solid) from Eq. (14.6)

Integrating Eq. (14.6) allows to closely simulate the epidemic spreading without the need of Monte Carlo simulations. To verify this claim and demonstrate the correspondence between continuous- and discrete-time epidemic models, we consider two different dynamics on real-world phenomena, modeled through ADNs: flu spreading in a university campus and trend diffusion on Twitter. System parameters are obtained from case studies [25, 98–101], as detailed in [37]. We compare the outcome of Monte Carlo simulations averaged over 200 trials for both the continuous- and the discrete-time processes, along with the integration of the deterministic ODE system (14.6). In both examples, the activity distribution is discretized over $k = 59$ equidistant activation classes. Figure 14.9 demonstrates the equivalence of our approach with respect to traditional ADNs in Monte Carlo simulations, along with the validity of system (14.6) to exactly predict the epidemic spreading.

The study of the k -dimensional system (14.6) is more amenable to analytical treatment if it is rewritten in terms of the first k macroscopic variables, x_1, \dots, x_k , resulting in the following system of ODEs:

$$\begin{cases} \dot{x}_1 = (\lambda\alpha_1 - \mu)x_1 + \lambda x_2 - 2\lambda x_1 x_2, \\ \dot{x}_2 = \lambda\alpha_2 x_1 + (\lambda\alpha_1 - \mu)x_2 - \lambda x_1 x_3 - \lambda x_2^2, \\ \dot{x}_3 = \lambda\alpha_3 x_1 + \lambda\alpha_2 x_2 - \mu x_3 - \lambda x_1 x_4 - \lambda x_2 x_3, \\ \dots \\ \dot{x}_k = \lambda\alpha_k x_1 + \lambda\alpha_{k-1} x_2 - \mu x_k - \lambda x_1 \sum \eta_h a_h^k \zeta_h - \lambda x_2 x_k, \end{cases} \quad (14.7)$$

where $\alpha_j = \sum \eta_h a_h^j$ are the moments of the activity rates distribution. This system is well-posed since the term $\sum \eta_h a_h^k \zeta_h$ in the k -th equation is a linear combination of the linearly independent variables x_1, \dots, x_k .

Studying system (14.7) leads to a significant characterization of the epidemic spreading, beyond the computation of the epidemic threshold in Eq. (14.1) obtained from linear stability analysis [37]. However, the selection of power-laws with exponent between 2 and 3 in the activity distribution induces numerical instabilities,

since statistical moments of the distribution blow up from the second onwards. Moreover, the prescription of initial conditions for macroscopic variables of order greater than 1 may result unfeasible in real-world applications.

A possible approach to address these issues is to project the k -dimensional dynamics to a lower dimensional space consisting of only $k^* \ll k$ equations. We approximate the term x_{k^*+1} using two elementary bounds: $a_1 x_{k^*} \leq x_{k^*+1} \leq a_k x_{k^*}$ and $x_{k^*+1} \leq \alpha_{k^*}$. Using these bounds, we can reduce the system of k ODEs (14.7) to a system of k^* ordinary differential inclusions (ODIs) [102], consisting of one inclusion and $k^* - 1$ equations.

If $k^* = 1$, we bound $a_1 x_1 \leq x_2 \leq \min\{\alpha_1, a_k x_1\}$, reducing system (14.7) to a single ODI. This one-dimensional system should not be contemplated to accurately predict the evolution of the process during the transient, between the zero-infected condition and the endemic equilibrium, due to the conservativeness of the bounds during such a transient phase. However, it can be effectively used to analytically determine an interval \mathcal{I} for the endemic equilibrium \bar{x}_1 , which is

$$\left[\max \left\{ \frac{\lambda \alpha_1}{\lambda \alpha_1 + \mu}, \frac{\lambda(a_k + \alpha_1) - \mu}{2\lambda a_k} \right\}, \frac{\lambda(a_1 + \alpha_1) - \mu}{2\lambda a_1} \right], \quad (14.8a)$$

if $\lambda \alpha_1 > \mu$, and

$$\left[\frac{\lambda(a_1 + \alpha_1) - \mu}{2\lambda a_1}, \min \left\{ \frac{\lambda \alpha_1}{\lambda \alpha_1 + \mu}, \frac{\lambda(a_k + \alpha_1) - \mu}{2\lambda a_1} \right\} \right], \quad (14.8b)$$

if $\lambda \alpha_1 < \mu$. Notice that, if $\lambda \alpha_1 = \mu$, we analytically compute $\bar{x}_1 = 1/2$.

We demonstrate the use of these two bounds through the two real-world case studies on flu spreading and Twitter [37]. Figure 14.10 illustrates the prediction of the endemic state using the bounds for $k^* = 1$, for the two case studies. Our simulations indicate that the accuracy of the bounds depends on the system parameters. Specifically, our results suggest that the closer is the endemic state to $\bar{x}_1 = 1/2$ (that is, $\alpha_1 \lambda = \mu$), the more precise the bounds are.

An improved prediction of the transient phase is obtained with $k^* = 2$, which leads to an ODI for the evolution of x_2 , coupled to the first ODE in system (14.7). As detailed in [37], we establish the two following ancillary ODEs:

$$\dot{x}_2 = \lambda(\alpha_2 - \phi_{\varepsilon, x_2}(x_1))x_1 + (\lambda \alpha_1 - \mu)x_2 - \lambda x_2^2, \quad (14.9a)$$

$$\dot{x}_2 = \lambda(\alpha_2 - \phi_{\varepsilon, x_2}(1 - x_1))x_1 + (\lambda \alpha_1 - \mu)x_2 - \lambda x_2^2, \quad (14.9b)$$

where $\phi_{\varepsilon, x_2}(x_1)$, is a continuous function that, in the limit $\varepsilon \rightarrow 0$, tends to the Heaviside function

$$\phi_{\varepsilon, x_2}(x_1) \rightarrow \begin{cases} a_1 x_2 & \text{if } x_1 < 1/2, \\ \min\{a_k x_2, \alpha_2\} & \text{if } x_1 > 1/2. \end{cases} \quad (14.10)$$

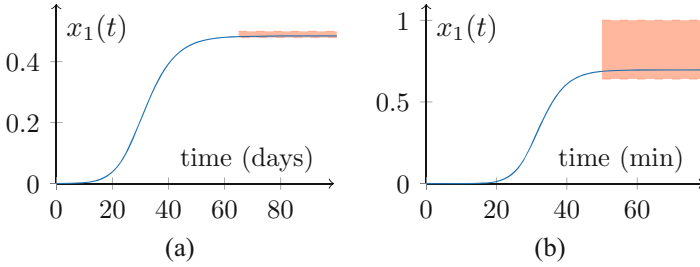


Fig. 14.10 (From [37]) Averaged Monte Carlo simulations of a discrete-time continuous-distribution ADN process (*blue*) and theoretical bounds on the endemic equilibrium state (computed for $k^* = 1$, in *red*), for flu (a) and Twitter (b) case studies. From data in [37], $\alpha_1 \lambda / \mu$ is equal to 0.988 in (a) and 1.785 in (b)

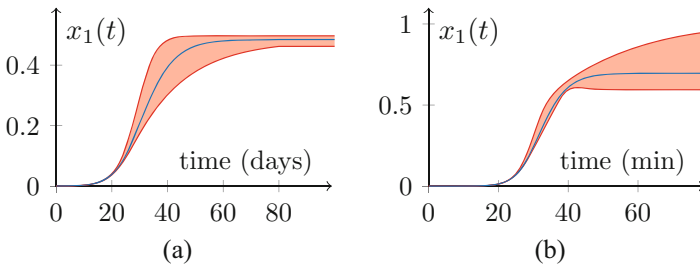


Fig. 14.11 (From [37]) Averaged Monte Carlo simulations of a discrete-time continuous-distribution ADN process (*blue*) and theoretical bounds on the dynamics of the epidemic spreading (computed for $k^* = 2$ with $\varepsilon = 10^{-3}$, in *red*), for flu (a) and Twitter (b) case studies

The upper- and lower-bounds for x_1 are obtained by coupling the first ODE in system (14.7) with Eqs.(14.9a) and (14.9b), and integrating in the limit as $\varepsilon \rightarrow 0$. Simulation results in Fig. 14.11 demonstrate the accuracy of the bounds in capturing the transient response. Higher endemic equilibria seem manifest into tighter prediction bounds during the transient, albeit the upper bound becomes conservative as time progresses. In general, the predictions of the endemic state from $k^* = 2$ are less precise than the simpler closed-form results for $k^* = 1$. This is related to the solutions of the ancillary ODEs (14.9a) and (14.9b) leaving the bounds for $k^* = 1$. With this in mind, the overall prediction accuracy could be improved by combining the bounds in Figs. 14.10 and 14.11.

Toward a further improvement in the prediction of the epidemic spreading, our framework can be utilized to produce accurate finite-time-horizon predictions, based on the availability of low-frequency epidemic data at the population level, such as the cumulative count case or the epidemic incidence [37].

14.6 Conclusions

Modeling of epidemic spreading has greatly advanced in the last decades, due to the availability of powerful models and computing power. However, much effort is needed to obtain models that are accurate and realistic, yet computationally affordable. To this aim, ADNs are a valuable tool to encapsulate the inherent heterogeneity in the characteristics of a population and to embrace the concurrent evolution of epidemic dynamics and the formation of the network of contacts on the present hyperconnected world. This chapter has presented our research effort, which aims at including realistic factors in epidemic modeling, while keeping the model computationally affordable and analytically tractable.

However, further work is needed toward steering the theoretical models presented herein toward effective tools for predicting epidemic spreading prediction and assisting interventions in the field. Future efforts will aim at tackling spatial and temporal memory in the network formation, which will help in encapsulating spatial locality and temporal recurrence in human contacts. Finally, effective techniques to achieve an analytical solution of the framework presented in the last section should be put forward.

Acknowledgements The authors warmly acknowledge the contribution of Mattia Frasca, Biagio Pedalino, and Lorenzo Zino in the development of the research efforts that this book chapter reflects.

This work was supported by National Science Foundation under grant No. CMMI-1561134, the Army Research Office under grant No. W911NF-15-1-0267, with Drs. A. Garcia and S.C. Stanton as program managers, and by Compagnia di San Paolo.

This chapter contains figures and excerpts from [35–37]. We acknowledge and thank Elsevier [36] and the American Physical Society [35, 37] for granting the permission to reuse the relevant material.

References

1. Allen, L.J., Brauer, F., Van den Driessche, P., Wu, J.: *Lect. Notes Math.* **1945**, 81 (2008)
2. Keeling, M.J., Rohani, P.: *Modeling Infectious Diseases in Humans and Animals*. Princeton University Press, Princeton (2011)
3. Keeling, M.J., Eames, K.T.D.: *J. R. Soc. Interface* **2**(4), 295 (2005)
4. Brauer, F., Castillo-Chavez, C.: *Mathematical Models in Population Biology and Epidemiology*. Springer, New York (2011)
5. van den Broeck, W., Giannini, C., Gonçalves, B., Quaggiotto, M., Colizza, V., Vespignani, A.: *BMC Infect. Dis.* **11**(1), 37 (2011)
6. Hethcote, H.W.: *Bltz Mathcal Biology*. **58**, 1019 (1996). <https://link.springer.com/article/10.1007/BF02459495>
7. Ferguson, N.: *Nature* **446**(7137), 733 (2007)
8. Funk, S., Salathé, M., Jansen, V.A.: *J. R. Soc. Interface* **7**(50), 1247 (2010)
9. Manfredi, P., D’Onofrio, A. (eds.): *Modeling the Interplay between Human Behavior and the Spread of Infectious Diseases*. Springer, New York, (2013)

10. Lewnard, J.A., Ndeffo Mbah, M.L., Alfaro-Murillo, J.A., Altice, F.L., Bawo, L., Nyenswah, T.G., Galvani, A.P.: *Lancet Infect. Dis.* **14**, 1189 (2014)
11. Merler, S., Ajelli, M., Fumanelli, L., Gomes, M.F.C., Pastore y Piontti, A., Rossi, L., Chao, D.L., Longini, I.M., Halloran, M.E., Vespignani, A.: *Lancet Infect. Dis.* **3099**(14), 1 (2015)
12. Barrat, A., Barthélemy, M., Vespignani, A.: *Dynamical Processes on Complex Networks*. Cambridge University Press, Cambridge (2008)
13. Perra, N., Gonçalves, B.: In: Gonçalves, B., Perra, N. (eds.) *Social Phenomena. From Data Analysis to Models*, pp. 59–83. Springer, Cham/New York (2015)
14. Holme, P., Saramäki, J.: *Phys. Rep.* **519**(3), 97 (2012)
15. Brauer, F.: *Bull. Math. Biol.* **70**(7), 1869 (2008)
16. Choe, S., Lee, S.: *Theor. Biol. Med. Model.* **12**(1), 28 (2015)
17. Ajelli, M., Gonçalves, B., Balcan, D., Colizza, V., Hu, H., Ramasco, J.J., Merler, S., Vespignani, A.: *BMC Infect. Dis.* **10**, 190 (2010)
18. Gomes, M.F.C., Pastore, A., Rossi, L., Chao, D., Longini, I., Halloran, M.E., Vespignani, A.: *PLoS Curr.* **6** (2014). Outbreaks. <http://currents.plos.org/outbreaks/article/assessing-the-international-spreading-risk-associated-with-the-2014-west-african-ebola-outbreak/sh>
19. Poletto, C., Gomes, M.F., Pastore Y Piontti, A., Rossi, L., Bioglio, L., Chao, D.L., Longini, I.M., Halloran, M.E., Colizza, V., Vespignani, A.: *Eurosurveillance* **19**(42), 20936 (2014)
20. Centola, D., González-Avella, J.C., Eguíluz, V.M., San Miguel, M.: *J. Confl. Resolut.* **51**(6), 905 (2007)
21. Volz, E., Meyers, L.A.: *J. R. Soc. Interface* **6**(32), 233 (2008)
22. Jolad, S., Liu, W., Schmittmann, B., Zia, R.K.P.: *PLoS One* **7**(11), e48686 (2012)
23. Schwartz, I.B., Shaw, L.B.: *Physics* **3**, 17 (2010)
24. Shaw, L.B., Schwartz, I.B.: *Phys. Rev. E* **81**, 046120 (2010)
25. Perra, N., Gonçalves, B., Pastor-Satorras, R., Vespignani, A.: *Sci. Rep.* **2**, 469 (2012)
26. Ghoshal, G., Holme, P.: *Phys. A Stat. Mech. Appl.* **364**, 603 (2006)
27. Butts, C.T.: *Science* **325**(5939), 414 (2009)
28. Moody, J.: *Soc. Forces* **81**(1), 25 (2002)
29. Morris, M., Kretzschmar, M.: *AIDS* **11**(5), 641 (1997)
30. Liu, S., Perra, N., Karsai, M., Vespignani, A.: *Phys. Rev. Lett.* **112**, 118702 (2014)
31. Sun, K., Baronchelli, A., Perra, N.: *Eur. Phys. J. B* **88**(12), 326 (2015)
32. Starnini, M., Pastor-Satorras, R.: *Phys. Rev. E* **89**(3), 032807 (2014)
33. Medus, A.D., Dorso, C.O.: *J. Stat. Mech. Theor. Exp.* **2014**(9), P09009 (2014)
34. Sousa da Mata, A., Pastor-Satorras, R.: *Eur. Phys. J. B* **88**(2), 38 (2015)
35. Rizzo, A., Frasca, M., Porfiri, M.: *Phys. Rev. E* **90**, 042801 (2014)
36. Rizzo, A., Pedalino, B., Porfiri, M.: *J. Theor. Biol.* **394**, 212 (2016)
37. Zino, L., Rizzo, A., Porfiri, M.: *Phys. Rev. Lett.* **117**, 228302 (2016)
38. Rizzo, A., Porfiri, M.: *Eur. Phys. J. B* **89**(1), 20 (2016)
39. Gómez, S., Gómez-Gardeñes, J., Moreno, Y., Arenas, A.: *Phys. Rev. E* **84**, 036105 (2011)
40. Vespignani, A.: *Nat. Phys.* **8**(1), 32 (2011)
41. Hung, L.S.: *J. R. Soc. Med.* **96**(8), 374 (2003)
42. Colizza, V., Barrat, A., Barthélemy, M., Vespignani, A.: *BMC Med.* **5**(34) (2007)
43. Ruan, S., Wang, W., Levin, S.: *Math. Biosci. Eng.* **3**(1), 205 (2006)
44. Ni, S., Weng, W.: *Phys. Rev. E* **79**(1), 016111 (2009)
45. Bajardi, P., Poletto, C., Ramasco, J., Tizzoni, M., Colizza, V., Vespignani, A.: *PLoS One* **6**(1), e16591 (2011)
46. Meloni, S., Perra, N., Arenas, A., Gómez, S., Moreno, Y., Vespignani, A.: *Sci. Rep.* **1**, 62 (2011)
47. Apolloni, A., Poletto, C., Colizza, V.: *BMC Infect. Dis.* **13**, 176 (2013)
48. Apolloni, A., Poletto, C., Ramasco, J.J., Jensen, P., Colizza, V.: *Theor. Biol. Med. Model.* **11**(1), 3 (2014)
49. Ginsberg, J., Mohebbi, M.H., Patel, R.S., Brammer, L., Smolinski, M.S., Brilliant, L.: *Nature* **457**(7232), 1012 (2009)
50. Bootsma, M.C.J., Ferguson, N.M.: *Proc. Natl. Acad. Sci.* **104**(18), 7588 (2007)

51. Fenichel, E.: Proc. Natl. Acad. Sci. **108**(15), 6306 (2011)
52. Chen, F., Jiang, M., Rabidoux, S., Robinson, S.: J. Theor. Biol. **278**(1), 107 (2011)
53. Bagnoli, F., Liò, P., Sguanci, L.: Phys. Rev. E **76**(6), 061904 (2007)
54. Poletti, P., Caprile, B., Ajelli, M., Pugliese, A., Merler, S.: J. Theor. Biol. **260**(1), 31 (2009)
55. Poletti, P., Ajelli, M., Merler, S.: PLoS One **6**(2), e16460 (2011)
56. Epstein, J.M., Parker, J., Cummings, D., Hammond, R.A.: PLoS One **3**(12), e3955 (2008)
57. Perra, N., Balcan, D., Gonçalves, B., Vespignani, A.: PLoS One **6**(8), e23084 (2011)
58. Funk, S., Gilad, E., Watkins, C., Jansen, V.A.A.: Proc. Natl. Acad. Sci. **106**(16), 6872 (2009)
59. Cotten, M., Watson, S.J., Zumla, A.I.: MBio **5**(1), e01062 (2014)
60. Chowell, G., Fenimore, P.W., Castillo-Garsow, M.A., Castillo-Chavez, C.: J. Theor. Biol. **224**(1), 1 (2003)
61. Riley, S., Fraser, C., Donnelly, C.A., Ghani, A.C., Abu-Raddad, L.J., Hedley, A.J., Leung, G.M., Ho, L.M., Lam, T.H., Thach, T.Q. et al.: Science **300**(5627), 1961 (2003)
62. Stolte, I.G., Dukers, N.H., de Wit, J.B., Fennema, J.S., Coutinho, R.A.: Sex. Transm. Infect. **77**(3), 184 (2001)
63. Truong, H.M., Truong, H.H.M., Kellogg, T., Klausner, J.D., Katz, M.H., Dilley, J., Knapper, K., Chen, S., Prabhu, R., Grant, R.M., Louie, B., McFarland, W.: Sex. Transm. Infect. **82**(6), 461 (2006)
64. Imrie, J., Lambert, N., Mercer, C.H., Copas, A.J., Phillips, A., Dean, G., Watson, R., Fisher, M.: Sex. Transm. Infect. **82**(1), 80 (2006)
65. Finlayson, T.J., Le, B., Smith, A., Bowles, K., Cribbin, M., Miles, I., Oster, A.M., Martin, T., Edwards, A., Dinunno, E.: Morb. Mortal. Wkly. Rep. Surveill. Summ. **60**(14), 1 (2011)
66. Van de Laar, M., Spiteri, G.: Eurosurveillance **17**(29) (2012). <http://www.eurosurveillance.org/ViewArticle.aspx?ArticleId=20225>
67. Deiss, R.G., Leon, S.R., Konda, K.A., Brown, B., Segura, E.R., Galea, J.T., C.F. Caceres, Klausner, J.D.: BMC Infect. Dis. **13**(1), 426 (2013)
68. World Health Organization. Ebola virus disease. <http://www.who.int/mediacentre/factsheets/fs103/en/>
69. González, M.C., Hidalgo, C.A., Barabási, A.: Nature **453**(7196), 779 (2008)
70. Poletto, C., Tizzoni, M., Colizza, V.: J. Theor. Biol. **338**, 41 (2013)
71. Legrand, J., Grais, R.F., Boelle, P.Y., Valleron, A.J., Flahault, A.: Epidemiol. Infect. **135**(4), 610 (2007)
72. Pandey, A., Atkins, K.E., Medlock, J.: Science **16**(6212), 991 (2014)
73. Fasina, F.O., Shittu, A., Lazarus, D., Tomori, O., Simonsen, L., Viboud, C., Chowell, G.: Eurosurveillance **19**(40), 20920 (2014)
74. Rivers, C.M., Lofgren, E.T., Marathe, M., Eubank, S., Lewis, B.L.: PLoS Curr. **6** (2014). Outbreaks. <http://currents.plos.org/outbreaks/article/obk-14-0043-modeling-the-impact-of-interventions-on-an-epidemic-of-ebola-in-sierra-leone-and-liberia/>
75. Webb, G., Browne, C., Huo, X., Seydi, O., Seydi, M., Magal, P.: PLoS Curr. **7** (2015). Outbreaks. <http://currents.plos.org/outbreaks/article/a-model-of-the-2014-ebola-epidemic-in-west-africa-with-contact-tracing-2/>
76. Meltzer, M.I., Atkins, C.Y., Santibanez, S., Knust, B., Petersen, B.W., Ervin, E.D., Nichol, S.T., Damin, I.K., Washington, M.L.: Morb. Mortal. Wkly. Rep. Suppl. **63**(3), 1 (2014)
77. Khan, A.S., Tshioko, F.K., Heymann, D.L., Le Guenno, B., Nabeth, P., Kerstiens, B., Fleerackers, Y., Kilmarx, P.H., Rodier, G.R., Nkuku, O., Rollin, P.E., Sanchez, A., Zaki, S.R., Swanepoel, R., Tomori, O., Nichol, S.T., Peters, C.J., Muyembe-Tamfum, J.J., Ksiazek, T.G.: J. Infect. Dis. **179**(Supplement 1), S76 (1999)
78. The WHO Ebola Response Team. N. Engl. J. Med. **371**(16), 1481 (2014)
79. World Health Organization. Ebola situation reports. <http://apps.who.int/ebola/en/current-situation/ebola-situation-report>
80. 2014 Ebola outbreak in West Africa – Case counts. <http://www.cdc.gov/vhf/ebola/outbreaks/2014-west-africa/case-counts.html>
81. Rivers, C.: Data for the 2014 Ebola outbreak in West Africa. <https://github.com/cmrvivers/ebola>

82. Nyenswah, T.G., Westercamp, M., Kamali, A.A., Qin, J., Zielinski-Gutierrez, E., Amegashie, F., Fallah, M., Gergonne, B., Nugba-Ballah, R., Singh, G., Aberle-Grasse, J.M., Havers, F., Montgomery, J.M., Bawo, L., Wang, S., Rosenberg, R.: *Morb. Mortal. Wkly. Rep.* **63**, 1 (2014)
83. World Health Organization. The Ebola outbreak in Liberia is over. <http://www.who.int/mediacentre/news/statements/2015/liberia-ends-ebola/en/> (2015)
84. Holme, P., *Phys. Rev. E* **71**, 046119 (2005)
85. Onnela, J.P., Saramäki, J., Hyvönen, J., Szabó, G., Lazer, D., Kaski, K., Kertész, J., Barabási, A.L.: *Proc. Natl. Acad. Sci.* **104**(18), 7332 (2007)
86. Tang, J., Scellato, S., Musolesi, M., Mascolo, C., Latora, V.: *Phys. Rev. E* **81**, 055101 (2010)
87. Cattuto, C., Van den Broeck, W., Colizza, V., Pinton, J.F., Vespignani, A.: *PLoS One* **5**(7), e11596 (2010)
88. Centers for Disease Control and Prevention. 2014 Ebola outbreak in West Africa – reported cases graphs. <http://www.cdc.gov/vhf/ebola/outbreaks/2014-west-africa/cumulative-cases-graphs.html> (2015)
89. Starnini, M., Pastor-Satorras, R.: *Phys. Rev. E* **89**(3), 032807 (2014)
90. Lei, Y., Jiang, X., Guo, Q., Ma, Y., Li, M., Zheng, Z.: *Phys. Rev. E* **93**, 032308 (2016)
91. Liu, C., Zhou, L.X., Fan, C.J., Huo, L.A., Tian, Z.W.: *Phys. A* **432**, 269 (2015)
92. Liu, M.X., Wang, W., Liu, Y., Tang, M., Cai, S.M., Zhang, H.F.: arXiv:1605.04557 (2016, preprint)
93. Zou, Y., Deng, W., Li, W., Cai, X.: *Int. J. Mod. Phys. C* **27**, 1650090 (2016)
94. Aoki, T., Rocha, L.E.C., Gross, T.: *Phys. Rev. E* **93**, 040301 (2016)
95. Ribeiro, B., Perra, N., Baronchelli, A.: *Sci. Rep.* **3**, 3006 (2013)
96. Olkin, I., Gleser, L., Derman, C.: *Probability Models and Applications*. Prentice Hall, Upper Saddle River (1994)
97. Kurtz, T.G.: *Approximation of Population Processes*, vol. 36. SIAM, Philadelphia (1981)
98. Kim, L., Abramson, M., Drakopoulos, K., Kolitz, S., Ozdaglar, A.: *Estimating Social Network Structure and Propagation Dynamics for an Infectious Disease*, pp. 85–93. Springer International Publishing, Cham (2014)
99. Zhao, K., Bianconi, G., *Front. Physiol.* **2**, 101 (2011)
100. Skaza, J., Blais, B.: *Phys. A* **465**, 289 (2017)
101. Aiello, W., Chung, F., Lu, L.: In: *Proceedings of the 32nd Annual ACM Symposium on Theory of Computing, STOC'00*, pp. 171–180. ACM, New York (2000)
102. Aubin, J.P., Cellina, A.: *Differential Inclusions: Set-Valued Maps and Viability Theory*, vol. 264. Springer, New York (2012)